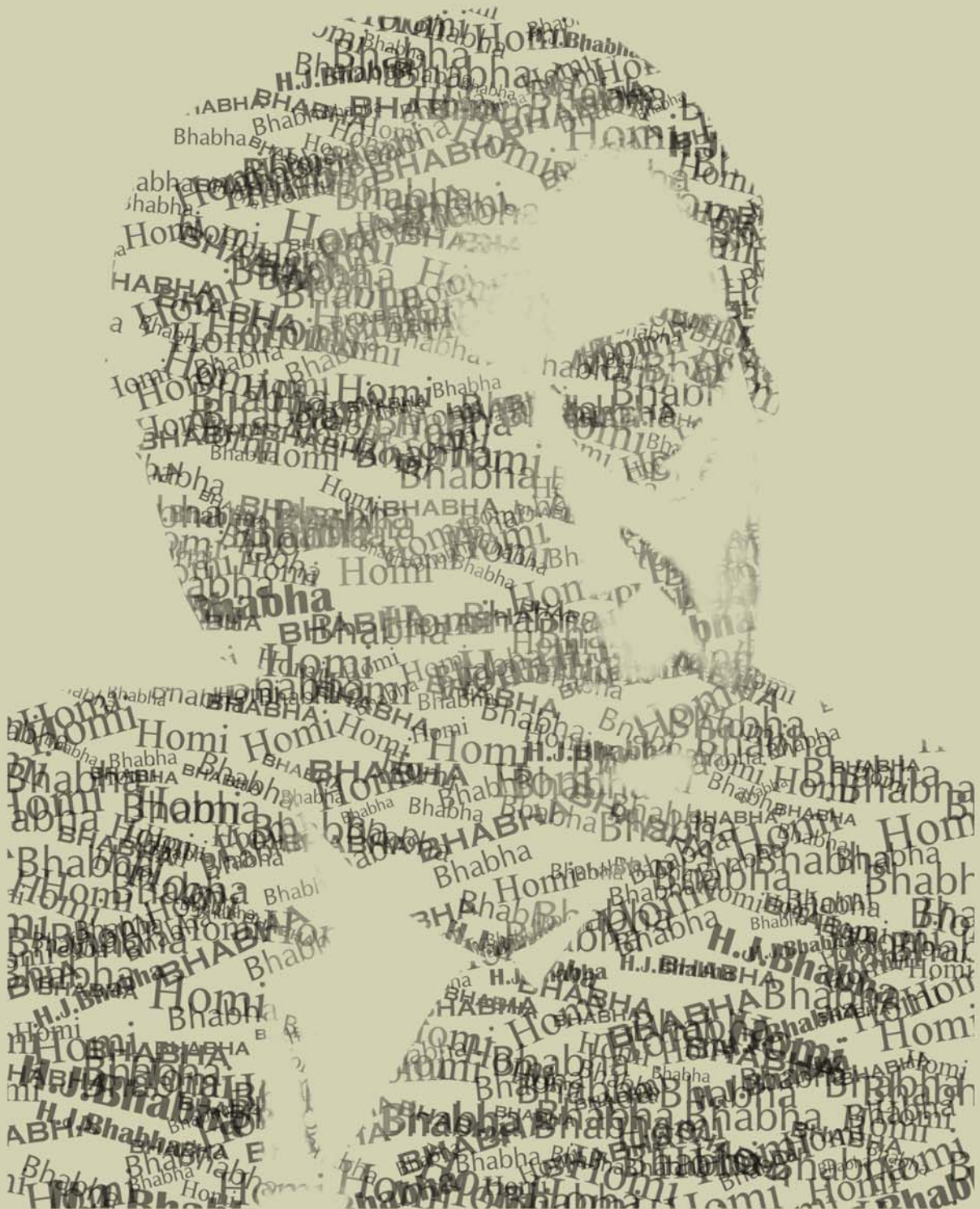


BARC NEWSLETTER

FOUNDER'S DAY SPECIAL ISSUE

OCTOBER 2011



BARC NEWSLETTER

FOUNDER'S DAY

SPECIAL ISSUE

OCTOBER 2011



भारत सरकार

Government of India

भाभा परमाणु अनुसंधान केंद्र

Bhabha Atomic Research Centre



CONTENTS

DAE Excellence Awards

- 1. Determination of neutron-induced fission cross sections by surrogate methods** 1
B.K. Nayak
Nuclear Physics Division
Dr. B.K. Nayak is the recipient of the DAE Homi Bhabha Science & Technology Award for the year 2009
- 2. Microstructure Characterization of Zr-2.5Nb Alloy Pressure Tube Manufactured by Novel Fabrication Routes and Irradiated Pressure Tubes by Transmission Electron Microscopy** 6
D. Srivastava
Materials Science Division
Dr. D. Srivastava is the recipient of the DAE Homi Bhabha Science & Technology Award for the year 2009
- 3. Remediation of radioactive wastes using novel extractants and novel separation techniques** 13
P.K. Mohapatra
Radiochemistry Division
Dr. P.K. Mohapatra is the recipient of the DAE Homi Bhabha Science & Technology Award for the year 2009
- 4. Talkative Organic Molecules** 19
S. Chattopadhyay
Bio-Organic Division
Dr. S. Chattopadhyay is the recipient of the DAE Homi Bhabha Science & Technology Award for the Year 2009
- 5. Challenges in Detector Grade Silicon Technology Demonstration** 26
Dr. Sadhana Mohan
Heavy Water Division



Dr. Sadhana Mohan is the recipient of the DAE Homi Bhabha Science & Technology Award for the year 2009

- 6. A Unified Approach for Deriving One-Dimensional Kinetic Equation for Non-Equilibrium Processes in Condensed Phase** **34**
Alok K. Samanta
Theoretical Chemistry Section, Chemistry Group, BARC
Dr. A.K. Samanta is the recipient of the DAE Scientific & Technical Excellence Award for the year 2009
- 7. Challenges in Neutron Transport Analysis for Nuclear Reactor Simulations** **37**
Anurag Gupta
Reactor Physics Design Division
and
R.S. Modak
Theoretical Physics Division
Dr. Anurag Gupta is the recipient of the DAE Scientific & Technical Excellence Award for the year 2009
- 8. Development and Application of Eddy Current Testing for Quality Assurance of Nuclear Components** **42**
Arbind Kumar, P.P. Nanekar and B.K. Shah
Quality Assurance Division
Mr. Arbind Kumar is the recipient of the DAE Scientific & Technical Excellence Award for the year 2009
- 9. Development of novel radionuclide generators for biomedical applications** **45**
Ashutosh Dash
Radiopharmaceuticals Division
Dr. A. Dash is the recipient of the DAE Scientific & Technical Excellence Award for the year 2009
- 10. Development of Optical Instruments for Spectroscopic and Nuclear Applications** **50**
D.V. Udupa, Sanjiva K. and N.K. Sahoo



Applied Spectroscopy Division

Dr. D.V. Udupa is the recipient of the DAE Scientific & Technical Excellence Award for the year 2009

- 11. Development of Software for Instrumentation in Power and Research reactors and Accelerator based Research** **55**
Padmini S., M.P. Diwakar, P.M. Nair, Swati Gaur, S.S. Pande and C.K. Pithawa
Electronics Division, E&I Group
and
Nilesh Gohel
Research Reactor Maintenance Division, Reactor Group.
Ms. S. Padmini is the recipient of the DAE Scientific & Technical Excellence Award for the year 2009
- 12. Development of Spent Fuel Handling Equipment and man-rem Saving Tools for Nuclear Reactors** **60**
Shyamal Roy, J.P. Singh and R.J. Patel
Refuelling Technology Division
Mr. Shyamal Roy is the recipient of the DAE Scientific & Technical Excellence Award for the year 2009
- 13. Development of Type B(U) Package for Cobalt-60 Teletherapy Source Transportation** **67**
D.C. Kar, K. Jayarajan and Manjit Singh
Division of Remote Handling and Robotics
Dr. D.C. Kar is the recipient of the DAE Scientific & Technical Excellence Award for the year 2009
- 14. Developmental study on metallic thorium and uranium-thorium alloy** **72**
Santanu Das, Raj Kumar, S.B. Roy and A.K. Suri
Materials Group
Mr. Shantanu Das and Mr. Raj Kumar are the joint recipients of the DAE Scientific & Technical Excellence Award for the year 2009



15. **The Formation of Mechanically Mixed Layer during Dry Sliding of Cu-15wt%Ni-8wt%Sn Bronze** 77
Jung B. Singh
Mechanical Metallurgy Division, BARC
Mr. Jung B. Singh is the recipient of the DAE Scientific & Technical Excellence Award for the year 2009
16. ***In-Situ* Mechanical Property Measurement System for Zr 2.5 wt% Nb Pressure Tube** 81
K. Madhusoodanan, S. Chatterjee, Sanjay Panwar and J.N. Kayal
Reactor Engineering Division
Mr. Madhusoodanan is the recipient of the DAE Scientific & Technical Excellence Award for the year 2009
17. **Molecular studies on mechanisms underlying the extreme radiation resistance in *Deinococcus radiodurans*** 85
H.S. Misra
Molecular Biology Division
Mr. H.S. Misra is the recipient of the DAE Scientific Technical Excellence Award for the year 2009 and of the P S Sarma Memorial Award presented at the 79th Annual Meeting of the Society of Biological Chemists(India) and National Conference on " Regulation of Biochemical and Cellular Processes in Diverse Systems held at the Indian Institute of Science, Bengaluru, during December 13-15, 2010
18. **Nuclear Analytical Chemistry: Developments and Applications** 93
R. Acharya
Radiochemistry Division
Dr. Raghunath Acharya is the recipient of the DAE Scientific & Technical Excellence Award for the year 2009
19. **Order-disorder transitions and thermodynamic properties of rare-earth iron perovskites and garnets** 98
S.C. Parida
Product Development Division



Dr. S.C. Parida is the recipient of the DAE Scientific & Technical Excellence Award for the year 2009

20. **Role and relevance of Radiopharmaceutical Chemistry Research in the Radiopharmaceuticals Programme of BARC** 103
Sharmila Banerjee
Radiopharmaceuticals Division
Dr. Sharmila Banerjee is the recipient of the DAE Scientific & Technical Excellence Award for the year 2009
21. **Structural Integrity Assessment of Nuclear Pressure Vessel and Piping Components: Some New Findings** 110
J.Chattopadhyay
Reactor Safety Division
Dr. J. Chattopadhyay is the recipient of the DAE Scientific & Technical Excellence Award for the year 2009
22. **Structure of Fluids at Interfaces: A Combined Simulation and Theoretical Study** 114
Chandra N. Patra
Theoretical Chemistry Section, Chemistry Group
Dr. Chandra N. Patra is the recipient of the DAE Scientific & Technical Excellence Award for the year 2009
23. **Technological Innovations in spent fuel handling and their implementation for fuel reprocessing plants** 119
Kailash Agarwal
Nuclear Recycle Project Special Equipment Design
Nuclear Recycle Board
Mr. Kailash Agarwal is the recipient of the DAE Scientific & Technical Excellence Award for the year 2009
24. **Ultrafast Fluorescence Spectroscopy and Supra-biomolecular Interactions of Organic Dyes** 124
A. C. Bhasikuttan
Radiation & Photochemistry Division
Dr. A.C. Bhasikuttan is the recipient of the DAE Scientific &



Technical Excellence Award for the year 2009

25. **Ultrafiltration Membrane Technology for Water Purification and Effluent Treatment** 128
R.C. Bindal, S. Prabhakar and P.K. Tewari
Desalination Division
Dr. R.C. Bindal is the recipient of the DAE Scientific & Technical Excellence Award for the year 2009
26. **Ultrasonic Measurement of Internal Diameter and Wall Thickness of Irradiated Zr-2.5%Nb Pressure Tube from KAPS-II Reactor** 133
J. L. Singh, N. Kumawat, M. P. Dhotre and P. M. Ouseph
Post Irradiation Examination Division
Shri J.L. Singh is the recipient of the DAE Scientific & Technical Excellence Award for the year 2009
27. **X-ray absorption Spectroscopy with Synchrotron Radiation** 138
Dibyendu Bhattacharyya
Applied Spectroscopy Division
Dr. D. Bhattacharyya is the recipient of the DAE Scientific & Technical Excellence Award for the year 2009
28. **Deployable Process Development in the Back-end of the Fuel Cycle: Spent Solvent Management & Actinide Partitioning of HLLW** 141
Smitha Manohar and P.K. Wattal
Process Development Division
Ms. Smitha Manohar is the recipient of the DAE Scientific & Technical Excellence Award for the year 2009
29. **Development of high performance electro hydraulic servo linear actuators** 145
Ramakrishna P., Shiju Varghese, Jay Shah & N.L. Soni
Fluid Power and Tribology Section
Refuelling Technology Division



Mr. Ramakrishna P. is the recipient of the DAE Young Applied Scientist and Technologist Award for the year 2009

- 30. Indigenous development of online radon and thoron monitors for applications in Uranium mining and Thorium processing facilities** **149**
J.J. Gaware, B.K. Sahoo, B.K. Sapra and Y.S. Mayya
Radiological Physics and Advisory Division
Shri B.K. Sahoo & Shri J.J. Gaware are the joint recipients of the DAE Young Applied Scientist & Technologist Award for the year 2009
- 31. Copper-curcumin complexes as superoxide dismutase (SOD) mimic: Structure activity relationship** **154**
Atanu Barik
Radiation & Photochemistry Division
Dr. Atanu Barik is the recipient of the DAE Young Scientist Award for the year 2009
- 32. Doped RE_3 (RE: Ce, Gd, Y) nanopowders: Phosphors for solid state lighting and bio-applications** **158**
V. Grover and A.K. Tyagi
Chemistry Division
Dr. Vinita G. Gupta is the recipient of the DAE Young Scientist Award for the year 2009. Dr. A. K. Tyagi is the recipient of the Rajib Goyal Prize in Chemical Sciences
- 33. Gas phase studies on interaction of clusters with laser and metal ions** **162**
Pramod Sharma
Chemistry Division
Dr. Pramod Sharma is the recipient of the DAE Young Scientist Award for the year 2009
- 34. CFD Analysis of Passive Autocatalytic Recombiner and its Interaction with Containment Atmosphere** **167**
B. Gera, P.K. Sharma, R.K. Singh and K.K. Vaze
Reactor Safety Division
and

**A.K. Ghosh**

Health, Safety & Environment Group

Mr. Bhuvaneshwar Gera is the recipient of the DAE Young Engineer Award for the year 2009

35. **'H₂-F₂ Reaction in a Tubular Reactor'** 172
A.K. Tiwari and C.S.R. Prasad
Chemical Technology Division
and
A.W. Patwardhan
Department of Chemical Engineering,
Institute of Chemical Technology, Mumbai
and
L.M. Gantayet
Beam Technology Dev. Group, BARC
Mr. A.K. Tiwari is the recipient of the DAE Young Engineer Award for the year 2009
36. **Indigenous Development of HDR Source Assembly for Brachytherapy** 178
M.K. Mishra, D.N. Badodkar and Manjit Singh
Division of Remote Handling & Robotics
and
K.V.S. Sastry and A.K. Kohli
Board of Radiation and Isotope Technology
Mr. M.K. Mishra is the recipient of the DAE Young Engineer Award for the Year 2009
37. **AKRUTI - DAE Societal Initiative AKRUTI - Advanced Knowledge & RUrual Technology Implementation** 182
K.B. Sainis
Bio Medical Group
and
A.M. Patankar
Technology Transfer & Collaboration Division
This Paper received the DAE Group Achievement Award for the year 2009



- 38. Design & Manufacture of Fuel Rod Cluster Simulators & Instrumented Steam Generators For FISBE Project of RED** **187**
R.L. Suthar
CDM
and
D. Saha
RED
This paper received the DAE Group Achievement Award for the year 2009
- 39. Design and Development of 10 MeV Industrial RF Electron Linac at Electron Beam Centre, Kharghar for Radiation Processing Applications** **193**
K.C. Mittal, D.P. Chakravarthy, V.T. Nimje, K.P. Dixit, S. Acharya, K.V. Nagesh, Vivek Yadav, Shiv Chandan, P.C. Saroj, A.R. Chindarkar, S.R. Ghodke, D. Bhattacharjee, A.R. Tillu, R. Barnwal, R.B. Chavan, D. JayaPrakash, R.L. Mishra, Mukesh Kumar, Vijay Sharma, P. Roychowdhury, Mahendra Kumar, R.R. Tiwari, Supriya S. Barje, N.K. Lawangare and N.Chaudhary
Electron Beam Centre, Accelerator and Pulse Power Division
and
R.L. Suthar, S.B. Jawale and S. Guha
Centre for Design & Manufacture
This paper received the DAE Group Achievement Award for year 2009
- 40. Design and Development of Fuel Rod Cluster Simulator** **198**
A.K. Vishnoi, A.K. Pal, D.K. Chandraker and P.K. Vijayan
Reactor Engineering Division
This paper received the DAE Group Achievement Award for the year 2009
- 41. Design, Manufacture and Deployment of Radiation and Corrosion Resistant Compact Custom Designed Motor for Centrifugal Extractors** **203**
R.K. Gupta



CM&DS, ChTG, BARC, Mumbai

and

**A. Sriramamurthy, P. Vijayasekaran, S. Sundaramurthy,
Felix Lawrence and A. Palanivel**

Reprocessing Group, IGCAR, Kalpakkam

and

P. P. Selvam

Reactor Engineering Group

IGCAR, Kalpakkam

This paper received the DAE Group Achievement Award
for the year 2009

- 42. Development, Installation and Commissioning of EDXRD & EXAFS Beamlines at Indus-2 Synchrotron Source Part-I** **207**
Energy Dispersive X-ray Diffraction Beamline at Indus-2 Synchrotron Source
H. K. Poswal, K. K. Pandey, A. K. Mishra, Nandini Garg, Abhilash Dwivedi, R. Vasanthi and Surinder M. Sharma
 High Pressure & Synchrotron Radiation Physics Division
Part-II
Dispersive Extended X-ray Absorption Fine Structure (EXAFS) beamline at INDUS-2 Synchrotron Source
S.N. Jha, D. Bhattacharyya, A.K. Poswal, S. Basu and N.K. Sahoo
 Applied Spectroscopy Division
 This Paper received the DAE Group Achievement Award
 for the year 2009
- 43. Man-rem Saving Tools for PHWR Coolant Channels** **213**
R. J. Patel
 Refuelling Technology Division
 This Paper received the DAE Group Achievement Award
 for the year 2009
- 44. Remote Disposal of Explosive Anti-Tank Mine Fuzes using Indigenous Mobile Robot System** **219**
Manjit Singh, P.K. Pal, K. Jayarajan, D.D. Ray, B. Sony,



**V.K. Shrivastava, R. Sahu, R.V. Sakrikar,
A.N. Jha and V.V. Agashe**

Division of Remote Handling & Robotics
and

Vivek Mahadev

Seismology Division

This paper received the DAE Group Achievement Award
for the Year 2009

- 45. Treatment of Intermediate level liquid waste of reprocessing origin-PREFRE, Tarapur** 223
D. Banerjee, A.K. Singh and I.J. Singh
Nuclear Recycle Group
and
T.P. Valsala, M.S. Sonawane, S. Chattopadhyay and U. Dani
Nuclear Recycle Board, BARC, Tarapur
This paper received the DAE Group Achievement Award
for the year 2009
- 46. Vibration as a Tool for Testing Healthiness of Defence Components** 227
A. Rama Rao, S.K. Sinha, K.K. Meher, Satyavir Singh and Anil Kumar Narayan
Vibration Laboratory Section
Reactor Engineering Division
This paper received the DAE Group Achievement Award
for the year 2009
- 47. Production of high specific activity ¹⁷⁷Lu and formulation of ¹⁷⁷Lu-DOTATATE for the treatment of neuroendocrine cancers** 231
Sharmila Banerjee, Sudipta Chakraborty, Tapas Das, K.V. Vimalnath Nair, Viju Chirayil and Archana Mukherjee
Radiopharmaceuticals Division
This paper received the DAE Group Achievement Award
for the year 2009



Merit Awards

48. **Cucurbituril-based Supramolecular Assemblies of Fluorescent Dyes: Their Prospective Applications** 236
Jyotirmayee Mohanty
Radiation & Photochemistry Division
Dr. (Ms.) Jyotirmayee Mohanty was awarded the "APA Prize for Young Scientists-2010" at the Asian Photochemistry Conference (APC-2010) held at Victoria University, Wellington, New Zealand, during November 14-18, 2010.
49. **Redox modulatory activities of dimethoxycurcumin, a synthetic analogue of curcumin** 240
Amit Kunwar and K. Indira Priyadarsini
Radiation & Photochemistry Division
This paper received the Lester Pecker Young Investigator Award at the 5th International Niigata Symposium on Diet & Health held at Niigata, Japan, during October 29-31, 2010
50. **Autoclave Leaching of Refractory Uranium Minerals** 242
T. Sreenivas, K. Anand Rao, M. Manmadha Rao, K.C. Rajan, Md. Serajuddin, P. Karthikayini and N.P.H. Padmanabhan
Mineral Processing Division
This paper received the MISRA award for Best Paper in Hydro, Electro and Bio metallurgy Category instituted by the Indian Institute of Mineral Engineers, at the International Seminar on Mineral Processing Technology, held at Jamshedpur during Dec. 2010
51. **Studies in Atomic Structure and Dynamics using Laser Spectroscopy** 249
Asawari D. Rath
Laser & Plasma Technology Division
This paper received the Best Thesis Presentation Award at the Topical Conference on EM interaction with Atoms, Molecules and Clusters, held at RRCAT, Indore, during March 3-6, 2010



- 52. Atoms, Molecules and Photons: From Precision Measurements to Quantum Control** **252**
B.N. Jagtap
Atomic and Molecular Physics Division
Dr. B.N. Jagtap is the recipient of the Platinum Jubilee Lecture Award (Physical Sciences) conferred on him at the 97th Indian Science Congress, held at Kerala University, Thiruvananthapuram, from 3-7 January 2010
- 53. Bioaccessibility of selenium from Se rich food grains of seleniferous region of Punjab, India as analyzed by Instrumental and Chemical NAA** **253**
Sumit K Jaiswal and N. Tejo Prakash
Department of Biotechnology & Environmental Sciences
and
Amit Goyal and Ranjana Prakash
School of Chemistry & Biochemistry, Thapar University, Patiala
and
R. Acharya and T.N. Nathaniel
Radiochemistry Division
and
A.V.R.Reddy
Analytical Chemistry Division
This paper received the IANCAS Best Paper Award (Oral Presentation), at the Fourth International Symposium on Nuclear Analytical Chemistry (NAC-IV), held at BARC, Mumbai, during November 15-19, 2010
- 54. High Pressure Freezing of Cyanobacteria for Immunolocalization Studies** **257**
Rachna Agarwal
Molecular Biology Division
and
Michael Melzer
Leibniz Institute of Plant Genetics and Crop Plant Research, Gatersleben, Germany
and
Jayashree Krishna Sainis
Molecular Biology Division
This Paper received the Best Oral Presentation Award at the



International Conference on Advances in electron microscopy and related techniques and XXXI annual meeting of EMSI, held at Training School Hostel, Anushaktinagar, from 8-10 March, 2010

- 55. Ion-transport characteristics in Nafion-117 membrane having mixed cationic composition** **260**
Sanhita Chaudhury, Chhavi Agarwal, A. K. Pandey and A. Goswami
Radiochemistry Division
This paper received the Best Oral Presentation Award (II prize) at the 2nd International Symposium on Application of Radiotracers in Chemical, Environmental and Biological Sciences (ARCEBS-2) held at SINP, Kolkata, during November 7-13, 2010
- 56. Nondestructive assay of Plutonium in empty stainless steel boxes by apparent mass method** **263**
C. Agarwal, S. Chaudhury, T. N. Nathaniel and A. Goswami
Radiochemistry Division
This paper received the Best Oral Presentation Award at the 4th International Symposium on Nuclear Analytical Chemistry (NAC-IV), held at Multipurpose Hall, TSH, BARC, from 15-19 Nov., 2010.
- 57. Catalytic decomposition of sulfuric acid over Fe₂O₃ and Pt/Al₂O₃: A comparative study** **266**
A.M. Banerjee, A.R. Shirole, M.R. Pai, A.K. Tripathi, S.R. Bharadwaj and D. Das
Chemistry Division
This paper received the Best Paper Award (II prize), at the International Symposium on Materials Chemistry (ISMC-2010), held at Mumbai, during December 7-11, 2010
- 58. Chemical compatibility between U-6wt.%Zr alloy and T91 cladding** **270**
Santu Kaity, T.R.G. Kutty and Arun Kumar
Radiometallurgy Division
and
Renu Agarwal
Product Development Division
and

**A. Laik**

Materials Science Division

and

H.S. Kamath

Nuclear Fuels Group, BARC

This paper received the Best Poster Award at the 9th International Symposium on Materials Chemistry (ISMC 2010), held at BARC, Mumbai, during December 7-11, 2010

- 59. Coincidence Doppler broadening studies of as grown CdSe nanoparticles** **274**
S.K. Sharma, P.K. Pujari, K. Sudarshan and P. Maheshwari
Radiochemistry Division
and
C.P. Shah, K.K. Singh, M. Kumar and P.N. Bajaj
Radiation and Photochemistry Division
This paper received one among the Best Poster Awards at the 3rd Asia Pacific Symposium on Radiation Chemistry and DAE-BRNS 10th Biennial Trombay Symposium on Radiation & Photochemistry, held at Lonavala, during September 14-17, 2010
- 60. Depth Profile of Polychlorinated Biphenyls in Sediment Core from Thane Creek Area of Mumbai, India** **277**
S.K. Sahu, G.G. Pandit and V.D. Puranik
Environmental Assessment Division
This paper received the Best Poster Award at the International Symposium on Trace Organic Pollutants in the Environment, held at Bharathidasan University, Tiruchirapalli, Tamilnadu, India, on January 23, 2010
- 61. Functional characterization of a DNA repair polymerase from a radiation resistant bacterium, *Deinococcus radiodurans*.** **281**
Nivedita P. Khairnar and Hari S. Misra
Molecular Biology Division
Dr. (Ms.) Nivedita P. Khairnar received the Best Research Paper Award in the Poster session of the International Conference on "Mutagens & Genetic Diversity for Health & Agriculture", Annual Meetings of EMSI-2010, held at Chandigarh, during March 12-14, 2010



- 62. Immobilization of glucose oxidase on synthetic and biological materials for biosensor development** **286**
Jitendra Kumar and S. F. D'Souza
Nuclear Agriculture and Biotechnology Division
This paper received the Best Poster Award at the 3rd International Symposium on Materials Chemistry (ISMC-2010) held at BARC, from 7th-11th Dec., 2010
- 63. Investigation of Magnetic Phase Transition in $TbCo_{2-x}Fe_x$** **290**
Madhumita Halder and S. M. Yusuf
Solid State Physics Division
This paper received the Best Poster Presentation Award at the 1) Advances in magnetism: Phenomena & Materials (AMPM-2010), at Manali, Himachal Pradesh and at the 2) International Conference on Magnetic Materials (ICMM-2010) held at the Saha Institute of Nuclear Physics, Kolkata, from 25th-29th Oct., 2010
- 64. Large Sample Neutron Activation Analysis of Dross for Gold and Silver** **294**
K. K. Swain, Nicy Ajith, R. Verma and A. V. R. Reddy
Analytical Chemistry Division
and
R. Acharya
Radiochemistry Division
This paper received the IANCAS Best Paper Award at the Fourth International Symposium on Nuclear Analytical Chemistry (NAC-IV), held at Mumbai from 15-19 November, 2010
- 65. Magnetic Ordering in $La_{1-x}Ce_xCrO_3$ ($0.0 \leq x \leq 1.0$) Nanoparticles** **297**
P. K. Manna, A. K. Bera and S. M. Yusuf
Solid State Physics Division
and
R. Shukla and A. K. Tyagi
Chemistry Division
This paper received the Best Poster Awards at the "Advances in Magnetism: Phenomena and Materials" (AMPM-2010), held at



Manali, during June 3-5, 2010 and "International Conference on Magnetic Materials" (ICCM-2010) held at Saha Institute of Nuclear Physics, Kolkata, during October 25-29, 2010.

- 66. Microstructural characterization of Al-base metallic foam developed by novel FSP technique** **302**
Kaushal Jha and K. N. Mahule
Engineering Design & Development Division
and
K. Bhanumurthy
Scientific Information Resource Division
and
G. K. Dey
Materials Science Division
This paper received the 3rd Prize in poster presentation, at the International Conference on Advances in Electron Microscopy and Related Techniques, held at Mumbai from 8-11 March, 2010
- 67. Prospective applications of biotechnological methods in salt accumulator halophyte sesuvium portulacastrum (L.) L.** **305**
Vinayak H. Lokhande and Tukaram D. Nikam
Department of Botany, University of Pune
and
Penna Suprasanna
Functional Plant Biology Section, Nuclear Agriculture and Biotechnology Division
This paper received the Best Poster Award at the International Conference on 'Biotechnology: A Global Scenario' organized by the Department of Biotechnology, held at Kakatiya University, Warangal, Andhra Pradesh from 2-4 November, 2010
- 68. Radiation synthesized stimuli-responsive HEMA-co-MAETC hydrogels** **310**
N.K. Goel, V. Kumar, Y.K. Bhardwaj and S. Sabharwal
Radiation Technology Development Division
This paper received the Best Poster Award at the 3rd Asia Pacific



Symposium on Radiation Chemistry and at the DAE-BRNS 10th Biennial Trombay Symposium on Radiation & Photochemistry (TSRP-2010), held at Lonavala, from September, 14-17, 2010

- 69. Room temperature synthesis of $MWO_4:Eu^{3+}$ (M = Ca, Sr, Ba) nanomaterials** **313**
B.S. Naidu, V. Sudarsan and R.K. Vatsa
Chemistry Division
and
B.Vishwanadh
Materials Science Division
This paper received the Best Poster Award at the International Conference on Materials Chemistry (ISMC 2010), held at BARC, Mumbai, during December 7-11, 2010
- 70. Standardization of correlation between measured radioactivity and observed dose using an activated concrete sample** **317**
Sanhita Chaudhury, Chhavi Agarwal and A. Goswami
Radiochemistry Division
and
M. Gathibandhe
Reactor Projects Division
This paper received the Best Poster Award at the 4th International Symposium on Nuclear Analytical Chemistry (NAC-IV) held at Mumbai, during November 15-19, 2010
- 71. Structural and electronic properties of Pdn (n=1-8) clusters deposited on alumina surface** **319**
Sandeep Nigam and Chiranjib Majumder
Chemistry Division
This paper received the Best Poster Award (II Prize) at the International Symposium on Materials Chemistry (ISMC 2010), held at Mumbai, during December 7-11, 2010
- 72. Studies on $BaO-CaO-Al_2O_3-B_2O_3-SiO_2$ glass system for use as SOFC sealant** **323**
M. Goswami, S. Singaravelan, A. Patil and G.P. Kothiyal
Glass and Advanced Ceramics Division



and

S. Bhattacharya

Technical Physics Division

This paper received the Best Oral Presentation Award at the International Workshop and Symposium on the Synthesis and Characterization of Glass (Glass-Ceramics (IWSSCGGC) held at C-MET, Pune, during July 7-10, 2010

73. Studies on the Production Feasibility of ^{64}Cu by (n, p) Reactions on Zn Targets in Dhruva Research Reactor 325

K.V. Vimalnath, A. Rajeswari, K.C. Jagadeesan, Viju C., P.V. Joshi and Meera Venkatesh

Radiopharmaceuticals Division

This paper received the Best Paper Award at the Fourth International Symposium on Nuclear Analytical Chemistry (NAC-IV), held at Mumbai, India from 15-19 November 2010

74. Study of interfaces in organic semiconductor heterojunctions 332

P. Maheshwari, D. Dutta, K. Sudarshan, S. K. Sharma and P. K. Pujari

Radiochemistry Division

and

S. Samanta, A. Singh and D. K. Aswal

Technical Physics Division

This paper received the Best Oral Presentation Award at the 12th International workshop on Slow positron Beam Techniques (SLOPOS-12) held at Magnetic Island, Australia, during 1-6 August, 2010.

75. Study of structural and thermal properties of barium strontium silicate glasses 337

K. Sharma, A. Dixit, A. Arvind and G.P. Kothiyal

Glass and Advanced Ceramics Division

This paper received the Best Poster Award at the International Workshop and Symposium on the Synthesis and Characterization of Glass-Ceramics (IWSSCGGC) held at C-MET, Pune, during July 7-10, 2010



- 76. Synthesis, characterization and luminescence study of $Y_2Sn_2O_7$: Tb nanoparticles co-doped with Sb^{3+}** **343**
Sandeep Nigam, V. Sudarsan and R. K. Vatsa
Chemistry Division
This paper received the Best Poster Award at the International Conference on Recent Trends in Materials Science and Technology (ICMST 2010), held at Thiruvananthapuram, Kerala, during October 29-31, 2010
- 77. Assessment of germplasm of Indian bread wheats for polymorphism at Xgwm261 locus: Microsatellite analysis, sequencing and relationship with agronomic traits** **347**
Suman Bakshi and S.G. Bhagwat
Nuclear Agriculture and Biotechnology Division
This paper received the Best Poster Award in the Biotechnology Section, at the Zonal Seminar on Physiological and Molecular Interventions for Yield and Quality Improvement in Crop Plant, held at the S.V. Patel University of Agriculture & Technology, Meerut, from 17-18 September, 2010
- 78. Bull's Multirule Algorithm, (M), An Excellent Means of Internal Quality Control for Hematology Analyzers** **351**
Shagufta. S, S.K.G. Shettigar, S. Gujral and R.K. Kulkarni
Medical Division, BARC
and
Manikchandra, T.
Tata Memorial Hospital, Mumbai
This paper received the Best Paper Award (II prize) at the All India Institute of Medical Technologists, 20th Congress of Biomedical Laboratory Science, held at Tiruchirapalli, Tamil Nadu, during December 18-19, 2010.
- 79. Carbondioxide Emissions and Alternative Electricity Generation Options** **356**
I.V. Saradhi, G.G. Pandit and V.D. Puranik
Environmental Assessment Division
This paper received the Best Poster Presentation Award (II prize), at the Workshop cum Seventeenth National Symposium on



Environment (NSE-17), held at the Indian Institute of Technology, Kanpur, during May 13-15, 2010

80. **Chemical stability and proton conductivity of $\text{BaCe}_{0.8}\text{Y}_{0.2}\text{O}_{3-\delta}$** 360
Pooja Sawant, A.N. Shirsat, S. Varma, B.N. Wani and S.R. Bharadwaj
Chemistry Division
This paper received the Best Poster Award (III prize) at t Thermal Analysis (THERMANS 2010), held at Kurukshetra, Haryana, India, during March 9-11, 2010
81. **Coherent Laser-Atom Interaction and its Application to Atomic Frequency Offset Locking** 365
Y. B. Kale and Ayan Ray
Laser & Plasma Technology Division
and
B. N. Jagatap
Atomic & Molecular Physics Division
This paper received the Best Poster Award at the Topical Conference on Atomic and Molecular Physics (TC-2010), held at the Raja Ramannna Centre for Advanced Technology, Indore from 3-6 March, 2010
82. **Conformational Changes in the Chromatin Structure of Human Peripheral Blood Mononuclear Cells Exposed to Low Dose Radiation** 368
Vinay Jain, Birajalaxmi Das and M.Seshadri
Low Level Radiation Studies Section
Radiation Biology & Health Sciences Division
and
P.A. Hassan
Chemistry Division
This paper received the Best Poster Award at the 7th International Conference on High Levels of Natural Radiation and Radon Areas (7HLNRRRA), held at Navi Mumbai, during November 24-26, 2010



- 83. Development of a plastic scintillator based large area ground surface contamination monitor** **371**
P. Ashokkumar, Anand Raman, D.A.R. Babu and D.N. Sharma
Radiation Safety Systems Division
This paper received the Best Poster Award at the 29th National Conference on (IARP NC 2010) Recent Advances in Radiation Dosimetry held at Mumbai, during February 3-5, 2010
- 84. Electrocatalysis of Fe(III)/Fe(II) Redox Reaction on Polyaniline Coated Platinum Electrode : Influence of Ionic Speciation of Analyte** **374**
Saurav K. Guin, Ruma Chandra, H.S. Sharma (Retd.) and S.K. Aggarwal
Fuel Chemistry Division
This paper was awarded the Best Poster Presentation (III Prize) at the 4th ISEAC Triennial International Conference on ElectroAnalytical Chemistry and Allied Topics (ELAC-2010) held at Puri, Orissa, during March 16-18, 2010.
- 85. Electrochemical Oxidation of Ascorbic Acid on Gold Nanoparticles Coated Pt** **378**
Manoj K. Sharma and Arvind Ambolikar
Fuel Chemistry Division
This paper was awarded the Best Poster Presentation (III) Prize at the 4th ISEAC Triennial International Conference on ElectroAnalytical Chemistry and Allied Topics (ELAC-2010) held at Puri, Orissa, during March 16-18, 2010
- 86. Electromagnetically induced transparency in a tripod atomic system** **382**
Niharika Singh
Homi Bhabha National Institute
and
R. D'Souza and B. N. Jagatap
Atomic and Molecular Physics Division
and
Q. V. Lawande
Theoretical Physics Division



This paper received the Best Poster Award at the National Laser Symposium (NLS-19), held at the Raja Ramanna Centre for Advanced Technology, Indore, from 1-4 December, 2010

- 87. Estimation of Distribution Coefficient of Uranium and its correlation with soil parameters around Turamdih Uranium Tailings Pond** **385**
Sukanta Maity, S. Mishra, S. Bhalke, C. B. Dusane, G.G. Pandit and V. D. Puranik
Environmental Assessment Division
and
H. S. Kushwaha
Health Safety and Environment Group
This paper received the Consolation Award in Poster Presentation Session, at the Workshop cum Seventeenth National Symposium on Environment (NSE-17), held at the Indian Institute of Technology, Kanpur, from 13-15 May, 2010
- 88. Estimation of radiation doses to members of the public in the northern corridor of India from intake of ^{238}U in drinking water** **388**
Sunil Bhalke, S. Mishra, Sukanta Maity, Chetan B. Dusane, G.G. Pandit and V.D. Puranik
Environmental Assessment Division
This paper received the Consolation Award in Poster Presentation, at the Workshop cum Seventeenth National Symposium on Environment (NSE-17), held at the Indian Institute of Technology, Kanpur from 13-15 May, 2010.
- 89. Feasibility Study of phosphorus determination in (Th-U) O_2 sample using different types of solvents for the extraction of phosphomolybdic acid** **392**
B.N. Mahanty, R. Gaikwad, V.R. Sonar, S. Raul, D.K. Das, A. Prakash, Md. Afzal and J.P. Panakkal
Advanced Fuel Fabrication Facility, BARC, Tarapur
This paper received the Best Paper Poster Award at the Symposium SESTEC-2010, held at IGCAR, Kalpakkam, from 1-4 March, 2010



90. **High Speed Cryogenic Turboexpander Rotor for stable operation up to 4.5 kHz Rotational Speed** 395
Rajendran Menon, Anindya Chakravarty, Mukesh Goyal, Mohananand Jadhav, Arun S., Satish Kumar Bharti and Trilok Singh
Cryo-Technology Division
This paper received the Best Paper Award at the Twenty Third National Symposium on Cryogenics (NSC-23) held at NIT, Rourkela, during October 28-30, 2010
91. **Laser Assisted Decontamination of Nuclear Fuel Elements** 401
J. Padma Nilaya and Dhruva J. Biswas
Laser & Plasma Technology Division, BARC
and
Aniruddha Kumar and Chandrakant Sharma
AFFF, BARC, Tarapur
This paper received the Best Paper Award at the National Laser Symposium held at RRCAT, Indore, during December 1-4, 2010
92. **Magnetism of geometrically frustrated quasi-one-dimensional-spin-chain compounds $\text{Ca}_3\text{Co}_{2-x}\text{Fe}_x\text{O}_6$** 405
A. Jain and S.M. Yusuf
Solid State Physics Division
This paper received the Best Poster Award at the Conference on Advances in Magnetism: Phenomena and Materials (AMPM-2010), held at Manali, Himachal Pradesh, during June 3-5, 2010
93. **Protactinium Recovery from Short-Cooled Spent Fuel and High-Level Waste Solutions in Thorium Fuel Cycle** 409
Neelam Kumari, P.N. Pathak, D.R. Prabhu and V.K. Manchanda
Radiochemistry Division
This paper received the Best Paper Award at the "Emerging Trends in Separation Science and Technology (SESTEC-2010)" held at Indira Gandhi Centre for Atomic Research (IGCAR), Kalpakkam, during March 1-4, 2010



- 94. Prussian Blue Analogue Molecular Magnets: Controlling Structural Disorder and Magnetic Properties** 413
N. Thakur, S.M. Yusuf and A. Kumar
Solid State Physics Division
and
J. V. Yakhmi
Physics Group
This paper received the Best Poster Award at the "Advances in Magnetism: Phenomena and Materials" held at Manali, Himachal Pradesh, during June 3-5, 2010
- 95. Response of aleurone layers from *Triticum dicoccum* genotypes to gibberellic acid (GA₃): Time course of amylase stimulation** 416
Chun Mei Chang and S.G. Bhagwat
Nuclear Agriculture and Biotechnology Division
This paper received the Best Poster Award (Third Place) at the Zonal Seminar on Physiological and Molecular Interventions for Yield and Quality Improvement in Crop Plants, held at S.V. Patel University of Agriculture & Technology, Meerut in 2010
- 96. The Central Monitoring Station of Indian Environmental Radiation MONitoring Network (IERMON): The Architecture and Functions** 419
Saurabh Garg, M.P. Ratheesh, T. Mukundan, M.D. Patel, A. Vinod Kumar, V.D. Puranik and C.K.G. Nair (Retd.)
Environmental Assessment Division
This paper received the Best Poster Award (I prize) at the Workshop cum 17th National Symposium on Environment held at Indian Institute of Technology (IIT), Kanpur, during May 13-15, 2010
- 97. Thermal cyclic hydrogen absorption desorption behavior of Ti₂CrV alloy** 423
Asheesh Kumar, K. Shashikala and C.G.S. Pillai
Chemistry Division
This paper received the Best Oral Presentation Award (III prize) at the 17th DAE-BRNS National Symposium and Workshop on Thermal Analysis, held at Kurukshetra, Haryana, during March 9-12, 2010



- 98. Thorium Intake due to consumption of locally grown vegetables by inhabitants of High radiation background areas by INAA** **427**
R.S.Sathyapriya, Suma Nair, R.K. Prabhath, Madhu Nair and D.D.Rao
Internal Dosimetry Section, Health Physics Division
and
V. Kamesh
SRM University, Tamilnadu, India
and
R. Acharya
Radiochemistry Division
This Paper received the Best Paper Award at the Fourth International Symposium on Nuclear Analytical Chemistry (NAC-IV), held at Mumbai, from 15-19 November, 2010
- 99. Transgenic tobacco plants expressing fungal copper and zinc transporter genes show enhanced acquisition of copper and zinc** **430**
Sudhir Singh, Prachy Dixit and Susan Eapen
Nuclear Agriculture & Biotechnology Division
This paper won the Best Poster Award at "The National Symposium on Plant Tissue & Organ Culture: the present scenario", held at University of Calcutta. during March 3-5, 2010
- 100. Transient plane source technique for measurement of thermal conductivity of U and T91 for fast reactor application** **434**
Santu Kaity, M.R. Nair, A.K. Sengupta and Arun Kumar
Radiometallurgy Division
This paper received the Best Poster Award at the 17th National Symposium on Thermal Analysis (THERMANS 2010) held at Kurukshetra, Haryana, during March 9-11, 2010
- 101. Sources identification using organic molecular markers in fine particulate matter collected at Trombay, Mumbai** **438**
S.K. Sahu, G.G. Pandit and V.D. Puranik
Environmental Assessment Division



This paper received the Best Poster Award at the Workshop cum Seventeenth National Symposium on Environment on advances in Environmental Monitoring and Modeling, held at the Centre for Environmental Science & Engineering, IIT Kanpur, from 13-15 May, 2010

102. Spectral narrowing of emission from ZnO inverse photonic crystals **441**

Sunita Kedia

Department of Physics, Indian Institute of Technology, Bombay, Mumbai
and

R. Vijaya

Department of Physics, Indian Institute of Technology Kanpur, Kanpur
and

Alok K. Ray, Sucharita Sinha and K. Dasgupta

Laser and Plasma Technology Division

This paper received the Best Paper Award at the 9th DAE-BRNS National Laser Symposium (NLS-09), held at BARC, Trombay, Mumbai from 13th to 16th January, 2010



Determination of neutron-induced fission cross sections by surrogate methods

B.K. Nayak

Nuclear Physics Division

Dr. B.K. Nayak is the recipient of the DAE Homi Bhabha Science & Technology Award for the year 2009

Abstract

Heavy ion reaction studies around Coulomb barrier have been usually used, to investigate projectile/target structure effects on reaction dynamics. Other than providing a basic understanding of the reaction dynamics, some of these reactions have been used as tools to serve as surrogates, for measuring neutron-induced reaction cross-sections involving unstable targets. In this paper, we present a new experimental technique known as "hybrid surrogate ratio method", which has been employed by us, to determine $^{233}\text{Pa}(n, f)$ cross-section of interest in Th-U fuel cycle for the first time, using $^6\text{Li}+^{232}\text{Th}$ transfer induced fission reactions. More candidate reactions for surrogate measurements have also been discussed.

Introduction

As a part of the large effort to reduce carbon emissions, support for alternative power sources, including nuclear has been growing all over the world. The renewed interest in nuclear power has led to a number of novel materials proposed, for fuels and reactor components. ^{232}Th , which constitutes the world's third largest reserve in India, is not fissile, therefore needs to be converted to a fissile material ^{233}U , by transmutation in a fast breeder reactor. A sequential three stage nuclear power program (for the optimum utilization of the indigenous nuclear resource profile of modest uranium and abundant thorium reserves) is being followed in India. The innovative design of reactors for direct use of thorium as a fuel, is also in progress. In this context, the frontier technologies being developed include Accelerator Driven Systems (ADS) and Advanced Heavy Water Reactor (AHWR) [1]. These new designs promote enhanced safety, reliability, and sustainability, in addition to proliferation resistance and

waste reduction. Accurate data sets, notably neutron-induced cross sections, are vital to the engineering and design of these systems.

Since some of the isotopes involved in the Th-U fuel cycle have half lives of a few days to a few minutes, some of the relevant cross sections are poorly known. The primary reaction of importance in the thorium cycle, is the one producing the fissile nucleus ^{233}U from neutron capture of ^{232}Th as shown in Fig. 1. The net production of ^{233}U is controlled by the 27 days half-life of ^{233}Pa isotope. As this isotope is produced in an intermediate step during the formation of the fissile ^{233}U nucleus, reactions competing with its natural decay, affect the production rate of the fissile fuel. In a thermal reactor, neutron capture of ^{233}Pa is totally dominating, but the situation is different in a fast reactor system such as the ADS. At fast neutron energies, the fission cross section increases and the capture cross section decreases. Thus, in this type of system, the magnitude of fission cross section becomes a key



parameter, which must be known with some precision. The accuracy with which the $n + {}^{233}\text{Pa}$ fission cross section is needed in fast breeding reactors and ADS, has been estimated to be less than 20% [2].

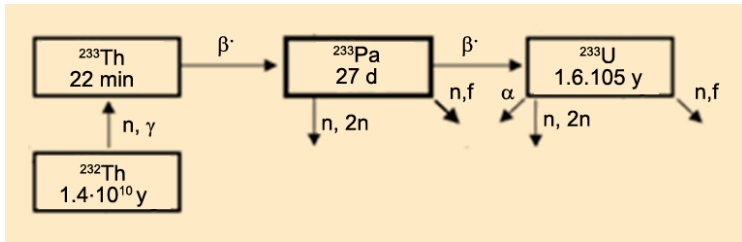


Fig. 1: Schematic view of production and decay of ${}^{233}\text{Pa}$ and ${}^{233}\text{U}$ isotopes in Th-U fuel cycle.

There is only one direct neutron energy resolved ${}^{233}\text{Pa}(n, f)$ cross section measurement which has been carried out with quasi-mono-energetic neutrons, where the ${}^3\text{H}(p, n){}^3\text{He}$ and ${}^2\text{H}(^2\text{H}, n){}^3\text{He}$ reactions have been used, to produce neutrons with energies of $E_n = 1.0\text{-}3.8$ MeV and $E_n = 5.0\text{-}8.5$ MeV, respectively [3,4]. Limited experimental data on direct measurement could be explained, by the short half life of ${}^{233}\text{Pa}$. In order to overcome these problems, the absolute surrogate reaction technique has been used [5] in the past, to measure the fission probability of ${}^{234}\text{Pa}$ formed in the ${}^{232}\text{Th}({}^3\text{He}, p){}^{234}\text{Pa}$ transfer reaction. The neutron-induced fission cross sections for the $n + {}^{233}\text{Pa}$ reaction have then been deduced, from the product of experimentally determined fission probability, with the compound nucleus formation cross section, determined from optical model calculations in the equivalent neutron energy range from threshold to 10.0 MeV [5]. None of this experimental data on ${}^{233}\text{Pa}(n, f)$ cross section in the energy range 6.0 MeV to 10.0 MeV, matches the recommended values for the neutron-induced capture and fission cross sections, extracted from ENDF/B-VII.0 [6] and JENDL-3.3 [7] evaluations.

Except for the present work, there is no experimental measurement on ${}^{233}\text{Pa}(n, f)$ cross section beyond 10.0 MeV neutron energy. The experimental data beyond 10 MeV is of importance for hybrid fusion-fission systems and for ADS. It can also give a stringent test to the neutron induced capture and fission cross sections, extracted from

various evaluations. More recently, the surrogate ratio method has been extensively used employing (α, α') and ${}^3\text{He}$ induced transfer reactions in the measurement of (n, f) cross sections [8,9]. In this method, the ratio of the cross sections of two compound-nucleus reactions, for same excitation energy (E_{ex}) is determined experimentally, using two different targets. An independent determination of one of the above cross sections then, allows one to infer the other by using the ratio. The (n, f) cross sections obtained in surrogate ratio methods, are observed to be consistent with ENDF/B-VII predictions for a large number of systems. But for the ${}^{233}\text{Pa}(n, f)$ cross section measurement, there are no suitable targets to employ surrogate ratio method with (α, α') or ${}^3\text{He}$ projectile.

Hybrid Surrogate ratio method

This is a unique method [10], which combines aspects of both absolute surrogate and surrogate ratio methods, for the determination of (n, f) cross sections. This method has been employed to derive ${}^{233}\text{Pa}(n, f)$ cross sections from the measurement of the ratio of the fission decay probabilities of ${}^{234}\text{Pa}$ and ${}^{236}\text{U}$ compound nuclei, over the excitation energy range of 17.0 MeV to 22.0 MeV. These nuclei are formed in ${}^{232}\text{Th}({}^6\text{Li}, \alpha){}^{234}\text{Pa}$ and ${}^{232}\text{Th}({}^6\text{Li}, d){}^{236}\text{U}$ transfer reaction channels respectively, as shown schematically in Fig. 2. The present measurement is unique in the sense, that the two compound residues are formed *in-situ* in the same experiment, with overlapping excitation energy spectrum, which has helped us to employ surrogate ratio method to extract the ${}^{233}\text{Pa}(n, f)$ cross section. The ground state Q-values (Q_{gg}) for ${}^{232}\text{Th}({}^6\text{Li}, \alpha){}^{234}\text{Pa}$ and ${}^{232}\text{Th}({}^6\text{Li}, d){}^{236}\text{U}$ transfer reactions are, 6.77 MeV and -6.05 MeV respectively. Because of the positive and negative Q-value of the deuteron and alpha transfer channels, it has been possible to populate the ${}^{234}\text{Pa}$ and ${}^{236}\text{U}$ compound systems at overlapping excitation energies, in ${}^6\text{Li} + {}^{232}\text{Th}$ transfer reactions. The possibility of positive and negative Q-value transfer channels is only possible in case of ${}^6\text{Li}$ and ${}^7\text{Li}$ -induced reactions. This is an example



how the structure of the projectile is affecting the reaction dynamics. In the present work, using a single target the compound nuclei, ^{234}Pa and ^{236}U are formed *in-situ* in two different direct reaction channels $^{232}\text{Th}(^6\text{Li}, \alpha)^{234}\text{Pa}$ and $^{232}\text{Th}(^6\text{Li}, d)^{236}\text{U}$ respectively. By using the same target to populate two compound systems, the uncertainty due to the target thickness is eliminated.

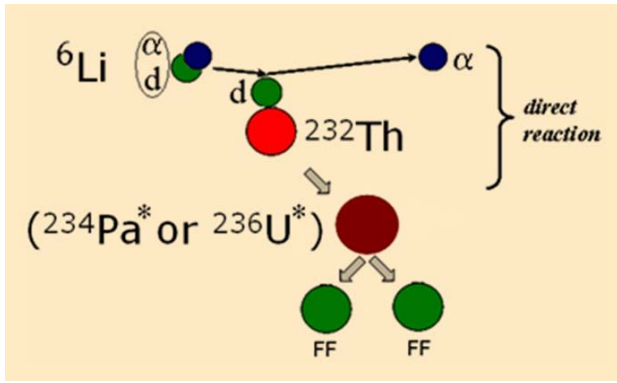


Fig. 2: Schematic view of ^{234}Pa and ^{236}U compound nuclei formed in $^6\text{Li}+^{232}\text{Th}$ reaction.

In this method, the Projectile-Like-Fragment (PLF)-singles and coincidence between PLF and fission fragment measurements are carried out, to determine the fission decay probabilities of the ^{236}U and ^{234}Pa compound nuclei produced in the transfer reactions, by dividing the number of PLF-fission coincidences (N_{α_i-f}) by associated PLF-singles (N_{α_i}) data as follows:

$$\Gamma_f^{CN}(E_{ex}) = \frac{N_{\alpha_i-f}}{N_{\alpha_i}}, \quad (1)$$

Where α_i denotes the α -particle or deuteron PLF channel, corresponding to ^{234}Pa or ^{236}U compound nucleus respectively. The relative fission probabilities of the compound nuclei are multiplied with relative neutron capture cross sections of corresponding surrogate reactions $\sigma_{n+^{233}\text{Pa}}^{CN}$ and $\sigma_{n+^{233}\text{U}}^{CN}$ to obtain the ratio of the compound nuclear reaction cross section at same excitation energies of $n+^{233}\text{Pa} \rightarrow ^{234}\text{Pa} \rightarrow \text{fission}$ and $n+^{235}\text{U} \rightarrow ^{236}\text{U} \rightarrow \text{fission}$ reactions as follows:

$$\frac{\sigma_f^{n+^{233}\text{Pa} \rightarrow ^{234}\text{Pa}}(E_{ex})}{\sigma_f^{n+^{235}\text{U} \rightarrow ^{236}\text{U}}(E_{ex})} = R(E_{ex}) = \frac{\sigma_{n+^{233}\text{Pa}}^{CN}(E_{ex})}{\sigma_{n+^{235}\text{U}}^{CN}(E_{ex})} \times \frac{\Gamma_f^{^{234}\text{Pa}}(E_{ex})}{\Gamma_f^{^{236}\text{U}}(E_{ex})}. \quad (2)$$

The $n+^{235}\text{U} \rightarrow ^{236}\text{U} \rightarrow \text{fission}$ cross section which is well measured, has been used as reference monitor, to determine $n+^{233}\text{Pa} \rightarrow ^{234}\text{Pa} \rightarrow \text{fission}$ cross section from the measurement. This is a new hybrid surrogate approach, which involves aspects of both the absolute and ratio surrogate method.

Experimental Details

A self-supporting thorium target of thickness 2.0 mg/cm^2 , was bombarded with ^6Li beam of energy $E_{lab} = 38.0 \text{ MeV}$, from 14MV Pelletron accelerator at Mumbai. A solid state ΔE -E telescope of thickness $150.0 \mu\text{m} - 1.0 \text{ mm}$ was kept at $\theta_{lab} = 90^\circ$ with respect to the beam direction around the transfer grazing angle, to identify the PLFs. A 16-strip solid state detector (each strip of size $2.0 \text{ mm} \times 64.0 \text{ mm}$) was placed at back angle covering laboratory angular range of 141° to 158° , to detect fission fragments in coincidence with PLFs. The ratio of the coincidence to single counts for $^{232}\text{Th}(^6\text{Li}, \alpha)^{234}\text{Pa}$ and $^{232}\text{Th}(^6\text{Li}, d)^{236}\text{U}$ reaction channels were determined, as a function of excitation energy.

Results and Discussion

The ratio of coincidence to single counts, corresponds to fission decay probability of the compound systems formed in the transfer reaction. The ΔE and E silicon detectors were energy calibrated by measuring elastic scattering at different energies and angles. The proton, deuteron, triton, α -particles and ^6Li are uniquely identified, by plotting ΔE against the total energy $\Delta E + E_{res}$. This plot was transformed to create an effective Particle Identification (PI) versus energy plot, which was generated using the linearization function ($\text{PI} = b(E_{tot}^{1.95} - E^{1.95})$), where E_{tot} is the total particle energy, E is the energy deposited in the E detector and 'b' is a constant. Fig. 3 shows a typical PI versus energy curve for the PLF telescope. The PI parameter has been zoomed to show p, d, t and α PLFs clearly, thereby the elastic channel has gone out of the scale and not shown in Fig.3. The excitation energy spectra of the target-like residues of ^{234}Pa and ^{236}U were determined,



employing two-body kinematics for ${}^4\text{He}$ and deuteron PLF channels. The excitation energy spectra so obtained for ${}^{234}\text{Pa}$ and ${}^{236}\text{U}$ nuclei, are shown in Fig. 4. The excitation energy spectra obtained for PLF-fission fragment

coincidence are also shown in the same figure. The ratio of coincidence to singles counts are determined for ${}^{234}\text{Pa}$ and ${}^{236}\text{U}$ nuclei, in the excitation energy range 17.0 MeV to 22.0 MeV in steps of 1.0 MeV .

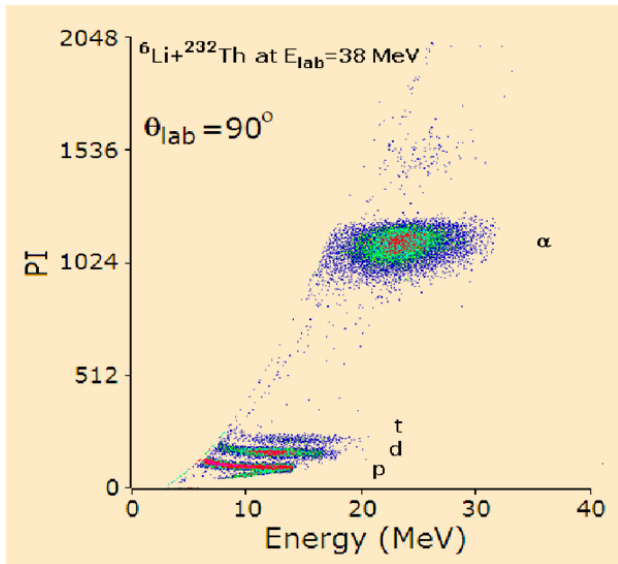


Fig. 3: Particle identification plot for ${}^6\text{Li}+{}^{232}\text{Th}$ at $E_{lab}=38$ MeV.

For each excitation energy bin, the ratio of fission decay probability of ${}^{234}\text{Pa}$ to ${}^{236}\text{U}$ is determined. The $n+{}^{235}\text{U} \rightarrow {}^{236}\text{U} \rightarrow$ fission reaction cross section is taken as reference monitor from ENDF/B-VII.0 [6]. The neutron capture cross sections are calculated by EMPIRE-2.19 code [11], for ${}^{235}\text{U}$ and ${}^{233}\text{Pa}$ nuclei in the excitation energy range 17.0 MeV to 22.0 MeV. Using Eqs. (1) and (2), the ${}^{233}\text{Pa}(n, f)$ cross sections as a function of excitation energy are obtained over the measured excitation energy range. The equivalent neutron energy, E_n , in the reaction ${}^{233}\text{Pa}(n, f)$ is related to excitation energy by the relation ${}^{233}\text{Pa}(E_{ex}, n, f) = {}^{233}\text{Pa}((233/234)E_n + S_n({}^{234}\text{Pa}), n, f)$, where S_n is the neutron separation energy of ${}^{234}\text{Pa}$ ($S_n = 5.22$ MeV). The ${}^{233}\text{Pa}(n, f)$ cross sections, as function of equivalent neutron energy so obtained, is shown in Fig. 5 along with the EMPIRE-2.19

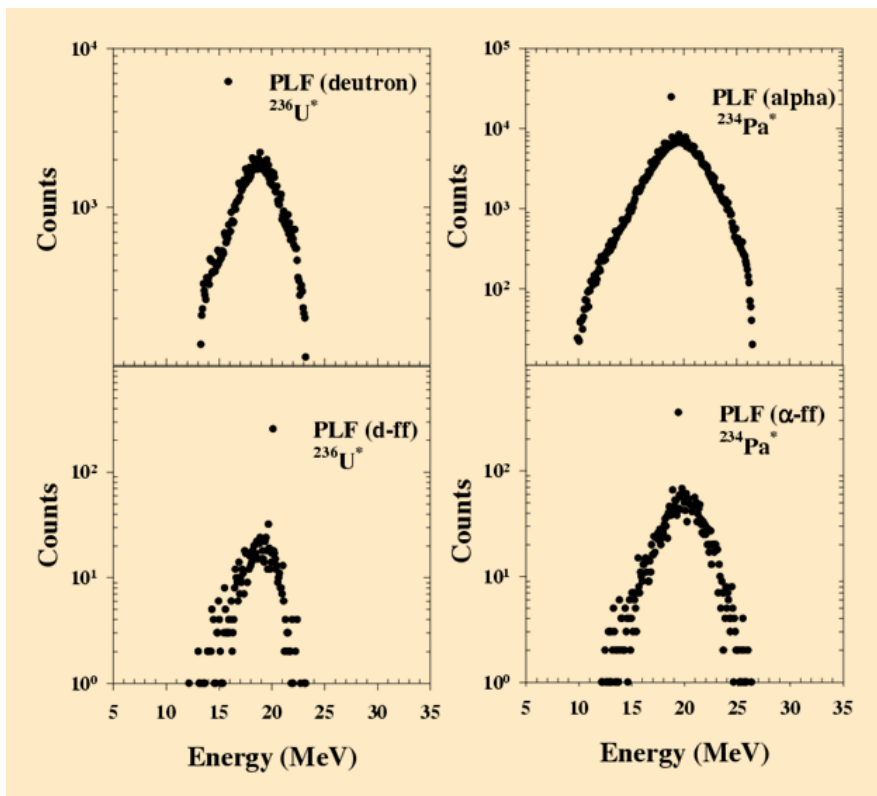


Fig. 4: Excitation energy spectra of target like fragments in ${}^6\text{Li}+{}^{232}\text{Th}$ reaction with (bottom) and without (upper) coincidence with fission fragments.

predictions in the neutron energy range 1.0 MeV to 20.0 MeV, for various sets of fission barrier parameters available from evaluations. The fission cross-sections predicted for RIPL-2 [12] fission barriers do not agree with experimental data at all energies. However, if one uses the fission barriers given by RIPL-1 [13], the calculated cross sections give good agreement with experimental data at low energies, but there is a significant disagreement at higher energies as shown in Fig. 5. The prediction of EMPIRE-2.19 using fission barrier heights obtained from Barrier Formula (BF) [14], compares reasonably well with the experimental data.

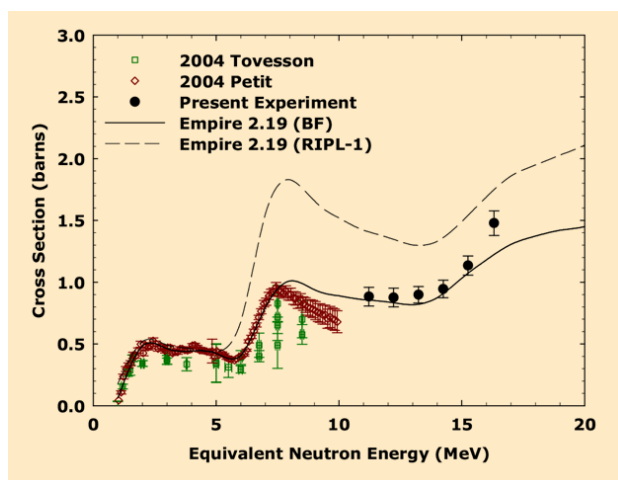


Fig.5: Experimental $^{233}\text{Pa}(n,f)$ cross-section along with EMPIRE-2.19 predictions (see text).

Summary and Conclusion

In summary, we have employed a new surrogate approach, which involves aspects of both absolute and ratio method in a unique way, to determine the $^{233}\text{Pa}(n,f)$ cross sections in the equivalent neutron energy range of 11.5 MeV to 16.5 MeV, using $^6\text{Li}+^{232}\text{Th}$ transfer-fission coincidence measurements. Present experimental data on $^{233}\text{Pa}(n,f)$ reaction cross section along with the data from the literature, covering equivalent neutron energy range 1.0 MeV to 16.5 MeV have been compared, with the predictions of EMPIRE 2.19 for fission barrier heights, corresponding to RIPL-1, RIPL-2, and Barrier Formula. In the present work, we have demonstrated the use of a surrogate reaction method, to determine $^{233}\text{Pa}(n,f)$ cross section. Recently, we have also carried out $^{234}\text{Pa}(n,f)$ cross section measurement by hybrid surrogate method, using $^7\text{Li}+^{232}\text{Th}$ reaction. The neutron-induced fission cross sections for a large number of reactions such as $^{241}\text{Pu}(n,f)$, $^{241}\text{Am}(n,f)$, $^{243}\text{Cm}(n,f)$, $^{244}\text{Cm}(n,f)$, and $^{245}\text{Cm}(n,f)$ can be measured by potential surrogate reactions, with ^6Li beam on available stable targets. The neutron induced fission cross section measurements by surrogate methods with $^6,7\text{Li}$ beams are being planned at the Pelletron-LINAC facility.

Acknowledgements

The author thanks Dr. S. Kailas for discussions and his keen interest in the present work. The author also acknowledges the collaboration in this work, with Drs. R.K. Choudhury, A. Saxena, D.C. Biswas, B. V. John, E. T. Mirgule, S. Santra, and S. Ganeshan.

References

1. <http://www.barc.ernet.in/publications/eb/golden/reactor/toc/chapter1/1.pdf>
2. V.G. Pronyaev, IAEA Report No. INDC(NDS)-408 (1999).
3. F. Tovesson, F.J. Hamsch, A. Oberstedt, B. Fogelberg, E. Ramstrom, and S. Oberstedt, *Phys. Rev. Lett.*, 88, 062502 (2002).
4. F. Tovesson *et al.*, *Nucl. Phys. A* 733, 3 (2004).
5. M. Petit *et al.*, *Nucl. Phys. A* 735, 345 (2004).
6. M.B. Chadwick *et al.*, *Nuclear Data Sheets* 107, 2931(2006)
7. K. Shibata *et al.*, *J. Nucl. Sci. Technol.* 39, 1125 (2002).
8. J. T. Burke *et al.*, *Phys. Rev. C* 73, 054604 (2006).
9. B. F. Lyles *et al.*, *PRC* 76, 014606 (2007).
10. B.K. Nayak, A. Saxena, D.C. Biswas, E.T. Mirgule, B.V. John, S. Santra, R.P.Vind, R.K. Choudhury and S. Ganesan *Phys. Rev. C* 78, 061602(R)(2008).
11. M. Herman, R. Capote, B.V. Carlson, P. Oblo•insky, M. Sin, A. Trkov, H. Wienke and V. Zerkin, *Nuclear Data Sheets*, 108, 2655-2715.
12. A. Mamdouh *et al.*, *Nucl. Phys.* A664, 389 (1998); A679, 337 (2001).
13. V.M. Maslov, in RIPL-1 Handbook, TECDOC-000, IAEA Vienna (1998).
14. S. K. Gupta and A. Saxena, in Proc. of 8th Korean Nuclear Data Workshop, held at Pohang, during 25th -26th August 2005.



Microstructure Characterization of Zr-2.5Nb Alloy Pressure Tube Manufactured by Novel Fabrication Routes and Irradiated Pressure Tubes by Transmission Electron Microscopy

D. Srivastava

Materials Science Division

Dr. D. Srivastava is the recipient of the DAE Homi Bhabha Science & Technology Award for the year 2009

Abstract

The Indian Pressurized Heavy Water Reactors (PHWRs) use Zr-2.5% Nb pressure tubes (PT) and the in-reactor performance of these tubes, such as irradiation creep and growth behaviour, depends strongly on their microstructure and texture. The microstructure and texture of the tube essentially depends on the combination of different thermomechanical treatments imparted during manufacturing of these pressure tubes. In the present paper, the microstructure evolution has been studied for pressure tubes, produced by novel heat treated condition. The finished microstructure consisted of fine α lamellae with distribution of nanometer size β phase, along the α/α interfaces having composition 75-80wt%Nb. Microstructure evolution in new optimized fabrication routes for manufacture of cold worked pressure tubes has been described here. The microstructure comprises of long α grain with higher aspect ratio and β being present as thin film having composition 15-20wt%Nb. This new fabrication route is proposed to be used, to manufacture pressure tubes for all upcoming PHWR reactors. The paper also shows irradiated microstructure characterization at different locations of the first pressure tube, obtained from the KAPS2 reactor. The study shows substantial modification in β morphology.

Introduction

The present generation of Indian PHWRs use Zr-2.5%Nb pressure tubes. KAPS-2 is the lead reactor in Indian PHWR reactors, using pilgered Zr-2.5% Nb PTs fabricated by the Nuclear Fuel Complex, Hyderabad. The satisfactory performance and the life of the pressure tubes depend mainly upon the extent of degradation of the mechanical properties, corrosion under the influence of high temperature coolant, neutron flux and dimensional instability as a result of irradiation creep and growth in the reactor condition [1-3]. Irradiation growth and irradiation creep govern the performance of the

cladding and the pressure tube material to a great extent. Since dimensional changes and mechanical property degradation can limit the life of PT, it is essential to study and develop an understanding of the microstructural evolution at different levels of manufacturing and its exposure to neutron irradiation. Creep and growth are greatly influenced by the microstructural parameters such as shape, size and aspect ratio of the α -lamellae, the distribution and morphology of the β -phase, the interfacial structure, dislocation density and the crystallographic texture [1-3]. These aspects are sensitive to the manufacturing process of the pressure tube.



The present paper describes the microstructure evolution in a new fabrication route, for cold worked pressure tubes. This route has been developed after an industrial scale trial of nine different routes at NFC. Heat treated pressure tubes are known to show improved creep performance [4]. The present paper describes the microstructure assessment at different stages of fabrication of heat treated pressure tube. Samples taken from an irradiated PT in KAPS2 are evaluated and compared with the microstructure of the unirradiated, as-fabricated material.

Results and Discussion

Microstructural Study of Zr-2.5Nb alloy Heat Treated Pressure Tube Fabrication

TEM micrographs after first extrusion showed dynamic recrystallization of the α grain. Refined and uniform microstructure suggested that, cast structure was completely removed during hot extrusion process, β phase was present at the α/α interface Fig. 1(a) [5-6]. The billet was β quenched to obtain homogenous microstructure, texture and chemical homogeneity. β quenched microstructure showed martensitic microstructure consisting of coarse lath martensites (Fig. 1(b)). The quenched billet was extruded to hollow blank. Microstructure after second hot extrusion showed that α grains become elongated in the axial direction of the tube and thin in the radial direction (Fig. 1(c)). The longitudinal section exhibited α phase of lamellar morphology aligned along the direction of the extrusion. Transverse section exhibited α lamellae, whose width and thickness were not similar. The average length, width and thickness of α lamellae were in the range of 15-20 μm , 1-2.5 μm and 0.3-0.5 μm respectively. β phase was present as thin wafer between two α lamellae, having average thickness of 0.02-0.05 μm . The extruded tube was further pilgered, which was showing heavily deformed microstructure. Subsequent to pilgering, $\alpha+\beta$ quenching was carried out, which is the most critical step in the fabrication of heat treated pressure tube. Quenching treatments were carried out in a controlled fashion, using quenching dilatometer, to study the evolution of microstructures as a function of different cooling rates.

Systematic studies on transformation from $\alpha+\beta$ phase field as a function of cooling rate are far from being extensive in published literature. In addition to cooling rate, effect of soaking temperature in the $\alpha+\beta$ phase field has been also examined in the present study. The samples cooled from 883 $^{\circ}\text{C}$ at different cooling rates in argon, showed primary α and transformed β phases. Samples cooled at the rate of 100 $^{\circ}\text{C}/\text{sec}$ and 50 $^{\circ}\text{C}/\text{sec}$ showed predominantly internally twinned martensite and internally slipped martensite structure respectively. Below this cooling rate, transformed β product was observed to be Widmanstätten $\alpha+\beta$. On the basis of these observations it could be concluded, that in order to obtain primary α and martensitic microstructure after $\alpha+\beta$ quenching, a minimum cooling rate is required which is a function of soaking temperature. On the basis of the results obtained during controlled heat treatment performed in quenching dilatometer, 883 $^{\circ}\text{C}$ was selected as soaking temperature and water as the quenching medium for $\alpha+\beta$ quenching operation for large dimension tube (100 mm OD X 4.5 mm WT X 500 mm length). TEM micrographs revealed $\alpha+\beta$ quenched microstructure consisting of fine martensite phase along with 20-25% primary α volume fraction (Fig. 1(d)). The $\alpha+\beta$ quenched samples were cold deformed (by pilgering) to the extent of 23%. Cold deformation of martensitic microstructure resulted in considerable increase in the dislocation density and dislocation substructure. (Fig. 1(e)). These defects acted as nucleation sites for precipitation of β_{Nb} from the supersaturated martensitic phase during subsequent aging process. Ageing temperatures 540 $^{\circ}\text{C}$ below the recrystallization temperature were used in the present study, after the 2nd pilgering operation. Complete tempering of martensite at 540 $^{\circ}\text{C}$ was observed whereas no recrystallization of the microstructure was observed. β precipitates (size less than 15nm) were observed only at the α/α lath interface (Fig. 1(f-g)). Energy Dispersive Spectroscopy (EDS) analysis in TEM of samples, aged at 540 $^{\circ}\text{C}$, showed 75-80%Nb in β phase. This study thus shows that a temperature of 540 $^{\circ}\text{C}$ is required to attain equilibrium concentration of Nb (85%) in β precipitates during aging. Finally autoclaving treatment was carried out at 290 $^{\circ}\text{C}$ for 120 hrs, which did not modify the microstructure to any noticeable extent (Fig. 1(h)).

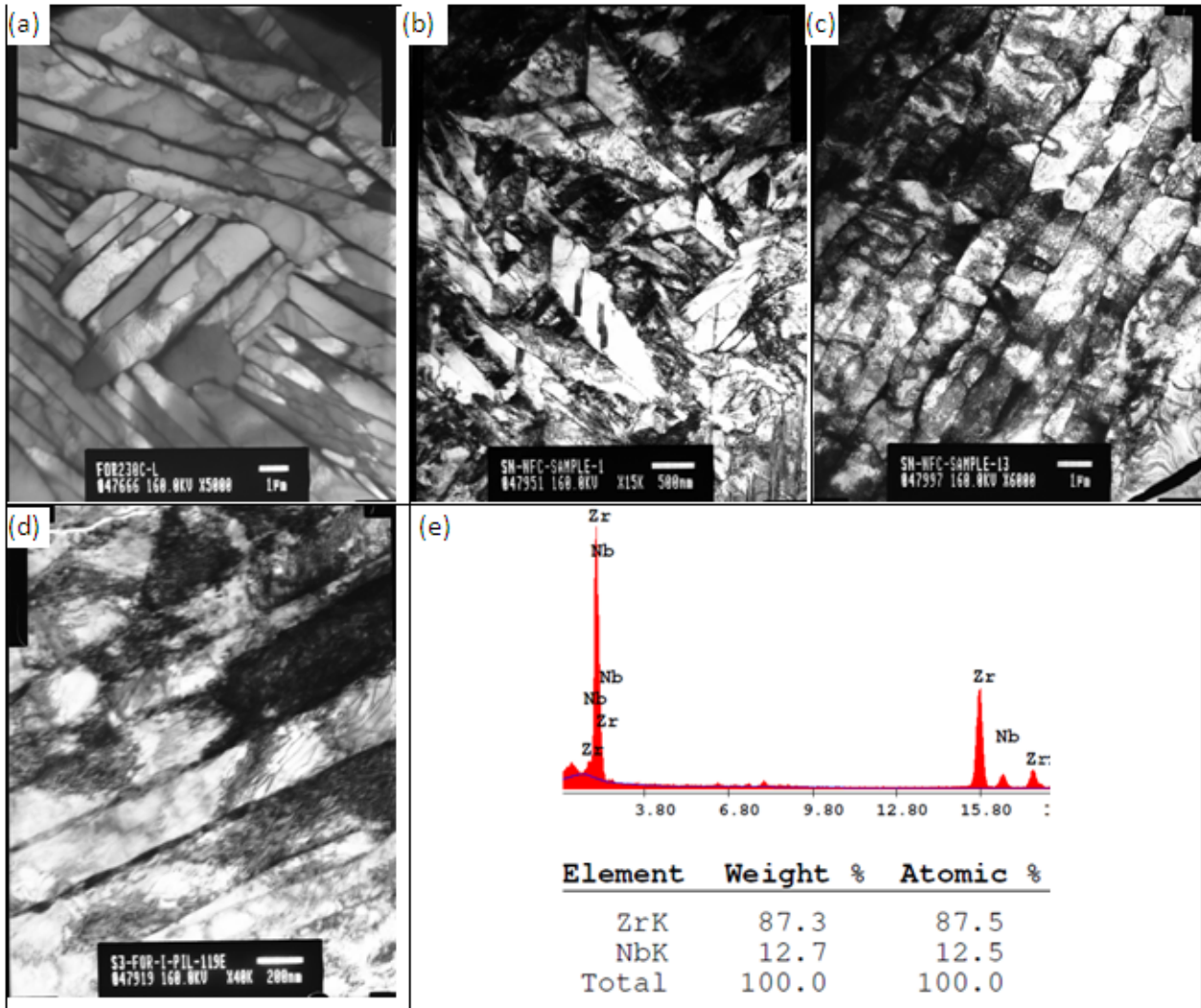


Fig. 1: TEM Microstructure evolution at different stages of new fabrication route of cold worked Zr-2.5Nb alloy pressure tubes (a)Forged (b) β quenched (c) first pilgered (d) autoclaved (e) EDS analysis of β phase

Microstructural Study of Zr-2.5Nb alloy Cold Worked Pressure Tube Fabrication by Optimized Fabrication Routes

The conventional method (CANDU) for fabrication of cold worked Zr-2.5Nb alloy pressure tubes, involves hot extrusion followed by 25 pct cold drawing. Zr-2.5% Nb alloy pressure tubes in NFC fabrication, involves hot extrusion (with lower extrusion ratio) and two-stage pilgering with an intermediate annealing treatment followed by autoclaving. The microstructure of the pressure tube fabricated at NFC has considerably different microstructure than those reported for CANDU pressure

tube. The α grains are much finer and aspect ratio is also small [7]. The β phase is mostly present in the globalised form unlike stringer in CANDU tube and it is substantially richer in Niobium. In order to examine the role of individual fabrication stages, in NFC, a campaign was carried out to fabricate pressure tube with different fabrication parameters. In all, pressure tubes were fabricated by nine different fabrication routes. The objective was to examine which route gives the best desirable microstructural, textural and mechanical properties. The important variations in Zr-2.5Nb pressure tube fabricated through different routes are given below:



- (i) Single stage forging and two step forging vs single stage extrusion process for breaking the ingot cast structure.
- (ii) Comparison of tube produced with different extrusion ratios.
- (iii) Comparison of the tube produced with two stage pilgering and with single stage pilgering
- (iv) Role of stress relief treatment after extrusion
- (v) Final 25 % cold work by single stage drawing versus single stage pilgering .

The important microstructural observations in the pressure tubes fabricated through above routes are summarized below:

1. Two step forging route has shown more homogenous microstructure. Grains were observed to be longer and aspect ratio was much higher, which is preferable.
2. There was variation in microstructure from leading end to trailing end in single stage forging and extrusion processes of breaking cast structure. In general, trailing end microstructure was more lamellar and homogenous.
3. Higher extrusion ratio has resulted in still higher aspect ratio (desired). The variation in microstructure from leading end to trailing end was much smaller in this case and microstructure appeared more uniform. Single pass always resulted in continuous β along the α/α interface.
4. Intermediate annealing treatment resulted in the globulization of β phase in several regions. The composition analysis has shown that these β were enriched to the level of 25 to 45 wt% of Nb.
5. Cold drawn process has shown that microstructure was very close to that observed in the tube produced by CANDU route
6. The α lamellae in CANDU pressure tubes were much longer upto 20 micron length and β phase was continuous and the composition was always in the range of 15 to 20 wt%.
7. NFC produced Pressure Tubes: The α grains were not lamellar in all the regions; the grain size was much smaller. The β was not continuous in many regions and they had globulized both at the α/α interface as well as within the α grains. The β phase composition varied from 15-45 %.

On the basis of this study described in detail in report [8], it has been proposed to fabricate Zr-2.5Nb alloy pressure, by the following fabrication route which involves two stages forging to billet followed by β quenching and extrusion to blank with higher extrusion ratio. The blank is then pilgered to final size and autoclaved at 400°C for 24 hours. The microstructure developed during each stage of this fabrication route is described in Fig. 2. The forged microstructure showed widmanstatten α phase and β phase being present at α/α interface (Fig. 2(a)). The grains were uniformly distributed from one end to the other end of the forged billet. The microstructure was also uniform from center to the edge of the billet. The β quenched structure showed complete martensitic microstructure. The extrusion of billet with higher extrusion ratio resulted in much longer α phase (15-20 μ m) and the aspect ratio was in the range of 1:10:70. The β phase was present as thin film between α lamellae. The single pilgering was done to obtain pressure tube in 25% cold worked condition. Microstructure showed higher density of dislocations within α grain. Autoclaving treatment reduced the dislocation density to some extent. However, the finished tube exhibited lamellar α with stringer of β phase in between. No globulisation of β phase was seen in this route and EDS analysis has shown that β composition was in the range of 15-wt20%Nb.

Microstructural Studies on Irradiated KAPS2 Zr-2.5Nb alloy Pressure Tube

TEM micrographs of the unirradiated S-07 pressure tube off cuts of KAPS2 reactor, is shown in Fig. 3(a). The samples showed typical lamellar microstructure of α and

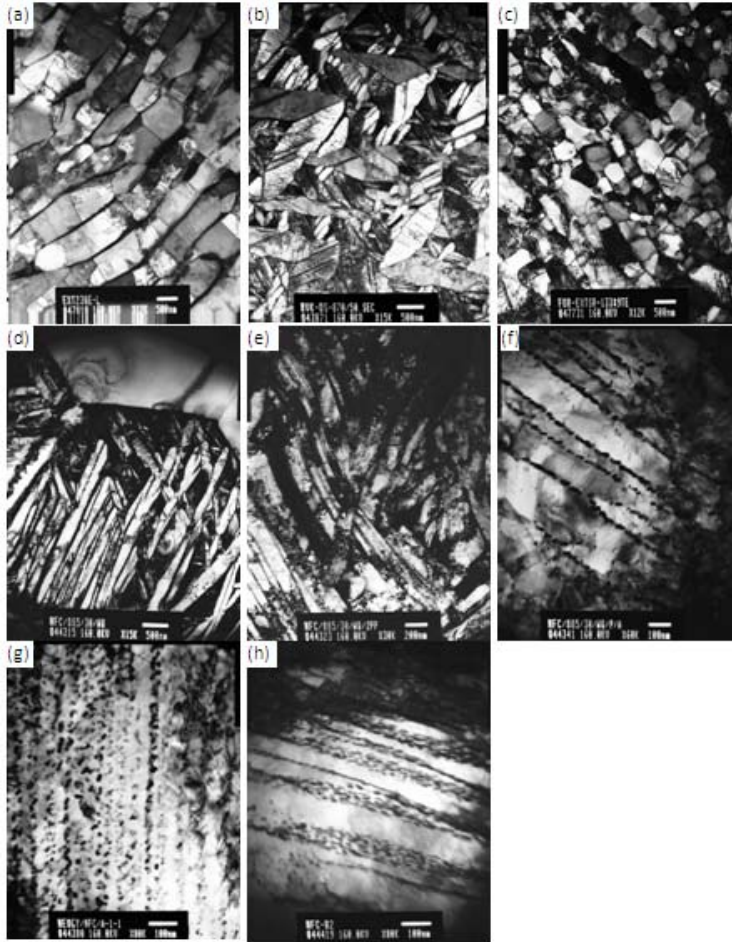


Fig. 2: TEM Microstructure evaluation at different stages of fabrication route of heat treated Zr-2.5Nb alloy pressure tubes (a)I-extrusion (b) β quenched (c)II extrusion (d) $\alpha+\beta$ quenched (e) ii pilgered (f) and (g) aged(h) autoclaved

β grains. However, many of the regions exhibited non-lamellar microstructure as well. The β -phase morphology varied from continuous fiber to globular. Niobium content was 10-12% in the continuous film of β and 20-40 % percent in case of globulised β -phase. TEM micrographs of the samples obtained from the different locations of the irradiated pressure tube are shown in Figs. 3(b)-(l) [10]. Unlike in the case of the reported irradiated Zircaloy-2 pressure tube samples [9], no significant defects, generated due to irradiation, could be seen. Hydride platelets were also absent in the irradiated Zr-2.5%Nb pressure tube, unlike the irradiated Zircaloy-2 pressure tube samples, which showed significant number of hydride platelets. The grain morphology of α -Zr phase did not

change appreciably after irradiation in the Zr-2.5%Nb alloy pressure tube. The major observations in the microstructure in different locations were as follows. In locations from inlet to 381 mm of PT, the microstructure did not change appreciably (Fig. 3(b)). Recovery of a part of the cold work could be seen. The α and β -phase morphology appeared to be similar as seen in the un-irradiated samples. In the region of 381 to 2000 mm from inlet, it was seen that lamellar structure of the α -phase was retained (Fig. 3(c)). Considerable recovery of the cold worked structure could be seen. The β phase had globulised in large number of regions but remained at the α/α interface. Further away (2000 to 4250 mm), the microstructures appeared to have changed considerably and extensive modification in β morphology was seen (Fig. 3(d-g)). It appeared that β phase had dissolved and re-precipitated within the α -Zr matrix. The volume fraction of the β phase had considerably reduced, suggesting that it had got enriched in Nb in most of the cases. Considering the reduction in the volume fraction of β phase, it is expected that β had got enriched to the level of 50-60 % Nb. The β phase had completely globulised and was present within the α lamellae and no β -phase could be seen at α/α interfaces in many regions (Fig. 3(h-j)). The region 4250mm from inlet to outlet at the end of the microstructure appeared to be similar to those seen near inlet. However, the extent of recovery of the cold worked structure was much higher and the β -Zr was marginally modified (Fig. 3(k-l)).

Conclusions

The present study shows the microstructure at different stages of fabrication characterized by TEM. The microstructure is shown for the heat treated pressure tube fabricated for the first time at NFC Hyderabad. The finished microstructure consisted of fine α lamellae with distribution of nanometer size β phase, along the α/α

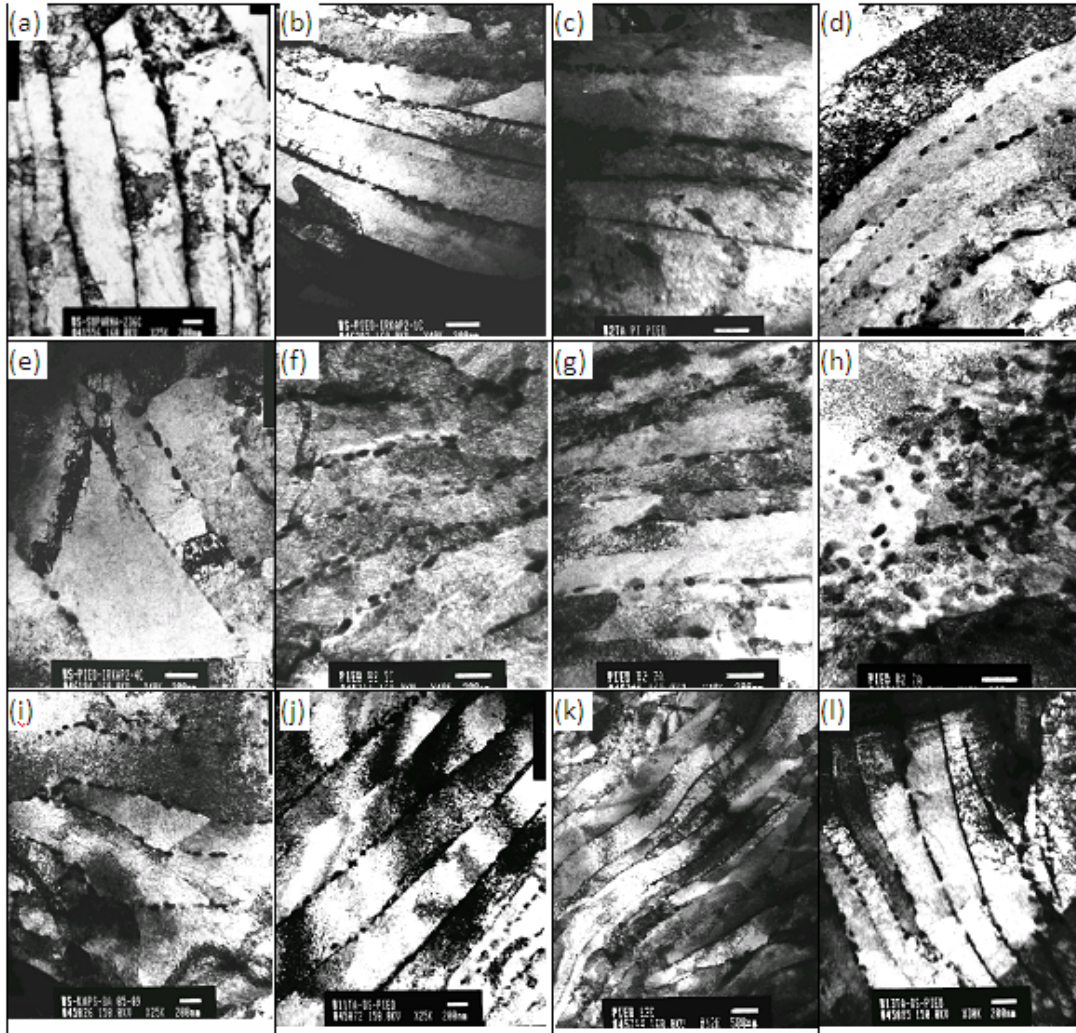


Fig. 3: TEM Microstructure Characterization of S-07 KAPS2 reactor pressure tube (a) unirradiated and (b-l) irradiated at different locations of pressure tube.

interfaces having composition 75-80wt%Nb. The microstructure developed during each stage of the new fabrication route, for fabrication of pressure tube of 700MW PHWR reactor, is also described. The final microstructure comprises of long α grain with higher aspect ratio and β being present as thin film having composition 15-20wt%Nb. The study also shows irradiated microstructure characterization at different locations of the first pressure tube obtained from the KAPS2 reactor. The study shows substantial modification in β morphology.

Acknowledgement

The author wishes to acknowledge that the work of pressure tube fabrication was carried out under the collaboration between Physical Metallurgy Section, MSD, BARC and Zirconium Fabrication Plant, Nuclear Fuel Complex, Hyderabad. The work on microstructural study of irradiated pressure tube material was carried out through collaboration between Physical Metallurgy Section, MSD, BARC and PIED, BARC. The contributions of K.V. Mani



Krishna, S. Neogy and Dr. G. K. Dey of MSD is thankfully acknowledged. The contributions of colleagues of ZFP, NFC, N. Saibaba, Phani Babu, S.K. Jha, V. Kumar, V. Deshmukh and V. Ramanna have been paramount, in the fabrication of the pressure tube and their support for carrying out this study is gratefully acknowledged. The contributions of Shri S.A. Anantharaman, E. Ramadasan and Suparna Banerjee for carrying out TEM studies of irradiated pressure tube material are appreciatively acknowledged.

References

1. B. A. Cheadle, C. E. Coleman and H. Licht, *Nucl Tech.*, vol. 57, 1982, p. 413
2. R. A. Holt, *JNM* 372 (2008) 182-214
3. D.K. Rodgers, C.E. Coleman, M. Griffiths, G.A. Bickel, J.R. Theaker, I. Muir, A.A. Bahurmuz, S. St. Lawrence, M. Resta Levi *JNM* 383 (2008) 22–27
4. M Koike and T. Asada *JNM* 159 (1988) 62-74
5. N. Saibaba, S. K. Jha, S. Tonpe, Kumar Vaibhaw, V. Deshmukh, S. V. Ramana Rao, K.V. Mani Krishna, S. Neogy, D. Srivastava, G. K. Dey, R. V. Kulkarni, B.B. Rath, E. Ramadasan and S. A. Anantharaman, In Press, 2011 Zirconium ASTM-STP, China.
6. N. Saibaba, S. K. Jha, S. Tonpe, V. Kumar, V. Deshmukh and Ramana Rao, D. Srivastava, S. Neogy, K.V. Mani Krishna, and G. K. Dey, E. Ramadasan, R. V. Kulkarni, B.B. Rath, and S. A. Anantharaman, BARC External Report BARC/2010/E/010.
7. D. Srivastava, G. K. Dey, and S. Banerjee *Metallurgical and Materials Transitions*, **26A**(1995) 2707
8. D. Srivastava, K.V. Mani Krishna, S. Neogy, G. K. Dey, S.K. Jha and N. Saibaba (to be published)
9. D. Srivastava, R. Tewari, G. K. Dey, B. P. Sharma and D. N. Sah BARC External Report No. BARC/2005/E/023, 2005
10. D. Srivastava, S. Neogy, Suparna Banerjee, E. Ramadasan, S. Anantharaman and G. K. Dey BARC External Report BARC/2011/E/007.



Remediation of radioactive wastes using novel extractants and novel separation techniques

P.K. Mohapatra

Radiochemistry Division

Dr. P.K. Mohapatra is the recipient of the DAE Homi Bhabha Science & Technology Award for the year 2009

Introduction

Radioactive waste remediation, especially, that related to High Level Waste (HLW), is essential, due to the presence of long-lived radionuclides with half lives as high as millions of years. Selective separation of the long-lived radionuclides, followed by their burning in high flux reactors/accelerator driven sub-critical systems are being proposed as key strategies, for Partitioning & Transmutation (P&T), in the safe management of radioactive wastes [1]. Selective separation is possible, by the design and synthesis of efficient extractants. Therefore, the future of actinide separations lies in the design and synthesis of selective, efficient, eco-friendly and radiation-resistant solvents, which can permit high actinide loading (without third phase formation), such as higher trialkyl phosphates and substituted monoamides, Carbamoyl Methyl Phospine Oxide, malonamides, glycolamides, etc. Some of these extractants relevant for actinide partitioning are shown in Fig. 1. As lanthanide - actinide separation is another key separation, step prior to the 'burning' of minor actinides, there have been considerable R&D efforts in such separation

studies, using N-donor ligands such as BTP (bis-triazinylpyridine) and BTBP (bis-triazinylbipyridyl) and S-donor ligands such as branched dithiophosphinic acids. Finally, there is a need to selectively separate ^{137}Cs , ^{90}Sr and Platinum Group Metals to enable recovery and utilization of these valuable isotopes, for a variety of purposes.

Novel separations employing microporous membranes, operating in the hollow fibre membranes, reverse osmosis / ultra-filtration modes, have found to be promising in many lab-scale studies. Membrane-based separation processes have shown rapid growth in the past few decades. In recent years, these processes have been found to be quite effective in areas such as treatment of industrial effluents, water purification, gas separation etc. with the ready availability of membranes of desired properties and configurations. Liquid membrane based separations, especially those involving Supported Liquid Membranes (SLM), have been found to be promising, as the selectivity displayed by the organic extractant can be suitably exploited [2]. Scale up issue is a challenge and modeling

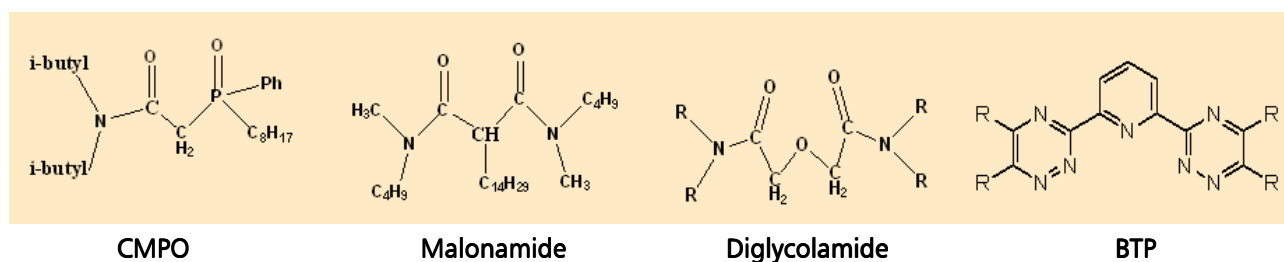


Fig. 1: Structures of reagents used for the extraction of trivalent actinides from acidic wastes



studies have indicated feasibility of the membrane separation methods for large scale applications.

Recovery of minor actinides

Current perception of radioactive waste management after operations involving the aqueous processing of the spent nuclear fuel materials, involves minor actinide partitioning using reagents such as CMPO, malonamides or diglycolamides (Fig. 1). At the Radiochemistry Division, BARC, extensive work has been carried out on solvent extraction studies involving these reagents, which include mixer-settler studies with simulated high level wastes, radiolytic stability and reusability [3,4]. Solvent extraction studies indicated that diglycolamides such as TODGA (N,N,N',N'-tetraoctyldiglycolamide) are by far the most suitable extractants for minor actinide recovery [1]. Subsequently, the transport behaviour of trivalent actinides and lanthanides has also been studied, using carriers such as CMPO, DMBDMDMA, TODGA and T2EHDGA (branched homolog of TODGA).

Transport of Am^{3+} from acidic feeds using either CMPO or DMBDMDMA in *n*-dodecane was limited, due to a very large co-transport of nitric acid. On the other hand, studies on the transport of Am^{3+} TODGA in *n*-dodecane as the carrier, were quite encouraging [5]. The transport studies on different actinide ions and fission products employing 0.1 M TODGA/*n*-dodecane as the liquid membrane in Flat Sheet Supported Liquid Membranes (FSSLM), from 3 M HNO_3 feed solutions, indicated quantitative transport of Am(III) and Eu(III) in 3 h, while about 5 h were needed for quantitative transport of Pu(IV) and Np(IV) (Fig. 2(a)).

In view of the low flux of Simulated High Level Waste feed, it was required to carry out studies with Hollow Fiber Supported Liquid Membrane (HFSLM), containing reagents such as CMPO, DMBDMDMA and the diglycolamides viz. TODGA and T2EHDGA. The transport of Am(III) with TODGA and T2EHDGA as carrier extractants, suggested quantitative transport of Am(III) within 30 minutes (Fig. 2(b)). Under identical conditions of feed and strip solutions, only ~65% and 50% Am(III) transport were observed for DMBDMDMA and CMPO, respectively which was attributed to very high acid

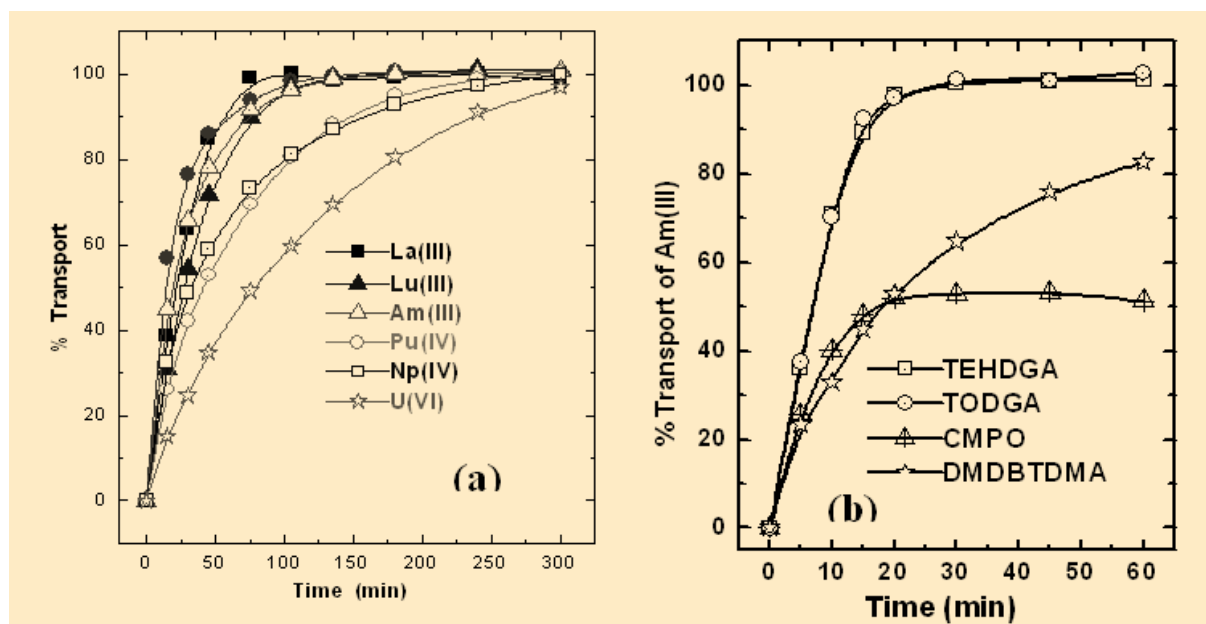


Fig. 2: (a) Transport of metal ions by TODGA-FSSLM; Membrane: 0.45 μm PTFE; Carrier: 0.1 M TODGA in *n*-dodecane; Feed acidity: 3M HNO_3 ; Strippant: Distilled water. (b) Transport of Am(III) by HFSLM of different solvents; Carrier: 0.1M TODGA + 0.5M DHOA, 0.2M TEHDGA + 30% iso-decanol, 1M DMBDMDMA and 0.2M CMPO + 1.2M TBP in NPH; Feed: 0.6g/L Nd at 3M HNO_3 (500mL); Receiver: Distilled Water (500mL); Flow rate: 200mL/min.



transport rates. Quantitative transport of Nd was seen in 30 minutes when 0.5 L feed solution containing 0.6 g/L Nd at 3 M HNO₃ was processed using 0.1 M TODGA + 0.5 M DHOA as carrier in the HFSLM technique. On the other hand, >99% transport of Nd was possible in 18 h using 20 L of feed and strip solutions. The product could be concentrated twice by maintaining a feed-to-strip volume ratio of 2:1 [6].

Lanthanide – actinide separations

Separation of lanthanides and actinides is a pre-requisite for the development of safer and economically viable methodologies of HLW management. We have carried out solvent extraction studies using di-alkyl-dithiophosphinic acids such as Cyanex-301, which under controlled conditions resulted in separation factor (D_{Am}/D_{Eu}) as high as 40,000 (Fig. 3 (a)) [7]. Our studies with substituted BTP and BTBP have not shown great promise, however, though it was possible to extract Am³⁺ from feeds containing as high as 0.1 M HNO₃. SLM studies using change to polypropylene membranes containing 0.1 M Cyanex-301 in *n*-dodecane as the carrier, pH 3.4

solution (sulphanilic acid buffer) as the feed and 0.1 M EDTA as the receiver, indicated quantitative transport (>99% in 4 h) of Am³⁺, while that of Eu³⁺ was negligible (Fig. 3 (b)) [8]. A synthetic solution containing ²⁴¹Am and several lanthanide radiotracers has revealed encouraging results, with DF values >100 for most of the contaminants. Lanthanide/actinide separation was also attempted by the HFSLM method, using Cyanex-301 and very encouraging results were observed. Feed Phase pH could be drastically brought down without affecting the separation efficiency. The decontamination factors for all the lanthanides were ~100, making this one of the most promising separation methods using HFSLM.

Bis-triazinyl pyridine (BTP, Fig. 1) derivatives have been suggested as alternative 'green' extractants, which also can separate trivalent lanthanides and actinides from acidic feeds. FSSLM studies carried out using Et-BTP in nitrobenzene + *n*-dodecane as carrier solvent, indicated preferential Am transport compared to the lanthanides used in the study, viz. La, Nd and Eu from a feed containing 0.1 M HNO₃ [9]. However, DF values were significantly lower (La: 34; Nd: 11; Eu: 4) as compared to those

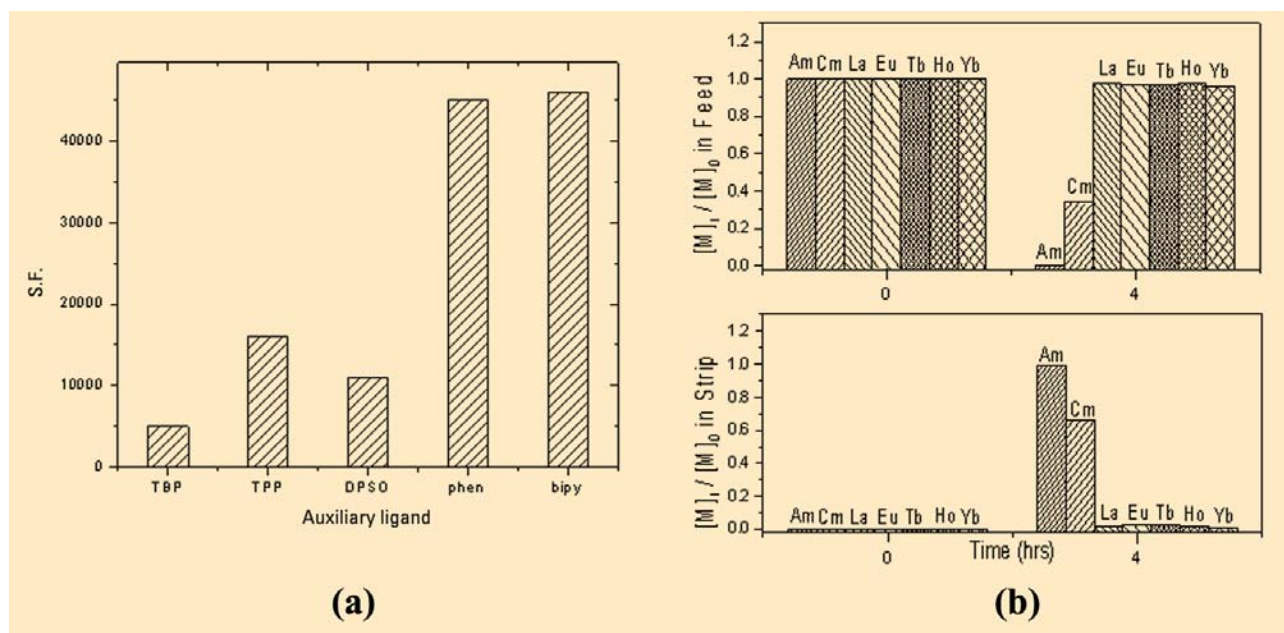


Fig. 3: (a) Separation factor values obtained from solvent extraction studies (data with phen and bipy are obtained at Radiochemistry Division, BARC). (b) FSSLM transport data showing efficient separation by the SLM method (top: feed; bottom: strip)



obtained with the Cyanex-301 system (>100 for all the lanthanides). Moreover, the membrane stability was poor.

Recovery of Pu from analytical waste using HFSLM

Compared to the application of SLM methods for U recovery, those for Pu separations are less common. Recovery of Pu from analytical wastes using liquid membrane technique appears challenging. Typically, major impurities in these wastes are Na, Fe, Ca, Al, Cr, Mg, Ni and Zn. Conventionally precipitation and ion exchange procedures are employed, for the recovery of Pu, which generates, large volume of liquid waste in glove box operations. In addition, radiation exposure to the operator due to ^{241}Am (daughter product of ^{241}Pu) is quite significant. At the Radiochemistry Division, HFSLM technique has been developed for the recovery of plutonium from analytical acidic waste, using 30%TBP/*n*-dodecane as the carrier.

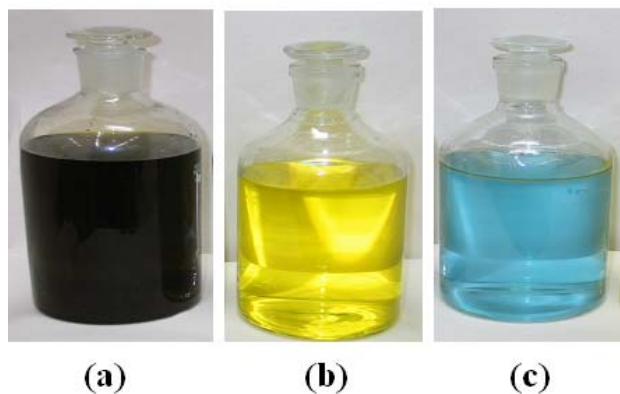


Fig. 4: The recovered plutonium and uranium from the analytical waste; (a) waste solution, (b) uranium solution, and (c) plutonium solution

The recovery of Pu from the waste was carried out in two stages. In the first stage, Pu(IV) and U(VI) were selectively transported into the receiver phase by TBP-HFSLM. About 96.2% U and 97.9% Pu were selectively transported into the receiver phase in 3 h. The Am(III) contamination in the product (U and Pu fraction) was found to be $<0.1\%$. In the subsequent stage, in the feed solution containing U and Pu, the valency of Pu was adjusted to Pu(III), which enabled separation of Pu from U. The TBP-HFSLM cycle was carried out using 0.1 M Na_2CO_3 as the receiver phase.

Samples of the recovered plutonium and uranium from the analytical laboratory waste, are shown in Fig. 4. Analysis of common metallic impurities in the Pu fraction was carried out by ICP-AES and the results indicated high DF values, suggesting purity of both U and Pu fractions as $>99\%$.

Recovery of Cs from high level waste

Cesium is one of the important elements formed from the fission of ^{235}U in the nuclear reactors. ^{135}Cs ($t_{1/2} = 2.3 \times 10^6$ years) and ^{137}Cs ($t_{1/2} = 30.1$ years) are major isotopes of Cs present in HLW). Separation of radio-caesium from the HLW is important for safe radioactive waste management. In addition, ^{137}Cs has many applications as a radiation source. Calix[4]-bis-2,3-naphtho-crown-6 (CNC, Fig. 5(a)) ligand was found to be very selective for the extraction of Cs(I) over other alkali metal ions. We have developed a method for the selective recovery of Cs from synthetic high level waste, using CNC in a mixture of nitrobenzene and toluene, which subsequently was applied for the lab-scale demonstration of radio-caesium recovery, from actual high level waste [10]. While attempting to develop alternative diluent system, NPOE was found to be quite good, though the D_{Cs} values were lower as compared to nitrobenzene. On the other hand, SLM transport studies on Cs(I) using CNC in 2-nitrophenyl cycloether as the carrier solvent, were found to be quite efficient for selective Cs recovery from acidic feeds. A mixture of 80% NPOE + 20% dodecane (dodecane was used to reduce viscosity) was optimized as a suitable diluent for CNC [11].

HFSLM transport of Cs(I) and other metal ions present in HLW (Cr, Fe, Sr, Am and Eu, etc.) was also investigated on 0.5 L scale, using CNC from a feed solution of 3 M HNO_3 , into a receiver phase of distilled water. With 1 mM CNC as the carrier, quantitative transport of Cs(I) was achieved in 6 h (Fig. 5(b)). The selectivity of Cs(I) over other radiotracers (^{214}Am , ^{154}Eu , $^{85,89}\text{Sr}$, ^{59}Fe and ^{51}Cr) was excellent with decontamination factors of ~ 100 with respect to various metal ions investigated in this study

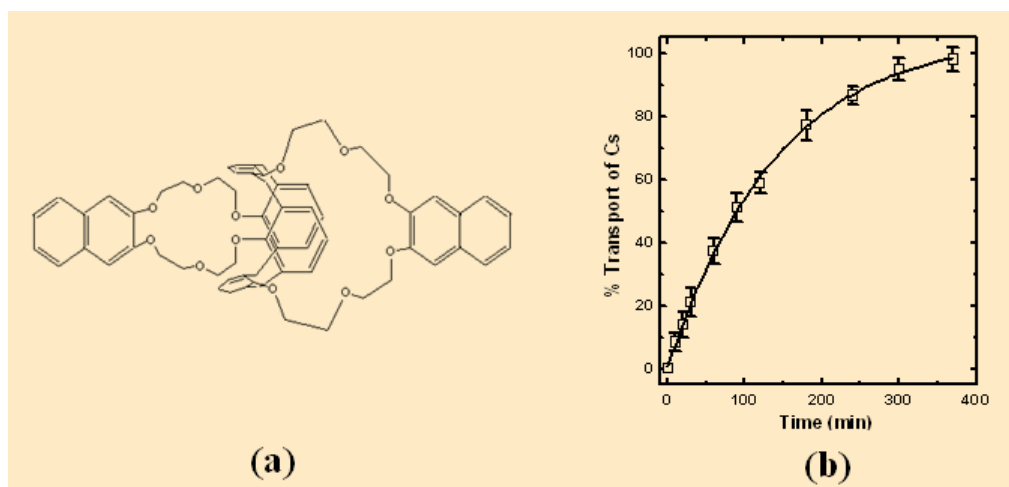


Fig. 5: (a) Structure of calix[4]-bis-2,3-naphtho-crown-6 (CNC), and (b) Transport of Cs by HFSLM; Carrier: 1mM CNC in 80% (v/v) NPOE + 20% (v/v) *n*-dodecane + 0.4% Alamine 336; Feed: 0.5 L HNO₃ spiked with ¹³⁷Cs; Strip: Distilled water; Flow rate: 200mL/min

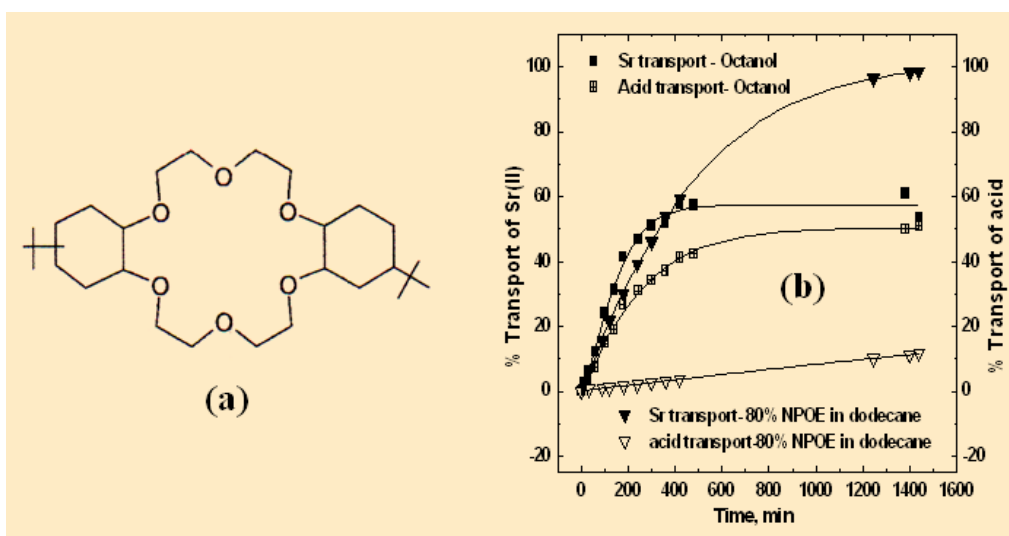


Fig. 6: (a) Structure of DTBu18C6; (b) Transport profiles of Sr(II) and nitric acid with the crown ether SLM system. Feed: 3M HNO₃; strip: distilled water, carrier: 0.1M DtBuCH18C6 in 80% NPOE / dodecane

[12]. High decontamination factors as well as throughputs, suggested possible application of the system for the recovery of radio-caesium from high level waste.

Transport of Sr by di-tertbutyl-di-cyclohexano-18-crown-6-SLM

Di-*tert*-butyl-di-cyclohexano-18-crown-6 (DTBuCH18C6, Fig. 6(a)), a substituted crown ether was found to be one of

the selective reagents for Sr(II) [13]. SREX (Strontium Extraction) process was developed at ANL, USA for the recovery of Sr from HLW. However, one of the drawbacks has been the co-extraction of significant amount of acid, which renders the separation method inefficient in the long run. We have developed a solvent extraction method for the selective extraction of radio-strontium from HLW, using a modified solvent [14]. An SLM-based method was also developed at our laboratory, using a mixture of



NPOE and dodecane for the quantitative transport of Sr from acidic feed solutions (Fig. 6(b)). Efforts are on, for scaling up of this method using HFSLM.

Conclusions

Novel selective extractants have been found to efficiently recover actinides and valuable fission product elements such as Cs and Sr from acidic wastes, including HLW. SLM-based methods have been found to be particularly promising, as the reagent inventory could be drastically brought down. One of the major obstacles, foreseen as this stage, has been the physical stability of the SLM, which could be enhanced by the judicious use of diluents. Selective pre-concentration using liquid membranes, may find use in the nuclear industry sooner than later. The low ligand inventory will not only reduce the cost of operation, but also can help in minimizing secondary waste volumes. The major concern in prolonged use, is the radiation stability of the reagent / polymer. This can be alleviated by the use of grafted membranes and radiation resistant polymers. Faster mass transport can be achieved by using HFSLM techniques.

References

1. S.A. Ansari, P.N. Pathak, P.K. Mohapatra and V.K. Manchanda, *Sep. Purif. Rev.* 40(2011)43-76.
2. P.K. Mohapatra and V.K. Manchanda; *Ind. J. Chem.*, 42A (2003) 2925.
3. R.B. Gujar, S.A. Ansari, D.R. Prabhu, P.K. Mohapatra, P.N. Pathak, A. Sengupta, S.K. Thulasidas, and V.K. Manchanda, *Solv. Extr. Ion Exch.* (in press).
4. R.B. Gujar, S.A. Ansari, D.R. Prabhu, D.R. Raut, P.N. Pathak, A. Sengupta, S.K. Tulsidas, P.K. Mohapatra and V.K. Manchanda, *Solv. Extr. Ion Exch.* 28 (2010) 764.
5. S.A. Ansari, P.K. Mohapatra, D.R. Raut, B. Rajeswari, M. Kumar and V.K. Manchanda, *J. Membr. Sci.*, 337 (2009) 304.
6. S.A. Ansari, R.B. Gujar, P.K. Mohapatra and V.K. Manchanda, *Radiochim. Acta*, in press (2011).
7. A. Bhattacharyya, P.K. Mohapatra and V.K. Manchanda, *Solv. Extr. Ion Exch.*, 17(2006)1.
8. A. Bhattacharyya, P.K. Mohapatra, and V.K. Manchanda, *Sep. Purif. Technol.*, 50 (2006) 278.
9. A. Bhattacharyya, P.K. Mohapatra, A. Roy, T. Gadly, S.K. Ghosh and V.K. Manchanda, *Hydrometallurgy*, 99 (2009) 18.
10. D.R. Raut, P.K. Mohapatra, S.A. Ansari and V.K. Manchanda; *Sep. Sci. Technol.* , 44 (2009) 3664.
11. D.R. Raut, P.K. Mohapatra, S.A. Ansari and V.K. Manchanda, *J. Membr. Sci.*, 310 (2006) 229.
12. P. Kandwal, P.K. Mohapatra, S.A. Ansari and V.K. Manchanda, *Radiochim. Acta*, 98 (2010) 493.
13. E.P. Horwitz, M.L. Dietz, D.E. Fisher, *Solv. Extr. Ion Exch.*, 8 (1990) 557.
14. D.R. Raut, P.K. Mohapatra and V.K. Manchanda, *Radiochim. Acta*, 97 (2009) 565.



Talkative Organic Molecules

S. Chattopadhyay

Bio-Organic Division

Dr. S. Chattopadhyay is the recipient of the DAE Homi Bhabha Science & Technology Award for the Year 2009

The 20th century has seen the birth of three Ages, called the Nuclear Age, the Electronic Age and the Chemical Age, each with profound social implications. Despite having a less dramatic impact, as a grandfather (beginning ca. 1930) the Chemical Age has more thoroughly and deeply permeated our day-to-day lives. Hence, we are now celebrating International Year of Chemistry 2011 (IYC-2011). Every single material in the universe is a chemical, and an impressive array of commonly used chemical "tools", ranging from modern food and drugs to plastics and computers to specialized coatings, fire retardants, and heat-transfer gases / liquids have become essential ingredients of our society. While chemistry is a science in its own right, in concert with biology, physics, medicine, materials science and other core disciplines, it makes effective contributions to the solutions of problems facing the world today and to the improvement of the condition of mankind tomorrow. The world would be a far more mysterious and less advanced place to live, without the development of chemistry. In future, it promises to stimulate and support innovation in all other branches of science and technology.

As a giant branch of science, chemistry has the ability not only to create the molecules, but also manipulate their properties and promises to take an increasing role as a creator and enabler, in materials science and biology. In particular, learning from nature how she assembles molecules and how such molecules recognize each other, it promises to build up new molecular world, not yet even imagined. Two aspects of chemistry primarily confer the extraordinary power of this branch of science. On one hand it can generate a huge molecular diversity of small and medium-sized molecules, pre-organized supramolecular assemblies *via* non-covalent interactions as well as nano-sized entities. On the other hand, each of these is bestowed with a specific property, and perhaps more importantly, this can be tuned by subtle structural variations. The importance of these molecules/assemblies lies not in their existence or exotic structures, but because they can execute certain specific jobs and are functional. The molecules/assemblies in question cross-talk (hence termed 'talkative') with completely alien molecules and / or get triggered by physical / biological factors to block / augment certain functions, generating detectable and /

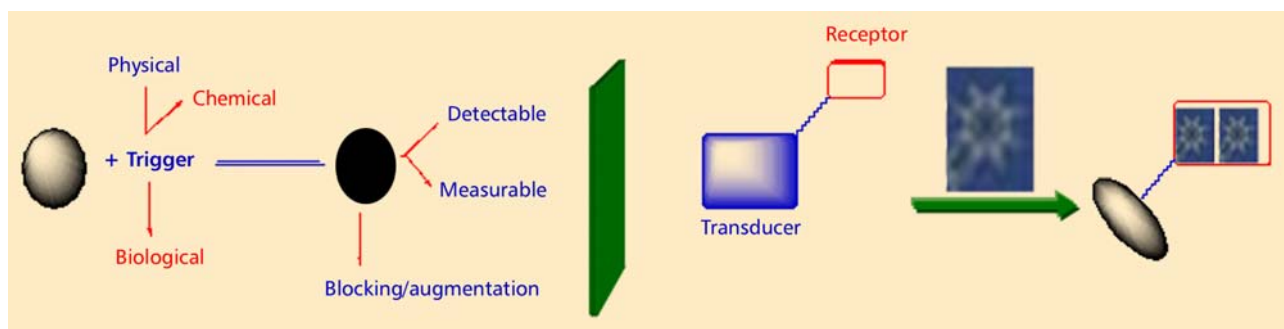


Fig. 1: Schematic description of talkative molecules



or measurable signals. Essentially, acting as a transducer, the molecules/assemblies exhibit the targeted functional property (Fig. 1).

Organic functional materials: prospects & challenges

Although traditionally well-known for their medicinal properties, the importance of organic molecules in seemingly unfamiliar areas such as nuclear and material sciences is increasingly being realized. Organic compounds offer the best potential for these due to the catenation property of the carbon atoms coupled with the possibilities of modulating their electronic properties as well as non-covalent interactions. Organic functional materials are also light-weight and can be processed easily, which offer distinct advantages especially in molecular electronics. The ease of tuning chemical structures and hence molecular properties can be appreciated from the following examples. A simple phenol can be derivatized to a bioactive flavone to be used as a drug, or calixarene derivatives that form cage structures of different geometries and are excellent hosts for application in separation science. Indeed some of these molecules are crucial in sequestering Cs⁺-ions

from the high level nuclear wastes. To cite another example, condensation of a pyrrole core with carbonyl compounds can furnish the bi-pyrroles (laser dyes and optical materials), calix-pyrroles (anions-specific ligands) or porphyrins/phthalocyanins (energy conversion and memory materials) (Fig. 2).

The idea of creating molecules with tailorable functions has fascinated chemists tremendously and the so called '*functional or talkative molecules*' have become the buzzword in design and development of novel materials. Considering the large gamut of atomic energy research activities, the requirement of a diverse array of organic materials need not be overemphasized. Especially the success of the programmes with regard to back-end fuel reprocessing, development of advance technologies and health promotion hinges on the availability of a wide range of molecules with different attributes. Organic materials, useful to recover valuables from HLW as well as for its safe management, are crucial in the back end of the nuclear fuel cycle. On the other hand, photo- and electro-active organic molecules / assemblies are in great demand in various nuclear and non-nuclear applications such as tunable dye lasers and molecular electronics. Likewise,

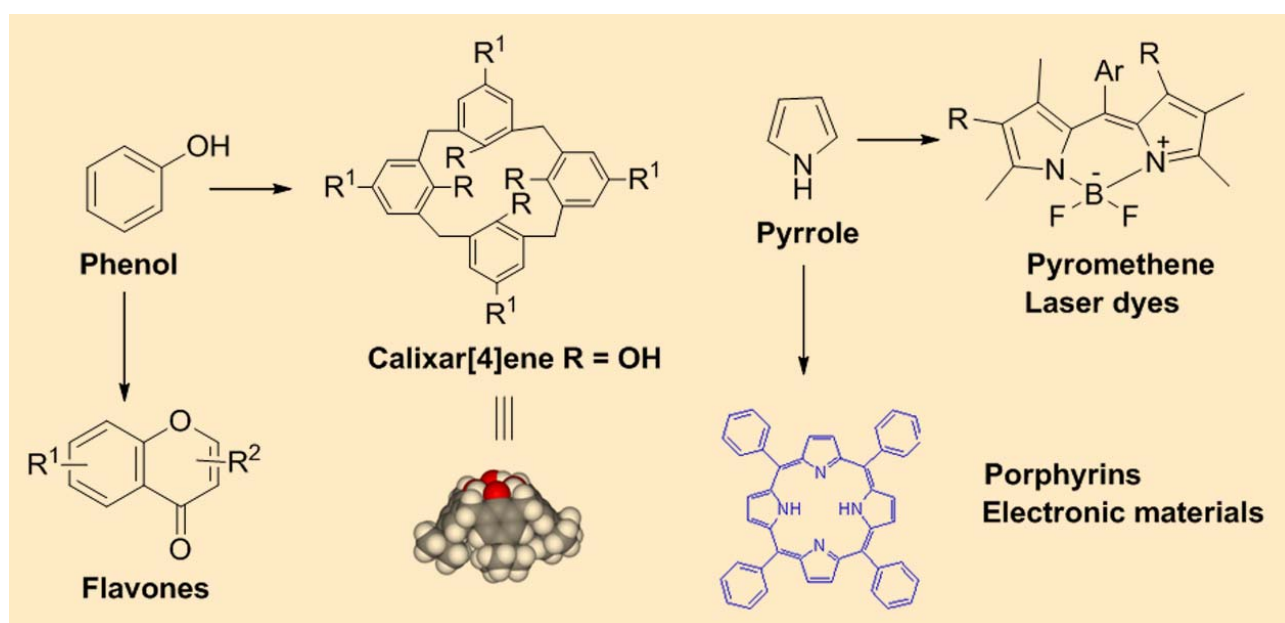


Fig. 2: Creation of diversity of talkative molecules



development of new redox compounds is essential for harnessing the medical benefits of radiation technology as well as formulating new drugs against various kinds of pathogenesis, caused by radiation exposure and other factors related to stress, pollution and lifestyle changes. These are speciality materials, generally required in low volumes (except the solvents), but are of high value and purity, and often commercially unavailable. Hence development of their indigenous synthesis is essential.

Unfortunately, even at the height of maturity of organic synthesis, production, processing, and use of chemicals in modern society has been accompanied by global-scale environmental pollution, natural resource depletion, and adverse health impact. The depletion of the stratospheric ozone layer by chlorofluorocarbon chemicals (CFCs), bioaccumulation of several organic pesticides / toxicants in the food chain etc., demonstrate the need for more comprehensive consideration of the potential impact of chemical use in society. Many of these problems can be substantially reduced by innovative design of synthetic protocols that have high atom efficiency, are carried out with recyclable / biodegradable catalysts in environmentally-benign media using minimum energy, and produce the targeted materials preferably from renewable sources. The modern concept is innovation of green chemistry that produces what you want and no waste.

Research & development of functional materials of societal relevance

From the beginning of my research career, I have tried to focus on developing organic materials of societal relevance, including those required in various departmental programmes. Understandably the programme of such a wide dimension can be sustainable only by effective molecular design, creating molecular libraries, and evaluation of the targeted function. The conventional approach of synthesizing single compounds and screening would be inadequate to realize the objectives. Instead, availability of a large number of organic compounds, their

screening and fine tuning for the designated activity by suitable modifications of the lead molecules would be essential. One of the major challenges associated with these, is that the molecules possess different complex structural motifs, and are often stereogenic. A large section of organic molecules are chiral, and their functional property is governed by the stereochemistry. Thus, a wrong stereomer of a target compound is a waste. Accordingly, development of asymmetric protocols is one of the major goals in organic chemistry research. Keeping in view of developing green synthesis, I have focused my research on (i) biocatalysis, (ii) asymmetric synthesis, and (iii) use of benign solvents (room temperature ionic liquids/H₂O) and/ or energy efficient techniques (microwave irradiation), to realize the goals, as are highlighted below with only a few examples.

Solvent engineering with biocatalysts

Enzymes are biodegradable agents that can catalyze most of the organic reactions under ambient conditions with high selectivity and turnovers. Hence, these are best suited for developing efficient green protocols for organic transformations with minimum side products and wastes. However, contrary to the conventional wisdom of enzymatic reactions in water medium, we have shown the feasibility of using enzymes even in organic media and even controlling the reaction course by subtle changes in the polarity / hydrophobicity of the reaction media. Such a strategy, known as 'solvent engineering' is very efficient and economic, compared to the typical biotechnological protocols. The advantages of using organic media are: better solubility of the substrates / products, easy product isolation, no / less enzyme deactivation and inhibition, reuse of the enzyme without immobilization, high temperature reaction etc. Together, these factors help in downstream processing and better turnovers. However, most importantly, this technique offers the possibility of designing new reactions as well as modulation of enantioselectivity and substrate-specificity. To cite some examples, enantio-selective esterification of (\pm)-3-hydroxybutyric acid (3-HBA) was



carried out at room temperature in toluene medium using *Candida rugosa* lipase (CRL) as the catalyst, and the enantioselectivity could be inverted by changing the chain length of the nucleophilic alcohol from *n*-butanol to *n*-hexanol. Likewise, the difficult task of entropically disfavoured macrolactonization can also be achieved enantioselectively, *via* a lipase catalyzed intramolecular *trans*-esterification of suitable α,ω -hydroxyesters, in an organic solvent. Conventionally, the reaction requires high dilution conditions and expensive reagents to activate the reacting groups, but still produce the racemic macrolide. Another lipase-catalyzed lactonization was also innovatively devised, to control the stereochemistry of three stereogenic centres in one step. These are schematically depicted in Fig. 3.

New asymmetric synthesis strategies

Majority of the natural and non-natural chiral organic molecules owe their chirality to the presence of a methyl

branching and / or carbinol function. Further, the stereogenic carbinol moiety can be transformed to various other complex structural motifs. Hence, we have introduced various new protocols for the syntheses of chiral methyl-branched and / or carbinol synthons (Fig. 4) and used them for the syntheses of a large array of complex organic compounds of departmental and societal relevance. For example, the asymmetric syntheses of methyl-branched chirons were developed starting from the naturally available terpene, pulegone, as well as a diosgenin-derived waste material, available in huge quantities from the pharmaceutical industries. The key step for the synthetic routes was a $\text{Pb}(\text{OAc})_4$ -catalyzed decarboxylation, to furnish the alkene in the presence of $\text{Cu}(\text{OAc})_2$ as a co-oxidant or the alkane, in its absence.

With regard to creating the chiral carbinol moiety and its derivative, both biocatalytic as well as various substrate controlled strategies were developed. Thus, the lipase-catalyzed esterification, *trans*-esterification, alcoholysis and

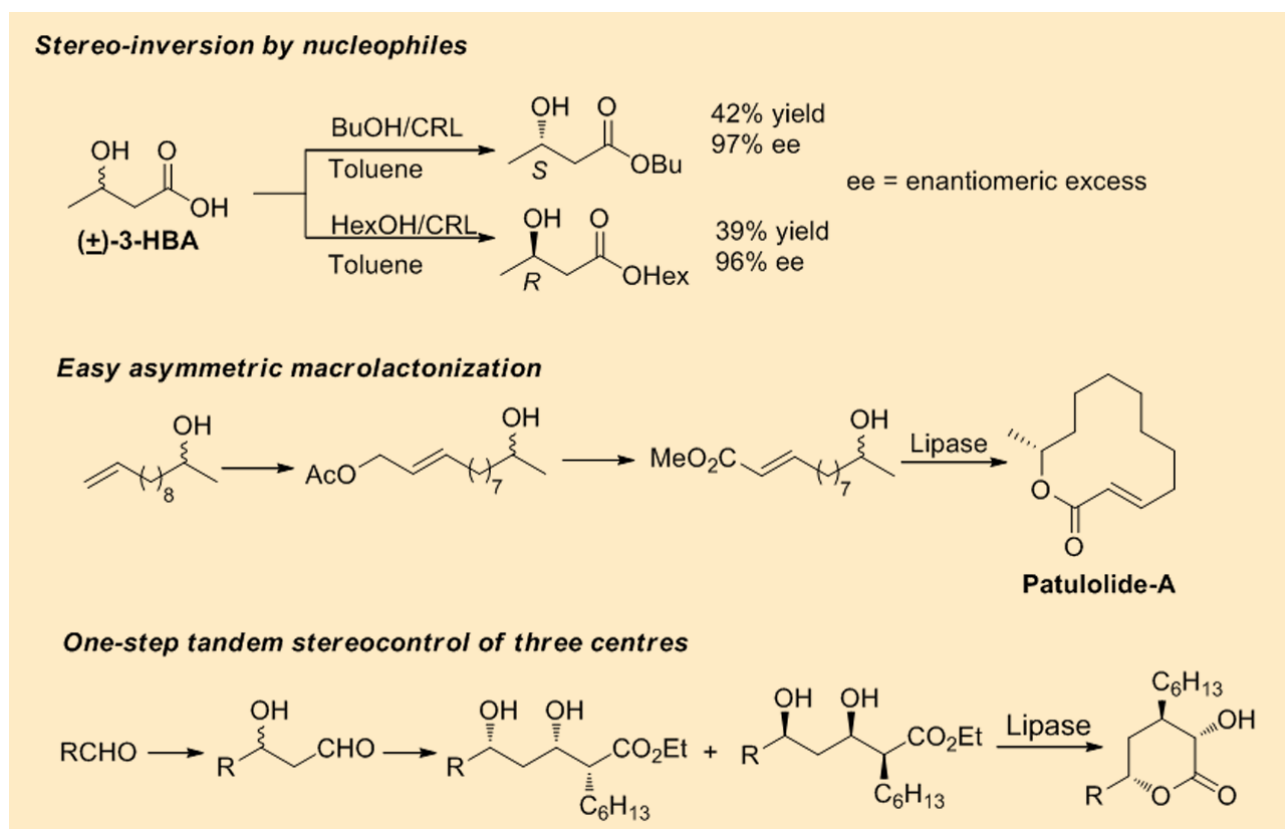


Fig. 3: Biocatalytic asymmetric syntheses

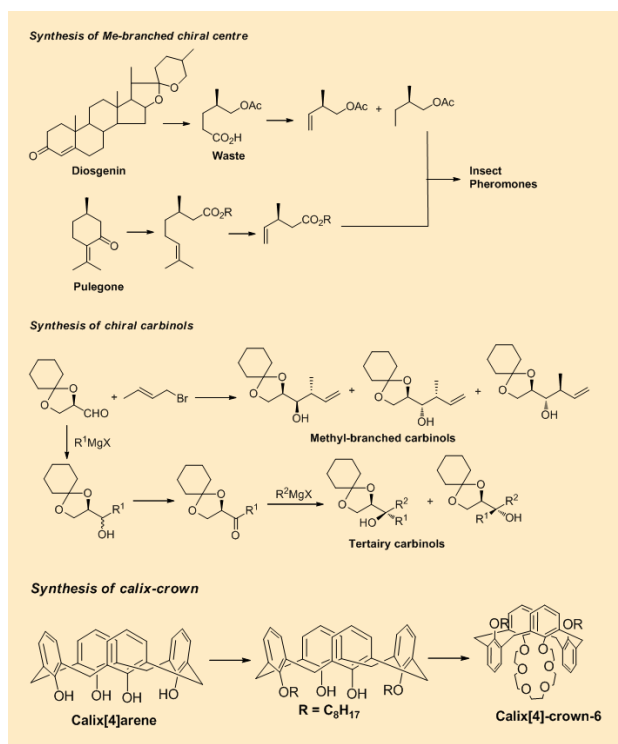


Fig. 4: New green synthetic strategies

aminolysis as well as oxynitrilase-mediated hydrocyanation were developed, to furnish a wide range of chiral carbinols. On the other hand, using a sugar-derived chiral aldehyde as the template, an efficient enantioselective synthesis of *tertiary*-alcohols was also achieved, via sequential addition of two Grignard reagents to suitable intermediates.

New media & techniques for efficient synthesis

Development of energy-efficient process, especially in safe reaction media is a major challenge in organic synthesis. We used [bmim][Br] as a new Room Temperature Ionic Liquid (RTIL) for asymmetric Barbier-type allylation reactions of γ -substituted allylic halides with a chiral aldehyde. This strategy enabled us to address the issue of chirality in an environmentally-benign solvent to furnish chirons, possessing both the above mentioned stereogenic centres. Another important aspect of the protocol was the metal-mediated stereoselectivity tuning. For example, while the Ga-mediated crotylation was found to produce the *anti*, *anti*-product with a diastomeric ratio (dr) of

3:5:92, the Bi-mediated reaction altered the diastereoselectivity in favour of the *anti*, *syn*-product with a dr of 10:83:7. The reactions failed in other media, establishing the role of the RTIL in metal activation.

Microwave-Assisted Organic Synthesis (MAOS) is a useful method for fast reaction, with better control on the product distribution. We have employed the MAOS route for regio-selective alkylation of the calix[4]arenes, and used some of the products to synthesize several calix[4]-crown compounds as potential metal-ions selective host molecules.

Talkative molecules of societal relevance

Materials for the back-end nuclear fuel cycle

Separation science plays a pivotal role at different stages of the nuclear fuel cycle, and techniques such as solvent extraction and ion-exchange are the backbones of this science. This warrants the development of novel metal ions-selective extractants and / or membranes that can be used to recover valuables from HLW as well as confine other toxic and hazardous radioactive metal ions of HLW, for their safe management / disposal. Besides showing high metal ions-selectivity, the materials need to be stable under highly acidic, oxidizing and radiolytic conditions. The low degradability, high selectivity and coordinating ability of the solvents would reduce their inventory, while good stripping parameters would increase their reusability. In my career, I have developed the syntheses of CMPO and a pentaalkyl malondiamide as actinide(III)-specific solvents and the process was transferred to the Heavy Water Board. More recently, one of the calix-crown derivatives, was found to be an efficient solvent for selective removal of the Cs^+ -ions from HLW. We also demonstrated that in the presence of a suitable plasticizer and additive, the same calix-crown derivative can be used as an Ion Selective Electrode (ISE) for the Cs^+ -ions with a linear response at concentration range (10^{-7} to 10^{-2} M) over the pH range of 4 to 11, and a detection limit of 8.48×10^{-8} M for the Cs^+ ions (Fig. 5). The lifetime of



the electrode was ~10-12 months, which is the highest for any membrane based Cs-ISE developed so far.

response became irreversible, which was attributed to the chemical reaction between Cl₂ and bis-porphyrin films.

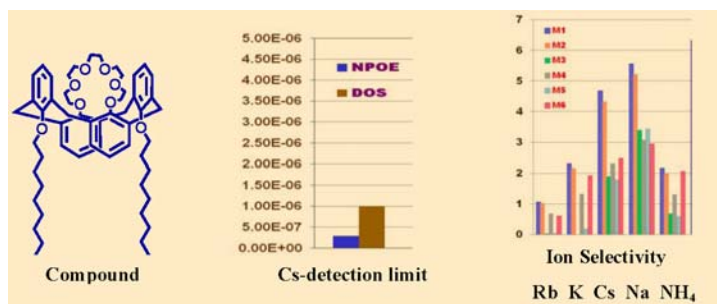


Fig. 5: ISE for Cs⁺ ions

Optical materials

Tunable laser dyes are important for various nuclear and non-nuclear applications. The pyromethene (PM) laser dyes are excellent fluorophors for these purposes, but suffer from photochemical degradation. In view of this, we have developed three PM laser dyes by incorporating a bulky *meso*-substituent, or replacing the F-atom at the B-centre, or a combination of both. The new laser dyes showed better photostability and equivalent lasing capacity compared to the commercially available PM-567 dye (Fig. 6).

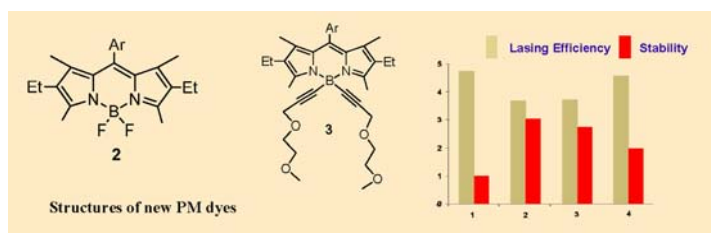


Fig. 6: New photo-stable laser dyes

Materials for molecular electronics

Developing sensors to selectively detect analytes, and quantifying them is of great relevance in the modern era. To this end, we developed spin-coated thin films of a bis-porphyrin molecule on glass, that acted as a selective chemiresistive sensor for the Cl₂ gas with fast response (3 s) and recovery (8 min) times, and sensitivity at 10–500 ppb range. However, beyond 1000 ppb of Cl₂, the sensor

Regarding molecular electronics, we developed molecular diodes based on donor–acceptor bilayers consisting of fullerene (C-60) and a tetraphenyl porphyrin derivative (TFPP), grafted on Si. The diodes were synthesized in by electrografting of a ~ 3.5 nm C-60 layer on H-terminated Si, followed by self-assembly of TFPP layers on the C-60 layer. The current rectification ratio (defined as: $RR = |I_{-1.8V} / I_{+1.8V}|$) for the diodes was ~1500, which could be rationalized using *ab initio* molecular-orbital theoretical calculations. Using a novel concept, a Si-wafer containing a bilayer of two different PM molecules was prepared, by first electro-grafting of one PM-moiety (containing a terminal olefin group) on Si-surface, followed by supramolecular attachment of the other PM molecule. The resultant molecular aggregate showed Negative Differential Resistance (NDR) property. This is the first report of a PM-based NDR system and is promising for its potential application in memory devices (Fig. 7).

Bio-materials for therapy

Oxidative Stress (OS), caused by intra-cellular and external stress (including radiation exposure) has been implicated for various pathogenic conditions such as gastric ulceration, cardio-vascular disease, cancer etc. At the same time, targeted creation of stress using chemicals and ionizing/ non-ionizing radiation are the only non-invasive option for cancer management. Given that the commercial synthetic drugs against these diseases are often toxic and expensive, we have explored various dietary factors as potential alternatives. To this end, three phenolics, isolated from the indigenous edible plants, *Piper betle* (pan) and *Myristica malabarica* (a spice) showed excellent anti-ulcer activities, while the pan-phenolic can be used against microbial skin infection. Contrary to the popular belief of gastro-toxicity of tea, our group has established the gastric ulcer healing property of various tea (green, black and

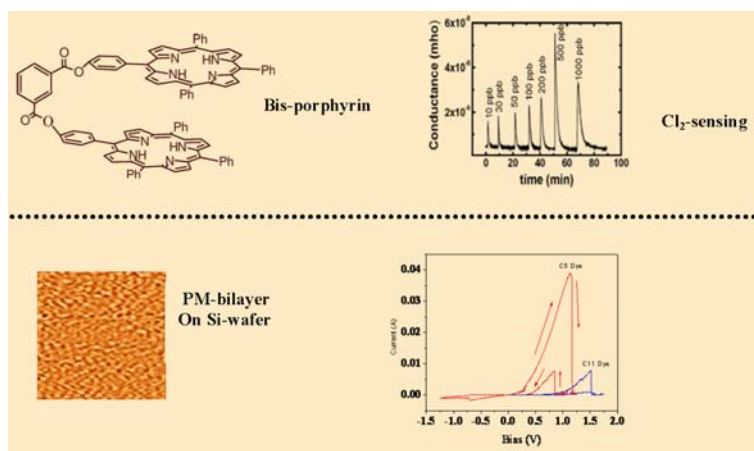


Fig. 7: Organics for molecular electronics

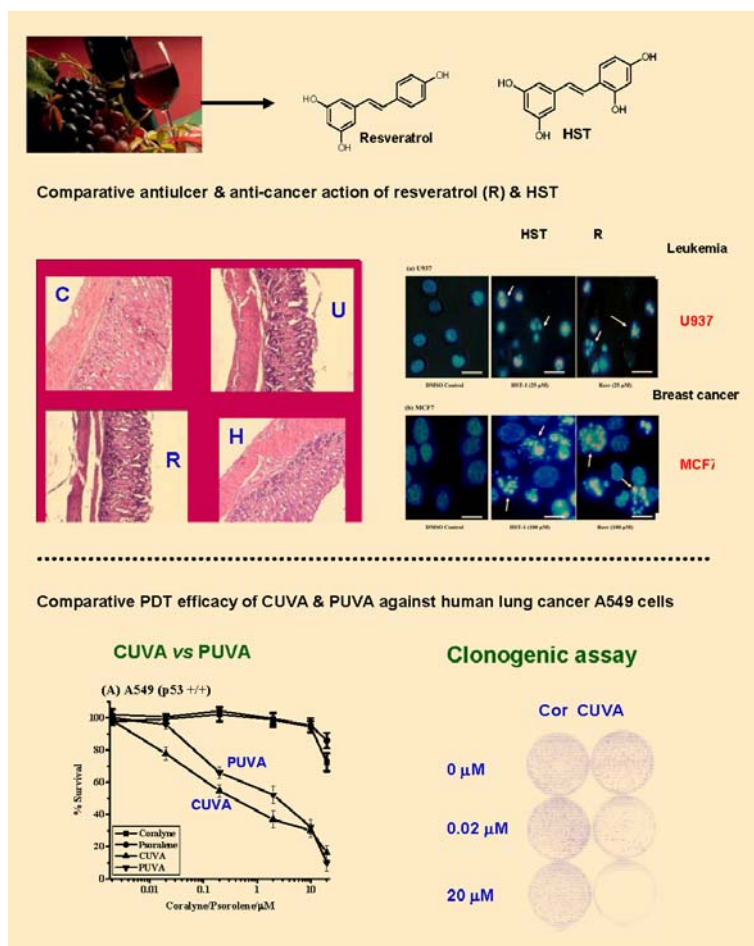


Fig. 8: Bio-organics for health

health benefit of the kombucha tea could be ascertained due to the reduction of its caffeine level during fermentation.

The clinical use of the grape-derived hydroxystilbene (HST), resveratrol against various oxidative stress-related diseases, is restricted due to its gastro-toxicity. Hence, we synthesized several of its analogues, and established better potency of one of these congeners as a chemopreventive agent against several human cancer cell lines than resveratrol. The HST also could heal indomethacin-mediated gastric ulceration in mice. In another approach, we have established the photo-dynamic action of a combination of coralyne, an alkaloid and UV-A light (CUVA) against lung and skin cancer cell lines, irrespective of their p53 status. The efficacy of CUVA was superior to that of psoralene and UV-A combination, that is used clinically for photo-dynamic therapy (Fig. 8).

Conclusions

Over the years, I have humbly tried to combine basic research in organic synthesis, chemical biology and supramolecular chemistry, to make molecules, that can talk with their environments and perform specific functions for which they have been designed. The synthetic strategies were formulated following the principles of green chemistry, wherein biocatalysts, ionic liquids, metallo-organics and micro-wave conditions were used, to develop comparatively clean protocols. The targeted deliverables viz. solvents and chemo-sensors, electronic materials, laser dyes and redox drugs were designed carefully for applications in various programmes (energy, separation science, health and advanced technology) of societal benefits. All these, perhaps, emphasize the utility of organic chemistry research, in building tomorrow's new world.

kombucha) decoctions. It was found, that oxidative transformation of the green tea-derived polyphenolic, epigallocatechin gallate (EGCG) to the theaflavins, present in black tea does not affect its healing action. Further, the



Challenges in Detector Grade Silicon Technology Demonstration

Dr. Sadhana Mohan
Heavy Water Division

Dr. Sadhana Mohan is the recipient of the DAE Homi Bhabha Science & Technology Award for the year 2009

Abstract

Economically viable high sensitivity radiation detector, demands negligible leakage current and high detection efficiency, to measure very small quantity of radiation such as charged particles and high energy neutrons. This is realized by using large-size, high-resistivity, high-carrier life time & defect-free silicon single crystal with large sensitive volume. In order to achieve detector-grade quality silicon, many technological challenges have to be met in terms of control of residual impurities up to sub ppb level, stress-free fine grain poly crystal ingot production & growth of large-size defect-free single crystal. Purification at this level cannot be achieved by direct conventional methods that are good enough for general purpose solar applications. It involves production and purification of highly toxic and hazardous precursor production in fluidized bed reactor, followed by distillation cascade, reconversion of volatile precursor to polysilicon ingot in a quartz reactor, to avoid leaching of reactor material at high temperature and contactless molten zone crystal, pulling in a class 10 clean room. These constraints make this technology very difficult to realize and is kept under close control by very few countries due to its high commercial value. Commercially available technologies are limited to photovoltaic level.

This paper highlights the technological issues for producing large-size high-resistivity silicon single crystal and the milestones reached during the course of time. Amongst the major milestones, 100 kg precursor production and 100 mm dia x 800 mm long single crystal drawn of $\langle 111 \rangle$ and $\langle 100 \rangle$ orientation are worth mentioning.

Key words: detector grade silicon, chemical vapor deposition reactor, float zone crystal pulling

Introduction

Silicon has a unique combination of properties which makes it special for use in day-to-day life as well as in high end advanced technologies. The largest application of elemental silicon with moderate properties is in metal alloy industry, representing about 55% of the world's silicon consumption, followed by silicones amounting to 40%. The remaining 5% of silicon consumption is in semiconductors, demanding stringent quality. Of late, it has also found its place in making of cosmic ray mirrors and MEMS devices.

Silicon is the most fascinating semiconductor material due to its favorable energy gap, ability to produce highest purity large-size defect-free single crystal by virtue of its better heat and mass transport properties, along with high stacking fault energy and critical resolved shear stress, in addition to the ease with which its electronic properties can be altered. It is needless to mention about its second largest natural abundance in the earth's crust after oxygen. No wonder silicon is termed as the work horse of the semiconductor industry. 80% of the semiconductor market is captured by commercial grade silicon whereas only 5% share is for detector grade. In fact as of today, silicon

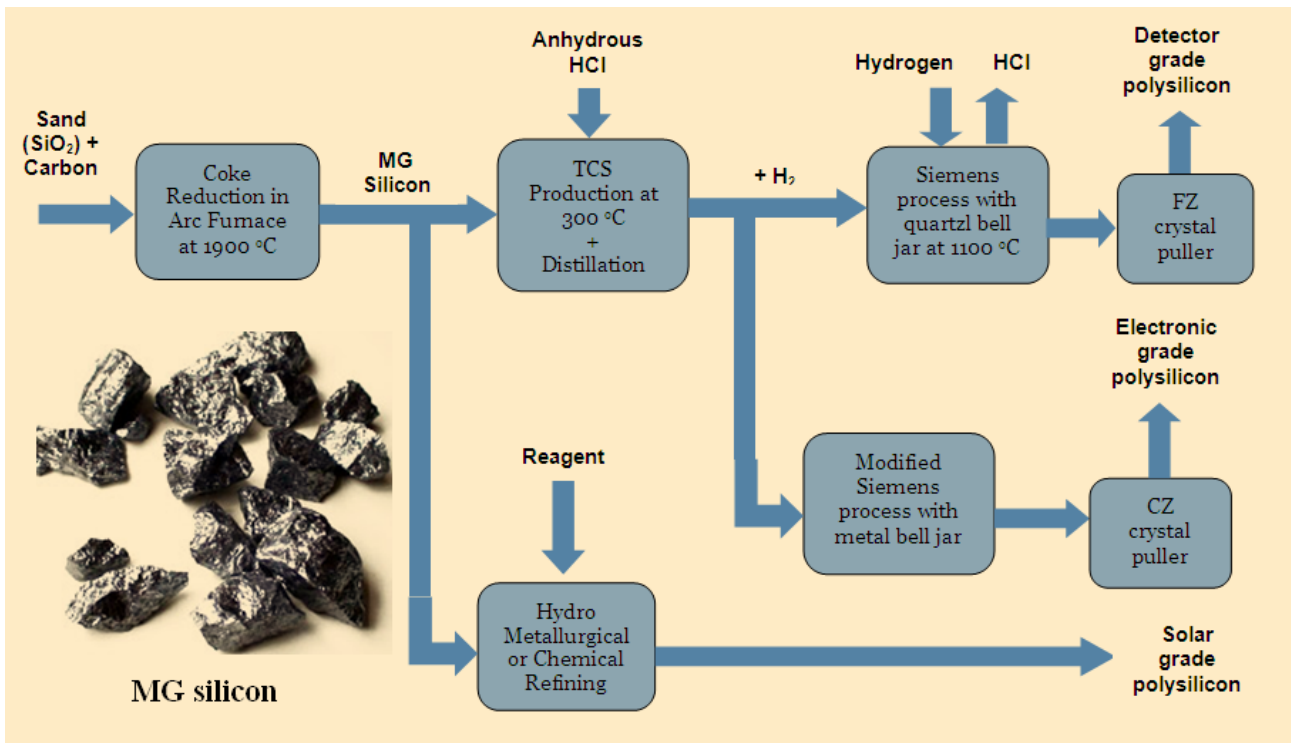


Fig. 1: Process flow sheet

manufacturing industries are not able to match the increasing global demand. Worldwide there is a sudden impetus on expansion programs in silicon industry.

Having realized the potential of silicon, Indian industries are now venturing into commercial grade silicon production technologies. BARC is committed to pilot scale detector-grade technology demonstration, to take care of our country's strategic programs in Atomic energy, Space and Defense. In an attempt to demonstrate this technology within a reasonable time frame, parallel approach for front end precursor production and wafer production in backend, with central thrust on large-size crystal pulling is adopted.

Detector grade silicon technology

Detector-grade silicon with properties close to intrinsic silicon is attached with high resistivity and almost nil compensation. Production technology is much more challenging as compared to commercial grade silicon. In absence of open literature and practically zero experience in the country, many hurdles were faced during

demonstration at each step. Continuous efforts in software and hardware development resulted in the success of milestones achieved.

Fig. 1 represents the various routes followed, for the production of various grades of silicon. Solar grade silicon requires less number of steps as compared to semiconductor grade whereas detector-grade demands much more stringent conditions from purity as well as growth technique considerations. Off grade silicon produced from detector-grade silicon production route can be recycled, to produce solar grade crystal in future.

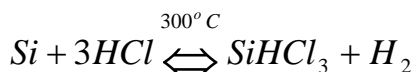
Detector grade silicon production: plant stages

Trichlorosilane (TCS) precursor production stage

Carbothermic reduction of sand results in metallurgical grade silicon with about 98% to 99% purity and is also known as crude silicon. Metallurgical grade silicon has significant impurity concentration and needs conversion to volatile material, to take advantage of high relative



volatility of most of the impurities even at atmospheric pressure. Volatile precursor TCS is produced by hydro chlorination of metallurgical grade silicon. TCS is primarily produced by the following reaction;



In addition to TCS, other halosilanes are also produced as byproducts. Reasonable TCS production yield is achieved, only after reaching a temperature greater than 250 °C. Undesired silicon tetrachloride formation increases beyond 350 °C. Optimum yield of TCS is experimentally found at 300 °C. The reaction is highly exothermic and needs efficient heat removal. Fluidized bed reactor is chosen to have uniform temperature profile across the reactor.

To study the feasibility of the process and generate design data for large-scale fluidized bed reactor (FBR), a pilot plant of 10 kg/day capacity and associated condenser scrubber system were designed, erected and successfully operated. The schematic diagram of pilot scale FBR experimental facility is shown in Fig. 2. Nitrogen as a diluent was used, to reduce the corrosion effect and sweeping of TCS product to achieve better yield.

In addition to high toxicity and fire hazard, major key issues faced in trichlorosilane production plant were: choking of sample lines due to solid silicon dioxide formation with traces of moisture, hardening of flexible tubes and increased byproduct formation at higher production rates. Further, undesired reaction products were not soluble in common material-friendly solvents. HF dissolves the choking product but needs careful procedure to avoid MOC attack.

The first milestone was reached after production of 100kg of TCS at near thermodynamic equilibrium composition.

TCS distillation

TCS produced in fluidized bed reactor plant had other chloro-silanes along with it and unacceptable level of electrical and heavy metal impurities. Squared off distillation cascade was designed, to purify TCS up to ppt level.

Cascade optimization is done, based on operating parameters as well as design parameters, to minimize plant volume and specific energy consumption. Typical

concentration profile and temperature profile are shown in Fig. 3. Purification at ppt level ends up at pinched conditions, leading to almost zero driving force and separation becomes extremely difficult. Impurity concentrations and temperature profile generated for all the five distillation columns showed, that the last two columns operate almost with flat temperature profile indicates that column performance control will be extremely difficult.

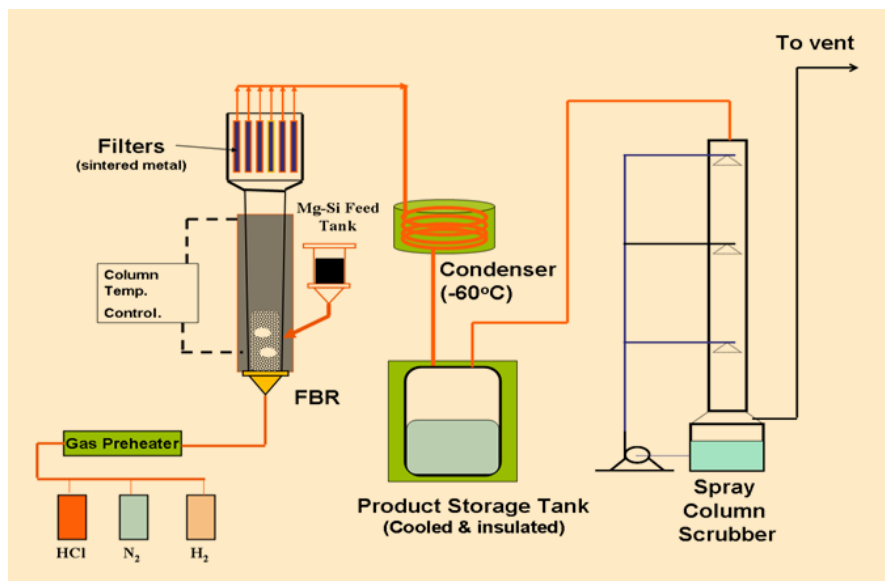


Fig. 2: Schematic diagram of Fluidized bed reactor system for TCS production

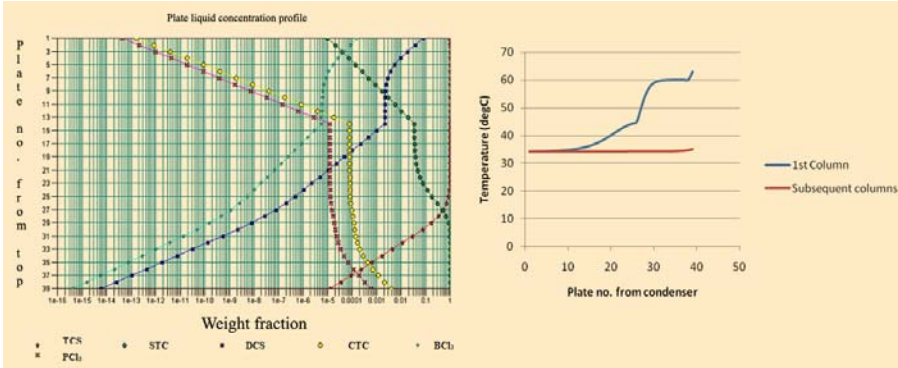
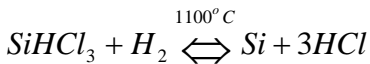


Fig. 3: Typical concentration & temperature profile of TCS distillation column

This step has many critical issues which might not have surfaced out in theoretical simulations but may be a matter of concern in the long run like leaching of material of construction elements, traces of corrosion products and analysis of impurities in TCS at ppt level.

Polysilicon production from TCS in CVD reactor

Distilled pure TCS is required to be reduced again by high purity hydrogen, to form polysilicon of desired purity in a Chemical Vapor Deposition (CVD) reactor by the following reaction;



Standard design methods for CVD reactor are limited to epitaxial CVD reactors. Ingot CVD design is not included

in any of the commercial software and thus needs in-house development of thermodynamic models, CFD models, incorporating multiple reaction kinetics for moving deposition boundary. Ingots CVD design and simulation with resistive heating of substrate itself is highly complex. Splitting the complex reactor design in stage wise software

development is adopted, for fixing the upper and lower bounds of operating parameters.

As a first attempt, thermodynamics of the system was studied independently and a computer code was developed, to estimate the equilibrium yield of the reactor under various operating conditions. The thermodynamic model of CVD reactor was developed, considering the seven thermodynamic viable reactions to estimate the extent of each reaction.

Reactor operating parameters like temperature, pressure and initial composition were evaluated for highest thermodynamic equilibrium yield in the reactor, by free energy minimization. The percentage thermodynamic yield of silicon for various reactor temperature and feed composition is shown in Fig. 4.

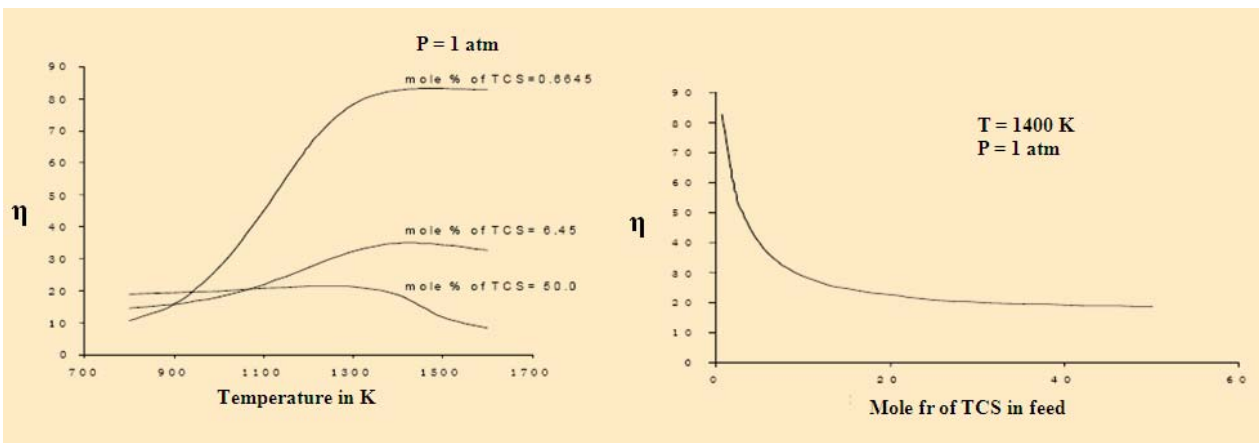


Fig. 4: Yield with reactor temperature and feed composition plots



Initial studies using Computational Fluid Dynamic (CFD) models including main reaction, while ignoring side reactions gave better idea of the operating conditions and nozzle position to obtain uniform growth. Temperature gradient inside the substrate rod was ignored. Real time complexities will be introduced later in a stage-wise manner.

Single crystal silicon production by FZ

Following are the industrial scale crystal pulling techniques from polysilicon;

1. Czochralski (CZ) crystal puller.
2. Float zone (FZ) crystal puller.

Over 90% of today's single crystal silicon is produced by CZ pullers and remaining by FZ. CZ puller needs container to hold the melt and contributes to impurity pickup while in FZ; molten zone is contact less & is held by surface tension in addition to RF inward pressure against gravity, turbulence and centrifugal forces. Typically oxygen impurities in FZ pulled silicon crystal, is 100-fold less as compared to the CZ pulled crystal, under same environmental and source material specifications. Due to better economics, ease of operation and moderate impurity acceptance, CZ pulled silicon crystals are preferred for low power electronic devices and in general

semiconductor industry; whereas FZ pulled silicon crystals having resistivity greater than 10 kΩcm are used in high power devices and radiation detectors.

Above all, CZ puller feed is in the form of silicon chunks of any size and shape, whereas float zone feed is fine grain, stress-free, cylindrical poly rod with almost 105mm dia x 1000mm length with proper cone and top hanger groove. Pre-stressed poly with high melting point impurities leads to crystal pulling failure runs. Unfortunate part is that, determination of these parameters is not possible by nondestructive techniques. Poly silicon ingot production qualifying for FZ is another big challenge.

Defect-free crystal pulling for desired orientation, needs high skill with thermal and hydraulic understanding to do *in situ* correction of power input, off centering of RF coil, upward and downward pull rate, adjustment of argon flow to push the dislocations and maintain desired temperature gradient, to avoid the violent molten zone from spilling.

Quick and precise response to avoid violent molten zone from spilling is the key to success. Floatzone machine requires very good balancing and clean environment for good performance. It was observed, that even a small vibration of ~15 Hz level is capable of destroying the crystal structure.

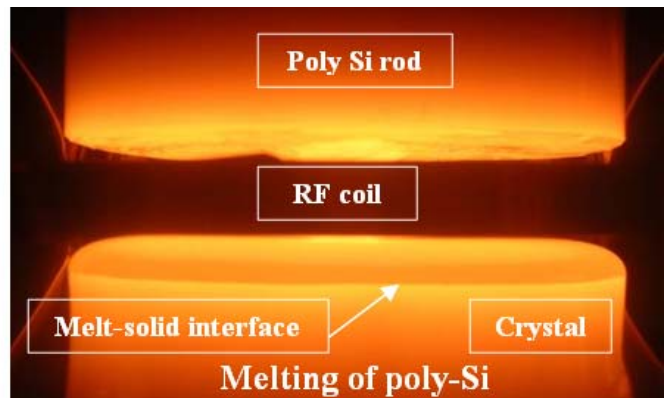
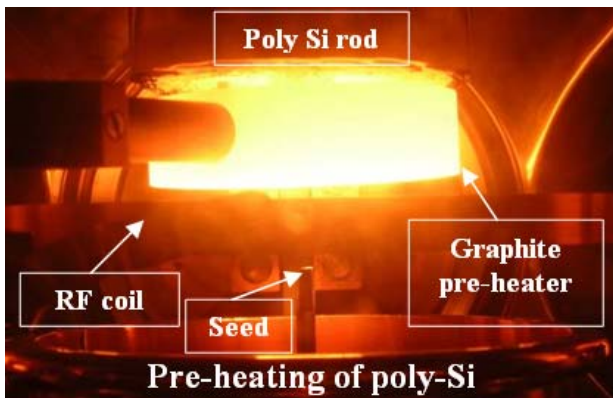


Fig. 5: Crystal pulling steps for FZ



Fig. 6: FZ crystal pulling machine at BARC in class10 cleanroom & Grown Si crystal on machine

Challenges faced during FZ crystal pulling

1. Arching: Impurities in poly resulted in silicon hillocks creating a spark while increasing the power to melt the flakes. Arching is one of the reasons for not going to vacuum zone refining in large crystals.
2. Blacking of crystals: Oxidation indicated by blackening of silicon was observed, due to oxygen impurity present in commercially available argon.
3. Zone instability: Spilling of molten float zone resulted in many failures due to destabilizing forces such as fast pulling speed, high power, high rotation speed, improper liquid solid interface shape.
4. Crystal structure damage: crystal got damaged due to slight increase in vibration level, improper support pin contact and improper alignment of the seed crystal.
5. Fractional freezing of melt: Insufficient power input led to freezing of top melt resulting in polysilicon flakes extending to single crystal interface finally leading to crystal structure failure. Poly and single

6. Thermal stresses cracking: Large linear thermal gradient due to improper pulling speed and large radial thermal gradient due to improper rotational speed, resulted in crystal cracking. Improper cooling and cold support pins contact also turned into crystal cracking.
7. In addition to the above mentioned issues, machine vibration and quality of clean room also affected the quality of crystal. Finally all issues were resolved by continuous practice with proper selection of rotational speed, upper and lower pull speeds, power input, off centering of coil and use of online purified argon gas.

The second major milestone was reached by demonstrating the largest single crystal pulled in the country, having size of 100mm dia and 800mm length.



Fig. 7: Single crystal silicon ingot (100 mm dia. & 800mm long pulled at HWD, BARC)



Silicon Wafer Production & Characterization

Major quality assurance check for silicon wafer in semiconductor industry, is to control variation in resistivity, minority carrier lifetime, carrier concentration and etch pit density. Special procedures are required to be followed for measuring these parameters in ultra-high purity silicon wafers. Conventional methods of measurement were found to be inadequate for effective measurements.

Single crystal silicon is sliced, lapped, etched, polished and cleaned, to produce final wafer in collaboration with

SSPL. Wafer resistivity is measured by high precision four point probe method.

Though, initially there was a large radial variation in resistivity, it was finally reduced by annealing. Average resistivity achieved was $\sim 30 \text{ k}\Omega\cdot\text{cm}$. Carrier life time of the wafers was measured by Laser assisted μ -PCD technique. It was further observed that high resistivity material needs proper passivation before carrier life time measurement, which may be ignored for low resistivity wafers. Typical minority carrier lifetime map is shown in Fig. 10.

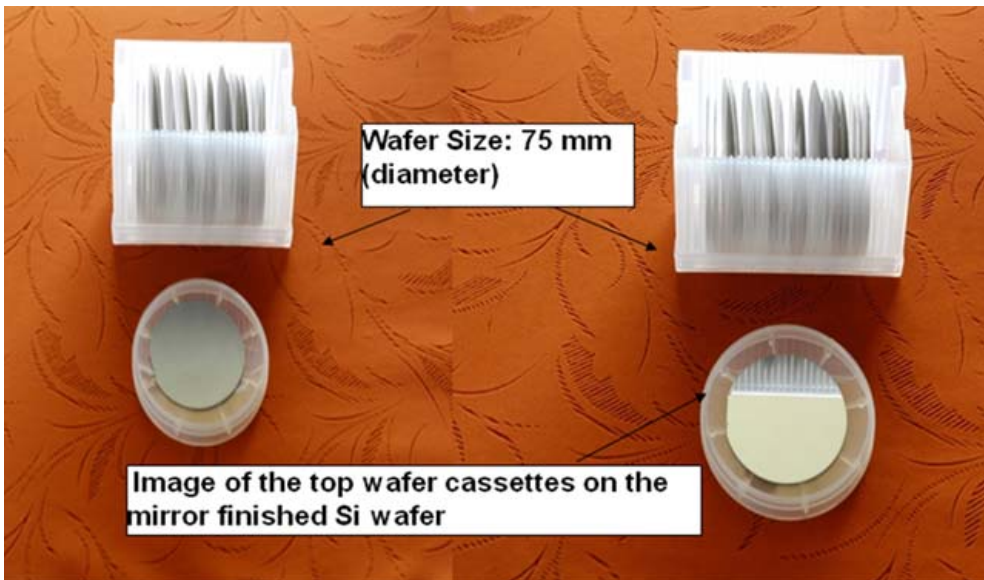


Fig. 8: As-cut and polished Silicon wafers produced at HWD

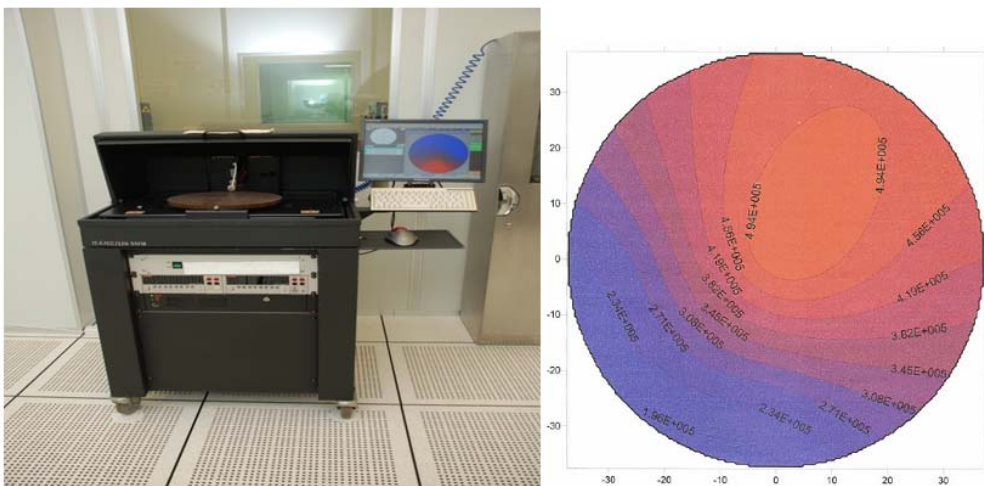


Fig. 9: Four point probe resistivity meter and typical output resistivity map

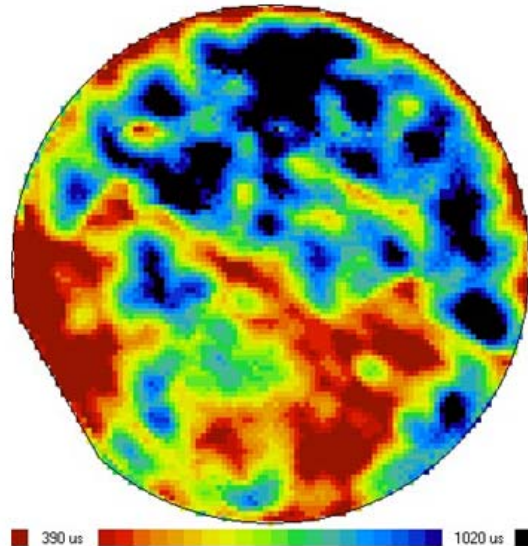
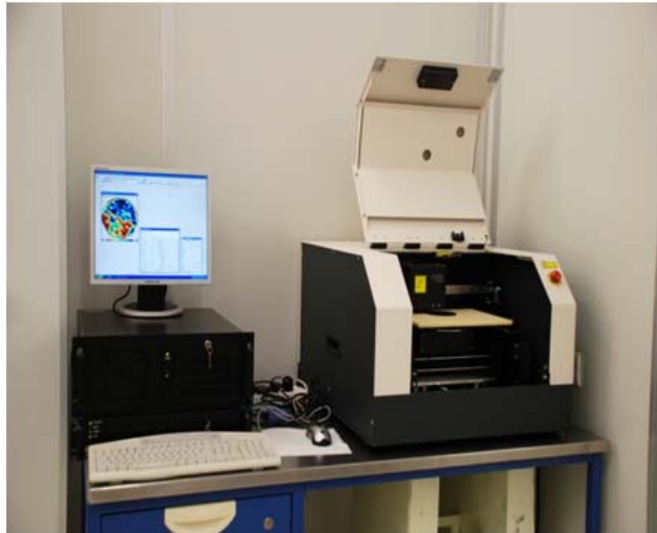


Fig. 10: Carrier lifetime measurement instrument and typical output lifetime map

Conclusion

Detector-grade single crystal silicon technology demonstration, is the first of its kind in the country. Most of the steps need in-house software, material, fabrication and hardware development. There is no standard recipe for detector-grade silicon wafer production. It's a

continuous evolving process, which is highly system-dependent. BARC has made a decent beginning with demonstration of clean room facility, TCS production, large size silicon single crystal ingot pulling and wafer slicing and characterization. There is still a long way in bridging the gaps and face the challenges in terms of purification, neutron transmutation and polysilicon ingot production.



A Unified Approach for Deriving One-Dimensional Kinetic Equation for Non-Equilibrium Processes in Condensed Phase

Alok K. Samanta

Theoretical Chemistry Section, Chemistry Group, BARC

Dr. A.K. Samanta is the recipient of the DAE Scientific & Technical Excellence Award for the year 2009

Abstract

We have derived here a kinetic equation of the probability distribution for the general reaction coordinates, non equilibrium solvation and energy diffusion co-ordinates, based on the first principle theory. The kinetic equations for the reaction coordinates or the relevant dynamical co-ordinates corresponding to reactions or dynamical processes, which lie in multi-dimensional Liouville space, become one dimensional. This is conceptually very simple and computationally highly economic and has wide applicability in different branches of science. As an illustrative example, we have investigated the dynamics of electron transfer reaction in condensed phase.

Introduction

Dynamical processes in the condensed phase such as electron transfer (ET) reactions, diffusive escape from potential wells, activated barrier crossing, non-equilibrium solvation etc. are of immense and long standing importance, in various frontier areas of research in physics, chemistry, and biology. A theoretical description of these phenomena [1-3] is, however, severely hindered by the multi-dimensional nature of the collective motion of the particles in condensed phase and also the difficulty in evaluating the non-equilibrium time correlation functions, for proceeding beyond the linear response theory. The objective of the present work is to bypass these difficulties, by developing alternative simpler approaches for describing various dynamical processes in the condensed phase. We obtain here a new simple one-dimensional theoretical framework, by identifying a proper reaction co-ordinate (or the relevant dynamical variable) and derive a kinetic

equation for its probability distribution function, which is shown to provide a generalized approach, for describing a wide class of dynamical phenomena.

Theoretical Formalism

In cases where the initial condition is non-equilibrium [3], the system is in multi-dimensional reactant potential well, and due to diffusion of phase-space coordinates Γ , the system is brought to the critical configuration and the reaction does take place with an intrinsic rate constant k_0 . The modified Liouville equation for such non-equilibrium reactive system can be written as

$$\frac{\partial \rho(\Gamma, t)}{\partial t} = -[iL + k_0 \delta(A(\Gamma) - \gamma^*)] \rho(\Gamma, t) \quad (1)$$



where L represents the Liouville operator and $\rho(\Gamma, t)$ is the probability density defined in phase space at time t . For most of the reactions, the phase space function is a function of the geometrical co-ordinates. However, in the case of energy diffusion controlled reactions, the total Hamiltonian H (function of phase space co-ordinates) of the diffusing particle is considered to be [2]. In this case, the particle moves with certain energy ($H=E$) in the potential well, and eventually through thermal fluctuations, the particle energy reaches the barrier energy (E_b) and it eventually escapes. In such situation, one has $E = E_b$. In our earlier work [3], we have shown rigorously using projection operator technique how the reaction dynamics defined in Liouville space can be mapped into the microscopic phase space $A(\Gamma)$. The one-dimensional kinetic equation for the distribution function $p(\gamma, t | \gamma_0, 0)$ in reaction co-ordinate space $A(\Gamma)$ can be written [3-8] as

$$\frac{\partial p(\gamma, t | \gamma_0, 0)}{\partial t} = \frac{\partial}{\partial \gamma} \left\{ D(\gamma) \left[\frac{\partial p(\gamma, t | \gamma_0, 0)}{\partial \gamma} + p(\gamma, t | \gamma_0, 0) \frac{\partial}{\partial \gamma} \{ \beta V^{eff}(\gamma) \} \right] \right\} - k_0 \delta(\gamma - \gamma^*) p(\gamma, t | \gamma_0, 0) \quad (2)$$

Here, the effective potential $V^{eff}(\gamma)$ is function of γ given by

(3)

where $\beta = (1/k_B T)$ and $H^r(\Gamma)$ respectively, denote the inverse temperature and Hamiltonian for the reactant in solvent medium. $D(\gamma)$ (3-11) corresponds to reaction co-ordinate dependent diffusivity. Here $p(\gamma, t | \gamma_0, 0)$ represents the probability of finding the $A(\Gamma)$ to have the value γ when its initial value is γ_0 . Although theory developed here is more general, as an illustrative example, in the following section, the dynamics of electron transfer reaction in condensed phase is illustrated.

Electron-Transfer Reaction

We consider here a typical ET process where a molecule donor-acceptor (DA) is excited from the ground state with an ultra-short laser pulse leading to the formation of the ion-pair D^+A^- . The system is initially prepared in a

constrained non-equilibrium state through photo chemical excitation and in the subsequent time, the constraint is removed as the system is no longer under laser field. The system then starts relaxing downward along its multidimensional potential energy surface (corresponding to the ion-pair D^+A^- in solvent medium) through relaxation of the surrounding polar solvent till it meets that of the molecule DA (in solvent medium) at the critical geometrical co-ordinates [3],

$$H_{sol}^r(\mathbf{R}) - H_{sol}^p(\mathbf{R}) = \gamma^* = \Delta G - \lambda_s \quad (4)$$

where back ET reaction does take place with an intrinsic rate k_0 . The quantity $H_{sol}^i(\mathbf{R})$ ($i = r, p$) represents the Hamiltonian for the solute - solvent and solvent - solvent interaction energy. Here \mathbf{R} represents a set of geometrical co-ordinates for the relevant system. ΔG corresponds to the free energy change of charge recombination (CR) reaction and λ_s denotes the solvent reorganization energy. As the ET reaction is assumed to proceed on a multidimensional surface of the theoretical description

we propose here for the ET system of interest, consists of a multidimensional space spanned by the low frequency solvent collective coordinates (multidimensional) characterized by the orientational polarization function $\mathbf{P}(\mathbf{r})$. In addition to it, we also consider here, low frequency harmonic molecular vibrational mode described by the coordinate (Q). Thus, the Hamiltonians H_{sol}^i ($i = r, p$) for ion pair (D^+A^-) and neutral solute (DA), respectively, are given as

$$H_{sol}^r = \int \mathbf{P}(\mathbf{r}) \cdot \mathbf{P}(\mathbf{r}) d\mathbf{r} + \int_{|\mathbf{r}-\mathbf{r}_D|>a}^{|\mathbf{r}-\mathbf{r}_A|>b} \mathbf{P}(\mathbf{r}) \cdot \left[\frac{e(\mathbf{r}-\mathbf{r}_D)}{|\mathbf{r}-\mathbf{r}_D|^3} - \frac{e(\mathbf{r}-\mathbf{r}_A)}{|\mathbf{r}-\mathbf{r}_A|^3} \right] d\mathbf{r} + \frac{1}{2}(Q+Q_0)^2 \quad (5)$$

$$H_{sol}^p = \int \mathbf{P}(\mathbf{r}) \cdot \mathbf{P}(\mathbf{r}) d\mathbf{r} + \frac{1}{2}Q^2 \quad (6)$$

where \mathbf{r}_D and \mathbf{r}_A stand for the positions for donor and acceptor, respectively and the second term on the right-hand side of Eq. (6) stands for the interaction energy between the charges and the polarization field $\mathbf{P}(\mathbf{r})$. The reaction co-ordinate $A[\Gamma]$ defined for the ET reaction is given as

$$A[\Gamma] = (H^r - H^p). \quad (7)$$



The effective potentials $V^{eff}(\gamma)$ in reaction co-ordinate space (γ) for the reactant state is derived based on Eqs.(3), (6) and (8), and the final expression for this quantity is defined as

$$(8)$$

where λ_v corresponds to vibrational re-organization energy and the transition point γ^* in γ space is defined as . The overall ET rate constant k for forward reaction can be written as

$$k = \frac{k_{TST}}{1 + \frac{k_{TST}}{k_d}} \quad (9)$$

where k_{TST} and k_d represent the rate of ET reaction calculated based on transition state theory and well dynamics, respectively, are defined as

$$[k_1^{TST}]^{-1} = k_0^{-1} (4\pi\lambda_r k_B T)^{1/2} \exp\left[\frac{\beta}{4\lambda_r} (\Delta G + \lambda_s)^2\right] \quad (10)$$

$$[k_1^d]^{-1} = \left(\frac{\beta\tau_r}{2\lambda}\right) (\pi\lambda_r k_B T)^{1/2} \int_{\Delta G \rightarrow \lambda_s}^{2\lambda} dz_1 \exp\left(\frac{\beta}{4\lambda_r} z_1^2\right) [1 - \text{erf}(z_1 / (4\lambda_r k_B T)^{1/2})] \quad (11)$$

where k_0 is the intrinsic rate and its expression can be written in terms of transfer integral J as $k_0 = (4\pi^2 / h) J^2$ and τ represents polarization relaxation time. Here and λ_s respectively represent total and orientational reorganization energies. The parameters used are: $J = 0.3\text{eV}$ and $\lambda_r = 1.5\text{ eV}$, $\tau_s = 0.3\text{ ps}$ and temperature $T = 300\text{ k}$. The calculated values are found to be very good with the available experimental results. Theory developed here is more general, can be extended to finite system [11] also.

Concluding Remarks

The kinetic equation (Eq.2) provide a generalized approach for describing a wide class of dynamical phenomena. Although theory developed here is more general, as an illustrative example we consider back ET reaction and the calculated results are found to be very good in agreement

with the available experimental results. Theory for non equilibrium solvation and escape of a particle from the potential well can easily be developed based on the generalized kinetic equation (Eq.2) by proper selection of $A[\Gamma]$ and $k_0 = 0$.

Acknowledgements

It is a great pleasure to thank Prof. S. K. Ghosh for his unstinted inspiration, invaluable guidance and keen interest, which helped me to venture into diverse fields of research. I express my sincere thanks to Prof. T. Mukherjee for his continuous support and encouragement. It is also a great privilege for me to thank D. K. Maity, S. M. Ali, K. Dhole, A. K. Pathak, B. Modak and A. Patra who have contributed to the present work. The author would like to thank K.R.S. Chandrakumar and A. K. Patra of SSPD, BARC for their encouragement towards this work.

References

1. R. Zwanzig, *J. Chem. Phys.*, **35**, 1420 (1961) 983.
2. R. Zwanzig, *Non equilibrium Statistical Mechanics*(2001), Oxford University Press.
3. A. Patra, A. K. Samanta and S. k. Ghosh; *Phys Rev E*. **83** (2011), 026104.
4. R. A. Marcus; *J. Chem. Phys.* **24**(1956), 979.
5. T. Asahi, N. Mataga, *J. Phys. Chem.* **95** (1991)1956.
6. A. K. Samanta and S. K. Ghosh, *J. Phys. Chem. A*, **112** (2008), 752.
7. K. Dhole, B. Modak, A. K. Samanta and S. K. Ghosh; *Phys Rev E*. **82** (2010), 016110.
8. K. Dhole, A. K. Samanta, S. K. Ghosh, *J. Phys. Chem. A*, **112** (2008), 4879.
9. A. K. Samanta, S. M. Ali, and S. K. Ghosh; *Phys. Rev. Lett.* **87** (2001), 245901.
10. A. K. Samanta, S. M. Ali, and S. K. Ghosh; *Phys. Rev. Lett.* **92** (2004), 145901.
11. A. K. Pathak, A. K. Samanta, D. K. Maity, T. Mukherjee and S. K. Ghosh, *J. Phys. Chem. Lett.* **1** (2010),



Challenges in Neutron Transport Analysis for Nuclear Reactor Simulations

Anurag Gupta

Reactor Physics Design Division

and

R.S. Modak

Theoretical Physics Division

Dr. Anurag Gupta is the recipient of the DAE Scientific & Technical Excellence Award for the year 2009

Abstract

The most fundamental task in a nuclear reactor, is to follow the neutron distribution in order to maintain and control the nuclear fission chain reaction. The fundamental equation governing the average behavior of neutrons, is the linear form of Boltzmann transport equation. The core design simulations with neutron transport method are most complex and CPU-intensive jobs, in reactor design and analyses. For a designer it is imperative to perform these calculations with good accuracy and efficiency to try out various options. It is important for the code developers to use techniques involving minimum approximations and to use most recent numerical methods applied in tandem with the huge computing power available today. The present paper discusses some of these challenges.

Introduction

In nuclear reactor design, the most fundamental task is to follow the neutron distribution as a function of space, direction, energy and time, in order to maintain and control the nuclear fission chain reaction. The fundamental equation governing the average behaviour of neutrons is given by the linear form of Boltzmann transport equation, which is an integro-differential equation. The core simulations involving the solution of the neutron transport equation are very CPU-time-intensive and require the best of numerical and computational schemes. It is because of this reason, most of the preliminary core design calculations are done with diffusion theory, which is a popular approximation to the transport theory.

Because of time consuming nature of transport simulations, huge efforts have been made internationally, over many decades, to obtain a reasonable solution in acceptable CPU-times. Over the years, researchers have proposed many new discretisation schemes, numerical techniques, acceleration methods and computing styles, to reduce the computing time. These schemes are devised or modified in tandem with the availability of computing power at that moment. High performance computing tools such as sophisticated programming styles and parallel computing are regularly used, to enhance the efficiency of the computer codes.

There are several numerical schemes applied to discretise the transport equation and its variants, for a variety of



geometrical configurations. Prominent among them are finite difference, nodal, modal and finite element methods. The current international interest is to have methods that work for general geometries such as Method of Characteristics, mesh-less methods etc. Discretisation of the neutron transport equation may give rise to either a system of linear equations (source problem) or to an eigenvalue system (criticality problem). These coupled systems are huge, involving millions of unknowns and there may or may not be an explicit generation of coefficient matrices. Sophisticated numerical algorithms are available to solve these systems efficiently. One such group of methods is the Krylov subspace class of algorithms which are of current international interest. The convergence properties of the Krylov methods are usually better and they are generally suitable for parallelization.

Challenges in Neutron Transport Simulation of a reactor core

A nuclear reactor in practice, is a very complex device. It contains a core which may have a series of fuel rods or pins arranged in a particular fashion. There can be a moderator material to slow down the high energy neutrons, a reflector to contain the neutrons within a domain and a coolant to remove the heat. There can be several controlling devices and measurement equipment. Then there are structural and appropriate shielding materials.

The challenge is to compute the power or neutron flux in each of the fuel pellets in the fuel pins, stacked as clusters in fuel assemblies and this has to be done:

- for complicated geometries and with challenging physics,
- as a function of time over a fuel cycle,
- various core configurations, control rod situations,
- with nuclides depletion and production,
- including feedbacks from coupled heat transfer and coolant flow,

- with novel structural and support materials,
- with acceptable accuracy and efficiency.

Complex Physics of neutron-nucleus interactions

The physics of neutron-nucleus interaction itself is complex. The cross-sections depend on energy as shown in Fig. 1 and there are resonances which further complicate the calculations of reaction rates. Thus, the cross-sections depend very sensitively on neutron energy and material temperature. Moreover, the neutron-nucleus scattering interaction can be anisotropic in lab frame. The time-dependent calculations present further challenges: a fraction (<1%) of fission neutrons are emitted with a delay. This does not affect steady state situations, but have a huge impact on transients, in fact they dominate any time dependent behaviour of the core. Hence it is imperative to calculate precursor concentrations and decay rates along with neutron flux.

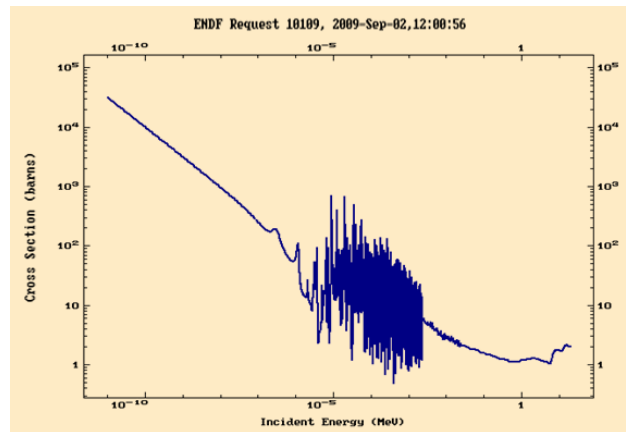


Fig. 1: Cross section as incident neutron energy

Multi-physics Multi-scale problem

The changes in the temperatures and densities of fuel, coolant and moderator materials, result in change in absorption and production of neutrons, leading to change in core reactivity. This leads to power gradients which further alter temperatures, densities and flows. Thus another challenge is presented in the form of a coupled multi-physics system with variable scale problems to handle (Fig. 2).

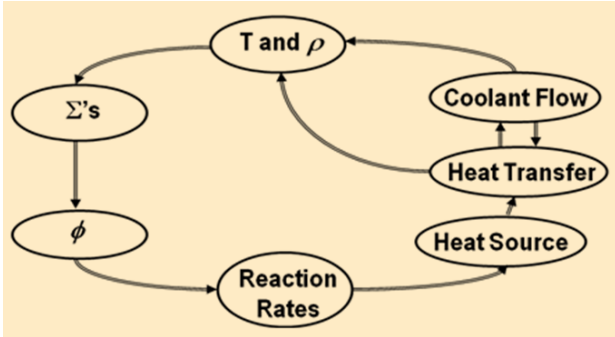


Fig. 2: A multi-physics problem (Ref:M.L. Adams)

Efforts to Solve the Problem

Conventionally, there are two steps of numerical transport simulations: lattice and whole core. Parameters are obtained by homogenizing a lattice and fed as input to the whole core calculations (Fig. 3). This may lead to a faster solution without significant loss of accuracy but still the whole core calculations are very CPU-time-intensive.

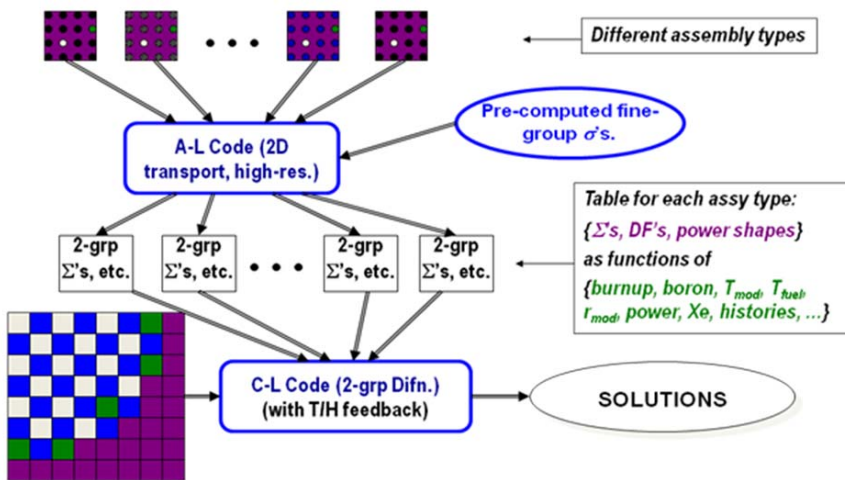


Fig. 3: A two step approach for core neutronics simulation (Ref: M.L. Adams)

The Neutron Transport Equation

The general neutral particle transport equation has seven dimensions (3 in space, 2 in directions, 1 each in energy and time). The most commonly used method to discretise the angular variable Ω is the Discrete Ordinate (S_N) method.

Similarly other variables are also discretised by appropriate schemes. The discretised transport equation is conventionally solved by the well-known inner-outer iterative procedure (Lewis and Miller, 1993). There are several computer codes developed over many decades which are based on inner-outer procedure.

Transport Core Calculation Without Spatial Homogenization

Traditionally, the core simulations are done in two steps: lattice and core. This procedure was followed as not enough computing power was available in the past. The accuracy of the homogenisation is a concern. With enormous computing power available today, there is a recent trend to explore the whole core simulations without any spatial homogenisation. Such simulations require the best of modelling, solution algorithms and massive parallelization techniques. Recently, an NEA benchmark (Fig. 4) was proposed to test the accuracy of modern deterministic transport methods when applied to reactor core problems without spatial homogenization (Smith et. al. 2006).

Solution of Source Problem: the TSA and Conjugate Gradient method

It is well-known that for optically thick and highly scattering regions, the convergence of inner iterations is very slow (Lewis and Miller, 1993) leading to large CPU times. Two major schemes have been suggested to accelerate these iterations: the Coarse Mesh Rebalancing (CMR) and the Diffusion Synthetic Acceleration (DSA). The DSA scheme was considered particularly attractive and considerable studies have been done (Adams and Larsen, 2002) on it. The Transport Synthetic Acceleration (TSA) is an improvement over the DSA, where the "corrective equation" is approximated by a transport

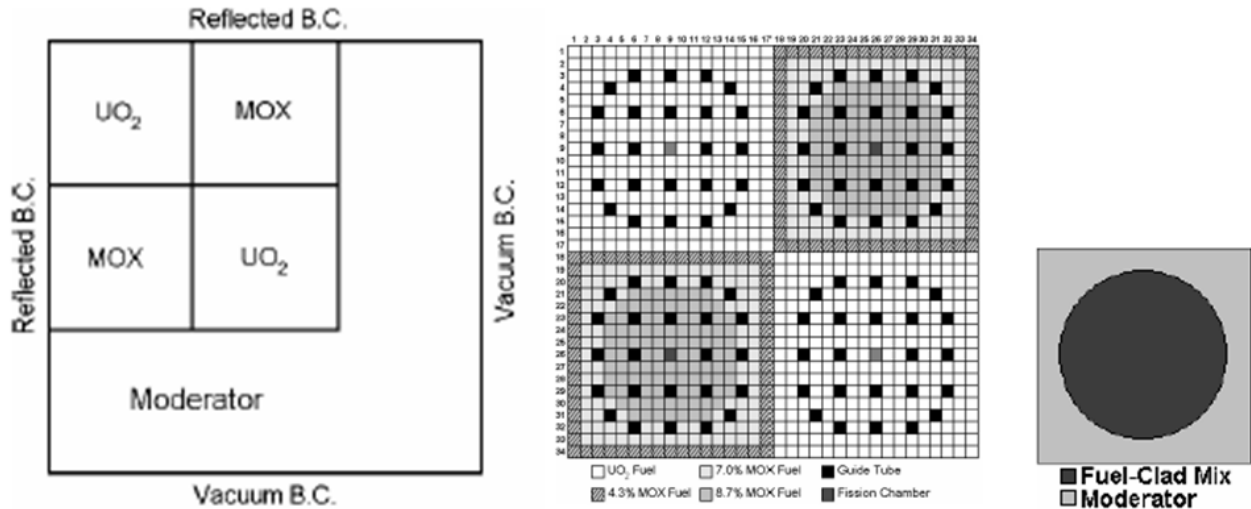


Fig. 4 : Benchmark for transport calculations without homogenisation

equation with lower quadrature order and strictly isotropic scattering rather than a diffusion equation. The TSA-CG method was applied to a variety of 2-D and 3-D cases (Gupta et. Al. 2008). In almost all the cases, a good speedup was obtained. Fig. 5 shows the reduction in the number of iterations with TSA-CG, for each of the 42 groups, for a representative 2-D case.

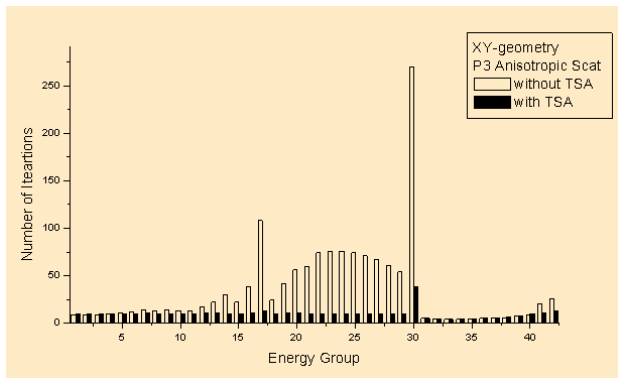


Fig.5: Effect of TSA on iterations for each group

Acceleration of K-eff Problem: Orthomin(1)

The solution of K-eigenvalue problem is commonly required for the analysis of fission-based systems. The prime interest is to evaluate the fundamental mode eigenvalue (K-eff) and the associated shape of neutron flux. The problem is usually solved by the power iteration method, to find the

fundamental mode. This involves solution of fixed source problem in each group which includes the well-known mesh-angle sweeping procedure (Lewis and Miller, 1993). Several attempts have been made (Adams and Larsen, 2002) to obtain an efficient solution of K-problem, such as shifted power iteration, coarse mesh rebalancing and Chebyshev acceleration.

A Krylov sub-space method called Orthomin(1) was proposed by Suetomi and Sekimoto (1991) for 2-D k-eff diffusion problems. An attempt has been made to apply this method to neutron transport problems. A direct implementation of the algorithm seemed very difficult as one has to generate coefficient matrices and there will be problems such as commonly occurring negative fluxes. To overcome this, a quite different approach based on fission-sources is suggested. In this approach, the K-eigenvalue problem can be written as $Pf = Kf$, where P is a square matrix called "fission matrix" and eigenvector f consists of mesh-wise fission source densities. The scheme was introduced in 3-D code ATE3 (Gupta and Modak, 2005) and applied to realistic 3-D cases. It was found that the Orthomin(1) works even better when applied with TSA. Fig. 6 show the effect of Orthomin(1) and TSA schemes on the CPU-times for a run for an LWR benchmark and AHWR critical facility:

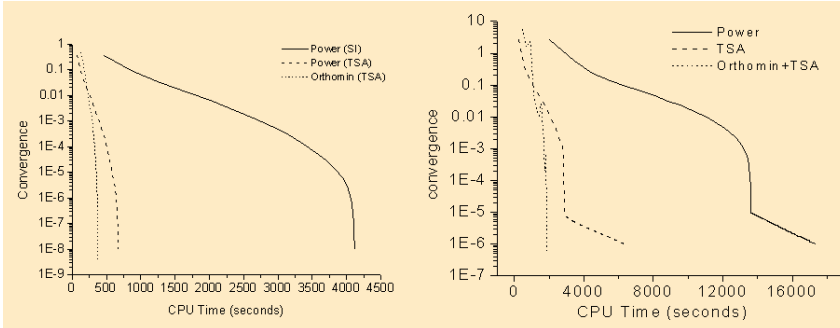


Fig. 6: Combined effect of Orthomin(1) and TSA

General Geometry methods

One of the disadvantages that deterministic solution of neutron transport simulations have, is that they require a geometrical grid for the solution. On the other hand, stochastic Monte Carlo methods are routinely used for core calculations as they have advantage of general geometry, but their use is limited. Researchers always wished for a deterministic general geometry method and MoC is one of current international interest. In MOC, the transport equation is solved along straight lines at the discrete number of spatial angles. These lines are known as characteristics. The method has advantages in terms of parallelisation too. There exist several codes now, which use MoC to whole core calculation (Smith et al. 2006).

Conclusions

The neutron transport simulation of a reactor core is one of the most challenging jobs in reactor design and analysis. The present article offers a glimpse into how the problem is tackled. We discussed methods which are developed in-house as well as current international trends. As more and more computing power becoming available, researchers are now exploring methods without spatial homogenization, general geometry capabilities and possible use of point data libraries. Apart from stochastic Monte Carlo simulations, approaches like *Method of*

Characteristics and Meshless methods are now gaining momentum along with irregular grid based deterministic solutions. Advanced solution algorithms like Krylov subspace methods are becoming popular to solve coefficient matrices. Research is now more focussed on methods which use minimal approximations and provide higher accuracy.

References

1. Adams M.L., Transport Methods for Nuclear Reactor Analysis, Computational Methods in Transport Tahoe City, September 11-16, 2004, www.ipam.ucla.edu/publications/tr2004/tr2004_4934.ppt
2. Adams M.L. and Larsen E.W., "Fast Iterative Methods for Discrete-Ordinates Particle Transport Calculations", *Prog. Nucl. Energy*, 40(1), 3-159, 2002.
3. Gupta Anurag, et.al, "Development of Neutral Particle Transport Code ATES3 & Further studies on Transport Synthetic Acceleration", Proceedings of PHYSOR-08, Interlaken, Switzerland, 2008.
4. Gupta Anurag and Modak R.S., "ATES3: Anisotropic Transport Equation Solver in 3D", Proceedings of 16th annual meeting of Indian Nuclear Society (INSAC-05), Mumbai, Nov 15-18, 2005.
5. Gupta Anurag and Modak R.S., "New Applications of Orthomin(1) algorithm for K-eigenvalue problem in Reactor Physics", *Annals of Nucl. Energy*, 33(6), p.538, 2006.
6. Smith M. A., Lewis E. E. and Byung-Chang Na, "Benchmark on Deterministic 3-D MOX Fuel Assembly Transport Calculations without Spatial Homogenization," *Progress Nucl. Energy*, 48, 383-393, 2006.



Development and Application of Eddy Current Testing for Quality Assurance of Nuclear Components

Arbind Kumar, P.P. Nanekar and B.K. Shah
Quality Assurance Division

Mr. Arbind Kumar is the recipient of the DAE Scientific & Technical Excellence Award for the year 2009

Abstract

Eddy Current Testing (ECT) is based on electromagnetic induction. It is used for detection of surface and sub-surface flaws, in electrically conducting material. Eddy Current test results are affected by lift-off, test material properties viz. electrical conductivity and magnetic permeability and test parameter such as frequency. Some of the difficulties faced during eddy current testing are: the control of lift-off, selection of the proper frequency and test technique, design of a suitable test probe, reproduction of the calibration standard and standardization of the test methods. To overcome these limitations, various developments were carried out and these developments were applied for quality assurance of nuclear fuels and in-service inspection of nuclear reactor core components as well as heat exchanger tubes of heavy water plants. The design and fabrication of eddy current test coils and development of indigenous eddy current test system for fuel inspection, in-service inspection of PHWR coolant channels and heavy water plants, is described in this paper.

Development of Indigenous Eddy Current Test System for Testing of PRP Fuel Element

Dispersion fuel is used for PRP. The intermetallic fuel is vibro-compacted inside a Zr-1%Nb fuel tube, having diameter 5.8 mm and length 1000 mm and Al-Si alloy is infiltrated through the fuel tube. The continuity of the fuel, inside the fuel tube, needs to be confirmed using eddy current testing. The selection of test frequency was a challenging task, as the materials of the fuel tube and fuel are different. The test frequency was standardized and the ECT probe was designed and fabricated. An indigenous automated ECT system was developed, for checking the continuity of Dispersion Fuel in PRP Fuel Element as shown in Fig. 1. There are three channels in this equipment for detection of surface flaws, subsurface flaws and variation in electrical conductivity. The feeding of fuel element, testing, recording of test results and sorting

of accepted and rejected fuel elements are carried out automatically.



Fig. 1: Automated Eddy Current Test System for Testing of PRP Fuel



Development of Indigenous Automated Inspection System for Metallic Fuel for Fast Breeder Reactor

Uranium oxide fuel is to be used in PFBR at Kalpakkam. This fuel has low breeding ratio, low thermal conductivity and linear heat rating, and low burn-up. The metallic fuel (U-Pu-Zr) can overcome these limitations of oxide fuel. Hence, it was proposed to develop the metallic fuel for PFBR. The metallic fuel (diameter -5 mm & length – 300 mm) is fabricated through melting and casting route. Being a cast product, the fuel rod may have physical discontinuities. The integrity of the fuel rod needs to be checked, using a non-destructive test method. An automated fuel inspection system, for checking the integrity of metallic fuel for fast breeder reactor was designed and fabricated as shown in Fig. 2. This system has facilities for weight measurement, length and diameter measurement using LVDT probe and flaw detection using eddy current testing. This system is installed under glove box and testing will be carried out remotely.

In-service Inspection of Coolant Channels of Pressurized Heavy Water Reactors (PHWRs)

The coolant channel of PHWR consists of a pressure Tube (Zr-2.5%Nb), a concentric calandria tube (Zircaloy-2) and four tight-fit garter springs (Zr-2.5%Nb-0.5% Cu) rested

on pressure tube, in the annular space between pressure tube and calandria tube. Heavy water coolant flows through the pressure tube, to remove the heat generated around the fuel bundles. The coolant channel components degrade during service, due to the hostile environment such as high temperature and high pressure of the coolant, fuel load, vibration and irradiation effects. Hence, periodic in-service inspection (ISI) is required, to monitor the integrity of these components. ECT is used to detect the location of garter springs and the gap between calandria tube and pressure tube. ECT coils for garter spring detection and CT-PT Gap measurement in coolant channels of PHWRs during pre-service as well as in-service inspection, were designed and fabricated as shown in Fig. 3. A few hundreds of coolant channels of PHWRs were inspected during pre-service and in-service inspection.

In-service inspection for Heat Exchanger Tubes of Heavy Water Plants

Heat Exchanger Tubes (AISI 316L) of heavy water plants degrade due to localized corrosion such as crevice corrosion, pitting corrosion and stress corrosion cracking at tube to tube sheet joints, support plate location, U-bend and tube internal surface during service. The integrity of these tubes needs to be monitored using non-destructive examination, to avoid the unplanned shutdown of the plants. Eddy current test coil was designed and fabricated



Fig. 2: Automated Fuel Inspection System for Testing of Metallic Fuel



Fig. 3: Inspection Head containing garter spring coil and CT-PT gap coil



and eddy current test procedure for testing of these tubes was standardised, using multi-frequency eddy current test methods. About 300 km of heat exchanger tubes of heavy water plants at Kota and Manuguru were inspected, during annual turn around.

Design of Eddy Current Test Coil and Development of Eddy Current Techniques for Quality Control of Dhruva Fuel

Eddy current test coils were designed and fabricated and an eddy current test technique was standardized, for quality control of Dhruva Fuel. Annually 1500 Natural Uranium Metallic Rods and Aluminum Finned Clad Tubes are tested, for surface and sub-surface flaw detection using these eddy current test coils and standardized test procedures.

Design and Fabrication of Eddy Current Test Coil and Development of Eddy Current Techniques for Testing of Various other Nuclear Components

Eddy Current test coils were designed and fabricated and ECT procedures were standardized for the many important applications as mention below.

- ◆ Electrical Conductivity Measurement of Rubber Strip containing Metallic Particle

- ◆ In-Service Inspection of Condenser Tubes at TAPS 1&2, Tarapur
- ◆ Detection of Discontinuity of Silumin in Fuel Rod Simulator
- ◆ Pre-Service Inspection of Condenser Tube of VVER, Kudankulam
- ◆ Detection of Discontinuity in Welded Austenitic Stainless Steel Pipes for Cable In Conduit Conductor for Superconductor wire
- ◆ In-Manufacturing Inspection of Titanium Tubes for LWRD Project

Conclusions

Eddy Current Testing is used for surface and sub-surface flaw detection in conductive metals. ECT results are affected by test coil variables as well as test material variables. Design of the ECT probe, selection of test parameters, standardization of ECT technique and signal analysis were carried out for non-conventional applications, such as testing of PRP B-core fuel element, uranium rod for Dhruva reactor and metallic fuel for PFBR, in-service inspection of PHWR coolant channels and heat exchanger tube testing of heavy water plants. ECT coils were designed, fabricated, utilized and ECT procedures were standardized, for various other applications too.



Development of novel radionuclide generators for biomedical applications

Ashutosh Dash

Radiopharmaceuticals Division

Dr. A. Dash is the recipient of the DAE Scientific & Technical Excellence Award for the year 2009

Abstract

This article provides a review on the innovative work, on the utility of nanomaterial-based sorbent and electrochemical technique, in the development of radionuclide generators for radiopharmaceutical applications. Extensive investigations on few generators, led to steady progress, achieved both in terms of process technology and final performance, in terms of product yield and purity.

Introduction

A radionuclide generator is a device, for effective radiochemical separation of a daughter radionuclide formed by the decay of a parent radionuclide. Radioisotope generator system represents a cost-effective way to ensure a continuous and reliable supply of short-lived radioisotopes, for clinical investigations and therapies, on an 'as needed' basis. Essentially, every conceivable approach has been used, for parent / daughter separation strategies. The column chromatographic process using a bed of sorbent, has emerged as the most popular approach. The inherent drawback of conventional sorbent used in column chromatographic system is the requirement of high specific activity parent radionuclide, owing to limited sorption capacity of the sorbent. Column chromatographic separation has also its limitation in working with long lived β -emitting radioisotopes, owing to the radiolytic degradation of the sorbent. Hence, fresh approaches are required to overcome these disadvantages.

Nanomaterials as sorbents in radionuclide generators

In recent years, the field of nano-sized materials has caught the attention and close scrutiny of scientists of diverse fields, owing to their extremely small size, large specific surface area and distribution of reactive surface sites. One of the specific properties of nanomaterials is that a high percent of the atoms are on the surface. The surface atoms of nanoparticulate metal oxides are unsaturated, exhibit intrinsic surface reactivity and can strongly adsorb metal ions in solution. Owing to the high surface area and intrinsic surface reactivity, nanomaterial based sorbents have higher sorption capacity and selectivity, compared to conventional sorbents. In order to tap the potential of nanomaterials as a new generation high capacity sorbent in the preparation of radionuclidic generator, our group for the first time, has successfully developed a few radionuclide generator systems using this class of material.



Electrochemical separation for radionuclide generator system

An equilibrium mixture of parent/daughter radionuclide having adequate difference in their formal potential values, in an aqueous electrolytic medium, can be mutually separated by selective electrodeposition of the daughter radionuclide on an inert electrode surface, under the influence of controlled applied potential. Aiming to electrodeposit the daughter radionuclide selectively from an aqueous electrobath, this novel approach has been directed towards the development of radionuclidic generators.

This article gives a brief overview of recent and ongoing researches of our group on the application of nanomaterial based sorbent and electrochemical technique to develop radionuclidic generators for biomedical applications.

Radionuclide generators system developed at Radiopharmaceuticals Division

Electrochemical $^{90}\text{Sr}/^{90}\text{Y}$ generator

Yttrium-90 is a therapeutic radioisotope of enormous interest. Owing to a long half-life of the beta emitting parent radionuclide, a chromatographic $^{90}\text{Sr}/^{90}\text{Y}$ generator can lead to substantial radiation degradation of the column matrix and restricts its utility. In an attempt to overcome the limitation of column chromatographic method, the use of electrochemical technique to avail ^{90}Y from ^{90}Sr was exploited. In this generator, the separation of ^{90}Y from ^{90}Sr is realized, owing to the difference between the standard electrochemical potentials. The generator involves two steps for electrolytic separation. The process involves electrolysis of a mixture of ^{90}Sr and ^{90}Y in nitrate form at $\text{pH} \sim 3$ at a potential of -2.5V , using platinum electrodes. The electrode containing ^{90}Y deposit is removed, used as the anode and subjected to a second electrolysis. The deposited ^{90}Y is leached in acetate buffer, a form suitable for

radiolabelling. Because the generator can be 'milked' virtually indefinitely, it was named 'Kamadhenu'[1]. The radionuclidic purity of ^{90}Y was assayed, based on a novel analytical technique called extraction paper chromatography [2]. This work encouraged ITD, an international commercial company, to design and build an automated ^{90}Y delivery system 'Kamdhenu' under the guidance of IAEA.

$^{188}\text{W}/^{188}\text{Re}$ generator

The $^{188}\text{W}/^{188}\text{Re}$ generator using a bed of acidic alumina column for chromatographic separation of ^{188}Re has remained the most popular procedure world over. The capacity of bulk alumina for taking up tungstate ions is limited ($\sim 50\text{ mg W/g}$) necessitating the use of very high specific activity ^{188}W ($185\text{-}370\text{ GBq/g}$), which can be produced only in very few high flux reactors available in the world.

Nanomaterial based $^{188}\text{W}/^{188}\text{Re}$ generator

In this context, the use of nanomaterial based sorbent possessing high capacity for W would not only mitigate the requirement of high specific activity ^{188}W , but also facilitate easy access to ^{188}Re . In order to realize the potential of nanomaterial based sorbent for the preparation of $^{188}\text{W}/^{188}\text{Re}$ radionuclide generators, three different nanomaterials such as polymer embedded nanocrystalline titania (TiP) [3], Nanocrystalline zirconia [4] and nanocrystalline $\gamma\text{-Al}_2\text{O}_3$ [5] were synthesized in our laboratory. X-ray diffraction and TEM micrograph of these nanomaterial based sorbent materials, are depicted in Fig.1 and Fig.2 respectively.

These nanosorbents were effective in providing carrier-free ^{188}Re (as $^{188}\text{ReO}_4^-$) with high yield with acceptable radionuclidic, radiochemical and chemical purity for clinical applications. Method to salvage the enriched ^{186}W from spent generators and to reuse it as target material was also demonstrated.

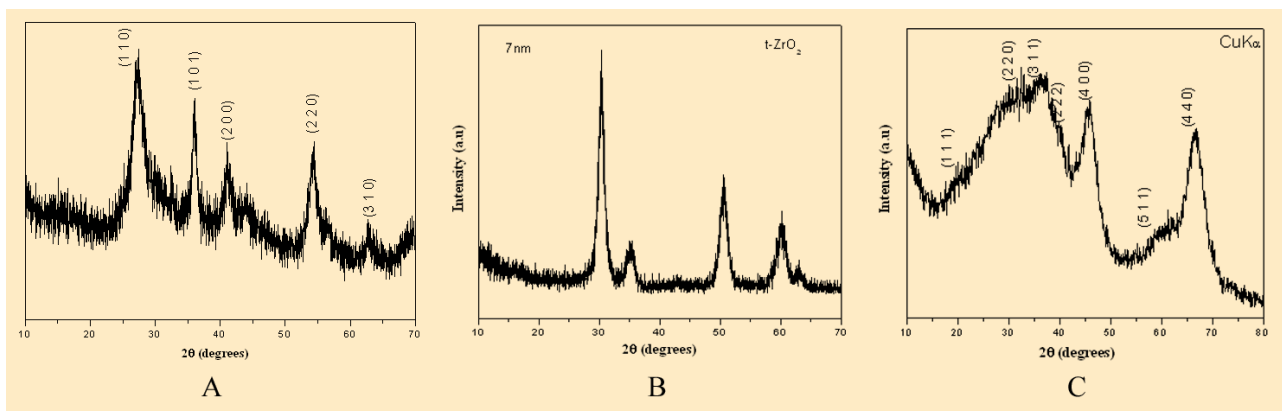


Fig. 1: XRD pattern of (a) polymer embedded nanocrystalline titania(TiP) (b) nanocrystalline zirconia (c) nanocrystalline γ -Al₂O₃

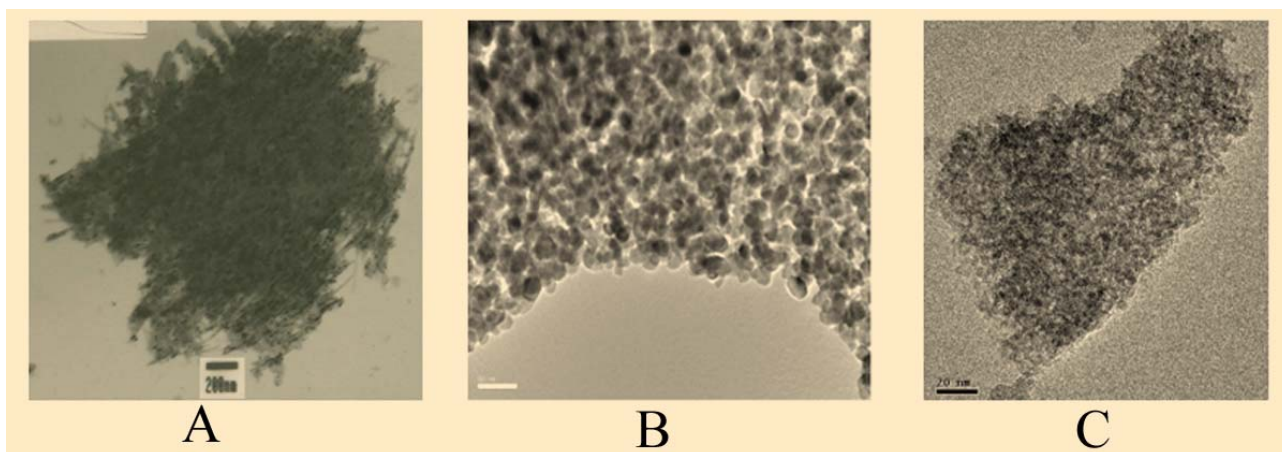


Fig. 2: TEM micrograph of (a) polymer embedded nanocrystalline titania(TiP) (b) nanocrystalline zirconia (c) nanocrystalline γ -Al₂O₃

Electrochemical ¹⁸⁸W/¹⁸⁸Re generator

An electrochemical separation technique to avail ¹⁸⁸Re from ¹⁸⁸W, adaptable for the use of low specific activity ¹⁸⁸W, was developed [6]. The electrolysis requires a time period of 60 minutes, at pH 1-2 at a potential of 7 V with 200 mA current, using platinum electrodes in oxalic acid medium. After electrolysis, the ¹⁸⁸Re deposited on the cathode was dissolved in 0.5 mL of 0.5 M HCl solution and passed through an alumina column preconditioned with saline. The overall decay corrected yield of ¹⁸⁸Re was >70%. The recovered ¹⁸⁸Re had high radiochemical (>97%) and radionuclidic purity (>99.99%).

⁹⁹Mo/^{99m}Tc generator

Of the isotopes currently in use, ^{99m}Tc has become the workhorse of diagnostic nuclear medicine. In order to reduce reliance on fission-produced ⁹⁹Mo, our group has explored the possibility of using (n, γ)⁹⁹Mo employing novel techniques, such as column chromatography using nanomaterial based sorbent and electrochemical process for accessing ^{99m}Tc.

Nanomaterial based ⁹⁹Mo/^{99m}Tc generator

The feasibility of using polymer embedded nanocrystalline titania(TiP) [7] and tetragonal nano-zirconia (t-ZrO₂) [8]



as the effective sorbents for developing a $^{99}\text{Mo}/^{99\text{m}}\text{Tc}$ chromatographic generator, have been demonstrated in our laboratory. Molybdenum-99 was both strongly and selectively retained by these sorbents at acidic pH and $^{99\text{m}}\text{Tc}$ could be readily eluted from it, using 0.9% NaCl solution with high yield with acceptable radionuclidic, radiochemical and chemical purity for clinical applications.

Electrochemical $^{99}\text{Mo}/^{99\text{m}}\text{Tc}$ generator

An electrochemical pathway for accessing $^{99\text{m}}\text{Tc}$ through the $(n,\gamma)^{99}\text{Mo}$ was also explored to avail $^{99\text{m}}\text{Tc}$ for radiopharmaceuticals application [9-10]. $^{99\text{m}}\text{Tc}$ from an equilibrium mixture of $^{99}\text{Mo}/^{99\text{m}}\text{Tc}$ was selectively deposited on a platinum cathode in an electrochemical cell by applying optimal potential of 5V over a period of 1 hour in NaOH electrobath voltage and stripped back again into the 0.9% saline solution. The overall yield of $^{99\text{m}}\text{Tc}$ was >90%, with >99.99% radionuclidic purity and >99% radiochemical purity. The compatibility of the product in the preparation of $^{99\text{m}}\text{Tc}$ labeled formulations such as $^{99\text{m}}\text{Tc}$ -DMSA and $^{99\text{m}}\text{Tc}$ -EC was found to be satisfactory in terms of high labeling yields (>98%).

Nanomaterial based $^{68}\text{Ge}/^{68}\text{Ga}$ generator

The commercially available $^{68}\text{Ge}/^{68}\text{Ga}$ generator systems are not optimally designed for direct applications in a clinical context. Our group has successfully used nanomaterial based sorbent such as ceria-polyacrylonitrile (PAN) composite [11] and nano zirconia [12], to develop chromatographic $^{68}\text{Ge}/^{68}\text{Ga}$ generator systems for accessing ^{68}Ga . These materials exhibit excellent column properties and are found to be promising materials for availing ^{68}Ga that could be directly used for the preparation of clinical grade radiopharmaceuticals. The compatibility of the product for preparation of ^{68}Ga labeled DOTA-TATE under the optimized reaction conditions, was found to be satisfactory in terms of high labeling yields (>99%).

Conclusion

This article briefly describes the first use of electrochemical technique and nanomaterial based sorbent, for the development of radionuclidic generator for radiopharmaceuticals application. The development not only offers alternative radionuclide resources to meet expanding demands for radiopharmaceuticals research, but also represents state-of-the-art separation chemistry, for radionuclidic generator development. Due to their special attributes, the interest in these radionuclide generators continues unabated and will find increasing acceptance in foreseeable future.

Acknowledgement

The technologies described in this paper are the result of valuable contributions of several scientists. Much of the reported work was done during the tenure of Dr. Meera Venkatesh as Head, Radiopharmaceuticals Division and Dr. V.Venugopal, as Director, Radiochemistry & Isotope Group. Application of electrochemical methodology for radionuclide generators development was a suggestion by Dr. M. R. A. Pillai. The use of high capacity adsorbents was also initiated in the early 2000. Shri Rubel Chakravarty has contributed immensely both intellectually as well as academically and together with Shri Ramu Ram carried out most of the experimental work. The authors' group has collaborated with Dr. A.K. Tyagi and his colleagues from Chemistry Division in nanomaterial based science. The author is thankful to all the above peers, colleagues and collaborators.

References

1. Chakravarty, R., Pandey, U., Manolkar, R.B., Dash, A., Venkatesh, M., Pillai, M.R.A., Development of an electrochemical $^{90}\text{Sr}/^{90}\text{Y}$ generator for separation of ^{90}Y suitable for targeted therapy, *Nucl. Med. Biol.* 35(2008):245–253.



2. U. Pandey, Dharni, P.S., Jagesia, P., Venkatesh, M., Pillai, M.R.A., A novel extraction paper chromatography (EPC) technique for the radionuclidic purity evaluation of ^{90}Y for clinical use, *Anal. Chem.* 80(2008):801-807
3. R.Chakravarty; A. Dash; M. Venkatesh, Separation of Clinical Grade ^{188}Re from ^{188}W Using Polymer Embedded Nanocrystalline Titania, *Chromatographia*, 69 (2009):1363-1372
4. Chakravarty, R., Shukla, R., Tyagi, A.K., Dash, A., Venkatesh, M., Nanocrystalline zirconia: A novel sorbent for the preparation of $^{188}\text{W}/^{188}\text{Re}$ generator, *Appl. Radiat. Isot.* 68 (2010):229-238.
5. Chakravarty, R., Shukla, R., Ram, R., Venkatesh, M., Tyagi, A.K., Dash, A., Exploitation of Nano Alumina for the Chromatographic Separation of Clinical Grade ^{188}Re from ^{188}W : A Renaissance of the $^{188}\text{W}/^{188}\text{Re}$ Generator Technology, *Anal Chem* (2011), *In press*.
6. Chakravarty, R., Dash, A., Kothari, K., Pillai, M.R.A., Venkatesh, M. A novel $^{188}\text{W}/^{188}\text{Re}$ electrochemical generator with potential for medical applications, *Radiochim. Acta*, 97(2009):309-317.
7. Chakravarty, R., Shukla, R., Gandhi, S., Ram, R., Dash, A., Venkatesh, M., Tyagi, A.K. Polymer embedded nanocrystalline titania sorbent for ^{99}Mo - $^{99\text{m}}\text{Tc}$ generator *J. Nanosci. Nanotechnol.* 8(2008):4447-4452.
8. Chakravarty, R., Shukla, R., Tyagi, A.K., Dash, A., Venkatesh, M., Practicality of Tetragonal Nano-Zirconia as a Prospective Sorbent in the Preparation of $^{99}\text{Mo}/^{99\text{m}}\text{Tc}$ Generator for Biomedical Applications, *Chromatographia* 72(2010):875-884.
9. Chakravarty, R., Dash, A., Venkatesh, M., A novel electrochemical technique for the production of clinical grade $^{99\text{m}}\text{Tc}$ using $(n, \gamma)^{99}\text{Mo}$, *Nucl. Med. Biol.* 37(2010)21-28.
10. Chakravarty, R., Venkatesh, M., Dash, A., A novel electrochemical $^{99}\text{Mo}/^{99\text{m}}\text{Tc}$ generator, *J. Radioanal. Nucl. Chem. In press*
11. Chakravarty, R., Shukla, R., Ram, R., Venkatesh, M., Dash, A., Tyagi A.K., Nanocerium-PAN composite-based advanced sorbent material: a major step forward in the field of clinical-grade $^{68}\text{Ge}/^{68}\text{Ga}$ generator, *ACS. Appl. Mat. Interface.* 2(2010):2069-2075.
12. Chakravarty, R., Shukla, R., Ram, R., Tyagi A.K., Dash, A., Venkatesh, M., Development of a nano-zirconia based $^{68}\text{Ge}/^{68}\text{Ga}$ generator for biomedical applications, *Nucl. Med. Biol.* 38(2011): 575-583.



Development of Optical Instruments for Spectroscopic and Nuclear Applications

D.V. Udupa, Sanjiva K. and N.K. Sahoo
Applied Spectroscopy Division

Dr. D.V. Udupa is the recipient of the DAE Scientific & Technical Excellence Award for the year 2009

Introduction

Optics and Spectroscopy have both historically evolved as companion sciences, with advances in optics leading to advancements in optical spectroscopy. Realizing the crucial role of optics in guiding spectroscopy research, the erstwhile Spectroscopy Division had envisaged the establishment of an advanced optics laboratory in the Division for in-house fabrication and testing of precision optical components and thin film optical devices. The Applied Spectroscopy Division has been actively engaged in the design and development of optical and spectroscopic instruments, in tune with this philosophy.

A brief overview of some of these indigenously developed optical instruments, consisting of Interferometers, Monochromators, Polychromators, Spectrographs and Periscopes is presented here.

22-channel Direct Reading Polychromator

A direct reading polychromator for simultaneous spectrochemical analysis of 22 elements in Uranium and other reactor materials, was

developed indigenously, in collaboration with CDM, BARC [1]. The instrument is based on concave grating dispersion and has 22 photo-multiplier tubes, for simultaneous detection of impurities by atomic emission spectroscopy.

A one meter Czerny-Turner scanning monochromator was developed, for sequential analysis of rare-earth impurities in uranium and other reactor materials, for the Kalpakkam Atomic Reprocessing Plant (KARP)[2]. This instrument has a scanning wavelength range of 200-450 nm and a resolution of 0.02 nm, giving a typical detection limit of 14 ng/ml, 39 ng/ml, 2.3 ng/ml and 5.3 ng/ml for Gd, Ce, Y and Mo respectively.

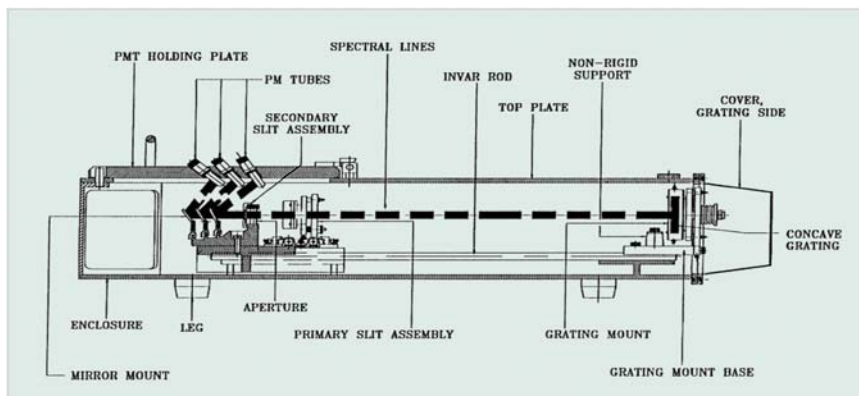


Fig. 1: Mechanical drawing showing the side view of polychromator



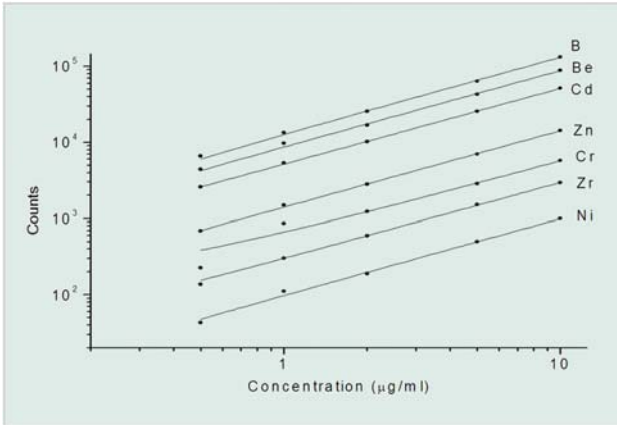


Fig. 2: Calibration curves for simultaneous analysis of seven elements using the instrument

6.65 meter vacuum ultraviolet high resolution spectrometer

A 6.65 m off-plane Eagle spectrometer has been developed indigenously, in collaboration with CDM, BARC, for high-resolution VUV spectroscopic studies, at Indus-I Synchrotron Radiation Source, RRCAT [3,4]. This optical instrument covers a wavelength range of 700-2000 Å in the vacuum ultraviolet region, with an estimated resolution of 0.01 Å.

Half meter Scanning Monochromator

A 0.5 meter scanning monochromator has been developed, for application in $^{15}\text{N} - ^{14}\text{N}$ isotopic analysis in nitrogen,



Fig. 3: One meter Czerny-Turner Scanning monochromator based sequential analysis system



Fig. 5: The 6.65 m Vacuum Ultraviolet spectrometer

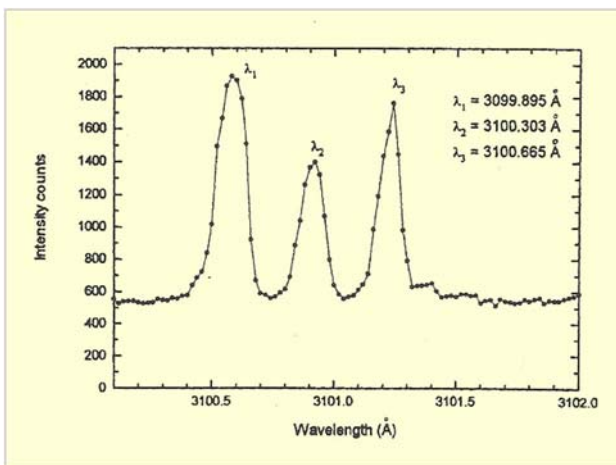


Fig. 4: Iron triplet lines with wavelength separation of 0.36 Å resolved by the monochromator

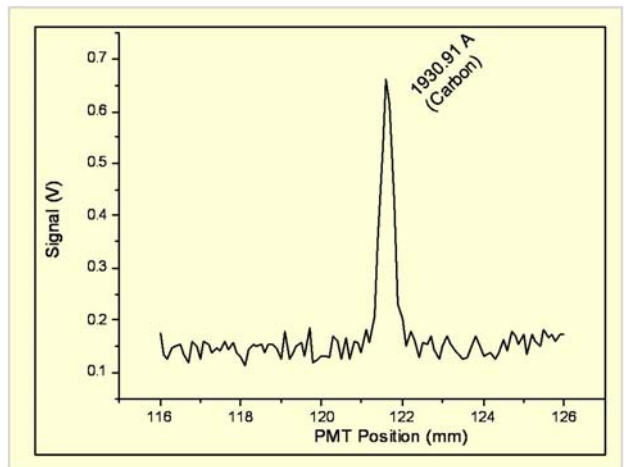


Fig. 6: Carbon emission line recorded using the Spectrometer



extracted from bio samples[5]. This instrument was developed in collaboration with CDM, BARC and has a wavelength range of 200-500 nm with a resolution of 0.04 nm.



Fig. 7: Half meter spectrometer with data acquisition system

Air spaced Fabry-Perot etalons

Fabry-Perot etalons useful for high-resolution spectroscopy and measurement of small wavelength shifts in laser beams, have been developed. This interferometer consists of highly flat polished optical mirrors (surface flatness $> \lambda/50$ and reflectivity $\sim 90\%$) aligned precisely parallel to each other (Parallelism < 0.1 arc-sec) at the exact specified separation. Fabry-Perot etalons with free spectral ranges of 30 GHz, 15 GHz and 7.5 GHz and a finesse of 22 have been developed.

Half meter Multi-Channel Spectrograph

A 0.5 meter multi-channel spectrograph using CCD detector has been developed, in collaboration with CDM, BARC, for micro-Raman spectroscopic applications[6]. This

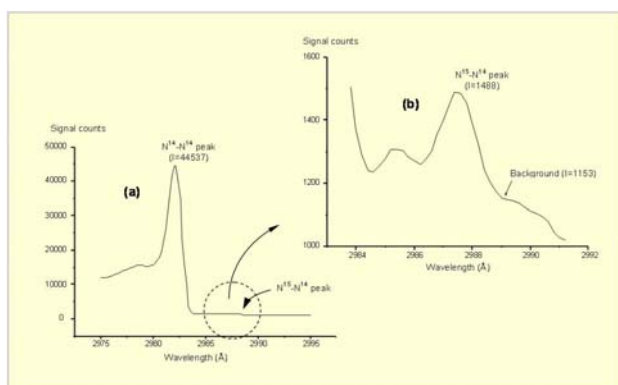


Fig. 8: Spectrum showing the peaks of $^{14}\text{N}-^{14}\text{N}$ and $^{14}\text{N}-^{15}\text{N}$ molecules recorded by the instrument.

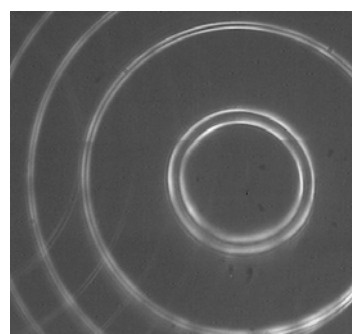


Fig. 10: Fabry-Perot fringes resolving two closely spaced laser modes



Fig. 9: Air spaced Fabry-Perot Etalon of free spectral range 7.5 GHz and aperture 25 mm

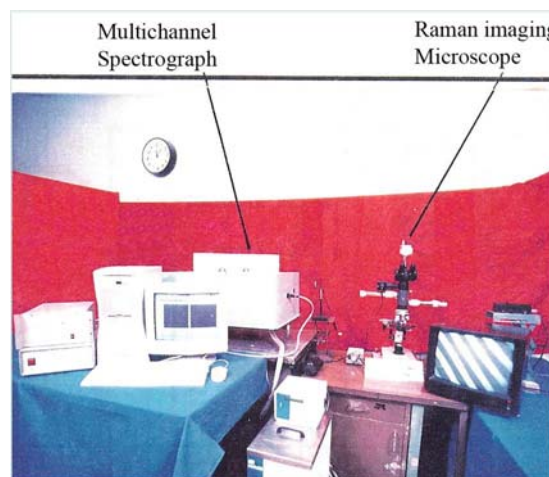


Fig. 11: Multi-channel spectrograph for Raman spectroscopic application

DAE Excellence Award



instrument has a wavelength range of 400-700 nm with a resolution of 0.1 nm and a recording bandwidth of 37 nm.

FBTR core viewing periscope

A 6 meter long optical periscope for in-service inspection of the core of the Fast Breeder Test Reactor at Kalpakkam was developed in collaboration with DRHR and CDM[7]. The periscope made using radiation stabilized glasses, facilitates viewing and photography /video recording of the objects in the core with a spatial resolution of 0.7 mm, with a field of view of 8° and a field scanning of 110°.

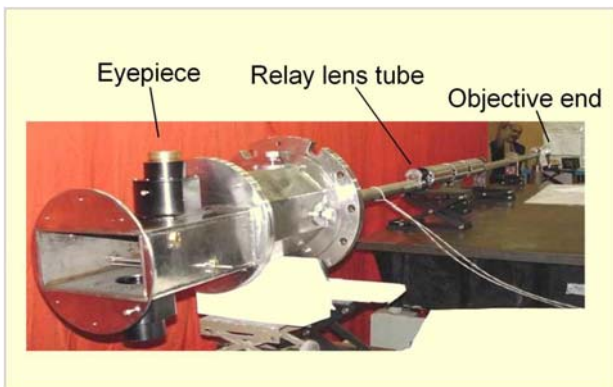


Fig. 12: Six meter FBTR periscope showing the optical canal housing the relay lenses, prisms and zoom objective.

Echelle Spectrograph

An echelle spectrograph with a 2-Dimensional CCD detector was designed and developed for the simultaneous spectrochemical analysis of up to 45 elements[8]. The spectrograph has a wavelength range of 210-400 nm with a resolution of 0.02 nm. The typical determination limit achieved with this instrument is 0.02 mg/ml for B, Cd and Gd.

10 meter PFBR Periscope

A 10 meter long optical periscope for visual inspection and video recording of components in the core of the Prototype Fast Breeder Reactor (PFBR) coming up at Kalpakkam has been designed and is currently under advanced stage of fabrication. This instrument is being



Fig. 13: Photograph of the analytical system using the echelle spectrograph

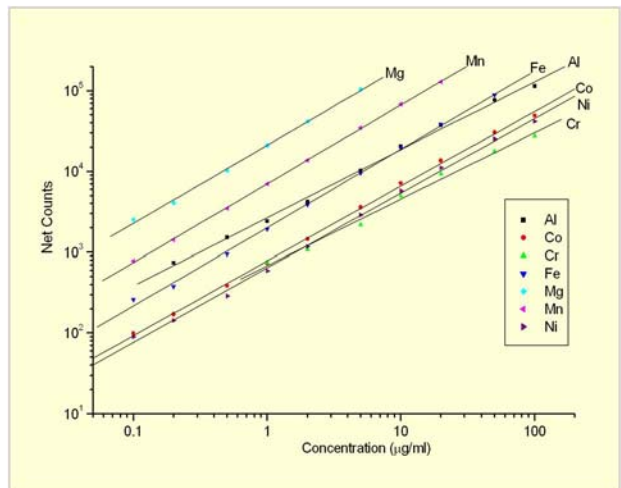


Fig. 14: Calibration plots for the simultaneous analysis of seven elements using echelle spectrograph



Fig. 15: Ten meter periscope under development for the PFBR Reactor

developed in collaboration with DRHR and CDM divisions of BARC and with IGCAR, Kalpakkam and will be used under reactor shut down condition. The instrument has a



spatial resolution of 0.4 mm and field of view of 15° with a field scanning of 110°.

References

1. R P Shukla, S Bhattacharya, D V Udupa, T Jayasekharan, P P Khanna, S M Marathe, Sampath Kumar, M N Patil, S V G Ravindranath, Sandeep Guha, M B Guhagarkar and A P Roy, "The Design Fabrication and Performance Evaluation of a 22 Channel Direct Reading Atomic Emission Spectrometer using Inductively Coupled Plasma as a Source of Excitation", *Sadhana*, Indian Academy of sciences 25, Part 1, (2000) 57-69.
2. R P Shukla, D V Udupa, S S Biswas, Manika Das, S V G Ravindranath, S M Marathe, A K Sinha, M B Guhagarkar and A P Roy, "The Design, Fabrication and Performance Evaluation of a Scanning Monochromator for Rare Earth Element Analysis", *Journal of Optics* 26, No.2, (1997) 47-65.
3. N C Das, R P Shukla, D V Udupa, N K Sahoo, D Bhattacharya, K Sunanda, P Saraswathy, Sampath Kumar, A K Sinha, S Bhat and V C Sahni, "Design, Development and Performance Evaluation of a High Resolution VUV Spectrometer at Indus-1 Synchrotron Source", *Journal of Optics* 32, (2003) 177-192.
4. N.C. Das, R.P. Shukla, D.V. Udupa, N.K. Sahoo, D. Bhattacharya, K. Sunanda, P. Saraswathy, Sampath Kumar, A.K. Sinha, S. Bhat and V.C. Sahni, "Development of a 6.65 m Off-plane Eagle Spectrometer for a High Resolution VUV Beam – line at Indus-1 Synchrotron Radiation Source", *Current Science* 87, No.11, (2004) 1523-1529.
5. R.P. Shukla, D.V. Udupa, Manika Mallick, S. P. Somkuwar, B.J. Shetty, A. K. Sinha and V.C. Sahni, "Design and Development of 0.5 m Scanning Monochromator and its Application to ¹⁵N Analysis", *BARC Newsletter*, July, (2005) 12-19.
6. R.P. Shukla, Sanjiva Kumar, Manika Mallick, S V G Ravindranath, S Thakur, N K Sahoo, N C Das and A K Sinha, "Multichannel Spectrograph using CCD as a Detector for Raman Spectroscopic Application", BARC Report: BARC/2002/E/019.
7. N.C. Das, Sanjiva Kumar, D.V. Udupa and R.P. Shukla, "The Design and Fabrication of an Optical Periscope for Core viewing of Fast Breeder Test Reactor (FBTR)", BARC Report no. E 017, (2004).
8. D. V Udupa, Sanjiva Kumar, B J Shetty, P B Patil, Omana N, R Sampath Kumar and Ajaya Kumar, "Development of an Echelle Spectrometer for Simultaneous Trace Elemental Analysis", *BARC Newsletter*, July, (2008) 9-12.



Development of Software for Instrumentation in Power and Research reactors and Accelerator based Research

Padmini S., M.P. Diwakar, P.M. Nair, Swati Gaur, S.S. Pande and C.K. Pithawa

Electronics Division, E&I Group

and

Nilesh Gohel

Research Reactor Maintenance Division, Reactor Group

Ms. S. Padmini is the recipient of the DAE Scientific & Technical Excellence Award for the year 2009

Abstract

The Electronics Division is mainly concerned in building systems for reactor instrumentation and nuclear physics experiments. Software forms a significant component of these systems. Applications for reactors have large overlapping functional requirements in addition to specific requirements. This has been captured into a reusable "Real Time Data Acquisition Framework." This application framework provides a platform and imposes high-level architecture for building embedded systems. The variability in these systems is taken care of by configuration points. Using this approach, the following systems have been developed: Flux Mapping System for TAPP-3&4, Digital Recording System for AHWR Critical Facility, Radiation Data Acquisition System, Fire Alarm System and RRS Data Acquisition System for Dhruva. Nuclear data acquisition software has been designed to dynamically exploit the number of available processor cores, making it scalable to meet throughput requirements of individual experiments. This paper describes some of the software technologies used, the software development process and the major applications that have been developed in the last few years.

Introduction

Software is a significant component of the instrumentation projects that have been undertaken by the Electronics Division, for Power Plants / Research reactors and accelerator based research. Systems developed for nuclear reactors have to address concerns of high reliability, real time performance, safety and interoperability. Nuclear data acquisition systems have to be designed to be scalable, handle large volume of event data and filter meaningful data through sophisticated software triggers. These systems need to have the ability to exploit advances in multicore architecture, to meet throughput requirements and allow programmability to the user. In order to meet

these challenges, some of the important decisions were concerned with the choice of technology to be used. Attempts were made to identify, evaluate, select, and absorb software innovations for improved performance. These include Modern Languages, Frameworks and software engineering practices. While adopting these technologies, a transition pattern was followed where these technologies are first adopted for nuclear physics applications and after a certain level of maturity is reached, they are applied for safety critical applications.

The paper is organized in three parts: Technologies that have been used to address the above challenges, applications that were developed using these technologies



and improvements made in the software development process.

Real time Data Acquisition Framework

Designing a distributed application, requires careful consideration of performance, scalability, reliability, security, maintainability, interoperability and extensibility. The concept of an architecture-based reuse has been used, which provides a common platform for a family of related applications. Variability between these applications has been analyzed and configuration points are provided, to take care of these variations. Handling the variant aspects is done by the Component configuration infrastructure, that supports dynamic, runtime (re) configurations and (re) deployments of objects. By reusing an appropriate architecture, not only development and testing effort is saved, but time to complete is reduced and architectural mistakes are avoided.

Multicore and Task-based Programming

It is a well-understood maxim in the technology industry, that software and hardware must evolve in parallel, and be well matched to achieve desired functionality and performance. Physical limits of semiconductor technology and improved manufacturing technologies, are driving processor architectures towards multi and many cores. Most desktop machines today have at least a dual-core microprocessor. Servers and advanced workstations are designed with quad-core and octal core microprocessors.

Traditional sequential code, does not take advantage of multiple cores, because the serial instructions run on only one of the available cores. Improving the throughput requires splitting algorithms into multiple threads, coordination among the different units of code, sharing information between them, and collecting the results. Threads created directly with native threading package are logical threads, that are mapped by the operating system onto the physical threads of the hardware. By using native threads directly, the developer becomes responsible

for matching the parallelism available in the application, with the resources available in the hardware. Creating too few logical threads will result in underutilization of available hardware resources. Creating too many logical threads will cause the operating system to incur considerable overhead, as it must time-slice access to the hardware resources.

We have used a lightweight concurrency model using the Tasks Parallel Library (TPL) in .NET Framework that is based on actor model. This model could express the logical parallelism in applications with large number of tasks, which are scheduled by the runtime library on to its internal pool of worker threads. Usage of tasks made it possible to focus on the logical parallelism in the application, without worrying about managing the parallelism. In addition, since tasks are much lighter in weight than threads, parallelism could be expressed at a much finer granularity. This design is scalable on many core architectures.

Modern Languages

Multi-paradigm is the paradigm of the future. The level of abstraction of programming languages is increasing with features like garbage collection, type safety, threading, exception handling, extensible data types, and code security provided in the language itself. The three major trends for programming languages are declarative, concurrent and dynamic. Recent developments in industry have resulted in big influence on languages. Many functional languages like Erlang, Scala, Haskell, Clojure, F# etc. are becoming popular, as they make concurrency a lot simpler. There is no sharing of state and mutating of state in these languages. F#, a functional language with strong typing, very succinct, type inferencing, pattern matching, active patterns, async workflows, units and measures, has some imperative constructs. Tools are getting sophisticated in finding and exploiting fine-grained concurrency when they are presented with abstract, declarative and functional codes.



In the systems designed, safe high-level programming languages have been used to the greatest extent possible. These prevent critical errors while facilitating development and use of accurate and efficient software-development tools. C++, an object oriented language has been used, for embedded system development on QNX RTOS. A multi-paradigm programming language C# on the .NET platform is currently being used, for development of Operator Consoles for Dhruva control room. With C# 4.0, explicit functional language extensions such as lambda expressions, closures, continuations and type inference have been used. LINQ technology built into C# encouraged declarative programming style. Currently F# is being explored for use in application areas like scientific computations, UI etc.

Software Development Process

An iterative incremental model of development was adopted for our projects. Classic software development processes follow the waterfall lifecycle where development proceeds linearly from requirements analysis through design, code & unit testing and system testing, with limited feedback on the results of the previous phases. In this approach, there is a lot of emphasis on "the specification" which is required to be complete. In a waterfall approach, many problems are resolved during the system integration activity.

The main advantage of iterative incremental is to bring more predictability to the outcome and the schedule. It brings higher quality products and satisfies the real needs of end-users, as there is time to evolve requirements, design and implementation. In the iterative process, the software that is developed comes first. The software architecture is driven by early lifecycle decisions. Planning is mostly based on risks and unknowns, which have to be addressed right from the onset.

Agile Methodology

The practices of traditional software development processes are inadequate to control projects with complex technology and sophisticated requirements. We have adopted agile development practices, which resulted in the ability to manage changing priorities, increased productivity, improved team morale and enhanced software quality. The Agile process implements empirical process control through iterations, frequent releases of working, tested software, emergence of requirements and architecture, self-organization of multiple small teams and collaboration with users.

Working closely with the users, the agile team delivers version of the software as early and as often as possible. Constant feedback is obtained from the code that is delivered. Automation is used for continuous building and testing the project. In order to preserve the design, the code needs to be re-factored. Work progresses in *iterations*: small blocks of time (a week or so) where a set of features are identified and implemented.

Software development infrastructure for agile process has been set up with tools and procedures for configuration management and automated unit testing, profiling, code coverage & dynamic testing. The tool set also includes refactoring tools, tools for automated build, test, release & deployment activities and acceptance testing tools.

Applications

Flux Mapping System for TAPS 3 & 4

The Flux Mapping System (FMS) of 540Mwe PHWR is a system, which is the first of its kind, used in Indian PHWRs. It is used to compute a detailed flux/ power distribution of the reactor core using modal synthesis method. The



main function of FMS is to monitor the in-core Vanadium self powered neutron detector signals, located at different locations in the core, generate neutron flux profiles, 14 zonal powers and other related information, compute, and send zone power correction factors to the Reactor regulating system. FMS also performs two additional functions namely: display of detailed flux maps and computation of burn up of Co⁵⁹ isotope and the build-up of Cobalt ⁶⁰ isotope.

The system is designed as three-tier distributed fault-tolerant system with dual redundant Ethernet optical links between nodes. The three tiers are: Nine Input Scanning Processor (ISP) sub-nodes, dual redundant Flux Mapping Processors (FMP) nodes, and dual redundant Operator Console (OC) nodes. ISP nodes are located in the reactor building, receive signals from SPND detectors and send the scanned data through dual redundant fiber optic link, to the FMP nodes located in the control equipment room. Each of ISP and FMP are PC- architecture-based, rugged embedded nodes.

The nodes of FMS are interconnected through dual redundant fiber-optic links. Fiber optical communication eliminated EMI interference. This network architecture has resulted in drastic reduction of cabling from reactor building to control room. In order to achieve the deterministic behaviour in the Ethernet based network, master-slave protocol was used, which avoids the potential packet collision.

The embedded nodes (ISP, FMP) run on QNX RTOS to meet safety standards. QNX Neutrino is ideal for embedded real-time applications, as it scales to very small sizes and provides multitasking threads. It has priority driven pre-emptive scheduling, and fast context switching. QNX Neutrino achieves this through fundamental principles: Microkernel architecture and Message-based inter-process communication.

Each of the FMS nodes periodically performs self-test, to identify faulty components. Watchdog continuously

monitors system integrity. The redundant FMP nodes change their roles to active (Master) and stand-by (Listener) role in alternate scan cycle. This ensures that all the software modules in each FMP node are active all the time. This helps in prompt detection of faults in the FMP nodes. Redundant network links are also used in the same way, for early detection of link problems. This resulted in achieving high availability of the system.

PC Based Systems for Research Reactors (Dhruva and AHWR Critical Facility (CF))

In Dhruva, a need for upgradation of some of the instrumentation was felt, in the data acquisition and processing systems, due to either obsolescence or for augmenting the facilities provided by the existing systems. Taking care of the retrofitting requirements of obsolete systems / instrumentation, the following systems were designed, developed and deployed at Dhruva: Radiation Data Acquisition System, RRS Data Acquisition System, Fire Alarm System and Operator Console for Alarm Annunciation System. Significant improvements that have been obtained using this approach are: completely redundant systems, convenient paperless large data storage, operator friendly interface and the facility to connect to other systems.

A digital recording system for AHWR CF was developed and installed, to record parameters from Reactor regulating system, Neutronic channel instrumentation & Process instrumentation and to monitor the actuation time of shutdown devices like Shut off rods and Moderator dump & Control valves. On-line estimate of critical height of moderator level based on inverse LCRM count could be computed which was very useful in first approach to criticality.

Ethernet CAMAC Crate Controller

CAMAC is currently the most widely used instrument standard for nuclear data acquisition and accelerator



control applications in accelerator labs in India. A new CAMAC controller (ECC) has been developed with an embedded processor and Ethernet as the communication medium to the host computer. Control applications need several physically distributed crates with regular scanning of all the parameters with control from a centralized PC. On the other hand, nuclear physics experiments need a high throughput with a large number of parameters. ECC is designed to achieve these objectives using single cycle mode, scan mode and list mode operations.

The ECC is designed with Single Board computer having PC architecture, which allows standard Ethernet services, such as TCP socket based communication protocol. The processor runs a version of real-time operating system QNX. The micro-kernel architecture of QNX allows for low memory footprint and gives deterministic performance. The multi-threading architecture permits the overlapping of the operations of data acquisition and delivery of data through the communication channel. This results in improved system performance even on a single processor system. Judicious use of multiple threads with lockless algorithms enables the system to take advantage of multi-core support in QNX to provide a scalable solution.

Conclusion

It has been observed, that when software development takes into consideration advances in software technology,

it results in radically new and powerful solutions. We have been able to embrace promising technologies, modern programming languages and good software engineering practices. Framework based approach not only resulted in speeding up the system development, but also cut down the time and effort required for testing and maintenance of these systems. Agile adoption improved productivity, reduced project risk, and enhanced software quality through collaboration, test-driven design and continuous integration.

Acknowledgement

The authors would like to acknowledge the encouragement and support provided by Shri M.D. Ghodgaonkar and Shri P. K. Mukhopadhyay. We acknowledge the contribution of Reactor Instrumentation Section, ED. in the design and development of hardware for FMS. We acknowledge the contribution of Data Processing Group, ED. in the design and development of hardware for CAMAC Controller. We are also thankful to the user community for their collaboration, which helped in making the transition to agile a success. We are thankful to Shri Kevin Fernandes, ED for shaping the UI and additional support provided in commissioning of the systems.



Development of Spent Fuel Handling Equipment and man-rem Saving Tools for Nuclear Reactors

Shyamal Roy, J. P. Singh and R. J. Patel
Refuelling Technology Division

Mr. Shyamal Roy is the recipient of the DAE Scientific & Technical Excellence Award for the year 2009

Abstract

On-power fuelling in Pressurised Heavy Water Reactor (PHWR) is essential, to maintain reactivity in the core. Due to this, the spent fuel transfer system interacts with the core in daily basis. Proper functioning of the spent fuel transfer system, enables the reactor to run smoothly and efficiently. The coolant channel used in Pressurised Heavy Water Reactor (PHWR) is a very important component, both from the point of view of reactor performance and reactor safety. It houses fuel bundles at high temperature and pressure. Life management of coolant channels is essential, to provide assurance of continued structural integrity of pressure tubes over reactor life time. Various life management tools viz. BARCIS, WEST and CHIP have been developed and are deployed in PHWRs. In India, as part of three stage nuclear power programme, Prototype Fast Breeder Reactor (PFBR) is being constructed. Inclined Fuel Transfer Machine (IFTM) is to be deployed for fuel transfer operation. The hoisting system of IFTM plays a very important role in terms of safety and reliability during fuel transfer operation.

Introduction

Natural uranium used in PHWR as fuel, has very little excess reactivity available in the core at any time. This makes it necessary to carry out fuelling operation almost on a continuous basis. The on-load Fuelling Machine (FM) is designed to remove irradiated fuel from the reactor core and load fresh uranium fuel. In 540 MWe PHWR, there are 392 coolant channels. Each channel contains 13 fuel bundles. Spent Fuel Transfer System (Fig. 1) facilitates the transport of irradiated fuel, removed from reactor building to the Spent Fuel Receiving Bay (SFRB). The light water filled SFRB and Spent Fuel Storage Bay (SFSB) are located away from reactor building. A typical

540 MWe PHWR has two identical Fuel Transfer (FT) systems, each dedicated for "North" and "South" sides of the reactor. Major FT equipment comprises, Transfer Magazine (TM) which receives the spent fuel from FM, Shuttle Transfer Station (STS) which receives fuel from TM, a shuttle transport system connects STS on one end and receiving bay equipment on the other end. It facilitates the transport of spent fuel by virtue of light water flow, through a shuttle transport tube. The SFRB equipment enables to receive the spent fuel and facilitates their transport further to SFIB occasionally, for fuel inspection or to adjacent SFSB for cooling and storage. Proper functioning of SFRB equipment enables smooth/efficient fuel transfer operation.

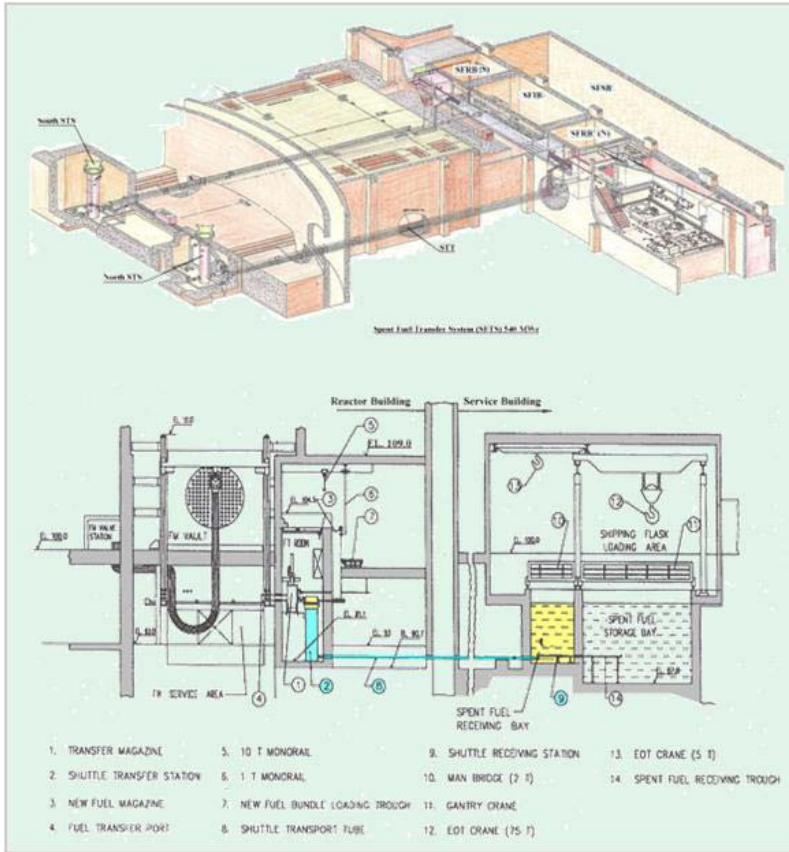


Fig. 1: Spent Fuel Transfer System for 540 MWe PHWR

The coolant channel in PHWR is a very important component, both from the point of view of reactor performance and reactor safety. The coolant tube basically consists of pressure tube which contains nuclear fuel and heavy water at high temperature & high pressure passes through these fuel. The pressure tube is surrounded by a concentric calandria tube. The annular gap between pressure tube and calandria tube filled by a suitable gas is essentially meant to thermally insulate the high temperature pressure tube from the relatively low temperature moderator (Fig. 2). End of the pressure tubes is connected with end fitting and closure seal plug, for isolation of pressure boundary. Every time fuelling machine

visits the channel needs to clamp on the end fitting remove closure seal plug and carry out the refuelling operation. This repeated operation on the channel is likely to lead to some damage on end fitting closure seal face. To rectify this damage, the channel needs to be isolated from the feeder of PHT supply. A Channel Isolation Plug (CHIP) has been developed for this purpose. In addition to this, any type of damage in pressure tube may lead, to crack or complete breakage of pressure tube. In other words, it affects the integrity of the coolant channel, which is of great importance in reactor performance and reactor safety. Life management of coolant channels of PHWRs is essential, to provide assurance of continued structural integrity of pressure tubes, over reactor life time. Some techniques have been developed, to maintain the mandate of life management. These are the BARC Channel Inspection System (BARCIS), and the Wet Sliver Sample Scraping Tool. The techniques are designed

with the objective of minimising radiation exposure to

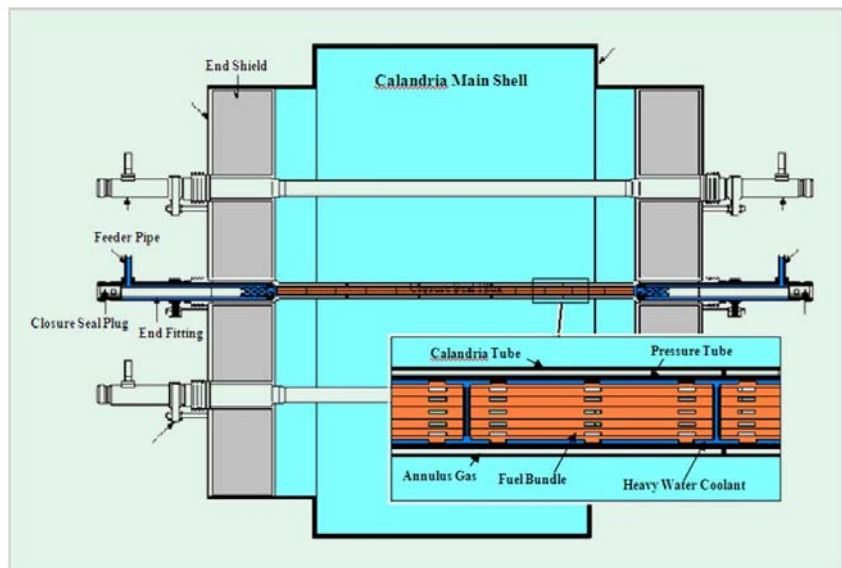


Fig. 2: Typical Coolant Channel for Indian PHWR



inspection personnel and completion of the inspection with minimum reactor downtime. The successful development and completion of all these indigenous techniques contributed to substantial savings on man-rem in operating plants.

PFBR is being constructed in India, as part of three stage nuclear power programme. IFTM is to be deployed for refuelling the PFBR in off-power mode. IFTM transfers fresh & irradiated core sub-assemblies (S/A) in/out of main vessel (MV) during fuel handling operations. To transfer Core Sub-Assemblies from In-Vessel Transfer Post (IVTP) to Ex-vessel Transfer Post (EVTP) and fresh Sub-assemblies from EVTP to IVTP a Transfer Pot (TP) is used. A Hoisting system mounted at the top of Rotatable Shielded Leg (RSL) at elevation 40m is used for hoisting and lowering of the TP (Fig. 3). The hoisting system plays a very important role in terms of safety and reliability, during fuel transfer operation. To achieve this requirement, the hoisting system for IFTM has been designed, using the international design codes and guides in a professional manner, to meet the stringent requirement of single failure criteria as stipulated by regulatory authority. Detailed drawing, design

documents, design calculations were prepared for the system. The system has been manufactured and is being tested, prior to installation in the reactor at Kalpakkam.

The following paragraphs explain the highlights of the above mentioned system:

Spent fuel receiving bay equipment for 540 MWe PHWR (Fig. 4)

SFRB is situated in the service building, about 45m away from the reactor building. The SFRB admeasuring 6m x 4.5m x 6.5m deep, is filled with light water. There are two separate SFRB's for north and south fuel transfer system. SFRB equipment mainly consists of Shuttle Receiving Tube (SRT), Pawl opening mechanism, Transfer Arm (TA) and set of hydraulic cylinders. All this equipment is operated under water. Out of various layouts worked out, the present layout has been considered, as this enables fuel transfer operation in one horizontal plane and the movement of fuel, visible from the top of the bay. A pair of fuel bundles is transported from reactor building to SFRB by virtue of light water flow inside a shuttle. The shuttle is decelerated and received in the Shuttle Receiving

Tube (SRT). Pawls of shuttle are opened by the help of pawl opening mechanism. After opening the pawls, SRT is rotated of and aligned with TA, the fuel is ejected by hydraulic ram on TA and pushed further for transferring to SFSB or SFIB. Detail design of the SFRB equipment was taken up. Challenges in design of SFRB equipment are that, spent fuel is highly radioactive hence it has to be handled inside shielding, the mechanisms need to be remotely operated, each likely abnormal situation needs to be visualized in detail, to provide built-in remedies and all safety principles have to be

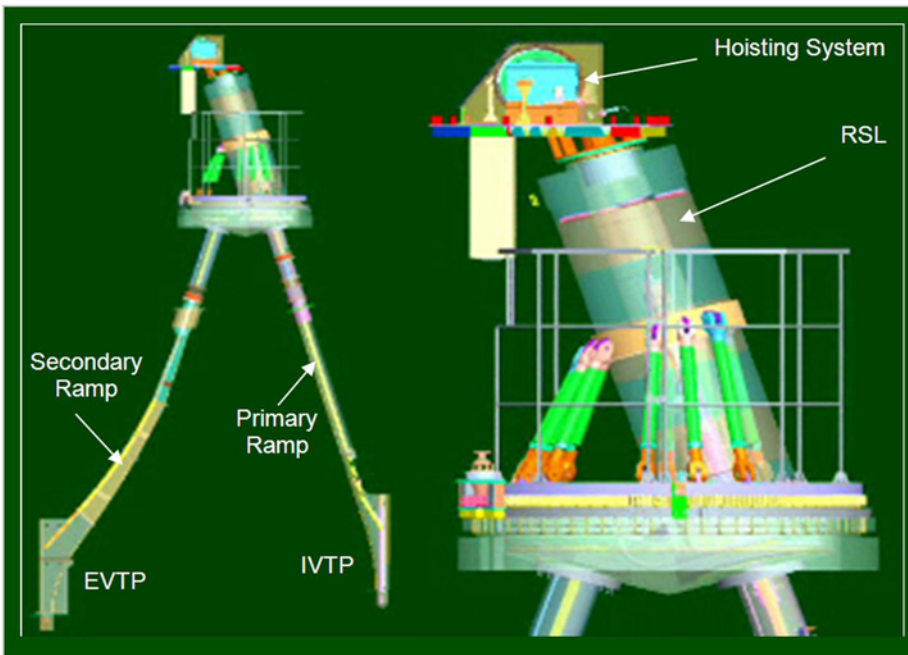


Fig. 3: Inclined Fuel Transfer Machine for PFBR

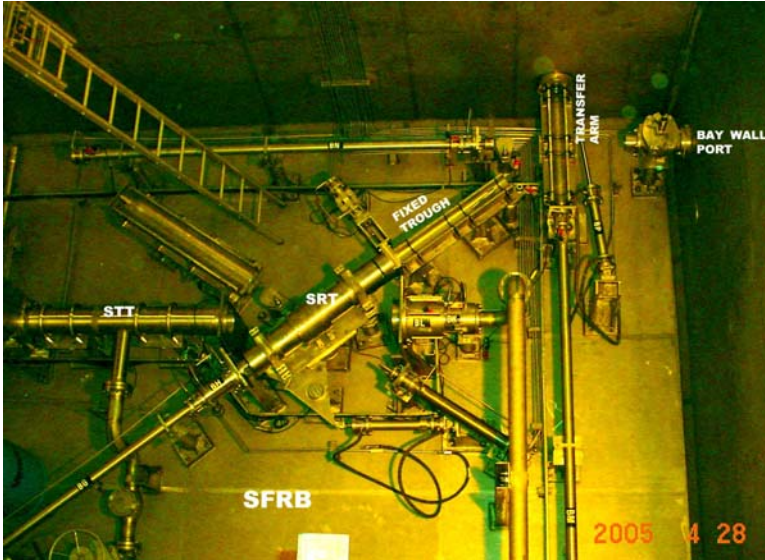


Fig. 4: Spent Fuel Receiving Bay Equipment for TAPS-3&4

considered. The design of the SFRB has been conceptualised, detail engineering has been done and handed over to NPCIL. Spent Fuel Transfer System design has been proven to be satisfactory at TAPS-3&4. Precise detail design, exploration of AutoCAD and 3D packages, design verification by experimentation and continuous interaction with other groups, has made it possible for the system for almost deviation-free manufacturing and commissioning. The system is being used satisfactorily in TAPS-3&4.

Life Management Tools for Pressure Tube of PHWRs (Fig. 5)

To enhance the performance of the PHWRs, ageing management programme for coolant channels plays an important role. In the past, various life management techniques/tools have been used for this purpose, which need channel in dry condition. Drying of the channel involves removal of fuel, ice freezing the feeders, putting feeder blanks and draining and cleaning of the channel. This involves time, reactor down time and man-rem expenditure. The present techniques can do the inspection jobs without draining or drying of the channel, while saving the fuel.

Techniques like BARCIS to monitor the health of the coolant channel, Wet Sliver Sample Scraping technique (WEST) for taking sliver samples from the inside surface of the pressure tube for Hydrogen analysis and Channel Isolation Plug (CHIP) which enable the repair of the damage seal face, have been developed. For all the above techniques, the existing Fuelling Machines (FMs) are used, which makes it possible to do the job remotely and quickly.

The overall system of BARCIS consists of an inspection head, a special sealing plug, a drive mechanism, a computerised control system and inspection equipment. The existing fuelling machine has been used to load/unload the assembly of special plug and inspection head, into the coolant channel. Design of Special sealing plug enables the BARCIS to do ISI job in heavy water filled condition. The plug acts as a pressure boundary at shut down



Fig. 5: Life Management Tools

DAE Excellence Award



condition of the reactor and also allows a leak-tight passage for carrying out inspection. The challenges in the design of the plug were, very confined space to accommodate the plug and incorporation of safety features. This has resulted in substantial reduction in cost and complexity of the system. The special sealing plug enables to installation of the inspection head remotely in the channel to be inspected by FM, allows the entry of drive tube to be connected to inspection head for transferring the collected data by inspection head to the computer outside. The drive tube is connected to a drive mechanism, which provides axial and rotary motions to the inspection head inside the channel. Thus special seal plug plays a major role in ISI operation. Different versions of plug have been evolved and are being used successfully for ISI in 220 MW (e) PHWRs.

Hydrogen concentration is an important parameter that must be assessed to evaluate the fitness for service of pressure tubes. Earlier assessing hydrogen content always led to removal of a pressure tube. This happened to be very costly, because of the long shut downtime requirements. In recognition of need of a better approach, a tool has been developed known as WEt Sliver Sample Scraping Tool (WEST). The tool collects oxide layer from the ID of pressure tube with the help of FMs. The tool has a carriage which moves on a pre defined path. The carriage has two tool bit cutter, to remove oxide layer and metal sliver. FM ram is applied to move the carriage. For proper assessment of hydrogen concentration, it is required to collect sample at different locations of the pressure tube. The FM used for the operation of WEST has limited stroke, hence collection of sliver sample at the furthest end from the channel is not possible. To overcome this problem, WEST extension has been developed. The WEST extension houses a spring loaded piston which allows force to transmit from one end to the other end. The extension bridges the gap between WEST and ram of FM. Ram force is applied on the piston of

extension which transfers the force to the carriage of WEST for taking the cut. With the help of WEST extension, it is possible to collect sliver sample at any axial location from the ID of pressure tube.

During operation of the reactor, sometime the closure seal face gets damaged. Temporarily this leakage can be blocked, by using End Fitting Blanking Assembly. However ultimately the closure seal face needs to be repaired and normalized. To enable this repair in water filled channel, a CHannel Isolation Plug (CHIP) has been developed. This helps in isolating the closure seal face and make it accessible for repair. This plug has been supplied to almost all power stations and is being used successfully.

Hoisting System for IFTM of PFBR (Fig. 6)

IFTM transfers Core Sub-Assemblies (CSA) in 17° inclined positions to the vertical. The irradiated CSA is put in a sodium filled Transfer Pot (TP) of IFTM by Transfer Arm (TA) at In-vessel transfer position (IVTP). Hoisting system is mounted at the top of the RSL hoists the TP along with irradiated CSA, up inside the Rotatable Shielded Leg (RSL). The RSL along with hoisting system is then rotated by 180° and gets aligned with secondary ramp. The TP is lowered in Ex-Vessel Transfer Position (EVTP), from where the irradiated CSA is replaced by fresh CSA. The fresh CSA is then hoisted from EVTP and lower to (IVTP) in the reverse manner. The IFTM internals are maintained at

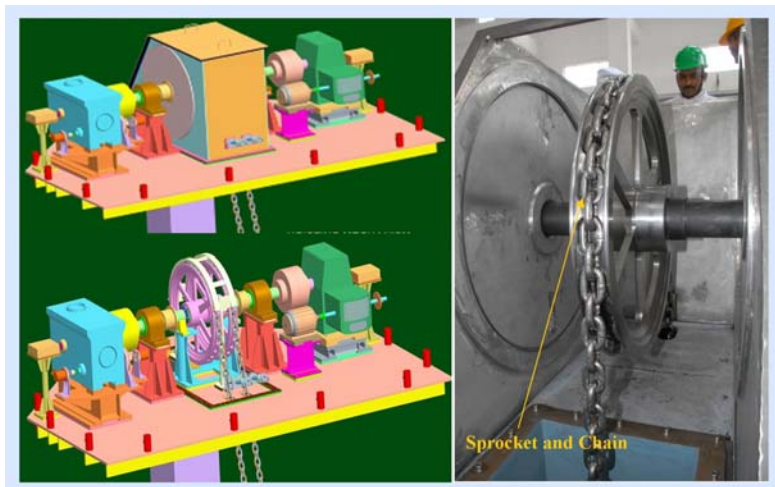


Fig. 6: Hoisting System for PFBR



Fig. 7: Experimental Set up for Study of material

423-473 K by hot argon, during fuel handling operation. Fuel transfer operation in PFBR performs in reactor shut down condition.

For hoisting of TP, double chain with separate pocket type sprocket mounted on a common shaft has been used. The shaft is connected to a motor through a reduction gearbox. For hoisting, welded link chain has been considered for reliability, flexibility, ease of operation etc. The one end of the link chain is connected to the TP and other end is connected to the Chain Collection Pot (CCP), after passing over the sprocket wheel. The link chain remains in tension in TP side and slack in CCP side. The pockets of sprocket wheel accommodate the link chain during rotation of the sprocket wheel. The sprocket wheel, welded link chain and drive shaft are enclosed in a leak-tight chamber, called argon chamber.

Considering the nature of job, mechanism and environment of the system, the hoisting system has been designed with special care. The code ANSI/ASME NOG-1 for design of conventional cranes and the guidelines given by French code RCC-MR subsection- K for components at high temperature has been followed, during the design of hoisting system. Considering the criticality and importance of the system, the design of the hoisting system has been included the features of single failure proof system and AERB guidelines. The design of pocket

type sprocket also needed special care, as the load being handled at an angle in hoisting system of IFTM. For better engagement/disengagement of chain and sprocket, the configuration of pockets has been modified, to suit the operating condition after careful analysis and experiments.

Experimental Setup for Study of Material (Fig. 7)

For carrying out shock-wave experiments on material, a 63mm diameter gas-gun facility has been built at BARC. It is capable of accelerating projectiles to velocities up to 1 km/s using Nitrogen and Helium gases. These on impacting a target, generate shock pressure up to 40 GPa. The facility consists of a pressure chamber called Breech, a 3m long barrel through which the projectile moves, a target chamber where the target is placed and a catcher tank to arrest the fragmented particles of the target. The system has been fabricated, erected and commissioned successfully. The gun has been performing well and is being used for shock-wave experiments. Further to this, to carry out experiments with higher velocities projectiles, a propellant gas test setup is being commissioned.

A 6m. diameter double-walled spherical vessel is being made, for studies of material property. The vessel is special in nature, made of 85mm thick plate and a 1500mm diameter opening.



Conclusion

New innovative concept of spent fuel receiving bay in 540 MWe PHWR, TAPS-3&4 has been proven, by performance. The system is operation & maintenance friendly and is able to cater to increased load of refuelling in 540 MWe PHWR.

Design & development of life management tools for 220 MWe PHWR, viz. Special Sealing Plug for BARCIS, Wet Sliver Sample Scraping Tool (WEST) and Channel Isolation

Plug (CHIP) have become standard tools in operating PHWRs. They facilitate quick deployment in plant with negligible man-rem expenditure.

Design & development of single-failure proof hoisting system, for Inclined Fuel Transfer Machine has increased the reliability of the system.

The successful commissioning of gas-gun facility, provided a new opening for study of material under shock wave.



Development of Type B(U) Package for Cobalt-60 Teletherapy Source Transportation

D.C. Kar, K. Jayarajan and Manjit Singh
Division of Remote Handling and Robotics

Dr. D.C. Kar is the recipient of the DAE Scientific & Technical Excellence Award for the year 2009

Abstract

Qualified package is essential, for the transportation of the source capsule between the manufacturer's site and the location of the cobalt-60 teletherapy unit. During transportation, consequences of any shielding failure can be catastrophic. The package has to fulfill the stringent safety requirements for normal operating conditions, as well as for accidental situations, as per the national and IAEA Safety Standards. Recently, we have developed a Type B(U) package, for the indigenously developed teletherapy machine Bhabhatron. This paper highlights some of the design and test procedures, followed during the development and qualification process of this package.

Introduction

Teletherapy source transportation packages are used, for transportation of Cobalt-60 source capsules, between the manufacturer's site and the cancer hospitals. As the sources are transported through public domain, consequences of any breach of shielding can be severe. Therefore, utmost care has to be exercised, to protect the people and the environment from the harmful effects of radiation. As part of our indigenous radiotherapy programme, we have developed a transportation package (Fig. 1) for transporting the cobalt-60 radioactive sealed sources, for our Bhabhatron series of indigenous teletherapy units. It is certified as Type B(U), which means that it is approved for international shipments as well. Here, important design challenges and regulatory issues are discussed in brief.

Background

Teletherapy is one of the established modes for the treatment of localized cancers. In cobalt teletherapy units,

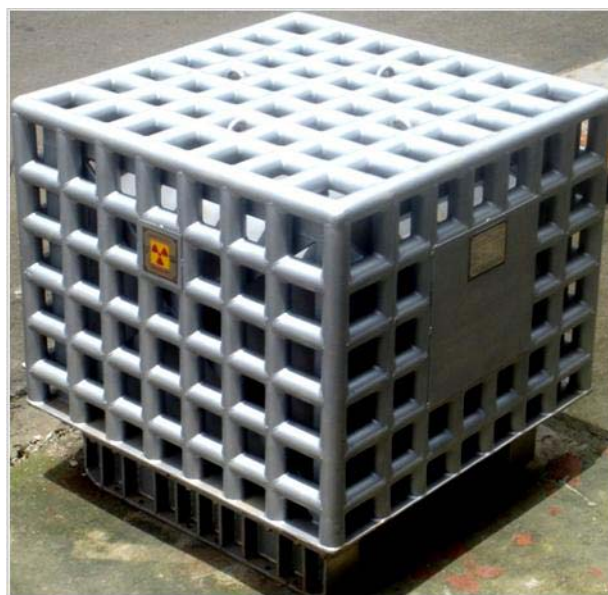


Fig. 1: Teletherapy Source Transportation Package



gamma radiation emitted from cobalt-60 radioisotope is utilized, for destroying cancerous tissues. Tiny pellets of cobalt-60 radioisotope are encapsulated and securely fastened, inside a source drawer. The radioactivity content of each fresh source capsule may be as high as 15000Ci. The source drawer is a part of the teletherapy machine and needs to be transported to the machine site (typically a hospital), for loading into the therapy unit.

The source transportation package is meant to:

- i) transport the drawer containing the source capsule safely from source fabrication facility to the hospital,
- ii) facilitate transfer of this drawer into the machine in hospital environment without undesired exposure,
- iii) serve as safe storage of the decayed source being replaced, and
- iv) transport the decayed source to the designated disposal facility.

Package Design

As per the IAEA Regulations for the Safe Transport of Radioactive Material [1, 2], radioactive material transportation packages are classified according to their activity contents. For Type-A package, quantitative limits on the contents are prescribed, and can't be used for the present application. We need Type-B package for which contents limits are indirectly restricted, by the need to comply with requirements relating to radiation emission, heat dissipation, internal pressure, criticality etc. Additionally, Type-B package is required to retain adequate shielding and containment, in case of severe accidents.

We have finalised the basic design of the package, based on the application requirements and the Transport Regulations of the IAEA. It has mainly two major sub-assemblies: a transport flask and a fire-shield(Fig. 2). The transport flask is a cylindrical lead-shielded steel container with two identical channels: one for the source drawer and the other for a dummy drawer. It is closed on either side by shielded detachable doors, attached to the body by hinges. These doors can be physically locked, to prevent any accidental exposure.

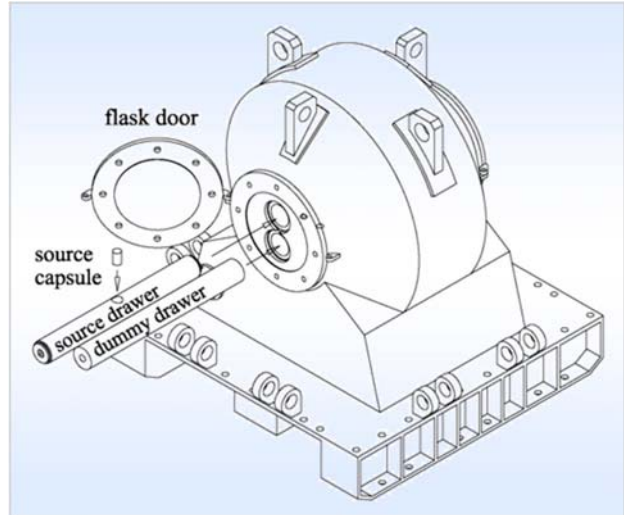


Fig. 2: The Flask and Operating details

The fire-shield is a box-like structure with open bottom. In the inner side, it has a layer of ceramic wool, protected by steel sheets. Its role is to prevent excessive heating of the flask during accidental fire. The structure on the outer surface of the fire-shield is made of thin tubes. These sacrificial tubes form a protective grid and absorb impact energy, to maintain the integrity of the fire-shield, during any accidental impact. During transportation, the fire-shield remains securely fastened to the flask.

Type-B package is capable of satisfying a sequence of tests, representing accident conditions on the same specimen. Most important among these are:

- i) free drop test from a height of nine metres onto an unyielding target, in an orientation causing maximum damage,
- ii) free drop from one metre onto a steel punch of 150mm in diameter and 200mm long, mounted on a rigid target, and
- iii) thermal test, in which the package is exposed to a fully engulfing fire at 800 °C for 30 minutes.

It is postulated, that during hypothetical accident conditions, the vehicle (carrying the package) speed will be limited to the regulatory test velocity (48 km per hour), which is equivalent to the speed at the end of nine-metre free drop. In practice, the equivalence to these hypothetical conditions is achieved, by placing control on carrier



movements viz. speed, amount of fuel, escort vehicle etc. It is essential to demonstrate, that the package is capable of satisfying the requirements as per IAEA regulations, which permits any of the following methods or combinations thereof:

- i) physical tests on prototype,
- ii) physical tests on a scaled model,
- iii) simulation using various computational tools and
- iv) reference to similar package successfully demonstrated earlier.

We have used analytical/software tools to validate the design. Subsequently, physical tests were carried out on full-scale package, to demonstrate safety during accident conditions of transport as stipulated in the regulations. During thermal performance analysis, it was observed that retaining the thermal shield is necessary, to prevent any loss of shielding (lead melting) during the regulatory fire test of the package. Initial design of the package is simulated and analysed using Nonlinear Dynamic FE Code – PAM-CRASH for safety against accidental collision. Detailed analyses for stresses, deformations, energy absorbed by various structural components of the package were performed. Primary objective was to ensure the integrity of the containment as well as the thermal insulation, during the regulatory tests of the package. After a series of iterations, the fire-shield was finalized to retain the integrity during nine-meter free drop test, irrespective of the orientation of the package while hitting the unyielding target.

Package Fabrication

After design finalization, two packages were fabricated under strict quality control. Wherever applicable, chemical analyses of the materials were performed. Non-destructive testing of all the welded joints of the lead containment was performed. Dye penetration testing and hydro testing were conducted, to ensure leak-tightness of the lead. The package was solution annealed to remove the residual stresses introduced during the fabrication process. Lead pouring was performed as per guidelines. After lead pouring, radiometry was performed to ensure the shielding integrity of the package.

Regulatory Tests

The regulatory tests under accident conditions were carried out at the Automotive Research Association of India (ARAI), a research institute of the Automotive Industry with the Ministry of Heavy Industries & Public Enterprises, Government of India.

For the nine-meter drop test, the package was instrumented with two accelerometers and 24-channel strain gauges (eight rosettes) at different positions of the package, to record the acceleration and strain information during the impact on the unyielding target. Two high-speed (3000 fps) cameras positioned orthogonally, captured the impact for visual understanding of the collision. A gantry type crane equipped with quick-release mechanism was used for lifting, positioning and dropping the specimen on to the target. The instrumented package (Fig. 3) was dropped in such a way that one of the sides (perpendicular to the source drawer axis) hits the target. This orientation was chosen, because FEA results indicated, that it is the most damaging one of all the possible drop orientations.



Fig. 3: Package before 9m free drop



After the drop, detailed visual inspections were performed for physical damages of the package. No damage was detected on the flask. However, a few bolts used for the assembly of the flask and the thermal shield were sheared off during the impact. The hitting surface of the sacrificial structure has deformed significantly by absorbing part of the impact energy. It was important to note that, the thermal insulation of the fire-shield was fully protected. The recorded parameters were analysed and found to be in line with the simulation results. Punch test was performed on the same package after this 9-m drop, using the remaining bolts. No significant damage was observed in punch test. The tube structure prevented the punch from reaching the thermal insulation layer. A photograph of the package after the 9-m drop test and the punch test is shown in Fig.4.

Thermal Testing was conducted in diesel-fired furnace at ARAI, Pune. For the fire test, the package was instrumented with 16 thermocouples at various locations of the fire-shield and the flask. The package was painted with PyroMark, to achieve the thermal emissivity and absorptivity properties, as prescribed in the regulations. The package was placed on a stand in such an orientation that the most damaged portion of the package (interface

between the flask and the fire-shield) faced the furnace bottom. During tests, it was ensured that average furnace wall temperature was maintained at 850°C for the entire duration of the test. After required preheating of the furnace, the package was placed inside the furnace and furnace door was closed. It was found that the package surface temperature reached 800°C within six minutes after closing the door. After 36 minutes, the furnace door was opened, the package was taken out to an open area and was left for natural cooling (Fig.5).

The temperature profiles of the package during heating and cooling are shown in Fig.6. A maximum temperature of 280°C was observed on the flask surface, near the flask door. The temperature at the source capsule location reached its maximum at 50 minutes after the removal from the furnace. No lead leakage was observed in the package.

Radiometry test was performed on the package, which was subjected to drop test, punch test and fire test. No significant deviation in leakage radiation levels was observed, compared to the test performed before these regulatory tests.



Fig. 4: Package after 9m drop and punch test

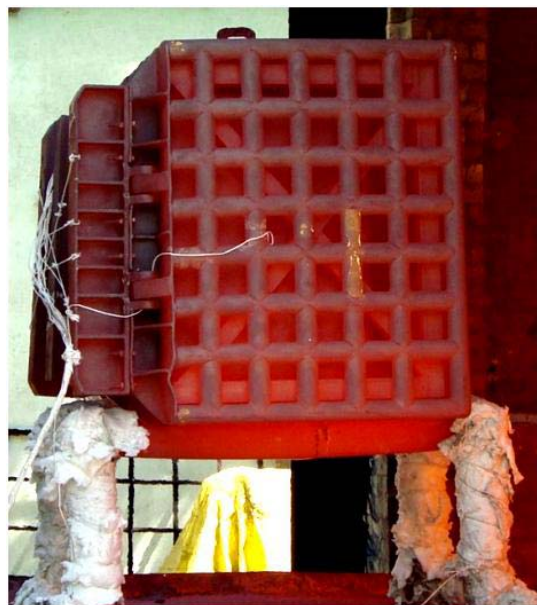


Fig. 5: Immediately after fire test

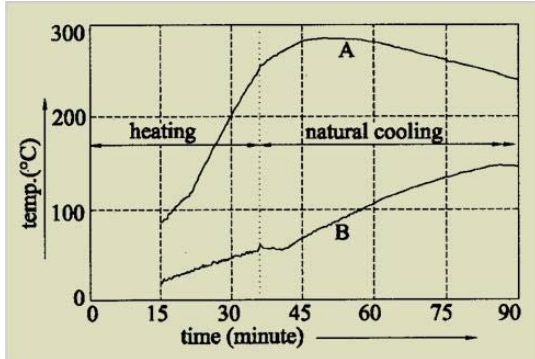


Fig. 6: Temperature profile during fire test
 A: at flask door outer surface;
 B: at source capsule location

Regulatory Approval

Design details, safety analysis report, QA programme, operation and maintenance details, production controls, test results during fabrication and test results before the first shipment were submitted to the Atomic Energy Regulatory Board (AERB). Subsequently, presentations were made to relevant committees. After thorough scrutiny and independent analyses by AERB, the package was granted Type B(U) certification, under the provision of the IAEA regulations.

Conclusion

Development of the source transportation package was essential for our indigenous teletherapy programme. Starting with the basic design, a number of modifications were implemented leading to the present model. Finally, regulatory tests were performed and the performance was demonstrated successfully. The process took around two years. Since its approval, a number of transportations were carried out between Trombay and various cancer hospitals in the country. One shipment was made to Vietnam along with the Bhabhatron, that India has donated through the Programme of Action for Cancer Therapy (PACT) initiatives of the IAEA.

Acknowledgement

Authors sincerely acknowledge the contributions of the Refuelling Technology Division and the Reactor Safety Division of BARC, in modelling, simulation and analysis of the package.

References

1. Regulations for the Safe *Transport of Radioactive Material*, Safety Series No. TS-R-1, 2005 Edition, IAEA, Vienna,
2. Advisory Material for the IAEA Regulations for the Safe Transport of Radioactive Material, IAEA Safety Guide No. TS-G-1.1 (ST-2).



Developmental study on metallic thorium and uranium-thorium alloy

Santanu Das, Raj Kumar, S B Roy and A.K. Suri

Materials Group

Mr. Shantanu Das and Mr. Raj Kumar are the joint recipients of the DAE Scientific & Technical Excellence Award for the year 2009

Abstract

Thorium and Uranium are elements of interest to nuclear reactor technology. It is expected that, with more and more importance given to nuclear power, efforts will also be directed towards developing various fuels, based on Th-U²³³ cycle. Thorium-uranium alloys are being considered due to their high temperature stability and than additional potential for breeder type reactors. Thorium-based metallic fuels are expected to have potential for higher breeding gains than other fuel forms of thorium. Data on irradiation properties of Th-U alloy fuels, though very less, looks promising. Thorium metal powder of purity more than 99% was prepared by the calciothermic reduction of ThO₂, followed by acetic acid leaching. Process parameters controlling the characteristics of powder have been studied and established. This thorium powder has been melted in arc furnace, to produce solid finger of metallic thorium. Preliminary characterizations have been carried out on thorium metal. Efforts have subsequently been furthered, to develop uranium-thorium alloy, using the same thorium metal. U-Th alloy has been characterized for physical metallurgical behaviour.

Introduction

Higher potential use of thorium, in future power generation in our country, is obvious [1,2,3,4,5]. Thorium are already being used as blanket materials in many reactors. However, the additional advantages of thorium metal and alloys in terms of high temperature applications in reactors such as ease of fabrication, high density and better thermal conductivity cannot be overlooked. Thorium metal has high melting point and negligible fission gas swelling below 800°C even after prolonged irradiation. Thorium exhibits only a single phase transition at a temperature as high as 1400°C. Stability of thorium under irradiation due to its isotropic structure, has aroused interest in the use of cubic thorium-uranium alloy fuels. Because of the nuclear properties of thorium, uranium is required to be used with thorium as a start up material.

Preliminary results on irradiation of thorium containing up to 10% U²³⁵, indicate excellent stability [6]. Two alloys containing 5.4 wt% and 7.6 wt% U were used as evaluation fuels in the Sodium Graphite Reactor. They were subjected to long burn up at high temperature. Problems, encountered in this first reactor experiment with thorium alloy fuel, were in the stage of preparation of the fuel itself. Want of a suitable crucible material, lack of compositional homogeneity in the alloy and low process yield were roadblocks.

An alloy containing 1 – 7.5 at% uranium was studied [7] in those early days, even when the phase diagram of Th-U system was not completely assessed [8]. Invariant reactions were also not properly identified. However, lowering of transformation temperature on alloying with uranium was reported. Phase changes from FCC to BCC



were also re-confirmed, but the difficulty in accurate measurement of the temperature at that high temperature regime (~1400 °C) was reported, with a spread over to the tune of 25 °C.

A handful of experiments were carried out on phase stability of unalloyed thorium and thorium alloy systems, other than thorium-uranium. Study [9] made on *theoretical aspects* on thorium alloy systems has recently been reported, but experimental studies, specific to U-Th system, have not been done so far.

Experimental

Thorium powder

Thorium powder was produced via calciothermic reduction of thoria. Thoria was obtained from M/s IREL. The various set of parameters e.g. soaking temperature, preheating temperature, lining thickness etc. were standardized for producing the thorium powder. After conducting characterizations e.g. C,O, N analyses, ICP-AES, particle size, SEM and XRD, thorium powder was taken for further processing. SEM image of thorium powder is presented in Fig. 1 along with an image of uranium powder,

produced via similar route, for an easy comparison of their widely varying morphological features.

The product thorium powder is 3 – 200 micrometer in size, silvery to grayish in colour and typically *dog-bone* or *peanut* shaped in appearance, under the microscope. Like uranium powder, thorium powder also is very sensitive to exposure to oxygen and turns blackish, gradually, in contact with air even at ambient temperature. The purity of the thorium powder was >99% (carbon ~ 200 ppm, O ~1300-2000 ppm).

Thorium metal and alloy

Thorium pellets were melted using a non-consumable arc furnace in argon atmosphere. Bright silver coloured thorium finger was produced. Fig. 2 presents photograph of thorium pellet and metallic thorium finger (20 g in weight).

Thorium like titanium and zirconium, attacks the crucible material at high temperature. In the present study, the alloy was melted in an induction furnace using Y₂O₃ coated graphite crucible. The photograph of the induction melting unit is presented in Fig. 3.

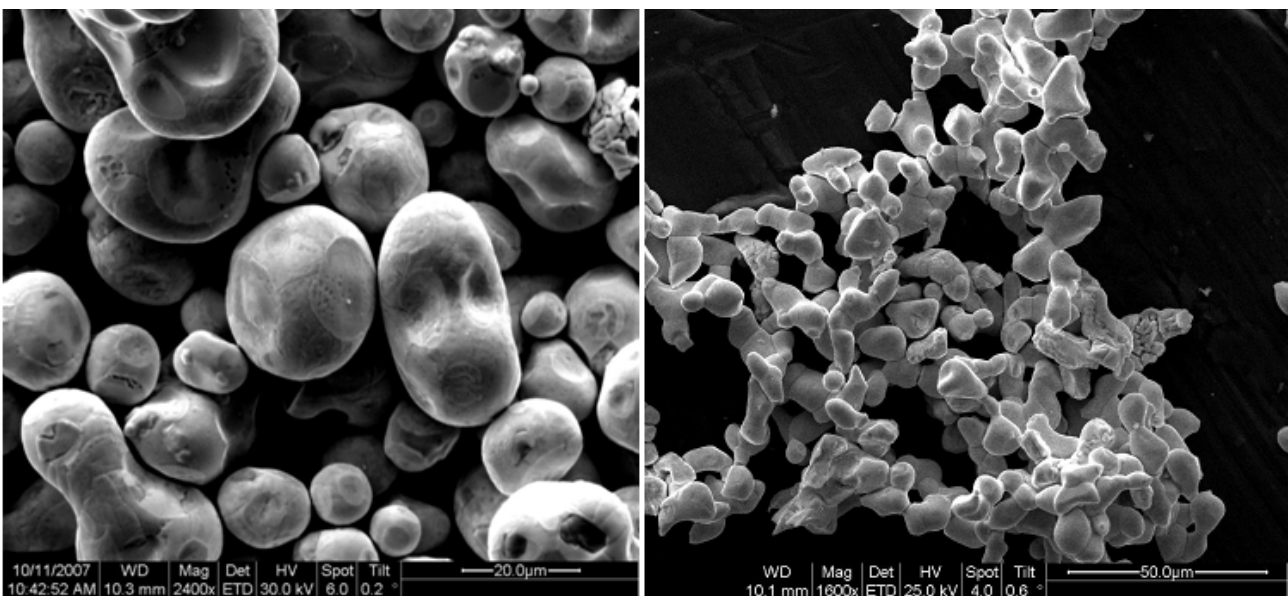


Fig. 1: SEM images showing uranium powder (L) and thorium powder (R)





Fig. 2: Photographs of pellet of thorium powder (L) and thorium metal finger (R), produced by melting the thorium pellet in arc furnace

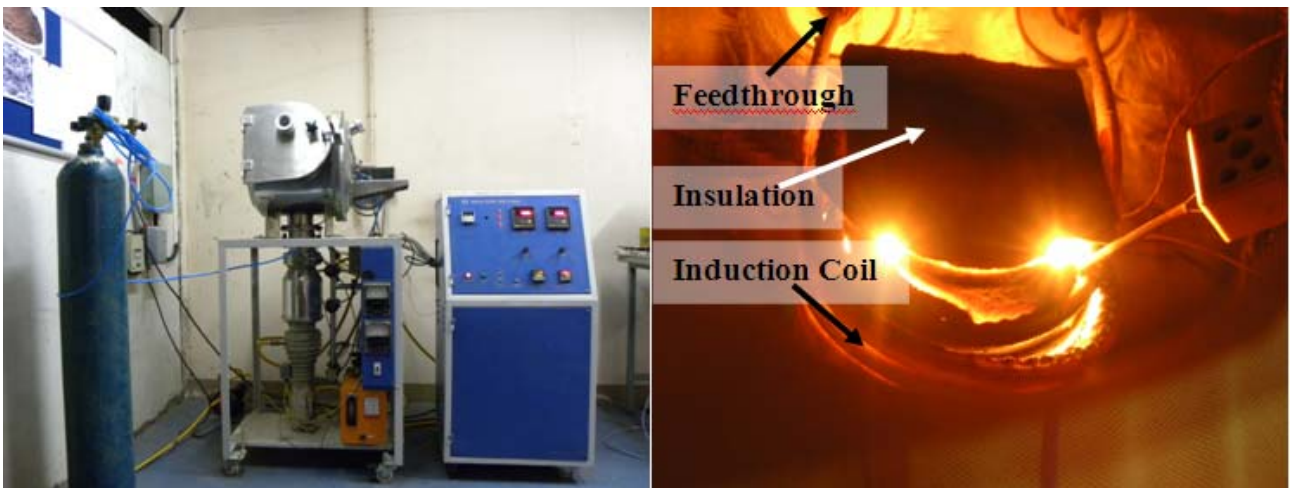


Fig. 3: Photographs of induction furnace (L) and melting of the alloy (R), captured using a Nikon P-90 camera

Results

The overall chemical compositions of alloys were confirmed through XRF analysis. XRF analysis, done on the alloy sample confirmed the target composition of thorium to be 35 wt%. XRD pattern also indicated, the presence of α thorium and α uranium phases, respectively. Moreover, changes in cell volume, (3.44% in α thorium and 0.18% in α uranium), indicated higher solubility of uranium in thorium. Optical micrograph and SEM image of U-35%Th are presented in Fig. 4. In as cast samples, *herringbone* type of microstructures, which is quite typical with thorium alloys, was seen.

SEM micrographs of U-35%Th alloy along with X-ray mappings of Th- M_α and U- M_α are shown in Fig. 5 a, b & C, respectively. These mappings show the presence of thorium-rich and uranium-rich phases.

Summary

1. Thorium powder of >99% purity was produced via calciothermic reduction of thorium. Powder production process parameters were standardized. Silvery grayish, *dog-bone* shaped thorium powders, having tap density of 2 g. cc⁻¹, were found to be in the size range of 3- 200 μ m.

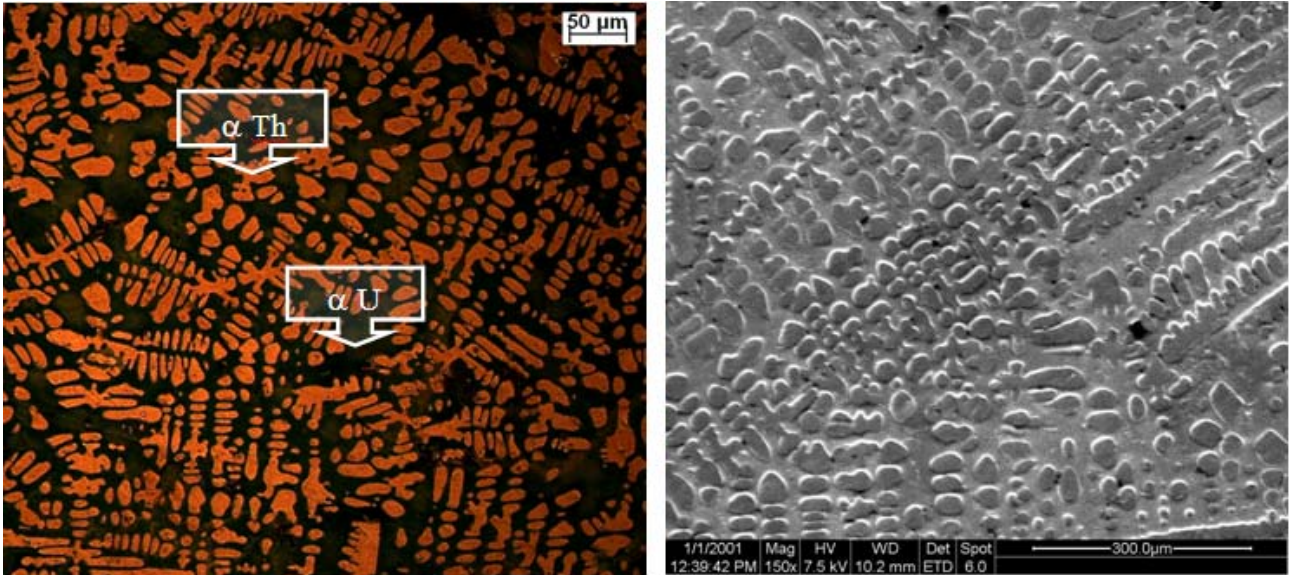


Fig. 4: Microstructures of U-35%Th alloy, optical (L) and SEM (R)

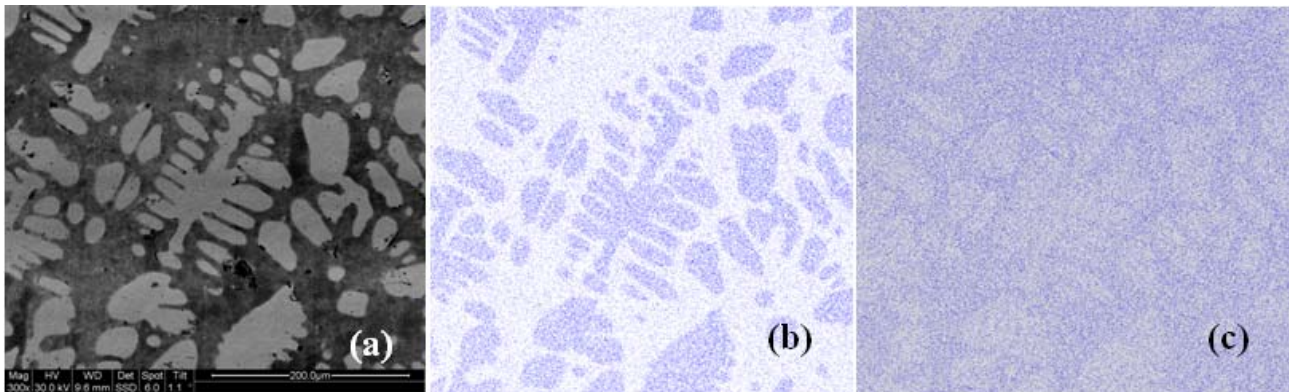


Fig. 5: SEM image of (a) U-35%Th alloy with elemental mapping for (b) Th-M_α and (c) U-M_α

2. The thorium metal powder was pelletized and arc-melted, to form solid metallic thorium finger. Thorium finger having unmistakable metallic luster was produced and characterized. The thorium powder was found to pick up more oxygen on melting.
3. The uranium-thorium alloy was prepared for the first time and indigenously. The alloy was produced by melting thorium metal fingers, produced in-house, and uranium slugs.
4. Characterizations were conducted. Microstructures showed two-phase *herringbone* type of structure. XRD pattern confirmed the presence of α thorium and α uranium phases. Those phases were identified with the help of EDS mapping.

At present, the work is being further followed up, with selected compositions from U-Th system.

References

1. B Prakash, S R Kantan and N K Rao, Metallurgy of Thorium Production, Review Series Collection Monographs, No. 22, IAEA, 1962.
2. P Rodriguez and CV Sundaram, Nuclear and materials aspects of the thorium fuel cycle, *Journal of Nuclear Materials*, 100 (1981) 227-249.
3. R K Sinha and A Kakodkar, Design and development of the AHWR – the Indian thorium fuelled innovative



- nuclear reactor, *Nuclear Engineering and Design* 236 (2006) 683-700.
4. K Anantharaman, V Shivakumar, D Saha, Utilisation of thorium in reactors, *Journal of Nuclear Materials*, 383 (2008) 119-121.
 5. K Balakrishnan and C Ganguly, Thorium Utilization in Indian power Programme, *Mater. Sci. Forum*, Vol 48-49, pp 125-138, (1989).
 6. B R Hayward and P Corzine, Thorium – Uranium Fuel Elements for SRE, 2nd International Conference on the Peaceful Uses of Atomic Energy, Geneva, 1958, P/785
 7. G H Bannister, J R Thomson, The body centered cubic to face centered cubic phase transformation in thorium and some uranium-rich alloys, *Journal of Nuclear Materials*, 12, 1 (1964) 16-23
 8. D.E Peterson, The Th-U (Thorium-Uranium) System, *Bull. Of Alloy Phase Diagrams*, Vol 6, No. 5, 1985
 9. Z S Li, X J Liu, C P Wang, Thermodynamic modeling of the Th-U, Th-Zr, Th-U-Zr systems, *Journal of Alloys and Compounds*, 476 (2009) 193-198

Acknowledgement

The authors are grateful to M/S IREL for supplying the thoria, Shri K.N. Hareendran, UED for XRF analysis, Shri C.B. Basak, MFD for the crucible coating, Dr. T.R.G. Kutty, RMD for the arc melting facility, Dr. K.B. Khan, RMD for C,O,N analyses, Dr. C.G.S. Pillai, Head, MCS, Ch.D, for SEM and Shri A K Sengupta, Head, FPES, RMD for XRD, Shri P.K. Rajagopalan, UED for his inspiration in the initial period of the work. Last but not the least, the authors are grateful to all the colleagues of SUMP-I for providing the valuable support in carrying out the above mentioned activities.



The Formation of Mechanically Mixed Layer during Dry Sliding of Cu-15wt%Ni-8wt%Sn Bronze

Jung B. Singh

Mechanical Metallurgy Division, BARC

Mr. Jung B. Singh is the recipient of the DAE Scientific & Technical Excellence Award for the year 2009

Abstract

Dry sliding wear of Cu-15Ni-8Sn (in wt%) bronze, against a stainless steel 440C counter surface is investigated in air and flowing Ar gas, using a pin-on-disc tester. The microstructure of the mechanically mixed layer formed during wear, has been characterized at the nanoscale level with an aim to identify its genesis and to establish its role in controlling the wear.

Introduction

During the sliding of two solid bodies, under friction and load, chemical composition of the near surface is modified, due to the interaction with the counter face material and the environment. This layer is termed as transfer layer or Mechanically-Mixed Layer (MML) and has characteristically distinct chemical composition and microstructure. The transfer layer can be continuous or patchy. The importance of this layer on affecting the friction of the sliding bodies and their wear rate, has been well acknowledged [1]. Debris generated during the wear process originates mostly from the transfer layer. Previous studies on pure Cu have shown, that transfer layers are a few microns thick and consist of nanocrystalline grains [2]. During a tribological process, the transfer layer is believed to be constantly in the process of making and breaking under steady state conditions. Despite the numerous past studies invoking the importance of transfer layer, there remains a poor understanding of MML, especially with regard to their microstructure and their formation. Further, it remains unclear whether the transfer layer is a part of the existing bodies or is formed by the debris particles, by the process of compaction on the sliding surface.

In the present work, the formation of the transfer layer, in a spinodally decomposed Cu-15wt%Ni-8wt%Sn bronze alloy (henceforth referred to as CuNiSn alloy) [3] has been studied. Microstructures of subsurface layers formed during wear were characterized up to nanoscale level by conventional and analytical Transmission Electron Microscopy (TEM), including energy dispersive spectroscopy and Electron Energy Loss Spectroscopy (EELS). The wear behavior of the bronze was interpreted in the light of microstructural changes, occurring in the surface during the wear process.

Experimental procedure

Wear tests of the CuNiSn alloy (~ 31 HRC hardness) were carried out, using a pin-on-disc tester against a martensitically hardened stainless steel (SS) 440 C disc (~ 60 HRC hardness). Details of the testing procedure are mentioned in [3,4]. The wear rates were estimated by direct measurement of the weight loss of the pin, to an accuracy of ± 0.1 mg as well as from the linear displacement versus time data plot, recorded *in-situ* by a Linear Variable Displacement Transducer (LVDT). TEM



samples of the worn pin were prepared as per the procedure described in ref. [4].

Results and Discussion

Wear Behaviour

Table 1 gives the weight loss, the coefficient of friction (μ) and the wear coefficient (K) for the worn CuNiSn alloy. At 10 Kgf load and 0.25 m/s sliding speed under air, severe wear of the pin against the SS 440C countersurface started, right at the beginning of the experiment. In flowing Ar atmosphere, under the same test conditions, the wear rate reduced by about 75% while it reduced further by about 50%, with a reduction of the sliding speed from 0.25 m/s to 0.10 m/s. The coefficient of friction versus time curves showed similar characteristic, throughout all the tests [3] – a negligibly short transient period followed by a steady-state period with only one type of transfer mechanism. Moreover, the value of friction coefficient was around 0.3 for all experiments, carried out against the SS counter surface. This suggested that similar wear mechanisms operated during these tests. A steady state coefficient of friction suggested, that there was only one mechanism of transfer and wear. However, in the self-mated tribological system, the wear rate increased significantly. The weight-loss increased by about 250% over the SS-mated system when tested in air at the sliding speed of 0.25 m/s under 10 Kgf load (Table 1).

Microstructure

Cross section microscopy of the worn pin revealed a Severely Plastically Deformed Layer (SPDL), capped by a thin MML (about 2 to 3 micron thick), separating the outer surface and the SPD layer. TEM characterization of the MML revealed it to be a nanocomposite comprised of equiaxed Cu-rich bronze grains and $(Fe,Cr)_2O_3$ -based oxide grains (Fig. 1). The MML was formed by the mechanical mixing of debris particles from both the bodies, viz., the bronze pin and the SS 440C counter face surface. Oxidation seemed to have played an important role, since the oxide particles generated from the SS counter face surface appeared to stabilize the MML. When a similar experiment, with the same loading conditions, was done under flowing

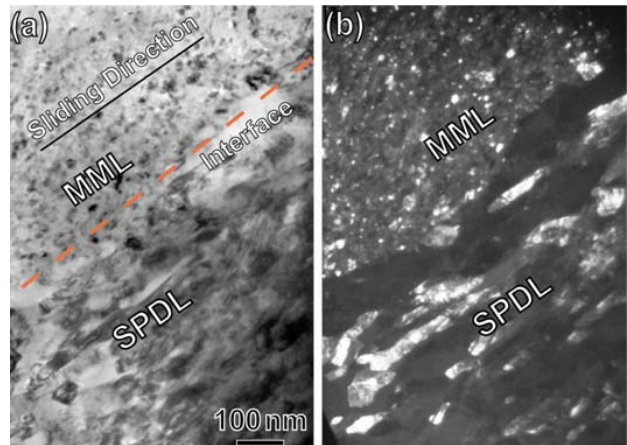


Fig. 1: (a) Bright field and (b) Dark field TEM micrographs of the subsurface layers formed in CuNiSn bronze worn in air against a SS 440C counter face.

Table 1: Table summarizing experimental conditions and the data extracted from the wear experiments

Expt. No.	Counter face Disc Material	Load (kgf)	Sliding Speed (m/s)	Time (s)	Environment	Coeff. Of Friction	Weight Loss (gm)	Wear Coefficient
1.	SS 440C	10.0	0.25	9000	Air	0.279	0.1311	6.42×10^{-5}
2.	SS 440C	10.0	0.25	9000	Argon	0.343	0.0321	1.57×10^{-5}
3.	SS 440C	10.0	0.10	9000	Argon	0.294	0.0151	1.85×10^{-5}
4.	Cu-Ni-Sn	10.0	0.25	9000	Air	0.517	0.3228	1.58×10^{-4}



Ar atmosphere, the MML formed was observed to be patchy (Fig. 2). In addition, when the source of Fe_2O_3 particles generation was removed and the experiment was done with a self-mated bronze disc, the surface was devoid of MML subsurface layer. The pin showed the formation of SPDL only. These findings have been published separately [4]. The SPDL consisted of a Cu-Ni-Sn solid solution with elongated nanograins, due to extensive dislocation glide and twinning. Since the wear rate in self-mated system had increased significantly, it was concluded that the formation of the MML had improved significantly the wear resistance of the bronze against SS 440C.

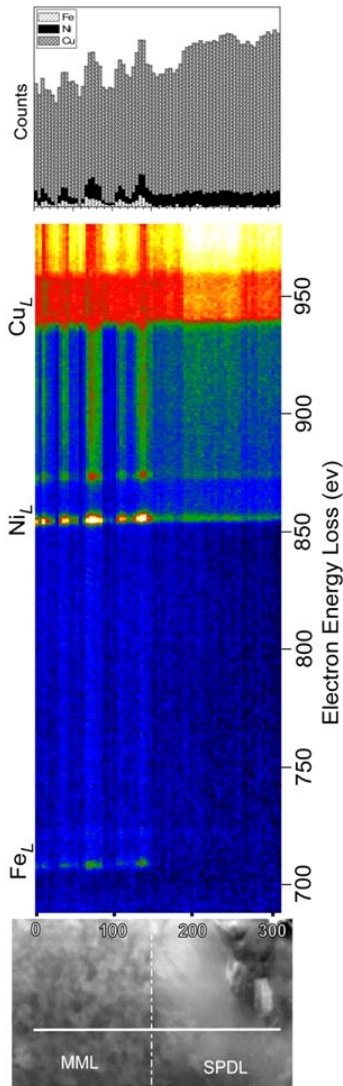


Fig.2: EELS line-scan across the MML/SPDL interface revealing that the phase separation has occurred only in the MML while SPDL has remained the single bronze phase.

The bronze phase in the MML, had the tendency to phase separate Cu and $(Ni + Fe_2O_3)$ phases. The decomposed phases in the MML were studied in detail, using core-energy-loss spectroscopy. This is illustrated in Fig. 3, which shows EELS line scan across the MML/SPDL interface. Details for the interpretation of the spectra can be found in ref. [5]. Evidently, the separation of the bronze phase into Ni-rich and Ni-lean particles within the MML could be seen in the histogram. Further, the Ni-rich particles also contained Fe (from the $(Fe,Cr)_2O_3$ particles). Length scale of this decomposition was about 20 nm (Fig. 3). In contrast, no such decomposition was found in the SPDL. The drastic change in composition and microstructural features across the MML/SPDL established, that MML was not part of the original (pin) body and must have formed by mechanical mixing and compaction of the debris from the two bodies. This was because, a continuous change of microstructural features across the interface would have been observed, if the MML was a part of the original body.

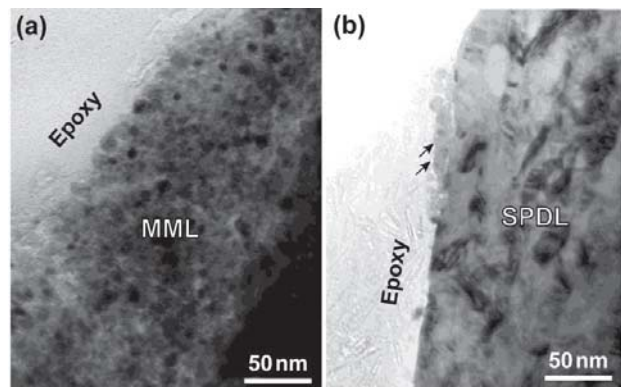


Fig.3: TEM micrographs revealing patching nature of the MML in CuNiSn worn against a SS 440C in flowing argon atmosphere. (a) and (b) micrographs are from adjacent regions where MML capped the SPDL in (a) while there was negligible MML (shown by arrow marks) in (b).

These investigations have also demonstrated, that the formation of a MML in the present context was beneficial in reducing the wear rate and this was most beneficial, when it was very thin and patchy. The MML played a role very similar to that of a solid lubricant. The presence of such an MML has advantages over an external solid



lubricant, since it rebuilds continuously and it forms everywhere along the contacting interfaces.

Conclusions

On the basis of nanoscale structural and chemical characterization of the transfer layer and its underlying material formed during the dry sliding of Cu-Ni-Sn bronze, it can be concluded that: (i) the transfer layer was not a part of the main body - a commonly held concept; and (ii) the formation of mechanically mixed layer, reduces the wear rate drastically.

Acknowledgements

This work was done as part of post-doctoral research work at the University of Illinois at Urbana-Champaign. The

financial support received during the research is gratefully acknowledged.

References

1. D.A. Rigney. Transfer, mixing and associated chemical and mechanical processes during the sliding of ductile materials. *Wear* 245 (2000):1-9.
2. P. Heilmann, J. Don, T.C. Sun, D.A. Rigney, W.A. Glaeser. Sliding Wear and Transfer. *Wear* 91 (1983): 171-190.
3. J.B. Singh, W. Cai, P. Bellon. Dry sliding of Cu-15 wt%Ni-8 wt%Sn bronze: Wear behaviour and microstructures. *Wear* 263 (2007) 830-841
4. J.B. Singh, J.-G. Wen, P. Bellon. Nanoscale characterization of the transfer layer formed during dry sliding of Cu-15 wt.% Ni-8 wt.% Sn bronze alloy. *Acta Materialia* 56 (2008): 3053-3064.



In-Situ Mechanical Property Measurement System for Zr 2.5 wt% Nb Pressure Tube

K. Madhusoodanan, S. Chatterjee, Sanjay Panwar and J.N. Koyal
Reactor Engineering Division

Mr. Madhusoodanan is the recipient of the DAE Scientific & Technical Excellence Award for the year 2009

Abstract

Periodic assessment of mechanical properties of Zr 2.5 wt% Nb pressure tube is required for ensuring its fitness for continued operation in Pressurised Heavy Water Reactors. An *In-situ* Property Measurement System, designed and developed in house, is capable of doing the measurement of mechanical properties in a non-intrusive manner. The measurement process consists of ball indentation, partial unload and reload sequences at a location. The load and corresponding depth of indentation recorded during the test are analysed, using custom made software to generate information on mechanical properties. The system has been qualified using specimens with known mechanical properties and the safety related issues have been addressed by analytical and experimental work.

Introduction

Measurement of mechanical properties of the pressure tube, made of Zr 2.5 wt% Nb in Pressurised Heavy Water Reactors (PHWRs) is an integral part of the material surveillance programme, necessary to ensure safe operation of the reactor. As a reactor operated pressure tube is highly radioactive, removal of the pressure tube and preparation of specimens from it for testing, consumes high doses of radiation. Considering this aspect, an *In-situ* Property Measurement System (IProMS), based on cyclic ball indentation has been developed, that can be used for *in-situ* measurement of the mechanical properties.

Technique of measurement

The technique of measurement used in IProMS is based on an analysis of the data, generated from multiple indentation cycles at the same location, on the surface of the testing material by a tungsten carbide ball. Each cycle consists of indentation, partial unload and reload

sequences. The load and corresponding depth of indentation are recorded during the test. Material properties like yield strength, Ultimate Tensile Strength (UTS) strain hardening exponent etc. are estimated from a post-processing of the data recorded. Schematic representation of ball indentation technique is shown in Fig.1.

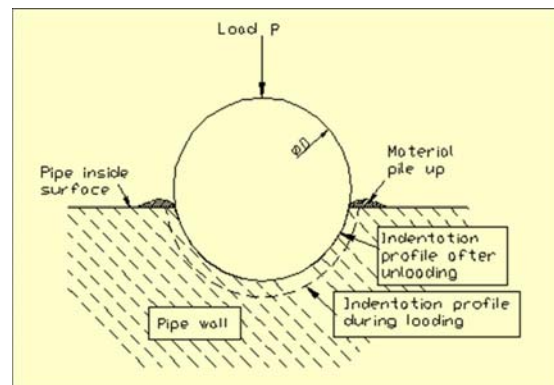


Fig. 1: Schematic representation of ball indentation technique.



Estimation of mechanical properties

The methodology used for estimation of mechanical properties from ball indentation test, is described in ref. [1, 2]. From the data recorded during the test, values of peak load, total depth of indentation and plastic depth of indentation, corresponding to each unload cycle are used, to estimate the mechanical properties.

System for measurement

IProMS mainly consists of a tool head, (Fig.2) that can be inserted in a pressure tube of 83 mm inside diameter, as shown in Fig.3. Indentation is carried out using a tungsten carbide ball of 1.5 mm diameter and the depth of indentation is measured, using a Linear Variable Differential Transformer. Design of the tool head is such that, there is minimum effect of global deformation on the measurement. System operation, control, data acquisition, analysis and display are achieved using a Control, Operation and Display (COD) Station.

Qualification trials

In order to qualify IProMS, tensile specimens were prepared from Zr 2.5 wt% Nb material, having different mechanical properties obtained through heat treatment, as given in Table 1. All the specimens were tensile tested at ambient temperature, as per the standard ASTM-E8M-1988, using a servo-hydraulic universal testing machine [3, 4]. Ball indentation test was carried out on three specimens each, from the four different categories.

Estimation of mechanical properties

Load deformation curve and variation of true strain vs. true stress for a typical case of H3-7, are shown in Fig. 4



Fig. 2: Tool head of IProMS



Fig. 3: IProMS tool head inside pressure tube.

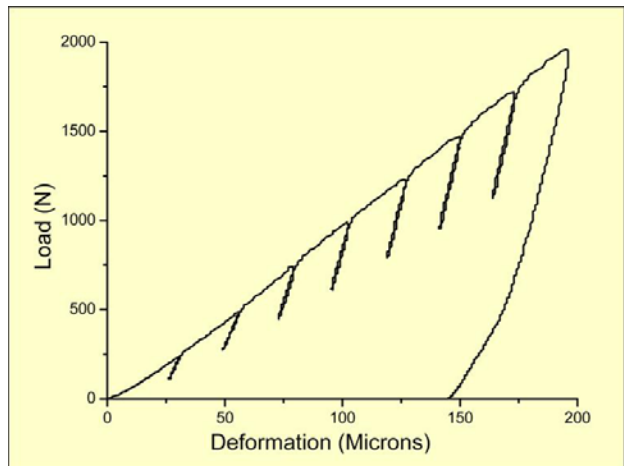


Fig. 4: Load deformation curve of specimen H3-7.

Table 1: Details of heat treatment carried out on different specimens

Sl. No.	Specimen identification	Soaking temperature (°C)	Soaking time (Hours)
1.	H3-1	No heat treatment (In as received condition)	-
2.	H3-6	700	2
3.	H3-7	550	6
4.	H3-8	800	0.5

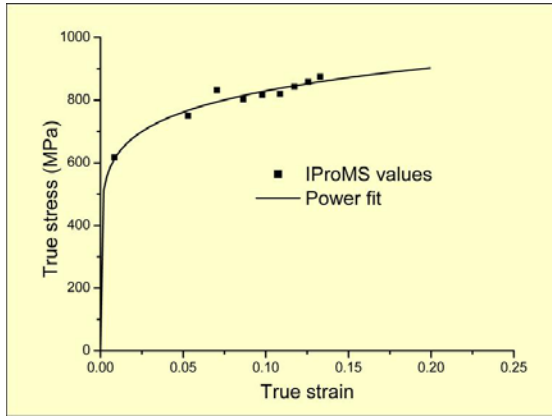


Fig. 5: True stress true strain curve of specimen H3-7

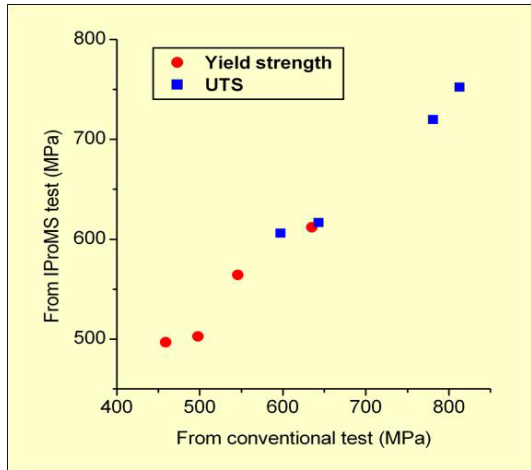


Fig. 6: Comparison between results from conventional and IProMS tests.

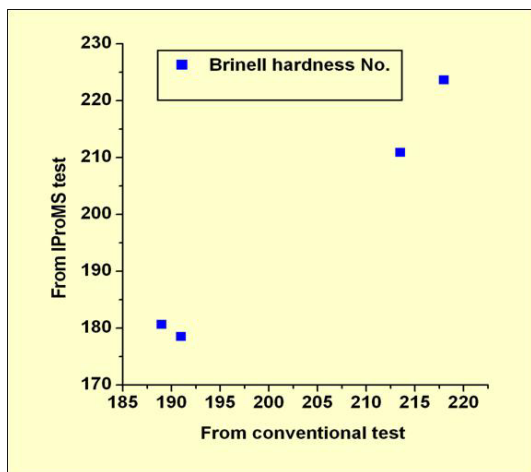


Fig. 7: Comparison between results from conventional and IProMS tests.

and Fig. 5 respectively. Comparison between the mechanical properties from conventional tests and IProMS tests are shown in Fig. 6 and Fig. 7. The difference between mechanical properties from conventional tests and IProMS tests is of the order of 5 to 10%.

Estimation of residual stress

When the residual stress introduced by indentation process along with operating stress exceeds a threshold value, hydrides present in the area can crack, leading to initiation of Delayed Hydride Cracking (DHC). Fig. 8 shows the residual stress contour in the tangential direction, obtained from an elastic plastic finite element analysis of the indentation process. It can be observed from Fig. 8, that the stress value exceeds the threshold on a considerably small area on the surface.

Qualification of indentation area against initiation of DHC

Pre-hydrated tensile specimens of Zr 2.5 wt% Nb material were subjected to ball indentation, and then tested for DHC as per standard procedure up to a tensile stress of 300 MPa. The indentation area observed under stereo microscope after the indentation test, shown in (Fig. 9), does not indicate initiation of any crack, thereby ruling out the possibility of initiation of DHC.

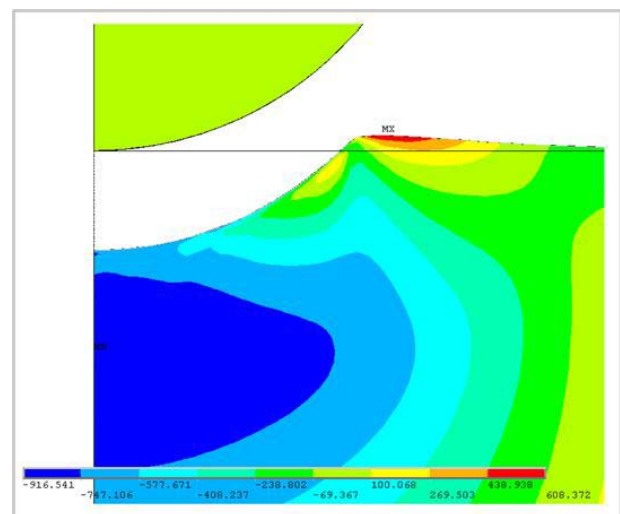


Fig. 8: Residual tangential stress contours around the indentation zone after final unloading

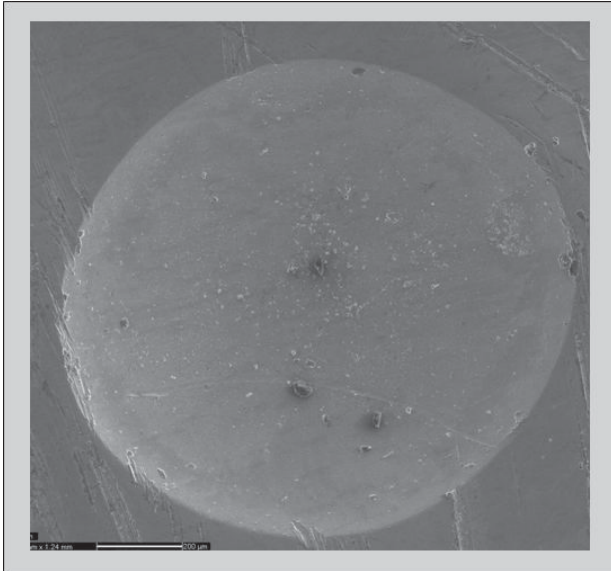


Fig. 9: Indentation area after DHC test observed through stereo microscope.

Conclusion

An '*In-situ* Property Measurement System (IProMS)' has been developed, which can be used for *in-situ* measurement of mechanical properties of pressure tube. Comparison with experimental results from conventional tests indicates, that IProMS will be able to capture the change in mechanical properties of the pressure tube during irradiation. Analytical and experimental studies indicate, that there is no possibility for initiation of DHC from the indentation area.

Acknowledgements

Authors are grateful to Dr R.N. Singh, MMD, BARC for providing the heat treated specimens and carrying out the conventional tests. Authors express their deep sense of gratitude to Dr R.K.Sinha, Director, BARC and Director, RD&DG, for his constant encouragement and support for this work. Authors also wish to record their gratitude to Dr P.K. Vijayan, Head, RED.

References

1. Haggag. F.M., "In-Situ Measurements of Mechanical Properties Using Novel Automated Ball Indentation System", ASTM STP 1204, pp 27-44, 1993.
2. Murty K.L., Mathew M.D., Wang Y., Shah V.N., Haggag F.M., *International Journal of Pressure Vessels and Piping* 75(1998)831-840.
3. ASTM Standard A370, "Standard Test Methods for Mechanical Testing of Steel Product".
4. ASTM Standard E646, 'Standard Test Method for Tensile Strain Hardening Exponents (n-values) of Metallic Materials".



Molecular studies on mechanisms underlying the extreme radiation resistance in *Deinococcus radiodurans*

H.S. Misra

Molecular Biology Division

Mr. H.S. Misra is the recipient of the DAE Scientific Technical Excellence Award for the year 2009 and of the P S Sarma Memorial Award at the 79th Annual Meeting of the Society of Biological Chemists(India) and National Conference on " Regulation of Biochemical and Cellular Processes in Diverse Systems at the Indian Institute of Science, Bengaluru, during December 13-15, 2010

Abstract

Gamma radiation acts directly on the cellular components or indirectly through oxidation of water in living cells, which could lead to the damage of genetic materials and the oxidative damage of other biomolecules. An organism which survives higher doses of γ radiation, would have to possess efficient mechanisms, to combat the deleterious effect of radiations. *Deinococcus radiodurans* a bacterium survives under extremely high doses of γ radiation. We used this bacterium as a model system, for understanding the molecular basis of its extreme phenotypes. Using both technological and intellectual capabilities developed inhouse, we demonstrated the novel mechanisms of radiation tolerance in *Deinococcus* mediated by (i) natural antioxidant and radioprotector such as pyrroloquinoline-quinone (PQQ) and (ii) the efficient recombination pathways contributing through DNA double strand break repair. We reported the involvement of signal transduction components in bacterial response to γ radiation for the first time, and proposed a unique alternate DNA damage response mechanism, yet to be shown in other bacteria.

Introduction

DNA damage caused by radiation, occurs in all organisms as a consequence of ultraviolet (UV) light, emanating from the sun and ionizing radiation (γ rays & X-rays) from natural sources, medical treatment and contaminated land. The repair of DNA damage is crucial for life and defects in DNA repair pathways can lead to genetic disease and cancer in mammals. Unlike eukaryotes, the cellular and molecular responses to DNA damage have not been fully characterized in prokaryotes except UV induced SOS response in certain bacteria, possibly because bacteria differ from higher organisms into both cellular complexity and tolerance to DNA damage. *Deinococcus radiodurans* a gram-positive bacterium is primarily known for its extraordinary resistance to both ionizing and non-ionizing

radiations [1, 2]. It can tolerate up to 6.5kGy γ radiation, without a measurable loss of cell viability [3]. The extraordinary tolerance of *D. radiodurans* (hereafter referred as *Deinococcus*), to other abiotic stresses including radiation and desiccation, has attracted both radiation biotechnologist and molecular geneticists for using it (i) in bioremediation of radioactive waste and, (ii) as a model organism for understanding the molecular basis of its extreme radioresistance. The radiobiotechnological use of this bacterium however, suffers a major setback because this microorganism is yet to be tested for any desirable traits, for its use in bioremediation of radioactive waste, except that it is resistant to both chronic as well as acute exposures of γ radiation, and has a number of proteins



that need to be characterized for their usefulness. On the contrary, there are microorganisms that do not possess such a magnitude of radiation resistance, but have numerous features that are useful in bioremediation of hazardous waste, mixed with metals and aromatic compounds. Therefore, the basic understanding of mechanisms underlying the radiation resistance and at least the identification of molecules required for the usefulness of this bacterium in radiobiotechnological applications, would be the core areas of basic research and worth pursuing. Further, both basic and applied research on this bacterium would require the development of technology for its genetic modification and for the expression of desirable characters in this bacterium. Our laboratory has been focusing on both of these aspects i.e. the development of both technological and intellectual capabilities for carrying out advanced research on this bacterium and the basic research on understanding the molecular basis of the extraordinary radiation resistance in this organism. Using in house expertise in these areas, significant contributions have been made in understanding the molecular basis of extraordinary radiation resistance in *Deinococcus*.

Development of technological expertise for easy manipulation of *Deinococcus radiodurans*

Genetic manipulation of any organism requires organism-specific genetic tools. These are developed depending upon the need of researchers. We were in need of technology for genetic manipulations of *Deinococcus* mainly on two aspects (i) the synthesis of proteins from other bacteria as well as over production of this bacterial proteins itself, and (ii) the inactivation of any gene of interest for studying their contributions in radiation resistance of *Deinococcus*. We developed many constructs for this work using the resources available in our laboratory. The notable ones were pRADgro (Fig. 1a) and pNOKOUT (Fig 1b). For the development of pRADgro, a 261bp DNA fragment containing regulatory sequences of *groESL* genes of *Deinococcus* (*Pgro*), Shine-Delgarno (SD) sequences for ribosome binding and five codons of GroE along with four new unique restriction enzyme sites for providing correct translation frame for recombinant protein synthesis, was cloned in pRAD1 [4] cloning vector. The pRADgro was checked for its nature as a shuttle expression vector between *Deinococcus* and *Escherihcia coli*, another model

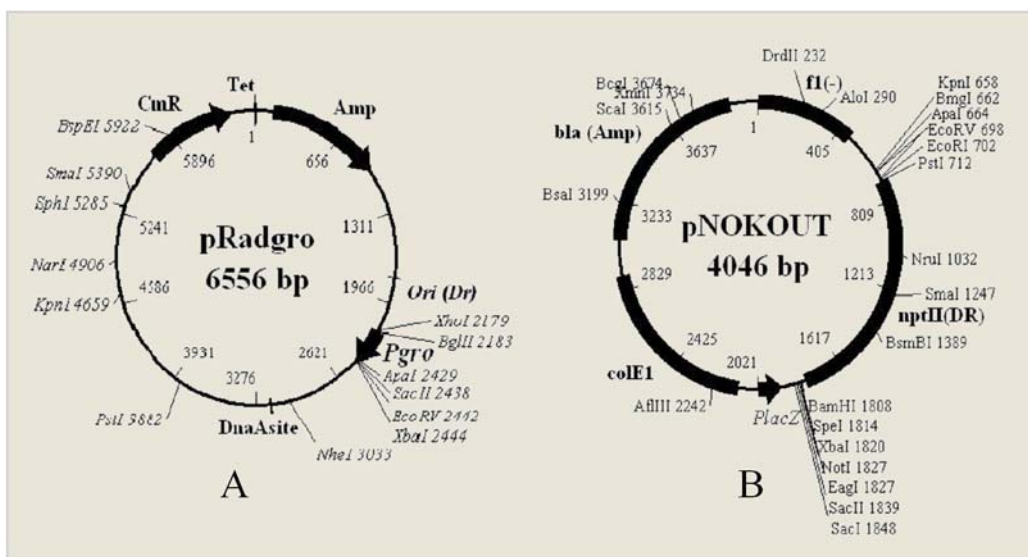


Fig. 1: Partial restriction map of pRadgro and pNOKOUT constructs. The 261bp BglIII-XbaI fragment containing promoter (*Pgro*) was cloned in pRAD1 to get pRadgro (A) and 937bp an expressing cassette of *nptII* (*nptII* (DR)) was cloned at *SmaI* site of pBluescript SK+ to get pNOKOUT (B).



organism mostly used for gene cloning and recombinant proteins synthesis, by checking the expression of transgenes in both the organisms [5,6].

Similarly, pNOKOUT was constructed by cloning the neomycin phosphoryltransferase II (*nptII*) selection marker cassette into pBluescript SK+ an *E. coli* cloning vector. The *nptII* cassette was earlier known for the expression of kanamycin resistance in *Deinococcus* and pBluescript SK+ should not be surviving in *Deinococcus*. Thus pNOKOUT was anticipated to carry an expressing *nptII* cassette into *Deinococcus* but would not be maintaining in it. This will make pNOKOUT a suicidal vector and the replacement of desired gene with *nptII* would take place through genetic recombination. These features of pNOKOUT were confirmed again in both *E. coli* and *Deinococcus*. The results showed the integration of *nptII* into *Deinococcus* R1 genome and expression of kanamycin resistance in these cells. Both of these constructs have been extremely useful in our ongoing program on this bacterium. A large number of proteins from both *E. coli* and *Deinococcus* have been expressed and a number of genetic knockout strains have been generated, and the roles of various proteins in radiation resistance have been ascertained in

this bacterium. These vectors have also been provided by several laboratories abroad on material transfer agreement (MTA) and are being used for basic research on *Deinococcus*. This allowed us to have complete autonomy in any kind of genetic manipulation, required for making *Deinococcus* suitable for both basic and applied work.

Functional significance of macromolecular interactions in radioresistance of *Deinococcus radiodurans*

Proteins are ultimate functional units that contribute to different characteristics in a living being. The protein functions are intimately regulated by the microenvironment around these molecules and therefore, the different organisms surviving in different environments would be expected to have different microenvironments inside their cells. Different organisms having similar array of proteins, might exhibit different characteristics, due to change in microenvironment in which these proteins are functioning in a particular living system. With these existing paradigms, we hypothesized that the possibility of DNA metabolic proteins, required for extreme phenotypes in this bacterium might be interacting and thus functioning differently in this bacterium. This assumption was further strengthened

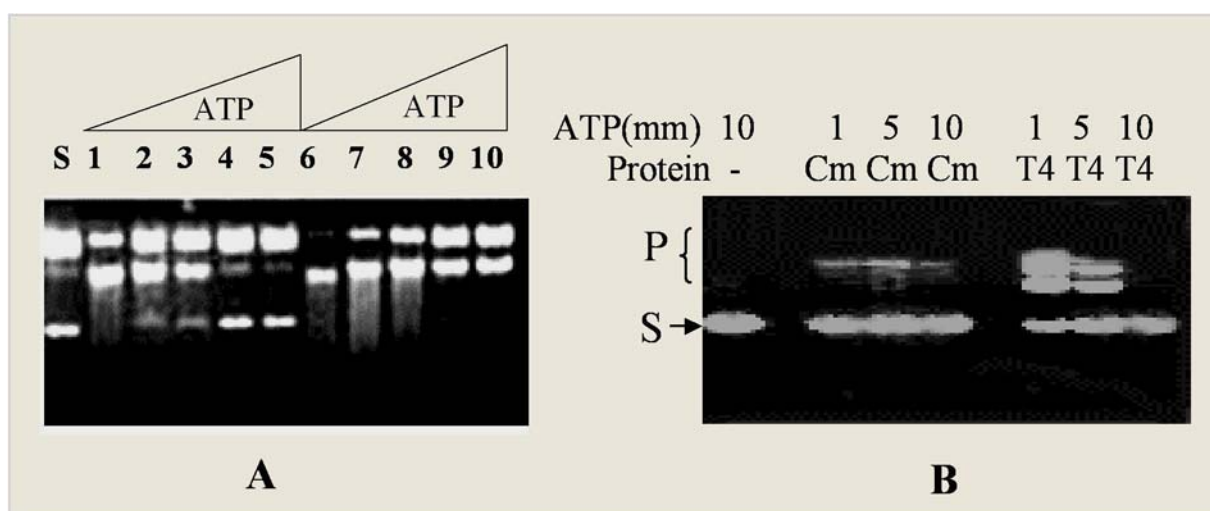


Fig. 2: Regulation of two incompatible functions in multiprotein complex. Multiprotein complex isolated from *D. radiodurans* was checked for nuclease activity on dsDNA in presence of Mg²⁺ (1-5) and Mn²⁺ (6-10) with increasing concentration of ATP (A). The DNA ligase activity of complex (Cm) was compared with T4 DNA ligase (T4) in presence of different concentration of ATP (B).



when we observed, that *Deinococcus* with *E. coli*, which exhibit just the opposite response to γ radiation, have nearly similar protein complements for DNA recombination and repair pathways. Therefore, to test our hypothesis, the possible existence of these proteins in form of macromolecular complex was first checked. The multiprotein complexes were isolated from stationary phase cells of *Deinococcus* and *E. coli* and compared for different DNA metabolic activities and presence of recombination repair proteins by immuno-detection [7]. Multiprotein complexes from both these organisms although have several of the DNA metabolic activities similar to each other, they differ grossly on some of the crucial functions. Unlike *E. coli*, the multiprotein complex from *Deinococcus* did not contain RecA but it had some of the other important DNA repair function like ATP sensitive nuclease (Fig. 2a) and ATP stimulated DNA ligase (Fig. 2b) and proteins associated with non-homologous recombination activities. The protein components of this complex were identified by mass spectrometry and 24 different polypeptides were detected, that included PprA, ATP type DNA repair ligase (DRB0100) and a 5' nucleotidase (DR0505).

The functional significance of some of these proteins like PprA, DRB0100 and DR0505 were characterized for their roles in γ radiation resistance of this bacterium. We

deleted *dr0505*, *pprA* and *drb0100* genes from *Deinococcus* genome and recombinant proteins were made in *E. coli* and purified. By checking the γ radiation effect on survival of these mutants and activity characterization of recombinant proteins, we demonstrated the roles of these proteins in γ radiation resistance of *Deinococcus* and the possible mechanisms of action were shown. Interestingly, the activity of recombinant DRB0100 ligase compulsorily required PprA and DRB0098, another protein of this bacterium for its enhanced activity (Fig. 3). Further DRB0100 supports radiation resistance in *Deinococcus* only when PprA, DRB0098 and DRB0099 were present [8]. These results suggested the functional significance of protein-protein interaction in macromolecular complex for its efficient functioning in γ radiation resistance of *Deinococcus*. Similarly, the recombinant DR0505 is characterized as an ATP sensitive nuclease and the novel phosphoesterase activities those that withstand up to 65°C *in vitro* [9] and implicated in the role of this protein, in nucleotide recycling.

Functional significance of known DNA recombination / repair proteins in radiation resistance of *Deinococcus*

There are two major DNA recombination pathways like RecF and RecBC, which have been implicated for repair

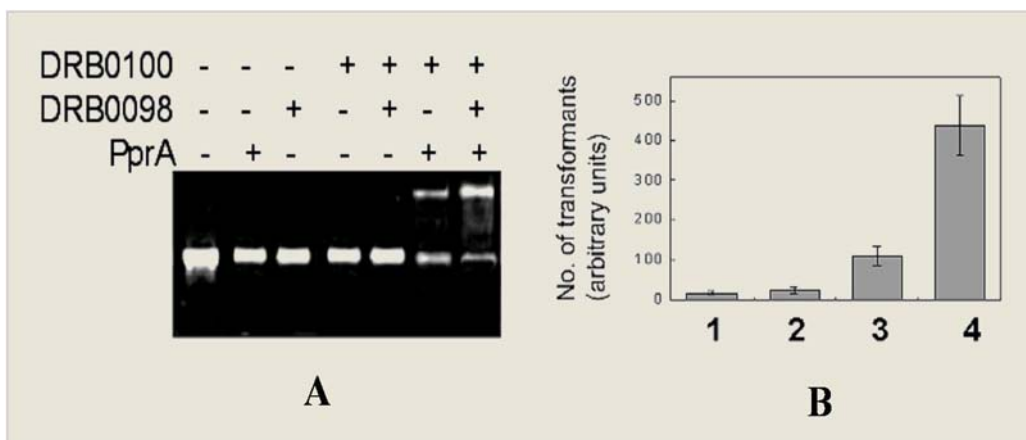


Fig.3: DNA end joining activity assay of DRB0100 identified from multiprotein complex. Purified proteins were incubated with PCR amplified linear DNA and checked on agarose gel (A) and linearised plasmid DNA ligated samples were checked for transformation in *E. coli* (B). Ligation efficiency directly correlates with the number of transformants obtained with each samples.



of radiation-induced DNA damage in most of the bacteria. RecBC enzyme complex has been characterized for its role in DNA double strand break repair, in many radiation-sensitive bacteria. Surprisingly, the genome of *Deinococcus* encodes all the components of RecF recombination pathway but lacks the components of classical RecBC pathway. How does this bacterium mend its shattered genome in the absence of RecBC enzymes was worth investigating. First the possibility of RecF contributing to efficient DNA strand break repair was checked by *in-trans* expression of SbcB, an exonuclease I, a known inhibitor of RecF pathway, and then by over expression of RecBC from *E. coli* into *Deinococcus*. *Deinococcus* cells expressing these proteins separately become sensitive to γ radiation but the levels of radiation sensitivity was more in SbcB expressing cells than RecBC, suggesting the involvement of RecF pathway in radiation resistance of this bacterium [5] and less significance of RecBC to these phenotypes at least in *Deinococcus* [10]. The role of RecF recombination pathway in radiation resistance of this bacterium was further supported from the observation, that the functions of other suppressors of RecBC pathway like SbcCD, is required for higher radioresistance [11].

Characterization of a novel antioxidant's role in radiation resistance of *Deinococcus*

There are two major components that mostly contribute to γ radiation resistance in living system. These are the efficient DNA strand break repair and the strong oxidative stress tolerance mechanisms. *Deinococcus* has been appreciated for both these characteristics. Along with extreme doses of γ radiation, the bacterium can also withstand the deleterious effects of hydrogen peroxide, by tolerating up to ~25 mM H_2O_2 without any measurable loss of cell viability. The oxidative stress tolerance is contributed by both enzymatic and non-enzymatic components. We addressed the

role of non-enzymatic components if any, in such higher levels of oxidative stress tolerance in *Deinococcus*. We searched the genome of this bacterium for metabolic pathways, associated with antioxidant synthesis in bacterial system. We observed that the genome of this bacterium confers a gene (we hereby designate as *pqqE*) that encodes an enzyme responsible for pyrroloquinoline quinone (PQQ) biosynthesis in bacterial system. This gene was cloned and expressed in *E. coli*. Transgenic *E. coli* producing PQQ showed several fold higher tolerance to oxidative stress *in vivo* and protected biomolecules from γ radiation damage *in vitro* [12]. PQQ was subsequently shown as strong antioxidant as vitamin C and Trolox [13] and could neutralize superoxide, hydroxyl and oxygen free radicals *in solution* without any indication of its consequential effect [13]. PQQ was subsequently shown as pro-oxidant in mammalian cells, by depleting the redox equivalents that act as antioxidants in mammalian cells. It showed higher rates of apoptotic cell death in tumor cells as compared to normal cells [14].

The role of PQQ in radiation resistance phenotypes of *Deinococcus* was investigated. The *pqqE* gene was deleted from the genome of *Deinococcus* and effect of different DNA damaging agents including γ radiation, on cell survival and DSB repair ability of mutant cells were

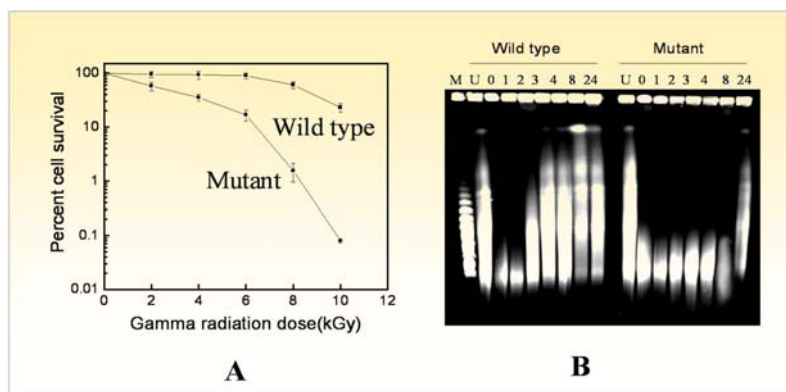


Fig. 4: Involvement of PQQ in radiation resistance of *D. radiodurans* through its role in DSB repair. *D. radiodurans* cells devoid of PQQ were generated and effect of γ radiation on survival of these cells (mutant) was compared with wild type (wild type) (A). The cells recovering from γ radiation effects were collected at different time interval (1-24 h) and analysed for shattered genome reassembly on pulsed field gel electrophoresis (B) and compared with unirradiated (U) controls.



investigated. Results showed, that the absence of PQQ makes this bacterium incompetent to withstand higher doses of DNA damage and γ radiation in particular (Fig. 4A). Molecular mechanisms contributing to this phenotype of PQQ was checked and found that PQQ has a role in DNA strand break repair (Fig. 4B) [15]. Subsequently, a PQQ inducible putative protein kinase encoded from *dr2518* gene was identified from this bacterium and its role in γ radiation resistance of *Deinococcus* through DNA strand break repair was demonstrated [16].

Gamma radiation response studies in *Deinococcus*

Every living cell exposed to any stress, exhibits rapid changes at cellular and molecular levels, to counteract the deleterious effect of both biotic and abiotic stresses. Such changes come under the processes termed as stress responses, which determine the tolerance levels of that organism to a particular stress. Similarly, the cells exposed to γ radiation also respond to both oxidative stress and DNA damage effects. Bacterial response to DNA damage has been studied, in terms of the effect of DNA damage on gene expression and on the functional modulation of proteins associated with DNA repair and cell division and is known as SOS response. *Deinococcus* does not exhibit SOS response mechanisms [17]. In spite of that, it shows DNA damage induced gene expression. The molecular mechanisms underlying the regulation of the synthesis and activity modulation of various proteins by γ radiation induced DNA damage, were not known. The systematic studies on changes occurring in *Deinococcus* cells exposed to γ radiation were carried out at both cellular and molecular levels. It showed that cells exposed to γ radiation, rapidly synthesized very high levels of signaling nucleotides including ATP, AMP and cyclic AMP etc and stress responsive

enzymes like adenylyl cyclase, phosphodiesterase, protein kinases [18] (Fig. 5). These molecules are well known for their roles in regulation of various cellular and molecular processes, suggesting that *Deinococcus* does respond to γ radiation induced DNA damage, which could be different from other bacteria as it does not confer classical SOS response mechanism.

DR2518 was earlier shown as a PQQ inducible protein kinase having a role in radiation resistance in *Deinococcus*. The effect of γ radiation induced DNA damage on expression and activity of DR2518 protein kinase was checked. Results showed, that both synthesis and activity of this kinase were regulated by γ radiation induced changes in the cells, which indicated that this kinase could be a typical candidate of an alternate DNA damage response mechanism of this bacterium. The ability of this kinase phosphorylating several important DNA repair proteins of *Deinococcus* and regulating the differential expression of genes in response to γ radiation induced DNA damage (Fig. 6), strengthened its role in radioresistance. The results obtained from this particular study suggested, that unlike other bacteria that confer SOS response, *Deinococcus* might have an alternate mechanism of DNA damage response and DR2518 kinase

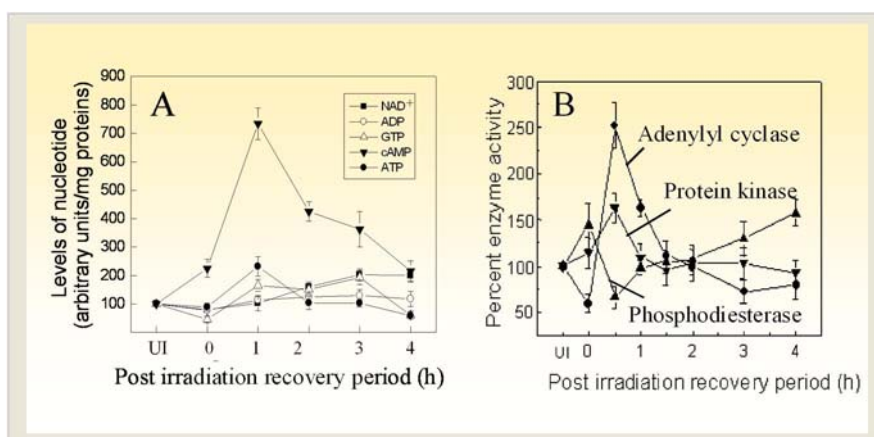


Fig. 5: Effect of γ radiation on levels of signaling molecules. *Deinococcus* cells treated with 6.5kGy γ radiation and cells were collected at different post irradiation recovery time. Total purine nucleotides (A) and stress responsive enzymes like adenylyl cyclase, protein kinase and phosphodiesterases were assayed using standard procedures.

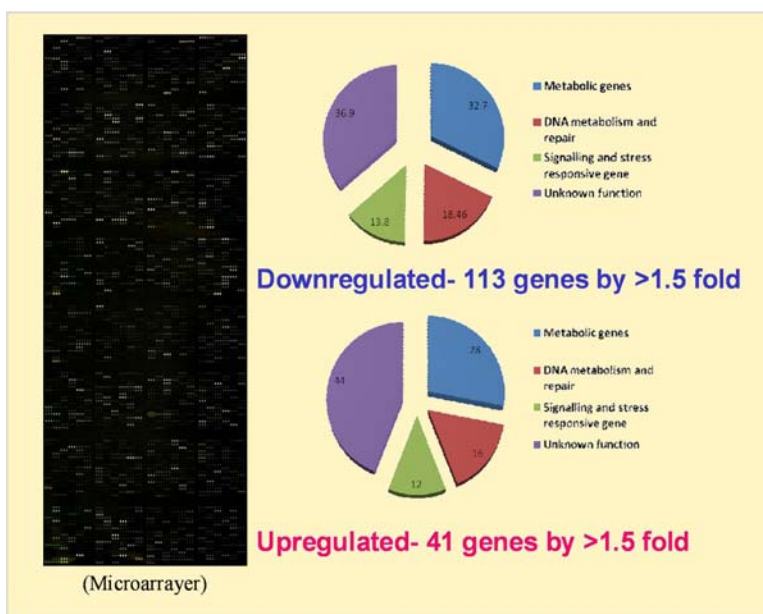


Fig. 6: Involvement of a radiation responsive serine/ threonine protein kinase (STPK) in regulation of gene expression in *D. radiodurans*. *Deinococcus* cells devoid of STPK were exposed with 6.5kGy γ radiation and global change in gene expression was measured by microarray analysis (Microarrayer) in collaboration with Prof. Yeujin Hua, Zhejiang University, Hangzhou China. Different numbers of genes showing reduced expression (downregulated) and increased expression (upregulated) by 15 fold or more were taken into consideration for making conclusions.

seems to be a candidate protein kinase playing crucial role in this process.

Conclusions

Molecular mechanism underlying extraordinary radioresistance of *Deinococcus* was not clear. Several laboratories globally, working on various aspects leading to a single question on how this bacterium possess unthinkable and unbelievable tolerance to γ radiation effect. Our work at BARC has contributed significantly to global efforts on this aspect. Some of our notable contributions are (i) the RecF recombination pathway in absence of RecBC enzymes, contributes to efficient DSB repair and radiation resistance (ii) an antioxidant metabolite PQQ has a role in both oxidative stress tolerance and DSB repair, (iii) the multiple proteins having greater significance in DSB repair and radiation resistance, are present and function together in a multiprotein complex, (iv) we

proposed an alternate DNA damage response mechanism leading to induced synthesis of signaling molecules, stress responsive enzymes and a DNA damage responsive membrane protein kinase in this bacterium, and (vi) the involvement of a eukaryotic type Ser/Thr protein kinase was reported for the first time on the role of a protein kinase in DSB repair and radiation resistance in any bacterium.

Acknowledgements

I am grateful to Dr K. B. Sainis, Director, BMG and Dr S. K. Apte, Associate Director, BMG for their keen interest in the subject as well as moral and intellectual support. I am thankful to Drs Hari Mohan, Indira K Priyadarshini, Atanu Barik, V.P. Joshi, Roja Gopalakrishnan and Professor Yeujin Hua for collaborative support. My special appreciation and gratitude to my colleagues Drs N. P. Khairnar, Vidya Kamble, Shruti Desai and Swathi Kota and Shri Y. S Rajpurohit, Shri A. D. Das, C. Vijay Kumar and Ms Kruti Mehta,

for keeping the pace of their research progress uninterrupted and their outstanding work output. Sincere efforts of Shri Sunil D. Dhotre for providing laboratory material for the work and of all the people in the section, deserve a heartfelt acknowledgement.

References

1. Makarova, K. S., Aravind, L., Wolf, Y. I., Tatusov, R. L., Minton, K. W., Koonin, E. V. and Daly, M. J. "Genome of extremely radiation-resistant bacterium *Deinococcus radiodurans* viewed from the perspectives of comparative genomics". *Microbiology and Molecular Biology Reviews* 65 (2001): 44-79.
2. Slade, D. and Radman, M. "Oxidative stress resistance in *Deinococcus radiodurans*". *Microbiology and Molecular Biology Reviews* 75 (2011): 133-191.



3. Battista, J.R. "Radiation resistance: the fragment that remain". *Current Biology* 10 (2000): R204-205.
4. Meima, R. Lidstrom, M.E. "Characterization of the minimal replicon of a cryptic *Deinococcus radiodurans* SARK plasmid and development of versatile *Escherichia coli*-*D. radiodurans* shuttle vectors". *Applied and Environmental Microbiology* 66 (2000): 3856–3867.
5. Misra, H.S., Khairnar, N.P., Kota, S., Srivastava, S., Joshi, V.P. and Apte, S.K. "An exonuclease I sensitive DNA repair pathways in *Deinococcus radiodurans*: a major determinant of radiation resistance". *Molecular Microbiology* 59 (2006):1308-1316.
6. Kota, S. and Misra, H.S. "PprA: a protein implicated in radioresistance of *Deinococcus radiodurans* stimulates catalase activity in *Escherichia coli*". *Applied Microbiology and Biotechnology* 72 (2006): 790-796.
7. Kota, S. and Misra, H.S. "Identification of a DNA processing complex from *Deinococcus radiodurans*". *Biochemistry and Cell Biology* 86 (2008): 448-458.
8. Kota, S., Kamble, V. A., Rajpurohit, Y. S. and Misra, H. S. "ATP-type DNA ligase requires other proteins for its activity *in vitro* and its operon components for radiation resistance in *Deinococcus radiodurans* *in vivo*". *Biochemistry and Cell Biology* 88 (2010) :783-90.
9. Kota, S., Kumar, C.V. and Misra, H.S. "Characterization of an ATP-regulated DNA-processing enzyme and thermotolerant phosphoesterase in the radioresistant bacterium *Deinococcus radiodurans*". *Biochemical Journal* 431 (2010): 149-157.
10. Khairnar, N.P., Kamble, V.A. and Misra, H.S. (2008) RecBC enzyme overproduction affects UV and gamma radiation survival of *Deinococcus radiodurans*. *DNA Repair (Amst)*, **7**, 40-47.
11. Kamble, V.A. and Misra, H.S. "The SbcCD complex of *Deinococcus radiodurans* contributes to radioresistance and DNA strand break repair *in vivo* and exhibits Mre11-Rad50 type activity *in vitro*". *DNA Repair (Amst)*, 9(2010): 488-494.
12. Khairnar, N. P., Misra, H. S. and Apte, S. K. "Pyrroloquinoline-quinone synthesized in *Escherichia coli* by pyrroloquinoline-quinone synthase of *Deinococcus radiodurans* plays a role beyond mineral phosphate solubilization". *Biochemical Biophysical Research Communications* 312 (2003): 303-308.
13. Misra, H.S., Khairnar, N.P., Atanu, B., Priyadarshin, I. K. I., Mohan, H. and Apte, S. K. "Pyrroloquinoline-quinone: a reactive oxygen species scavenger in bacteria". *FEBS Letters* 578 (2004) :26-30.
14. Shankar, B., Pandey, R., Amin, P., Misra, H. S. and Sainis, K. B. "Role of glutathione in augmenting the anticancer activity of pyrroloquinoline quinone (PQQ)". *Redox Report* 15 (2010): 146-154
15. Rajpurohit, Y.S., Gopalakrishnan, R. and Misra, H.S. "Involvement of a protein kinase activity inducer in DNA double strand break repair and radioresistance of *Deinococcus radiodurans*". *Journal of Bacteriology* 190 (2008): 3948-3954.
16. Rajpurohit, Y.S. and Misra, H.S. "Characterization of a DNA damage-inducible membrane protein kinase from *Deinococcus radiodurans* and its role in bacterial radioresistance and DNA strand break repair". *Molecular Microbiology* 77 (2010): 1470-1482.
17. Narumi, I., et al. "The LexA protein from *Deinococcus radiodurans* is not involved in RecA induction following gamma irradiation". *Journal of Bacteriology* 183 (2001):6951-6956.
18. Kamble, V.A., Rajpurohit, Y.S., Srivastava, A.K. and Misra, H.S. "Increased synthesis of signaling molecules coincides with reversible inhibition of nucleolytic activity during postirradiation recovery of *Deinococcus radiodurans*". *FEMS Microbiology Letters* 303 (2010): 18-25.



Nuclear Analytical Chemistry: Developments and Applications

R. Acharya

Radiochemistry Division

Dr. Raghunath Acharya is the recipient of the DAE Scientific & Technical Excellence Award for the year 2009

Abstract

The article gives a brief summary of developments and applications of nuclear analytical methods namely (i) single comparator Neutron Activation Analysis (k_0 -NAA), (ii) k_0 -based Internal Monostandard NAA (IM-NAA) for large size and non-standard geometry samples including reactor materials, (iii) k_0 -based Prompt Gamma ray NAA (PGNAA) for non-destructive analysis of materials for low Z elements and neutron poisons, (iv) instrumental and chemical NAA (INAA and CNA) methods for total and/or species concentrations of elements namely As, I and Se and (v) Particle Induced Gamma ray Emission (PIGE) methods for non-destructive determination of F in borosilicate glass and Li in ceramic samples.

Introduction

The k_0 -based NAA method was adopted at the Radiochemistry Division in the year 1995, for multielement determination in various matrices [1-4]. This method is more attractive than relative method, as it uses a single comparator like gold instead of multielement standards. This method needs reactor and detector-based input parameters namely sub-cadmium to epithermal neutron flux ratio (f), epithermal neutron flux shape factor (α) and absolute detection efficiency of the detector (ϵ) in addition to nuclear constants like k_0 and Q_0 [2,3]. The k_0 -NAA was standardized by determining f and α for the irradiation sites of research reactors at BARC and determining the k_0 -factors for some analytically important isotopes, validated by analyzing reference materials (RMs) of different origin and applied to samples of diverse matrices [1-10]. Routine analysis by conventional NAA and k_0 -NAA deals with small size samples (tens of mg-500 mg). Often sub-sampling of solids and small size sample analysis are questionable

in terms of true analytical representation. In this case, large size sample (g-kg scale) analysis is advantageous for better analytical representativeness. A k_0 -based Internal Monostandard NAA (IM-NAA) method, using *in-situ* relative detection efficiency, was developed for the analysis of large size and non-standard geometry samples and applied to nuclear reactor materials, wheat grains, uranium ore and archaeological potteries [11-16]. IM-NAA method was also applied to small size samples of diverse matrices including meteorites [17] and uranium ores [18]. Our expertise on k_0 -method was advantageously utilized, to carry out R&D work on k_0 -based Prompt Gamma ray NAA (PGNAA), using neutron beam facilities at Dhruva reactor [19-23,4]. R&D work on PGNAA includes determination of prompt k_0 -factors, analysis of RMs, compositional analysis of nuclear structure materials, meteorites and cement standard and determination of H in zircalloys and B in RMs, chemical compounds and borosilicate glass samples. The R&D work on k_0 methodologies in NAA and PGNAA was carried out for the first time in India.



R&D work on k_0 -NAA and IM-NAA

Irradiation positions of Apsara (core and thermal column, TC), CIRUS (self serve, SS, and pneumatic carrier facility, PCF), Dhruva (PCF), and AHWR critical facility (CF) were used. Neutron monitors like Au, Zr, In, Mo and Zn were used for neutron spectrum characterization. The k_0 -NAA method was validated by determining concentrations of about 30 elements in several Reference Materials (RMs) [3] obtained from IAEA NIST & USGS and applied to many samples including ruby [1], beryl and emerald [5], sediments [6], manganese nodules and encrustations [7,8], cereals [9], medicinal and edible leaves [10]. For NAA of short-lived activation products, PCFs at CIRUS and Dhruva reactors were used. The k_0 -factors of the short-lived nuclides (half-lives – 11 s to 37 min) for the elements namely F, Se, Sc, Al, V, Ti, Cu, Ca, Mg, I and Cl with respect to gold (^{197}Au) were determined [24]. For validation of the IM-NAA, Synthetic MultiElement Standards (SMELS) and IAEA RMs SL-3 and Soil-7 were analyzed using Au and Sc monostandards respectively [25]. Concentrations of 23 elements were determined and the % deviations were within $\pm 8\%$ with respect to certified values.

Large Sample NAA (LSNAA)

The IM-NAA method was applied for the analysis of some large and non-standard geometry samples (2-100 g), as shown in Fig. 1. This includes nuclear fuel cladding cum structure materials namely zircalloys (zircaloy 2 and 4) [11,12], stainless steels (SS 316M, D9 and SS 304L and

BCS RMs) [11,13,14], 1S grade aluminium [11], wheat grains [14], uranium ores [15] and ancient clay potteries [15,16]. The results of Zircaloy 2 and SS-316M are given in Table 1. The elements determined in zircaloy samples are Zr, Sn, Fe, Cr, Ni, In, Mn, As, Co, W and Ta whereas in Stainless steel samples, the determined elements are Fe, Cr, Ni, Mo, Mn, Co, As and W. Since all the major and/or minor elements Zr, Sn, Fe, Cr and/or Ni in zircalloys and Fe, Cr, Ni, Mn and/or Mo in SS were amenable to NAA, concentration values were obtained by mass balance approach. The results are in good agreement with the literature/reported compositions. In the case of 1S aluminium, impurities could be determined as the mass of the sample was entirely due to Al.

The IM NAA method was used to analyze samples of wheat grains to investigate the applicability of large sample NAA and to examine the effect of heterogeneity on the routinely practised sub-sampling method [14]. The results indicated, that it would be better to analyze one large sample (> 1 g) instead of replicate sub samples. One of the best applications of IM-NAA is the analysis of large and non standard geometry ancient potteries for the provenance study. A total of 30 large size ancient potteries, obtained from excavated Buddhist sites of Andhra Pradesh, were analyzed [16]. The concentration ratios of 15 elements Na, K, Cr, Fe, Co, Ga, Cs, As, La, Ce, Sm, Eu, Lu, Hf and Th with respect to Sc were determined. Values of La/Ce and statistical cluster analysis using concentration ratios were used for the grouping.

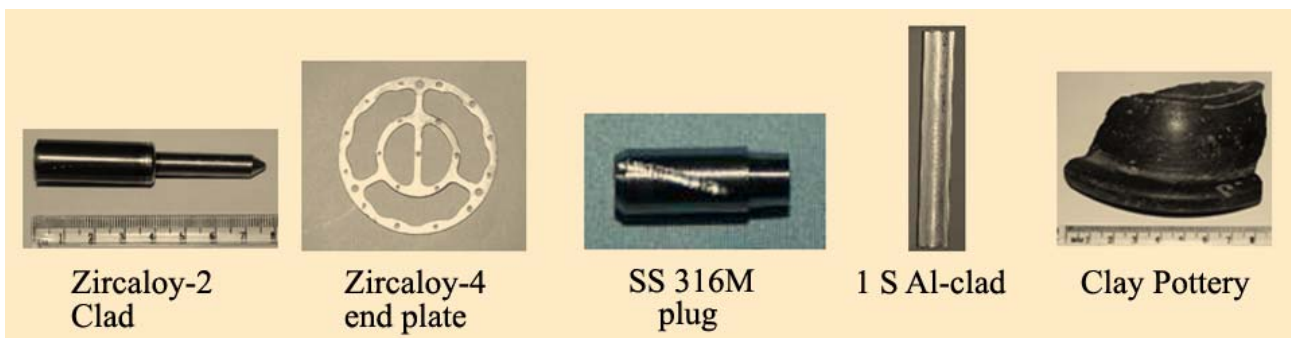


Fig 1: Photos of some large size samples

DAE Excellence Award



Table 1: Composition results of large samples of Zircaloy 2 and SS 316 M by IM-NAA

Element	Zircaloy 2	Specifications	Element	SS 316M	Specifications
Zr%	98.2±0.7	Balance	Fe%	65.1 ± 0.9	Balance
Sn%	(15.8±0.3)×10 ⁻¹	1.2-1.7	Cr%	17.1 ± 0.1	16.5-17.5
Fe%	(1.8±0.2)×10 ⁻¹	0.07-0.2	Ni%	13.5 ± 1.3	13.00-14.00
Cr%	(8.3±0.1)×10 ⁻²	0.05-0.15	Mo%	2.3 ± 0.1	2.00-2.75
Ni%	(7.8±0.4)×10 ⁻²	0.03-0.08	Mn%	(18.8 ± 0.1) ×10 ⁻¹	1.5-2.0
In ^a	(1.0±0.1)×10 ⁻¹	NA	Co ^a	144.8±4.2	300 max
Co ^a	6.8±0.1	20	As ^a	52.5±2.6	NA
Ta ^a	16.3±1.1	200	W ^a	25.5±2.5	NA
Hf ^a	24.0±0.7	100			
Mn ^a	10.7±0.1	50			
As ^a	4.5±0.4	NA			

a – concentration in mg kg⁻¹, NA – not available

R&D work on Prompt Gamma ray NAA (PGNAA)

Since 1999, we have been carrying out studies on PGNAA using thermal and reflected neutron beam lines at Dhruva reactor [19-23]. As part of the quality assurance program, prompt k_0 -factors for isotopes of elements like H, B, N, Mg, Si, S, K, Ba, Cd, Sm, Hg and Gd were determined, with respect to 1951 keV gamma-ray of ³⁶Cl, using both thermal and reflected neutron beams [19,20]. The internal mono-standard method of PGNAA was used to analyze IAEA RMs like SL-3 (sediment) and 153 (Milk powder) [21] for method validation. Composition analysis of SS 361M and BCS CRM 466 was carried out by standard-less approach. It was also applied to "Jagannath meteorite" and concentrations of Fe, Cr, Si, K, Mg, Ca and Ni were determined. A methodology for correcting the self-shielding effect was standardized, which was validated with synthetic samples containing neutron poisons like B, Cd and Gd. The method developed was used to determine elements namely B, Ti, Mo, Cr and Si in TiB₂ alloy [22] and boron in chemical compounds and borosilicate glass samples [23]. Low concentrations of boron were determined in several RMs, with a detection limit of 1 mg kg⁻¹ [23].

Applications of instrumental and chemical NAA methods

Thermal and Epithermal NAA (TNAA and ENAA) methods were standardized for U and Th in mixed oxides and zircon, U, Th and Rare Earth Elements (REEs) in uranium ores, and trace amounts of Th in uranium oxide. Trace amounts of REEs and other elements in a purified ²⁴¹Am sample could be determined by NAA. INAA and Chemical NAA (CNAA) methods were used for total arsenic and inorganic arsenic species (arsenite and arsenate) concentrations in potable water [26]. ENAA method using boron carbide filter was optimized to determine concentrations of iodine in food, food products including milk, baby foods and iodized salts and iodine values were found to be in the range of 0.16- 5.5 mg. kg⁻¹ except for iodized salt (10-33 mg. kg⁻¹) [27]. An anion exchange Polymer Inclusion Membrane (PIM) was used in conjunction with NAA, to determine low levels of I⁻ in aqueous samples and applied to milk and milk powder sample for iodide contents [28]. Selenium (Se) in crop products from seleniferous areas of Punjab was estimated by INAA. Se concentrations are in the range of 10-670 mg kg⁻¹, whereas the values of wheat and mustard grains are 100 and 670 mg kg⁻¹, respectively [29].



PIGE methodology for low Z elements (F and Li) using proton Beam at FOTIA, BARC

Quantitative estimation, of low Z elements like Be, Li, B, C, N, O, F, Si, P and S is difficult by many analytical techniques, including wet chemical methods, if the sample is difficult to dissolve. PIGE methods, with proton or deuterium beams are found to be unique due to the non-destructive nature, negligible matrix effect and no spectral interference. Recently a PIGE facility (Fig. 2) has been set up at FOTIA, BARC. We have standardized a PIGE method using 4 MeV proton beam for non-destructive determination of F in barium borosilicate glass samples [30,31]. Barium BoroSilicate Glass (BaBSG) is a potential candidate for vitrification of thorium-based nuclear waste. The prompt gamma rays of 110 and 197 keV from ^{19}F ($p, p'\gamma$) ^{19}F were measured by high resolution gamma ray spectrometry. Samples containing F in the range of 0.1-4 wt%, prepared at WMD, BARC, were analyzed to study the F retention in glass matrix during vitrification. In a similar way, a PIGE method was standardized for Li, in lithium incorporated $\text{Nd}_2\text{Ti}_2\text{O}_7$ ceramic sample, determination non-destructive. The prompt gamma rays of 478 and 429 keV from ^7Li ($p, p'\gamma$) ^7Li and ^7Li ($p, n\gamma$) ^7Be were used for this study. The method is promising for Li estimation in samples like Lithium nitrate and silicate without chemical destruction of sample.



Fig. 2: PIGE set up at FOTIA

Acknowledgments

Author gratefully acknowledges the co-operation of the personnel of Reactor Group and Author is thankful to all contributors and collaborators. Special thanks to Dr. A.V.R. Reddy, Ex-RCD and Head, ACD, Dr. A. Goswami, Head, RCD, Dr. P.K. Pujari, Head, NCS, RCD, Dr. S.B. Manohar, Ex-Head, RCD, Dr. A.G.C. Nair, Shri P.P. Burte, Dr. K. Sudarshan, Dr. A.K. Pandey, Dr. R. Tripathi, Dr. S. Sodaye, Dr. K.K. Swain, Dr. Preeti Bhagat, Shri K. B. Dasari and Shri Sumit Chhillar. Author is grateful to Dr. S. Cahplot, Head, SSPD, Dr. R.K. Choudhary, Ex-Head, NPD & Dr. S. , NPD and Dr. P. Singh, Dr. S.K. Gupta & Mr. A. Agarwal, LEHIPA. PG, Dr. C.P. Kaushik & Dr. R.K. Mishra, WMD, BARC. Author is thankful to Dr. V.K. Manchanda, Ex-Head, RCD, Dr. V. Venugopal, Ex-Director, RC&I Group, Dr. S.K. Aggarwal, AD, RC&I Group and Dr. K.L. Ramakumar, Director, RC&I Group for their keen interest and encouragement.

References

1. R.N. Acharya, P.P. Burte, A.G.C. Nair, A.V.R. Reddy and S.B. Manohar, *J. Radioanal. Nucl. Chem.*, 220 (1997) 223.
2. R. Acharya, Ph.D Thesis, University of Mumbai, Mumbai, 2000.
3. R.N. Acharya, A.G.C. Nair, A.V.R. Reddy S.B. Manohar, *Appl. Radiat. Isot.*, 57 (2002) 391.
4. R. Acharya, A.G.C. Nair, K. Sudarshan, A. Goswami, A.V.R. Reddy, *J. Radioanal. Nucl. Chem.*, 278 (2008) 617.
5. R.N. Acharya, R.K. Mondal, P.P. Burte, A.G.C. Nair, N.B.Y. Reddy, L.K. Reddy, A.V.R. Reddy, S.B. Manohar, *Appl. Radiat. Isot.*, 53 (2000) 981.
6. S.K. Jha, R.N. Acharya, A.V.R. Reddy, S.B. Manohar, A.G.C. Nair, S.B. Chavan, S. Sadasivan, *J. Environ. Monit.* 4 (2002) 131.
7. R.K. Dutta, R. Acharya, A.G.C. Nair, S.N. Chintalapudi, V. Chakravorty, A.V.R. Reddy, S.B. Manohar, *J. Nucl. Radiochem. Sci.*, 6 (2005) 139.



8. R.K. Dutta, R.N. Acharya, V. Chakraborty, A.G.C. Nair, A.V.R. Reddy, S.N. Chintalapudi, S.B. Manohar, *J. Radioanal. Nucl. Chem.*, 237 (1998) 91.
9. T. Balaji, R.N. Acharya, A.G.C. Nair, A.V.R. Reddy, K.S. Rao, G.R.K. Naidu, S.B. Manohar, *Sci. Tot. Environ.*, 253 (2000) 75.
10. T. Balaji, R.N. Acharya, A.G.C. Nair, P.P. Burte, G.R.K. Naidu, A.V.R. Reddy, S.B. Manohar, *J. Radioanal. Nucl. Chem.*, 243 (2000) 783.
11. A.G.C. Nair, R. Acharya, K. Sudarshan, S. Gangotra, A.V.R. Reddy, S. B. Manohar, A. Goswami, *Anal. Chem.* 75 (2003) 4868.
12. R. Acharya, A.G.C. Nair, A.V.R. Reddy, A. Goswami, *J. Nucl. Mat.*, 326 (2004) 80.
13. R. Acharya, A.G.C. Nair, A.V.R. Reddy, A. Goswami, *Anal. Chim. Acta*, 522 (2004) 127.
14. R. Acharya, A.G.C. Nair, K. Sudarshan, A.V.R. Reddy, A. Goswami, *Appl. Radiat. Isot.*, 65 (2007) 164
15. R. Acharya, K.K. Swain, K. Sudarshan, R. Tripathi, P.K. Pujari, A.V.R. Reddy, *Nucl. Instr. and Meth. A*, 622 (2010) 460.
16. K. B. Dasari, R. Acharya, K. K. Swain, N. Lakshmana Das, A. V. R. Reddy, *J. Radioanal. Nucl. Chem.*, 286 (2010) 525.
17. A.G.C. Nair, R. Acharya, A.V.R. Reddy and A. Goswami, B.Adur, H.B. Mali, J. Rathod, R. Patil, K. Vora, *Current Science*, 87 (2004) 654.
18. S. Tiwari, A. G. C. Nair, R. Acharya, A.V.R. Reddy, A. Goswami, *J. Nucl. Radiochem. Sci.*, 8 (2007) 25.
19. R.N. Acharya, K. Sudarshan, A.G.C. Nair, Y.M.Scindia, A. Goswami, A.V.R. Reddy, S.B. Manohar, *J. Radioanal. Nucl. Chem.*, 250 (2001) 303.
20. A.G.C.Nair, R.Acharya, K.Sudarshan, R.Tripathi, A.V.R.Reddy, A.Goswami, *Nucl. Inst. Meth. A*, 564 (2006) 662
21. K. Sudarshan, R. Tripathi, A. G. C. Nair, R. Acharya, A. V. R. Reddy and A. Goswami, *Anal. Chim. Acta*, 535 (2005) 309.
22. K. Sudarshan, R. Tripathi, A. G. C. Nair, R. Acharya, A. V. R. Reddy and A. Goswami, *Anal. Chim. Acta*, 549 (2005) 205.
23. R. Acharya, *J. Radioanal. Nucl. Chem.*, 281 (2009) 291.
24. R. Acharya, K. K. Swain, Amit Kumar, Nicy Ajith, R. Verma, A.V.R. Reddy, *J. Radioanal. Nucl. Chem.*, 286 (2010) 507.
25. R. Acharya, K. K. Swain, A.V.R. Reddy, *Nucl. Instr. Meth. A* 622 (2010) 411.
26. R. Acharya, A.G.C. Nair, A.V.R. Reddy, *J. Radioanal. Nucl. Chem.*, 281 (2009) 279.
27. P.R.Bhagat, R. Acharya, A.G.C. Nair, A. K. Pandey, N.S. Rajurkar, A.V.R. Reddy, *Food Chem.*, 115 (2009) 706.
28. Preeti Bhagat, A.K. Pandey, R. Acharya, A.G.C. Nair, N.S. Rajurkar and A.V.R. Reddy, *Talanta*, 71 (2007) 1226.
29. Neetu Sharma, R. Prakash, A. Srivastava, U.S.Sadana, R. Acharya, N.Tejo Prakash, A.V. Ramana Reddy, *J. Radioanal. Nucl. Chem.*, 281 (2009) 59.
30. R. Acharya, R. Tripathi, K. Sudarshan, A.V.R. Reddy, et al., *Exploration and Research for Atomic Minerals*, 19 (2009) 188.
31. S. Chhillar, R. Acharya et al., *J. Radional. Nucl. Chem.*, (Accepted).



Order-disorder transitions and thermodynamic properties of rare-earth iron perovskites and garnets

S.C. Parida

Product Development Division

Dr. S.C. Parida is the recipient of the DAE Scientific & Technical Excellence Award for the year 2009

Abstract

Magnetic order-disorder transitions in rare-earth orthoferrites, $RFeO_3$ and rare-earth iron garnets (RIGs) $R_3Fe_5O_{12}$ (R = rare earth elements) were investigated by calorimetric method and different contributions to the total heat capacities of these oxides were computed by statistical thermodynamical methods. Thermodynamic properties of these oxides as a function of temperature were computed, using the experimental data. Various types of stability diagrams in the R-Fe-O systems were computed, in order to understand the thermodynamic stabilities of these compounds in different physico-chemical environments.

Introduction

Rare-earth iron perovskites ($RFeO_3$) and rare-earth iron garnets ($R_3Fe_5O_{12}$), where R represents a rare-earth element, are some of the important magnetic materials. $RFeO_3$ compounds belong to perovskite structure-types and are termed as orthoferrites to distinguish them from cubic spinel ferrites. The orthoferrites crystallize in an orthorhombically distorted perovskite structure, with four molecular unit per unit cell. The crystallographic distortion of the unit cell increases, with decrease in ionic radii of R^{3+} across the lanthanide series. The main distortion is related to the tilts of octahedra around the b and c orthorhombic axes. These tilts are made evident in the Fe-O-Fe bond angles, that are lower than the ideal value of 180° in the cubic perovskite. The Fe^{3+} ion is octahedrally coordinated by oxygen, giving an FeO_6 octahedra. The larger the R^{3+} , the nearer is the super-exchange bond angle to 180° (Fig. 1) and hence the order-disorder transition temperature is higher. Thus, $LaFeO_3$ has the highest Néel

temperature and $LuFeO_3$ the lowest. The magnetic ordering of the Fe^{3+} ions is essentially antiferromagnetic. Due to the low symmetry of the magnetic unit cell, which is equal to the crystallographic one, weak ferromagnetism is observed (canted moment). Starting from the paramagnetic state at high temperature, the magnetic moment of Fe^{3+} orders antiferromagnetically around 600-700 K on cooling. Canting of the magnetic moments results in weak ferromagnetism in the Fe^{3+} ordered state. On further cooling, many rare-earth orthoferrites undergo spin reorientation transitions, where the direction of the net magnetic moment rotates continuously or abruptly from one crystallographic axis to another, due to the antisymmetric and anisotropic-symmetric exchange interactions between Fe^{3+} and R^{3+} . In some orthoferrites with antiparallel configurations of Fe^{3+} and R^{3+} moments, vanishing net magnetization occurs at a compensation temperature. The magnetic moment of R^{3+} orders around or below liquid helium temperature in some systems. The Fe-Fe coupling is very small because of the perovskite



structure. Magnetic couplings of the type Fe-R and R-R are at least two orders of magnitude below the Fe-Fe coupling. The different types of magnetic interactions between Fe^{3+} and R^{3+} follow a hierarchy of Fe-Fe, Fe-R and R-R with decreasing order of strength as shown in Fig. 2.

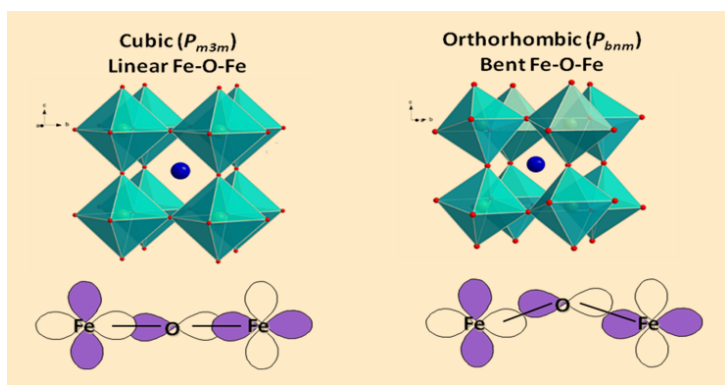


Fig. 1: Structural distortion showing the superexchange Fe-O-Fe angle in RFeO_3

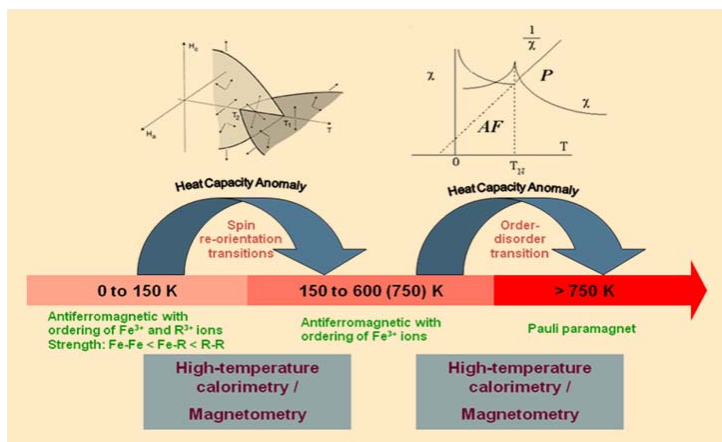


Fig. 2: Different types of transitions in RFeO_3 with increasing temperature

Magnetic garnets crystallize in the dodecahedral or 12-sided structure related to the mineral garnet. The structure of rare earth iron garnets is described by a body centered unit cell with space group $1a3d(230)$, containing eight formula units (160 atoms). In the Wyckoff notation, R^{3+} cations occupy special position c (twenty four dodecahedrally co-ordinated sites), whereas Fe^{3+} cations share special positions a (sixteen tetrahedrally co-ordinated sites) and d (twenty four octahedrally coordinated sites). The Fe^{3+} ions on the a sites are strongly coupled

antiferromagnetically to those of the d sites. The resultant magnetization of these two sublattices is in turn antiferromagnetically coupled to the spins of the R^{3+} ions on the c sites. The magnitude of the Fe-Fe interaction is stronger than the R-Fe interactions. The coupling between the a and d sites is responsible for the Curie temperature

at about 550 K, which is approximately same for all the RIG. Below 70 K, the Fe^{3+} ions on the a and d sites are nearly aligned and the effective molecular field (MF) acting on the Fe^{3+} ion is of the order of 5×10^6 G. In contrast, the MF acting on the R^{3+} ions on the c sites is of the order of 2×10^5 G, which produces energy level splitting of the order of 20-50 cm^{-1} . In $\text{R}_3\text{Fe}_5\text{O}_{12}$, the R^{3+} ions are subjected to a crystalline electric field. For S -state R^{3+} ions, the effect of the crystalline field is negligible in comparison to that of the exchange field. When the R^{3+} is not in an S -state, the crystalline field splitting is of the same order as the exchange splitting. Therefore, the magnetic moment of each level will be different from that of the free ion, and in general anisotropic. Under these conditions, the number of effectively inequivalent c sites is reduced from six to two, at sufficiently low temperatures, and hence one expects different splitting for each level. The levels of R^{3+} split by the exchange field will be appreciably populated above 4 K and will give a large contribution to the heat capacity.

We have investigated the phase transitions in these magnetic oxides using calorimetric method, measured their heat capacities, magnetic order-disorder (second order) transition temperatures. We have determined the standard molar free energy of formation of these oxides using solid state electrochemical method. We have derived Debye temperatures, magnetic entropies of these compounds by using the experimental data and statistical thermodynamical methods. Further, we have constructed thermodynamic data tables for these compounds and constructed different types of stability diagrams for the R-Fe-O systems.



Heat capacities of $RFeO_3$ and $R_3Fe_5O_{12}$

The heat capacity data obtained in our study is shown in Fig. 3 which shows heat capacity anomalies for all these compounds, in the temperature range of 600-750 K for $RFeO_3$ and 530-570 K for $R_3Fe_5O_{12}$ compounds, resembling the λ -type transition. Form the earlier studies on the orthoferrites and garnets, it has been observed that the phase transition is second order in nature and involves magnetic order-disorder transition. For the $RFeO_3$ compounds, the order-disorder transition is from antiferromagnetic (AF) to paramagnetic state, characterized by the Néel temperature (T_N) where as for

values of T_C for $R_3Fe_5O_{12}$ show a systematically decreasing trend, with decrease in ionic radii of R^{3+} ions as one goes from $Sm_3Fe_5O_{12}$ to $Lu_3Fe_5O_{12}$. However, this decrease is not significant as compared to that observed for $RFeO_3$, because the extent of structural distortion with decrease in ionic radii of R^{3+} ion in cubic $R_3Fe_5O_{12}$, is less as compared to that in orthorhombic $RFeO_3$.

The heat capacity data obtained in the present study, in the temperature range of 130 to 860 K are combined with the very low temperature heat capacity data available in the literature, using spline fitting procedure in order to get smooth values of $C_{p,m}^o$ for $RFeO_3$ and $R_3Fe_5O_{12}$, in the entire temperature range from 0 K to 860 K.

This heat capacity data is then used to calculate the different components of heat capacity contributions like lattice, electronic and magnetic contributions and Debye temperature, using statistical thermodynamical methods as shown in Fig. 5.

The entropy of transition due to magnetic order-disorder transition can be calculated, by integrating the plot of $(C_{magnetic}/T)$ against T in the temperature range from 0 K to the high temperature tail of the λ -peak. For the compound $LaFeO_3$, magnetic entropy ($S_{magnetic}$)

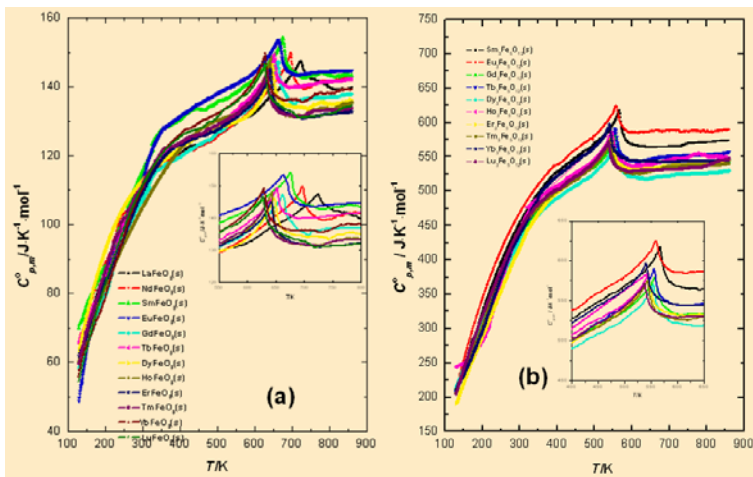


Fig. 3: Plot of heat capacity of (a) $RFeO_3$ and (b) $R_3Fe_5O_{12}$

the $R_3Fe_5O_{12}$, the transition involves magnetic order-disorder transition from ferrimagnetic to paramagnetic state, characterized by the Curie temperature (T_C). The values of T_N for $RFeO_3$ and T_C for $R_3Fe_5O_{12}$ observed from the heat capacity plot are shown in Fig. 4 and compared with published data.

It can be seen from Fig. 4 that the values of T_N for $RFeO_3$ show a systematic decreasing trend with decreasing the ionic radii of R^{3+} ions as one goes from $LaFeO_3$ to $LuFeO_3$. This trend is expected on the basis of increasing structural distortion. The

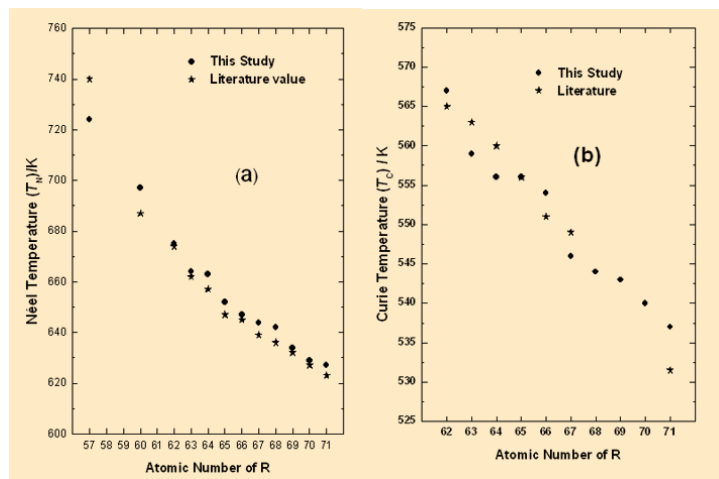


Fig. 4: Order-disorder transition temperatures of (a) $RFeO_3$ and (b) $R_3Fe_5O_{12}$

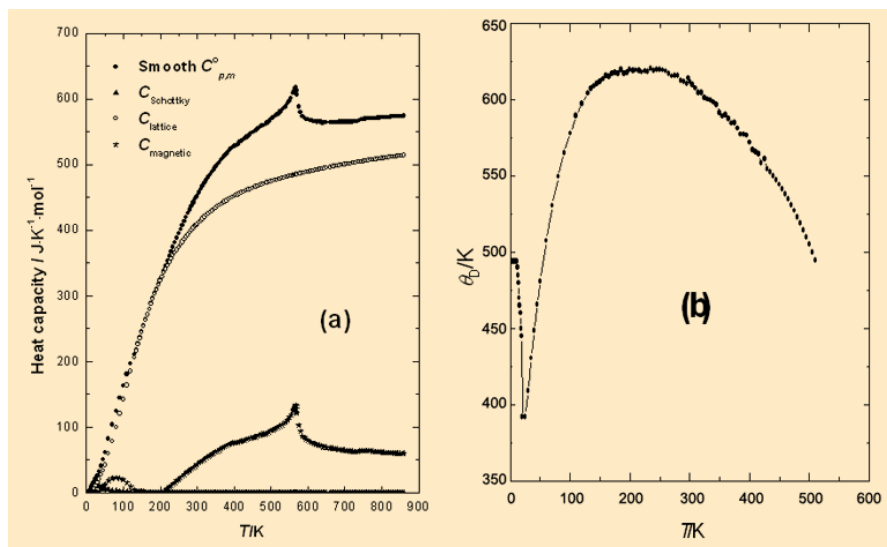


Fig. 5: (a) Plot of heat capacity against T and (b) Plot of (θ_D) against the absolute temperature (T) for $\text{Sm}_3\text{Fe}_5\text{O}_{12}(\text{s})$

Table 1: Values of $\theta_{D(0\text{K})}$, $\theta_{D(\text{effective})}$ and $S_{(\text{magnetic})}$ for RFeO_3 and $\text{R}_3\text{Fe}_5\text{O}_{12}$ compounds.

Perovskite	$\theta_{D(0\text{K})}/\text{K}$	$\theta_{D(\text{effective})}/\text{K}$	$S_{(\text{magnetic})}/\text{J}\cdot\text{K}^{-1}\cdot\text{mol}^{-1}$	Garnet	$\theta_{D(0\text{K})}/\text{K}$	$\theta_{D(\text{effective})}/\text{K}$	$S_{(\text{magnetic})}/\text{J}\cdot\text{K}^{-1}\cdot\text{mol}^{-1}$
LaFeO_3	407	582	17.5	-			
NdFeO_3	402	574	29.9	-			
SmFeO_3	-	-	-	$\text{Sm}_3\text{Fe}_5\text{O}_{12}$	494	662	107.6
EuFeO_3	-	-	-	$\text{Eu}_3\text{Fe}_5\text{O}_{12}$	-	-	-
GdFeO_3	358	555	22.8	$\text{Gd}_3\text{Fe}_5\text{O}_{12}$	490	655	113.0
TbFeO_3	356	552	18.3	$\text{Tb}_3\text{Fe}_5\text{O}_{12}$	455	656	81.8
DyFeO_3	352	551	21.1	$\text{Dy}_3\text{Fe}_5\text{O}_{12}$	422	657	62.6
HoFeO_3	342	550	25.9	$\text{Ho}_3\text{Fe}_5\text{O}_{12}$	419	646	107.8
ErFeO_3	339	548	23.8	$\text{Er}_3\text{Fe}_5\text{O}_{12}$	418	648	82.7
TmFeO_3	337	544	19.2	$\text{Tm}_3\text{Fe}_5\text{O}_{12}$	414	645	108.0
YbFeO_3	335	542	18.7	$\text{Yb}_3\text{Fe}_5\text{O}_{12}$	414	646	96.2
LuFeO_3	333	541	15.1	$\text{Lu}_3\text{Fe}_5\text{O}_{12}$	392	650	78.3

obtained by integrating the area of the plot, equals to $17.5\text{ J}\cdot\text{K}^{-1}\cdot\text{mol}^{-1}$. This value is in good agreement with the value obtained from the formula: $S_{\text{magnetic}} = R \ln(2S + 1)$. For LaFeO_3 this value becomes $14.897\text{ J}\cdot\text{K}^{-1}\cdot\text{mol}^{-1}$ because for Fe^{3+} (d^5 electronic configuration) in high spin state, $S = 5/2$. For other compounds, the same method is applied to derive the entropy associated with magnetic transition. The values are listed in Table 1.

Construction of thermodynamic tables for RFeO_3 and $\text{R}_3\text{Fe}_5\text{O}_{12}$

Various thermodynamic measurements on these compounds, conducted in the author's laboratory, are reported in literature. Mostly, the authors have used solid-state electrochemical methods to find out the standard molar Gibbs energy of formation, $\Delta_f G_m^\circ(T)$, of these compounds as a function of temperature. This data



was used in conjunction with the heat capacity data from calorimetry to derive various thermodynamic parameters for these compounds using the standard thermodynamic relations. After calculation of all the thermodynamic functions, the values have been tabulated at selected temperatures. The thermodynamic functions which are usually tabulated are: $C_{p,m}^{\circ}$, S_m° , $\{H_m^{\circ}(T) - H_m^{\circ}(298.15 \text{ K})\}$, H_m° , $\Phi_m^{\circ}(T)$, $\Delta_f H_m^{\circ}(T)$ and $\Delta_f G_m^{\circ}(T)$. The values generated in this study for $R\text{FeO}_3(\text{s})$ ($R = \text{La, Nd, Sm, Eu, Gd, Tb, Dy, Ho}$ and Eu) and $R_3\text{Fe}_5\text{O}_{12}(\text{s})$ ($R = \text{Sm, Eu, Gd, Tb, Dy, Ho}$ and Eu) are published in literature [1].

Conclusions

Heat capacity anomalies were observed for $R\text{FeO}_3(\text{s})$ (orthoferrites) and $R_3\text{Fe}_5\text{O}_{12}(\text{s})$ (garnets), which were attributed due to magnetic order-disorder transitions. The Néel temperatures (T_N) observed for the orthoferrites show a regular decreasing trend across the lanthanide series from 725 K for $R = \text{La}$ to 623 K for $R = \text{Lu}$. The Curie temperatures (T_C) observed for the garnets, also show the

same decreasing trend from 567 K for $R = \text{Sm}$ to 532 K for $R = \text{Lu}$. The values of T_N and T_C measured in this study, are in good agreement with those reported in literature by other techniques like Mössbauer and Magnetic measurements. Thermodynamic tables showing the tabulated values of $C_{p,m}^{\circ}$, S_m° , H , G , $(H_T - H_0)$, $(H_T - H_{298.15 \text{ K}})$, $-(G_T^{\circ} - H_{298.15 \text{ K}}^{\circ})/T$, $\Delta_f H_m^{\circ}$ and $\Delta_f G_m^{\circ}$ at different temperatures, were computed for the compounds $R\text{FeO}_3$ and $R_3\text{Fe}_5\text{O}_{12}$. The thermodynamic data generated in this study will be helpful to assess the stability of these compounds under different physico-chemical conditions in application environments.

Acknowledgement

The contribution of all co-authors in this research work is gratefully acknowledged.

References

1. S.C. Parida, S.K. Rakshit and Z. Singh, *J. Solid State Chem.*, 181 (2008) 101.



Role and relevance of Radiopharmaceutical Chemistry Research in the Radiopharmaceuticals Programme of BARC

Sharmila Banerjee

Radiopharmaceuticals Division

Dr. Sharmila Banerjee is the recipient of the DAE Scientific & Technical Excellence Award for the year 2009

Abstract

Development of new radiopharmaceuticals requires multidisciplinary support. This is extended most significantly with respect to building a synthetic organic chemistry expertise, for envisaging novel molecules and synthetically manipulating them into the desired form, prior to radiolabeling. Therefore, synthetic organic chemistry plays a major role in radiopharmaceuticals research, leading to development of new molecules. Efforts toward cost-effective and indigenous development of new molecules, intended for use after radiolabeling with either diagnostic or therapeutic radioisotopes, with an aim to catering to the requirements of various Nuclear Medicine Centres in India, is therefore of prime importance. A few of the radiolabeled agents, indigenously developed in the Radiopharmaceuticals Division, BARC, following extensive research, have shown considerable promise in clinical trials and are awaiting approval of the appropriate regulatory authorities, for use as radiopharmaceuticals by Nuclear Medicine clinicians in India. This article aims at highlighting the recent developments in research in radiopharmaceutical chemistry in the Radiopharmaceuticals Division, which have yielded promising outcomes warranting further development into products.

Keywords: Radiopharmaceutical chemistry, target-specific agents, bifunctional chelating agents, radiolabeling, ^{99m}Tc -radioprecursors.

Introduction

The development of new and improved approaches for targeted delivery of radiolabeled agents for diagnosis and therapy, is currently one of the most intensively pursued areas of radiopharmaceutical research. An aptitude and capability to visualize and design lead molecules or the 'pharmaceutical' component of the radiopharmaceutical agent, constitutes one of the key factors in the development of new molecules for use as radiopharmaceutical precursors. The identification of the ideal targeted radiolabeled agent for each potential clinical application is a challenging task, because of the multitude of variables

that must be considered, some relating to the radioisotope and others to the biological carrier. Radiopharmaceuticals Division has an access to a host of reactor-produced isotopes, with varying radiochemical properties, to meet the requirement of a wide range of radiopharmaceutical formulations, with applications in varied physiological disorders. This, in turn, gives rise to the possibility of envisaging new molecules with the desired chelating moiety, which can form stable complexes with the radioisotope under consideration. While designing the chelating moiety, it is pertinent to keep in mind, that not only does each metallic radioisotope has its affinity for chelating with a particular array of donor atoms with which



they form stable complexes, but the resultant radiolabeled agent should also retain its desired target-specificity, intended for the particular application. All these factors which need to be considered while arriving at the stable inorganic complex of a target-specific vector, intended for a specific application in biological systems, constitutes the challenges involved in radiopharmaceutical research. This article attempts to present an overview of the efforts of the Radiopharmaceutical Chemistry Group in the Radiopharmaceuticals Division, towards envisaging lead molecules as precursors for radiolabeling with potential radioisotopes, resulting in development of potential radiopharmaceutical preparations.

Diagnostic agents

The interest in the field of research on diagnostic radiopharmaceuticals based on ^{99m}Tc has recently gained momentum, due to the identification of several novel ^{99m}Tc -synthons as precursors viz. $[\text{}^{99m}\text{Tc}(\text{CO})_3(\text{H}_2\text{O})_3]^+$, $[\text{}^{99m}\text{TcN}]^{2+}$, $[\text{}^{99m}\text{Tc}(\text{PNP})]^{2+}$ and ^{99m}Tc -HYNIC (hydrazinonicotinamide) for carrying out radiolabeling with target-specific vectors. These precursors have harnessed the versatile chemistry of the various oxidation states of Tc. In the designing of the site-specific agents, the primary aim is to prepare high specific activity complexes of ^{99m}Tc and the aforementioned radiosynthons yield high specific activity complexes, which is an essential requirement for targeting the limited receptor expression on specific tumors. The ligating molecules chosen for radiolabeling with these synthons act as vectors for a specific target, which could be an organ, a receptor overexpression on malignant tumors or diseased condition, specific antigens as well as physiological conditions such as hypoxia. Keeping the various targets in mind, our efforts are directed to identify and synthesize new molecular vectors, which can be radiolabeled directly or in most cases carry out synthetic modification, which render them suitable for complexation with the radiometals.

Tumor-avid molecules

The challenging syntheses of a variety of unsymmetrically substituted water soluble porphyrins in pure form, have been accomplished. In carrying out radiolabeling of the porphyrin derivatives, necessary synthetic modification of the peripheral substituents has been carried out, for incorporation of the chelating groups. These porphyrin derivatives have been radiolabeled with ^{99m}Tc using the novel 'Click' route. With an aim to exploring the potential of radiolabeled porphyrins in targeting tumor and their suitability for PET imaging, an unsymmetrical porphyrin derivative, viz. 5- $[\rho$ -ethyloxy(mesyl)phenyl]-10,15,20-tris(ρ -methoxyphenyl) porphyrin has been synthesized, involving a four-step synthetic procedure. Initial studies of radiolabeling the porphyrin derivative with ^{18}F , has indicated interesting potential of this radiolabeled molecule. Other small molecules such as chlorambucil, colchicine have been synthetically manipulated for complexation with ^{99m}Tc .

Hypoxia

Nitroimidazoles show an affinity to target tumor hypoxia owing to their inherent capability of getting reduced under hypoxic conditions and binding to intercellular components. In our efforts to identify an ideal hypoxia marker, a series of differently substituted 2-,4-,5-nitroimidazoles conjugated with different chelators such as iminodiacetic acids, diethylene triamine and aminoethylglycine have been synthesized and conjugated with the $[\text{}^{99m}\text{Tc}(\text{CO})_3(\text{H}_2\text{O})_3]^+$ core yielding complexes of different charges and lipophilicities, the two prime factors which need to be carefully optimized for obtaining the ideal residence time of the radiolabeled species in hypoxic cells. The ^{18}F -analogue of Fluoromisonidazole is currently being used as a gold standard, in the clinical evaluation of hypoxic tumors. Towards envisaging a ^{99m}Tc analogue for similar purpose, an iminodiacetic acid derivative of



misonidazole was synthesized and radiolabeling procedure with $[^{99m}\text{Tc}(\text{CO})_3(\text{H}_2\text{O})_3]^+$ core optimized. Preliminary bioevaluation studies indicated, that the molecule has a significantly higher potential, to target hypoxic tumors and further studies are underway.

Functional imaging agents

While the iminodiacetic acids are used as chelating ligands for labeling with the $[^{99m}\text{Tc}(\text{CO})_3(\text{H}_2\text{O})_3]^+$, xanthate and dithiocarbamate derivatives of differently substituted long chain fatty acids and tert-butyl dithiocarbamate, methoxyisobutyl dithiocarbamate are used for radiolabeling with the $[^{99m}\text{TcN}]^{2+}$ core. The resultant complexes prepared under rigorously optimized conditions, are intended for use as potential agents for myocardial and brain perfusion studies. The use of yet another novel ^{99m}Tc -core viz. ^{99m}Tc -HYNIC has been demonstrated in the radiolabeling of isoniazid, an antitubercular drug. In this regard, a comparative study of the relative merits of radiolabeling using the novel cores such as $[^{99m}\text{Tc}(\text{CO})_3(\text{H}_2\text{O})_3]^+$ and ^{99m}Tc -HYNIC over that of the conventionally used $[^{99m}\text{Tc}=\text{O}]^{3+}$ core has been demonstrated, using differently derivatized isoniazid molecule.

Receptor-specific agents

The synthetic strategy involves multi-step syntheses to derivatize the parent molecule to the required derivative which becomes amenable for chemical conjugation with the bifunctional chelating agent (BFCA) following which the radiolabeled complex is prepared via the use of a ^{99m}Tc synthon. Towards targeting the over-expression of specific receptors in diseased conditions, syntheses of suitable derivatives of receptor-specific molecules viz. N-benzyl piperidine, N-methylpiperidine (sigma receptor), 5-hydroxytryptamine (serotonin receptor), steroidal derivatives (estradiol, testosterone, progesterone) have been carried out for, labeling with ^{99m}Tc . Different radioprecursors of ^{99m}Tc have been used for radiolabeling of these ligands.

Peptides as vectors

RGDs (arginine-glycine-aspartic acid) are extracellular matrix proteins with the exposed tripeptide sequence and are specific towards extracellular integrin $\alpha_v\beta_3$ receptors. Therefore, for the early diagnosis as well as development of therapeutic drugs, appropriately radiolabeled RGD molecules serve as vectors, for targeting the receptors over-expressed on rapidly growing and metastatic tumors. With the prior knowledge that RGD dimer exhibits better receptor binding potential, in the present strategy, a novel concept of utilizing a suitably functionalized RGD monomer, to form a tetracoordinated complex with $[\text{TcN}]^{2+}$ is envisaged, as it results in a species which is the mimic of the RGD dimer. The lysine amino group of cyclic RGD monomer was derivatized to dithiocarbamate, for radiolabeling with $[^{99m}\text{TcN}]^{2+}$ core. The radiolabeling studies have been optimized and formation of $^{99m}\text{TcN}-(\text{RGD})_2$ as a predominantly single species has been confirmed by HPLC. Preliminary biological studies carried out in mice bearing melanoma tumor, reveals interesting results.

Click-route for preparation of ^{99m}Tc -labeled molecules

'Click chemistry' is the reaction between an azide and an alkyne, resulting in the formation of a triazole ring. While this reaction earlier was reported to take place at high temperatures, recent finding reveals, that in the presence of Cu(I) catalyst, this reaction could be carried out at room temperature/lower temperature and this has significantly increased its practical utility, in synthetic organic chemistry. For application in radiopharmaceutical chemistry, if the alkyne is propargyl glycine, the resulting triazole derivative can function as a good tridentate ligand (the amine, carboxylic acid and one of the nitrogen of the triazole ring acting as the donors). This reaction leads to the formation of a 1,2,3-triazole which acts as a tridentate chelate for the $[^{99m}\text{Tc}(\text{CO})_3(\text{H}_2\text{O})_3]^+$ precursor. Progesterone receptors are expressed in breast cancers, making them favorable targets for development of radiotracers for imaging as well as for therapy. In this direction, 11-



hydroxyprogesterone, was synthetically modified to 11-azidoprogesterone for radiolabeling with ^{99m}Tc -tricarbonyl core, via the click chemistry route. This route provides the advantage of a single-step one-pot preparation of a ^{99m}Tc -labeled biomolecule, in high yield, under mild reaction conditions in aqueous media. The Cu(I)-catalyzed click reaction between an alkyne and an azide is essentially a [3+2] cycloaddition reaction. In similar lines, for targeting the androgen receptor over-expression $^{99m}\text{Tc}(\text{CO})_3$ -17 α -triazolylandrost-4-ene-3-one has been obtained via the click route from 17-azidotestosterone. The complexes were characterized by reversed phase HPLC and *in vitro* cell binding studies of the complexes, using appropriate cancer cell lines known to over-express specific receptors, revealed interesting results.

Developmental work

The challenging synthetic protocols and purification techniques to arrive at the right stereoisomer for obtaining several key ligands, which are organic precursors of well-established radiopharmaceutical preparations, have been rigorously standardized and revisited. These ligands include ethylenedicycysteinate (ECD) and hexamethylenepropylene aminoxime (HMPAO) which on complexation with $[\text{Tc}(\text{V})=\text{O}]^{3+}$, yield radiopharmaceuticals which are commercially available for brain perfusion studies. Methoxyisobutyronitrile (MIBI), is yet another ligand which complexes with ^{99m}Tc to give $[\text{MIBI}]_6^+$, an agent which is used for myocardial perfusion studies. The lack of the local capability of making this ligand, has been affecting the continuation of the supply of this product by BRIT. The synthetic route to some of the aforementioned ligands requires, handling the intermediates under stringent anhydrous and inert conditions, as well as extensive standardization and fabrication of high-pressure reaction vessels. The synthetic expertise has enabled a cost-effective indigenous sourcing of the important raw material, required in radiopharmaceutical preparations as import substitution.

Therapeutic radiopharmaceuticals

The work carried out towards the development of new radiopharmaceuticals for targeted radiotherapy, encompasses the broad areas involving syntheses of novel target-specific organic molecules, for use as chelating agents for radiolabeling with different indigenously developed therapeutic radionuclides, such as ^{177}Lu , ^{90}Y , ^{186}Re , ^{188}Re , ^{166}Ho , ^{153}Sm , ^{175}Yb , ^{109}Pd and ^{170}Tm . The efforts toward development of therapeutic agents, which have yielded promising results and subsequent development into products, are outlined in the sequel.

Agents for targeted radiotherapy

A host of biologically avid molecules, which can constitute vectors for targeted delivery have been synthesized. Our initial efforts to use ^{186}Re and ^{188}Re as the therapeutic isotope, required syntheses of suitable ligands possessing a tetradentate donor array consisting of N_2S_2 substituents. A number of molecules have been functionalized, to conjugate with BFCA possessing the suitable donor atoms, for complexation with ^{186}Re and ^{188}Re . One such agent $^{186/188}\text{Re}$ -EC (ethylene dicycysteinate) which has been synthesized and extensively studied for application in Intra Vascular Radionuclide Therapy, has indicated promising potential. In our studies, water soluble porphyrins have emerged as promising candidates with respect to their tumor affinity and localization therein. In this connection, the ^{188}Re labeled 5,10,15,20-tetrakis[3,4-bis(carboxymethylenoxy)phenyl]porphyrin has indicated promising potential in tumor regression studies, carried out in Swiss mice models, bearing thymic lymphoma and fibrosarcoma. It is pertinent to note that, since this porphyrin possesses a bis-carboxymethylenoxy substituent in each of the aromatic residues in the periphery, which are suitable for complexation with the radiometal $^{186/188}\text{Re}$ in +5 oxidation state, introduction of a BFCA was not required. The therapeutic radionuclides which have been used by us are mostly radiolanthanides for which the preferred BFCA



is a macrocyclic DOTA (1,4,7,10-tetraazacyclododecane-1,4,7,10-tetraacetic acid) conjugate. In this respect, syntheses of peptide conjugates such as somatostatin analogues viz. lanreotide- and octreotide-DOTA conjugates for radiolabeling with ^{90}Y and ^{177}Lu have yielded interesting results. The symmetric and unsymmetrically substituted water soluble porphyrins, which have been mentioned earlier, have been conjugated with DOTA as the chelator in the periphery and used for radiolabeling with ^{90}Y , ^{177}Lu . Similarly, 2-,4-,5-nitroimidazole, metronidazole and sanazole have been derivatized, to a form suitable for conjugation with DOTA derivatives and the resultant species have thus become suitable, for labeling with the radiolanthanides.

^{177}Lu -based products

The indigenous production of high specific activity ^{177}Lu , using in-house facilities, which have been rigorously standardized, has resulted in the commercial deployment of this promising therapeutic isotope, as a regular product from the Radiopharmaceuticals Division. The availability of this promising isotope has provided the necessary impetus to research, aimed at exploring the possibility of designing agents for a variety of applications as radiopharmaceutical preparations. In this direction, porphyrins (tumor-avid substrates), nitroimidazoles (hypoxia markers), steroid derivatives (specific for receptors over-expressed in certain cancers) and peptides (somatostatin analogues over-expressed in neuroendocrine tumors) have been conjugated with polyazamacrocyclic BFCAs such as DOTA derivatives, for complexing with ^{177}Lu . A novel ^{177}Lu -labeled porphyrin derivative, 5,10,15,20-tetrakis [4 carboxymethyleneoxyphenyl] porphyrin coupled with *p*-amino-benzyl-DOTA has shown considerable promise in tumor regression studies, both in fibrosarcoma and thymic lymphoma, with respect to increasing the average tumor doubling time and decreasing the average specific growth rate.

Radiolabeled-phosphonates as agents for bone pain palliation

One of the most extensively used class of ligands which has been synthesized and investigated by our Group, is the series of acyclic and cyclic tetramethylene phosphonic acids. The promising candidates among this class of compounds are EDTMP (ethylenediaminetetramethylene phosphonic acid) and DOTMP (1,4,7,10-tetraazacyclododecane-1,4,7,10-tetramethylene phosphonic acid). ^{177}Lu with its suitable nuclear decay characteristics [$T_{1/2} = 6.73$ d, $E_{\beta(\text{max})} = 497$ keV, $E_{\gamma} = 113$ keV (6.4%) and 208 keV (11%)] and large-scale production feasibility with adequate specific activity using moderate flux research reactors, was envisaged to be an excellent radionuclide in the +3 state, for forming stable complexes with the multidentate phosphonic acid donor arrays present in ligands such as EDTMP and DOTMP. With this feasibility in mind, the possibility of preparation and subsequent evaluation of ^{177}Lu -EDTMP and ^{177}Lu -DOTMP as potential bone pain palliatives became a relevant subject of research. Multidentate polyaminophosphonic acids have already been proven as carrier molecules of choice, for radiolanthanides and similar +3 metal ions, in designing agents for palliative radiotherapy of bone pain, due to skeletal metastases. ^{177}Lu complexes of EDTMP and DOTMP are being considered as potential products for use in human patients. After the successful completion of pre-clinical dosimetry studies, clinical evaluation of ^{177}Lu -EDTMP was initiated in human patients, suffering from prostate carcinoma with bone metastases. No adverse effect due to the therapy has been detected in any of the patients and all of them have experienced excellent pain-relief. The formulation of ^{177}Lu -EDTMP which is awaiting appropriate regulatory clearance, is thus a totally indigenous product, developed by the Radiopharmaceuticals Division.



Conclusion

Synthetic organic chemistry plays a significant role in radiopharmaceutical research, carried out in the Radiopharmaceuticals Division. The development of ^{177}Lu -EDTMP as a bone pain palliative for use in human patients, is one of the major outcomes of the above input. The expertise of the group has enabled standardization of the challenging synthetic protocols, for cost-effective sourcing of potential ligands, used as radiopharmaceutical precursors. There are a number of other agents which have considerable potential and can be developed into promising products, following further studies. However, there are considerable limitations posed due to regulations on clinical trials, using new radiopharmaceutical formulations. Despite this, we expect that our efforts will lead to deployment of a few other radiopharmaceuticals, for the benefit of cancer patients and therefore our effort towards turning these expectations into reality, will be continued.

Acknowledgements

The work described in this article is a collective effort of a group of scientists of the Radiopharmaceuticals Division. The author is one of the major contributors towards

building the synthetic capabilities and expertise of the Radiopharmaceutical Chemistry Section of the Division. The author sincerely acknowledges the guidance and encouragement given by Dr. M.R.A. Pillai, Head, Radiopharmaceuticals Division toward the success of this program right from its conception. The support extended by Dr. H.D. Sarma, Radiation Biology and Health Sciences Division, by carrying out animal experiments essential to establishing the potential of the radiosynthetic products, is being gratefully acknowledged. The support provided by the erstwhile Head of Division, Dr. Meera Venkatesh and Dr. V. Venugopal, Director, Radiochemistry and Isotope Group, is also being gratefully acknowledged.

References

1. Evolution of Tc-99m in diagnostic radiopharmaceuticals. Sharmila Banerjee, M.R.A. Pillai, N. Ramamoorthy. *Semin. Nucl. Med.* 31, 2001, 260-277.
2. Emergence and present status of Lu-177 in targeted radiotherapy: The Indian scenario. Sharmila Banerjee, Tapas Das, Sudipta Chakraborty, Meera Venkatesh *Radiochim. Acta*, 2011 (In Press).



Structural Integrity Assessment of Nuclear Pressure Vessel and Piping Components: Some New Findings

J.Chattopadhyay

Reactor Safety Division

Dr. J. Chattopadhyay is the recipient of the DAE Scientific & Technical Excellence Award for the year 2009

Abstract

A comprehensive *Component Integrity Test Program* (CITP) was initiated at RSD, BARC, to address various unresolved issues related to integrity assessment of pressure vessel and piping components. In this program, large number of full scale tests on straight pipes, elbows and cruciform specimens of various sizes with various crack configurations, subjected to different loading conditions, were carried out. The test data was numerically analyzed by elastic-plastic finite element analyses as well. In parallel, a comprehensive analytical program was taken up, in which, several new equations have been proposed for more optimized and accurate integrity assessment of piping components. The test database generated as part of CITP has been utilized, for experimental validation of the newly proposed equations.

Keywords: Pipe, pipe bend, fracture test, integrity assessment, finite element analysis

Introduction

Leak-Before-Break analyses of the Primary Heat Transport (PHT) system piping and safety assessment of Reactor Pressure Vessel (RPV) during a Pressurized Thermal Shock (PTS) event, needs detailed integrity assessment of the RPV and piping components, which needs several numerical tools and analytical equations. While significant amount of research has been done worldwide to develop these equations for several decades, there are many issues that are still not resolved or partially resolved. To resolve some of these issues, a comprehensive CITP was initiated in RSD, BARC several years ago. The present paper very briefly enumerates some of the new findings of these investigations.

Experimental Work

In the experimental investigations, fracture mechanics tests are carried out on cracked pipes and elbows, under quasi-

static monotonic loading. Large number of pipes of various sizes (200-400 mm diameter) with circumferential cracks of various angles (30°-150°), configurations (throughwall/surface), materials (base/weld) subjected to various loading conditions e.g. 4 point bending load and combined bending moment and internal pressure, have been tested. Similarly, large number of elbows of various sizes (200-400 mm diameter) with throughwall cracks of various angles (60°-120°), locations (extrados/intrados/crown), configurations (circumferential/ axial) under in-plane bending modes (opening/closing) have also been tested (Fig. 1). Also fracture tests have been carried out on six cruciform specimens (Fig. 2) at room temperature and -70°C, to study the effect of biaxial loading to simulate fracture encountered by a nuclear RPV under PTS event. Elastic-plastic finite element analyses of these tested components have also been carried out (Fig. 3).



Fig.1: Photograph of pipe and elbow fracture test set-up

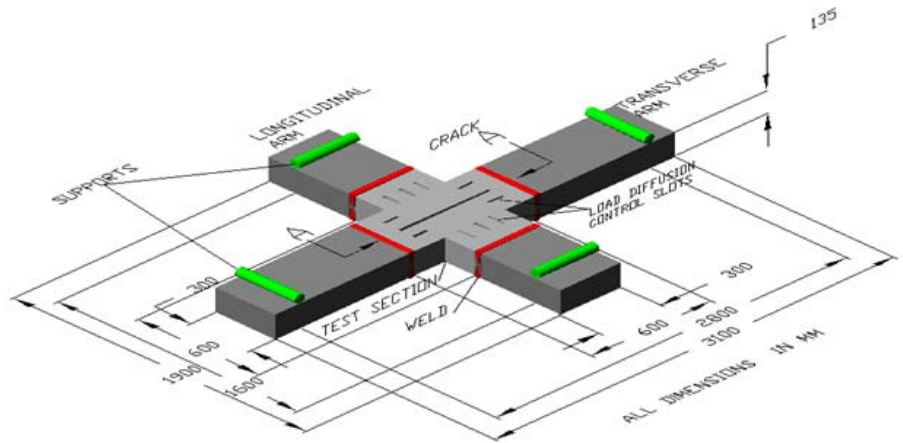


Fig.2: Photograph of Test Set-up and schematic of cruciform test specimen

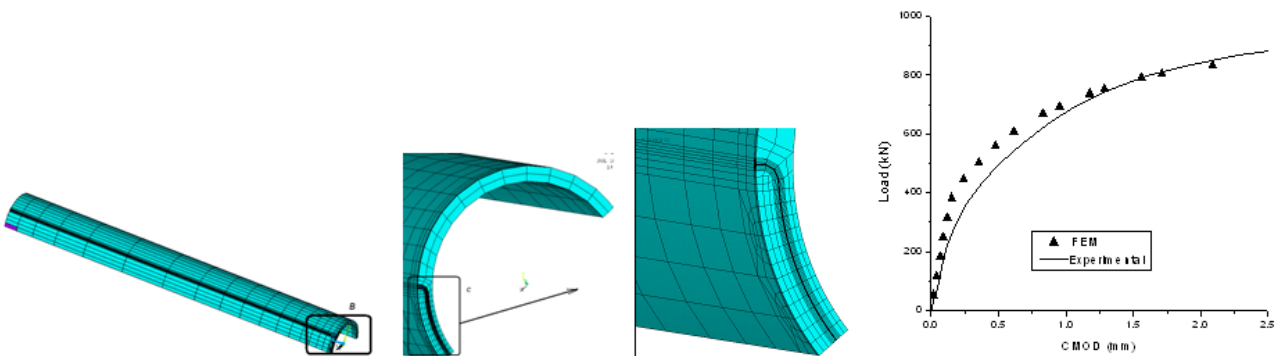


Fig.3: Finite element mesh and comparison of test results with numerical predictions for a part-throughwall cracked pipe



Analytical Work

Various analytical work has been undertaken in RSD, BARC, to propose improvements in the existing equations, for optimized and more accurate integrity assessment of piping components. The test data developed above has been extensively used for experimental validation of the proposed improvements. Major analytical work is as follows:

Generalized equation of h_{pl} and g to evaluate J-R curve

The evaluation of plastic J-integral from test data, needs ' η_{pl} ' and ' γ ' functions that are geometry and loading-dependent. Earlier ' η_{pl} ' and ' γ ' functions had been derived from dimensional analyse that were specific to the geometry and loading conditions. No general formula was available. The limit load-based general expressions of ' η_{pl} ' and ' γ ' functions are derived as follows:

$$\eta_{pl} = -\frac{\partial F_L}{\partial A} \cdot \frac{1}{F_L} \quad \text{and} \quad \gamma = \frac{\partial^2 F_L / \partial a^2}{\partial F_L / \partial a} \quad (1)$$

where, F_L is the limit load expression of the cracked component as a function of crack size (a) and A is the crack area. Utilizing these general expressions, new ' η_{pl} ' and ' γ ' functions for various pipe/elbow geometry under

various loading conditions, (for which no solutions are available in the open literature) have been derived.

Study of transferability of fracture properties from specimen to component

It is now well-known, that J-R curve shows geometry dependence due to influence of stress triaxiality. If the triaxial conditions are found to be similar, then it is believed that the J-R curves are transferable. For several piping components with various crack configurations and small laboratory TPB specimens machined from these components, constraint parameters have been calculated and J-R curves compared [5]. Figs. 4 & 5 show that constraint conditions of various piping components are identical and so are the J-R curves.

Development of New Limit Load Equations for Pipe Bends

Pipe bends or elbows are commonly used components in a piping system. It is important to know its limit moment, for the safe operation of the plant. However, the limit moment equations for pipe bends are very limited in open literature. As a part of the comprehensive program initiated by RSD, BARC, new closed-form equations have been

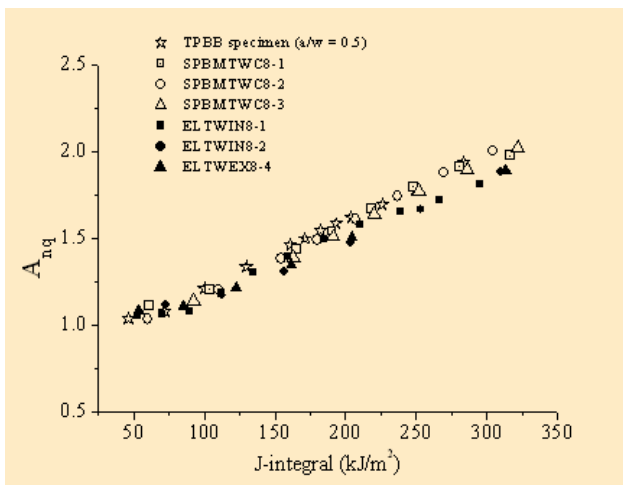


Fig. 4: Variation of constraint parameter (A_{nq}) with J-integral for various pipes and elbows

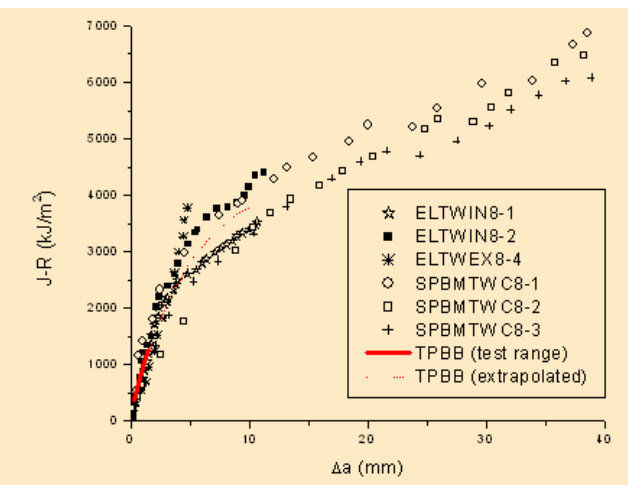


Fig. 5: Comparison of J-R curves from TPB specimen and through-wall cracked pipes and elbows



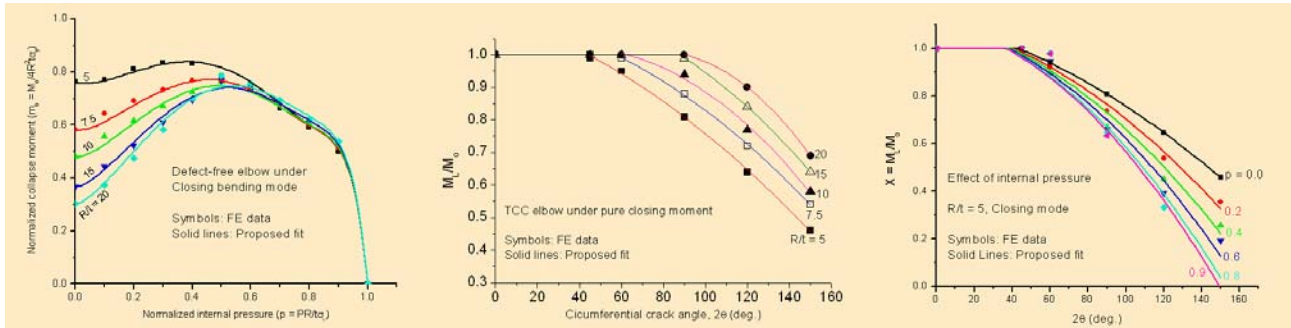


Fig. 6: Variation of normalized limit moment of throughwall circumferentially cracked elbow

proposed, to evaluate plastic collapse moments of pipe bends. Total 607 cases have been analyzed [6].

Three crack configurations are considered: (i) Defect free elbow, (ii) Throughwall Circumferentially Cracked (TCC) elbow and (iii) Throughwall axially cracked elbow.

For each crack configuration, two in-plane bending modes: (i) Closing and (ii) Opening mode.

For each bending mode, two loadings: (i) Pure in-plane bending moment and (ii) Combined loading of internal pressure and in-plane bending moment.

For each of the above geometry and load configuration, several radii-to-thickness ratio (R/t) and crack sizes (for cracked elbows) have been considered and new limit moment equations are proposed for these cases. Fig. 6 shows typical results for defect-free and TCC elbows.

Development of elastic-plastic J and COD estimation scheme for throughwall circumferentially cracked elbow under in-plane bending moment

LBB qualification of nuclear power plants requires detailed fracture analysis of piping components with postulated throughwall cracks. For this purpose, the estimation of elastic-plastic J-integral and COD is very essential. In the present investigation, simple J and COD estimation schemes for elbow with throughwall circumferential crack

at extrados/intrados, subjected to in-plane closing/opening bending moment, have been proposed. The proposed J-integral and COD equations are as follows [7-9]:

$$J = J_e + J_p; \delta = \delta_e + \delta_p; J_e = K^2 / E; \delta_e = 4MV^2 / (\pi D_o^2 E)$$

$$J_p = \alpha^{n+1} \sigma_y \varepsilon_y \pi R \left(1 - \frac{\theta}{\pi}\right)^2 h_1 \left(\frac{\theta}{\pi}, n, \frac{R}{t}\right) \left(\frac{M}{M_L}\right)^{n+1} \quad \text{for } \frac{M}{M_L} \leq 1.0 \quad (2)$$

$\alpha^{1/(n+1)}$ in the above eqn. is replaced with α for $M/M_L \geq 1.2$ and it is linearly interpolated for $1.0 < M/M_L < 1.2$

$$\delta_p = \alpha^n \varepsilon_y \pi R h_2 \left(\frac{\theta}{\pi}, n, \frac{R}{t}\right) \left(\frac{M}{M_L}\right)^n \quad \text{for } \frac{M}{M_L} \leq 1.0 \quad (3)$$

$\alpha^{1/n}$ in the above eqn. is replaced with α for $M/M_L \geq 1.2$ and it is linearly interpolated for $1.0 < M/M_L < 1.2$, where, the subscripts 'e' and 'p' indicate the elastic and fully plastic values respectively, M_L is the limit moment.

Conclusions

Several new equations have been proposed for improved and more accurate integrity assessment of piping components. These equations have also been experimentally validated using the test data generated as part of the comprehensive Component Integrity Test Program by RSD, BARC.

Acknowledgement

The author is grateful to Mr. H.S.Kushwaha, ex-Director, HS&EG and RRF, Mr. K.K.Vaze, AD, RD&DG and Head,



RSD, Dr.B.K. Dutta, Head, CMS, RSD for their great inspiration and motivation to carry out this work. The author also acknowledges the contributions of his junior colleagues, Mr. M.K. Sahu and Mr.A. Pawar, RSD for some work mentioned in this paper. The author also acknowledges the contribution of FTL, SERC, Chennai in the conduction of the fracture experiments.

References

1. Chattopadhyay,J., Dutta,B.K. and Kushwaha,H.S., "Experimental and analytical study of three point bend specimens and throughwall circumferentially cracked straight pipe", *International Journal of Pressure Vessels and Piping*, Vol.77, 2000, pp 455 – 471
2. Chattopadhyay,J., Pavankumar,T.V., Dutta,B.K. and Kushwaha,H.S., "Fracture experiments on throughwall cracked elbows under in-plane bending moment: Test results and theoretical/numerical analyses", *Engineering Fracture Mechanics*, Vol.72, 2005, pp 1461 – 1497
3. Rice,J.R., Paris,P.C. and Merkle, J.G., 1973, "Some Further Results of J-integral Analysis and Estimates", *Progress in Flaw Growth and Fracture Toughness Testing*, ASTM STP 536, American Society for Testing and Materials, Philadelphia, pp 231 – 245
4. Chattopadhyay,J., Dutta,B.K. and Kushwaha,H.S., "New ' η_{pl} ' and ' η ' functions to evaluate J-R curves from cracked pipes and elbows: Part I – Theoretical derivation", *Engineering Fracture Mechanics*, Vol.71, Issue no.18, 2004, pp 2635 - 2660
5. T.V.Pavankumar, Chattopadhyay,J., Dutta,B.K. and Kushwaha,H.S. "Importance of stress triaxiality at crack tip in elastic-plastic fracture mechanics", 8th International Symposium on Plasticity and Impact Mechanics, IMPLAST 2003, 16-19th March, , New Delhi, India, 2003
6. Chattopadhyay,J., Kushwaha,H.S. and Roos,E., "Improved Integrity Assessment Equations of Pipe Bend", *Int. J. of Pressure Vessel and Piping*, Vol.86, 2009, pp 454 - 473
7. Zahoor,A., 1989-1991, "Ductile Fracture Handbook", Vol.1-3, EPRI-NP-6301-D, N14-1, Research Project 1757-69, Electric Power Research Institute
8. Chattopadhyay,J.,Tomar, A.K.S., Dutta, B.K., and Kushwaha, H.S., "Elastic-plastic J and COD estimation schemes for throughwall circumferentially cracked elbow under in-plane closing moment", *Engineering Fracture Mechanics*, Vol.72, 2005, pp 2186 - 2217
9. Chattopadhyay,J., Acharyya, S., Kushwaha, H.S., "Elastic-plastic J and COD estimation schemes for 90° elbow with throughwall circumferential crack at intrados under in-plane opening moment", *International Journal of Fracture*, Vol.144, No.4, pp 227 - 245, 2007.



Structure of Fluids at Interfaces: A Combined Simulation and Theoretical Study

Chandra N. Patra

Theoretical Chemistry Section, Chemistry Group

Dr. Chandra N. Patra is the recipient of the DAE Scientific & Technical Excellence Award for the year 2009

Abstract

Understanding the microscopic structure and macroscopic properties of condensed matter from a molecular perspective is important for modern chemistry. The very basis of such understanding is provided by statistical mechanics through bridging the gap between molecular events and the physicochemical properties of macroscopic systems. With ever-increasing computational capabilities, molecular simulations and *ab initio* calculations hold promise in providing a nearly exact route to statistical mechanics. However, phenomenological and semiempirical methods still remain quite relevant because of their simplicity and versatility in solving complex chemical problems. Under this scenario, amalgamation of analytical theories and computer simulation offers a serious compromise. Recent advances in such methods are summarized with emphasis on quantitative modeling of the interfacial behavior of fluids and soft materials, including simple fluids, colloids, polymer solutions and polyelectrolytes. Attention is also given to some potential applications of these methods to nanomaterials and self-assemblies.

Introduction

The primary objective of statistical mechanics is to interpret and predict the properties of macroscopic systems in terms of their microscopic counterparts.¹ It provides a cornerstone in understanding numerous natural phenomena and for design and optimization of chemical processes.² The importance of statistical mechanics in many different branches of basic and applied chemistry has long been realized, although its tunability to specific structural and dynamical problems has become feasible only recently. The obvious reason for such a systematic development is its suitability in covering the entire spectrum of physicochemical problems, thereby providing an inherent proximity to real experimental data. As a corollary, a number of approximate and semiempirical methods emerge which use ingenious combinations of basic concepts from statistical mechanics. The quanta of

sophistication in statistical mechanical methods are naturally driven by the specificity of problems used to represent various physicochemical systems. So far, a number of more rigorous theoretical methods have been devised,³ which are based on molecular simulations, liquid-state theories, Self-Consistent Field (SCF) theory and classical Density Functional Theory (DFT).

The rich variety of equilibrium and dynamical phenomena associated with the solid-fluid interfaces have been a subject of wide variety of research in view of their applications in biological, electrochemical and colloidal nanosystems. In recent years, there has been an upsurge of interest in this field due to significant progress in computer simulation as well as availability of sophisticated tools in theoretical formulations. Most of the earlier developments, however, have been based on simple model systems to mimic the characteristics of the real complex



systems. This article presents some recent developments in the modeling of interfacial properties of fluids and soft materials, carried out in our laboratory. Following a brief introduction to the basic concepts and new developments, the main text is concerned with applications of these methodologies to the interfacial behavior of simple fluids, electric double layers, colloids and structure of polymeric materials. This article concludes with a brief discussion on some possible future applications of theoretical chemistry to fabrication of novel materials, biomolecular engineering and molecular self-assembly.

Basic Concepts and New Developments

Statistical mechanical description of classical systems¹ involves the concept of an ensemble, which is an arbitrarily large collection of imaginary systems, all of which are characterized by the same macroscopic parameters, but each member of the ensemble has different sets of coordinates and momenta of the particles. The system dealing with an interface is an open system in general, and is characterized by fixed values of volume V , temperature T , and chemical potential μ with the ensemble designated as a grand canonical ensemble. Theoretical description of classical fluids at an interface starts with the description of the single particle density, $\rho(\mathbf{r})$, of the fluid, conveniently expressed as³

$$\rho^{(1)}(\mathbf{r}) = \rho(\mathbf{r}) = \langle \hat{\rho}(\mathbf{r}) \rangle = \left\langle \sum_{i=1}^N \delta(\mathbf{r} - \mathbf{r}_i) \right\rangle \quad (1)$$

The determination of this fundamental quantity has led to a large number of methodologies, which can be broadly classified, into four categories. The first one is based on the Integral Equation Theory (IET),⁴ which has been found to be quite successful in both homogeneous and inhomogeneous forms of description. The second one belongs to methods based on Density Functional Theory (DFT),⁴ which have been applied to simple and complex fluids in then various forms of description, viz. perturbative and non-perturbative methods like Weighted Density

Approaches (WDA). The hybrid methods that include both the density functional and the integral equation theory constitute the third method, which has been applied quite recently, to study the fluid mixtures⁵ and the electric double layer.⁶ The fourth one involves the Monte Carlo (MC) and Molecular Dynamics (MD) simulations,⁷ which provide direct physical insights into different important aspects of the structure of fluids. The present interest lies mainly in hybrid methods, viz. the Self-Consistent Density Functional Approach (SCDFA)⁸ from DFT and IET and the Monte Carlo density functional theory (MCDFT)⁹ from MC and DFT. Whereas the former is based on the calculation of density functional quantities from IET and mostly applied to simple fluids including the ionic systems, the latter requires single chain simulation with enumeration of configurations and finds applications in complex polymeric fluids.

Representative Applications

As indicated earlier 1, there have been numerous applications of the newer theoretical developments and computer simulation methods, to the calculation of various interfacial properties of fluids. Rather than attempting to review the entire work, we have selected only the recent developments in these fields from our laboratory.

Electric Double Layers

The Electric Double Layer (EDL),¹⁰ represents the system of nonuniform ionic fluids originated at the electrode-electrolyte interface and it has direct relevance to many aspects of electrochemistry and biophysics. We have developed a weighted density functional theory, where the only input required is the second order correlation function of the uniform fluid. The calculated ionic density and the mean electrostatic potential profiles compare quite well with the simulation results. Such a study is able to predict¹¹ the experimental inner layer capacitances (c_H) quite well as is evident from Fig. 1.

Solvation and Surface Forces

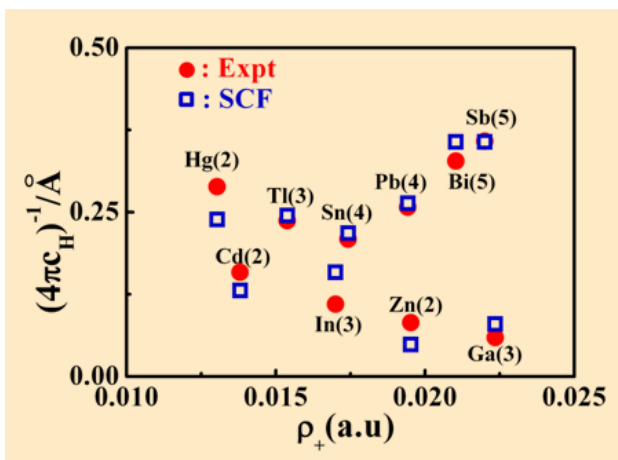


Fig. 1: The inverse inner layer capacitance for various metals immersed in an aqueous solution against the metallic electron density.

The forces¹² between hydrophobic surfaces immersed in polyelectrolyte solutions is of practical importance such as waste water treatment and protein precipitation. Several experimental measurements have shown, that these forces are oscillatory in nature; this turned out to be attractive in the presence of small amount of salt, whereas excess salt causes the same to become purely repulsive. In the present work, we have proposed a new weighted density approach for predicting the so-called solvation forces in simple liquids. As shown in Fig. 2, it can predict¹³ the interaction energies between two mica surfaces immersed in

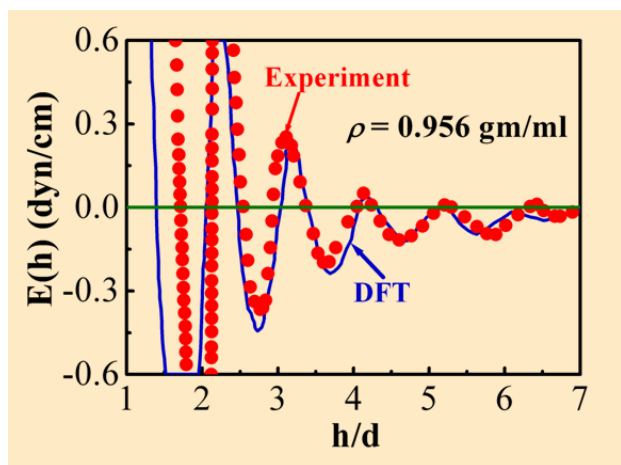


Fig. 2: Interaction energy between two mica surfaces immersed in Octamethylcyclotetrasiloxane vs the surface separation.

octamethylcyclotetrasiloxane and liquid tetradecane, comparable with experimental values.

Polymers at interfaces

The structure of polymer melts at interfaces¹⁴ is of immense technological importance in diverse applications such as surface finishing, lubrication, nanotechnology and cybernetics. Theoretical description of polymer molecules starts with united atom model with the two most widely studied²³ are the Freely Jointed Chain (FJC) and the Fused Hard Chain (FHC) models. Among the various theoretical developments, the notable contribution which warrants mention here is the Monte Carlo Density Functional Theory (MCDFT),¹⁵ where it is required to only simulate of a single chain in a self-consistent field, due to the other molecules and surfaces, which is calculated with a prescribed formulation of DFT. Fig. 3 depicts¹⁵ the calculated density profiles of athermal equimolar mixture of polymer and solvent. It is amply clear, that at high polymer density, packing entropic effects force the polymer molecules to pack against the surface. Theoretical developments along the same line for polyelectrolyte systems¹⁶ have predicted many interesting observations for binding interactions including the negative total electrostatic free energy in the presence of multivalent salt.

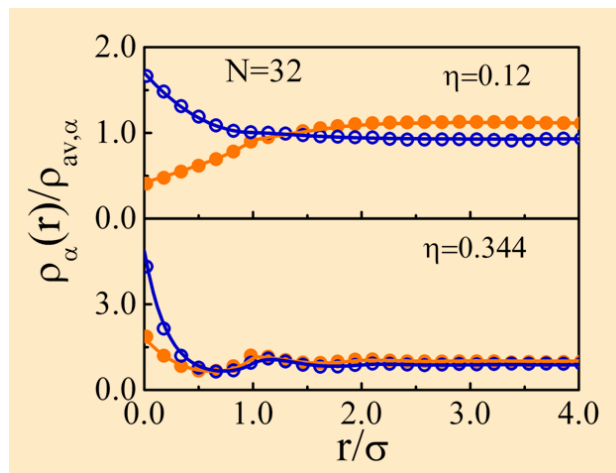


Fig. 3: Comparison between DFT predictions (lines) and Monte Carlo simulations (symbols) for the density profiles of athermal equimolar mixture of 32-mers and solvent at wall separation $H=10$ and volume fraction η as indicated.



Self-assembly of Nanoparticles and Colloids

Self-assembly of large particles into ordered arrays is supposed to be an efficient way of preparing microstructured materials¹⁷ with interesting versatility of

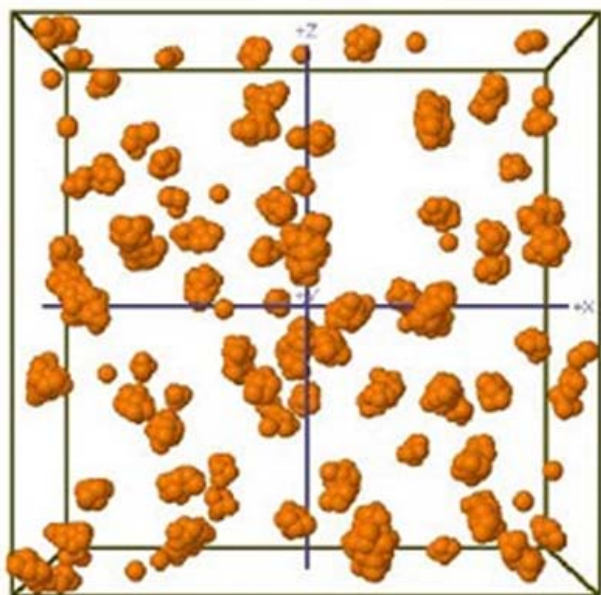


Fig. 4: Representative snapshot of 1000 bare C_{60} fullerenes in aqueous solution, volume fraction $f=0.07$ and 298K (water is not shown) after 2 ns in MD simulation.

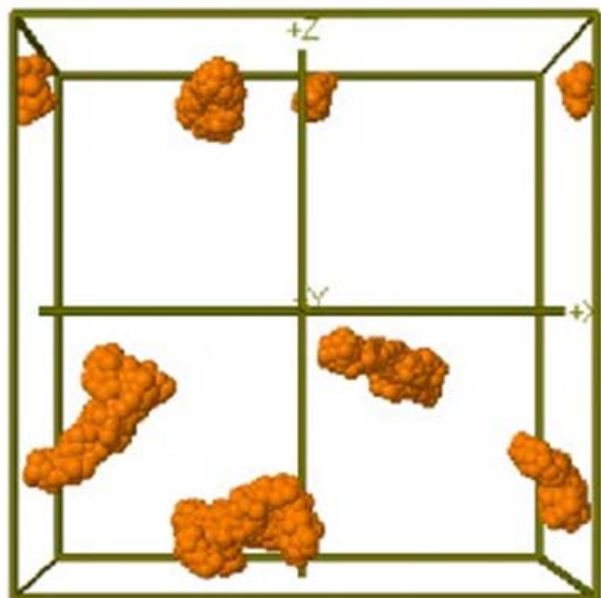


Fig. 5: Representative snapshot of 1000 bare C_{60} fullerenes in aqueous solution, volume fraction $\phi=0.07$ and 298K (water is not shown) after 2 ns in combined MD with LB simulation.

desired properties. In the present work, we have carried out a systematic study of the structure and dynamics of self-assemblies, formed from C_{60} fullerene nanoparticles in aqueous solution, by using our molecular dynamics lattice Boltzmann (MD-LB) simulation method. Fig. 4 depicts the structure of C_{60} fullerenes in aqueous solution when coarse-grained MD simulation is carried out. However, representation of accurate solvent correlations through LB simulation leads to C_{60} aggregating into larger clusters as reported in experiments and which can be visualized from Fig. 5.

Concluding Remarks and Future Directions

The contents discussed in the present article are illustrative rather than exhaustive. A number of topics of current interest like the DNA salt binding, the molecular self-assembly, the solvation dynamics, the wetting transition are not covered in the present article. Colloidal macroion in the presence of electrolyte is another fascinating area¹⁸ of R&D. Although much current work in the literature concerns relatively simple models with emphasis on the performance of various versions of the theory for representing the qualitative or semiquantitative physicochemical properties in the bulk or near surfaces, much of it in the coming years will depend upon the development of more realistic intermolecular force fields for more complex systems. Important advances are already emerging in applications of these methods to material fabrication, environmental protection, biomolecular engineering, transport processes through ion channels, and nanotechnology¹⁹ for various highend applications in space, atomic energy and defence equipment. Modeling and simulation will play an extremely crucial role in all these areas of developments for mankind in the foreseeable future!

Acknowledgements

I am greatly indebted to Swapan K. Ghosh for inspiration and assistance leading to this work and for numerous fruitful discussions. I greatly acknowledge my



collaborators Arun Yethiraj and Grant D. Smith for their helpful guidance at various stages of my research. I am also benefited from insightful discussions with L.B. Bhuiyan, A.L. Benavides and Teena Goel. It is a pleasure to thank Tulsi Mukherjee for his kind interest and constant encouragement.

References

1. McQuarrie, D.A., *Statistical Mechanics* (Harper & Row, New York, 1976).
2. Davis, H.T., "Statistical Mechanics of Phases, Interfaces, and Thin Films", VCH, New York, 1996.
3. Hansen, J.P. and McDonald, I.R., "Theory of Simple Liquids", Academic Press, New York, 1990.
4. "Fundamentals of Inhomogeneous Fluids", edited by Henderson, D., Dekker, New York, 1992.
5. Patra, C.N. and Ghosh, S.K., *J. Chem Phys.* 116, (2002) 8933.
6. Goel, T.; Patra, C.N.; Ghosh, S.K. and Mukherjee, T., *J. Chem. Phys.* 132 (2010) 194706; Patra, C.N. *J. Phys. Chem. B* 113 (2009) 13980.
7. Frenkel, D. and Smit, B., *Understanding Molecular Simulation* (Academic Press, New York, 2002).
8. Patra, C.N. and Ghosh, S.K., *J. Chem. Phys.* 118 (2003) 8326.
9. Patra, C.N., *J. Chem. Phys.* 121 (2004) 3930.
10. Schmickler, W., *Interfacial Electrochemistry* (Oxford University Press, New York, 1996).
11. Patra, C.N. and Ghosh, S.K., *J. Chem. Phys.* 102 (1995) 2556.
12. Israelachvili, J., *Intermolecular and Surface Forces* (Academic Press, New York, 1992).
13. Patra, C.N. and Ghosh, S.K., *Phys. Rev. E* 50 (1994) 5123.
14. Yethiraj, A., *Adv. Chem. Phys.* 121 (2002) 89.
15. Patra, C.N., *J. Chem. Phys.* 126 (2007) 074905.
16. Chang, R.; Patra, C.N. and Yethiraj, A., *J. Phys. Chem. B* 108 (2004) 9126.
17. Glotzer, S.C. and Solomon, M.J., *Nature Materials* 6 (2007) 557.
18. Patra, C.N., *J. Phys. Chem. B* 114 (2010) 10550.
19. Hall, J.S., *Nanofuture: What's Next for Nanotechnology* (Prometheus Books, New York, 2005).



Technological Innovations in spent fuel handling and their implementation for fuel reprocessing plants

Kailash Agarwal

Nuclear Recycle Project Special Equipment Design
Nuclear Recycle Board

Mr. Kailash Agarwal is the recipient of the DAE Scientific & Technical Excellence Award for the year 2009

Introduction

Spent fuel reprocessing involves a good amount of nuclear material handling in very harsh environment of high radiation, coupled with corrosive nitric acid. For long, it has been felt that there is a strong need to provide automation in the field of head-end operations; i.e. spent fuel storage, under-water handling, charging and feed clarification, which will lead to higher plant throughput and shorter plant shut down periods. All the reprocessing plants in NRG/NRB have manually intensive operations, especially in the field of spent fuel handling. There was a strong need felt to put efforts for improvements in these areas. The feed back from KARP, PREFRE and PP were utilized in conceptualizing the ideas and converting them into full scale systems, before implementation in the plants.

The various innovative ideas which were developed in-house and implemented, are as follows,

Spent Fuel Storage Facilities (SFSF)

Design of safety features such as Infiltration system for keeping the ground water table below the raft of the pool, Leak detection system for pool liners, pool bridge design with

automation features for positioning, locators for seismic qualification of stack of trays and single failure-proof cask handling crane, qualified for seismic event, for Spent Fuel Storage Facilities (SFSF) at Tarapur and Kalpakkam.

The pool walls are lined with 3 mm thick SS plate and the floor is lined with 6 mm thick SS plate, to avoid ingress/egress of pool water. The fuel pool is provided with an elaborate leak collection/detection system. The leak

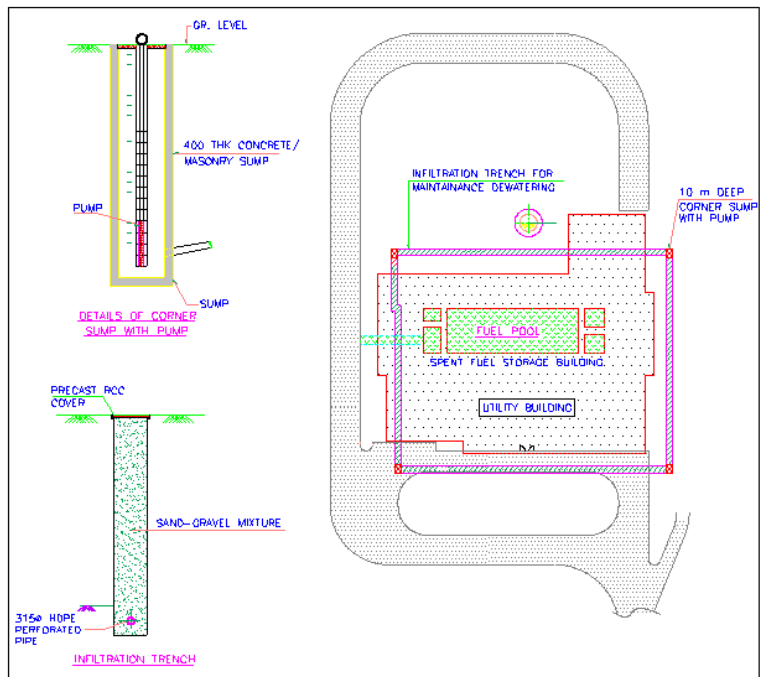


Fig.1: Infiltration Trench

DAE Excellence Award



collection channels on the backside of the pool liners play the dual role of supporting the liners, and collecting of any water leakage through the welding. These channels are connected to pipe headers terminating at a deep leak detection and collection pit. In addition to the above, there are infiltration bore wells/infiltration galleries provided around the SFSF building, to maintain the ground water below the pool raft. In the infiltration system, four deep wells are connected to HDPE slotted pipes, covered by layers of gravel and soil around the pool. Ground water from the surrounding area travels into these pipes and gets collected in these four wells, where submersible pumps take care of pumping the water to storm water drains automatically. This system is quite useful in keeping the ground water table, below the raft of the pool in all the seasons.

Fuel bundles are handled underwater in the fuel pool in the following ways:

- a) Handling of trays from shipping cask to storage locations.
- b) Handling of tray from one location to another designated location.
- c) Loading of fuel bundles from tray loading platform into the charging cask.

All the storage locations of the trays in the fuel pool and loading platform are at fixed co-ordinates, due to locators provided on the floor for the trays. This is useful for automation of the Pool Bridge for all these operations. The pool bridge has been provided with rack and pinion type positive drive arrangement, for long travel and cross travel motions. The PLC controls all x, y and z co-ordinates of the tray handling tool, with reference to the corner of the pool. The trays and casks are located at designated positions with the help of guiding locators. (Fig. 2).

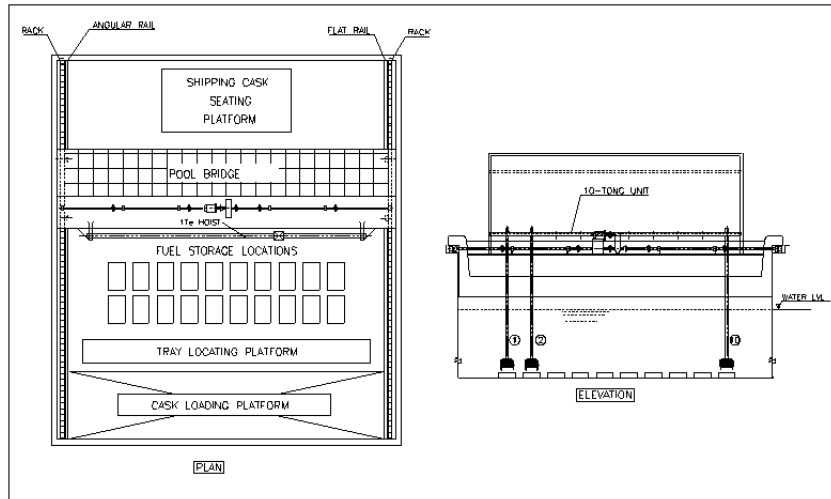


Fig.2: Layout of Pool Bridge

Direct Fuel Transfer System

This innovative concept of direct fuel transfer, from pool to spent fuel chopper, eliminates the use of heavy charging casks. This gives an added approach towards total automation in fuel handling, at the reprocessing plants.. Direct fuel transfer system is required, for remote transfer of the spent fuel bundles, from fuel pool of Fuel Handling Area (FHA) to the dissolver cell in an automated way, eliminating manual operation, saving man hours, eliminating dependency on skilled manpower and minimizing man-rem consumption. This will be achieved by connecting the fuel pool to the dissolver cell, through an underground tunnel and a tray transfer trolley running into it, from fuel pool to dissolver cell and vice versa. The system utilizes electro-mechanical wire rope driven trolley, for transferring of fuel bundles, from storage pool to the Cell; motorized X-table for movement of bundles from trolley position to the chopper position; pushing arrangement for transfer of bundles (from trolley to the X-table and later from X-table to the chopper) and various in-built interlocks/safety features. A small cycle time is required, in order to achieve high plant throughput capacity of INRP-1; the handling of 220 Mwe spent fuel bundles & system adaptable to 540 Mwe fuel bundles, low radiation exposure during the operation, less



maintenance, remote maintainability, ruggedness and safe handling of fuel. These critical factors were taken into account during the design of the system .Fig. 3 shows an elevational view of the Automation System Layout.

This automation system has been proposed for the first time, for nuclear reprocessing plants. The system is designed with built-in safety margin giving high service life, redundancy giving high reliability and modular construction with ease of maintenance. System design is aimed at simplicity in system assembly, operation & maintenance.

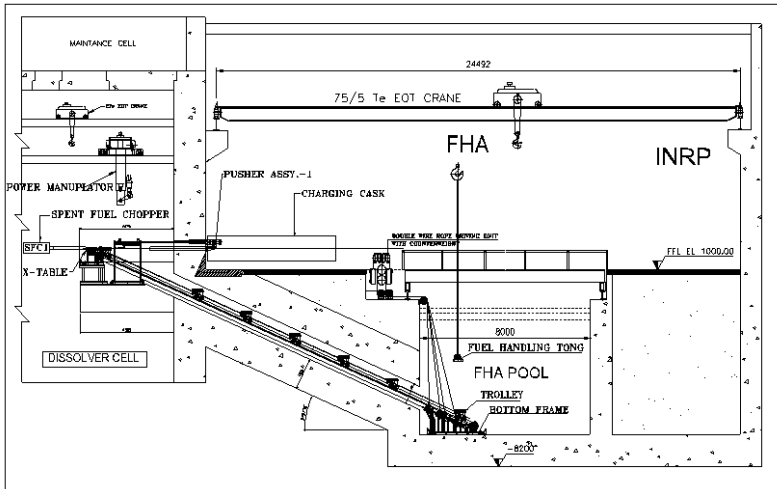


Fig.3: Elevation of the Automation System Layout

Feed Clarification Filter

Design and development of a vacuum-based filtration system for feed clarification is required, for filtration of zircalloy fines from the dissolved solution, before further processing. It also has features for remote handling and replacement. The new filter envisages zero by-passing of liquid solution through the gaskets, as it is compressed by a spring-loaded top cover. The development was systematically carried out and tested with simulated plant conditions, before implementation. This system has been recently implemented at KARP, PREFRE-2, PR-3A and the future recycle plant, INRP-1. The plant chocking problems in metering pumps and valves seats have been solved to a large extent. The performance of the system at KARP for the last two years has been excellent.

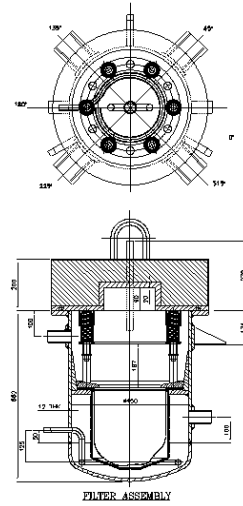


Fig. 4: Filter Assembly

Development of an Automated Charging System for Reprocessing Plants

This system is required to integrate and automate all the operations of transfer port, charging dolley, charging cask door, automatic coupling and de-coupling of pusher rods, pushing of fuel bundles and retracement of all pushers. This system is the first of it's kind in a reprocessing plant and required a multi-disciplinary approach, for successful completion. The introduction of this system at KARP has improved the performance of the plant, it has reduced dependence on skilled operators required for spent fuel charging and reduced man-rem exposure. Spent fuel charging has been completely automated with these stupendous efforts for the last 5 years. The first unit is already operational at KARP and has successfully carried out two years of operations. This machine has been functioning well and has optimized the requirement of operators from six to just one and reduced man-rem exposure, being a non-contact automatic operation. A similar system has been provided for PREFRE-2, Tarapur and PR-3A Kalpakkam. The ACF for Power Plant operations is also being implemented. This development has been a major break-through for head-end operations of a reprocessing plant.

DAE Excellence Award



Fig. 5: Automated Charging Facility

The system essentially has a trolley-mounted indexing pushing device, placed behind the charging cask dolley and run on a common set of rack and guide rails (Fig. 5). The system operates on a PLC controlled environment, which has a servo pusher, mechanical couplers for push rods and indexing system for alignment of push rods. The linear indexing device holds 4 liner and fuel pusher actuator rods on an X- table, mounted on LM guides and moves the actuators from home position to pushing position. The actuation is done by a pneumatic cylinder with reed switches at end positions. A locking cylinder confirms the alignment after each indexing.

A servo drive (servomotor with two pole resolver) with rack and pinion transmission and Linear Motion (LM) guides has been used, for pushing the liner and fuel bundles. Two types of grippers have been mounted on servo drive, one for pushing of liner actuator and the other for fuel pusher actuator. To place these grippers in position, a rotary indexer and vertical slide have been used. Rotary indexer has a pneumatic rotary actuator and the vertical slide is operated on LM guides, with the help of a pneumatic cylinder.

The control console system configuration uses a suitable CPU for PLC and a suitable station for Modbus. A MMI is mounted on this console, for setting the parameters. The PLC gives actuation signals depending on pre-conditions to be met, for each subsequent operation as per the ladder diagram. The PLC has been programmed according to ladder diagrams with defined inputs and outputs. There are about 160 sequences of operations during a single cycle of charging and these are repeated for subsequent charging. In the event of breakdown of any of these systems, fuel charging can be continued manually, either using the ACF unit or without the ACF as was practiced earlier.

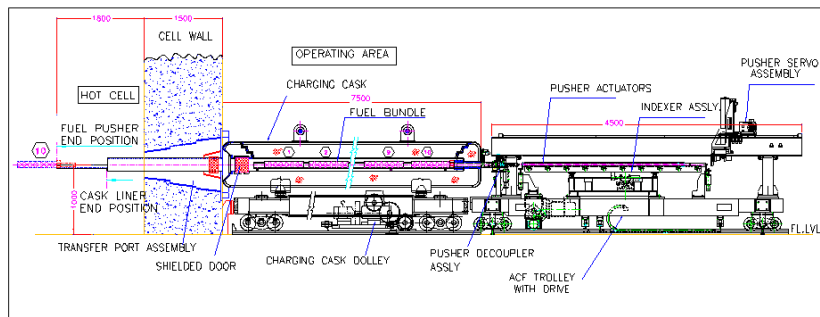


Fig.6: General Arrangement of Automated Charging Facility (ACF) along with charging cask

Development of an Indexing Cask

This has very high benefits for reducing the number of cask visits to pool, thereby increasing efficiency in head-end operations. A 40 (10X4) bundle charging cask has been developed, to replace the 10 bundle charging cask at KARP and PR-3A. The system is under field trials before implementation at PR-3A. Similar casks are being provided for ROP, which will allow simultaneous head-end operations in PREFRE and ROP and will help in achieving plant throughput.

Charging cask is a lead shielded container, which serves the purpose of transferring the spent fuel bundles from fuel pool to SFC, without any radiation exposure to the



personnel. Existing Charging Cask has a capacity of 10 fuel bundles and is required to be handled underwater eight times per batch. In order to reduce the underwater handling of Charging Cask considerably, an Indexing charging cask has been developed. It accommodates 40 fuel bundles at a time, in place of existing 10 fuel bundles. It reduces the number of handling times of Charging Cask from 8 to 2, for one batch. The challenges in the design of the indexing mechanism were: keeping the half-cut open portion of cavity pipe (4 sets) always on the top to load the fuel bundles from top into the liner and to avoid falling of bundles in the cask cavity and rotation of indexing mechanism in a controlled manner, to load and charge the fuel bundles in all the 4 sets of cask liners.

To achieve positive rotation of cavity pipes, a sun and planetary gear system has been used. (Fig. 7) The speed of rotation of central shaft is in such a ratio, that the top cut portion of cavity pipe always faces the top, irrespective of speed.

As the indexing is required underwater during loading of the fuel bundles as well, the drive is enclosed in a hermetically sealed container, with suitable feed-throughs for electrical supply and pneumatic lines. To achieve

indexing of the mechanism within allowable tolerances, a PLC with encoder has been employed. The PLC controls the motor as per a set programme and stops at every 90° rotation of the indexing mechanism. It takes feedback from the encoder mounted on the drive shaft. Additionally, a pawl and ratchet mechanism has been used, to achieve positive locking of indexing mechanism at every 90°.

The cavity pipes are held in bearings at two end plates. To avoid deflection in the pipes, these are supported at two intermediate places, with the help of plate and roller assemblies. The supporting plate rollers are guided in the recessed plates fixed to cask cavity. As this mechanism operates both, in fuel pool and in air, corrosion and radiation aspects were taken into consideration, for material selection of various components.

Acknowledgement

The author thanks Shri S. Basu, Chief Executive, NRB for his valuable guidance and continuous support in carrying out above activities. Author is also thankful to all the engineers and support staff in NRPSD, KARP and PREFRE-2, Tarapur for day-to-day interactions.

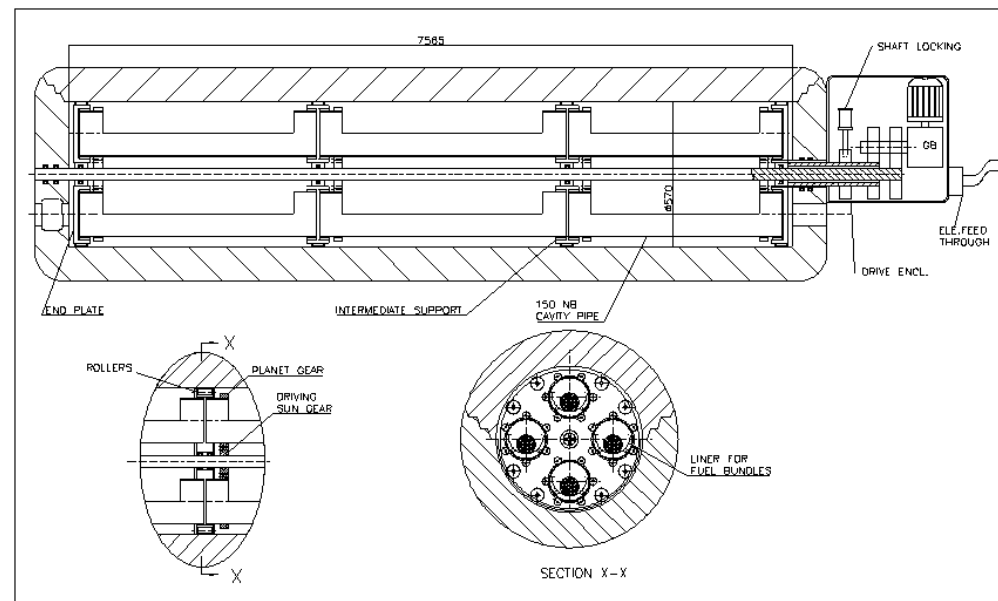


Fig. 7: Indexing Charging Cask





Ultrafast Fluorescence Spectroscopy and Supra-biomolecular Interactions of Organic Dyes

A. C. Bhasikuttan

Radiation & Photochemistry Division

Dr. A.C. Bhasikuttan is the recipient of the DAE Scientific & Technical Excellence Award for the year 2009

Abstract

This short article presents a glimpse of the select photochemical research in our group, along with a brief account of the femtosecond fluorescence up-conversion facility, developed in RPCD, that offers a convenient and sensitive ultrafast fluorescence detection, to cater to the photochemical research in the Division. In the present article, the discussion is restricted to typical molecular systems like triphenylmethane (TPM) dyes and thioflavin T, that shows significant structural modulations in the excited state. Understanding the relaxations and modulations of excited state properties on binding to ss-DNA, BSA or with macrocyclic hosts, are the motivations of the present study. The topics covered are (i) intriguing ultrafast excited state relaxation dynamics in malachite green (ii) G-quadruplex formation in ss-DNA in the presence of malachite green (iii) the cooperative interaction of brilliant green with BSA and cucurbit[7]uril and (iv) formation and breakage of a stimulus-responsive supramolecular capsule, formed by thioflavin T, metal ions and cucurbit[7]uril.

Key Words: Fluorescence up-conversion, Triphenylmethane dyes, Thioflavin T, Cucurbit[7]uril, G-quadruplex

Introduction

In photochemical studies, one of the major issues is to understand, the geometric and electronic distribution of the molecule, the surrounding medium, and other extrinsic factors which influence the molecular properties and to what extent can one use this information to control excited-state dynamics. In the event of molecular interaction, physico-chemical processes like, electron transfer, proton transfer, charge transfer, solvation, torsional dynamics etc., occur in the picosecond to femtosecond timescales and a detailed investigation of such processes warrants sensitive and reliable experimental facilities. In general, fluorescence-based techniques are very sensitive to investigate various photochemical processes. In our group, steady-state as well as time-resolved fluorescence with a wide time resolution from nanosecond to femtosecond have been

extensively used, to investigate various complex photochemical processes including excited state relaxation, electron transfer processes, modulation of excited state properties via supramolecular interaction and others. This article presents some of the studies carried out using ultrafast fluorescence technique like fluorescence up-conversion with time resolution down to ~ 100 femtosecond and also the intriguing photophysical properties and their advantageous modulation in some of the potential organic dyes, exploiting their interaction in a supra-biomolecular environment.

Femtosecond fluorescence up-conversion facility

Understanding the details of molecular events in real time, is of utmost importance to execute controlled chemical reactions and to channelize them into various applications.



The concept of obtaining the ultrafast time resolution in the fluorescence measurements, relies on the non-linear effect of generating sum-frequency photons from the mixing of the fluorescence photons with a gate light pulse, which are spatially separated in sequence, to introduce a path difference in steps of 2 micron each, which is equivalent to a 6.6 fs time delay. Depending on the changes in the fluorescence intensity of the sample at different delay periods, the intensity of the up-converted light also changes accordingly and the latter is detected with a sensitive photon counter to generate the kinetic traces. The schematic and the actual arrangement of the femtosecond fluorescence up-conversion setup, developed in our Division is shown in Fig.1. With this set up, the instrument resolution is ~ 100 fs [1].

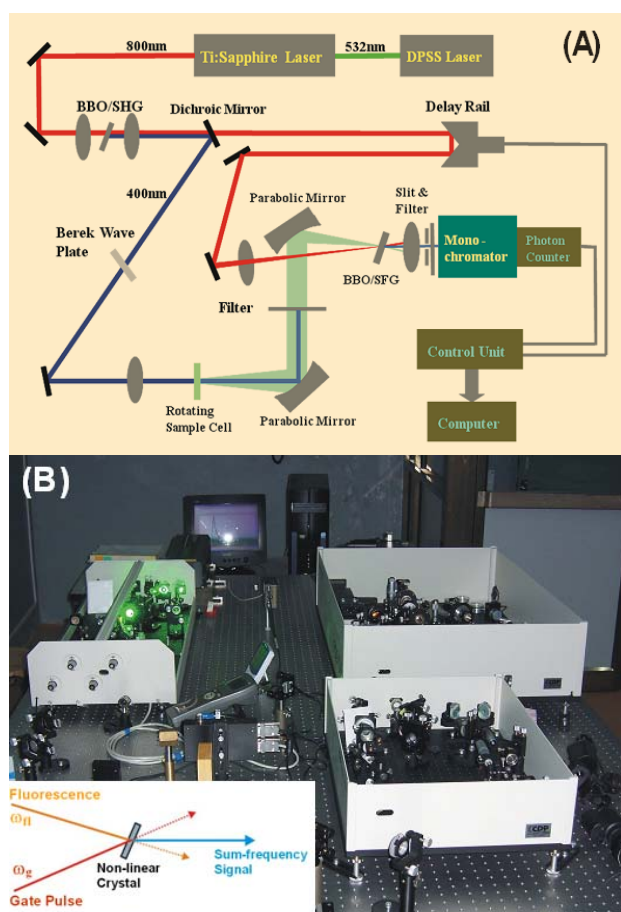


Fig.1: Schematic (A) and the actual photograph (B) of the femtosecond fluorescence up-conversion setup developed in RPCD during Xth plan period.

Ultrafast excited-state dynamics of malachite green

Triphenylmethane (TPM) dyes are one of the earliest organic molecules investigated, to understand the ultrafast torsional motions in the excited states and to exploit their advantages in areas ranging from laser dyes to photodynamic therapy. For the TPM dye, Malachite Green (MG), employing the fluorescence up-conversion and other optical measurements and following S_2 state excitation, the data revealed a cascade population relaxation along the S_2 state, with a time constant of ~ 130 fs, that is almost independent of solvent viscosity, contrary to the relaxation dynamics of the S_1 state (Fig. 2A).

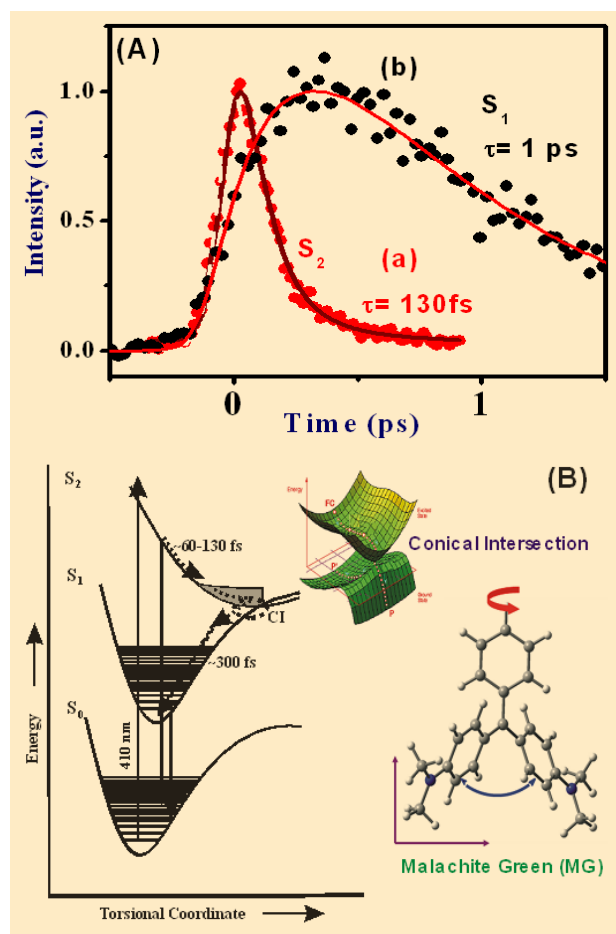


Fig.2: (A) Fluorescence decay traces obtained in an ethanol solution of MG on excitation at 410 nm (a) at 450 nm (b) at 680 nm. (B) Schematic representation of the proposed relaxation pathways in malachite green.



Following wavelength-dependent time-resolved anisotropy measurements along the S_2 and S_1 emission bands, we propose a relaxation pathway along a conical intersection of S_2 and S_1 potential surfaces, supported by the torsional motion of the unsubstituted phenyl ring (Fig. 2B). Present study identifies the major structural changes associated with the excited state of TPM dyes, which are of direct relevance to the application of these dyes in different areas [2,3].

Interaction of malachite green with G-quadruplex

As discussed, due to the structural relaxation in the excited states, the radiative lifetimes of TPM dyes are, in general, very short (< 1 ps) in low viscosity solvents. The lifetime, however, increases substantially upon binding of the TPM dyes with bio-macromolecules like DNAs and proteins, that possess potential applications in photodynamic therapy, drug delivery, catalysis, site/sequence specificities and therapeutics. Oligonucleotide sequences containing guanine-rich stretches can form unique, mutually hydrogen-bonded, internally-folded, or inter-strand G-quadruplexes (see Fig. 3), which are active in chromosomal telomeres, gene promoters, immunoglobulin switch regions.

Using photochemical methods, we demonstrate the binding interactions of a guanine-rich single strand oligomer sequence $d(G_2T)_{13}G$ with the biologically active chromophoric dye, MG. Convincingly, malachite green supports the formation of G-quadruplex and forms a strong complex with it, resulting in ~ 100 fold enhancement in its fluorescence yield. This specific interaction as compared to other poly nucleotide sequences, is a convenient method, to detect the G-quadruplex formation in DNAs and RNAs [4].

Brilliant green with BSA and cucurbit[7]uril: an enhancer strategy

The advantage of placing dye/drug in a supra-biomolecular environment has immense applications in enhancing the photochemical activity. In our study, we observed a fluorescence enhancement by a factor of ~ 300 and a largely increased binding affinity, when the TPM dye, Brilliant Green (BG), binds to bovine serum albumin (BSA) in the presence of a macrocyclic host cucurbit[7]uril (CB7). Observed results indicate a cumulative (multiplicative) fluorescence enhancement as compared to the effects observed in the presence of CB7 alone (factor of 6) or BSA alone (factor of 45) (Fig. 4). The present

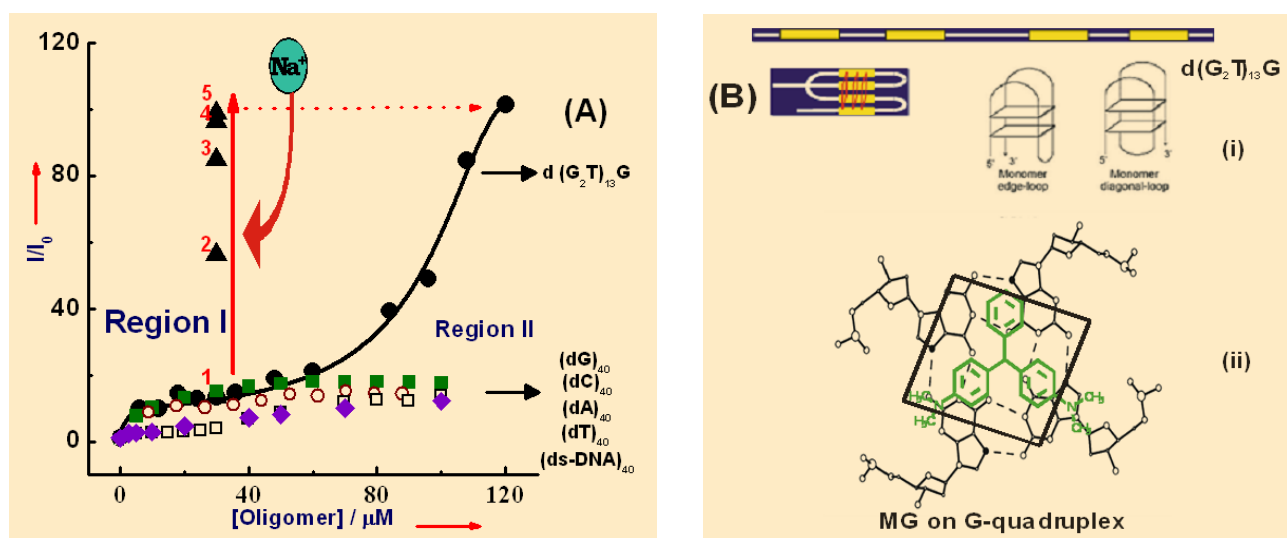


Fig.3: (A) Binding curves for MG with the oligomers. \blacktriangle denotes the increase in emission intensity with the addition of NaCl upto 500 mM (5). (B) Representation of the folding patterns in the G-rich oligomer (i) and a schematic representation of the binding of MG on the quadruplex (ii).



observation suggests a new supramolecular 'enhancer strategy', to improve the binding of selected organic dyes to biomolecules, which could improve their sensitivity in sensor applications and their activity in medicinal applications, prominently photodynamic therapy [5].

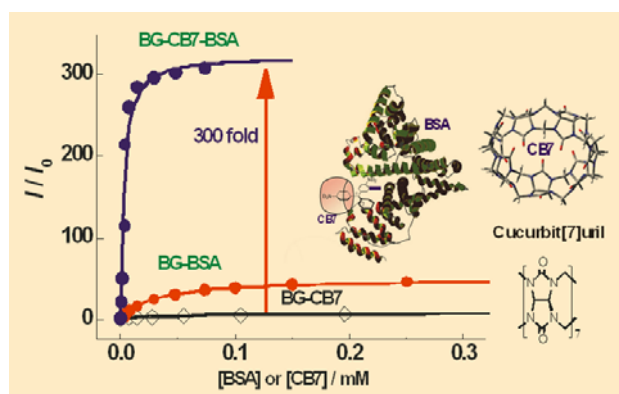


Fig. 4: Plots of the fluorescence intensity ratio (I/I_0) for BG with addition of CB7 (\diamond), BSA (\square) or both (\circ). Inset: Schematic representation of the proposed supra-biomolecular complex and the structure of CB7.

Stimulus-responsive fluorescent supramolecular capsule

Non-covalent interaction through host-guest approach, where a guest molecule is encapsulated into the macrocyclic host cavity, can introduce pronounced effects on, as well as, fine-tuning of the physico-chemical properties of the included guest, which find immense importance in photostability, drug delivery, photodynamic therapy, catalysis and sensor applications. In our study, we observed an intriguing non-covalent interaction of Thioflavin T (ThT), a fibril diagnostic dye, with CB7 in the presence of metal cations [6]. In the absence of metal ions ThT forms 2:1 (CB7:ThT) complex with CB7. Incorporation of metal ion to the 2:1 complex solution, leads to an unusual enhancement in the fluorescence emission (~ 270 fold in the presence of Ca^{2+}). Detailed photophysical characterization with support from NMR and anisotropy data has revealed, a novel stimulus-responsive cooperative metal ion, binding to the stoichiometrically selected $(\text{CB7})_2 \cdot \text{ThT}$ complex, demonstrating a highly fluorescent supramolecular nano-

capsule, which responds to stimulants like adamantyl amine (AD) and provides a controlled release of the components as presented in Fig. 5. Such stimulus-responsive capsular complexes are projected to find application in areas like drug-delivery vehicles, nanoreactors or metalloenzyme models.

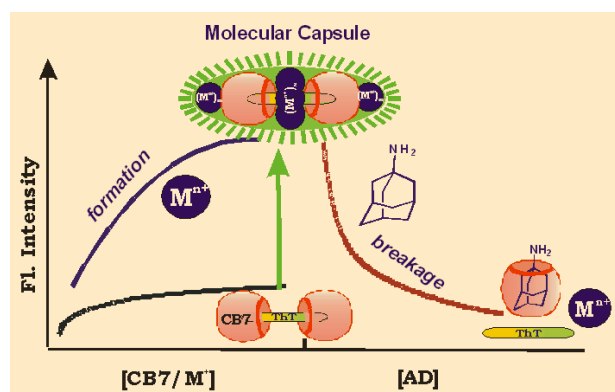


Fig. 5: Schematic representation of the formation and stimulus responsive breakage of the supramolecular capsule.

Acknowledgements

I acknowledge the contributions of all collaborators and co-authors of our published works. My special thanks are due to Dr. S. K. Sarkar, Head, RPCD and Dr. T. Mukherjee, Director, Chemistry group, BARC for their encouragement and support.

References

1. P. K. Singh, M. Kumbhakar, J. Mohanty, S. Nath, A. C. Bhasikuttan, H. Pal, S. K. Sarkar, T. Mukherjee, BARC Report, 2009, E-1843, 1-21.
2. A.C. Bhasikuttan, M. Suzuki, S. Nakashima, T. Okada, *J. Am. Chem. Soc.* 2002, 124, 8398.
3. A.C. Bhasikuttan, A.V. Sapre, T. Okada, *J. Phys. Chem. A*, 2003, 107, 3030.
4. A. C. Bhasikuttan, J. Mohanty, H. Pal, *Angew. Chem. Int. Ed.*, 2007, 46, 9305.
5. A. C. Bhasikuttan, J. Mohanty, W. M. Nau, H. Pal, *Angew. Chem. Int. Ed.*, 2007, 46, 4120.
6. S. Dutta Choudhury, J. Mohanty, H. Pal, A. C. Bhasikuttan, *J. Am. Chem. Soc.*, 2010, 132, 1395



Ultrafiltration Membrane Technology for Water Purification and Effluent Treatment

R.C. Bindal, S. Prabhakar and P.K. Tewari
Desalination Division

Dr. R.C. Bindal is the recipient of the DAE Scientific & Technical Excellence Award for the year 2009

Abstract

A variety of ultrafiltration (UF) membranes and membrane-assisted devices have been developed at the Desalination Division (DD), BARC, for water purification and water decontamination with respect to iron, arsenic and fluoride, both at domestic and community scale. The UF membrane processes have got tremendous potential in treatment of radioactive effluents both at front and back end of the nuclear fuel cycle. The paper presents a brief overview of work carried out in DD, in this direction.

Introduction

Population growth, rapidly expanding urbanisation and industrialisation coupled with overexploitation of good quality water sources, are putting tremendous pressure on water-related infrastructural facilities. At the same time, pollution and environmental issues call for ecofriendly technologies in these areas. In the last decade, the ultrafiltration (UF) membrane technology has developed in to one of the valuable tools towards addressing these issues of concern. UF membrane process essentially works on size exclusion principle, with pore sizes ranging from 2 nm to 100 nm, at relatively low operating pressure (1-5 bar) with minimum chemical intervention. In many cases, UF membrane process offers the advantages of water recovery for recycle and the possibilities of recovering valuable materials from the concentrate. With the growth of synthetic polymer technology, it has become possible to tailor-make variety of UF membranes to suit specific applications.

The Desalination Division is extensively involved in the development and deployment of various types of UF membranes and UF membrane-assisted devices for wide range of applications, like domestic water purification, removal of hazardous contaminants like fluoride, arsenic and iron and treatment of industrial effluents including nuclear industry. This paper aims at presenting the R&D work carried out in this direction in our laboratory in BARC.

UF membrane for water purification

Development and deployment of UF membrane in innovative forms for the purification of drinking water is the most important area of research in membrane field, as this application has direct societal implication. Keeping various constraints of existing processes and field conditions in mind, BARC has undertaken extensive R&D to develop the "point of use" devices with features like: 1) Affordability, 2) Minimal maintenance, 3) Independent



of the power source, 4) Minimal wastage of water (almost 100% recovery) and 5) Quality.

UF membrane devices for domestic water purification

Based on polysulfone UF membrane in cylindrical, candle-like configuration, BARC has developed a point-of-use device (Fig.1) for purification of domestic drinking water, capable of removing bacteria, viruses, suspended solids, colloids, colour, odour and organics. The characteristics of this device are given in Table 1.

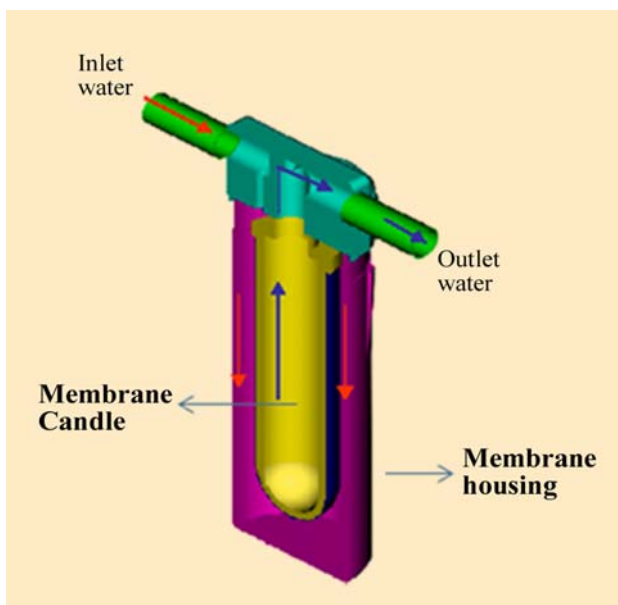


Fig. 1: UF Membrane device for domestic water purification

This device consists of mainly two parts:

1. A membrane candle comprised of a porous polypropylene candle laminated with a thin ultrafiltration membrane of polysulfone polymer with silver impregnated activated charcoal, filled in the hollow space of candle.
2. A housing unit, which is an outer container having provision to fix the membrane candle in it, with an inlet for supply water and an outlet for purified water come out as a product from the membrane candle.

The device developed at BARC, has superior characteristics and advantages over all other competing devices, which are mostly based on ultraviolet radiation. The main advantages are:

1. The device is very effective as it almost completely filters out bacteria and turbidity, thereby producing crystal-clear water.
2. The device is very compact, a small inexpensive portable gadget, that can be easily installed and needs no electricity or addition of any chemicals.
3. As the device physically filters out bacteria, there will not be any dead or decayed bacteria in purified water, unlike ultraviolet radiation or chemical addition devices.
4. The operational cost of device is almost negligible as the device works on hydrostatic pressure head. The device is almost maintenance-free, except for occasional cleaning of the membrane surface, to remove deposited suspended solids.

Table 1: Characteristics of domestic water purifier based on UF membrane

Removal of bacteria and viruses	Almost total (>99.99%)
Removal of suspended solids	Almost complete
Avg. pore size based on MWCO	<10 nm
Candle size	Area: 314 cm ²
Operating pressure	Hydrostatic pressure head of 5 to 35 psig
Product flow rate	40 ltrs of pure water per day at about 5 psig head
Membrane's chemical stability	i) Stable in molar acid and alkali ii) Stable w.r.t. residual Chlorine



- The device works in a dead-end manner and hence not a single drop of water is wasted.

Know-how of this technology has been transferred to 22 private parties for commercialization, out of which 11 have already been marketed under different brand names.

UF membrane devices for community and industrial scale water purification applications

Based on commercial success of domestic water purifier, we in BARC, have developed a "backwashable spiral UF membrane device" for purification of water at community level as well as for industrial applications. The technology consists of the following three parts:

- Preparation of UF membrane in sheet form by phase inversion technique, consisting of a 50 micrometer thick polysulfone coating over a porous nonwoven fabric support (sizes upto 1 m width and 20 m length) and subsequent post treatment.
- Rolling of these UF membranes in spiral configuration of 2512 or 4040 sizes, accommodating about 1 sq. meter and 5 sq. meter membrane area respectively.
- A procedure to provide backwashing effect.

Brief features and specifications of this device are presented in Table 2 below. This technology has been transferred to three private parties for commercialization.

UF membrane assisted processes for water decontamination

Many parts of our country suffer from water-borne diseases, due to natural contamination of water with fluoride, iron and arsenic. At present, there is no fool-proof and economically viable technology available for removal of these contaminants. For removal of these contaminants, various physico-chemical processes like adsorption and aeration have been suggested by various laboratories. However, most of these processes suffer from secondary contamination problems. For example, during defluoridation using activated alumina, it is found that defluoridated water gets contaminated with aluminium beyond the permissible limit. Similarly, for removal of arsenic by adsorption on iron, or removal of iron by aeration, product water has iron contamination beyond acceptable limits. In our laboratory at BARC, we have demonstrated that these physicochemical processes coupled with UF membrane devices can produce water free from original as well as from secondary contaminants. The technologies of iron, fluoride and arsenic decontamination have been transferred to separate private parties. A simple schematic of these UF membrane assisted processes is presented in Fig. 2.

Table 2: Salient features and specifications of backwashable spiral UF membrane device

Salient Features	Specifications
<ol style="list-style-type: none"> Physical elimination of suspended solids, microorganisms, colloidal species, turbidity Ensure continuous operation, low foot-print area, stable flux and output quality Useful as community water purifier Useful as pretreatment for desalination 	<ol style="list-style-type: none"> Operating pressure: 2-3 kg/cm² Backwashing pressure: up to 2 kg/cm² Cross-flow mode of operation for higher turbidity feed Dead-end mode operation for feed quality up to 10 NTU Membrane flux of 1000 LMD per bar Backwashing by filtrate/pure service water

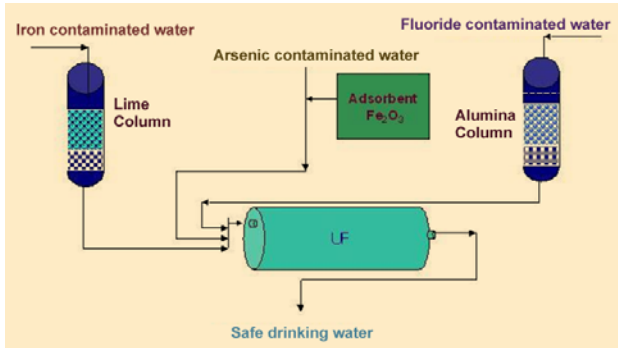


Fig. 2: A schematic of UF membrane-assisted physicochemical processes for water decontamination

Application of UF membranes in nuclear waste treatment

Fabrication and/or reprocessing of nuclear fuel invariably leads to the generation of waste in which significant amount of actinides are present, which require either recovery as a valuable material or treatment for safe disposal of this waste. In most cases, these waste effluents are highly acidic or alkaline. In many cases, large parts of these actinides are present in fine colloidal form. Conventionally, special grade ion exchangers with vigorous pre-conditioning are used for removal of these actinide materials from effluent. However, this process has many inherent drawbacks and also generates substantial amount of secondary waste during regeneration and thereby makes it difficult to recover these valuable species. In order to demonstrate/evaluate the potential of ultrafiltration membranes for such application, few laboratory scale and pilot plant studies were conducted and these are described in the following sections.

Pilot plant scale study of UF membrane technology for treatment of fuel pond water in reprocessing plants

Spent fuel from nuclear power reactors are stored in fuel pond filled with water before reprocessing. For handling of these high radioactive rods, the fuel pond water should be very clear, and should have as low activity as possible

in dispersed form. For this purpose, a pilot scale study was conducted at PREFRE, BARC, Tarapur, using in-house made UF membrane and spiral module.

The objective of the study was : 1. To clarify turbid fuel pond water, 2. To evaluate the performance of UF module after back-washing and 3. To make a Radiation survey of the hot spot if required.

During the course of this study, about 12000 L of fuel pond water containing 4.6×10^{-6} mCi/L gross alpha and 3.2×10^{-4} mCi/L gross beta-gamma activities was treated. Incidentally, a steady DF of about 4 was achieved, for both gross α and gross β - γ activities, and the treated water was almost turbidity-free (<0.1 NTU). The flux value declined by about 15% that could be regained by back washing with pH 2 solutions. No hot spot on the membrane module has been observed so far.

UF membrane for electrochemical process

Electrochemical processes are widely used for production of various chemicals. One of the most important parts of an electrolyser unit is the separator or diaphragm, which separates catholyte from anolyte. This part plays an important role in determining the purity and concentration of the desired chemical as well as the amount of electrical energy consumption. Most of the time, electrochemical processes involve the use of highly acidic or alkaline electrolytes and hence the diaphragm should be chemically stable under these conditions.

One of the most critical operations in the processing of spent fuel is partitioning, wherein the plutonium is separated from the organic solution containing uranium, by selectively reducing Pu(IV) to Pu(III). The reduction of Pu(IV) to Pu(III) is accomplished with the reducing agent, uranous nitrate, which is produced at PREFRE, Tarapur, by electrolytic reduction of U(VI) using NAFION 90209 membrane in the electrolyte cell, as a separator between anode and cathode. The Nafion membrane is of US origin

DAE Excellence Award



and hence not available for DAE applications. Subsequently, the development of suitable polymeric separator for this purpose was taken up by the Desalination Division. The said diaphragm can withstand hostile chemical environment of the electrolytic cell, which involves the use of 3 M nitric acid and about 0.8 molar hydrazine nitrate. The diaphragm was successfully tested at PREFRE and it was observed, that by manipulating the process operating conditions, it is capable of yielding 100 % conversion of uranyl to uranous. This UF diaphragm was also successfully tested under field condition for the production of ammonium persulfate from ammonium sulfate by electrochemical process. After successful field trials, this technological know-how was transferred to a private chemical manufacturer for their in-house use.

Conclusion

UF membrane process is not only an important separation process by itself, but is also a base process for all other types of pressure-driven membrane processes. UF membranes are finding increasing use in other non pressure driven processes also, like electrolytic processes, hemodialysis/hemofiltration, diffusion dialysis etc. and are being used on industrial scale for a variety of applications. It has shown a very good potential for treatment of radioactive effluents too. Tailor-making of UF membranes for specific applications and introduction of nanotechnology are opening up innovative and promising possibilities, leading to the development of high flux and highly selective membranes, with high-impact applications, and hence in the advancement of UF membrane technology.



Ultrasonic Measurement of Internal Diameter and Wall Thickness of Irradiated Zr-2.5%Nb Pressure Tube from KAPS-II Reactor

J. L. Singh, N. Kumawat, M. P. Dhotre and P. M. Ouseph

Post Irradiation Examination Division

Shri J.L. Singh is the recipient of the DAE Scientific & Technical Excellence Award for the year 2009

Abstract

In Indian Pressurized Heavy Water Reactors (PHWRs), Zr-2 pressure tubes were replaced by Zr-2.5%Nb tubes, made through cold pilgering route. Low corrosion rate and low H/D pickup, favoured selection of Zr-2.5%Nb alloy. Wall thickness of pressure tubes was reduced to 3.32 mm due to higher strength of Zr-2.5%Nb alloy, while retaining the internal diameter. The present pressure tubes are operating at higher hoop stress due to reduced wall thickness. The channel S-07 from KAPS-II reactor was removed after 8 Effective Full Power Years (EFPY), to carry out detailed Post Irradiation Examination (PIE). Internal diameter and corresponding wall thickness were measured by an innovative ultrasonic testing technique. It was found that diametral creep was more in a location, where initial wall thickness was lowest.

Introduction

High temperature and high-pressure heavy water coolant, flows through the pressure tubes (PT) over years of reactor operation. High-pressure coolant generates tensile Hoop stress inside the PT wall, subjecting it to expand outwardly, aided by high temperature. Hoop stress is mainly responsible for increase in internal diameter (creep) though, it also depends on several other parameters like temperature, fluence, texture, cold work, grain shape and size etc. Hoop stress is determined by coolant pressure, internal diameter and wall thickness. Coolant pressure is an operational variable while, the other two parameters viz-internal diameter and wall thickness are affected by irradiation over long duration. It also undergoes irradiation enhanced creep and growth, both axially and diametrically. An irradiated Zr-2.5%Nb pressure tube S-07 was received for detailed post irradiation examination. To estimate the diametral creep, changes in wall thickness (WT) and

internal diameter (ID) have been measured by ultrasonic testing technique, developed in-house.

The Zr-2.5%Nb pressure tubes are estimated to operate continuously for 30 years, due to lower corrosion and H/D pick up. If total hydrogen does not exceed 30 ppm, it may have adequate load carrying capacity. Diametral increase causes flow bypass around the fuel bundles and hence, may result in fuel failures. The increase in pressure tube length (elongation) may lead to problems for the support at the ends and feeder pipes. Creep sag and increase in diameter may cause an early CT/PT contact, for blister formation. Hence, creep rate is one of the factors, determining the life of pressure tubes. Diametral creep due to Hoop stress is dependent on local internal diameter and wall thickness, around a particular circumference. These two parameters have been measured by ultrasonic testing technique and results are discussed in this paper.



Probe holder design

To determine the actual hoop stress ($H=PD/2t$) around a particular circumference, it is essential to measure WT and ID both on the same circumference, to determine local Hoop stress. The two fabrication parameters may vary from inlet to outlet end in a pilgered tube. Two 10 MHz normal beam immersion transducers, facing in opposite directions, were fitted along the diameter line, inside an annular perspex cylindrical probe holder, shown in Fig. 1. To keep the probe holder in the center inside the PT, four spring loaded steel ball rollers were used, for easy entry and smooth movement of the probe assembly. The ultrasonic beam gets reflected back from ID surface, and

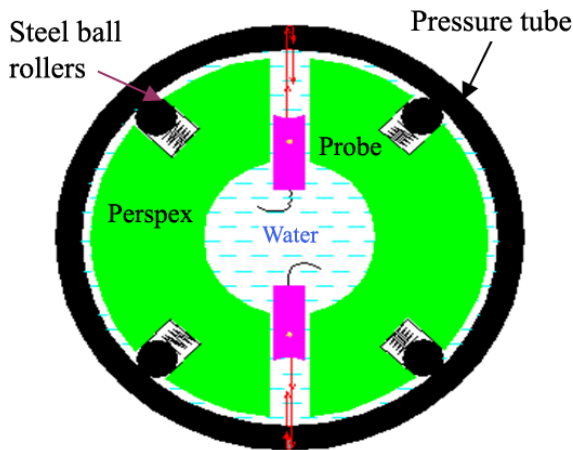


Fig. 1: Schematic probe arrangement

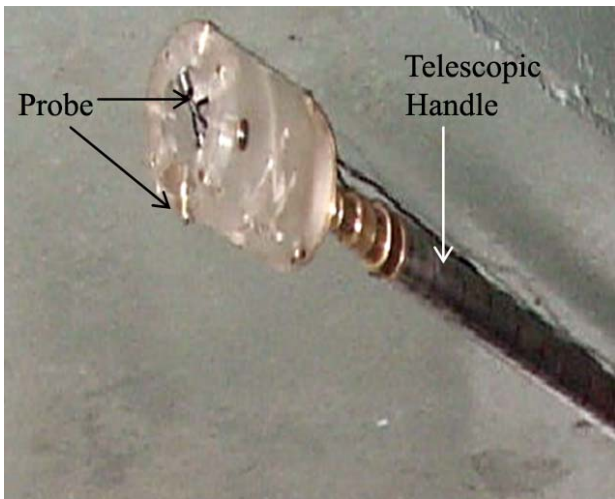


Fig. 2: Probe holder with telescopic handle

a part of it enters the wall of the pressure tube to be returned from OD surface. Water path in front of the two probes are added to the distance between the probe, to estimate ID of the pressure tube. Thus at the same circumferential location ID and WT measurements are carried out simultaneously. One set of ID measurement is accompanied by two wall thickness readings. The probe holder is rotated by 90° to get another ID measurement and two more wall thickness readings.

The pressure tube removed from the reactor is around 5.1 meter long. A 6-meter long telescopic handle was fabricated, to cover the entire length of the irradiated pressure tube. Six 1-meter long stainless steel tubes of different diameters with end stoppers were assembled, giving smooth sliding movement over each other. Small grub screws were provided, to lock the fully expanded segmental tubes, to make a 6-meter long handle as shown in Fig. 2.

Permanent markings were inscribed at intervals of 50 mm on each segment, to be visible at a distance away from the shielding cask end. The 6-meter long stainless steel pipe is filled with water from the top open side, for ultrasonic coupling of the probes.

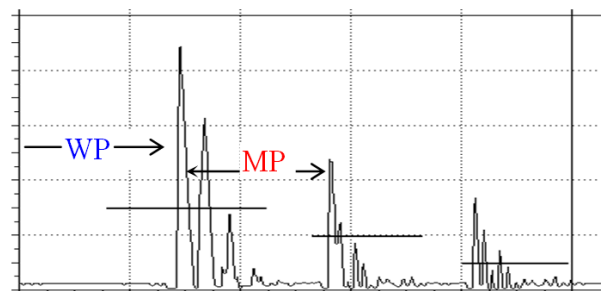


Fig. 3a: Typical signal for single probe

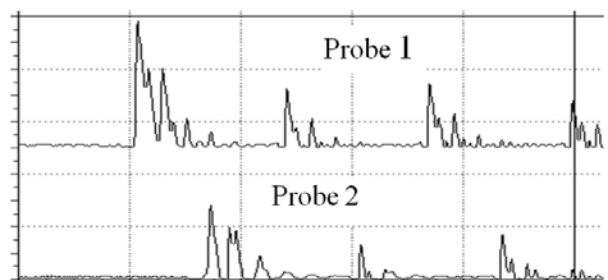


Fig. 3b: Typical signals for two probes



Calibration

The UT probes were calibrated using Zr-2.5%Nb PT spool piece with machined steps and a two channel ultrasonic testing machine with an accuracy of ten microns. Ultrasonic velocity in water was used to measure water path (WP) for a known internal diameter, to calculate the distance between the two probes. For pressure tube wall thickness, ultrasonic velocity in Zr-2.5%Nb alloy was set and confirmed, by measuring wall thickness at known locations. Corrections were provided for phase reversal effects. The signal appearing first is from water /PT ID interface and the latter two are from OD of the pressure tube. Typical signal waveforms are shown in Fig. 3a. & 3b. for single and double probes respectively.

Measurements

A 6 meter long S.S. pipe of 116 mm OD was used inside a shielding cask to hold the irradiated pressure tube to ensure complete immersion of the 5.1 meter long irradiated PT in water (Fig. 4a). To hold water and also protect workers from harmful radiations, the shielding cask was carefully tilted using overhead crane. The lower bottom ends of S.S. pipe and cask were sealed leak-tight by a common rubber bung, having drainage tube and a valve (Fig. 4b). Water was filled in the S.S. pipe ensuring full immersion of the pressure tube. The probe holder was introduced from the top open end of the S.S. pipe, projecting out of the cask. Measurements were taken at every 50 mm distance, inside the pressure tube.

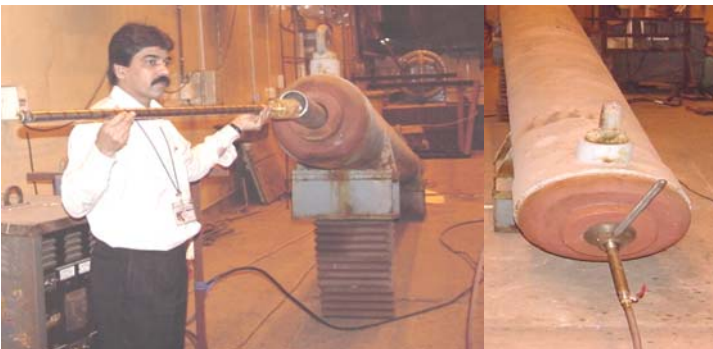


Fig. 4a: Trial set up with PT inside the S.S. pipe in the tilted shielding cask.

Fig. 4b: Back side of the cask sealed leak-tight with drainage system

Result

The measured diameter and thickness readings were plotted against pressure tube length. Internal diameter was found to have increasing trend from inlet to outlet end. But, there is an abrupt increase in the ID distinctly seen around 3.2 meters from inlet end as seen in Fig. 5. The as fabricated ID at the peak region was found to have increased by ≈ 0.9 mm after 8 EFPY. Thinning was

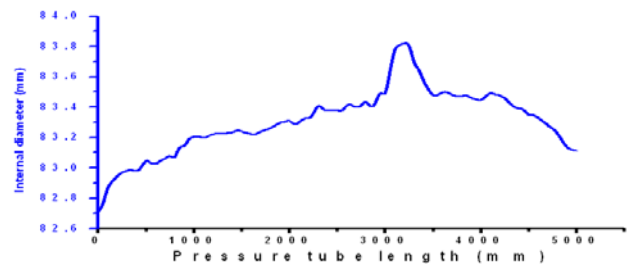


Fig. 5: Internal diameter variation along the irradiated pressure tube

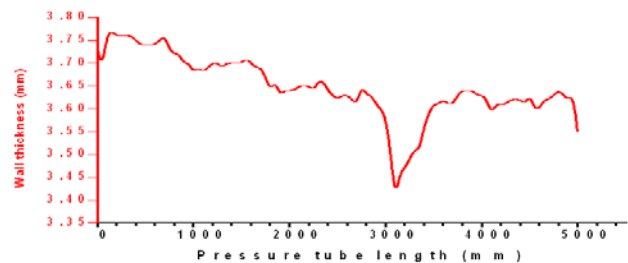


Fig. 6: Wall thickness variation along the pressure tube

also observed in the pressure tube from inlet to outlet end (Fig. 6). A localized wall thinning is clearly seen in the same region (peak ID) on the pressure tube, around 3.2 meter from inlet end and spanning over 600 mm length. ID and WT both plotted together can be seen in Fig. 7 which shows the kink in ID, corresponding to the wall thinning. It was not clear whether the peak in ID and wall thinning were irradiation-induced or from the manufacturer's side, at the time of measurement.

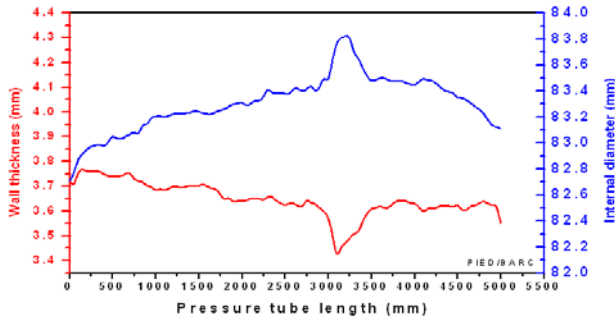


Fig. 7: Combined plot of internal diameter and wall thickness

Discussion

As fabricated ID were also plotted and compared with data generated during PIE. It is seen that as fabricated ID was on the upper end of specification as shown in Fig. 8. But, a slightly higher initial ID that is still within specified range, may not cause a localized peak in diameter creep. The increase in ID up to 0.9 mm does not account for so much wall thickness reduction due to creep, from constancy of volume consideration, unless a lower WT existed from the very beginning. The reason behind diametral creep is Hoop stress, which is determined not only by ID but also by WT.

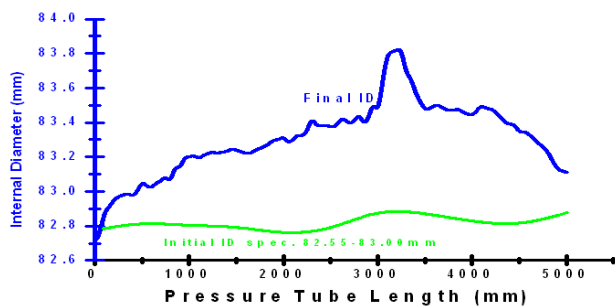


Fig.8: Comparison of as fabricated ID (green) and ID measured after 8 EFPY

There is thickness variation around the same circumference in the as-fabricated tube. The minimum WT value (3.452mm) available from the recorded data for this tube is in the central region, around 3.2 meters from the inlet end as shown in Fig. 9.

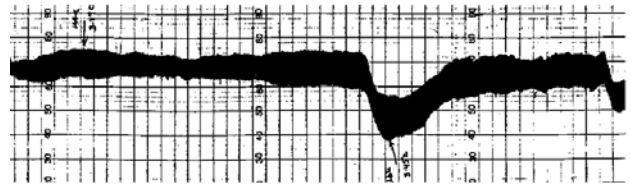


Fig. 9: As fabricated initial wall thickness chart

The level of hoop stress is determined dominantly by initial wall thickness than by initial diameter. It is the lower wall thickness from manufacturing, which raises the hoop stress deterministically and causes higher diametral expansion. As a result of which, the lower wall thickness region gets thinned down more, by in reactor creep. The initial lowest wall thickness 3.452 mm was further reduced to 3.4 mm, after 8.0 EFPYs of operation in the reactor core. The final wall thickness profile is the result of initial WT profile superimposed by thinning, due to addition of thermal and irradiation diametral creep, which is more from center to outlet end. Higher temperature and fast neutron flux enhance the diametral creep more towards outlet end.

Since, two wall thickness readings were available at the end of the diameter line, it was possible to calculate outer diameter as well. The wall thickness readings were added to the respective ID to get outer diameter. The difference between final ID & OD is not as much as that in initial ID & OD (Fig. 10).

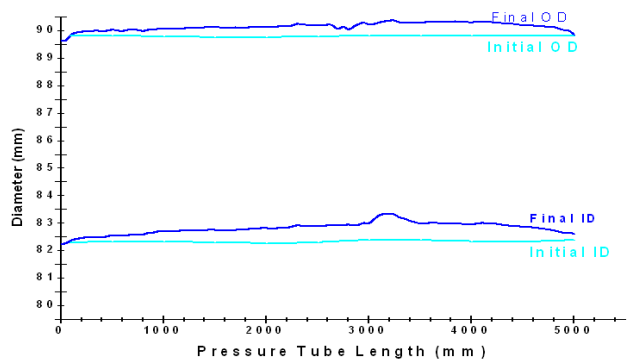


Fig. 10: Comparison of initial and final internal & outer diameters



This shows that outer diameter is not increasing as much as internal diameter, due to compensation by wall thinning. This information is useful for removable AHWR type pressure tube.

Conclusion

1. Ultrasonic testing technique has been developed and used, to measure simultaneously ID & wall thickness of irradiated pressure tubes, to evaluate the effect of hoop stress and irradiation on creep.
2. Measurement on irradiated pressure tube S-07, indicates a maximum diametral increase of 0.9 mm
3. Cold pilgering route of manufacturing gives thickness variation all along the pressure tube. At the location where minimum thickness occurred during manufacturing, higher hoop stress lead to enhanced diametral creep. The proper selection of thickness and control of its variation is very important.
4. The reason for localized enhanced diametral creep in S-07 pressure tube from KAPS-II is lower initial wall thickness, though it was under specified range of manufacturing.

at a location 3.2 meter from inlet end; where as tabrical lower wall thickness reduced further.



X-ray absorption Spectroscopy with Synchrotron Radiation

Dibyendu Bhattacharyya
Applied Spectroscopy Division

Dr. D. Bhattacharyya is the recipient of the DAE Scientific & Technical Excellence Award for the year 2009

Introduction

X-ray absorption spectroscopy (XAS) generally deals with measurement of absorption coefficient, as a function of X-ray photon energy, around an X-ray absorption edge of an element, in a material. X-ray absorption spectrum consists of two parts: (i) The spectrum near the absorption edge (viz., the X-ray near edge structure or the XANES part) gives information about the external perturbations in the valence states to which electrons make transitions from core levels, upon absorption of X-ray photon energy and hence can yield information regarding hybridization of orbitals in case of molecule or long range order existing in a crystalline sample, apart from the oxidation states of the absorbing atom in the material. (ii) The second part of the spectrum which extends from 50 eV to ~700 eV above the absorption edge, is generally called the Extended X-ray absorption fine structure (EXAFS) part, which is generally characterized by the presence of fine structure, oscillations and can give precise information regarding the short range order and local structure around the particular atomic species in the material. This determination is confined to a distance given by the mean free path of the photoelectron in the condensed matter, which is between 5-7 Å radius from the element. The above characteristic along with the fact that EXAFS is an element specific tool, makes EXAFS a powerful structural local probe. With the advent of modern bright Synchrotron radiation sources, this technique has emerged to be the most powerful local structure determination technique, which can be applied to any type of material viz.

amorphous, polycrystalline, polymers, surfaces and solutions. Furthermore, EXAFS does not require any particular experimental conditions, such as high vacuum and hence, samples of various physical forms can be adapted for measurements in the experimental stations [1-5].

Theoretical formulation

The X-ray absorption coefficient for an atom in the photon energy range of 1-100 keV is generally dominated by Photoelectric effect as shown in Fig.1, which is a monotonically decreasing function of energy, with several discontinuities known as absorption edges. These discontinuities occur when the energy of the incident photons equals the binding energy of different core levels of the atom and are classified with capital letters (K,L, M...) according to the principal quantum number of the core level ground state ($n = 1, 2, 3...$). The edge energy is characteristic of each atom. In the case of an isolated atom (monatomic gas), the absorption coefficient decreases monotonously between two subsequent edges. However, in a real material the spectrum always shows oscillations as shown in the inset of Fig. 1 for Ge K edge. An incident photon is able to extract a core electron, if its energy is equal to or greater than the edge energy. If the absorbing atom is isolated in space, the photoelectron propagates as an unperturbed isotropic wave, but in a real material since the absorber is surrounded by several neighbouring atoms, photoelectrons get backscattered and the final state of the photoelectron can be described, by

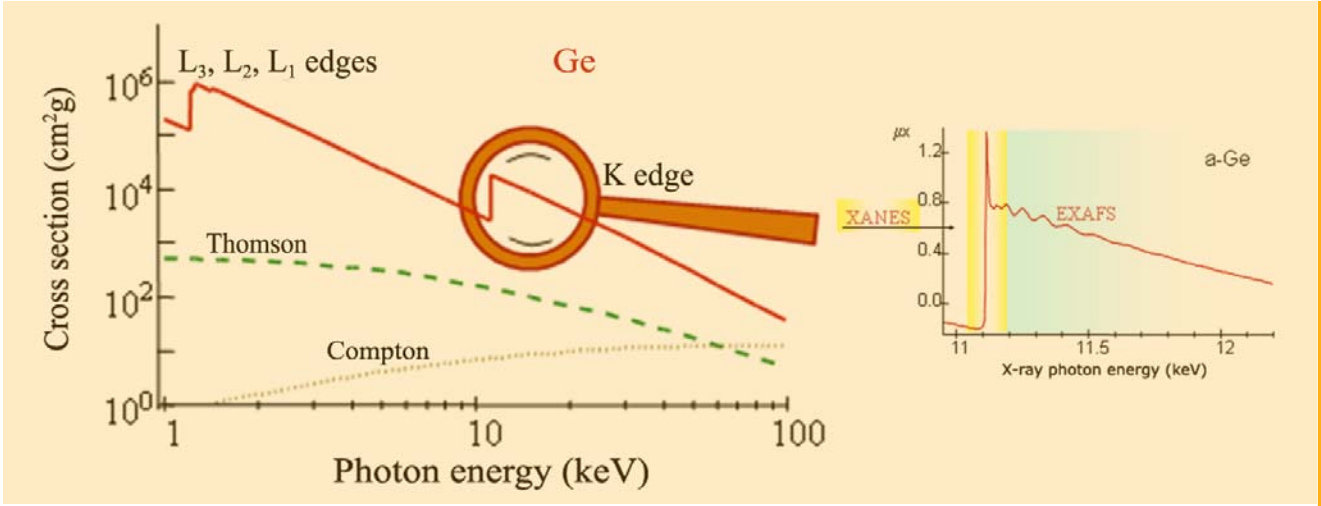


Fig. 1: K edge of Ge crystal with inset showing the fine structure oscillations

the superposition of the original and scattered waves. This leads to an interference phenomenon that modifies the interaction probability between core electrons and incident photons. Constructive interference increases while destructive interference decreases the absorption coefficient of the atom. This interference phenomenon, for a given energy of the photoelectron, depends on the distance between emitting and scattering atoms and their scattering strengths and coordination numbers.

Since the oscillations in the absorption spectra are important, the experimentally obtained μ versus E data is first plotted as $\chi(E)$ versus E , where $\chi(E)$ is defined as follows:

$$\chi(E) = \frac{\mu(E) - \mu_0(E)}{\Delta\mu_0(E_0)} \quad (1)$$

where, E_0 is the absorption edge, $\mu_0(E)$ is the bare atom background and $\Delta\mu_0(E_0)$ is the step in the $\mu(E)$ value at the absorption edge. The energy scale is also converted to the wave number scale k , given by:

$$k = \sqrt{\frac{2m(E - E_0)}{\hbar^2}} \quad (2)$$

$\chi(k)$ is weighted by k^2 to amplify the oscillations at high k and finally the $\chi(k)k^2$ versus k spectra is Fourier transformed to generate the $\chi(R)$ versus R spectra in terms of real distances from the centre of the absorbing atom.

Under the dipole approximation, an analytical expression of the EXAFS signal can be derived as follows [6]:

$$\chi(k) = \sum \frac{N_j f_j(k) e^{-2k^2 \sigma_j^2} e^{-\frac{2R_j}{\lambda}}}{kR_j^2} \sin[2kR_j + \delta_j(k)] \quad (3)$$

where, N_j is the number of j th neighbours of the absorbing atom sitting at a distance of R_j , having a scattering amplitude of f_j and creates a phase change of δ_j as the photoelectron get scattered by its potential. The term σ_j represents the fluctuation at the atomic positions (having both structural as well as thermal effect) and λ is the mean free path which determines the probability of the scattering photoelectron to come back at the absorber, after being backscattered by the neighbour.

Different relevant parameters from the EXAFS signal are determined by fitting the experimental EXAFS spectra with the above theoretical expression. The amplitude, distance, phase and degeneracy of the different contributions corresponding to different interactions (nearest neighbour and further interactions), are used as fitting parameters



for fitting the experimental data. Different codes for EXAFS data analysis programme are available among which, IFEFFIT package is mostly commonly used [7].

Experimental methods

The most important experimental requirement to carry out EXAFS measurements is a continuous X-ray source of high intensity and only Synchrotron radiation sources match this criterion. EXAFS measurements with synchrotron radiation are generally carried out in two different modes viz., scanning and dispersive. In the scanning mode, the experimental arrangement (generally called a beamline) uses a Double-Crystal-Monochromator (DCM) to select a particular energy from the incident synchrotron beam, which is then made incident on the sample and the intensity of the transmitted beam passing through the sample, or that of the fluorescence beam emerging out of the sample, is recorded with suitable detectors along with the incident intensity at each energy, by scanning the DCM crystals. In the dispersive mode, a bent crystal polychromator is used to select a band of energy from the white synchrotron beam, which is horizontally dispersed and focused on the sample. The transmitted beam intensity from the sample is recorded on a position sensitive CCD detector, thus enabling recording of the whole EXAFS spectrum around an absorption edge in a single shot. At INDUS-2 Synchrotron radiation source a RRCAT, Indore, a dispersive EXAFS beamline is already commissioned and operational [8,9] and another Scanning type EXAFS beamline will be commissioned soon.

References

1. N. C. Das, N. K. Sahoo, D. Bhattacharyya, S. Thakur, N.M. Kamble, D. Nanda, S. Hazra, J. K. Bal, J. F. Lee, Y. L. Tai and C. A. Hsieh, *J. Appl. Phys.* 108 (2010) 023515.
2. D. Lahiri, R. Ningthoujam, D Bhattacharyya and S. M. Sharma, *J. Appl. Phys.* 107 (2010) 054316.
3. K. Bhattacharyya, S. Varma, A.K. Tripathi, D. Bhattacharyya, O. Mathon and A.K. Tyagi, *J. Appl. Phys.* 106 (2009) 093503.
4. A.K. Bakshi, S.N. Jha, L. Olivi, D.M. Phase, R.K. Kher and D. Bhattacharyya, *Nuclear Instruments Method. in Phys. Res. B* 264 (2007) 109.
5. D. Bhattacharyya, A. K. Bakshi, G. Ciatto, G. Aquilanti, A.S. Pradhan and S. Pascarelli, *Solid State Communication*, 137 (2006) 650.
6. *X-Ray Absorption: Principles, Applications, Techniques of EXAFS, SEXAFS and XANES*, edited by D.C. Konigsberger and R. Prince (Wiley, New York, 1988).
7. M. Newville, B. Ravel, D. Haskel, J.J. Rehr, E.A. Stern, and Y. Yacoby, *Physica B* 154, 208 (1995).
8. D. Bhattacharyya, A.K. Poswal, S.N. Jha, Sangeeta and S.C. Sabharwal *Nuclear Instruments Method. in Phys. Res. A* 609 (2009) 286.
9. Abhijeet Gaur, B. D. Shrivastava, D. C. Gaur, J. Prasad, K. Srivastava, S. N. Jha, D. Battacharyya, A. Poswal and S. K. Deb, *Journal of coordination Chemistry*, 64 (2011) 1265.



Deployable Process Development in the Back-end of the Fuel Cycle: Spent Solvent Management & Actinide Partitioning of HLLW

Smitha Manohar and P.K. Wattal

Process Development Division

Ms. Smitha Manohar is the recipient of the DAE Scientific & Technical Excellence Award for the year 2009

Abstract

Conversion of process developmental activities into a deployable technology, for the back-end of the fuel cycle, calls for a multi-disciplinary set of activities culminating in demonstration of the process using actual waste, before it gets adopted for regular processing. The successful operation of the spent solvent management facility at ETP, Trombay and setting up of another such facility at Tarapur, is one example of many such efforts carried out at NRG. An integrated approach has also led to the setting up of the Actinide Separation Demonstration Facility (ASDF) at Cell 4, SSSF Tarapur for High Level Liquid Waste (HLLW) of PHWR origin. Operational experiences of this facility are expected to serve as useful inputs, towards designing such facilities in the future.

Introduction

Radioactive waste management being a case of sustainable development, there is enough scope for upgrade of technology on one hand and development & induction of cross-cutting technologies on the other, leading to a positive impact on the environment in terms of smaller waste volumes for disposal and lower discharges to the environment. Among the processes and technologies that have been developed in-house and have been adopted on plant-scale is the Spent Solvent Treatment Facility set up and operated at BARC. Another example is a facility for demonstration of partitioning of actinides from HLW, including recovery of Uranium as a value resource & partitioning of Minor Actinides from HLW set up at, SSSF, Tarapur which is presently under commissioning. A spent solvent management facility has been integrated with the actinide separation facility, to address the spent solvents

stored at Tarapur and those generated from the operations of the actinide partitioning facility.

Spent Solvent Management

Spent solvents of reprocessing origin (30% TBP in n-paraffin) constitute a major portion of radioactive liquid organic wastes, arising from nuclear activity. An in-depth study of this waste stream has led to the evolution of a complete management option, which addresses not only the concern of radioactivity but also its organic nature. This is based on alkaline hydrolysis of TBP¹, which converts it into aqueous soluble products, viz. sodium salt of dibutyl phosphoric acid and butanol. During the process of alkaline hydrolysis, almost all the activity associated with the waste gets transferred into the aqueous phase. The recovered diluent virtually free of activity and TBP can be recycled, and in case of it not meeting reprocessing



standards, can be incinerated. The process generated aqueous waste is found compatible with cement and can be immobilized in cement matrix. Fig. 1 depicts the operating screen at ETP, Trombay showing the overall process schematic.

The simplicity of the alkaline hydrolysis process made it an obvious choice for future spent solvent management plants. Its capability to render the diluents, free of TBP

and activity has been well recognized. However, the process suffers from a drawback of producing almost equal volumes of secondary aqueous waste that contains almost all the activity associated with spent solvents. Immobilizing these secondary wastes in cement matrix, leads to an increase in waste volume for final disposal. The question of managing this bottom phase would determine the sustainability of alkaline hydrolysis process for spent solvent management. Enough incentive therefore

exists to carry out further research so as to minimize these waste volumes for final disposal. Long stored spent solvents have been observed to have very low levels of beta-gamma activity and some alpha contamination. For such wastes, it makes sense to concentrate the activity several times, so as to minimize secondary waste volumes. Efforts were therefore undertaken to study the recyclability of the aqueous bottoms². The experimental result for modified alkaline hydrolysis process with NaOH recycle, is shown in Fig. 2. A modified flow sheet has therefore been developed for spent solvents presently stored at Tarapur, addressing recycle, of unreacted alkali & bringing the bulk of the secondary waste to dischargeable limits. This can have a substantial impact on the waste volumes to be immobilized in cement based matrices.

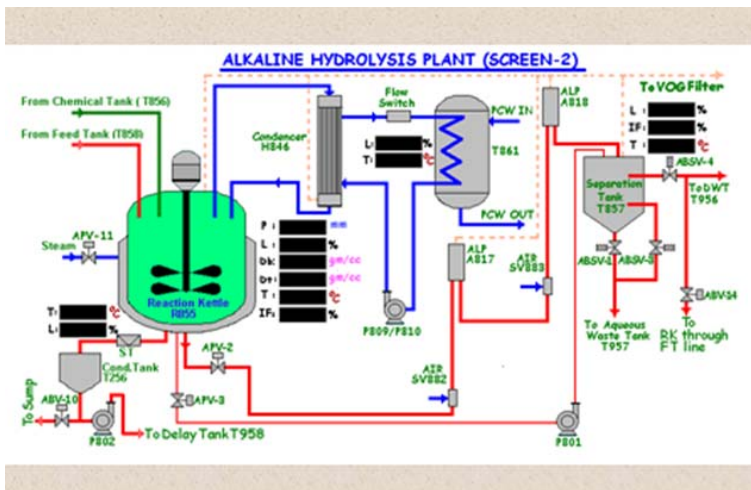
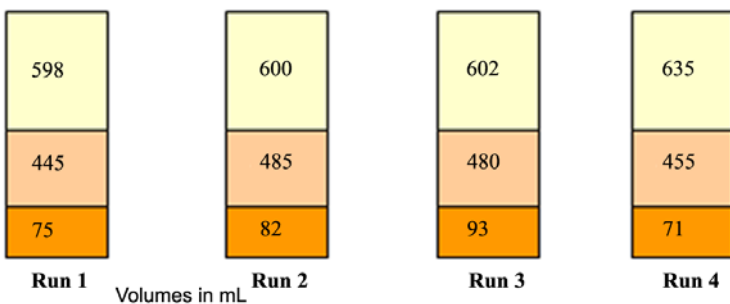


Fig. 1: Schematic for alkaline hydrolysis facility

- Activity associated with feed α : 88Bq/ML γ : 158 Bq/mL
- 4 repeat runs using same waste and recycled bottom phase were carried out using 1 L waste and 200 mL (11 M) NaOH



Top Dodecane (~600 mL) α : BDL γ : 2Bq/mL Recovery/incineration	Middle NaDBP (~500 mL) α : BDL γ : 70-200 Bq/mL For Discharge with Dilution	Middle Butanol (160 mL) α : BDL γ : 2 Bq/mL Incineration	Bottom NaOH phase (85-90 mL) ** α : 4255 Bq/mL γ : 6678 Bq/mL ** Recycled in run 1-4 ** For Immobilization after 4 th Run/actinide recovery
--	--	---	--

Fig. 2: Results of the modified alkaline hydrolysis process

R&D Programme for actinide partitioning of high level liquid waste

A structured R&D framework is being pursued, to develop and deploy processes & technologies for actinide partitioning of HLLW. One of the most defining steps in this programme, is selection of potentially successful extraction system, based on the systematic study on extraction properties and their optimization for full scale studies³. Design of appropriate contacting devices & equipment for in-cell application, along with its evaluation, calls for a second important set of activity. Performance

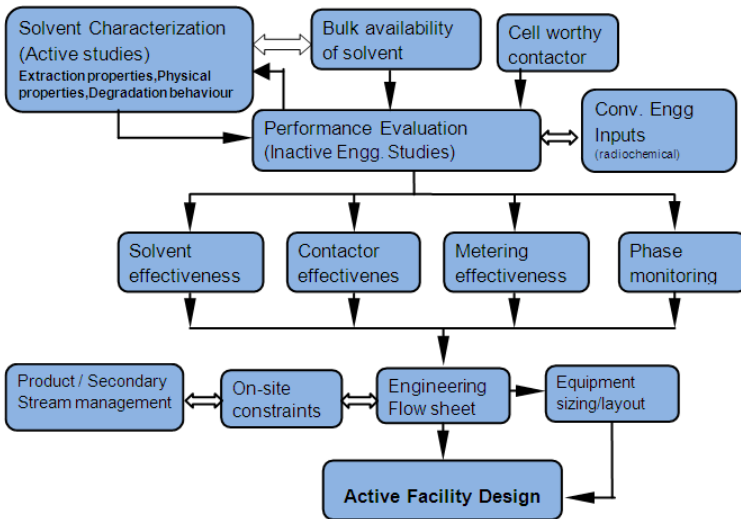


Fig.3: Overall R&D Programme for Actinide Partitioning from HLW

Table 1: Extraction and Stripping Results of CMPO & TEHDGA solvent system

Element	CMPO (0.25 M CMPO + 1.2 M TBP in n-dodecane)		TEHDGA (0.2 M TEHDGA in n-dodecane with iso-decyl alcohol)	
	% Extracted A/O (1:1)	% Stripped A/O (1.25:1)	% Extracted A/O (2.5:1)	% Stripped A/O (1.25:1)
Ln	97.58	99.60	97.27	99.71
Ce	98.45	~100	99.72	~100
Mo	88.31	95.68	16	94.56
Ru	20.0	~100	15	~100
Sr	NA	NA	3.0	94.85

Aq. Simulated HLW with acidity of 4 M
 Aq. Flow rates(Aq) : 30LPH
 No. of stages: Extraction - 5 Stages & Stripping - 5 Stages

evaluation of the selected contactors with the solvent system, provides the basis for the engineering flow sheet design, for such a process (Table 1). Efforts have also been directed towards identification of the various secondary streams, that would emanate out of such a facility along with their storage and management. Fig. 3 gives the overall R&D objectives for such a programme.

Technology demonstration of actinide partitioning with real HLLW

Technological demonstration of the partitioning of HLLW from PHWR waste, could serve to be a benchmark for the adoption of this process for all future plants. With this objective, an "Actinide Separation Demonstration Facility" (ASDF) is being set-up at Cell 4, SSSF, Tarapur, to demonstrate the bulk separation step and also with provision to try out group separation⁴. This facility has been designed as per the conventional basis of design of a radiochemical plant. Engineering results of this facility will serve as useful inputs, for design of partitioning facilities for its adoption. Fig. 4 shows a photograph of the facility and Fig. 5 depicts a live control room screen for this facility.

This facility has been designed with dedicated and well engineered provisions, for separately demonstrating the stepwise partitioning of minor actinides. The throughput of this facility is expected to match the vitrification capacity of about 30 l/hr. In addition to being adequately instrumented to measure engineering scale parameters such as flow rates, level, density,

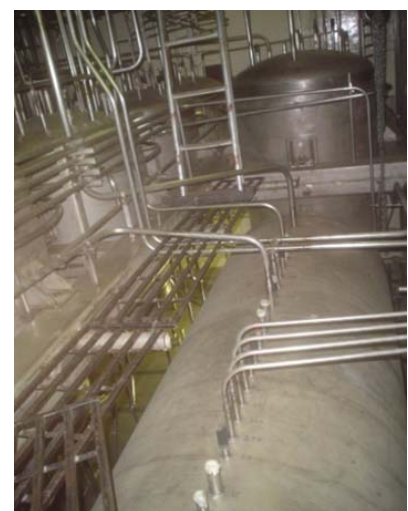


Fig. 4: Actinide Separation Demonstration Facility

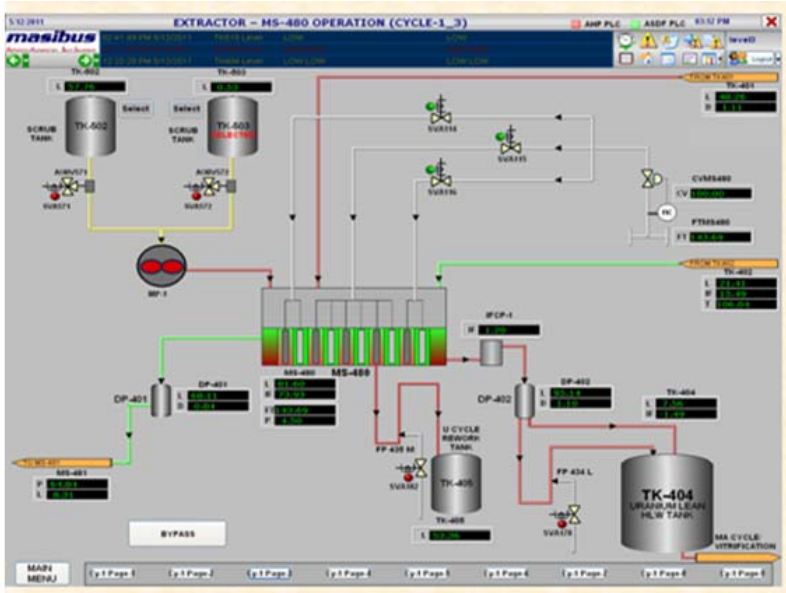


Fig. 5: Control room screen for ASDF

interface and temperature, this facility has provision to manage all primary and secondary streams that are expected to emanate from the processes. The spent solvent management facility has been integrated with the ASDF, for managing the spent solvents emanating out of this facility.

References

1. Smitha Manohar, C.Srinivas, M.P.Dandekar, S.Y.Bakre, D.S.Deshingkar, and P.K.Wattal "Organic Radioactive Waste Treatment Methods" Book on Nuclear Fuel Cycle Technologies- closing the fuel cycle, 2006, BRNS
2. Smitha Manohar, K. N. Kutty, D.S. Deshingkar and P. K. Wattal 'Minimization of Secondary Waste during the Alkaline Hydrolysis Process for treatment of Spent Solvent', SESTEC 06.
3. Smitha Manohar, 'Technological Development for Partitioning of High Level Liquid Waste: An Engineering perspective' invited talk in SESTEC-10.
4. Smitha Manohar, J.N.Sharma, B.V.Shah, P.K.Wattal 'Process Development for Bulk Separation of Trivalent Actinides and Lanthanides from Radioactive High level Liquid Waste', Vol 156, No 1 May 2007, Nuclear Science & Engineering, American Nuclear Society.



Development of high performance electro hydraulic servo linear actuators

Ramakrishna P., Shiju Varghese, Jay shah & N.L. Soni

Fluid Power and Tribology Section
Refuelling Technology Division

Mr. Ramakrishna P. is the recipient of the DAE Young Applied Scientist and Technologist Award for the year 2009

Abstract

Conventional hydraulic linear actuators cannot be used in demanding applications like seismic shake table and material testing, as these require good precision and high bandwidth actuators. For indigenous development of such actuators, improvements such as hydrostatic bearings, advance control algorithms, indigenous digital controller and hydraulic system improvements, were incorporated in hydraulic linear actuator. Performance of these actuators was demonstrated to the user by setting up a single degree of freedom shake table on a test bench. The developed actuators have a resolution of 5 micron and flat response up to 50 Hz in bode plot. These special actuators also have many other industrial applications like hydraulic manipulator, special press etc.

Introduction

High performance Electro Hydraulic Servo Linear Actuators (EHSLAs) have been developed. Innovative techniques were employed in electro hydraulic servo linear actuators to improve their characteristics in static and dynamic conditions. These actuators have demonstrated high fidelity reproduction of earthquake time history, in a single degree of freedom (DOF) on a test bench and using the same type of actuators, indigenous development of six degree of freedom 5 Ton shake table is in progress.

Various improvements in the development of high performance electro hydraulic servo linear actuators are:

Hydrostatic bearings

Coulomb friction in conventional hydraulic actuators easily reaches from 5% to 15% of the maximum load capacity

which not only reduces the force generated, but also reduces the control accuracy and bandwidth of hydraulic actuators. For accurate control of acceleration, friction should be minimized. Hydrostatic bearings keep the piston floating in the cylinder, thus minimizing coulomb friction and improving the performance of the hydraulic actuator.

Several Frictionless Hydraulic Linear Actuators (FHLAs) were fabricated with strict inspection on dimensions and assembled in clean environment. An experimental test facility was built and the frictionless condition using hydrostatic bearing (Fig.1) was demonstrated. Since no elastomeric seal was used, excellent dynamic response was achieved.

Advance control algorithms

Band width obtained by simple proportional controller is limited. A better approach to obtaining a fast response, is

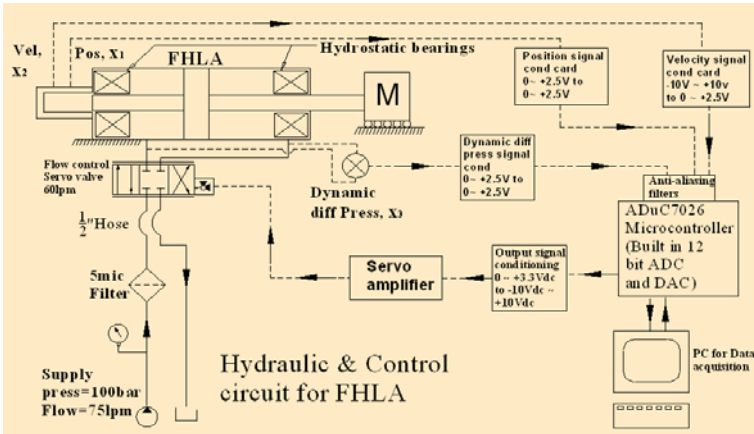


Fig. 1 : Schematic of hydraulic and control system

to model the dominant dynamics of the system and use this knowledge of the dynamics in the controller design. The fifth order state space model of EHSLA was developed, starting from the first principles and it was validated with experimental results. To overcome the limitations of proportional controller, State feedback controller, Fig. 2 was designed using Eigen value map and implemented in

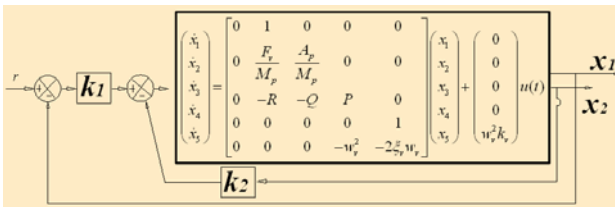


Fig. 2: State feedback control

EHSLA. In the Eigen value map, the uncontrolled movement of complex poles due to servo valve dynamics in a simple proportional controller, was overcome in state feedback controller. For state feedback control, various sensors (Fig.1) were used to measure three states (displacement of piston, velocity of piston & dynamic differential pressure across piston) of hydraulic actuator. For a step response (Fig. 3) a close match obtained between theoretical prediction (continuous blue line) and experimental results (red plus sign) can be clearly seen for displacement, velocity, dynamic differential pressure and control output of servo hydraulic actuator. State feedback controller improved the bandwidth of EHSLA to 40Hz

with a position resolution of 5 micron. In-house developed servo-controller card 42MHz, 32 bit ARM processor with RS232 Interface, 12 Bit 1MSPS ADC & DAC, EEPROM 62KB and digital controller, currently running at 1KHz, was used. Advanced control algorithm was developed in-house and programmed into these controllers. Further improvement in the bandwidth was attained by use of pole placement compensator. The design of compensator was carried out in SISOTOOL of MATLAB. In the Eigen value map, the undesired poles of the servo actuator were compensated by zeros of the controller. This

optimized compensator was discretised as seen in Fig. 4 and loaded in digital controller. The improvement of its performance (-3dB at 56Hz) was experimentally

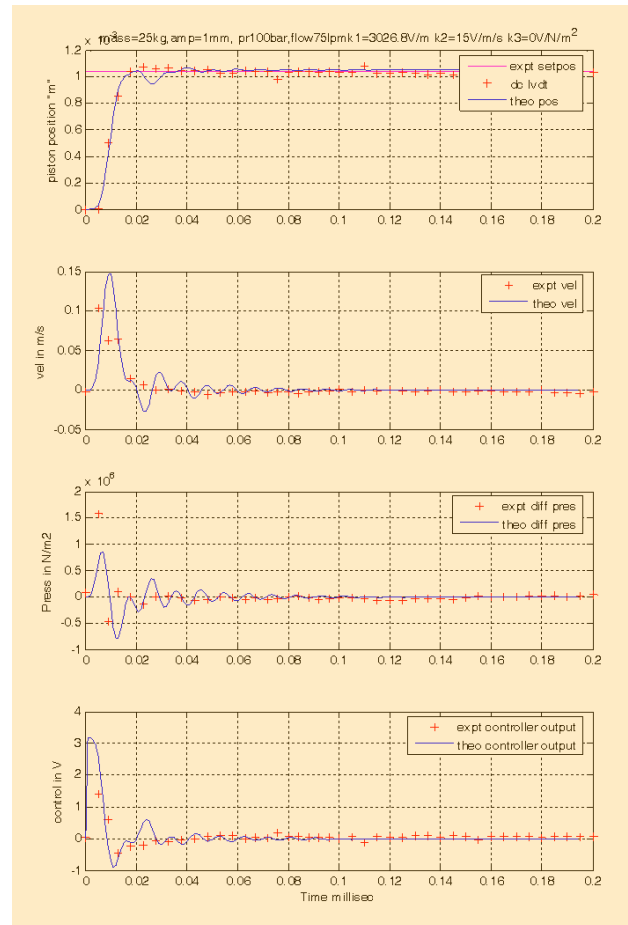


Fig. 3: Variation of states for velocity feedback in proportional control

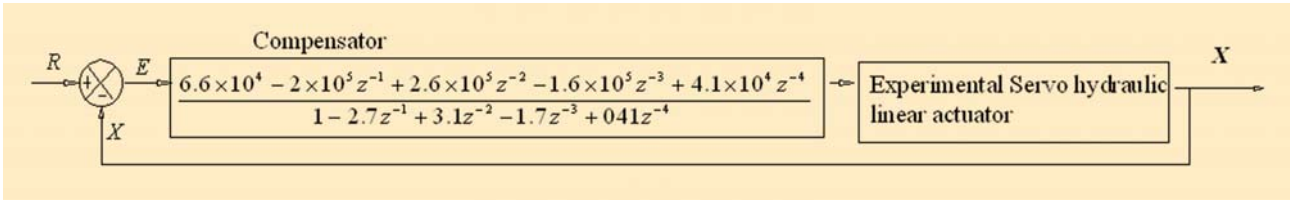


Fig.4: Discrete pole placement Compensator

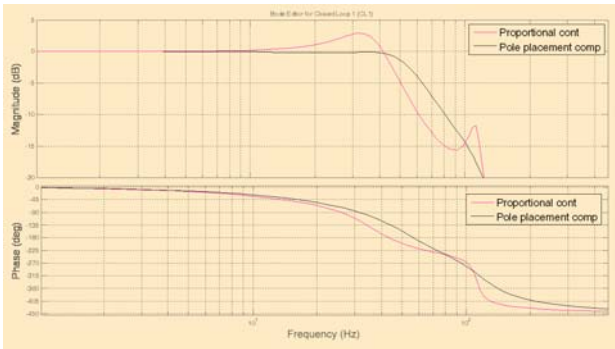


Fig.5: Bode plot analysis of proportional controller & pole placement compensator

demonstrated. In the bode plot, Fig. 5 peaking observed in proportional controller is due to undesired poles of servo valve. The improved performance can be clearly seen in bode plot of pole placement compensator, where the reduced damping due to undesired poles of servo valve have been compensated.

Hydraulic system improvements

It is very important to supply clean, cool and pressurized hydraulic fluid to the EHSLA. This is provided by hydraulic power supply system. To achieve and maintain the above performance of EHSLA, it is required to maintain NAS5 cleanliness hydraulic oil (ENKLO-68) and increase the effective bulk modulus of fluid.

In addition to use of 3 micron mechanical filter in hydraulic power supply system, electrostatic oil cleaner and magnetic filter were

used. Mechanical filter is effective in removing particles greater than 5 microns whereas electrostatic oil cleaner is effective in removing particle lesser than 5 microns. Ferrous and other magnetic particles are removed by magnetic filter. To monitor the actual cleanliness achieved by the above filtration system, automatic particle counters were used and ferrography was used for qualitative analysis of hydraulic system Fig. 6 Hydraulic power pack & Condition monitoring system. Air present in hydraulic oil reduces the effective bulk modulus which directly influences the natural frequency of EHSLA. Effective bulk modulus of hydraulic oil was improved, by removing air from oil, by degassing using vacuum degassing unit specially developed for this purpose in FPL.

Shake table on test bench

Using the above improvements, EHSLA as a drive of single degree of freedom shake table, (Fig. 6) was successfully demonstrated for the user, by subjecting it to design response spectra compatible time history. The EHSLA with the advanced control algorithm faithfully reproduced time

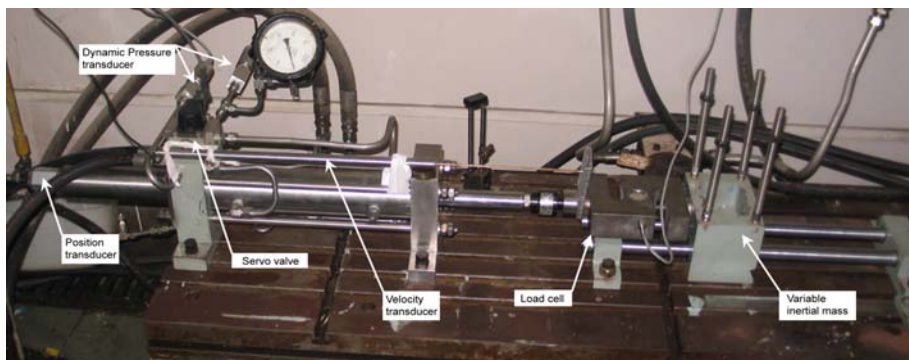


Fig.6: Single DOF shake table on test bench

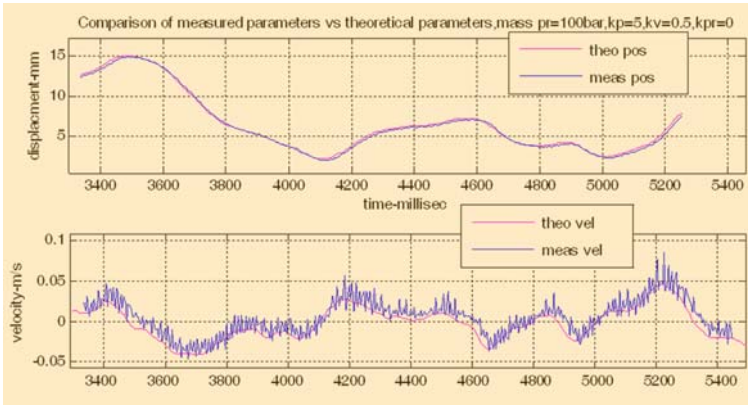


Fig.7: Displacement and velocity profile

histories in displacement and velocity, (Fig. 7) and proved that, EHSLA with indigenous servo controller card is capable to be used as a drive for a shake table. Its performance was better than imported counterparts.

Conclusion

Indigenous electro hydraulic servo linear actuators have been developed for demanding applications like seismic shake table meeting good precision and high bandwidth requirements, by incorporating many improvements in servo hydraulic actuators. Dominant dynamics of the EHSLA was modelled, advance control algorithms –state feedback controller and pole placement compensator were designed and implemented in indigenous servo controller cards. Performance of these actuators was demonstrated by qualifying them on a single degree of freedom shake table. Since these servo actuators have flat response till 50Hz in bode plot, they can give high fidelity reproduction of earthquake time histories.

DAE Excellence Award



Indigenous development of online radon and thoron monitors for applications in Uranium mining and Thorium processing facilities

J.J. Gaware, B.K. Sahoo, B.K. Sapra and Y.S. Mayya

Radiological Physics and Advisory Division

Shri B.K. Sahoo & Shri J.J. Gaware are the joint recipient of the DAE Young Applied Scientist & Technologist Award for the year 2009

Abstract

Using the conventional ZnS(Ag) detector, two different continuous radon monitors and an online thoron monitor have been developed, for application in underground U mine and thorium processing plant respectively. Special features of these monitors include low cost, high sensitivity and non-interference of humidity and trace gases. The capability of the radon monitor in networked radon monitoring in U mines, has been demonstrated. The thoron monitor is designed for stack monitoring of thoron release, in a thorium processing facility. Being highly sensitive, these monitors can also be used for environmental studies such as emission measurement from soil, building materials, thorium powders and monazite sands in High Background Radiation Areas. These indigenous monitors have the potential to serve as import substitutes for the Indian radon/thoron research programmes.

Introduction

The measurement of radon in air, is primarily based on the detection of alphas from radon and its decay products. Measurement could either be passive time-integrated or active measurement through grab or continuous sampling radon (Lucas, 1957; Abbady et.al., 2004). Time-integrated measurement of radon is mainly limited to dosimetric applications, where as-continuous measurement yields insight into spatio-temporal correlations, build-up in confined spaces, hourly variations induced by pressure and temperature variations, atmospheric transport, extreme excursions, duration of specific highs and lows etc. While increased computational capabilities on environmental modeling have given rise to greater needs for real time data, the corresponding developments in networking and data transmissions have made it possible, to achieve large scale simultaneous measurements. Such facilities are being

increasingly developed as part of systems for earthquake predictions, in uranium mining, for environmental monitoring and geophysical research. Apart from these general applications, monitoring radon concentrations in Uranium mining and thorium processing facilities is important in evolving effective strategies to reduce radiation doses to occupational workers. With this in view, automatic online radon and thoron monitors have been developed as detailed in the following sections.

Description of systems

Online Radon Monitor

Using an innovative algorithm developed for correlating the total counts with the radon concentration, two versions of radon monitor have been developed. The portable version called SRM (Scintillation Radon Monitor), utilizes



a ZnS:Ag based scintillation cell for measurement of alpha from radon and its decay products. The other version named ECAS (Electrostatic Collection and Alpha Scintillation) is developed using an electrostatic chamber for collecting the charged decay products of radon on the ZnS:Ag surface. The details are as follows:

Portable Radon Monitor - SRM

The schematic of the microprocessor based SRM and its photograph are shown in Fig. 1a and Fig. 1b respectively. Radon is sampled into the scintillation cell (150 cc) through a "progeny filter" and "thoron discriminator" eliminating radon progenies and thoron gas respectively. The thoron discriminator based on "diffusion-time delay" does not allow the short lived thoron ^{220}Rn (half life 55.6 sec) to pass through. The alpha scintillations from radon and its decay products formed inside the cell, are continuously counted for a user-programmable counting period by the PMT and the associated counting electronics. The alpha counts obtained are processed as per the developed algorithm, to display the concentration of radon. Considering the limitations on the range of the alpha particles (~6 cm), the dimensions of the scintillation cell were optimized to achieve high sensitivity (1.2 cph/Bqm^{-3}) with lower detector volume (150 cc). This configuration is very useful for measurement of mass exhalation and surface exhalation of radon from various naturally occurring radioactive materials.

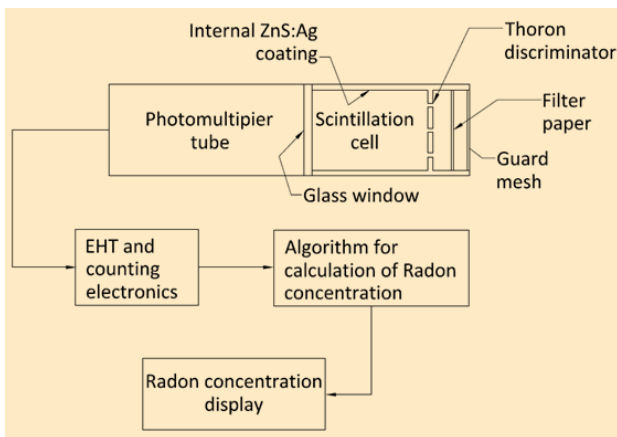


Fig.1a: Schematic diagram for Portable Radon Monitor (SRM)



Fig.1b: Photograph of Portable Radon Monitor (SRM)

High Sensitivity Radon Monitor - ECAS

The low range of the alpha particles (~ 6 cm), makes it difficult to enhance the sensitivity of the SRM monitor, by just increasing the volume of the scintillation cell. Hence, an electrostatic collection technique for charged decay products of radon, on the ZnS:Ag scintillator has been used. The schematic and the photograph of ECAS are shown in Fig. 2a and Fig. 2b respectively. As in SRM, the sampling of radon into the detector volume (1000 cc) is carried out by diffusion, through "progeny filter" and "thoron discriminator" in succession. The electric field for various detector geometries and dimensions were modeled using commercial software and the optimal field with this simple-to-fabricate cathode and anode design was obtained. Accordingly, an electrical potential

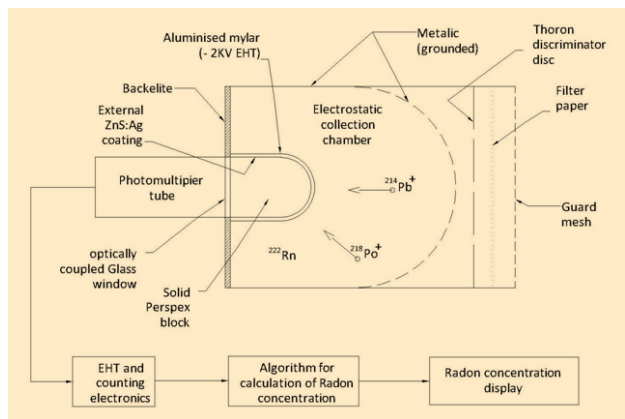


Fig. 2a: Schematic diagram for high sensitivity radon monitor (ECAS)

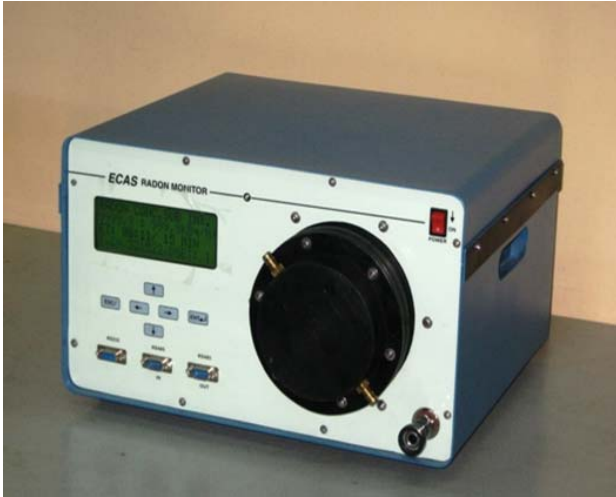


Fig. 2b: Photograph of high sensitivity radon monitor (ECAS)

of -2 KV is applied to an aluminized mylar ($12\mu\text{m}$ thickness) covering the ZnS:Ag scintillator coated on the cathode, which is a solid perspex cylindrical block with a hemispherical head. The alpha scintillations produced by ^{222}Rn , ^{218}Po and ^{214}Po are detected by the PMT and the associated counting electronics. The alpha counts obtained are processed by a microprocessor unit, to display the concentration of radon.

Online Thoron Monitor

The indigenously developed, microprocessor-based thoron monitor consists of two Lucas Scintillation Cells (LSCs) which are coupled to a separate photomultiplier tube with associated pulse preamplifier and scalar. Its schematic diagram and photograph are shown in Fig. 3a and Fig. 3b respectively. The LSC is a 2" dia and 3" height cell, made of S.S. 316 material with two inbuilt levels of radon-thoron progeny pre-filters for reducing background contamination. The flow to either of the LSCs is switched by the microprocessor at the intervals specified through programmable parameters. During each interval, while one cell counts the background, the other cell measures counts due to both thoron and the background activity. The unit automatically calculates and logs the thoron concentration data in the memory.

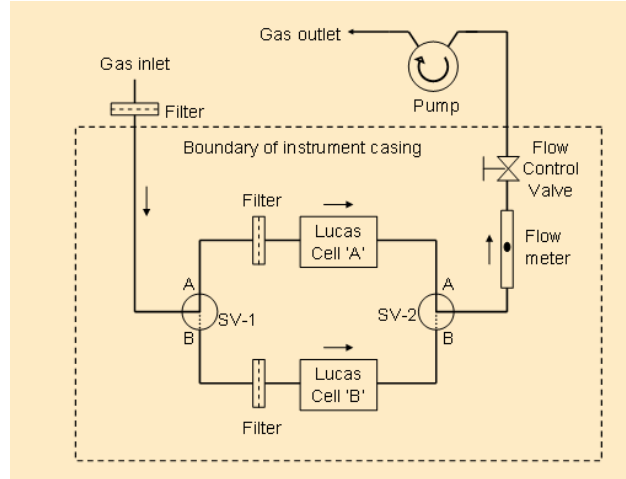


Fig. 3a: Schematic diagram for online thoron monitor



Fig. 3b: Photograph of online thoron monitor

Performance evaluation

Various tests were carried out under controlled conditions in a chamber, to evaluate the performance of the monitors. The first set of experiments was carried out, to compare the measurements of online radon monitors against the commercially available system AlphaGUARD. A fair agreement was seen between ECAS, SRM and AlphaGUARD as shown in Fig. 4. Similarly, measurements with the indigenous thoron gas monitor were compared with that obtained using the commercial unit RAD-7 (Fig. 5). Since the background is high at higher thoron concentrations, the thoron monitor is tested upto



2 MBq/m³. For both the monitors, the variations were within 3%.

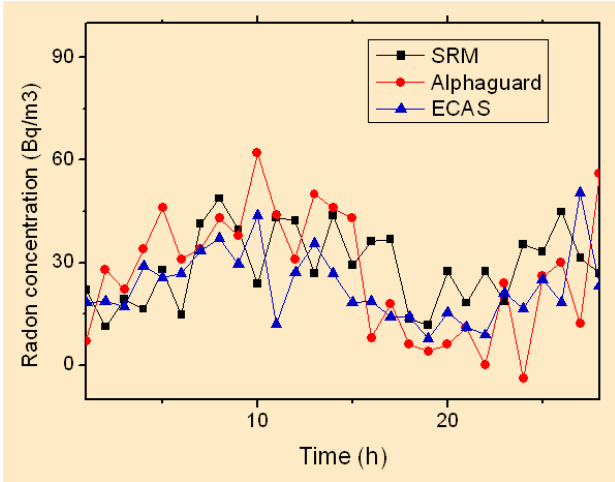


Fig.4: Comparison of radon measurements by SRM and ECAS against AlphaGUARD

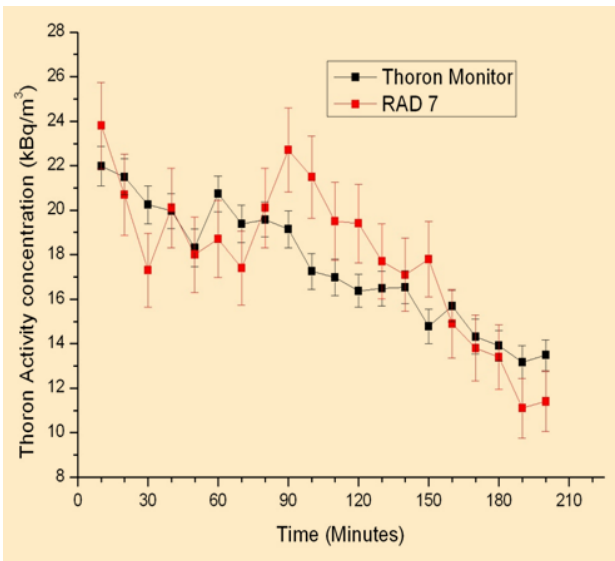


Fig.5: Comparison of measurements of Thoron monitor with RAD7

Applications of radon monitor

Features such as uninterrupted online operation, high sensitivity and free from humidity/ trace gas interference, open up diverse applications in radon and thoron studies. These include calibration of passive detector systems, indoor/outdoor radon monitoring, network-based online radon monitoring in workplaces such as underground uranium mines, radon emission studies from soil/water/

building materials, field survey and site monitoring such as uranium tailings pond. Some of the potential applications have been demonstrated below.

Measurement of radon emission from soil and building materials

We have demonstrated the use of ECAS for measuring the rate of radon emission from soil, using the “accumulator” technique. The soil is covered with the accumulator and the radon build up in it is monitored, using ECAS connected in a closed loop with an external pump. The buildup data is fitted to an appropriate model, to extract the radon emission rate from soil. For the experiment conducted in an open ground (Fig. 6), the accumulator technique (Sahoo and Maya (2010)) gave



Fig. 6: Measurement of radon emission from soil using SRM



Fig. 7: Measurement of radon emission from a cement sample using ECAS

DAE Excellence Award



the radon emission rate as $80 \text{ Bq m}^{-2} \text{ h}^{-1}$, close to the value obtained using RAD-7. Since building materials are the second most important source of radon, ECAS was also used, to measure radon emission from cement samples (Fig. 7) according to the measurement procedure (Sahoo et al. (2007)). The emission rate was found to be $7.2 \text{ mBq kg}^{-1} \text{ h}^{-1}$.

Networking in Uranium mines at Turamdih - field trial

The networking capability with fast response of ECAS is useful for monitoring uranium mines and tailings pond, to give real-time spatial profiles of radon. In this context,

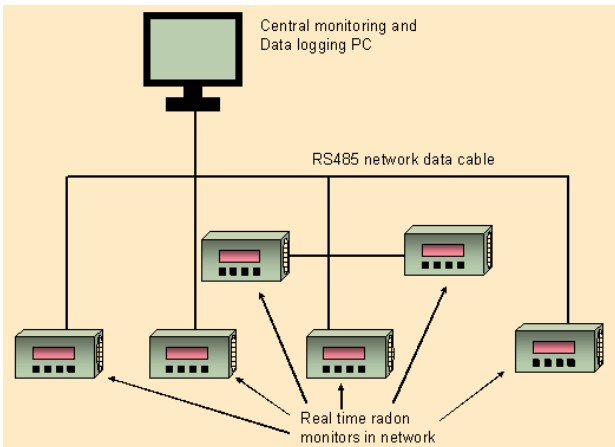


Fig. 8: Schematic diagram of Radon monitoring network at Turamdih U Mines

few online monitors were installed inside the uranium mines (Fig. 8) at locations where the concentration of radon is expected to be high. Results of the measurements are shown in Fig. 9.

Acknowledgements

The authors would like to thank Sh. H.S. Kushwaha, Ex-Director, HS&EG and Dr. A.K. Ghosh, Director, HS&EG, BARC, for their constant encouragement and support towards this work.

References

1. Abbady A, Abbady AG, Michel R., Indoor radon measurement with the Lucas cell technique, *Appl Radiat Isot.*, 61(6) (2004):1469-1475.
2. Lucas F.H. Improved low-level alpha-scintillation counter for radon. *Rev. of Sci. Inst.*, 28 (1957): 680-683.
3. Sahoo BK, Mayya YS. Two dimensional diffusion theory of trace gas buildup in soil chambers for flux measurements. *Agric. and Forest Meteorol.* 150 (2010):1211-1224.
4. Sahoo BK, Nathwani D, Eappen KP, Ramachandran TV, Gaware JJ, Mayya YS. Estimation of radon emanation factor in Indian building materials, *Rad. Meas.* 42 (2007): 1422-1425.

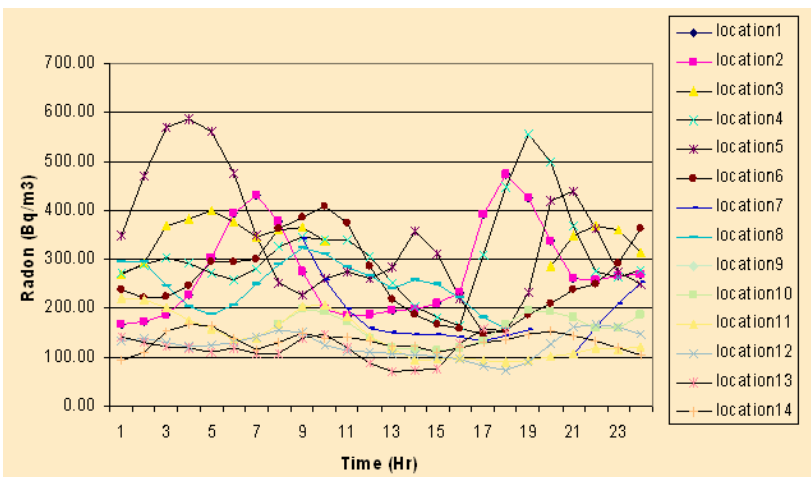


Fig. 9: Radon levels monitored at various locations inside Uranium mines



Copper-curcumin complexes as superoxide dismutase (SOD) mimic: Structure activity relationship

Atanu Barik

Radiation & Photochemistry Division

Dr. Atanu Barik is a recipient of the DAE Young Scientist Award for the year 2009

Abstract

Copper (II) complexes of curcumin with different stoichiometry (1:1 and 1:2 for copper:curcumin) were synthesized and characterized by different spectroscopic techniques. Both the complexes were examined for superoxide dismutase (SOD) activity. The formation constants of the complexes were measured by cyclic voltammetry. SOD activity of the complexes was measured by xanthine/xanthine oxidase assay, by using cytochrome c. The structural geometry of the complexes was established from EPR spectrometer, suggesting distorted square-planar geometry for 1:1 complex and square-planar geometry for 1:2 complex. The SOD activity of the complexes was correlated with the structural distortion; more the structural distortion higher the SOD activity of the complex.

Introduction

Superoxide dismutase (SOD) is an antioxidant enzyme present in living systems.¹ It plays a major role in protecting the cells against oxidative damage caused by superoxide ($O_2^{\cdot-}$) radicals. SOD catalyzes $O_2^{\cdot-}$ radical to oxygen and hydrogen peroxide. The active center of this enzyme is occupied by copper and zinc. In the electron transfer chain of mitochondrial process $O_2^{\cdot-}$ radicals are formed due to incomplete reduction of molecular oxygen. Although $O_2^{\cdot-}$ radicals themselves are not so reactive, but in the presence of metal ions like Cu, Fe it is converted to more damaging $\cdot OH$ radicals.² Under normal circumstances, the native SOD enzyme is capable of removing the $O_2^{\cdot-}$ radical, by dismutation process. But the balance of this process is lost when there is excess production of $O_2^{\cdot-}$ by various oxidative stress generating factors. These situations often lead to different physiological disorders. To overcome

these situations, new SODs are being explored as useful therapeutic agents.^{3,4} Unlike the native SOD enzyme, the synthetic SOD mimics should be designed, by taking into consideration longer shelf life, higher lipid solubility and penetration into cells. It would be preferable to have SOD mimics of redox active metal complexes with antioxidants and other inflammatory drugs, because of added pharmacological activity, and reduced toxicity of the ligands. Curcumin is a wonder molecule for its remarkable pharmacological activity including anti-inflammatory, anticarcinogenic and antioxidant activity with almost no side effects.⁵ It has two *o*-methoxy phenolic OH groups attached to the α , β unsaturated β -diketone moiety. With this aim, 1:1 and 1:2 Cu (II)-curcumin complexes (Fig. 1) were synthesized and their SOD activity was compared and further correlated with their structural properties.

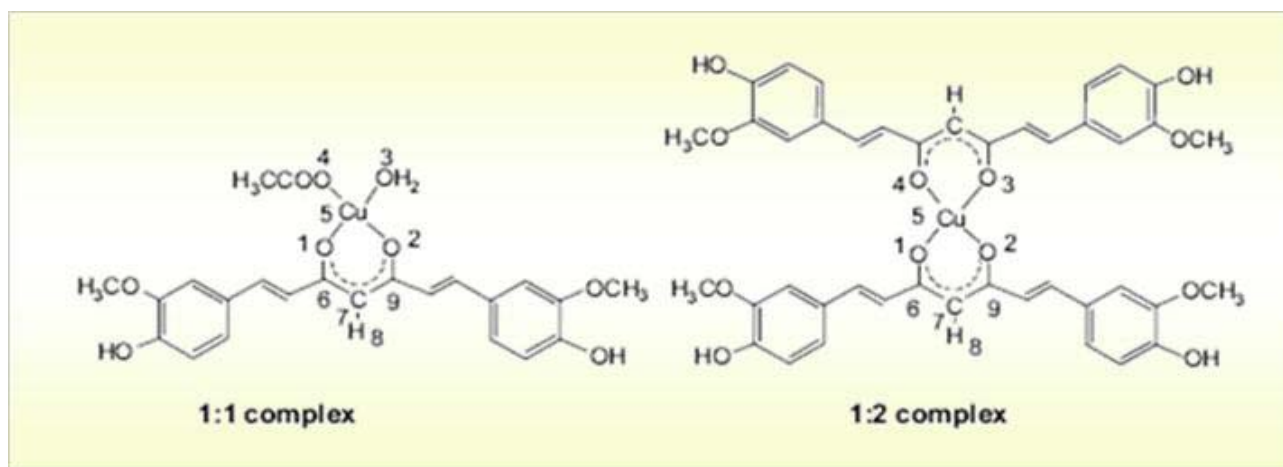


Fig. 1: Molecular structures of Cu(II)-curcumin complexes (1:1 and 1:2).

Results and Discussion

Synthesis and characterization of complexes

1:1 Cu (II)-curcumin complex was synthesized by refluxing equi-molar ratios of cupric acetate and curcumin in ethanol under nitrogen atmosphere at 60 °C for 3 hours.⁶ Similarly for 1:2 Cu (II)-curcumin complex, cupric chloride and curcumin (Cu: curcumin, 1:2 mole ratio) was used as starting material and the same procedure was adopted.⁷ The separated solid was dried in vacuum to obtain dry powder after filtration. Both the complexes were characterized by elemental analysis, IR, NMR and mass spectroscopic techniques. The complexes are insoluble in water and soluble in DMSO. UV-visible spectra of 1:1 and 1:2 complex were recorded in DMSO solvent. The 1:1 complex have absorption maxima at 426 nm and two shoulders at 410 and 450 nm, whereas 1:2 complex has absorption maxima at 370 nm.

Electrochemical properties of the complexes

SOD is a class of oxido-reductase enzyme, thus the redox potential of the complexes would have important role for designing new SOD mimics. The redox potential for the couple $O_2/O_2^{\cdot-}$ is -0.33 Vs NHE at neutral pH. The redox potentials of the complexes were recorded in DMSO solvent against Ag/AgCl reference electrode. The potentials for Cu(II)/Cu(I) redox couple for 1:1 and 1:2 complexes were calculated to be 0.38 and 0.42 V vs. NHE,

respectively. The data indicates that the reduction potential values of the complexes are not very much different and are within the range of compounds, that are expected to show SOD activity.⁸ The stability (i.e. formation constant) of the complexes was also measured by electrochemical method. The formation constant was determined to be 3.7×10^{14} and 3.9×10^{15} for 1:1 and 1:2 complex respectively and indicated that the complexes are considerably stable in the experimental medium.⁷

Superoxide radical scavenging activity of the complexes

For these studies, $O_2^{\cdot-}$ radicals were generated by enzymatic method using xanthine/xanthine oxidase system and detected by reduction of cytochrome c (Fe^{+3}). In the presence of the complexes, the absorbance at 550 nm due to cytochrome c (Fe^{+2}) decreases with increasing concentration of the complex. The IC_{50} value (i.e. the concentration required to decrease the absorbance by 50% with respect to blank) for the complexes was determined to be 6.7 μM and 68 μM for 1:1 and 1:2 complexes, respectively.⁷ This data suggests that 1:1 complex has almost 10 times higher SOD activity than 1:2 complex. Under the same experimental condition, the IC_{50} value for curcumin was estimated to be 86.8 μM . The rate constant of $O_2^{\cdot-}$ radical with the complexes was estimated by employing competition kinetics between cytochrome c and the complexes with $O_2^{\cdot-}$ radicals. Using the rate



constant as $5.8 \times 10^5 \text{ M}^{-1}\text{s}^{-1}$ for the reaction of $\text{O}_2^{\cdot-}$ radical with cytochrome c, the rate constant for 1:1 and 1:2 complexes with $\text{O}_2^{\cdot-}$ radical, was estimated at $7.1 \times 10^5 \text{ M}^{-1}\text{s}^{-1}$ and $1.0 \times 10^5 \text{ M}^{-1}\text{s}^{-1}$ respectively.⁷ This data also suggests that 1:1 complex has a higher rate constant than 1:2 complex and supports the earlier observation. EPR spectroscopy is an excellent technique to study free radicals or transition metal complexes. Superoxide radical (3.5 mM) in the form of KO_2 -crown ether system dissolved in DMSO was used for recording EPR spectra. At 77 K, the characteristic EPR signal of $\text{O}_2^{\cdot-}$ radical significantly reduced by the addition of 1:1 complex (as low as 36 μM), and the signal disappeared completely within 2–3 min.⁶ Similar reduction of signal was also observed for 1:2 complex. This confirms that 1:1 and 1:2 complex scavenges the $\text{O}_2^{\cdot-}$ radical directly. It may be noted that in the present study, the $\text{O}_2^{\cdot-}$ radical is scavenged immediately after the addition of the complex, while for curcumin this took nearly an hour. To correlate the structural aspects with the SOD activity, EPR spectra of both complexes were recorded at 77K in DMSO. The recorded EPR spectra for both complexes were fitted with simulated spectra, to get the structural parameters. The EPR spectrum of 1:2 complex showed axial symmetry ($g_{\parallel} = 2.295$, $g_{\perp} = 2.0852$, $A_{\parallel} = 170 \text{ G}$) which is associated with square planar coordination of four equivalent oxygen atoms around Cu(II) ion.⁷ On the other hand, 1:1 complex has distorted square planar structure around Cu(II) ion and the values of orthorhombic g tensor have been estimated to be $g_1 = 2.325$, $g_2 = 2.071$, $g_3 = 2.062$, $A_1 = 155 \text{ G}$.⁷ Diaz et al. have reported a good correlation between f factor ($g_{\parallel}/A_{\parallel}$, where A_{\parallel} is expressed in cm^{-1}) and SOD like activity, for a series of Cu(II) complexes.⁹ A f factor value smaller than 135 cm^{-1} is obtained for square planar Cu(II) complexes, and this value increases with increasing square planar distortion. The f value for native SOD is 160 cm^{-1} , indicating a tetrahedral distortion from square planar geometry, which is one of the features that enhance the catalytic activity of the enzyme. From the above EPR data, the f values for 1:1 and 1:2 complexes were determined to be 150 ($g_{\parallel}/A_{\parallel}$) and 135 cm^{-1} ($g_{\parallel}/A_{\parallel}$) respectively.

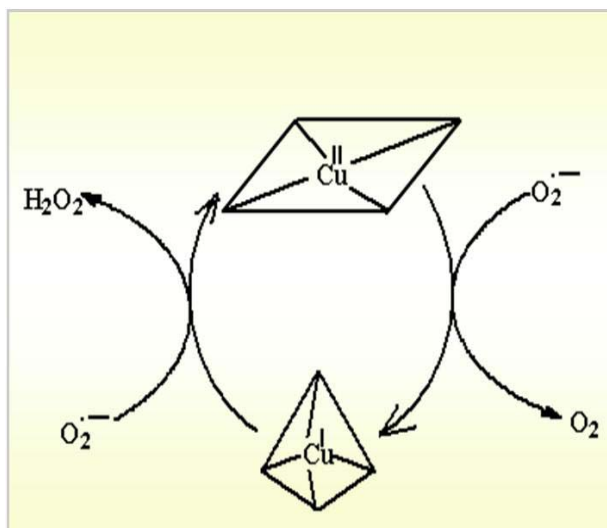


Fig. 2: Schematic representation for the change of coordination geometry around Cu ion during SOD activity.

During the process of SOD activity, there is change in the oxidation state from Cu (II) to Cu (I) ion. In Cu (I) 3d orbitals are completely filled, whereas for Cu (II) ion it is partially filled. Partially filled orbitals get extra stabilization due to Crystal Field Stabilization Energy (CFSE) during the complex formation process, whereas completely filled orbitals will tend to have a tetrahedral geometry which will have minimum ligand-ligand repulsion (Fig. 2). Thus flexible ligands around the Cu ion will help to shuttle between different oxidation states. In the case of 1:2 complex, Cu (II) ion is attached with two chelated curcumin ligands and for 1:1 complex, Cu (II) ion is attached with one chelated curcumin ligand and other two monodentate ligands. Thus for 1:1 complex, the change from distorted square planar to tetrahedral geometry would be an easier process compared to 1:2 complex, which has more rigid square planar geometry. Therefore 1:1 complex exhibiting appreciable square planar distortion is expected to show higher SOD activity.

Acknowledgement

I would like to thank Dr. K. I. Priyadarsini, Head, Radiation Chemistry Section, and all my collaborators and co-authors of our published papers. Encouragement and support from Dr. S. K. Sarkar, Head, RPCD and Dr. T. Mukherjee, Director, CG, BARC are gratefully acknowledged.



References

1. Fridovich, I. "Superoxide radical and superoxide dismutase". *Acc. Chem. Res.* 5 (1972): 321–322.
2. Halliwell, B.; Gutteridge, J. M. C. "Free Radicals in Biology and Medicine", second ed., Oxford, Clarendon Press, 1989.
3. Riley, D. P. "Functional mimics of superoxide dismutase enzymes as therapeutic agents". *Chem. Rev.* 99 (1999): 2573–2587.
4. Czapski, G.; Goldstein, S. "Requirements for SOD mimics operating in vitro to work also in vivo". *Free. Radic. Res. Comm.* 12–13 (1991): 167–171.
5. Aggarwal, B. B.; Sundaram, C.; Malani, N.; Ichikawa, H. In *Curcumin: The Indian solid gold*; Aggarwal, B. B.; Young-Joon, S.; Shishodia S. Eds., The Molecular Targets and Therapeutic Uses of Curcumin in Health and Disease, New York, Springer, 2007.
6. Barik, A.; Mishra, B.; Shen, L.; Mohan, H.; Kadam, R. M.; Dutta, S.; Zhang H. Y.; Priyadarsini, K. I. "Evaluation of a new copper(II)–curcumin complex as superoxide dismutase mimic and its free radical reactions". *Free Radic. Biol. Med.* 39 (2005): 811–822.
7. Barik, A.; Mishra, B.; Kunwar, A.; Kadam, R. M.; Shen, L.; Dutta, S.; Padhye, S.; Satpati, A. K.; Zhang, H.-Y.; Priyadarsini, K. I. "Comparative study of copper(II)-curcumin complexes as superoxide dismutase mimics and free radical scavengers". *Eur. J. Med. Chem.* 42 (2007): 431–439.
8. Durackova, Z.; Mendiola A. M.; Sevilla, T. M.; Valent, A. "Thiohydrazone copper(II) complexes. The relationship between redox properties and superoxide dismutase mimetic activity". *Bioelectrochem. Bioenerg.* 48 (1999): 109–116.
9. Diaz, A.; Cao, R.; Fragoso, A.; Sanchez, I. "Interpretation of the SOD-like activity of a series of copper(II) complexes with thiosemicarbazones". *Inorg. Chem. Commun.* 2 (1999): 358–360.



Doped REF_3 (RE: Ce, Gd, Y) nanopowders: Phosphors for solid state lighting and bio-applications

V. Grover and A.K. Tyagi
Chemistry Division

Dr. Vinita G. Gupta is the recipient of the DAE Young Scientist Award for the year 2009
Dr. A. K. Tyagi is the recipient of the Rajib Goyal Prize in Chemical Sciences

Abstract

Rare earth nanofluorides (YF_3 , CeF_3 and GdF_3) were explored as potential phosphors, for UV-based LEDs for solid state lighting. Apart from multicolored phosphors, novel white light emitting compositions, containing Tb^{3+} , Eu^{3+} , Dy^{3+} , have also been successfully synthesized, by soft chemical routes. Representative doped CeF_3 nanophosphors have been embedded into polymers like PMMA and PVA giving transparent nanocomposites and they are found to emit bright colors. Preliminary studies on human breast cancer cells have shown good uptake of doped GdF_3 nanoparticles by carcinoma cells, which give bright colors corresponding to that of nanoparticles after being illuminated with UV light.

Keywords: Rare-earth fluorides Nanophosphors, Photoluminescence, Polymer-Composites

Introduction

Solid state lighting has been a key research area that involves the quest for novel phosphors, which can efficiently absorb UV light given by LED to emit desired colors (1,2). The fluoride lattice provides for the high coordination number for the doped rare-earth ions and the high ionicity of the rare-earth to fluorine bond, results in a very wide band gap, low vibrational energies and low probability of inter-configurational transitions. This results in long lifetimes of their excited states and high luminescence quantum yields. A lot of research is devoted to synthesize nano-sized rare earth fluorides as colored/white light emitting solid phosphor, wherein all the RGB (red, green, blue) components are contained within the same host matrix. The introduction of inorganic nanoparticles into a polymer matrix is an effective method to bring them into a functional form. They have promising

applications in high-grade optoelectronic devices such as light emitting diodes (LEDs), security labeling, lasers, displays as well as bio-applications. Among the rare earth fluorides, YF_3 , CeF_3 and GdF_3 doped by rare-earth ions is capable of producing efficient visible emission under vacuum UV irradiation. YF_3 has a large band gap (10 eV) and does not give an emission of its own in the wavelength region of interest and hence is a suitable matrix. On the other hand, the advantage associated with CeF_3 and GdF_3 is, efficient absorption and energy transfer by host to the activator. A facile one pot synthesis of redispersible doped REF_3 nanoparticles and their composites is reported, with the aim of developing white light emitting solid state phosphor, excitable by single wavelength UV excitation. The preliminary results on bio-applications have also been demonstrated.



Experimental

The stoichiometric amounts of $\text{RE}(\text{NO}_3)_3 \cdot 6\text{H}_2\text{O}$ were precipitated with sodium fluoride in ethylene glycol solvent and the mixture was refluxed. Various single and multiple-doped nominal compositions of $\text{RE}_x(\text{Do})_{1-x}\text{F}_3$ ($0.025 \text{ d}'' \times \text{d}'' 0.10$, RE^{3+} : Y^{3+} , Ce^{3+} , Gd^{3+} and $\text{Do}^{3+} = \text{Eu}^{3+}$, Tb^{3+} and Dy^{3+}) were prepared. Nanocomposites were synthesized by sonication-assisted dispersion, followed by solvent casting. The starting materials and all the synthesized nominal compositions were characterized by powder XRD, HR-TEM, FT-IR and photoluminescence studies. The CIE color coordinates (x , y) were calculated with the equidistant wavelength method.

Result and Discussion

The as-prepared products were characterized by powder XRD, which revealed hexagonal symmetry (SG: $\text{P6}_3\text{22}$) for (doped and undoped) CeF_3 and orthorhombic symmetry for YF_3 nanopowders (SG: pnma). Interestingly, for GdF_3 , doping small amounts of activators stabilized the metastable hexagonal form. The average crystallite size of the samples was found to be ~ 15 nm. High resolution-TEM data recorded on a few representative compositions, showed distinct fringes indicating high crystallinity of the samples. The particles were fairly regular in shape and size. The FTIR spectroscopic studies confirmed the stabilization of the nanoparticles' surface by ethylene glycol molecules which play a vital role in making them dispersible. Good dispersibility is an important criterion that aids ease of fabrication and also facilitates the use of nanoparticles for biological assays and imaging.

Photoluminescence and decay studies on CeF_3 and GdF_3 host lattice

Detailed photoluminescence studies were carried out on REF_3 doped with varying concentrations of the activator ions. In case of Dy^{3+} doped compositions, characteristic Dy^{3+} emission profile at 478 nm (${}^4\text{F}_{9/2} \rightarrow {}^6\text{H}_{15/2}$ (blue-green color)) and 571 nm (${}^4\text{F}_{9/2} \rightarrow {}^6\text{H}_{13/2}$ (yellow color)) were observed at host excitation (Fig. 1). The respective excitation spectra showed a broad hump peaking at 252

nm (for CeF_3), which can be assigned to the host Ce^{3+} transition (4f-5d) and a peak at 275 nm for GdF_3 . For REF_3 doped with Tb^{3+} , sharp emission peaks at 487 nm, 542 nm, 580 nm and 620 nm (${}^5\text{D}_4 \rightarrow {}^7\text{F}_j$ of Tb^{3+}) were observed, on host excitation. Similar studies on GdF_3 : Eu^{3+} showed the emission peaks at 612 nm and 590 nm. However, it is noteworthy that CeF_3 : Eu^{3+} didn't show any characteristic Eu^{3+} peaks in the emission spectrum. It has been postulated that in presence of Ce^{3+} , quenching of emission in Ce^{3+} and Eu^{3+} co-doped systems occur. The lifetime studies revealed that optimum luminescence properties were observed for 2.5 mol% Dy^{3+} and 7.5 mol% Tb^{3+} in CeF_3 and 2.5 mol% Tb^{3+} in GdF_3 . The observations that host excitation peaks appear on monitoring the emission characteristic of the dopant ion and very poor emission spectra were obtained on direct excitation of the dopants prove, that energy transfer seems to be the major mode for activator excitation. Energy transfer efficiency values were found to be 89% for CeF_3 : Tb^{3+} (7.5 mol%) nanoparticles and 60% for CeF_3 : Dy^{3+} (2.5 mol%) nanoparticles. Further, GdF_3 nanoparticles co-doped with Tb^{3+} and Eu^{3+} (2.5 mol% each and 5 mol% each) showed emissions corresponding to both the dopants at host excitation. Lifetime measurements indicated towards the energy transfer taking place from Tb^{3+} to Eu^{3+} also. The decay studies showed a bi-exponential decay for the activators which can be attributed to the dopant ion present in the different surroundings (presumably in the bulk and on the surface). With the aim of synthesizing white light emitting solid state phosphor, REF_3 lattices were doped with all the three activators Tb^{3+} (green), Dy^{3+} (blue) and Eu^{3+} (red) and their concentrations were optimized to get a mixed white emission. The white light emission could be achieved with CeF_3 : 2.0 mol% Tb^{3+} , 3.5 mol% Dy^{3+} and 4.5 mol% Eu^{3+} and GdF_3 : 2.0 mol% Tb^{3+} , 3.5 mol% Dy^{3+} and 4.5 mol% Eu^{3+} . Their CIE co-ordinates were found to be very close to broad day light and are depicted on the chromaticity diagram (Fig. 2). Highly transparent nanocomposites could be obtained for the green emitter CeF_3 : 5.0 mol% Tb^{3+} , blue emitter CeF_3 : 2.5 mol% Dy^{3+} and white light emitter CeF_3 : 2.0 mol% Tb^{3+} , 3.5 mol% Dy^{3+} , 4.5 mol% Eu^{3+} with PMMA (Poly methyl



methacrylate) and PVA (Poly vinyl alcohol). These films gave good emission spectra at host excitation, indicating retention of energy transfer.

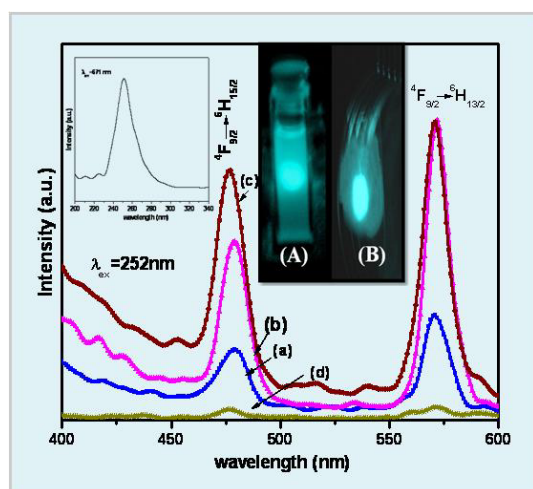


Fig. 1: The emission and excitation spectra of $CeF_3: xDy^{3+}$. Inset shows blue luminescence emitted by nanoparticles on UV excitation

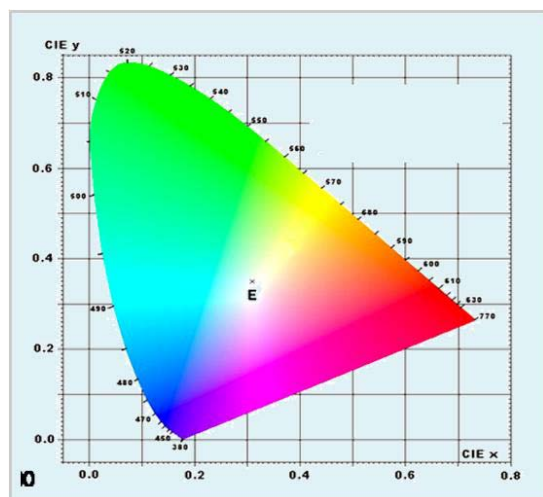


Fig. 2: Representation of CIE co-ordinates on Chromaticity diagram for triply doped composition; $GdF_3: 2.0 \text{ mol}\%Tb^{3+}, 2.0 \text{ mol}\%Eu^{3+}, 2.0 \text{ mol}\%Dy^{3+}$.

For bio-applications, the non-specific binding of these nanoparticles to human breast cancer cells (MCF-7) was studied, using fluorescence spectrometry and confocal microscopy. The incubation of cancer cells with nanoparticles under physiological buffered condition,

resulted in significant fluorescence intensity and the magnitude of fluorescence intensity and the pattern of binding of nanoparticles, was found to be dependent on stabilizing agent.

Single wavelength excitable multicolored YF_3 nanocrystals

Doped redispersible YF_3 nanocrystals were obtained as earlier and were found to crystallize in an orthorhombic phase. FT-IR studies showed the stabilization of nanoparticles by ethylene glycol moiety. The highly intense emission spectra of various activators (Dy^{3+} , Tb^{3+} , Eu^{3+} and Sm^{3+}) in the presence of Ce^{3+} , their long lifetimes ($\sim ms$) and significant reduction in the lifetime of Ce^{3+} proved an efficient energy transfer operating in the nanocrystals. The time resolved emission studies indicated the presence of two different sites for the emitting ion. Bright blue (Dy^{3+}), green (Tb^{3+}), red (Eu^{3+}) and purple (Sm^{3+}) emissions were observed on irradiating corresponding $YF_3: Ce^{3+}, RE^{3+}$ nanocrystals, under ultraviolet light (Fig. 3).

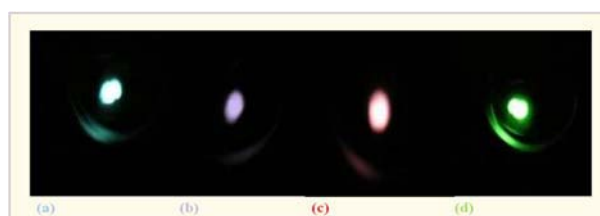


Fig. 3: Bright emission from variously doped $YF_3: Ce^{3+}, RE^{3+}$ nanopowders upon irradiating the sample with UV light where RE^{3+} is (a) Dy^{3+} (b) Sm^{3+} (c) Eu^{3+} (d) Tb^{3+}

Conclusions

Highly dispersible rare earth doped REF_3 nanoparticles (size: 15-20 nm) were successfully synthesized and extensively characterized. Efficient energy transfer was observed from the host

lattice to activator ions, resulting in bright luminescence. White light emitting phosphors could be synthesized which had CIE co-ordinates, very close to broad day light.



PVA and PMMA based transparent nanocomposites of some representative green, blue and white light emitting compositions were synthesized and these films were shown to emit bright luminescence upon UV irradiation. Preliminary experiments suggested the application of these nanoparticles in cell labelling.

References

1. Sivakumar, S., Van Veggel, F.C.J.M., Raudsepp, M. "Bright White Light through Up-Conversion of a Single NIR Source from Sol-Gel-Derived Thin Film Made with Ln^{3+} -Doped LaF_3 Nanoparticles". *Journal of the American Chemical Society* 127 (2005): 12464-65.
2. Yi, G., Lu, H., Zhao, S., Ge, Y., Yang, W., Chen, D., Guo, L.H. "Synthesis, Characterization, and Biological Application of Size-Controlled Nanocrystalline $\text{NaYF}_4:\text{Yb,Er}$ Infrared-to-Visible Up-Conversion Phosphors". *Nano Letters* 4 (2004): 2191-96.



Gas phase studies on interaction of clusters with laser and metal ions

Pramod Sharma
Chemistry Division

Dr. Pramod Sharma is the recipient of the DAE Young Scientist Award for the year 2009

Abstract

Clusters provide an ideal medium for investigating several fundamental condensed phase physicochemical phenomena in the gas phase. This is possible because of their near solid-like local density which mimics the condensed phase, while their secluded existence in the gas-phase, facilitates probing of elementary reactions under well-defined conditions, unperturbed by external factors that prevail in the condensed phase. Present article describes studies related to interaction of laser and metal ions with matter, using clusters as a reaction medium.

Introduction

Flanked between isolated atoms/molecules and bulk materials at two extremes, there exists a unique class of matter known as clusters, which is aggregate of a few to thousand of atoms or molecules. These clusters are held together by interactions ranging from weak vander Waals forces to strong ionic bonds¹. The structural and electronic properties of these low-dimensional materials, bear resemblance neither to atoms/molecules they are composed of, nor to the corresponding bulk matter they eventually get transformed in to. Over the last few decades, studies on cluster, especially as a function of their size, have been of particular interest due to the potential of these studies to improve understanding of how physical and electronic properties evolve, as particles grow from atoms/molecules through finite clusters to the bulk phase².

This unique form of matter has been widely exploited for basic understanding of different physical, chemical and biological problems. Under the influence of laser field, clusters exhibit anomalous photochemical behavior as a

function of cluster size, which is quite different as compared to its constituent monomer counterpart. For example, clusters have been found to exhibit intra-cluster photochemistry which opens up new reaction channels that are inaccessible for its monomer constituent³. In addition, employing clusters as model reactors, reactivity of metal ions towards different types of organic reagents have been investigated. In our laboratory similar studies have been carried out in the gas-phase to investigate:

- Photochemical behavior of clusters as a function of laser-wavelength and degree of aggregation.
- To screen catalytic activity of different metal ions
- To probe elementary reactions under well-defined conditions unperturbed by external factors that prevail in the condensed phase.

An abstract of these studies is given in the following sections, describing observation of unique phenomenon of Coulomb explosion (CE), when molecular clusters were interacted with nanosecond laser pulse of $\sim 10^9$ W/cm²,



which resulted in generation of energetic multiply charged atomic ions and electrons. While studies related to reaction of metal ions with acetylene clusters were carried out, to screen catalytic activity of metal ions towards acetylene polymerization.

Instrumentation

Fig. 1 illustrates a photograph of the cluster setup coupled with time-of-flight mass spectrometer, designed and fabricated indigenously at the Chemistry Division⁴. Supersonic expansion of gases through a nozzle into vacuum, provides a convenient means for generating gas phase clusters of atoms and molecules. In our studies, a pulse valve mounted in the expansion chamber acts as a cluster source for the generation of molecular clusters. In this set-up, typically an inert carrier gas (helium or argon) at a stagnation pressure of 1–8 bar is bubbled through the liquid organic sample of interest, for the formation of the desired clusters. The resultant gas mixture is then supersonically expanded through a pulse nozzle. Under these jet-cooled conditions, translational and rotational temperatures drop to a few Kelvin. At such low translational temperatures, condensation of atoms and molecules leads to formation of clusters. The resultant supersonic jet is skimmed with the help of a skimmer (a truncated cone) and a cold beam of molecular clusters is introduced in the analyzer chamber, where these clusters



Fig. 1: Photograph of time-of-flight mass spectrometer indigenously designed and fabricated at Chemistry Division, BARC.

are subjected to mildly focused nanosecond laser pulses from a Nd : YAG laser. The ions produced upon laser–cluster interaction are accelerated by a Wiley-McLaren assembly and are mass separated in a time-of-flight mass spectrometer.

For studies involving reaction of metal ions with clusters, a metal rod was placed at an appropriate distance from the nozzle and the metal ions generated upon laser ablation of metal rod were synchronized to interact with the molecular clusters generated upon supersonic expansion. The resultant metal–cluster ions generated were skimmed and extracted into the time-of-flight mass spectrometer by utilizing a pulsed voltage.

Photochemistry of acetone clusters as a function of size and laser wavelength

Acetone monomers in the gas phase have been widely studied at different laser wavelengths. To understand how photochemistry of acetone alters upon clusterization, studies on acetone clusters were carried out at different laser-wavelengths, as a function of cluster size. Generation of acetone clusters of varying size was realized, by taking into account the fact, that “upon supersonic expansion, clusters are produced as a result of three body collisions between the molecules and the carrier gas”. The rate of three body collisions is expressed as (Z_3)-

$$Z_3 \propto P_0^2 d / T_0^2 \quad (1)$$

Where P_0 is stagnation pressure, d is nozzle diameter and T_0 is pre-expansion gas temperature. The above relation suggests, that the probability of cluster formation increases with increase in the stagnation pressure as well as the nozzle diameter. Based on the above relation, studies on acetone clusters were carried out, by varying nozzle diameter (d), which is directly related to average cluster size generated upon supersonic expansion, at different laser wavelengths. Fig. 2(a) shows time-of-flight mass spectrum of acetone clusters, obtained using 0.5 mm nozzle subjected to 532 nm laser pulses of intensity $\sim 4.5 \times 10^9$ W/cm². It can be seen that clusters generated using smaller diameter (0.5 mm) nozzle exhibited simple multiphoton dissociation/ionization behaviour, resulting



in generation of fragment ions like CH_3CO^+ , $(\text{CH}_3\text{COCH}_3)_n^+$ ($n=1-4$), $(\text{CH}_3\text{COCH}_3)_n\text{CH}_3\text{CO}^+$ ($n=1-3$) etc., consistent with earlier studies reported on multiphoton ionization of acetone clusters. In contrast, when clusters of acetone generated using 0.8 mm nozzle were subjected to 532 nm laser pulses under identical experimental conditions, (Fig. 2(b)), the acetone clusters were found to exhibit the phenomena of Coulomb explosion, resulting in generation of multiply charged atomic ions of carbon and oxygen i.e. C^{m+} ($m=1-4$) and O^{n+} ($n=1-3$), in addition to other fragment ions. This experiment clearly demonstrates the size dependent photochemical behavior of acetone clusters⁵.

In addition, acetone clusters were also subjected to $\sim 10^9 \text{ W/cm}^2$ intensity laser pulses of 355 and 266 nm, under identical expansion conditions, as those employed for 532 nm studies using 0.8 mm diameter nozzle. At these wavelengths in the UV region, no signature for the

occurrence of Coulomb explosion phenomenon, i.e. observation of multiply charged atomic ions with large kinetic energy could be detected even up to higher laser intensities (i.e. $\sim 10^{10} \text{ W/cm}^2$). These studies also point towards the crucial role of excited intermediate states. Though 355 and 266 nm photons are more energetic as compared to 532 nm photon and the probability of causing multiphoton excitation would be higher at these wavelengths, yet acetone clusters undergo only primary multiphoton dissociation/ionization behavior at 355 and 266 nm (Figs. 3 (a) & (b)).

Interaction of acetylene clusters with laser ablated metal ions: Observation of polymerization and mechanism of intra-cluster reaction

In another study, different first-row transition metal (TM) ions generated upon laser ablation were interacted with acetylene clusters. Based on time-of-flight mass spectrum,

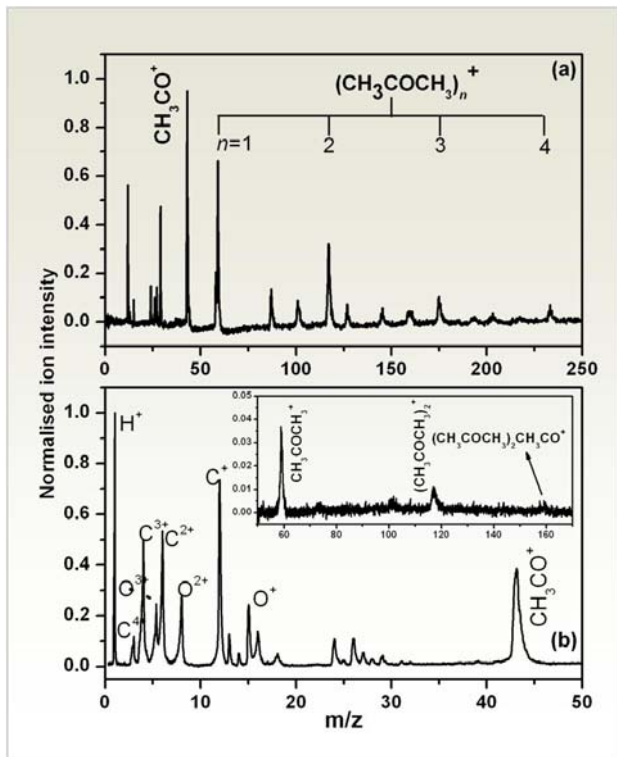


Fig. 2: Time-of-flight mass spectra of acetone clusters subjected to $\sim 4.5 \times 10^9 \text{ W/cm}^2$ laser intensity pulses at 532 nm (a) using 0.5 mm diameter nozzle and (b) using 0.8 mm diameter nozzle at 2 bar helium stagnation pressure. Inset shows the cluster fragment ions.

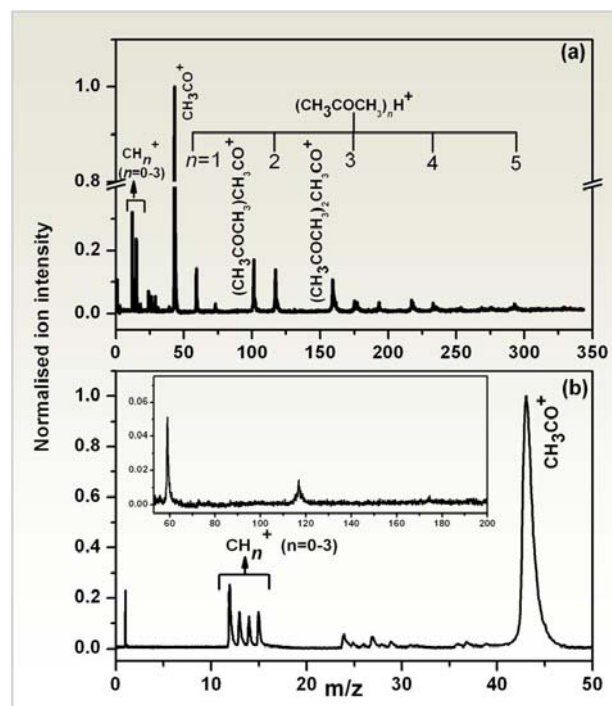


Fig. 3: Time-of-flight mass spectra of acetone clusters, generated using 0.8 mm diameter nozzle at 2 bar helium stagnation pressure subjected to (a) $\sim 1.4 \times 10^9 \text{ W/cm}^2$ laser intensity pulses at 355 nm and (b) $\sim 1 \times 10^9 \text{ W/cm}^2$ laser intensity pulses at 266 nm. Inset shows the cluster fragment ions.



generation of hydrocarbon fragments (namely $C_6H_4^+$, $C_6H_5^+$, $C_8H_6^+$ and $C_8H_7^+$), with different compositions and intensities from the reactions of TM ions and acetylene clusters, suggested regarding varying order of reactivity of the TM ions towards polymerization of acetylene. Fig. 4 represents the time-of-flight mass spectra obtained upon interaction of acetylene clusters with metal ions Ti^+ , V^+ and Cr^+ produced by laser-ablation of their respective metal targets. The spectra revealed, generation of metal-acetylene complexes with varying order of clusterization. Vanadium-acetylene clusters in addition, exhibited hydrogen abstraction reaction, which resulted in generation of clusters of the type $VC_{2n}H_{2n-m}^+$ (see Figs. 4(b) inset). Similarly, Fig. 5 displays ion signal obtained upon interaction of Fe^+ , Co^+ and Ni^+ with acetylene clusters. In addition to metal ion-acetylene cluster adducts, ion signal corresponding to acetylene clusters and their fragments were also observed in the mass spectra. These cluster fragments are believed to be covalently bonded hydrocarbon fragments, formed as a result of metal ion induced catalytic polymerization. A sequential addition

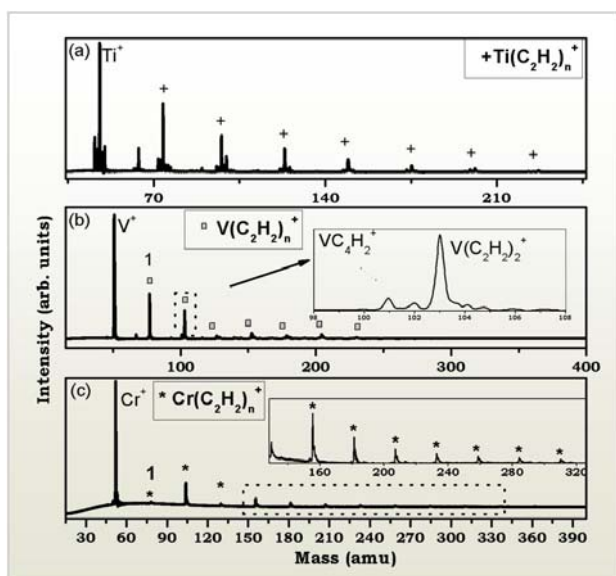


Fig. 4: Time-of-flight mass spectra of metal acetylene clusters for Ti^+ , V^+ and Cr^+ . Inset figure 4 (b) depicts hydrogen abstraction reaction for $V(C_2H_2)_2^+$ cluster. Inset figure 4 (c) shows higher clusters for $Cr(C_2H_2)_n^+$ clusters, up to $n=11$.

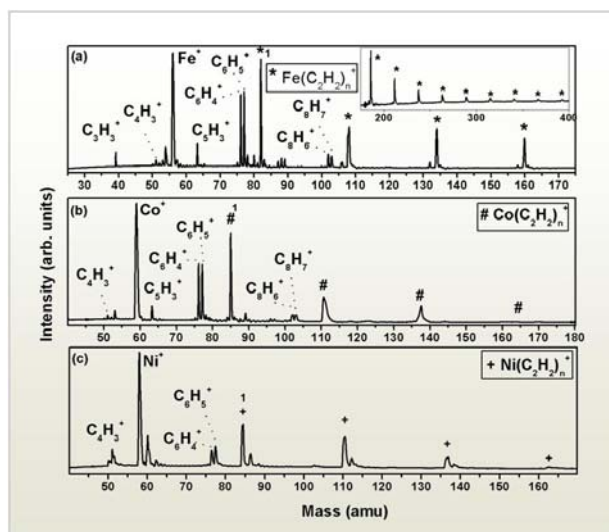


Fig. 5: Time-of-flight mass spectra of metal acetylene clusters for Fe^+ , Co^+ and Ni^+ . Inset figure 5(a) depicts higher clusters of $Fe(C_2H_2)_n^+$.

of acetylene molecules to the metal-ion activated acetylene monomer within the clusters, is proposed as a possible mechanism for polymerization of acetylene, initiated by C-H bond activation. The proposed mechanism suggests intermediacy of $C_4H_3^+$ in the generation of higher hydrocarbon species such as $C_6H_4^+$, $C_6H_5^+$, $C_8H_6^+$ and $C_8H_7^+$ observed in the time-of-flight mass spectra⁶.

Summary

Clusters provide an ideal medium for investigating the alteration in physical and chemical properties of a species, as they transform from atomic/molecular level to condensed phase. Clusters exhibit altogether different photochemistry, as new photochemical reaction channels open up, which are not observed for the molecule. Because of their high local electron density, they interact efficiently with laser radiation and serve as attractive targets for studying several nonlinear phenomena including Coulomb explosion. Present studies, suggest that clusters exhibit complex yet efficient laser-cluster interaction mechanism, resulting in the generation of multiply charged atomic ions. Feasibility of utilizing clusters as nano-reactors for screening reactivity of different metal ions in gas phase, unperturbed by external factors, has also been explored.



Acknowledgements

The author is grateful to Dr. T. Mukherjee, Director, Chemistry Group, Dr S.K. Kulshreshtha, Dr. D. Das, Head, Chemistry Division, Prof. D. Mathur (TIFR) and Dr. R. K. Vatsa for their helpful scientific discussions, constant encouragement and support.

References

1. Jena, P., Rao, B. K., Khanna, S. N. *Physics and Chemistry of small clusters*. New York, Plenum, 1987.
2. Levy, D. H. "Van der Waals molecules". *Adv Chem Phys* 47 (1981): 323-362.
3. Brown, C., Vaida, V. "Photoreactivity of oxygen dimers in the ultraviolet". *J Phys Chem* 100 (1996): 7849-7853.
4. Majumder, C., Jayakumar, O. D., Vatsa, R. K., Kulshreshtha, S. K. "An experimental set-up for generation and characterization of metal clusters". *Indian J Chem* 40 (2001): 577-582.
5. Sharma, P., Vatsa, R. K. "Photochemistry of acetone clusters: Size dependent observation of Coulomb explosion in the multiphoton ionisation regime". *Europhysics Letters* 84 (2008): 43003(1-6).
6. Sharma, P., Attah, I., Momoh, P., El-Shall, M. S. "Metal acetylene cluster ions $M^+(C_2H_2)_n$ as model reactors for studying reactivity of laser-generated transition metal cations". *Int J Mass Spectrom* 300 (2011): 81-90.



CFD Analysis of Passive Autocatalytic Recombiner and its Interaction with Containment Atmosphere

B. Gera, P.K. Sharma, R.K. Singh and K.K. Vaze

Reactor Safety Division

and

A.K. Ghosh

Health, Safety & Environment Group

Mr. Bhuvaneshwar Gera is the recipient of the DAE Young Engineer Award for the year 2009

Abstract

In water cooled nuclear power reactors, significant quantities of hydrogen could be produced due to metal water reaction, following a postulated Loss-Of-Coolant-Accident (LOCA) along with non availability of Emergency Core Cooling System (ECCS). Passive Autocatalytic Recombiners (PAR) are implemented in the containment of water cooled power reactors to mitigate the risk of hydrogen combustion. For the assessment of the PAR performance in terms of maximum temperature of catalyst surface and outlet hydrogen concentration, an in-house 3D Computational Fluid Dynamics (CFD) model has been developed. In addition, CFD analysis of interaction of a representative nuclear power plant containment atmosphere with PAR was simulated, using the commercial CFD code for PAR Interaction Studies (PARIS benchmarks) exercise.

Keywords: hydrogen, containment, nuclear power plant, catalytic recombinder, CFD.

Introduction

Within the nuclear industry, PARs are installed in advanced water cooled power reactor containments, as combustible gas control systems during severe accident conditions. During a severe accident in a nuclear power plant, the high temperature zirconium fuel cladding can react with high-temperature steam, to produce hydrogen. Hydrogen thus generated has the potential to cause uncontrolled combustion in the containment building, which represents a threat to the integrity of the confinement, due to pressure and temperature levels. Numerous techniques have been developed, for mitigating the potential for such accidents. Pre-inerting, post-accident inerting, electrical recombinder, catalytic recombinder, igniters, mixing by use of fans are several methods, to mitigate the hydrogen hazards in nuclear containments. Passive catalytic recombination of

H₂ with O₂ in air, appears to be the most promising one [1]. Autocatalytic recombiners are passive, since they are self-starting and self-feeding; they have no moving parts and require no external energization. The gas mixture flows through the recombinder by natural convection, pushed by the gas heated as a result of the reaction. These natural convective flow currents, promote mixing of combustible gases in the containment. To provide optimal and reliable conditions and to understand the internal processes inside the recombinder, modeling of the device in detail is required. For the analysis of the processes inside a passive autocatalytic recombinder, such as reaction kinetics or heat and mass transfer, a 3D in-house CFD code has been developed. The code calculates the catalyst temperature and the concentration regression along the catalyst plates.



The code has been validated against REKO experiment [2] and has been used to predict maximum catalyst surface temperature and recombiner outlet hydrogen concentration.

Apart from this, a PAR model is developed based on the manufacturer's correlation to integrate with commercial CFD codes, used for hydrogen distribution modeling. The model has been used to simulate PAR Interaction Studies (PARIS-1) benchmark problem. A 2D geometrical model of the simulation domain was used. The containment was represented by an adiabatic rectangular box with two passive autocatalytic recombiners located at intermediate elevations near opposite walls. In this approach, PAR volume has been modeled as fluid region and separate

energy equation was solved, for heat transfer to solid plate from reaction and from solid plates to fluid media, through user coding.

CFD Analysis of PAR

The REKO test facility consists of a vertical flow channel with a rectangular cross section 46 mm wide (W) and 146 mm deep. The simplified geometry for the computation is shown in Fig. 1. The channel is 504 mm high ($L_1 + L_2 + L_3$) with about 180 mm of channel length above the sheets (L_3). For the current experiments, four sheets made of stainless steel and coated with wash coat/platinum catalyst material were arranged in parallel, inside the flow channel. The plates used were 1.5 mm thick and 143 mm high (L_2). In the experimental setup, they were arranged in parallel with a separation of 8.5 mm. Experiments have been performed for different flow velocities (0.25, 0.50, and 0.80 m/s) at different inlet temperatures (298, 343 and 383 K). Inlet hydrogen concentrations were varied between 0.5 and 4% v/v. REKO-3 experimental data was used to validate our in-house code [3]. Figs. 2 and 3 show the steady state average hydrogen concentration and catalyst surface temperature along the catalytic sheet, obtained from present computation along with experimental results. As the

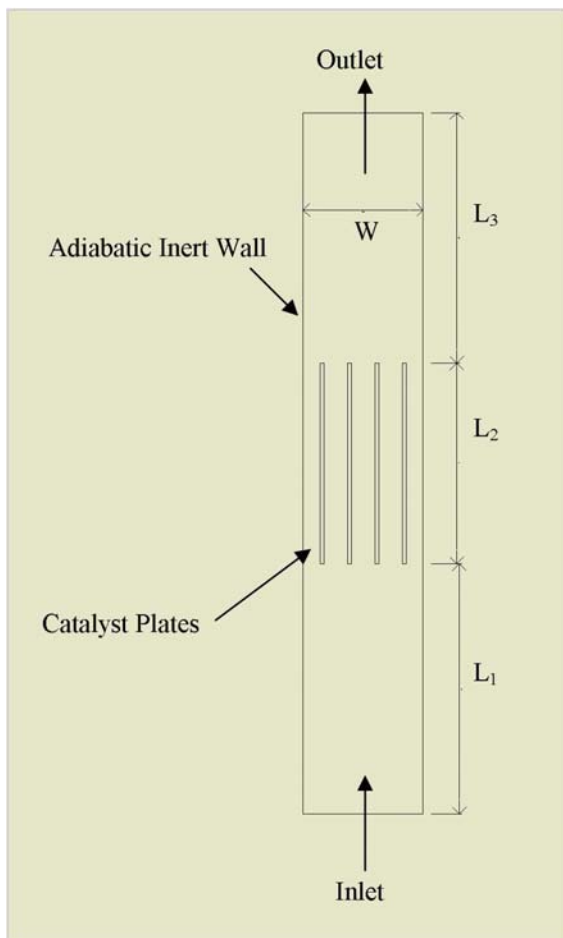


Fig. 1: Simplified geometry for CFD computation (All Dimensions are in mm)

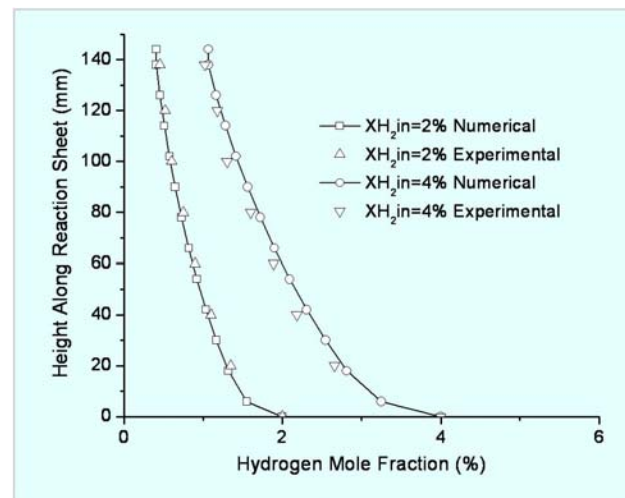


Fig. 2: Steady state average hydrogen concentration in the recombiner section for REKO facility, comparison of CFD results with experimental results for inlet hydrogen mole fraction 2% & 4% and temperature 343 K

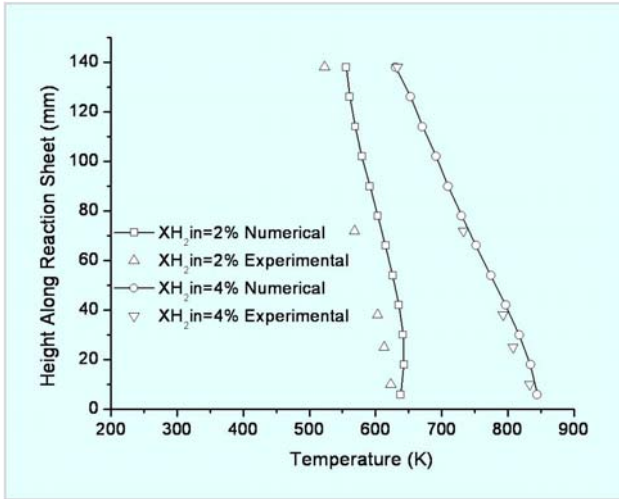


Fig. 3: Catalyst surface temperature along the catalytic sheet (central plate) for REKO facility, comparison of CFD results with experimental results for inlet hydrogen mole fraction 2% & 4% and temperature 343 K

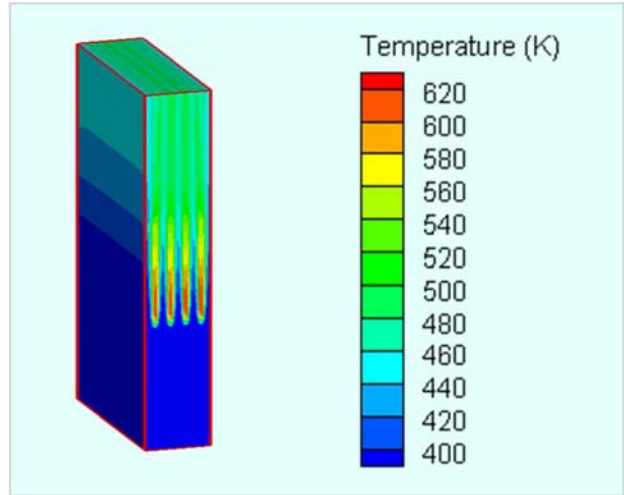


Fig. 4: Temperature contour for simulation performed for REKO facility for inlet hydrogen mole fraction 2% and temperature 383 K

mixture enters the recombiner section, the reaction occurs at the leading edge of the catalyst sheet. The reaction rate is highest at the leading edge of the plate. This is manifested by sharp decrease in hydrogen concentration and maximum catalyst surface temperature near the leading edge of the plate. As flow takes place over catalytic plate, boundary layer is formed over the plate surface and hydrogen diffuses from the bulk of the mixture towards plates for recombination. With the flow along the catalyst sheet, concentration gradient decreases, thus reaction rate also decreases along the sheet. Both reaction kinetics and diffusional mass transport phenomenon control the recombination. Figs. 4 and 5 show the temperature and hydrogen concentration, for air hydrogen mixture of 2% v/v hydrogen concentration entering at 383 K for REKO test facility.

CFD Analysis of PAR Interaction with Containment Atmosphere

As part of this study, a PAR of the AREVA FR90/1-150 design was considered in a 2D rectangular domain. Height of PAR (h) was 1 m and width (w) was 0.2 m. PAR entry and exit section widths are also equal to 0.2 m. Each PAR has 15 autocatalytic plates with dimensions of 0.15 m x 0.15 m x 0.0001 m (height x depth x width), and an

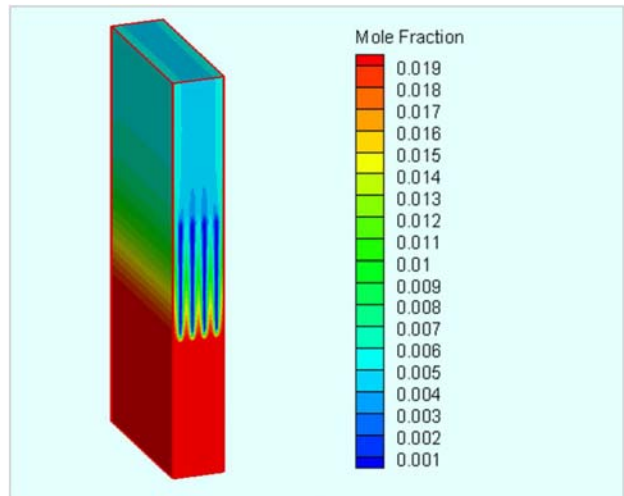


Fig. 5: Hydrogen mole fraction contour for simulation performed for REKO facility for inlet hydrogen mole fraction 2% and temperature 383 K

inter-space of 0.01 m. There are two PARs located in the containment (Fig. 6). No heat or mass transfer (steam condensation) occurs on the walls. The starting point for the calculation was a homogeneous mixture at 3.36 bar, 393 K, oxygen mass fraction 0.1203, hydrogen mass fraction 0.0018 and steam mass fraction 0.4817. The 2D transient Navier-Stokes equation along with the energy and species transport was solved, using commercial CFD

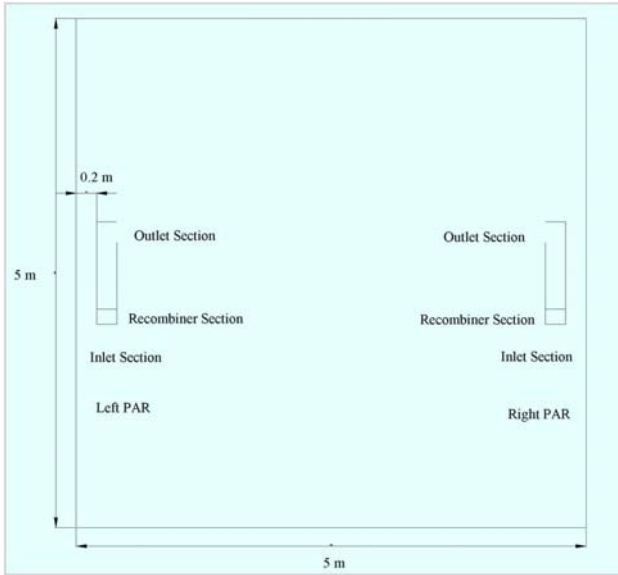


Fig. 6: PARIS-1 model geometry with 2 PARs;

software CFD-ACE+ [4]. The pressure loss across the catalyst plates was modelled as a sink term in momentum equation through user coding. The hydrogen conversion was modelled by means of the empirical AREVA correlation [5]. The heat generated due to recombination and taken by solid plates was further transferred to fluid in the recombiner section, by natural convection. Hydrogen conversion rate was used, to obtain the solid plate temperature based on energy balance and then the heat convected by fluid mixture through the recombiner section was computed and was used as source term, for energy equation solved for recombiner section [6].

Initially, the hydrogen concentration was high, the conversion rate was directly proportional to hydrogen concentration thus hydrogen removal takes place sharply. Fig. 7 shows the amount of total hydrogen in the representative containment, as a function of time. As the hydrogen is consumed, heat is generated and a flow field is developed and hydrogen moves from the bottom of the recombiner towards the top outlet. Fig. 8 shows the variations of the average temperature in the containment vessel. Fig. 9 shows the hydrogen mass fraction contour inside the representative containment at 20 s. The recombiner reduces the hydrogen concentration in the upper region significantly in nearly 900 s. After that, only

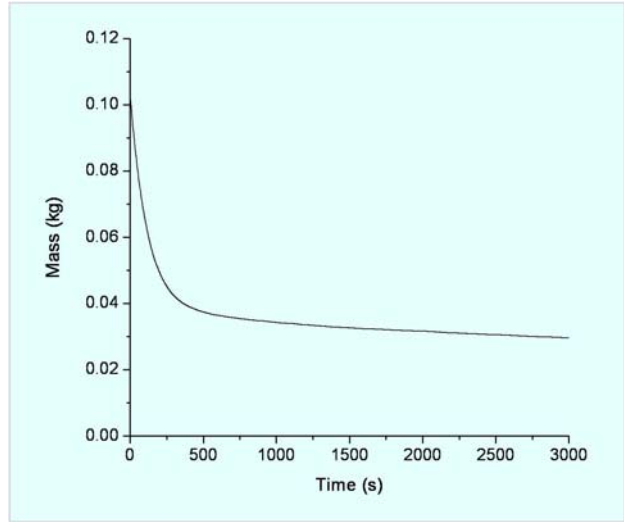


Fig. 7: Average Hydrogen Mass in the Representative Containment

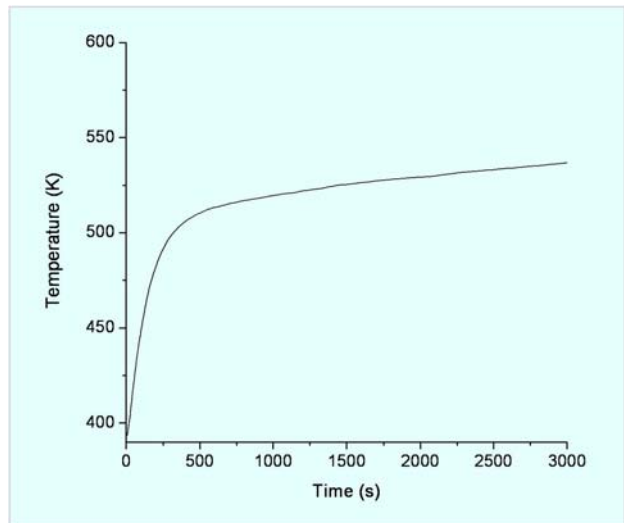


Fig. 8: Average Temperature in the Representative Containment

diffusional control recombination takes place and concentration reduces very slowly.

Conclusion

A 3D CFD analysis of PAR has been carried out, for the literature quoted experimental geometries. The present in-house CFD model can be used, for a plate type recombiner of any chosen dimensions for predicting its behaviour. Apart from this, homogeneous transient model of

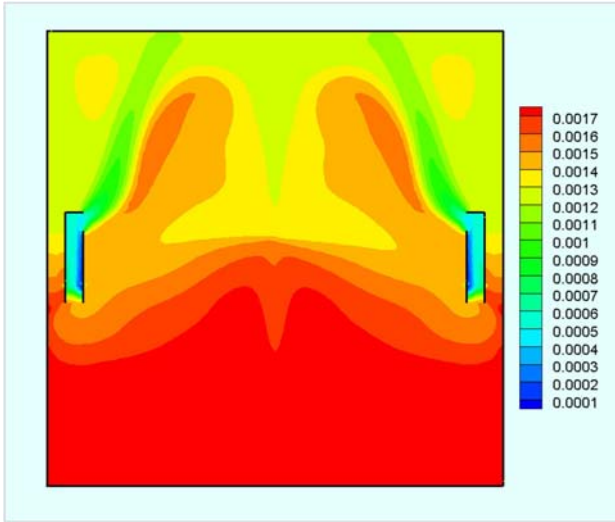


Fig. 9: Hydrogen Mass Fraction at 20 sec

hydrogen recombiner, to simulate the PAR in accidental condition inside containment atmosphere has been developed. Specific PARs with prescribed manufacturer's correlations for hydrogen conversion can be simulated for its performance evaluation, with the methodology presented in this paper. The present approach can be used for optimizing PAR location inside the reactor containment and assessing PAR efficiency in different scenarios.

References

1. Mitigation of Hydrogen Hazards in Water Cooled Power Reactors, IAEA, Vienna, IAEA-TECDOC-1196, 2001.
2. Reinecke, E. A., Tragsdorf, I. M., and Gierling, K., "Studies on Innovative Hydrogen Recombiners as Safety Devices in the Containments of Light Water Reactors", *Nuclear Engineering and Design* 230 (2004): 49–59.
3. Gera, B., Sharma, P. K., Singh, R. K. and Ghosh, A. K., "Numerical Simulation of Passive Catalytic Recombiner", *Kerntechnik* 74 (2009): 286-291.
4. CFD-ACE+ V2009.2, User Manual, ESI CFD Inc., Huntsville, AL 35806.
5. Bachellerie, E., Arnould, F., Auglaire, M., Boeck, B. de, Braillard, O., Eckardt, B., Ferroni, F., Moffett, R., "Generic Approach for Designing and Implementing a Passive Autocatalytic Recombiner PAR-System in Nuclear Power Plant Containments", *Nuclear Engineering and Design* 221 (2003): 151–165.
6. Gera, B., Sharma, P. K., Singh, R. K. and Vaze, K. K., "CFD Analysis of Passive Autocatalytic Recombiner Interaction with Atmosphere", *Kerntechnik* 76 (2011): 98-103.



'H₂-F₂ Reaction in a Tubular Reactor'

A.K. Tiwari and C.S.R. Prasad

Chemical Technology Division

and

A.W. Patwardhan

Department of Chemical Engineering,
Institute of Chemical Technology, Mumbai

and

L.M. Gantayet

Director, BTDG, BARC

Mr. A.K. Tiwari is the recipient of the DAE Young Engineer Award for the year 2009

Abstract

Reaction between potentially explosive mixture of H₂ and F₂ has been studied both experimentally and computationally. It was carried out in a tubular reactor, graduating from one stage to the other, so as to handle the reaction in a safe and sustained manner. The ratio of H₂ to F₂ flow and the flow rate of nitrogen, affect the reactor temperatures. The experiments have been performed over a wide range of flow ratios to generate reliable data. It was observed that the flame due to reaction between hydrogen and fluorine is formed in front of the fluorine feed nozzle. Numerical simulations have been carried out and temperature profiles predicted by these simulations are compared with experimental ones. Good match is observed between the two. This study will be helpful in designing a large scale H₂-F₂ flame reactor.

Key words: H₂-F₂ reaction, turbulent flame, reactor temperature, flame reactor.

Introduction

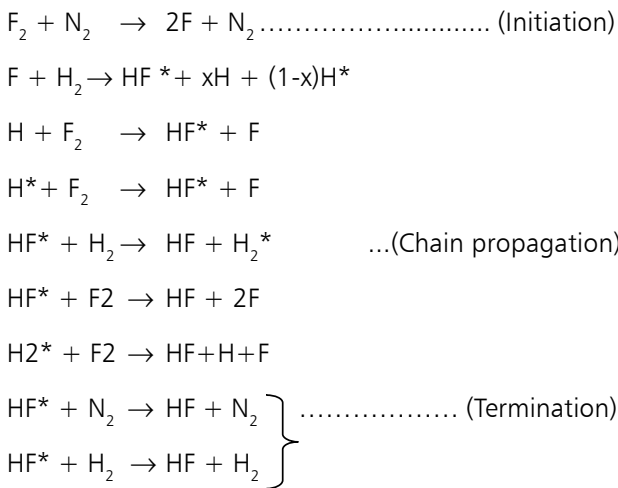
The energy needed for many chemical reactions of industrial importance may be provided externally, by heating or internally by carrying out an exothermic chemical reaction in the region of interest. One such example is the reaction between H₂ and F₂. The reaction between the two produces a high temperature flame. Majority of the published work deals with this reaction in the context of HF lasers [Chen et al. (1975), Kapralova et al. (1976), Kim and Cho (1994)]. Very little work has been reported on its utilization for material processing in chemical and nuclear industries. Scanty information is available for potentially explosive mixtures like H₂ and F₂.

It was reported by Grosse and Kirshenbaum (1955) that, self ignition takes place whenever fluorine gas issues into hydrogen atmosphere, even at room temperature. Table 1 gives the flame temperature for pure hydrogen-fluorine reaction, mixed in different proportions at atmospheric pressure and room temperature, as reported by Wilson et al. (1951). Basov et al. (1969) consider that the reaction between H₂ and F₂ involves a branched chain mechanism. According to Sullivan et al. (1975), H₂-F₂ reaction is of chain type, where free radicals help in the propagation of the reaction steps. In a mixture of F₂, H₂ and N₂, the envisaged reaction steps are as follows:



Table 1: Theoretical flame temperature by Wilson et al.(1951)

Mole% F ₂	Mole% H ₂	Theoretical Flame Temperature at 1atm(K)
10	90	1920
33.3	66.7	3550
50	50	4300
66.7	33.3	3800



The fluorine atoms required to initiate the reaction are formed either by dissociation at higher temperature or by collision of fluorine molecule with another high velocity molecule. Rabideau et al. (1972) found the specific rate constants for H+F₂ and F+H₂ reactions at 300K to be 2.5±0.2x10¹² cm³/mole.sec and 4 ± 1x10¹² cm³/mole.sec respectively. The concentration profile presented by Zebib et al. (1975) showed, that H₂ and F₂ never co-existed as the reaction was immediate. In the present work, the reaction between H₂ and F₂ has been carried out in a long tubular reactor, operating at low pressure. Effect of the ratio of F₂ and H₂ flow rates on reactor temperature has also been studied. Nitrogen is always present along with fluorine when it is produced from electrolysis of HF. Therefore, studies on effect of nitrogen flow rates on reactor temperatures were also performed. The experimental data was used to validate a numerical model. The model, thus established, can be used as a tool to simulate cases involving higher reactant flow rates for reactor design and scale up.

Experimental set up

Fig. 1 shows the block diagram for the H₂-F₂ reaction system. The experimental set up consists of a tubular reactor, feeding arrangements and a scrubber. Hydrogen is supplied from a cylinder, while fluorine is generated by electrolysis of hydrogen fluoride in an electrolytic cell using KF.2HF as the electrolyte. The F₂ from the electrolytic cell is premixed with a known quantity of N₂. Flow rates of hydrogen and fluorine mixed with nitrogen are regulated through respective flow control valves. The reactor wall is preheated to 423 K using an on-off temperature controller. Four B-type thermocouples tagged T1 to T4 have been used near the feed nozzles, while five K-type thermocouples are placed away from them. Further details of thermocouple location are given in Table 2. The exit points of fluorine and hydrogen nozzles in (r, θ, z) format are at (10,0,140) and (10,180,130) respectively. The reactor wall temperature is controlled by removing the heat of reaction by regulated air/water cooling. One pressure transmitter and two pressure switches are installed in the reactor. Safety interlocks are invoked to guard the reactor from high temperature and pressure surges. HF, F₂ and H₂ sensors are installed appropriately to detect the release of gases and alert for corrective action. As a redundant safety measure, one rupture disc is also attached to the reactor which opens directly to the scrubber. The effluents are routed to scrubber, where HF is neutralized with KOH solution. Excess hydrogen is vented to the atmosphere through a flame arrester and a water seal. The reaction is carried out remotely from control room using PLC and data is recorded through SCADA.

Experimental observations

The cases with varying flow rates of F₂ and H₂ are listed in Table 3. Adiabatic flame temperatures for these cases are also shown in this table, which varies from ~1100 to 3000 K. It was practically impossible to measure this high temperature, that too in a highly corrosive atmosphere. Therefore, the temperature sensors (T1 to T4) were placed in such a way, that they do not lie in the flow path of the fluorine stream. Thermocouple T1 recorded the highest temperature in all the runs. As seen in Figs. 2 and 3,



Table 2: Location of thermocouples in cylindrical coordinates

Thermocouple	Angle in anticlock wise direction	Radius in mm	Distance in mm from Top of reactor flange
T1	270	4.5	178
T2	90	4	173
T3	197	5.7	161
T4	15	18.5	154
T5	115	26	260
T6	90	25	260
T7	33	20	260
T8	135	16	594
T9	135	16	764

thermocouple T3, which is radially farther from the F₂ nozzle tip as compared to T4, always recorded higher temperature than the latter. It indicates that the flame expands to a radius of ~ 16 mm at a longitudinal distance of 20 mm. Thermocouples T5, T6 and T7 which are relatively closer to the reactor wall, recorded temperatures in the range of 490-570 K, which are much higher than the preset wall temperature. The temperature profile is flattened down the length of the reactor as the difference between T6 and T7 was 60-70 K as compared to 500-700 K, the difference between T1 and T2 placed at the top. During the experiments, no rise in reactor pressure was recorded through the transmitter.

In cases 3 to 11, effect of volumetric excess of hydrogen was studied on reactor temperature profile and the results are shown in Figs. 7a - c. In all the cases, the drop in the value of T1 was in the range of 20-80 K. The net change in T1 decreased at higher fluorine flow rates, suggesting that the effect of excess hydrogen reduces, when higher amount of energy is liberated inside the reactor. At low fluorine flow rate, the heat evolved is comparatively less and the high temperature zone is confined to a small region. As the hydrogen flow increases, more hydrogen molecules reach near the fluorine nozzle where the reaction takes place. Since hydrogen has higher thermal diffusivity, the rate of lateral heat dissipation increases, resulting in increase in temperature being recorded by T4 which is

slightly away from the nozzle radially. As the fluorine flow rate increases, more heat is liberated leading to higher temperatures near the nozzles. The high temperature zone also expands due to local turbulence. Therefore, with higher H₂ to F₂ flow ratio, both T1 and T4 values go down while T7 gains temperature. The gap between the values of T4 and T7 goes on decreasing with increase in hydrogen flow rate. There is almost no

variation in the values of T8 as flow of hydrogen increases. This suggests that the effect of excess hydrogen on the reactor temperature is limited to a distance of ~120 mm from the F₂ nozzle tip.

Study on the effect of nitrogen on reactor temperatures was performed through cases 12 to 17. From Figs. 8a - c, drop in temperatures as indicated by T1 and T4 was between 200 and 300 K, when nitrogen flow was increased from ~0.4 slpm to 3.5 slpm. Thermocouples T4 and T7 are located almost at the same radial distance but T7 is ~110mm farther from T4. When the nitrogen flow was varied for 0.2 slpm of fluorine, initially, at lower nitrogen flow rate (0.4 slpm), the value of T4 was more than T7 [Fig. 8(a)]. But, as the nitrogen flow was increased, T7 exceeded T4 by almost 100 K. When the nitrogen flow rate was increased to 3.4 slpm, the drop in T4 was close to 180 K while the rise in T7 was nearly 100 K. The gap between T1 and T7 reduced with increasing nitrogen. The temperatures as indicated by T8 and T9 were almost unaffected. Similar effects of nitrogen flow on reactor temperatures were observed for the other two flow rates of F₂, that is, at 0.3 and 0.4 slpm. Dip in T1 and T4 values and simultaneous rise in the value of T7 imply the expansion of the high temperature jet. More nitrogen adds momentum to the fluorine stream, leading to increase in its velocity. It also results in spreading of species and dissipation of reaction heat to a larger volume. However,



as observed in the case of excess hydrogen, this effect too appears to be limited to a length of ~120 mm as reactor temperatures below this length did not show any notable change.

Modeling

In order to simulate the reaction under consideration, a 3-D geometry model of reactor was made using GAMBIT 2.2.30. FLUENT version 6.2 was used as a CFD solver and also for post processing. To capture the mixing as well as the reaction phenomena, a fine mesh was adopted near the nozzle exit region. Fluorine and hydrogen issuing into the reactor have lower velocities, and un-mixed flows of these gases are in laminar region. However, when the gases mix and react together, temperature goes up to such an extent, that the flow becomes turbulent. Therefore, a turbulent flow model has been considered here. Species transport model has been used to study the mixture of species in the reactor. As the reaction is instantaneous, the overall rate of reaction is controlled by turbulent mixing. Rate of change due to reaction source has been calculated

by Eddy Dissipation Model (EDM). Mass flow inlet in kg/s is given as the inlet boundary condition for both the nozzles. Thermo-physical properties for all the species namely F₂, H₂, HF and N₂ and their mixture are selected from the Fluent data base. 'Outflow' is given as the outlet

boundary condition which assumes zero diffusion $\left(\frac{\partial \phi}{\partial x} = 0\right)$ flux at the outflow cells, where ϕ is

any flow variable. Inlet gas temperature for both the hydrogen and fluorine gases is given as 423 K. Wall temperature is maintained at 423K. The reactor pressure is given as 1000 mbar (abs).The radiation heat transfer has not been considered in the simulation, due to low emissivity values of flames. Ideal gas law has been used to take care of the density variation due to temperature change. No-slip boundary condition is employed at the walls. Relaxation factors of 0.3, 0.7, 0.8 and 0.8 have been used for pressure, momentum, turbulent kinetic energy and turbulent dissipation respectively. Simulations

Table 3: Gaseous flow rates and adiabatic flame temperature

Case no.	Flow Rate,F ₂ (slpm)	Flow Rate,H ₂ (slpm)	Flow Rate,N ₂ (slpm)	Adiabatic flame temp in K
1	0.44	2	0.52	2488
2	0.5	2	0.5	2691
3	0.2	0.63	0.4	2682
4	0.2	0.85	0.4	2367
5	0.2	1.27	0.4	1954
6	0.3	0.95	0.45	2830
7	0.3	1.27	0.45	2487
8	0.3	1.91	0.45	2025
9	0.4	1.27	0.5	2911
10	0.4	1.7	0.5	2545
11	0.4	2.54	0.5	2067
12	0.2	0.85	0.9	1933
13	0.2	0.85	3.4	1090
14	0.3	1.27	1.9	1715
15	0.3	1.27	3.4	1333
16	0.4	1.7	1.5	2043
17	0.4	1.7	3.5	1500



have been carried out with flow rates of hydrogen, fluorine and nitrogen as given in Table 3. The steady state condition is assumed and the solution was iterated until the stipulated convergence criterion of residue $< 10^{-4}$ was achieved for each run.

Modeling results and comparison with experimental observations

Initially, simulation was carried out using 0.75 and 1 mm grids, in order to verify the grid independency. The difference in temperatures at various locations for both the grid sizes as shown in Fig. 2 is not significant. However, there is a large difference between the computational time requirements for the two grid sizes. Therefore, further simulations were carried out with 1 mm grid size. In order to check the effect of turbulence model, simulations were carried out for 'case 2' using both standard $k-\omega$ and standard $k-\epsilon$ models. The temperature values of T1 through T9 are compared with the experimental data in Fig. 3. It is seen that the predictions with $k-\epsilon$ model are closer to the experimental data. Therefore, $k-\epsilon$ model for turbulence was chosen for simulations. The temperature contours are presented in Fig. 4 for cases 1 and 2. It can be seen that, reaction flame does not touch the reactor wall, and its length is around 120 mm in both the cases. Experimentally also, high temperatures are observed at locations of T5, T6 and T7 at ~ 120 mm from the nozzle, which further confirms the hypothesis. Fig. 5 shows the Y velocity contours for the two cases. From this figure, it is seen that velocity in the downward direction is predominant near the fluorine nozzle. A part of the hydrogen flow has upward motion suggesting some recirculation in the region near the hydrogen feed nozzle. The nozzles were inspected after the reaction had been carried out. Both the nozzles were found to be intact and clean, as if they have been passivated with diluted fluorides. One of the reasons attributed to the occurrence of this phenomenon, could be some length taken for hydrogen molecules to diffuse, mix with fluorine molecules and react. This observation is further confirmed by the simulation results shown in Fig. 6 where, hydrogen streamlines are seen bending towards the fluorine

streamlines and intersecting them slightly away from the nozzle tip. Since the velocity of hydrogen stream is lower, it is dragged by the relatively high velocity fluorine and nitrogen stream. The validated model used for cases 1 and 2 was deployed in simulating another 15 cases as mentioned in Table 3. Fig. 9 shows the comparison of simulated and experimental reactor temperature readings for few selected cases. There is a good match between the two. The computed data follows the experimental trend of increase and decrease in temperatures when a particular parameter is changed.

Conclusion

The reaction between hydrogen and fluorine has been carried out in a tubular reactor for different flow rates of reactant gases and also has been computationally simulated. The assumption made during the simulation that the reaction between hydrogen and fluorine is instantaneous and the flow field is turbulent has produced results, which match well with experimental observations. The reaction between hydrogen and fluorine takes place along the axis of fluorine flow jet. The flame does not form right at the nozzle tip because of insufficient fuel present locally. The flame temperature is affected by parameters such as excess of hydrogen and fraction of nitrogen present in the fluorine. With increasing flow of hydrogen, the temperature near the nozzle drops while the reactor temperature away from them increases. The drop in temperatures near the nozzle area is substantial with increasing nitrogen flow rate. The computational results also show similar behaviour. The good match between the experimental results and the numerical predictions validate the computational model. This tool can now be used to assist in the design of a scaled up H_2-F_2 -flame reactor.

References

1. Basov, N.G., Kulakov, L.V., Markin, E.P., Nikitin, A.I. and Oreavskii, A.N. Emission spectrum of a chemical laser using H_2-F_2 mixture. *ZhETF Pisva Red* 9 (1969): 613.



2. Chen, Hao-Lin; Daugherty, J. D.; and Fyfe, W. TA5- H_2/F_2 flame propagation and repetitively pulsed hydrogen fluoride (HF) chain-reaction chemical laser. *IEEE Journal of Quantum Electronics*, QE-11 (8) (1975): 648-653.
3. Grosse, A.V. and Kirshenbaum, A.D. The premixed H_2-F_2 flame and its burning velocity. *J. of American Chemical Society*, 77 (1955): 5012-5013.
4. Kapralova, G. A.; Trofimova, E .M.; Chaikin, A.M. Chain branching in the fluorine-hydrogen reaction. *Reaction Kinetics and Catalysis Letters*, 4(3) (1976): 381-387.
5. Kim, Sung-Ho; Cho, Ung-In. Theoretical investigation on the effects of additive oxygen in HF chemical laser performance, *Bull. Korean Chem. Soc.*, 15(9) (1994): 724-729.
6. Rabideau, S.W., Hecht, H.G. and Burton, L.W. A study of the Kinetics of the reaction between H_2-F_2 by EPR Methods. *J. of Magnetic Resonance*, 6(1972): 384- 395.
7. Sullivan, J.H., Feber, R.C. and Starner, J.W. Mechanism and types of explosives behavior in hydrogen-fluorine systems. *The Journal of Chemical Physics*, 62(5) (1975):1714-1725.
8. Wilson, R.H., Conway, J.B., Engelbrecht, A., and Grosse, A.V. The temperature of hydrogen-fluorine flame. *J. of American Chemical Society*, 73 (1951): 5514
9. Zebib, A., Williams, F.A. and Kassoy, D.R. Effects of Kinetic Mechanism on Diffusion-Controlled Structure of Hydrogen-Halogen Reaction Zones. *Combustion Science and Technology*, 10(1-2) (1975): 37-44.



Indigenous Development of HDR Source Assembly for Brachytherapy

M.K. Mishra, D.N. Badodkar and Manjit Singh

Division of Remote Handling & Robotics

and

K.V.S. Sastry and A.K. Kohli

Board of Radiation and Isotope Technology

Mr. M.K. Mishra received the DAE Young Engineer Award for the Year 2009

Abstract

Indigenous development of High Dose Rate (HDR) source assembly for Brachytherapy was taken up at the Division of Remote Handling & Robotics (DRHR) jointly with the Board of Radiation and Isotope Technology (BRIT). Recently, HDR source assembly was successfully qualified as per regulatory requirements and was approved for commercial use. The paper brings out the evolution of the design, development of gadgets for handling & welding inside the hot cell and its qualification.

Introduction

Treatment of cancer by using radiation emitted from radioisotopes or the radiation from the accelerators, is a well established procedure and is in practice for decades. Teletherapy and Brachytherapy are widely used for this purpose. In teletherapy, the cancerous tissue is irradiated by gamma rays emitted by radioisotopes. In brachytherapy mode of treatment, the radioactive source is kept near the cancerous tissue.

"Brachy" is a Greek word meaning short; hence Brachytherapy means short distance therapy. It is also known as internal radiotherapy or sealed source radiotherapy. This is a form of radiotherapy, where a radiation source is placed inside or next to the area requiring treatment. It allows use of a high dose of radiation, while reducing the risk of damage to nearby healthy tissues and increasing the

likelihood of cancerous tissue being destroyed. Brachytherapy is commonly used as an effective treatment for cervical, prostate, breast, localized uterus, head and neck and skin cancers.

Applicators in the form of catheters are arranged on the patient. A high dose rate source (often Iridium- 192) is then driven along the catheters on the end of a wire by a machine, while the patient is isolated in a room. The source remains in a preplanned position for a preset time, to allow controlled doses of radiation to be delivered to the cancerous tissues, without damaging the healthy tissues. Brachytherapy equipment requires accurate positioning of radioactive source of Ir¹⁹² within the close proximity of the cancerous area by ensuring safety of patient, operator, and general public with respect to radiation related hazards, achieving fail-safe, forward-backward movements of the radioactive source, etc.



The capsules that hold the radioactive 'seed' are only a few millimetres long, and about a millimeter in diameter and have a wall thickness of around 200 μm .

Description

The Brachytherapy source is sealed, so that the radioactive material is fully encapsulated within a protective capsule. HDR source assembly consists of radioactive material, miniature housings, end cover and metallic wire ropes. The assembly has five laser-welded joints between stainless steel wire ropes and miniature components. The component detailing and its design have evolved through ease of manufacture, assembly, handling and welding considerations. Laser welding parameters were finalized through several trials. Initially, laser-welded joints were studied through X-ray tomography for ensuring their quality followed by pull tests, to check the joint strength and its consistency.

A typical HDR source assembly is shown in Fig. 1. It has four miniature stainless steel micro-machined components viz.; machine end terminal, rope joining sleeve, source retaining capsule and cover and two stainless steel wire ropes of dia 0.91 and 0.73 mm. Overall size of the assembly is $\text{\O}1.1 \text{ mm} \times 2.1 \text{ metres}$ long. There are four laser-welded joints between stainless steel wire ropes and miniature stainless steel components and one laser-welded joint, between two miniature stainless steel components. The weld that joins the source-retaining capsule with its cover,

is needed to produce a hermetic seal, with a smooth weld bead. All the laser welding spots are very fine and perfect, devoid of any imperfections such as micro cracks, air bubble void etc. For each of these welded joints, laser welding parameters were optimized through series of trials at various stages.

Handling, Assembly and Welding

Considering miniature components and their handling inside the hot cell, laser welding was chosen. Wire rope end preparation went through several trials for avoiding flaring of wire rope strands and achieving ease of assembly with the matching part.

The welding system consists of industrial Nd:YAG laser, a motorised rotary unit, self centering holding device for miniature parts, inert gas purging arrangement, a CCD camera with 100X magnification to view the weld joint remotely.

Fig. 2 (a) shows laser welding system, Fig. 2 (b) shows welded joints and Fig. 2 (c) shows full-length welded HDR source assembly. In order to qualify the assembly, dummy source was used. In the final assembly, weld joint namely LW₅ (Fig.1) involving the source, is carried out inside the hot cell. In order to facilitate handling of miniature components during active welding inside the hot cell, assembly gadgets were developed and demonstrated for their capability in holding the assembly in position during

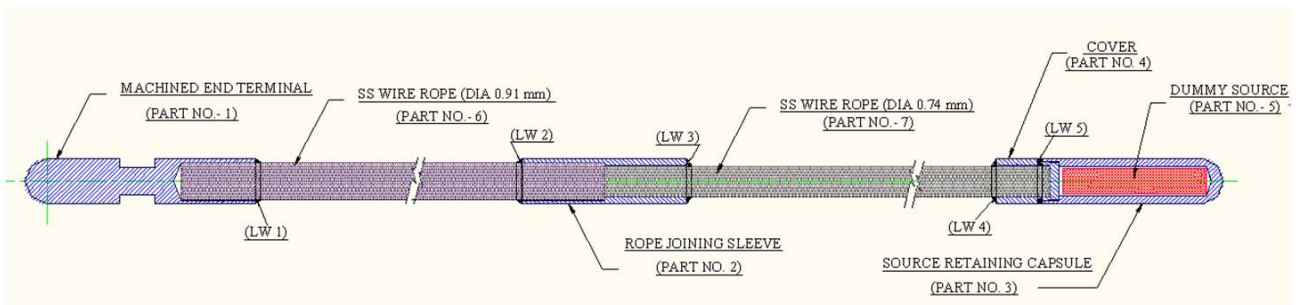


Fig. 1: HDR Source Assembly for Brachytherapy (Overall Dimension: $\text{\O}1.1 \text{ mm} \times 2.1 \text{ meter}$ long)



laser welding. A motorized semi-automated welding unit for welding inside the hot cell was designed and manufactured for this purpose (Fig. 3).



Fig.2 (a): Laser Welding System



Fig. 2 (b): Welded Joints



Fig. 2 (c): Full Length welded HDR Source Assembly



Fig. 3: Semi-automated welding system used for welding inside the hot-cell

Testing and Qualification

Laser parameters were optimized and several samples were prepared to carry out load tests. Initially, a few samples were subjected to non-destructive examination through 3D X-ray micro-tomography, which provided a good insight into its three-dimensional spatial distribution. Some samples were tested for pull strength on the Hounsefield Tensometer, based on which weld parameters were finalized.

After finalizing the welding parameters of all the joints, four samples were randomly selected from the lot of twenty full-length HDR source assemblies and subjected to qualification tests as per AERB/SS/3/Rev. 1 and source classification C-53312. The qualification tests included high pressure, low pressure, high temperature, low temperature, impact and puncture tests. Fig. 4 shows the tested samples along with impact and puncture tools used for the test. After each of these tests, the samples were subjected to helium leak testing.

All the samples have successfully passed the tests. Based on the successful qualification, the Atomic Energy Regulatory Board (AERB) approved and granted permission for production and deployment of indigenous HDR Source assembly for commercial use.



Fig. 4: Impact and puncture testing

Acknowledgement

Authors are thankful to Head, CDM and his team for helping in manufacturing of stainless steel miniature parts and testing. Authors are thankful to Dr. S. M. Oak, Shri B. N. Upadhyaya and the team at RRCAT for laser welding. Authors are also thankful to Dr. A. Sinha, Shri P.S. Sarkar, LNPS, BARC for their help in X-ray micro-tomography.

References

1. B. N. Upadhyaya, M. K. Mishra, S. C. Vishwakarma, R. K. Jain, A. Choubey, D. K. Agrawal, D. N. Badodkar, Manjit Singh, K. V. S. Sastry, B. N. Patil, and S. M. Oak, "Laser micro-welding of brachytherapy assembly having high dose rate source", *DAE-BRNS National Laser Symposium (NLS-08)*, 7-10 Jan. 2009, LASTEC, New Delhi.
2. P S Sarkar, A Sinha, M K Mishra, D N Badodkar, M Singh, K V S Sastry and A K Kohli, "X-ray micro-tomography-based non-destructive evaluation of microwelds in HDR source assembly used for brachytherapy", *Journal of The British Institute of Non-Destructive Testing: Insight* Vol. 53, No. 1, January 2011; pp: 25-28.
3. Safety Standard for Testing and Classification of Sealed Radioactive Sources, Document No.: AERB/SS-3, Rev. 1, Issue 2001.



AKRUTI - DAE Societal Initiative

AKRUTI - Advanced Knowledge & RUrAl Technology Implementation

Dr. K.B. Sainis

Bio Medical Group

and

A.M. Patankar

Technology Transfer & Collaboration Division

This Paper received the DAE Group Achievement Award for the year 2009

Abstract

To derive nuclear technology enabled societal benefits, the Advanced Knowledge and RUrAl Technology Implementation (AKRUTI) programme has been formulated and implemented in collaboration with many divisions of BARC, DAE units, the Rajiv Gandhi Science & Technology Commission (RGSTC) of the Government of Maharashtra (GoM) and NGOs working on technically oriented activities in rural sector. Seven AKRUTI nodes in Maharashtra and seven in other states of India have been set up, and most of them are functional for more than a year. Technologies deployed in various villages by NGOs, through village working groups under the guidance of BARC experts are: NISARGRUNA, Domestic Water Purifier, Soil Organic Carbon Detection Testing Kit, Foldable Solar Dryer, Vibro Thermal Disinfestor and Isotope Hydrology for investigation of underground water resources. A Tissue Culture Laboratory for micropropagation of banana plants with field hardening facility and Fruit Processing Unit has also been set up. A Rural Human and Resource Development Institute is being proposed, to train a committed work force to further spread the AKRUTI programme. This institute will work as a centre for DAE outreach programmes, for DAE technologies.

Background

Large-scale deployment of Non Power Applications (NPAs) and spinoffs, is the 4th key driver of major programmes of the DAE. As one of the schemes of this major programme to deliver or reach nuclear technology enabled societal benefits to the rural population, a structured programme called "AKRUTI-KRUTIK-FORCE" has been formulated and it is being implemented by BARC, for techno-economic growth of the rural sector. This programme has been worked out to complement, supplement and augment the efforts of similar programmes of different organisations,

departments and ministries. The programme, more popularly known as AKRUTI programme, is promoted as part of DAE Societal Initiative. AKRUTI programme is the culmination of interactions of a very large number of divisions of BARC and DAE units and collaborative experience of BARC-DAE scientists and engineers with National R&D laboratories, Agricultured Universities, KVKS, Farmers' Co-operatives, other Government Departments, Industries and NGOs. Technologies deployed in this programme cover areas related to water, land improvement, agriculture, food processing and urban-rural waste processing for value addition.



Programme Structure

The programme AKRUTI-KRUTIK-FORCE is designed to create structured and scalable network of technology nodes in rural areas, providing easy access to modern technologies to all villagers in their own villages. 'AKRUTI' is an acronym for 'Advance Knowledge and RUrAl Technology Implementation' programme. Through this programme, AKRUTI node is set up in a village, where technologies are deployed and demonstrated.

The programme is run under the guidance of BARC, through NGOs working to bring science and technology to that village. AKRUTI node parks a number of BARC developed technologies for use by villagers. These technologies are set up and demonstrated by village working groups. They take technologies to different villages around the AKRUTI node via working centres called KRUTIK established in different villages around AKRUTI. KRUTIK stands for 'Knowledge and RUrAl Technology Implementation Kendra, which works with villagers and farmers' groups and helps them to deploy these technologies in their own villages and in the fields. These groups are known as **FORCE** meaning **F**armers' **O**rganised group for **R**ural **C**reative **E**ntrepreneurship. Each member of a FORCE group is made familiar with technologies of AKRUTI through KRUTIK (Fig. 1). AKRUTI and KRUTIKS

are managed by technology oriented NGOs operating in the village. All the activities are carried out by villagers and managed by NGOs under the guidance of BARC-DAE scientists/engineers.

Current Status

Three AKRUTI nodes are set up in Maharashtra State (MS) financed by Rajiv Gandhi Science and Technology Commission (RGSTC), Govt. of Maharashtra, in collaboration with three NGOs viz. CARD, PARIVARTAN and NIRMITEE as follows:

- 'AKRUTI-NIRMITEE' - by NIRMITEE at Uddhar, Dist. Raigad, MS
- 'AKRUTI-PARIVARTAN' - by PARIVARTAN at Chiplun, Dist. Ratnagiri, MS
- 'AKRUTI-CARD' - by Community Action for Rural Development Society (CARD), at Anjangaon Surji, Dist. Amravati, MS

Out of the above three functional AKRUTIs, AKRUTI-PARIVARTAN and AKRUTI-NIRMITEE were inaugurated by Dr. Anil Kakodkar, the then Chairman, AEC and Secretary, DAE on 8th June 2008 at Chiplun and Dr. Srikumar Banerjee, the then Director, BARC, on 1st Nov. 2008 at Uddhar near

Pali, respectively. Due to visits of many NGOs from all over India to these three functional AKRUTIs, eight more AKRUTI nodes came into existence through self financed mode; one each in Andhra Pradesh (AP), Madhya Pradesh (MP), Karnataka, Assam (NER) and four in Maharashtra at the following locations described hereunder.

- AKRUTI-YMC by Yusuf Meherally Centre, Tara Village, Dist. Raigad, MS



Fig.1 : AKRUTI Programme Format



- AKRUTI-ANKUR by Ankur Pratihthan & Sanshodhan Sanstha, Ambajogai, Dist Beed, MS
- AKRUTI by Vivekanand Ashram at Hiwara Bk, Tal. Mehkar, Dist. Buldhana, MS
- AKRUTI by Loknayak Jayaprakash Narayan Leprosy Eradication Trust, at Waliv Tal., Vasai (East), Dist. Thane, MS
- AKRUTI by Fresh-O-Veg Krishak Club at Indore, MP
- NAYUDAMMA's AKRUTI at Kaviti Mandal, Dist. Srikakulam, AP
- AKRUTI by Malenadu Education & Rural Development Society at Sirsi, Dist. Uttara Kannada, Karnataka
- AKRUTI by Shanti Sadhana Ashram (SSA) at Basistha, Guwahati, Assam, NER

Further, to demonstrate application of AKRUTI for CSR and R&R (Rehabilitation & Redeployment) plan, three departmental AKRUTIs have been initiated as follows :

- AKRUTI-Nongjri, Nonghyllam, West Khasi Hills Dist, Meghalaya, NER [AMD-CSR]
- AKRUTI-Dorbar Shnong, Nongmensing, Shillong, Meghalaya, NER [AMD-CSR]
- AKRUTI-SEZ at Dibbapalam, Vizag, AP [BARC-VIZAG - R&R]

Andhra Pradesh Industrial Infrastructure Corporation-APIIC gifted land of three acres to BARC at Dibbapalem village for AKRUTI-SEZ.

Setting Up Akruti Node

Setting up of each AKRUTI node involved a number of steps, including preliminary survey of the location and the NGOs working in the area, selection of the S&T oriented NGO with good credentials, a series of discussions and finally signing of MoU after approvals from competent authority of BARC. Field deployment of technologies in a stepwise manner is coordinated by TT&CD in close association with various Divisions of BARC such as NA&BTD, FTD, DD, IAD and RTD and AMD-Shillong and BARC-Vizag involving a number of scientists and engineers engaged in developing these technologies. The group of scientists and engineers is recognized as AKRUTI team (Fig. 2, Annex-I) and works synergistically to guide and deploy technologies through village working group, under the AKRUTI NGO. This enables the villagers to acquire the knowledge to use, operate, run and maintain the equipment. NGOs in turn, set up KRUTIKs in surrounding villages, in consultation with BARC and create FORCE groups.

Technology Deployment Activities

Seven NISARGRUNA plants in AKRUTI nodes of Maharashtra are running successfully. Four of them are generating electricity using bio-gas. During inauguration, electricity generation was demonstrated by connecting 10KW, biogas generator to Nisargaruna Biogas plant at



Fig. 2: AKRUTI Team with Dr. R. K. Sinha, Director, BARC (seated fourth from left) on the occasion of award distribution ceremony of "Group Achievement Award – 2009". Also seen are Shri S. K. Ghosh, Director, ChEG & Dr. V. Venugopal, Director, RCh&IG (seated 1st and 3rd from left).



AKRUTI-PARIVARTAN (Fig. 3), whereas at AKRUTI-NIRMITEE, public address system, lighting and electrical equipment were run on electricity, generated through NISARGRUNA plant.

Demonstrations of Foldable Solar Dryer (FSD), Vibro Thermal Disinfestor (VTD), Domestic Water Purifier (DWP), Soil Organic Carbon Detection Testing Kit (SOCDTK), SHRI Sludge and New Seeds utilization are carried out, in different villages and fields. DWPs (without electricity) to meet the village needs of clean, bacteria-free drinking water are being assembled, in all the three AKRUTIs of Maharashtra. Foldable Solar Dryers (FSD) are also fabricated in AKRUTI nodes and more than 35 products have been developed using FSD (Fig. 3). Soil testing using SOCDTK has been carried out, by more than 300 farmers in their fields.

Exploration for sustainable underground water source using Isotope Hydrology technique has been initiated, in five sites in different AKRUTIs. At AKRUTI-CARD in Amravati, in a water scarce area, sustainable underground water source with capacity of 30,000 LPH has been identified and established, for use of farmers (Fig. 3).

Laboratory training in tissue culture technology for village farmers as an 'AKRUTI TRAINEE' in BARC, has also been initiated. CARD, Amravati is the first beneficiary of this programme in addition to four more from different



Fig. 3 : AKRUTI Field Activities



Fig. 4 : Tissue Culture Facility at AKRUTI-CARD

AKRUTIs. A tissue culture laboratory and field hardening facility (Fig. 4), with a capacity to produce 50,000 banana plantlets has been set up and completely functional in AKRUTI-CARD, Amravati. One more Tissue Culture facility at AKRUTI-Vivekanand Ashram in Buldhana, has been upgraded

Seven varieties of groundnut, soyabean and mustard seeds weighing 4310 kg have been sown on 250 different plots. AKRUTI node at Indore, MP has reported an average 19% increase in the yield for TPG-41 BARC groundnut variety, as compared to local seeds. This is based on the production of 76.07 quintals from 4.2 quintals of sowed TPG-41 seeds, in eight different fields of four villages viz. Datoda, Badiya, Nirmar, Khadi and Sulgaon. New seed varieties of BARC have been sown for the third time, in more than 100 locations around these AKRUTI nodes through KRUTIKs amongst the villagers and farmers in the surrounding villages. All the above activities are carried out by locals and managed by NGOs, under the guidance of BARC experts.

Rural Techno-Entrepreneurship

A technology package called AKRUTI Tech Pack (ATP) for technically oriented individuals/ entrepreneurs/industry/ companies to promote techno-economic activity in rural sector through AKRUTI programme is offered for EXCLUSIVE RURAL DEPLOYMENT at an affordable price. ATP is made of four technologies - NISARGRUNA, SOCDTK, FSD and VTD and one optional technology - DWP with



consultancy. Women Entrepreneurs (WEs) are further encouraged by providing additional concession on ATP deployment charges with other conditions remaining same.

Community Managed Drinking Water Plant

A number of technologies useful for purification of water by removal of microbes and / or contaminating ions like Iron/Fluoride/Arsenic have been developed at DD, BARC. Some of which have been transferred to industry for effective dissemination in to communities. Actual implementation of these technologies for rural sustainable field use and collection of data is therefore highly relevant. A first BWRO plant with 300 LPH capacity has been installed and commissioned in the field through AKRUTI-PARIVARTAN in Dapoli in the coastal village called Farare for data collection regarding economic sustainability of the deployed technology in field.

Future Direction for Akruti Programme

A dedicated, trained work force needs to be created to speed up the growth of AKRUTI programme and support the growing network of AKRUTI nodes. Creation of Rural Human and Resource Development Institute (RHnRDI), co-located with educational institutes has been proposed, for creation of opportunities in rural sector and for local technical guidance through participation of educational institutes, for healthy growth of AKRUTI programme.

Conclusion

AKRUTI programme complements, supplements and augments the efforts of existing programmes of different organizations, departments and ministries, to facilitate large scale deployment of several useful technologies in rural areas. AKRUTI programme enables the villagers to deploy and use DAE technologies evolved with local adaptations under guidance from BARC. 'AKRUTI-KRUTIK-FORCE' format, enables transfer of the fruits of technology to grass-root level and to every villager in the remote corners and provides inclusive growth to the rural sector

and tap the hidden innovative capability of the large rural Indian population.

References

1. AKRUTI-KRUTIK-FORCE Inclusive Rural Advancement through Technology Deployment, Patankar, A.M., *Nuclear India* (Nov-Dec 2007) Vol. 41/No.05-06, pp 9-12.
2. Website : <http://www.barc.gov.in/akruti-tp/index.html>

Annexure

Group Achievement Award-2009

AKRUTI TEAM

1. Dr K B Sainis, Director, BMG
2. Dr S F D'Souza, AD, BMG
3. Dr S P Kale, NA&BTD
4. Dr S J Jambhulkar, NA&BTD
5. Dr K S Reddy, NA&BTD
6. Dr J G Manjaya, NA&BTD
7. Dr A M Badigannavar, NA&BTD
8. Dr V M Kulkarni, NA&BTD
9. Dr S T Mehetre, NA&BTD
10. Dr A K Sharma, Head, FTD
11. Dr R Chander, Ex-SO/H, FTD
12. Dr M P Jain, FTD
13. Shri D D Shinde, FTD
14. Dr P K Tewari, Head, DD
15. Dr S Prabhakar, DD
16. Dr R C Bindal, DD
17. Smt S T Panicker, DD
18. Shri V S Somarajan, DD
19. Dr G Singh, Head, IAD
20. Dr K Shivanna, IAD
21. Dr S Sabharwal, Head, RTDD
22. Shri M R Shah, RTDD
23. Shri A Ramaiah, IFA
24. Shri P Prabhu, Ex CAO, PD
25. Shri G S Ravi, BARC-Vizag
26. Dr R Mohanty, AMD-NER
27. Smt S S Murudkar, TT&CD
28. Shri T H Salunke, TT&CD
29. Dr N Khalap, TT&CD
30. Smt S S Mule, TT&CD
31. Shri A M Patankar, Head, TT&CD, Group Leader



Design & Manufacture of Fuel Rod Cluster Simulators & Instrumented Steam Generators For FISBE Project of RED

R.L. Suthar, CDM & D. Saha, Head, RED
 S.B. Jawale, P.K. Vijayan, C.P. Mahajan, H.B. Panse, S.P. Srivastava
 & 57 Officers / Technicians of CDM & RED

This paper received the DAE Group Achievement Award for the year 2009

Introduction

Design & Manufacturing of both these systems was an example of dedicated & meticulous group effort. The team could successfully manufacture & supply these high pressure high temperature systems with extensive instrumentation tapings, a manufacturing engineer's challenge, which was an all time first achievement for India and only the second one in the world. The group activity involved the following:

Product development; Critical fabrication of intricate and complex product; Quality control as per QA plan; Extraction of all Instrumentation tapings through two high temperature high pressure boundaries; using various feed thru ports; Meticulous assembly of the complete system and Successful transportation to RED site were the tasks carried out by this group from CDM. Also, this group has contributed extensively to the design modifications for manufacturing feasibility and optimization by mutual discussions for both these products.

CDM has successfully manufactured and delivered two Instrumented Steam Generators for Facility for Integral System Behavior Experiments (FISBE) as per design and drawings provided by RED, BARC.

FISBE facility simulates the Primary Heat Transport (PHT) system of a 235 MWe PHWR, viz., the Fuel Rod Cluster Simulators (FRCS), the Steam Generators (SGs), the

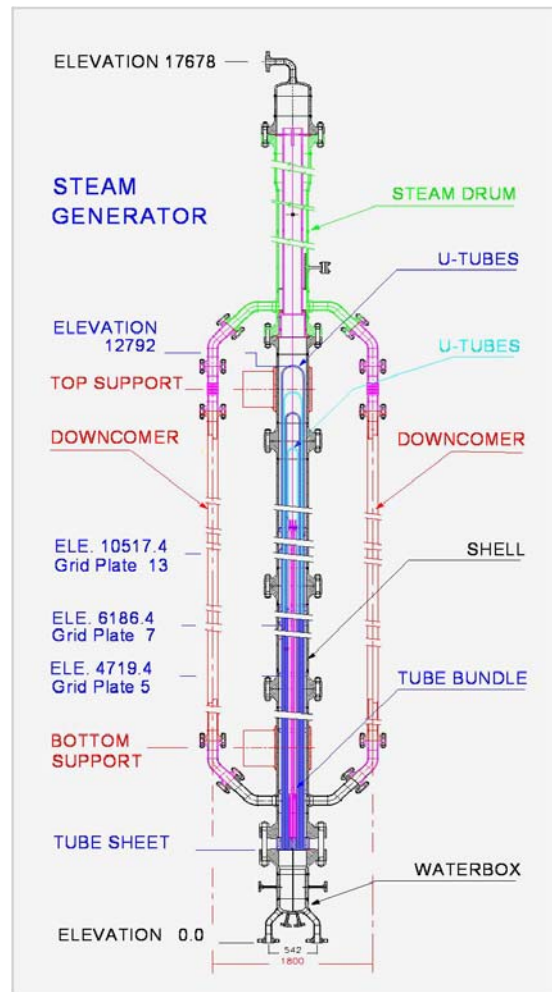


Fig. 1: Steam Generator vertical Assembly

DAE Excellence Award



Emergency Core Cooling System (ECCS), the Feed and the Bleed systems, along with their associated control systems. The facility is to be used for conducting thermal hydraulic experiments, by simulating steady state, transient and accidental conditions, which may occur in a PHWR.

Steam Generator

The Steam Generator (SG), Fig.1, is one of the key components in the FISBE loop, which contributes a great deal in simulating the behavior of the PHT system of the PHWR. It is a U-tube type, scale down model / replica of the SG of a PHWR. It's scaling down is only for the quantity of the U-tubes, keeping the elevations of all components, the same as that of the Steam Generator of a PHWR, thus making it a highly compact equipment with a high slenderness ratio. The Temperature, Pressure and flow conditions of the Primary and Secondary sides of the fluids are maintained the same as that in a PHWR, to realistically simulate the heat transfer characteristics in the FISBE Steam Generator. A total of 96 tapping points: 84 for Temperature, 6 for Pressure, 4 for Flow rates, 2 for Level and Differential pressure measurements are provided.

Its design conditions are as follows: (Designed as per ASME B&PV Code, Sec. VIII

Primary (Tube) Side Pressure. = 112.5 bar, Temp. = 315°C
 Secondary (Shell) Side: Pressure = 70.0 bar, Temp. = 285°C

Manufacturing of the highly compact, slender scaled-down models / replicas of high-temperature and high-

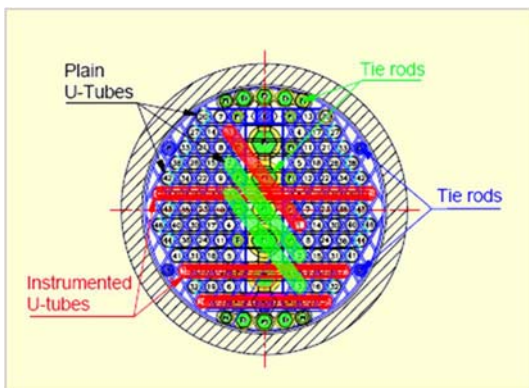


Fig. 2: Cross Sectional view of Steam Generator Assembly



Fig. 3; Vertical set up for Tube Bundle for welding of tube to tube sheet

pressure systems, was a challenging task for CDM, as the outside industries quoted exorbitant cost for the manufacture of the same. The assembly and safe installation of the instrumented tubes, Fig. 2, without damaging the thermocouples, was a painstaking effort.



Fig. 4: Tube Bundle final Assembly

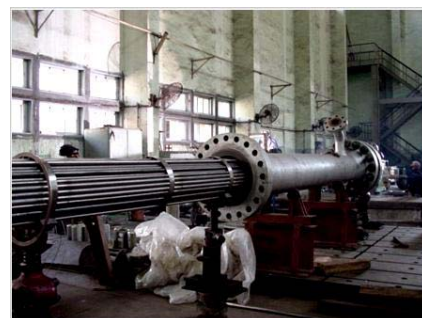


Fig. 5: Assembly, one by one of the shells, on the 11.5 meter long Tube-Bundle



Their manufacture required a lot of innovation and development of manufacturing processes. This work also involved incorporation of many design modifications in consultation with the designer.

The successful fabrication of the Steam Generators involved development of the following manufacturing processes.

- 1) Welding process for cladding of C.S. Tube Sheet with Inconel-600.
- 2) Manufacturing processes for fabrication of U-tubes:
 - 2a) Forming of U-bend of Incoloy-800, 16 mm dia. / 1mm wall thick tubes on 1st leg to the desired radius at the same time controlling the ovality and wall thinning (within 10% of wall thickness).
 - 2b) Development of the welding process as per Section IX of the code, by automatic orbital pulse TIG welding method, for butt-welding of Incoloy-800, tubes of the 2nd straight leg to the U-bend formed 1st leg of U-tubes.
 - 2c) Development of Brazing process as per the Code for joining SS sheathed Mica clad 1mm dia. thermocouples to SS-304L capillary tube thermo wells (to introduce the thermocouples into the U-tubes) compatible for the given high pressure and high temperature service.
 - 2d) Development of brazing process as per the code for installation of the SS Sheathed Mica clad 1 mm dia. thermocouples in the grooves machined on Incoloy-800 U-tubes, and Fork Strips, compatible for the given high pressure & high temperature service.
 - 2e) Development of machining process for machining of miniature grooves on the 11.5 meter long Incoloy-800 U-tubes, at various locations, and machining of fork strips for installation of the SS Sheathed Mica clad 1 mm diameter thermocouples.
 - 2f) Insertion activities for the instrumented U-tubes, without damaging their thermocouples, into the Tube-bundle skeleton / structure was more painstaking and required a lot of patience and skill.
- 3) Manufacturing processes for fabrication, Welding and brazing of components on the Instrumented U-tubes:
 - 3a) Development of welding processes as per Section IX of the code for welds of Incoloy-800, 16 mm dia. /1 mm wall thick, U-tubes to 10 mm dia. /0.8 mm wall thick SS-304L tubes for Impulse line tapings. (Fig. 6.)
 - 3b) Development of welding processes as per the Code for welding, by pulse TIG welding process, for welding the SS 304L Capillary Tube thermo wells to the Incoloy-800, U-tubes, for introducing the thermocouples into the U-tubes. Ref.Fig.5.



Fig. 6: U-tubes with tapings for Thermocouples and Impulse tube



Fig. 7: Steam Generator final Assembly



- 4) Development of manufacturing processes for joining of Tube to Tube sheet:

 - 4a) Process parameters were established, by mockup trials. The joining process was qualified by DP test, Helium leak test, Pull-out test and Micro-etching tests of the welds to ascertain minimum leak path. Minimum leak path of 1 mm for tube-to-tube sheet joint could be achieved for all the tube joints.
 - 4b) Welding of Tube-to-Tube sheet was done by TIG welding process, in 1G position by holding vertical the 11.5 meters long slender and delicate Tube Bundle assembly on a special handling fixture. (Ref. Figs. 3)
 - 4c) Contact rolling (expansion) of tube inside the tube sheet was done for full tube sheet thickness, by three stage over-lapped contact rolling method, because long rollers (equal to thickness of tube sheet) are not available in the market for the given diameter. Percentage of expansion was controlled, within 3 to 4% wall thinning, during the contact rolling operation.

- 5) Assembly of the Tube bundle was very critical, as only 0.5 mm clearance is available for insertion of the 11.5 meter long U-tubes in the openings in the

grid plates. All the 14 Grid plate assemblies are required to be aligned to the best possible extent to permit the assembly of very long U-tube. Tube bundles of both the Steam Generators, were successfully manufactured and the tube side of the bundle assemblies were successfully Hydro-tested at 320 bar pressure.

- 6) Fabrication of the Shells of the Steam Generator was done by qualified welders and as per approved welding procedure/WPS as per Section IX, inspected as per Section V and accepted as per Section VIII of the ASME B&PV Code.
- 7) Final Assembly of the individual shells: The segmental 4 nos. shells were assembled over the 11.5 meter long Tube bundle, one by one, and with safe extraction of thermocouples without damaging them through their respective extraction ports on Shells. Supports for the Tube bundle are to be removed and Thermocouples are to be extracted through the outlet Thredolets nozzles progressively, while the Shells, held by the crane, are slowly being moved in to its position on the bundle. The two completed Steam Generator Assemblies.(Fig.7), have been successfully subjected to Hydro-tests as follows:

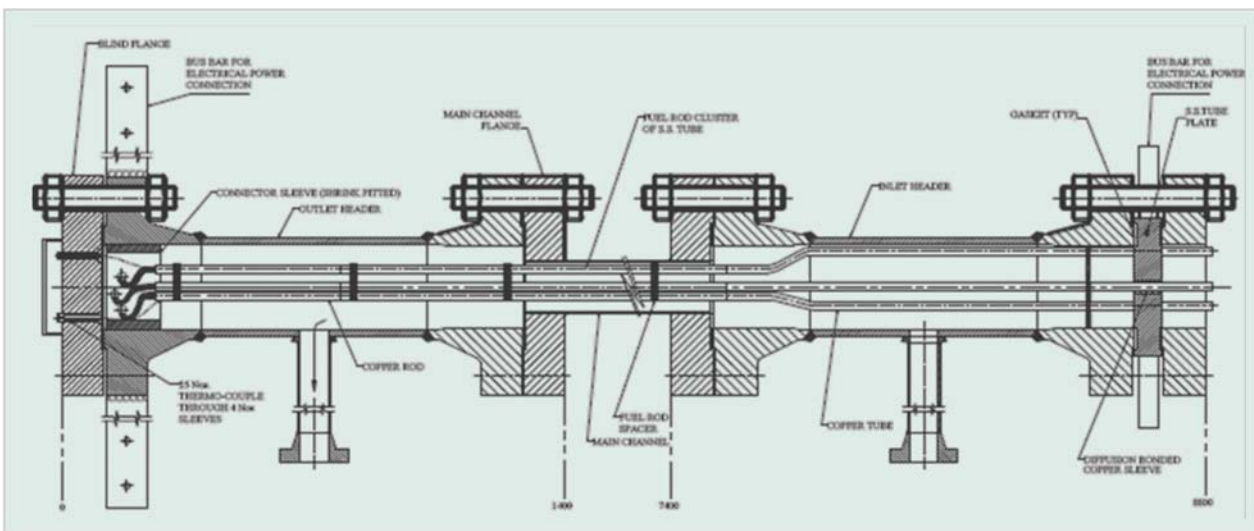


Fig. 8: Cross-section of Fuel Rod Cluster Simulator Assembly



Tube Side Pressure: 320 bar, at Room temp.

Shell Side Pressure: 115 bar, at Room temp.

- 8) Safety during transportation of the Steam Generators: For protecting the vulnerable (spiral wound metal) gaskets at the flanged bolted joints during transportation, special protective close fitting spacers / packing were machined and fixed on all the flanged joints. This special care is needed as the gaskets once assembled are non-replaceable during the life of the Steam Generator. Also Special handling fixture and supporting brackets were fabricated for lifting, handling transportation and storage at Hall 7 site.

Fuel Rod Cluster Simulators

The 19 Element Fuel Rod Cluster Simulators (FRCS) represents one Fuel Channel of 230 MWe PHWR. FRCS converts electrical power into equivalent thermal power, to simulate power generation by nuclear reaction in a fuel channel. It consists of 19 6-meter long heater elements (Fig.1), bundled together to form a cylindrical shape of 83 mm dia, with the help of six spacers. Each heater element is a thin walled 16mm dia SS304L tube filled with Ceramic pellets with Copper leads brazed at either ends. At the Outlet end, the Copper lead is a 750mm long solid rod, with flexible braided Copper lead of its end, and at the Inlet end, the lead is a Copper tube 1250mm long, which in turn is brazed to the SS Tube



Fig. 10: Fuel Rod Cluster Ready for Insertion into the Channel

Plate. (Fig.10). The Copper lead tubes are diverted to form a larger array to facilitate simultaneous brazing of all 19 Fuel Rods. The brazed joints with Tube Plate form the pressure boundary at the Inlet end. (Fig.9).

Five of the Fuel rods are instrumented, each carrying 4 thermocouples and another 5 thermocouples are attached to the five spacers. All 25 thermocouples are extracted through the blind Flange, at the Outlet end through brazed joints, and these brazed joints form the second pressure boundary. The Heater Element section of the FRCS is housed in a Channel made up of 100 mm N.B. SS304L Tube with appropriate flanges at both it's ends, and insulated by means of Ceramic sleeves. Both Inlet and Outlet Headers contain the Copper lead sections of the FRCS, with provision for electrical power connections in the form of bus-bars. (Fig. 8).



Fig. 9: SS Tube Plate End Of Fuel Rod Cluster



Fig. 11: FRCS Channel Assembly under Hydro-Testing



Fig. 12: Full FRCS Assembly ready for dispatch

The individual components, Channel & Full FRCS assembly were subjected to the following tests:

Fuel Rods (S.S. / Copper)

- (i) Helium Leak Test
- (ii) Hydro-test (internal) – 90 kg/sq. cm
- (iii) Hydro-test (external) – 175 kg/sq. cm

Channel With Headers Hydro-test - 240-kg/sq. cm

FRCS Full Assembly (Fig. 11) Hydro-test - 240-kg/sq. cm

The FRCS was fabricated developing the following processes:

- (i) Fabrication of Fuel Rods, involving Copper to SS brazed joints. The Fuel Rods fabricated as per this process were also subjected to Helium Leak Test.



Fig. 13: FRCS Assembly Being Transported To Hall 7, BARC

- (ii) Development of Tube Plate with Copper bushes diffusion bonded in it. This new process facilitated Copper-to-Copper brazed joints between Fuel Rod and Copper bushes fixed in the 35 mm thick Tube Plate. Direct brazing of Copper end of Fuel Rod to SS tube plate was not found to be feasible. Penetration of brazing up to 35 mm depth could be achieved using the new process.
- (iii) Brazing process for joining Copper (Rods & Tubes) to SS (Fuel Rods Tubes) and Copper tube to Copper Sleeve diffusion bonded to SS tube plate, to withstand the given pressures.
- (iv) Brazing process for simultaneous brazing of all the 19 Fuel Rods with appropriate brazing alloy were also developed.
- (v) Installation of the Thermo-couples, involving appropriate brazed joints. Personnel from RED, BARC were associated during this delicate process.

The two Fuel Rod Cluster Simulator Assemblies have successfully been completed, (Fig.12), tested and delivered at RED's Hall-7 site.

For transporting the 9 Meter FRCS Assembly, survey was made to select suitable mode of transport at the designated site behind Hall 7, through a very narrow lane, the only access route available to the site. Finally, two trolleys (Fig. 13) (with rubber tyres as cushions), were attached below the FRCS Assembly and these were pulled using one fork lift, at front end and one fork lift at the rear end, to lift and shift the trolleys as required. It would not have been possible to deliver it to site in any other way.



Design and Development of 10 MeV Industrial RF Electron Linac at Electron Beam Centre, Kharghar for Radiation Processing Applications

K.C. Mittal, D.P. Chakravarthy, V.T. Nimje, K.P. Dixit, S. Acharya, K.V. Nagesh, Vivek Yadav, Shiv Chandan, P.C. Saroj, A.R. Chindarkar, S.R. Ghodke, D. Bhattacharjee, A.R. Tillu, R. Barnwal, R.B. Chavan, D. JayaPrakash, R.L. Mishra, Mukesh Kumar, Vijay Sharma, P. Roychowdhury, Mahendra Kumar, R.R. Tiwari, Supriya S. Barje, N.K. Lawangare and N. Chaudhary

Electron Beam Centre, Accelerator and Pulse Power Division

and

R.L. Suthar, S.B. Jawale and S. Guha

Centre for Design & Manufacture

This paper received the DAE Group Achievement Award for year 2009

Abstract

At the Electron Beam Centre, a 10 MeV Linac has been indigenously designed, developed, commissioned and is operational at high power, for radiation processing. This is an on-axis coupled cavity standing-wave type of RF linac, operating with 50-70 keV electron gun having LaB₆ cathode and klystron-based RF source, at 2856 MHz. The linac is currently operating at an output beam power of 3 kW and is being routinely used for various experiments. Long-term operation (continuous 24 hour run) of the linac has been carried out successfully, to establish the reliability of the linac system for industrial use. This is the first indigenous RF linac in the country, which is operational at 3 kW. Technological development of various subsystems, operating experience and utilization for industrial applications, will be described in this paper.

Introduction

The extensive use of electron accelerators for industrial applications has spurred the industrial accelerator programme in APPD/BARC. The programme involves building and operating high power electron accelerators, in the energy range of 200 keV to 10 MeV, to cater to most of the applications. There has been a constant focus to develop the core technologies required for these accelerators indigenously and this effort has yielded successful results, which are evident in the present operation of these accelerators. The design and development of the 10 MeV RF Industrial Electron linac

[1] is one such project, taken up and successfully implemented by APPD/BARC. The specifications of the linac are listed in Table 1.

Table 1: Specifications of 10MeV RF Electron linac

Operating Frequency	2856 ± 2 MHz
Output Beam Energy	10 MeV
Peak Beam Current	250 mA
Beam Pulse Width	10 µsec
Pulse Repetition Frequency	400 Hz
Average Output Beam Power	10 kW
Microwave I/P Power to LINAC	6 MW peak, 25 kW average
Electron source	50 – 70 keV, 1 A (peak); LaB ₆ based
Length of Accelerator section	871 mm (33 cells)



System Description

The 10 MeV RF linac, shown in Fig.1, has an on-axis coupled cavity bi-periodic $\pi/2$ structure, operating at a frequency of 2856MHz and delivers electron beam pulses of 10 μ s duration at 5-400 Hz repetition rate. The injector is an LaB₆-based electron gun [2] in the triode configuration. Klystron-based RF source powers the linac [3,4]. The 10 MeV output beam is scanned over a length of 1 m with the help of a scan magnet [5]. The electrons emerge into the atmosphere through the 75 micron thick titanium window and are incident on the products to be

irradiated, which are placed on the conveyor. This linac can be used in the x-ray mode too, during which, the electron beam impinges on a tantalum target to produce Bremsstrahlung. Each of the sub-systems is described briefly in the following sections.

The triode gun uses LaB₆ as the cathode material, which is indirectly heated. The indigenously-developed cathode assembly is shown in Fig. 2. Locally available ceramic is used as insulation between the anode and cathode, to withstand voltages up to 70 kV (pulsed). The gun has been tested upto \sim 1000 mA and \sim 60 kV High Voltage Extraction. This gun is operational and delivers a beam of \sim 500 -600 mA. The anode-cathode potential is provided by a line-type modulator, shown in Fig. 3. This modulator, developed in-house, provides an output of 50-60 kV ,



Fig.1: Photograph of 10 MeV, 10 kW RF



Fig. 2: Cathode assembly of gun



Fig.3: Line type e-gun modulator



2A, 10 μ s, 400 Hz and is being used for regular electron gun operation.

One of the main technological challenges of this linac, has been the design and development of the RF cavity, which forms the main heart of the system. The on-axis coupled cavity bi-periodic $\pi/2$ structure operates at a frequency of $\sim 2856 \pm 1.5$ MHz, with Q_0 of ~ 12000 . When the Linac is in operation, the cavity dissipates ~ 5 kW of heat load and this load is removed by water cooling. The linac cavity, shown in Fig. 4, made of OFHC copper, has a complicated geometry and requires dimensional tolerances in the range of 10 - 20 microns and surface finish better than 0.2 microns. Each cell of this cavity is manufactured separately and then the cells are brazed in a vacuum furnace. This challenge has been successfully implemented using indigenous facilities available at CDM/BARC and the private industry in and around Mumbai. This is the first of its kind, developed in the country.



Fig.4: Brazen RF structure with 33 cells

The RF power source needed to develop the acceleration gradient, is based on the 6 MW (pk), 25 kW (avg.) multi-beam klystron (Toriy KIU147A), as shown in Fig. 5. The Line-type Modulator (55 kV, 280 A, 10 μ s, 415 Hz), required to power the klystron, has been designed, developed and tested jointly by SAMEER and BARC. A view of the modulator is shown in Fig. 6.

Scan magnet, made of silicon steel laminations, is used to generate a maximum magnetic field of ~ 1.5 kG, to scan the beam along a length of ~ 100 cm on the target. Fig. 7 shows the Scan magnet positioned above the

scan horn. Scan horn and beam extraction window (Ti-foil 75 μ m) at the bottom of Scan Horn, has been designed and developed indigenously, with the help of CDM/BARC. The electron beam comes out of the vacuum through Ti foil into the air and used for the experimental purposes.

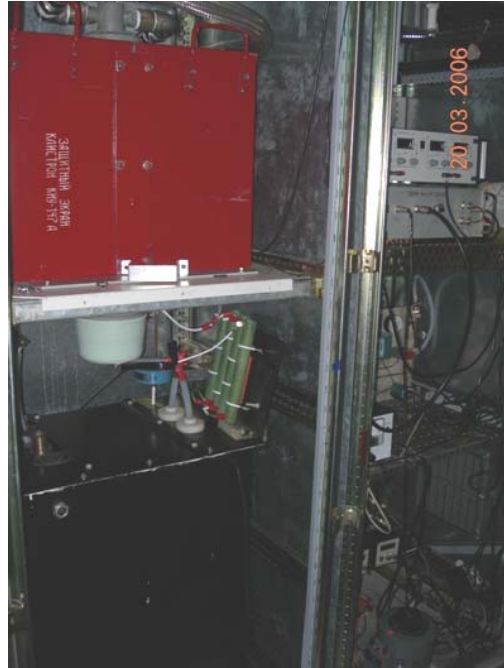


Fig. 5: View of klystron with lead shielding (in red)



Fig. 6: Line-type klystron Modulator



Fig. 7: Scan magnet mounted above horn



Fig. 8: View of Conveyor system outside the cell area

Thermal analysis of the linac cavity [6] has been carried out, to assess the temperature distribution and cooling water requirement. A demineralized water system [7] caters to all systems which require cooling. Distributed turbo-cum-sputter-ion pumping system, enables a vacuum level of 10^{-7} in the linac system. Fast current transformer is used to measure the beam current. Energy measurements have been carried out with the use of indigenous magnetic analyser, as well as the depth dose technique. Conveyor system, shown in Fig. 8, can be moved with speed, in the range of 0.1-7 m/min, to achieve variable dose requirements. Radiation monitoring system, ozone blower system and other infrastructural facilities/services have been successfully integrated with the linac system.

Control and interlock systems, including hard-wired interlocks, to enable remote and safe operation of the

linac, have been designed and developed in-house. With this system, it is possible to control the beam parameters as well as machine parameters.

Linac Operation

After integration of the sub-systems, RF conditioning of the linac [8] was carried out, with RF power input varying from 0.5 – 4 MW at 400 Hz. In the initial trials, conditioning time was ~250 hours, but subsequently, this time was reduced to <40 hours. During the RF conditioning of the linac cavity, a vacuum of 3.0×10^{-7} mbar was maintained throughout the complete linac system. The reflected power was <10% of the forward power at resonance, for all the forward power levels.

RF conditioning was followed by operation of the linac with electron beam. At an injection voltage of ~ 50 kV, electron beam was injected into the linac cavity. linac was operated for > 5hours at each beam power of 1kW to 4kW, without any breakdown. Fig. 9 shows the E-Gun injection voltage, Klystron current & Output beam current. Dependence of Beam energy on beam current and RF power (Theoretical analysis) is shown in Fig. 10. With injection voltage of 67kV, output beam current of 165mA has been obtained. linac System was operated at maximum beam parameters of 10MeV, 5.6kW for ~1hour.

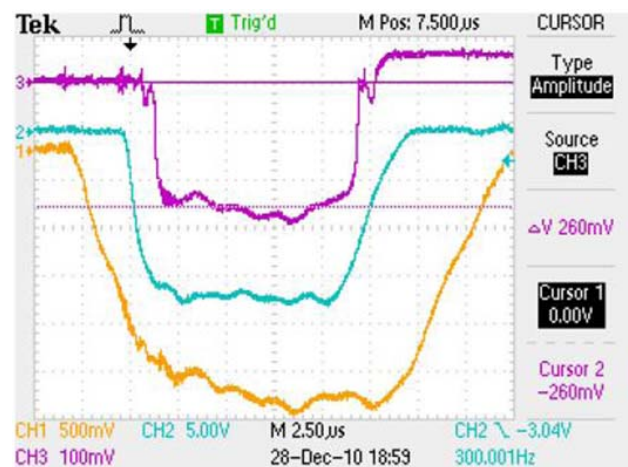


Fig. 9: Envelopes of E-Gun voltage (CH1), Klystron current (CH2) & Output beam current (CH3)

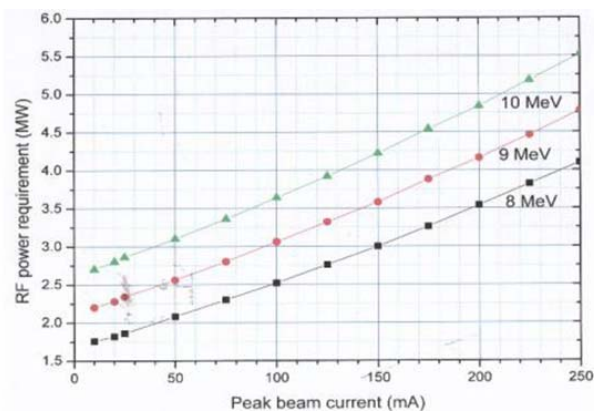


Fig.10: Beam Energy Relation with Beam current & RF Power

operated at beam energy of 10MeV at beam power of 3kW, i.e., beam current of 100mA with PRF of 300Hz. Input microwave power was set at 3.25 MW. For the x-ray mode operation, a 1.8mm thick tantalum sheet was placed at a distance of 150mm from the titanium window, to produce X-rays. X-ray measurement was done at different electron beam energies. X-ray energies from 3.0 MeV to 3.8MeV were measured, by varying the Klystron forward power at different beam currents.

Dosimetry studies [9] have established dose uniformity in the static and dynamic mode of $\pm 8\%$ and $\pm 5\%$ respectively. These experiments were done using B3 films at 10MeV, 3kW linac parameters for full 1m of beam scan width. This was done at 460mm from Ti exit window at various conveyer speeds. For 0.1m/min of conveyer speed, dose rate of 21kGy/min was measured. This dose was linearly dependent on the conveyer speed.

Linac Utilization

The linac is being used for a number of applications [10], both industrial and research. Industrial applications include irradiation of PE gaskets to enhance mechanical properties, coloration of gems, irradiation of food products to increase shelf-life, irradiation of semiconductor diodes to reduce the reverse recovery time, etc. Photofission experiments and delayed-neutron fraction studies have been successfully carried out in the 10 MeV linac facility. Now the linac is

routinely being utilized by several users, at a maximum beam power of 3 kW.

Conclusion

Design and development of electron accelerators for industrial and other applications has now reached a mature level at BARC. Experience in the successful installation, commissioning and operation of the 10 MeV RF linac will now prove as the major asset for development of various types of electron accelerators for several applications.

References

1. K.C. Mittal, "Accelerators at Electron Beam Centre, Kharghar," Proc. InPAC 2006
2. Dhruva B, et al, "Operational Experience and modifications in Electron Gun for the 10 MeV RF linacs ", Proc.InPAC2011
3. A.R.Tillu, et al, "Line-type modulator development for Multi-beam klystron in 10 MeV Industrial Electron Linac", Proc.InPAC2011
4. Shiv Chandan, et al, "Development of S-band RF Power Source for 10 MeV Industrial Linac", Proc.InPAC2011
5. S.Acharya, et al, "Design, development and operation of a scanning power supply for an RF Electron linear accelerator", Proc.InPAC2011
6. R.Barnwal, et al, "Thermal simulation of linac cavity of 10 MeV RF system", Proc.InPAC2011
7. P.C.Saroj, et al, "Cooling System for 3 MeV, 30 kW DC and 10 MeV, 10 kW RF Accelerators", Proc.InPAC2011
8. K.C.Mittal, et al, "Operating Experience of 10 MeV Industrial RF Linac", Proc.InPAC2011
9. N.Chaudhary, et al, "Monte Carlo Simulation & Dosimetric Studies for a 10MeV RF Electron Linear Accelerator", Proc.InPAC2011
10. K.C.Mittal, et al, "Utilization of 10 MeV linac facility for industrial applications and research experiments", Proc.InPAC2011.

DAE Excellence Award



Design and Development of Fuel Rod Cluster Simulator

A.K. Vishnoi, A.K. Pal, D.K. Chandraker and P.K. Vijayan
Reactor Engineering Division

This paper received the DAE Group Achievement Award for the year 2009

Abstract

The designer of a nuclear reactor system, has to ensure its safety during normal operation as well as accidental conditions. This requires, among other things, a proper understanding of the various thermal hydraulic phenomena occurring in the reactor core. In a nuclear reactor core, the fuel elements are the heat source and highly loaded components of the reactor system. Therefore, their behaviour under normal and accidental conditions must be extensively investigated. The complex nature of these phenomena calls for exhaustive experimental investigations. Fuel Rod Cluster Simulator (FRCS) is a very important component, required for the experimental investigation of the thermal hydraulic behaviour of reactor fuel elements. This paper brings out various design aspects and challenges in the design of the FRCS. Some of the main features of directly heated FRCS have also been presented in the paper.

Keywords: *Fuel Rod Cluster Simulator, Fuel Rod Simulator; Critical heat flux*

Introduction

Thermal hydraulics plays a vital role in the safety evaluation of a nuclear reactor. The safety analysis envisages prediction of the thermal hydraulic parameters under normal operating conditions and anticipated transients as well. The licensing criteria demand, that critical parameters like fuel temperature, clad temperature and critical heat flux, should be well within the prescribed limit, for the safe operation of the reactor. To meet this requirement, various computer codes are developed, to analyze the normal operating conditions and the accidental scenarios. However, these codes need to be validated to minimize, the prediction uncertainties of various models, incorporated in the code. Thus validation of the codes demands generation of experimental data, under conditions of

interest. Since thermal hydraulic experiments in the actual operating nuclear fuel bundle is not possible due to radiation hazard and limitations on the instrumentation of the fuel bundle, in-pile experiments are generally ruled out. Also, this data needs to be made available, before the licensing of the reactor at the commissioning stage. Thus, in view of the safety requirement and limitation of the in-pile experiments, the research community generally relies on the out-of-pile experiments. In the out-of-pile experiments, the nuclear fuel bundle is simulated using electrical heating and other systems like MHT, ECCS etc. are simulated to conduct transient experiments. The success of the experiments depends on the simulation of the fuel bundle using the electrical heating and



measurement of the important parameters like fuel clad surface temperature. Also, a part of the FRCS needs to be instrumented heavily in order to detect the location of dryout. For this purpose, probable location of dryout needs to be decided judiciously. Thus, the design of Fuel Rod Cluster Simulator (FRCS) poses challenges in terms of the required electrical resistance, power profile simulation (radial and axial), geometrical simulation and mounting of a large number of instruments like thermocouples, on the fuel rod surface. Various thermal hydraulic facilities world-wide use the FRCS which are proprietary in nature and hence complete design details are generally not made available in open literature. The various thermal hydraulic facilities like ATLAS, Heat Transfer Research Facility Columbia, HTL (PNC), ITL[6], ATTF[7] etc. use either directly heated FRCS or indirectly heated FRCS.

V. Casal [10] described different design aspects of FRCS and developed high performance indirectly heated FRCS for thermodynamic experiments. S. M. Balahov et al. [9] presented various FRCS designs used for thermal-hydraulics investigations for different facilities simulating VVERs. Erbacher et al. [5] designed tight-lattice FRCS of Advanced Pressurized Water Reactor (APWR) to carry out experiments on reflooding and deformation behaviour during LOCA. A. Borgohain et al. [1], A. K. Pal et al. [2] and A. K. Vishnoi et al. [3] developed high power rating directly-heated 54 - rods and 37- rods FRCS, simulating AHWR and PHWR fuel clusters respectively. N. K. Maheshwari et al. [8] developed indirectly heated FRCS. The FRCS developed in BARC is a vital equipment for design validation of the AHWR and are used in different facilities like Integral Test Loop (ITL), Facility for Integral System Behaviour Experiments (FISBE) and AHWR Thermal hydraulics Test Facility, Tarapur (ATTF).

Design Requirement of FRCS

The FRCS has to meet a number of requirements. These include:

- i) Simulation of geometry of the fuel bundle including the spacer.
- ii) Simulation of heat flux, power and coolant volume of the reactor fuel channel.
- iii) Capability of withstanding high temperature, high pressure conditions simulating reactor conditions.
- iv) Adequate instrumentation for experimental data generation, control & safety purposes.
- v) Achieving required electrical resistance to suit power supply for maximum power generation.
- vi) Proper insulation (electrical) of the heater pin from the rest of the experimental setup.
- vii) Capability to withstand repeated cyclic (temperature & pressure) operations.
- viii) Ease of assembly and disassembly.

Two types of FRCS commonly used are: direct resistance heating type and indirect resistance heating type.

- i) **Direct resistance heating type:** In this type of FRCS, current is passed directly through the tube, which geometrically simulates the cladding of a nuclear fuel rod. This type of FRCS finds application in experiments related to steady state heat transfer in single and two-phase flow of fluids, which are non-conductors of electricity. Very high uniform heat flux can be easily achieved. However, for unsteady state tests, simulation of stored heat is extremely difficult in directly heated FRCS design.
- ii) **Indirect resistance heating type:** In this type, a heater pin having central resistance heating element is insulated from the outer tube, which simulates the fuel clad. Heating element is concentrically located within the outer tube. This type of FRCS can be used for all types of fluids. Both steady state and unsteady state tests with single and two-phase flow can be carried out. But it is very essential to maintain uniform and minimum thermal resistance between heating element and the outer (cladding) tube. Special equipment is required for the fabrication of FRCS. All these result in considerable increase in cost and complexity during fabrication. If the gap between



outer tube and heater is filled with gas gap for better insulation, then the FRCS is called gas type indirectly heated FRCS.

Design and Development of Direct Resistance Heating type FRCS

A directly heated FRCS has been designed and developed in the Reactor Engineering Division of BARC, Mumbai. The design of the FRCS is based on power-to-volume scaling philosophy. The FRCS (Fig. 1, Fig. 2 and Fig. 3) consists of 54 Fuel Rod Simulators (FRS), which generates heat electrically, shell assembly, center tube for ECCS and provision for electrical connection and insulation. Each FRS is made up of a heater section, both ends of which are welded to connector rods, which simulates the unheated portion and provides electrical connection to the heater section. The connectors are made of nickel rods. The downstream connectors are connected to stainless steel electrical bus bars through top tie plate. On the other end, the connector rod is connected to bus bars

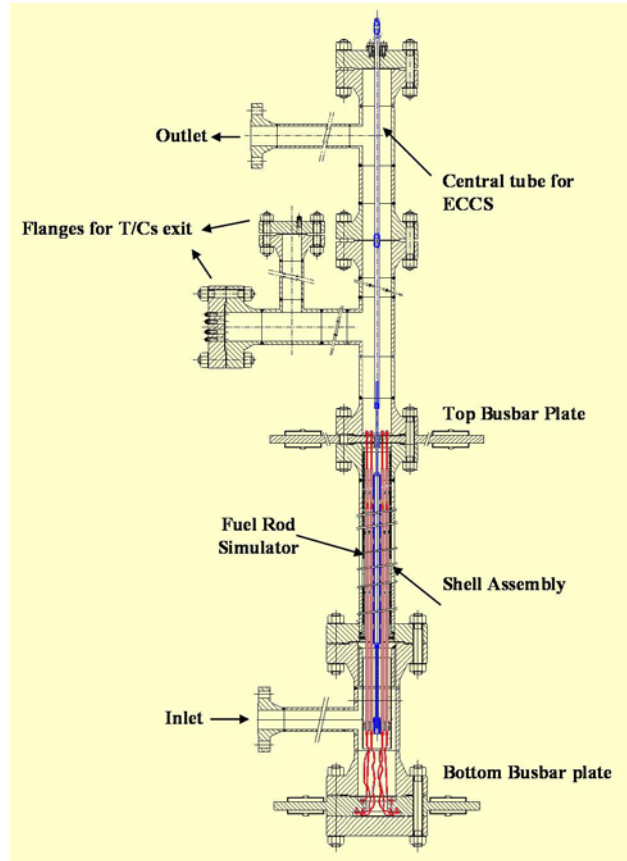


Fig. 2: Schematic of FRCS Assembly

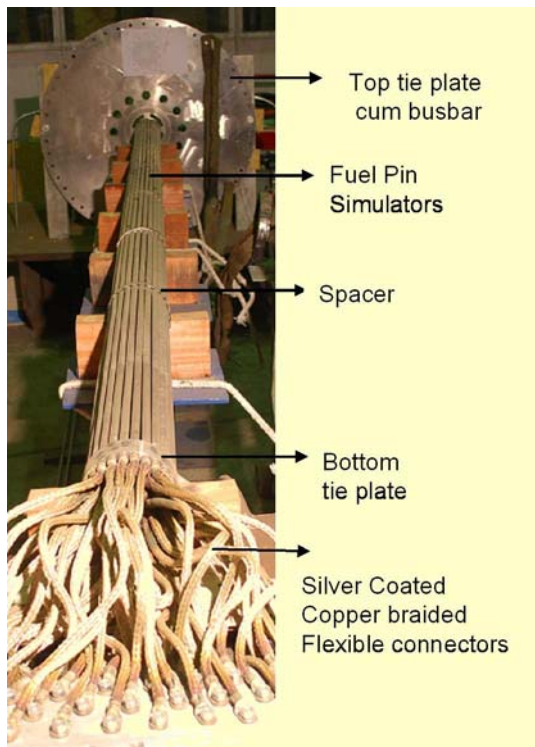


Fig. 1: FRS Bundle Assembly

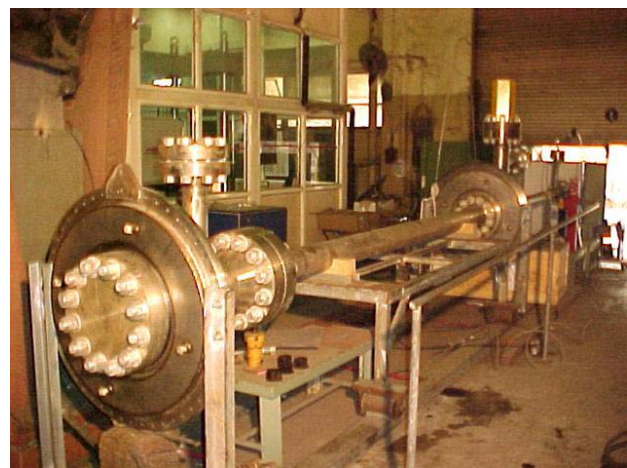


Fig. 3: Assembled FRCS

through silver coated flexible copper braided wires, to accommodate thermal expansion. Six stainless steel spacers are provided, to maintain the spacing among the FRS,



which exactly simulate the spacers of the reactor. The top tie plate and bottom tie plate could not be simulated exactly, because of the provision required for electrical connections. Ceramic liner tubes are used, to electrically insulate the current carrying heaters from the outer flow tube, which simulates the flow tube. Compressed asbestos material is selected as flange gasket, which also isolates the FRS electrically from the rest of the system. The main design parameters and other details are given in Table 1.

Table 1: Design Parameters of the FRCS

Design Parameters	
Pressure	100 bar
Temperature	315°C (Shell) and 550°C (heater tube)
Max. Flow rate	6 kg/s
Maximum Power	3 MW (with 30kA current rating)
Heater Element	
Number of heater rods	54
Tube material (Cladding)	INCONEL-600
Filler material	Ceramic (99% and above Alumina)
Heater length (mm)	3500
Heater tube outer diameter(mm)	11.2
Heater Tube thickness (mm)	0.6
Heater Rod PCD (mm)	
Inner	51.39
Middle	77.39
Outer	103.69
Max. linear heat rating	159 W/cm
Connector rod material	Nickel
Coolant	Light Water
Inlet Coolant Temperature	270°C
Shell Material	SS316L
Insulating Material	Ceramic and Compressed Asbestos
Sealing Material	Graphoil

Conclusion

FRCS is a vital element of a thermal hydraulic facility, to simulate the nuclear heating in the coolant channel. However, the simulation of the nuclear fuel bundle using electrical heaters for out-of-pile experiments poses a lot of challenges. Different types of Fuel Rod Cluster Simulators have their own advantages and disadvantages. Direct resistance heating type FRCS is easy to design and fabricate and a very high heat flux can be easily achieved, but it cannot be used for transient cases and electrical conductive coolants. Indirect resistance heating type FRCS is somewhat difficult to fabricate, but can be used for steady state as well as transient cases. In this type of FRCS, axial variation can also be easily achieved, by varying current carrying conductor thickness. The detailed design of a 3 MW power rating directly heated FRCS has also been presented and compared with the actual fuel assembly.

References

1. A. Borgohain, A.K. Pal, P.K. Vijayan and D. Saha "Design and development of directly heated fuel rod cluster simulator of AHWR", BARC Report, BARC/2006/I/017, 2006.
2. A.K. Pal, D Saha, and V. VenkatRaj, "Development of simulator for rod cluster fuel element", Symposium on indigenous nuclear equipment, Bombay, Feb'1987.
3. A.K. Vishnoi, D.K. Chandraker, A.K. Pal, A. Dasgupta, P. K. Vijayan and D. Saha, "Design and development of 3 MW power rating dieclrtly heated 54-Rod fuel rod cluster simulator", BARC Report, BARC/2010/R/004.
4. Cunningham, M.E., Hann, C.R., Olsen, A.R., "Uncertainty analysis and thermal stored energy calculations in nuclear fuel rods", *Nuclear Technology*, 47 (1980): 457-467.
5. Erbacher, F.J.; Wiehr, K., "Experimental investigations on the reflooding and deformation behavior of an advanced pressurized water reactor tight-lattice fuel



- rod bundle in a loss-of-coolant accident", *Nuclear Technology*, 80 (1988): 153-160.
6. G.S.S.P. Rao, P.K.Vijayan, N.V. Satish Kumar, A.K. Nayak, D.G. Belokar, A.K. Pal, A. Borgohain, Vikas Jain, Manish Sharma and D. Saha, 'AHWR Integral test loop scaling philosophy and system description', Divisional Report, RED, BARC, Mumbai, 2001.
 7. Mukesh Kumar, A. Dasgupta, A.K., Vishnoi, Vikas Jain, Naveen Kumar, Kapil Bodkha, D.K. Chandraker, A. K. Nayak, A.K. Pal, P.K. Vijayan, "Scaling philosophy and system description of AHWR thermal-hydraulic test facility (ATTF)", BARC Report, BARC/2010/E/007, June, 2010.
 8. N. K. Maheshwari and D. Saha, S.K. Srivastava, S.V. Paibhale and V. G. Date " Development of indirectly heated fuel rod simulators for thermohydraulic safety experiments", BARC Report, BARC/2001/I/002.
 9. S. M. Balashov, V. V. Kumskoi, A. M. Pavlov and A. A. Ulanovskii, "Fuel-element simulator for investigating thermal-hydraulic accidents in water-water reactors", *Atomic Energy*, Volume 73, Number 6: 981-984.
 10. V. Casal, "Design of high-performance fuel pin simulators for thermodynamic experiments with nuclear fuel elements", *Nuclear Technology*, 47 (1980) : 153-161.



Design, Manufacture and Deployment of Radiation and Corrosion Resistant Compact Custom Designed Motor for Centrifugal Extractors

R.K. Gupta

CM&DS, ChTG, BARC, Mumbai

and

A. Sriramamurthy, P. Vijayasekaran, S. Sundaramurthy, Felix Lawrence and A. Palanivel

Reprocessing Group

and

P. P. Selvam

Reactor Engineering Group

Indira Gandhi Centre for Atomic Research, Kalpakkam

This paper received the DAE Group Achievement Award for the year 2009

Abstract

Centrifugal extractors are vital for the successful reprocessing of Fast Reactor fuel. The development of motors for these extractors is challenging due to the adverse environment, such as radiation and corrosion. In this paper, some aspects of design and manufacturing of special purpose motor for centrifugal extractors has been discussed.

Introduction

High plutonium content fuels with maximum burn up and low cooling periods, pose challenges in the reprocessing of fast reactor fuel, with demanding requirement of alpha containment during operation and maintenance of the plant. While hot cells have been constructed and operated for over three decades in India, hot cells for processing nitric acid bearing radioactive solutions, with high plutonium content are being operated for the first time.

The hot cell in which the operations have been carried out is part of the CORAL facility in the Reprocessing Development Laboratory (RDL) at Kalpakkam. This hot cell is an α -tight stainless steel containment box, housed

inside a lead shielding which is provided with radiation-shielding windows and many devices for carrying out remote operation and maintenance such as articulated arm type Master-Slave Manipulators (MSM) and in-cell crane, pneumatic transfer system etc. While the process equipment requiring remote operation and maintenance viz. chopper, dissolver, centrifugal extractors (CE) etc., are housed inside the containment box, all the other process vessels that do not have these requirement are placed outside the containment box but inside the lead shielding.

During the design, validation, operation and maintenance phase of CE in the facility, many challenges were addressed and many spent fuel reprocessing campaigns were successfully carried out, which enabled the designing of



future commercial plants on a sound footing. One of the development activities of electrical drive for these extractors, is described here.

Brief description of Centrifugal Extractors

Centrifugal Extractor is a liquid–liquid mass transfer system in which solute transfer can occur between two immiscible liquid phases. Centrifugal extractors are very useful for the reprocessing of Fast Breeder Reactor (FBR) fuels which have burn-ups, many times more than that of PHWR fuels [1,2]. Since FBR fuels are reprocessed with much lower cooling periods, the associated radioactivity of the fuel is very high. This calls for deployment of short residence time contactors such as centrifugal extractors, to reduce the problems associated with the degradation of the solvent used in solvent extraction. The fast reactor reprocessing plant requires many banks of centrifugal extractors, each bank consisting of stages driven by an independent motor. The motor runs at the required speed and in the event of any motor not running, the whole bank has to be stopped immediately. The motors have a sufficiently long life as replacement of motor is not only time consuming but may also involve generation of radioactive waste. As there are no standard motors available in the market to meet the required specifications, they have to be designed and developed indigenously. The development of CE motors is an interdisciplinary activity and the validation of design involves not only non-radioactive field trials, but also in hot cells. The CORAL, in which FBTR spent fuel is reprocessed, provides the test bed for such validation.

An individual stage of the centrifugal extractor has a bowl at the bottom, in which the process solution goes through and the motor is fixed at the top. It is possible to take the motor remotely using MSM and incell crane, along with the bowl for maintenance. The motor is designed as a hermetically sealed type, for preventing the ingress of corrosive nitric acid vapour. A protective coating is also given to reduce the corrosion in the unlikely event of ingress of vapour.

Evolution of Motor Design

The motor (Fig.1) is a three phase squirrel cage induction type, with a power rating of approx 20 – 50 watts, operating around 3250 ± 250 rpm. The motor housing is made of stainless steel 304 L. The motors are driven by a variable frequency inverter with a common bus configuration. The motors are deployed for actual production runs in CORAL facility after extensive trials. The operational feedbacks are used for improving the design.



Fig.1 Typical motor of a CE stage

Design features of initial version

The initial design (version-1) was a 2 pole, 60 V, 20 W at 100 Hz squirrel cage induction motor, with stator bore dia of 31 mm and core length of 30 mm. The stampings were cut from CRGO, M4 Grade (0.27 mm thick) lamination sheets with an insulation of C5 on both sides. The stator winding was of class H, dual coated copper wire provided with a base coat of Terebec TR 543.38 and a top coat of Terebec AI 1013 BV 35 formulation. Slot insulation lining was of Nomex 410 (Polyamide) paper (5 mil thick). Glass Fibre card was used for overhang binding. Impregnating varnish was Elmotherm H-71 and finishing



varnish was Siliconit E 233. An air purge was provided, to limit the concentration of nitric acid fumes entering the motor.

A speed pick-up was provided inside the motor housing, based on variable magnetic reluctance principle for which two alnico magnet bars wound with coil are used. The two coils are connected in series to get more voltage for speed sensing. The electrical connection to the motors and the signal output of speed pick-ups is through multi-core radiation-resistant cable, through special radiation resistant connectors.

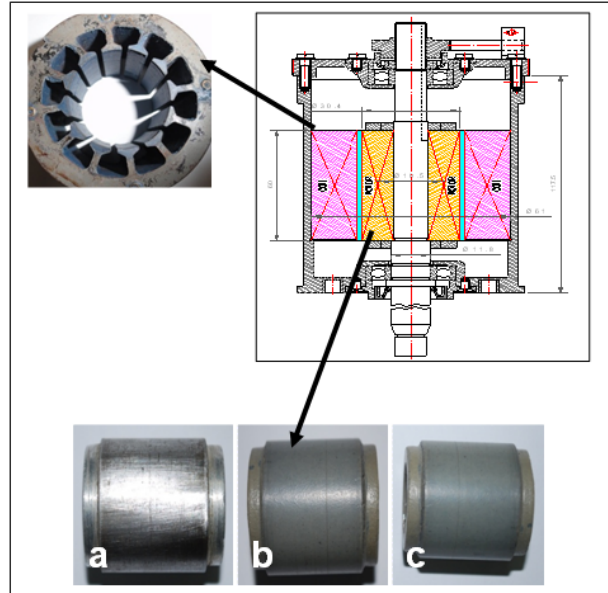
Based on the operating experience for the last six years, it has been found that these motors fail frequently, the MTBF being less than six months. The failures are mainly due to accumulation of products in the air gap between stator and rotor, due to corrosion of their surfaces which increases friction. It is also due to accumulation of the corrosion products in the bearings, leading to further increase in friction. In view of this, the starting torque of version-1 motor was not sufficient. Further, failure of speed pick-up coil due to corrosion was also noticed.

Based on the above experience, it was decided to design a new motor (version-2) with the following objectives:

1. reduction of corrosion of the stator and rotor stampings by suitable coating
2. modification of the bearing housing so that the corrosion products do not increase the friction
3. modification of the motor housing such that the acid vapour ingress into the motor is reduced
4. providing a reliable speed sensor which would give prompt indication of motor's status.

Design Features of New Motor

The version-2 motor (Fig. 2) is designed to enhance the life of motor with corrosion resistant coating on stator and rotor cores.



Rotors of CE motors (a) without coating, (b) with coating before testing and (c) with coating after testing
 Coating thickness: 80-90 micron; Hardness value: 80-84 Shore D Electrical, Surface resistivity: 10^{11} - 10^{12} ohm/sq.
 No swelling, thickness change and peeling observed after testing

Fig. 2: Features of Version-2 motor

The lamination sheets used for motor stampings have coating of MgO and SiO₂ on both sides. The exposed part of stampings undergoes corrosion in nitric acid vapour. To provide protection against corrosion, Poly Ether Ether Ketone (PEEK) coating was chosen, as it is a high performance engineering thermoplastic which has a radiation resistance of 10^9 rads and is also resistant to a wide range of chemicals at elevated temperatures, in harsh environment prevailing inside the containment box. Applied PEEK coating was of sufficient thickness so that allowance of machining to the required thickness was possible.

The performance of the coating was evaluated by continuous running of the rotor in nitric acid environment. There was no swelling and no change in the coating thickness. Hardness and surface resistivity of the coating also did not change after exposure to the acid vapour. As there was no peeling of the coated layer, it was confirmed



that the PEEK coating gave adequate protection against corrosion.

Acid and radiation resistant grease sealing was provided, to effectively reduce the acid vapour entering through motor housing.

To increase the life of speed sensor, the magnet and coil assembly was covered with PEEK. Also to enable maintenance of speed sensor, the design was modified in which the signal cable from the top end cover is connected with a separate connector, embedded in the top end cover. This makes it easy for dismantling the top end cover without affecting the signal cable.

In order to standardize the capacity of the motor for the range of operations required for FBR fuel reprocessing, the power was increased by increasing the stack length.

Evaluation of New Motor

Load tests were conducted to assess the performance degradation due to the increased air gap in both versions of the motor. The performance was evaluated by measuring the shaft torque at different operating speeds, by varying the supply frequency. Experiments were carried out before and after increasing the air gap. Fig. 3 gives a comparison of torques produced by motor version 1 and 2. At the operating supply frequency (60 Hz), the starting torque is

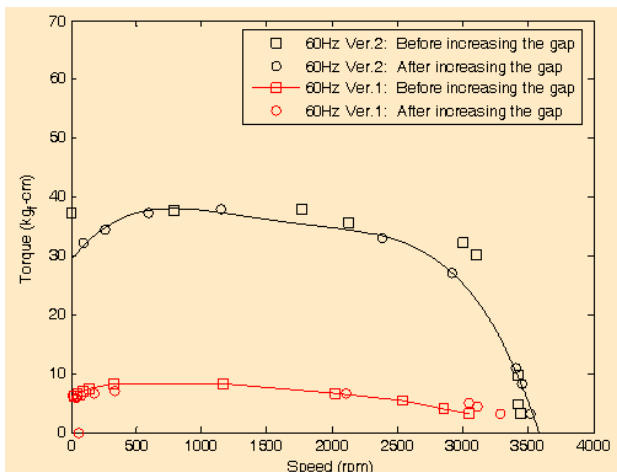


Fig.3 Comparative performance of two motors

30 kgf-cm for version-2 motor which is much higher than the starting torque (6 kgf-cm) of version-1 motor. It is also seen that the increase in the gap to 0.1 mm does not have much impact on the performance of the motors at 60 Hz operation. It can also be seen that the version-2 motor has favorable torque- speed characteristics and can operate at almost constant speed with marginal increase in torque requirement. Hence it can tolerate more friction than the version-1 motor.

Conclusion

Various designs have been tested and a viable design, meeting the target requirements has been finalized, fabricated and installed in the hot cell and is in service for more than 6 months, without any single failure. This gives reasonable confidence that the problem of frequent replacement of the version-1 motor due to accumulation of corrosion products in the air gap and bearing friction due to corrosion is significantly reduced with the improved torque-speed characteristics of the version-2 motor. It is planned to give PEEK coating on the stator core also, to further increase the motor life.

Acknowledgement

Authors wish to thank Shri R. Natarajan (RpG, IGCAR), G. Gouthaman, A.Y. Dangore and A.K. Wankhede (ChTG, BARC) for their kind support and encouragement throughout this work. The discussions with Shri V. Vijayakumar, M. Venkataraman, Shekhar Kumar (RpG), B.K. Nashine (FRTG) and P.R. Swaminathan (ROMG) are greatly acknowledged.

References

1. Sandesh S. Deshmukh, Vedantam Sripriya, Jyeshtharaj B. Joshi and Sudhir B. Koganti, *Ind. Eng. Chem. Res.*, vol. 46, (2007), pp 8343.
2. Sreepriya Vedantam, Jyeshtharaj B. Joshi and Sudhir B. Koganti, *The Canadian J. Chem. Engg.*, Vol.84, (2006), pp 279.



Development, Installation and Commissioning of EDXRD & EXAFS Beamlines at Indus-2 Synchrotron Source

Part-I

Energy Dispersive X-ray Diffraction Beamline at Indus-2 Synchrotron Source

H. K. Poswal, K. K. Pandey, A. K. Mishra, Nandini Garg, Abhilash Dwivedi,
R. Vasanthi and Surinder M. Sharma

High Pressure & Synchrotron Radiation Physics Division

This Paper received the DAE Group Achievement Award for the year 2009

Structure of materials is a vital input for determining their physical properties. X-ray diffraction is the most widely used technique, for investigation of structure of materials under various thermodynamic conditions viz, temperature and pressure. There are two variants of the x-ray diffraction technique: Angle Dispersive X-Ray Diffraction (ADXRD) and Energy Dispersive X-Ray Diffraction (EDXRD). EDXRD is known to be an efficient methodology for use in the constrained geometries. In this technique, white x-ray beam is incident on the sample and the diffracted signal is recorded at a fixed angle and is energy analyzed. Since

all the reflections are recorded simultaneously, EDXRD is also useful in kinetics related measurements and in glassy systems, where one requires data up to large Q values.

The High Pressure & Synchrotron Radiation Physics Division has developed an EDXRD beamline at a bending magnet port BL-11 of Indus-2 synchrotron radiation source. This beamline has also been optimized for carrying out diffraction measurements at high pressures. The schematic layout of the beamline is shown in Fig 1. Synchrotron Radiation (SR) from abending magnet is transported to

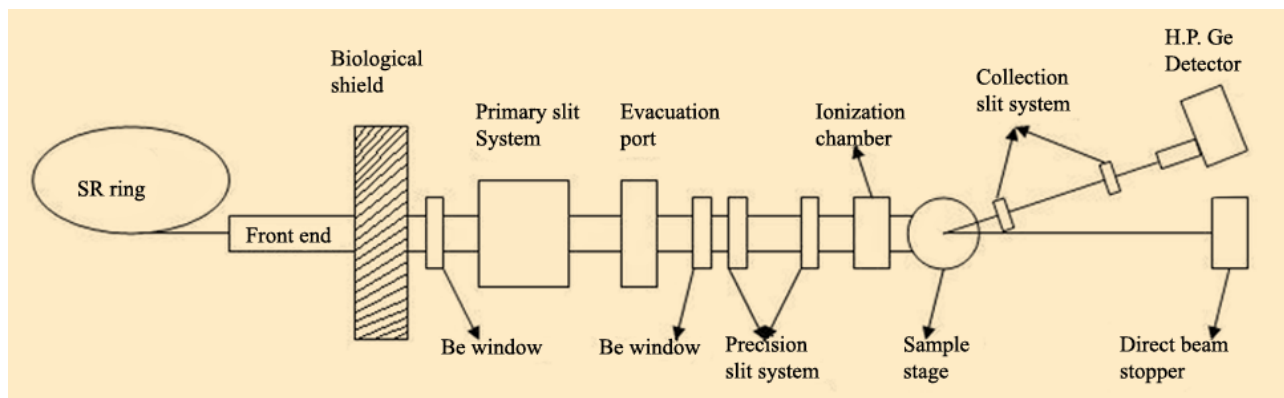


Fig. 1 : Schematic of EDXRD beamline

DAE Excellence Award



the optical hutch of the beamline through the frontend with 1 mrad horizontal beam acceptance. The storage ring vacuum is isolated from the beamline vacuum, by 200 μm thick water cooled beryllium window. The white beam is coarsely defined to $\sim 200 \times 200 \mu\text{m}^2$, using a water-cooled primary slit system and as it propagates further, it is collimated to less than $100 \times 100 \mu\text{m}^2$, using a set of two precision tungsten slit systems. The sample is mounted on a 8-axis motorized goniometric stage. The goniometer consists of co-axial θ - 2θ stage with detector arm, XY translation stage for 2θ axis alignment with SR beam and XYZ χ stages for sample maneuverability. The diffraction angle and gauge volume of sample is defined, using a set of cleaning slit system mounted on 2θ arm of sample stage. Finally diffraction signal is analyzed using liquid nitrogen cooled energy-sensitive high-purity germanium (HPGe) detector, mounted on the same 2θ

For high pressure experiments, pressure inside Diamond Anvil Cell (DAC) may be monitored, using equation of state of internal pressure calibrant e.g. Au, Cu etc. Since x-ray diffraction peaks from internal calibrants may interfere with the sample diffraction peaks, ruby fluorescence method is widely used. For this, a grain of Ruby is loaded along with the powdered sample inside a DAC. Ruby fluorescence spectrometer installed by us at the beamline, uses 532 nm frequency doubled diode pumped solid state laser as an excitation source and the fluorescence signal is collected using a microscope objective and is analyzed using a spectrograph.

Since this beamline is primarily optimized for high pressure measurements using DAC, where the sample size is $\sim 100 \mu\text{m}$, a provision has been made to focus white SR beam using Kirkpatrick Baez mirror system. It will focus 200 μm white SR beam to less than $\sim 30 \mu\text{m}$ with an intensity gain of \sim two orders of magnitude.

First set of benchmark EDXRD patterns of several elemental metals viz. Au, Cu, W, Ta, Zr, Mo etc, were recorded in May, 2008. The energy resolution of diffraction patterns was analyzed and the results are presented in Table 1.



Fig. 2: EDXRD beamline installed at BL-11, Indus-2 (RRCAT, Indore)

arm (Fig. 2). The final resolution of diffraction data at EDXRD beamline is $\sim 2\%$, limited by the detector resolution. For better inter-planar distance (d_{hkl}) resolution and structural determination, one needs to have diffraction data up to higher Q values. In the case of EDXRD beamline, it is determined by the spectral range of white SR beam and the collection angle i.e., 2θ . This beamline provides flexibility of changing the 2θ angle in a range of $\pm 25^\circ$, which allows one to record EDXRD pattern up to $\sim 15 \text{ \AA}^{-1}$ with energy range up to 70 KeV.

Table 1: Energy resolutions of various diffraction and x-ray fluorescence peaks

Peak details	$\Delta E/E$
Au $L\alpha_1$ (9.713 keV)	0.021
Au $L\beta_1$ (11.442 keV), Au $L\beta_2$ (11.584 keV)	0.026
Au (111)	0.014
Au (200)	0.013
Au (220)	0.012
Au (311)	0.011



Since then, this beamline is being extensively used for carrying out high pressure EDXRD experiments. A few recent studies using this beamline are discussed below:

Equation Of State (EOS) measurement of natural Uranium

At ambient conditions, natural uranium crystallizes in the orthorhombic structure (α -U). Previous high pressure experimental and theoretical studies on natural uranium, have shown discrepancy in the compressibility behavior. We have performed high pressure EDXRD experiments on natural U up to 25 GPa. Our measurements show, that ambient α phase is stable up to the highest pressure studied and the bulk modulus and its derivatives are determined to be $B_0 = 108$ GPa and $B_0' = 6.2$ respectively, which agree excellently with the published results obtained at ESRF ($B_0 = 104$ GPa and $B_0' = 6.2$)

EOS measurement of U- Mo alloy

Alloys of Uranium, stabilized in body-centered cubic structure (γ -phase), have been perceived to be more suitable fissile materials. Particularly, U-Mo alloys are formed in the γ -phase, at a relatively higher range of solute concentration and has an additional advantage of lower parasitic capture cross-section for neutrons. Besides irradiations effects, structural stability as a function of pressure is also important for these materials. We have studied high pressure behavior of U-10 wt. % Mo alloy, stabilized in γ -phase, up to 63 GPa at our EDXRD beamline. It has been found, that this structure remains stable up to the highest pressure of our measurements.

High pressure behavior of sesquioxides (Dy_2O_3 , Gd_2O_3 , Yb_2O_3 , Nd_2O_3)

Rare earth sesquioxides crystallise in three different structural forms, depending on the rare earth element ionic radius viz. cubic, monoclinic and hexagonal. Larger ionic radii sesquioxides stabilize in hexagonal phase, whereas for smaller ones, cubic phase is more stable.

High pressure studies on the cubic and hexagonal structured sesquioxide, would provide further insight into the high pressure structural behaviour of rare earth sesquioxides. Therefore, we carried out high pressure experiments on cubic Dy_2O_3 , Gd_2O_3 , Yb_2O_3 and hexagonal Nd_2O_3 . Our measurements at the EDXRD beamline showed structural transitions in all these sesquioxides. In particular, cubic phase was shown to transform into hexagonal phase, through a monoclinic phase which is similar to the ambient monoclinic phase found in some sesquioxides. The hexagonal phase of Nd_2O_3 also showed phase transition to a monoclinic phase at ~ 27 GPa, but this phase was different from the monoclinic phase, found in case of the other cubic rare earth sesquioxides.

GIXRD measurements on thin films

As an extension to the experimental capabilities of our beamline, we have augmented EDXRD beamline for Grazing Incidence X-Ray Diffraction (GIXRD) measurements, in energy dispersive mode. Recently, we carried out GIXRD measurements on various thin film samples viz. LB films of Cd-arachidate of different thickness ranging from 300nm to 1200nm, Co thin film deposited on anisotropically profiled silicon substrate, thin films of Co-Cu, semiconductor TiO_2 , NbC-Si thin films etc. These experiments were carried out, in order to study the in-plane structure and the effect of SR beam on the thin films, especially in the case of LB films. It has been found, that SR beam degrades LB films depending on the grazing incidence angle of SR beam. Since GIXRD data acquisition is relatively faster and has better signal-to-noise ratio in this mode as compared to that in scanning angle dispersive method, we could study the time dependence of degradation quantitatively, as a function of SR beam exposure.

References

1. High pressure phase transitions in Nd_2O_3 K. K. Pandey, Nandini Garg, A. K. Mishra and Surinder M. Sharma, Accepted in AIRAPT 23, 2011.



Part-II Dispersive Extended X-ray Absorption Fine Structure (EXAFS) beamline at INDUS-2 Synchrotron Source

S.N. Jha, D. Bhattacharyya, A.K. Poswal, S. Basu, and N.K. Sahoo

Applied Spectroscopy Division

Extended X-ray Absorption Fine Structure (EXAFS) technique, enables the measurement of fine structures in the X-ray absorption spectra, above the absorption edge of the atoms in a material. Generally, an EXAFS spectra extends from ~ 100 eV below the absorption edge of the particular atom to ~ 700 eV above the absorption edge. The spectrum near the absorption edge (viz., the XANES part) gives information about the long range order existing in the material and the oxidation states of the atoms involved, while the part of the spectrum well above the absorption edge (the EXAFS part) gives information regarding the short range order and local structure around the atomic species. With the advent of modern bright Synchrotron radiation sources, this technique has emerged to be the most powerful, for local structure determination which can be applied to any form or derivative of the material viz. amorphous, crystalline, polycrystalline, polymers, surfaces and solutions.

EXAFS measurements with synchrotron radiation are usually carried out in two different modes viz., scanning and dispersive, targeting different types of sample structures. Under the X plan, the Applied Spectroscopy Division, BARC developed an EXAFS beamline at INDUS-2 Synchrotron source, which works in the dispersive mode, using a 460 mm long Si (111) crystal mounted on an elliptical bender and a position sensitive CCD detector having 2048 x 2048 pixels. The beamline is designed to cover the photon energy range of 5 to 20 keV, providing energy band widths of 0.3 keV, 1.0 keV and 2.0 keV and with resolution of ~ 0.5 eV, 1 eV and 2 eV per pixels, at photon energies of 5 keV, 10 keV and 20 keV, respectively. An optical layout of the beamline is shown in Fig. 1 while the photograph of the beamline is shown in Fig. 2. The emission from the synchrotron source is first passed through a Be window (B) and the beam aperture system (K,K) and is then made to fall on the slit system (S,S)

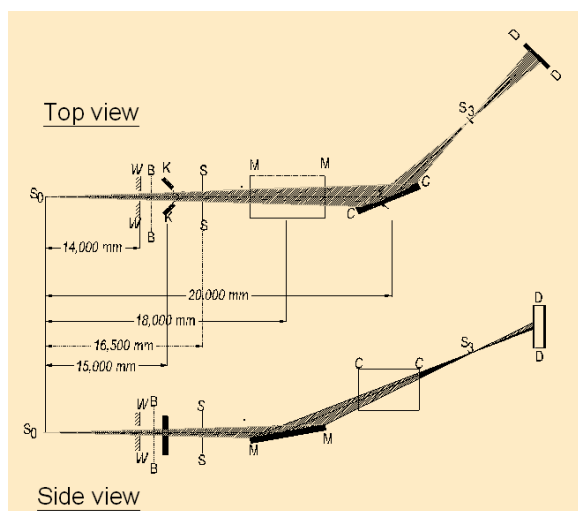


Fig.1. Optical layout of the EXAFS beamline



Fig.2. Photograph of the EXAFS beamline



which defines the final horizontal and vertical divergence of the synchrotron beam, using two sets of water-cooled tantalum jaws. The beam emerging from the slit system falls on vertically focusing mirror (M,M) and then on the silicon crystal (C,C) mounted on a bender. Depending upon the angle of incidence of the beam and its radius of curvature, the crystal reflects a particular central energy (E_o) with a certain band-width (ΔE) and this spatially dispersed polychromatic radiation is focused at the sample position (S_3), which is detected finally by a position-sensitive detector (D,D). Thus, the energy dispersed absorption spectra of the sample, over the whole band width (ΔE) around the central energy (E_o), can be simultaneously recorded by the detector.

The beamline was commissioned in February 2008. Since then, the beamline has been used extensively and several EXAFS investigations on technologically important materials prepared at various laboratories have been carried out [2,3], as discussed in the following sections:

(i) EXAFS study of uranyl ions, sorbed onto the surfaces of silica and alumina from aqueous suspensions of uranyl nitrate at varying pH have been carried out, at the uranium L_{III} edge (17.17 keV). The EXAFS analysis shows two oxygen atoms at 1.76 Å (due to axial O=U=O) and varying number of equatorial oxygen atoms (with pH), which were found to be in two groups, corresponding to U-O bond distances of 2.3 and 2.4 Å. These are attributed to the oxygen atoms from coordinated water molecules and those belonging to the silica or alumina surfaces. The above studies are important in modeling the sorption-based immobilization process of high level radioactive waste in silica and alumina rich minerals.

(ii) EXAFS study of binuclear hydroxo-bridged copper (II) complexes have been carried out at Cu K edge on four types of bi-nuclear copper complexes, which are important for their catalytic activity for oxidative coupling reactions[4,5].

(iii) EXAFS measurements have been carried out on doped ZrO_2 systems synthesized for Solid Oxide Fuel Cell (SOFC) applications, with 11% Nd and La doping and with 7,9,11 and 13% Gd doping. It has been observed, that though for Gd doping, the oxygen vacancies in ZrO_2 host matrix are created near the Zr site, for Nd and La doping with relatively larger ionic radii, the Zr-O shell remains more or less unperturbed and the oxygen vacancies are located near the dopant cations. It has also been found, that Gd doping of 9% is optimum for creation of vacancies near the Zr sites and hence, for increasing its ionic conductivity.

(iv) EXAFS measurements have been performed on doped $BaCe_{0.8-x}Zr_xY_{0.2}O_{3-\delta}$ ($0 < x < 0.8$) compounds, important for their potential application as electrolytes in SOFC, at the Yttrium K-edge. EXAFS data analysis show $BaCe_{0.8-x}Zr_xY_{0.2}O_{3-\delta}$ compounds to have orthorhombic structure for $x < 0.6$ and tetragonal structure for $x = 0.8$, which is consistent with X-ray diffraction measurements.

(v) EXAFS measurements have been carried out on two types of magnetically important ferrite spinel systems (a) magnetite doped with 50 mol % of Co and Zn ($Co_{0.5}Zn_{0.5}Fe_2O_4$), and (b) magnetite doped with 50 mol% Co and Ni ($Co_{0.5}Ni_{0.5}Fe_2O_4$). Analysis of EXAFS spectra has shown, that the bond distances of all samples are slightly higher than that expected for pure magnetite (Fe_3O_4) sample, due to the presence of the larger size dopant cations (Co, Ni and Zn) in the Fe sites.

(vi) EXAFS measurements have been carried out on ZnO nanoparticle gas sensors with varying particle size (between 5-100 nm) at the Zn K-edge (9659 eV). It was observed that for all the samples, the first Zn-O shell has lower coordination than the nominal value, which is a manifestation of presence of oxygen vacancies in the ZnO samples as expected. It was also observed, that with decrease in the particle size of the ZnO samples, Zn-Zn site is mostly affected with a gradual decrease in coordination number and increase in the Debye-Waller factor and bond distance.



Presently, *in situ* measurements in the beamline up to 600 K under different ambients is possible and facilities to carry out experiments in low temperatures up to 10 K and high temperature up to 1200 K, will be introduced soon.

Acknowledgements

The front-ends of both the beamlines were installed by our colleagues from the Synchrotron Utilization Division of RRCAT, Indore. Developments of several components of the beamlines, such as primary slit, precision slits and installation of goniometer of EDXRD beamline and crystal-bender and 19-axes goniometer for EXAFS beamline were done with the help of several colleagues of CDM (group leader Sh. A.K. Sinha) who were also the co-recipients of the group achievement award.

References

1. D. Bhattacharyya, A.K. Poswal, S.N. Jha, Sangeeta and S.C. Sabharwal *Nuclear Instruments Method. in Phys. Res. A* 609 (2009) 286.
2. D. Bhattacharyya, A.K. Poswal, S.N. Jha, Sangeeta and S.C. Sabharwal *Bull. Mater. Sci.*, 32 (2009) 103.
3. D. Bhattacharyya, S.N. Jha, A.K. Poswal, Sangeeta and S.C. Sabharwal *Bull. Mater. Sci.*, 2011 (in press).
4. Abhijeet Gaur, B. D. Shrivastava, D. C. Gaur, J. Prasad, K. Srivastava, S. N. Jha, D. Bhattacharyya, A. Poswal and S. K. Deb *Journal of coordination Chemistry*, 64 (2011) 1265.
5. Abhijeet Gaur, Ajita Johari, B. D. Shrivastava, D. C. Gaur, S. N. Jha, D. Bhattacharyya, A. Poswal and S. K. Deb *Sadhana (India)*, 36 (2011) 339.



Man-rem Saving Tools for PHWR Coolant Channels

R. J. Patel

Refuelling Technology Division

This Paper received the DAE Group Achievement Award for the year 2009

Abstract

Pressure Tubes in PHWRs are required to be monitored periodically, for assessing of their fitness for service. Closure seal face of end fitting, requires maintenance/repair jobs to be performed, to salvage it when damaged. All these activities are performed in radiation intensive areas like fuelling machine vault. Earlier generation techniques required the channel to be drained/dried for such tasks. These resulted in huge expenditure of man-rem and costly reactor shut down time. New generation tools and schemes have been developed, to carry out these activities remotely and in water-filled channel condition.

Introduction

Coolant Channels are important components of PHWRs consisting of mainly end fitting, liner tube, pressure tube, calandria tube and garter springs (Fig. 1). At both ends of the channel, shield plugs and seal plugs are used, for providing shielding and sealing. Heavy Water coolant circulates at high pressure and temperature through the

coolant channels and cools the fuel bundles. A remotely operated fuelling machine (Fig. 2) is used, for refuelling of the channel. The machine is like a robot which can be used for tasks other than refueling also.

Due to continued operation in the harsh environment of neutron flux, high pressure and temperature, coolant channel components especially the pressure tube are

subjected to degradation mechanisms, resulting in dimensional changes. In view of this, it is required to periodically monitor certain parameters like creep of the channel of operating PHWRs, to ascertain their fitness for service. Previously used methods consumed considerable man-rem and reactor shut down time. Fuelling machine-based remotely operated techniques have been developed, for checking the change in length of the channel, which can be operated remotely and thus can be deployed quickly. The total time taken for scanning the entire reactor face for creep measurement, is also considerably reduced.

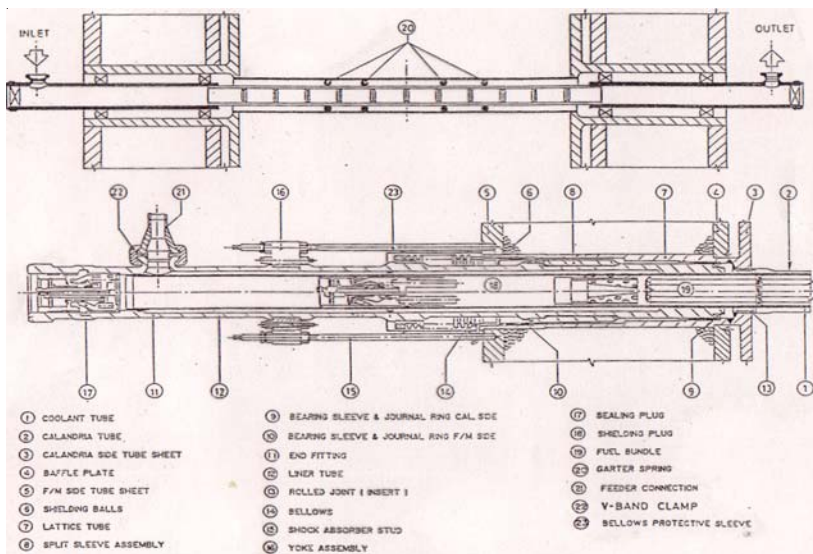


Fig. 1: Coolant Channel Assembly

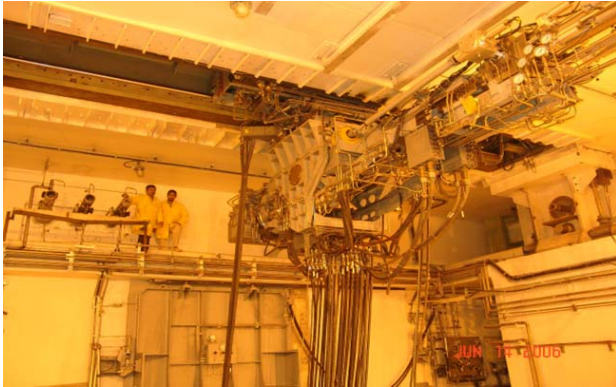


Fig 2: Fuelling machine for 540 MWePHWRs

The closure plug seal face of end fitting, used for sealing the channel, may get damaged during refueling operation, due to entrapment of particle between seal plug and seal face. The situation calls for immediate attending to the problem and may pose heavy economic penalty in terms of reactor shut down. It is desired to arrest such seal plug leakage temporarily, using a specially developed device. End Fitting Blanking Assembly is developed to meet the above requirement. For repairing the seal face, a device is required enabling the seal face to be accessible, without requiring draining and drying of the channel. Channel Isolation Plug is developed for this purpose, which makes the seal face accessible. In PHWRs, many a times the channel is required to be drained and isolated, for carrying out certain tasks such as In Service Inspection, replacement / repair of coolant channel assembly components. This is accomplished by ice plugging the feeder pipes and subsequently blanking the channel. To enable the ice plugging, it is necessary to stop the flow through the coolant channel. In the absence of isolation valves in the

PHT, Channel Flow Arrestor Assembly is developed, to enable the blocking of flow through the channel.

Creep measurement Schemes

Pressure tube of the coolant channel is subjected to neutron flux, pressure and temperature during reactor operation, and elongates (creep) under the influence of these conditions. This change in length is monitored regularly and adjustments are made in the yoke assembly of the channel, to prevent the restraining of the channel and consequent loading of the pressure tube. Previous methods required the use of theodolite and consumed lot of men-rem even for one channel monitoring. The following Fuelling machine-based techniques have been worked out, for this purpose.

Technique for Measurement of Axial Creep (TMAC)

The Z-cylinders of the fuelling machine are provided with linear potentiometers. This requires FMs on both sides to

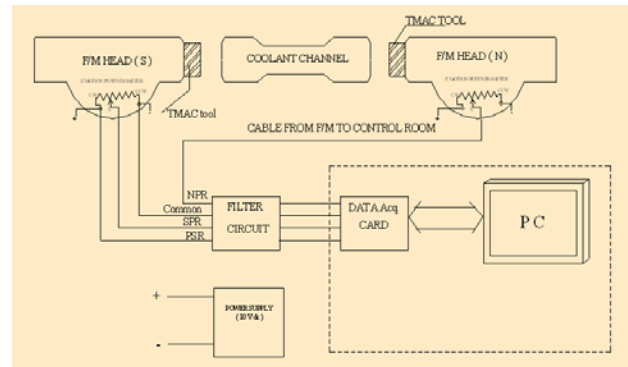


Fig. 3: Block diagram of TMAC

TMAC COMPONENTS


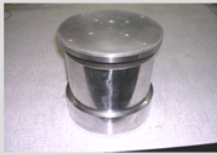


			
Sensor	TMAC tool	DOS based Operator Interface	Data Acquisition (PC) Card

Fig. 4: Components of TMAC



butt on the coolant channels. The change in length of the channel as compared to the non-creeping channel can be measured, with the help of the potentiometers, which is the measure of the creep.

This is a remote-operated method of creep measurement and has been extensively used in all the operating PHWRs. This provides creep data within an accuracy of ± 1.0 mm. Measurement can be completed in about 16-20 hrs. A specially developed data acquisition system and software collects and analyzes the data and a report is generated instantly, in tabular as well as core lattice formats.

Ultrasonic Measurement of Axial Creep (UMAC)

To further minimize the time taken for measuring the axial creep, a technique called Ultrasonic Measurement of Axial Creep is developed. This uses non contact type ultrasonic sensors, for measurement of distance of the E-face of the channel, with respect to non creeping channel. The sensor is mounted on the fuelling machine snout using a specially designed fixture. Fuelling machine moves across the reactor face carrying this sensor. A specially designed data

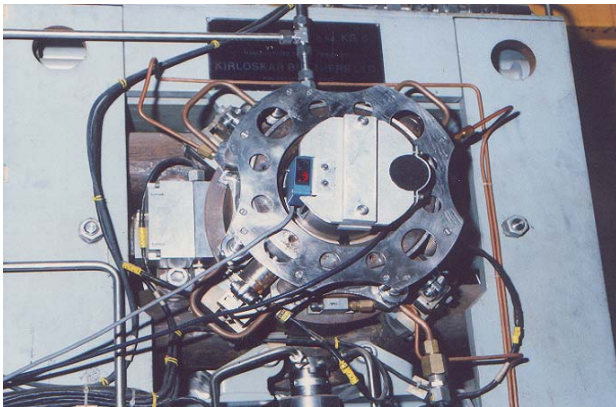


Fig 5 : Output from UMAC

acquisition system is used, for recording the data collected during scanning. Software is developed which analyses the data collected on both ends of the channels and evaluates the creep for all channels. The technique takes about 4 to 6 hrs in scanning of one reactor. The technique also facilitates the measurement of free expansion of the

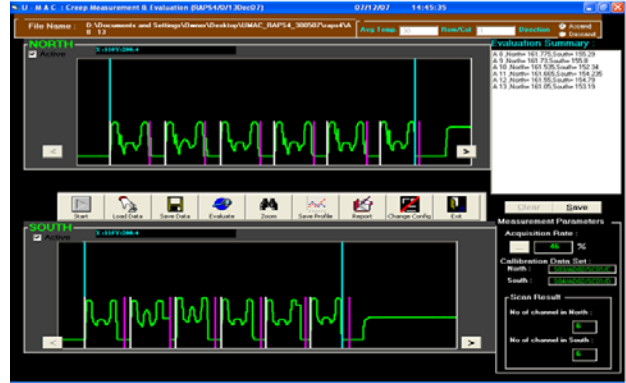


Fig 5 : UMAC tool mounted on FM

channels. The system has been delivered to all units of PHWRs and is in use.

Coolant Channel Maintenance Tools for 540 MWe PHWRs

End fitting of the coolant channel may require maintenance of its components during the life time of the reactor. These operations are taken up during shut down of the reactor and may require the channel to be drained and dried. Hence it is envisaged to develop techniques, which avoid draining and drying of the channel and enable the maintenance operation to be taken up quickly. End Fitting Blanking Assembly and Channel isolation Plug are two such devices, used in case of damage of the seal face. However it may be necessary on few unforeseen occasions, to drain the channel to take up any maintenance or inspection of its components. This requires feeder pipes to be frozen after stopping the flow through them. A fuelling machine-based tool, Channel Flow Arrestor Assembly is developed, to enable stopping of flow through the channel.

End Fitting Blanking Assembly

Coolant channel is sealed at either end using sealing plugs. The seal plug sits against the seal face of the end fitting and provides sealing of the channel. Many a times, a foreign material gets entrapped between the sealing plug



Fig 6 : End Fitting Blanking Assembly

seal disc and sealing face of the end fitting, resulting in damage to both the components and unacceptable leakage from the sealing plugs. The situation calls for immediate attending of the problem and may pose heavy economic penalty in terms of reactor shut down. It is desired to arrest such seal plug leakage temporarily using a specially developed device. End Fitting Blanking Assembly is developed, to meet the above requirement. End fitting blanking assembly uses elastomer seals for providing sealing, can be installed quickly and conveniently in about a minute's time and does not impose restriction on refueling of neighboring channels. It also has pressure release mechanism, to release the pressure while removing it from channel. It is designed to withstand the channel pressure and temperature. End fitting blanking assembly has been manufactured, qualified and handed over to TAPS-3&4 for use.

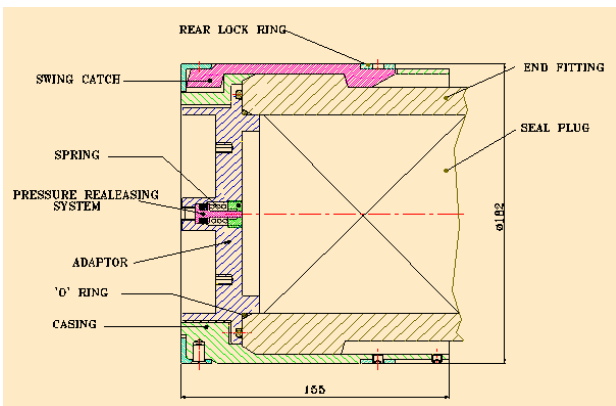


Fig 7: Sectional view of End Fitting Blanking Assembly

CHannel Isolation Plug (CHIP)

In case of damaged seal face, problem is mitigated temporarily using end fitting blanking assembly. Though the end fitting blanking assembly provides means to arrest the leakage due to damaged seal face temporarily, the



Fig 8 : Channel Isolation Plug



Fig. 9: Delivery Adaptor

seal face requires to be lapped, to bring back the end fitting to normal service. In normal circumstances, the channel is defueled, drained and dried to make the seal face accessible for repair. To facilitate lapping in water filled condition, a Channel Isolation Plug is required, which will isolate the channel, without the need for draining and exposes the seal face for carrying out lapping.

Channel isolation plug works along with a specially made delivery adaptor and installed in the end fitting using fuelling machine. After installing the channel isolation plug, the fuelling machine moves away along with delivery adaptor and the sealing face is available for inspection and repairing (lapping operation). In earlier designs for 220 MWe PHWRs, after installation by the fuelling machine, human intervention was required for getting access to the seal face. This requirement has been



eliminated in the channel isolation plug for 540 MWe PHWR. It uses elastomeric O-ring for sealing purpose. It is installed in the grooves meant for shielding plug and has safety features similar to shield plug and seal plug. Overall length of the channel isolation plug and delivery adaptor is less than 990 mm and is accommodated in the fuelling machine magazine. The plug has been designed, manufactured, qualified and delivered to TAPS 3 & 4.

plugging of the feeder pipes and subsequently blanking of the channel. To enable the ice plugging, it is necessary to stop the flow through the coolant channel.

Channel Flow Arrestor Assembly enables the blocking of flow through channel. Fuelling machine installs it in respective shield plug groove of end fitting. Elastomer O-ring in the front portion of flow arrestor assembly, blocks the flow and ice plugging of feeder can be taken up.

The sealing is required to be located beyond liner tube holes. In case of 540 MWe PHWR, the distance between shield plug groove and pressure tube being large, the channel flow arrestor assembly is made in two parts, consisting of flow arrestor plug and its extension. Mechanism is provided for joining and disjoining both parts and this is accomplished by the fuelling machine.

The Channel flow arrestor assembly is manufactured, qualified for simulated reactor conditions and is ready for use in reactor whenever necessary.

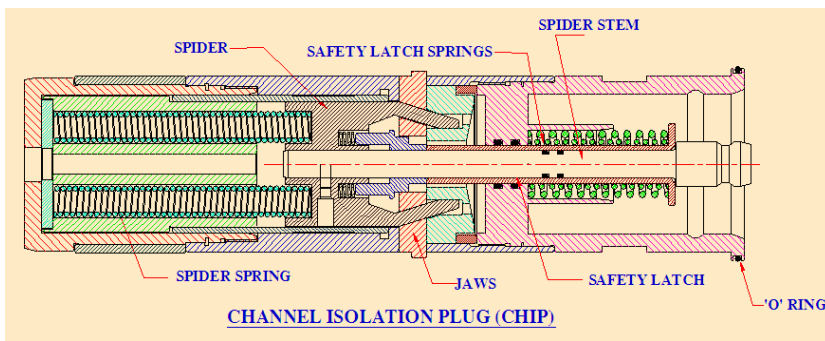


Fig. 10: Sectional view of Channel Isolation Plug

Channel Flow Arrestor Assembly

In PHWRs, many a times, channel is required to be drained and isolated for carrying out certain task such as In Service Inspection, replacement / repair of coolant channel assembly components. This is accomplished by ice

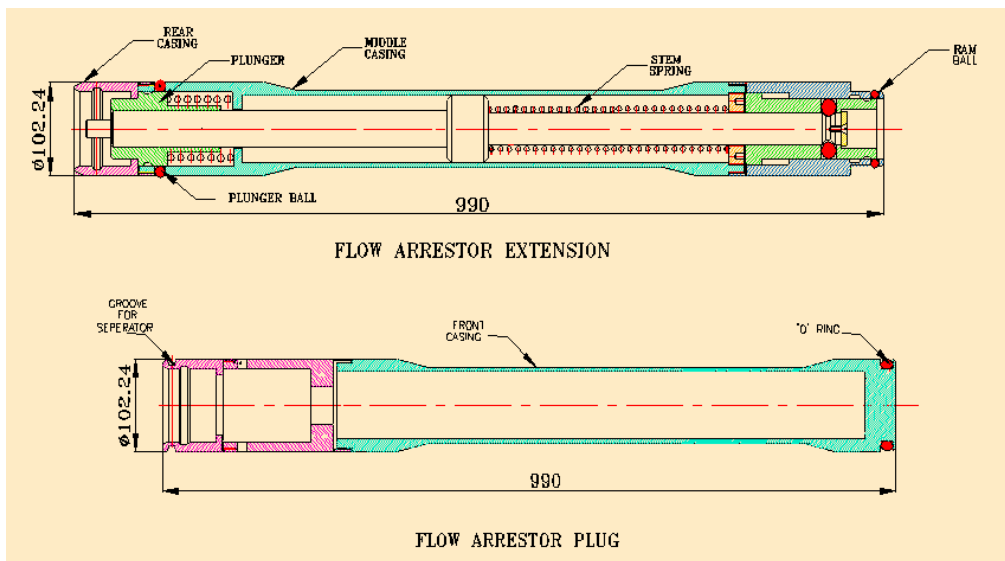


Fig. 11: Channel Flow Arrestor Assembly



Conclusion

Coolant channel components of the PHWRs require regular monitoring and maintenance. Capacity factor of PHWRs is influenced by the time taken to carry out these tasks. Use of fuelling machine to carry out part of the task/entire operation was envisaged, to optimize the time taken for such activities and the man-rem consumed. With continuous evolution, the methodologies have matured and resulted in reliable tools. Satisfactory performance of the tools in the operating units has established the soundness of the design.

Acknowledgement

Development of man-rem saving tools is a product of team work comprising of design engineers, operation engineers and supporting technical staff of the Refuelling

Technology Division. Shri Mahender Dev, SO (G) and Shri Monesh Chaturvedi, SO (E) have contributed in the development of Channel Isolation Plug. Shri Rites Ranjon, SO (F) and Shri S. Bhattacharyya, SO (D) have contributed in the development of Creep measurement techniques. Shri V.P. Bodile, SA/D and Shri S. Bhattacharya, have contributed in development of End Fitting Blanking assembly and Channel Flow Arrestor assembly. Team of technical staff comprising of S/Shri V.V. Kshrisagar, SA/E, S.V. Kulkarni, F/A, V.M. Vaity, T/G, R.G. Suryavanshi, T/G, B.S. Bhosale, T/D, V A Gaikwad, T/C, V P Patil, WA/A has made significant contribution in development and qualification of all man-rem saving tools. Fuelling machine testing crew comprising of Shri N. K. Mandal, SO(F) Shri C K Birla, SO(D) and Shri M.G. Gopalan, FM/B have contributed in performing Fuelling Machine compatibility tests on the developed tools. Author acknowledges the contribution of Shri. Mahender Dev in preparing this paper.



Remote Disposal of Explosive Anti-Tank Mine Fuzes using Indigenous Mobile Robot System

Manjit Singh, P.K. Pal, K. Jayarajan, D.D. Ray, B. Sony, V.K. Shrivastava,
R. Sahu, R.V. Sakrikar, A.N. Jha and V.V. Agashe

Division of Remote Handling & Robotics

and

Vivek Mahadev

Seismology Division

This paper received the DAE Excellence (in Science, Engineering and Technology)
Awards for the Year 2009

Abstract

A large number of ammunition boxes, containing potentially explosive anti-tank mine fuzes, were stored at Ordnance Factory Khamaria, Jabalpur for a long time. Using an indigenous remote-controlled mobile robot system, we safely disposed all the fuzes, after transporting them to a remote site. The system consists of a six-wheeled vehicle, an articulated manipulator and a mechanism for removing the fuzes from the ammunition boxes. The article describes the problem and the methodology adopted to solve the problem.

Introduction

About 300 boxes containing more than 13,000 rejected fuzes of anti-tank mines, were lying in two storage rooms at Ordnance Factory Khamaria (OFK), Jabalpur, for more than 25 years. Based on past experience, it was felt that some of these fuzes could have become very sensitive and might explode at the slightest disturbance. As their presence in the factory premises was a threat to the people, the factory and the surroundings, the boxes had to be removed from the site and their contents had to be disposed off at the earliest. Remote handling option was adopted, to avoid possible injury or loss of life during handling of these boxes. Based on a request from the Centre for Fire, Environment & Explosive Safety (CFEES), Delhi, we developed a mobile platform with an on-board manipulator for remotely transporting the boxes from the storage rooms to the disposal site. Another remote controlled mechanism was developed for opening the ammunition boxes at the disposal site and removing the

fuzes from the boxes. All the fuzes were disposed off by burning them in a controlled manner, after transporting them from the storage room to the disposal site, in the year 2006.

Problem Description

The site layout showing the storage rooms and disposal site are given in Fig. 1. The buildings and disposal site are connected through an over-bridge and cemented pathways. The buildings are separated by traverses, which are earth walls constructed to protect the buildings from accidental explosion in adjacent building.

The fuze boxes containing rejected fuzes were stacked up to a height of 1.5 m in two adjoining rooms, as shown in the Fig. 2. Two types of boxes, with dimensions of 600 mm x 250 mm x 320 mm height and 645 mm x 345 mm x 200 mm height, were stacked in the rooms. They were made up of 1 mm thick steel and weighed about 30 kg with their contents. Each box had a body, a lid,

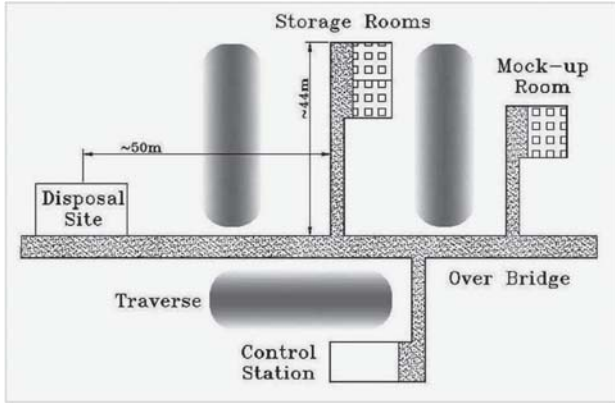


Fig 1: Site Layout



Fig. 2: Stacked Boxes in the Storage Room

two spring-clips and two hinges. The lid was retained in position by two spring clips.

We had to build a robot to remotely pick up a box from the stacks, bring it to the disposal site along the road and the over-bridge, open the spring clip of the box and pour its fuzes into a pit for disposal. This had to be done carefully to avoid any possibility of explosion.

Design Philosophy

Although robots are manufactured and sold all over the world for disposal of explosives, they were not found to be suitable for our application, due to the size and weight of the ammunition box, the space constraints and the safety requirements. Although the users had approached a few robot manufacturers for development of ordnance disposal systems, the cost of development was prohibitively high. This prompted us to work towards an indigenous solution.

We decided to set up the control station in one of the available buildings, which was protected by traverses and was close to the storage rooms and the disposal site, as shown in Fig. 1. Wireless stations were setup on the top of the traverses, to ensure proper connectivity within the working zones. A full scale mock-up facility was set up in another room, to test and qualify the operation of the scheme.

We also developed a pneumatic device, for remotely removing the spring-clip of the box and then tilting the box to pour its contents into the disposal pit. Both the robot and the unclipping device were to be operated remotely from the control station. The robot was connected to the control room PC through wireless Ethernet. Video feedback was available to the operator sitting in the control room, from cameras mounted on the mobile robot, the storage rooms and the disposal pit. The operator issued commands for the mobile robot and the manipulator, based on the video feedback.

Safety was given prime consideration in the scheme. Some of the safety considerations are given below:

- Avoid direct handling of the ammunition box by the operator.
- Provide sensors and interlocks on the vehicle to prevent the collision of the vehicle with the explosive boxes, walls or any other objects.
- Ensure that the robot joints would remain in their positions, during power failure.
- Ensure that the gripper would not drop the box, in case of power failure.

Mobile Platform

A six-wheeled battery-powered vehicle with on-board manipulator designed for handling and transportation of ammunition boxes, as shown in Fig.3. Each side of the vehicle had three wheels, which were powered by a single motor and coupled by chains and sprockets. By controlling the relative speeds of the left and right sets of wheels, the vehicle could be made to move in a straight line, move over an arc or take a turn around itself. The combination



Fig. 3: Mobile robot with manipulator

of motions helped in manoeuvring vehicle in cramped spaces, like storage rooms and room entrances.

Bumpers were provided around the vehicle to stop the vehicle during inadvertent collisions. Two Pan-Tilt-Zoom (PTZ) cameras were mounted on the vehicle, to monitor its path. One camera was mounted on the manipulator to view the gripper and box handling. The cameras sent video signals to the control room using wireless transmitters.

Manipulator

A four-axis articulated manipulator was developed for handling the ammunition boxes. It had a big gripper with 800 mm opening, to hold the ammunition box. Using a set of 4-bar mechanisms, the gripper was mechanically constrained to remain in vertical orientation, to prevent it from getting tilted during movement. Although the manipulator had a reach of 2 m radius from its base, it could be folded back to accommodate in the vehicle. Electromagnetic brakes were provided on the joints to prevent uncontrolled movement of the manipulator, during accidental break in the power supply to the motors.

Remote Box Opening Mechanism

The lids of the ammunition boxes were retained in position by a pair of spring clips. A setup was designed for opening the spring clips and removing the fuzes from the boxes, as shown in the Fig. 4. It has features for locating the box, clamping the box, opening the spring clips and

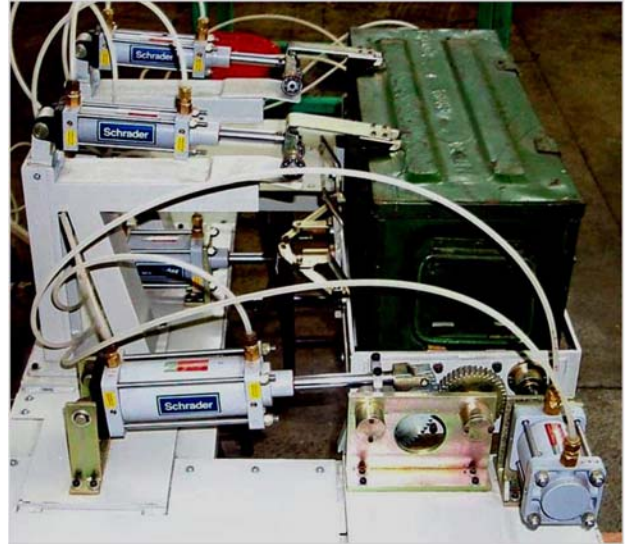


Fig. 4: Setup for spring clip opening and unloading of fuze box

rotating the box for removal of the fuzes. All these operations were done remotely from the control station.

Control Architecture

The overall control architecture of the Robot is as shown in Fig. 5. The on-board Single Board Computer (SBC) formed the master controller for the system, in which the high level application of the robot was executed. The SBC has a wireless Ethernet link with the host computer. The host, which is a standard desktop computer, executed the application on the SBC, via the VNC (Virtual Network

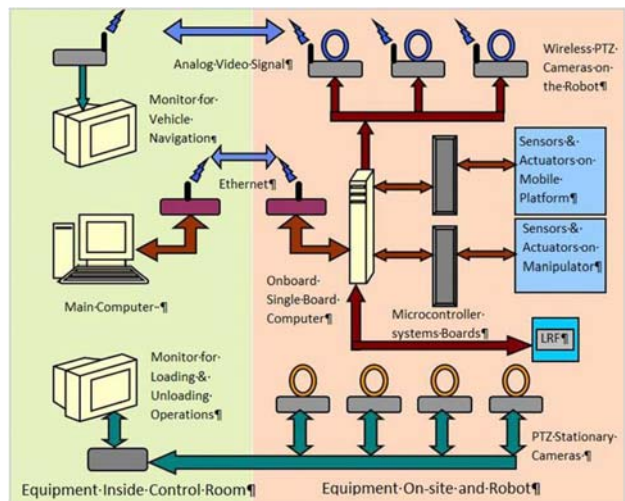


Fig. 5: Control architecture of the system

DAE Excellence Award

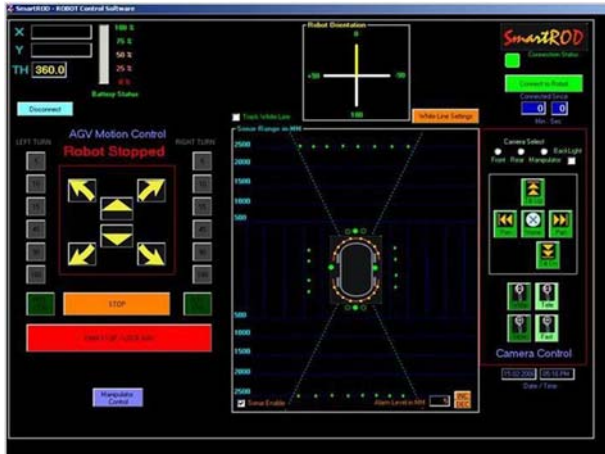


Fig. 6: HMI for Vehicle Operation

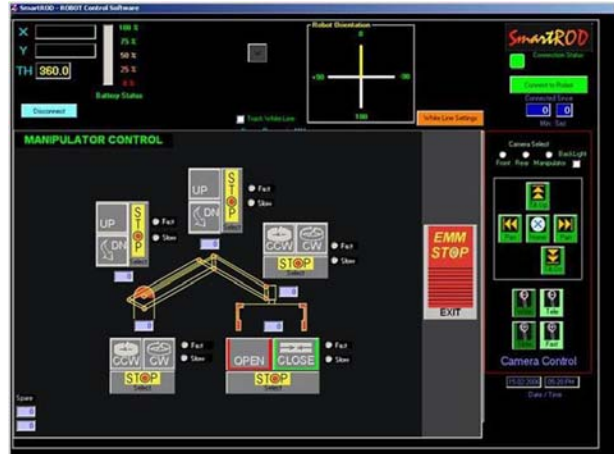


Fig. 7: HMI for Manipulator Operation



Fig. 8: Control Room Layout

Computing) server installed on the SBC. The SBC issues commands to the controller of the vehicle and the manipulator through two serial ports, as per instructions from the Human Machine Interface (HMI) programme.

One of the serial ports of the SBC was used for Pan-Tilt-Zoom controls of the on-board cameras of the mobile robot. The PTZ movements could be controlled from the same HMI of the robot. The video signals from the onboard cameras were directly transmitted through a wireless video link to the display, which is a standard television set. This display is used for the navigation of the robot throughout the operation.

Another serial port of the SBC was used for connecting to the SICK Laser Range Finder (LRF). The LRF generated range data over an angle of 180° in front of the robot. This data could be used for building a line map of the area.

Human Machine Interface for Control and Monitor

Figs. 6 and 7 show the graphical interface on the host computer, for the remote operation of the mobile robot.

It has provisions for driving the platform forward, backward and taking a turn. In addition, the interface displays the status of the battery, position and orientation of the mobile platform and a line map of the area in front of the platform.

The Fig. 8 shows the interiors of the control room setup for the operation and monitoring of the system.

Conclusion

We have developed a mobile robot system for remotely disposing the potentially explosive fuzes, stored at Ordnance Factory Khamaria, Jabalpur. The system was to be used for a specific application over a limited period. In a short time, we have developed a remote handling system with available know-how. The 25-year old problem of the Factory was solved by disposing all explosives safely, using this indigenous system.

Acknowledgements

The authors acknowledge the contributions of K. C. Boipoi, B. Das, D.S. Rajapure, Jacob Peter, P. S. Ghadge, M. Padhy, Abhijit Burman, Y. R. Pathan, S.R. More, G. L. Bhandare, M.S. Sawant, R. S. Hirlekar, A. R. Kotwal, R.J. Bamane, P. B. Patil, V. B. Gaikwad, A. A. Gonsalves, K. M. Wavhal, R. G. Koli and S. K. Pednekar for fabrication, assembly and testing of the system at BARC and carrying out the operations at OFK, Jabalpur.



Treatment of Intermediate level liquid waste of reprocessing origin-PREFRE, Tarapur

D. Banerjee, A.K. Singh and I.J. Singh

Nuclear Recycle Group

and

T.P. Valsala, M.S. Sonawane, S. Chattopadhyay and U. Dani

Nuclear Recycle Board, BARC, Tarapur

This paper received the Group Achievement Award for the year 2009

Abstract

Industrial scale treatment of alkaline intermediate level liquid waste stored in waste tanks at PREFRE, Tarapur has been carried out successfully, utilizing an indigenously developed process, involving ion exchange removal of ^{137}Cs and ^{90}Sr , followed by combined chemical treatment of the down-stream effluent. More than 250 M³ of the waste was decontaminated and discharged. This achievement has paved the way for creating adequate tank space, as a result of which the operation of PREFRE could be carried out uninterrupted. A brief description of the process and highlights of the achievement are summarized in this paper.

Keywords: Intermediate level waste, decontamination, ion exchange, chemical treatment.

Introduction

Intermediate level liquid waste (ILW) generated from reprocessing plants is made alkaline by the addition of Na_2CO_3 and NaOH and stored in underground carbon steel tanks. This waste is characterized by high salt loads and high gross β activity, mainly due to the presence of ^{137}Cs and traces of ^{90}Sr , ^{106}Ru etc. This alkaline ILW is treated by adopting an indigenously developed ion exchange based process, utilizing in-house synthesized, Cs-selective, Resorcinol Formaldehyde Polycondensate Resin (RFPR), followed by a commercially available Sr selective Iminodiacetic Acid Resin (IDAR). Industrial scale application of the process has been successfully demonstrated earlier, at Trombay [1-3], wherein large volumes of ILW originating from reprocessing of research reactor spent

fuel have been decontaminated. Operation was made easily mobile, by installing the whole ion exchange facility on a 40 Te trailer, which could be taken to the waste tank for treatment.

Excellent decontamination performance of the process and confidence gained during treatment of the ILW, encouraged us in setting up the facility for treatment of alkaline ILW, stored in underground tanks at PREFRE Tarapur plant. This plant is under continuous operation since commissioning, for reprocessing of spent fuels irradiated in power reactors. Unlike processing of ILW at Trombay, adaptation of the process for treatment of the ILW of PREFRE reprocessing plant origin, posed major challenges, mainly due to the presence of some trace quantities of chemical and radiochemical constituents in the waste.



Notably, the presence of traces of dissolved organics, generated from degradation of tri-butyl phosphate (TBP), interfered significantly in the decontamination of the waste. Further, presence of substantial amounts of ^{106}Ru and ^{99}Tc activity in the down-stream of ion exchange process entailed development of efficient processes, to bring down the activity level below discharge limits. Although it is known that ^{99}Tc in reprocessing waste is present mostly as TcO_4^- anion, presence of the radioelement in ILW was found for the first time in India. Apart from the chemistry aspects, implementation of the process within a very short time period was another challenge to engineers, as it involved shifting and refurbishment of the mobile facility, installation and its commissioning. All the challenges were met easily and more than 250 M^3 of the ILW including 200 M^3 of Tank-6 and 50 M^3 of Tank-5 waste was decontaminated, thereby creating adequate tank space and ensuring sustainability of PREFRE operation. A summary of the treatment campaign including a brief description of the processes used for treatment, are highlighted in the following sections.

Characteristics of waste

Detailed characterization of WTF-06 and WTF-05 waste of PREFRE Tarapur was done, prior to the treatment

campaign. Further, radiochemical characterization with respect to the minor constituents was obtained, by analyzing the samples generated after removal of major radionuclide, ^{137}Cs by ion exchange. A typical characteristic of both the tank's contents before and after ion exchange treatment, is shown in Table 1. It can be seen that, both the wastes are similar with respect to their chemical and radiochemical constituents although their concentrations vary widely. The total dissolved solids are mainly due to the presence of NaNO_3 and Na_2CO_3 . The salient features of both wastes include: presence of dissolved organics, significantly higher amounts of ^{106}Ru and ^{99}Tc activity and ^{137}Cs being the major radionuclide. In comparison to WTF-06, the WTF-05 waste contained about 2.5 times higher ^{137}Cs and, more importantly, about 35 times higher ^{106}Ru activity.

Removal of ^{137}Cs and ^{90}Sr by Ion exchange

A thumbnail view of the ion exchange system is shown in Fig.1. The waste was pumped at a flow rate of 400 L/h to the system, which comprised of a pre-filter (F1), three ion-exchange columns (two of them are loaded with RF resin for Cs-removal and one with imino diacetic acid resin for Sr-removal), each of 100 liters capacity in series and a resin trap. The ion exchange columns are installed on a self shielded cubicle. This was further enclosed by a

Table 1: Characteristics of ILW before and after ion exchange treatment

Constituent	WTF-06		WTF-05	
	Before IX treatment	After IX treatment	Before IX treatment	After IX treatment
pH	12.8	12.8	12.5	12.7
TDS, g/L	140	140	180	180
Total P as TBP, g/L	1.8	1.8	2.0	2.0
Gross \hat{a} , mCi/L	21.5	0.17	54.6	0.34
^{137}Cs , "	21.1	0.10	48.8	0.02
^{90}Sr , "	2.0×10^{-3}	1.4×10^{-3}	2.0×10^{-3}	2.0×10^{-3}
^{106}Ru , "	5.2×10^{-3}	5.2×10^{-3}	0.18-0.10	0.18-0.05
^{99}Tc , "	5.1×10^{-2}	5.1×10^{-2}	0.10	0.09



bigger cubicle within which all the piping, valves, instrument gadgets have been installed. The whole facility is installed on a 40 Te trailer. The treated effluent was collected in a monitoring tank. At the end of loading run, only lead RF column was eluated and then flow path between the two RF columns was interchanged for the next cycle to use the regenerated column as guard column, in every cycle. About 25 -35 M³ of waste was treated in each cycle. The performance of the ion exchange column was found to be almost invariant throughout the campaign and thus a typical profile of the treated effluent is shown in Table 1. This treated effluent from monitoring tank was routed to the LWTP for further treatment as described below.

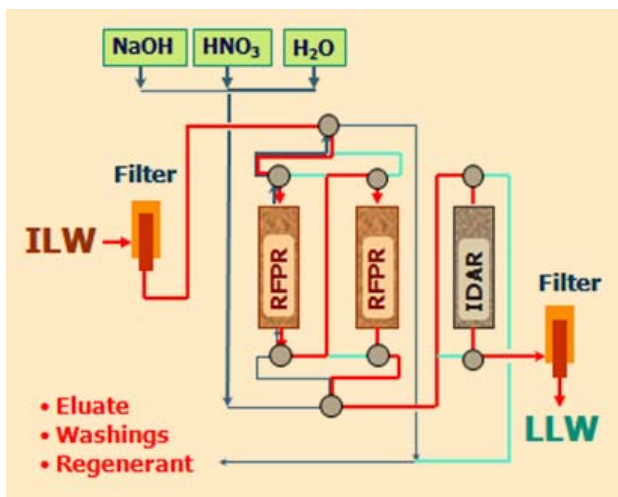


Fig.1: Schematic of ion exchange process

Decontamination of down-stream of ion exchange by chemical treatment

The down-stream of ion exchange is highly alkaline and mainly ¹⁰⁶Ru and ⁹⁹Tc rich. Decontamination of the down-stream of ion exchange process was done at LWTP, by adopting waste-specific chemical treatment formulations. Two processes have been used, for treatment of effluents generated during the campaign. Evaluation of processes and optimization of process parameters have been discussed in detail, in our earlier communications [4-5]. In summary, all the processes involve adjustment of pH to 2 by addition of acid, followed by addition of coagulant

and adjustment of final pH to 7-8. The initial adjustment of effluent pH <2 was necessitated for destruction of carbonate, which interferes significantly in ¹⁰⁶Ru decontamination. For adjustment of pH of the effluents, instead of using HNO₃, the acidic ILW generated from evaporation of high level waste in Advanced Vitrification System (AVS) was used. The AVS waste was an acidic (4M) effluent, containing about 0.1 mCi/L of ¹³⁷Cs and traces of ¹⁰⁶Ru activity. After pH adjustment, the effluent was treated by a two-step chemical treatment, involving precipitation of ferrous hydroxide in the presence of sulphite, FeS, copper ferrocyanide and barium sulphate. After the two-step treatment using the same formulation, the gross beta activity of the supernatant was reduced to 1 x10⁻³ mCi/L and therefore it was discharged after suitable dilution. The organics present in the waste were found to be separated in the form of an oily layer, at laboratory scale trials and in the form of a yellow layer at plant scale. A file photograph of the layer can be seen in Fig. 2. Interference of the presence of organics on Ru decontamination was overcome by using higher dosing of coagulants. The sludge generated from precipitation



Fig. 2: Photograph of the organic mass separated during chemical precipitation

was conditioned, cemented and disposed off as solid waste.

In the case of WTF-05 effluent, the Fe(OH)₂-based precipitation process, was found to be ineffective mainly



due to the presence of higher concentration of ^{106}Ru activity and high organic interference. An improved process was adopted for decontamination of the effluent. In this process, the organics, mainly dibutyl phosphate, were separated by the addition of Fe^{3+} in pH 2 solution for its precipitation as Fe-DBP complex. Then precipitation of CoS along with FeS, copper ferrocyanide and barium sulphate, was carried out. After Step-I treatment in the first trial (batch size: 12 M^3), the reduction of gross beta activity from 0.34 mCi/L to 7.2×10^{-3} mCi/L was achieved. Since only ^{106}Ru activity remained, Step-II treatment was therefore carried out, by adding 1000 ppm of Fe^{2+} as $\text{Fe}(\text{OH})_2$ and a decontaminated effluent containing $< 1.7 \times 10^{-3}$ mCi/L was obtained. During 2nd trial, $\text{Fe}(\text{OH})_2$ precipitation (500 ppm Fe^{2+}) was included along with CoS and FeS precipitation in the 1st Step which resulted in a decontaminated effluent containing $< 2.7 \times 10^{-3}$ mCi/L. The effluent was then discharged after suitable dilution.

Executive summary of the campaign

About 200 M^3 of WTF-06 and 50 M^3 of WTF-05 waste was treated successfully in the first phase of the campaign. Waste specific chemical treatment processes have been used, for decontamination of the down-stream effluent in a cost-effective manner. The highly ^{99}Tc and ^{106}Ru -rich effluent, generated from treatment of WTF-05, was also treated successfully. Experience gained in this campaign will be utilized in future treatment efforts.

Acknowledgement

Authors wish to thank all the staff of WMF(T), WMD and BETDD, who have worked directly or indirectly during various stages of this work to make the campaign

successful. The authors are grateful to Shri S.D. Misra, Director NRG, Shri P.K. Wattal, Head, PSDD, Shri Kanwar Raj, Head, WMD, Shri R.D. Changrani, CS, PREFRE and Shri Y. Kulkarni, PS, WMF(T) for their encouragement and support during various stages of this work.

References

1. Samanta, S.K, Ramaswamy, M. Misra, B.M. Studies on cesium uptake by phenolic resins, *Separation Science and Technology*, 27 (2) (1992):255-267.
2. Ozarde, P.D.; Samanta, S.K.; and Raj, K. (2002) *Management of intermediate level wastes from past reprocessing using cesium-specific resorcinol formaldehyde resin*, International Conference on Issues and Trends in Radioactive Waste Management, December 9-13, International Atomic Energy Agency, Vienna, Austria.
3. Banerjee D and Samanta S.K, "Process chemistry and resin performance in the treatment of alkaline intermediate level reprocessing waste by selective ion exchange", Proc. Ind. Nucl. Soc. Annual Conf. (INSAC-2003), Indira Gandhi Centre for Atomic Research, Kalpakkam (2003).
4. Banerjee D, Manjula A Rao, Annie Joseph, Manjrekar A, Singh I.J, Changrani, R.D and Wattal P.K, *Chemical Treatment Formulation for Decontamination of ^{106}Ru and ^{99}Tc Bearing Effluents of Power Reactor Spent Fuel Reprocessing Plant Origin*, Proc. of DAE-BRNS Symp. on Emerging Trends in Sep. Sci. Technol. SESTEC-2010, IGCAR, Kalpakkam, March 1-4, 2010, page -327.
5. Sonar N.L., Raghvendra Y., Kore S.G., Yadav V.K., De Vaishali., Valsala T.P. Sonavane M.S. and Kulkarni Y. *Decontamination of alkaline radioactive Low level liquid waste using chemical co-precipitation*, Procd, Nuclear and Radiochemistry symposium (NUCAR-2009), Mumbai.



Vibration as a Tool for Testing Healthiness of Defence Components

A. Rama Rao, S.K. Sinha, K.K. Meher, Satyvir Singh and Anil Kumar Narayan

Vibration Laboratory Section
Reactor Engineering Division

This paper received the DAE Group Achievement Award for the year 2009

Abstract

Vibration analysis as a diagnostic tool, for monitoring the health of machinery, structures and equipment is a well proven technique and acknowledged by almost all the industries. Realizing the inherent benefit of implementing the results of vibration analysis, industry is investing in vibration diagnostic equipments. Testing components for vibration is another area where substantial amount of money and efforts are being invested. These are largely required for qualifying defence components. This developmental work of high vibration techniques for testing two important components manufactured for advanced missiles, was undertaken for DRDO.

Key words: Vibration, Testing, Tool, Health, Machinery, Components.

Introduction

The Defence Research and Development Organization entered into a joint venture with Military Industrial Consortium of Russia, to form Brahmos Aerospace, with the aim to develop the supersonic cruise missile BrahMos. The ship and ground-launched versions have a range of 300 km, while the air-launched version has a range of 500 km. The ship and ground-launched version is 8.2 m in length, has a body diameter of 0.67 m, carries a 300 kg payload, and has a launch weight of 3000 kg; the air-launched version is 8.0 m in length, has a diameter of 0.67 m, carries a 200 kg payload, and has a launch weight of 2200 kg. Both versions have four clipped tip delta wings at mid-body, with four small delta control fins at the rear. The BrahMos carries either a 200 or 300 kg high explosive semi-armor-piercing warhead or a 250 kg submunitions warhead [1].

The formation of the company set an example for promotion in the world market through participation of several Indian industries in private and public sector. M/s Godrej was identified as one of the major players in view of its strong manufacturing base.

DRDO emphasized on indigenizing many techniques, in order to strengthen the testing base instead of relying on imported knowledge at high cost of foreign exchange. With this view, DRDO requested the Vibration Laboratory Section of BARC, to develop two technologies for testing the delta wing panels and fins and for testing bonding of BOKMY thermal insulation coating on the missile. There were no other inputs given except for oral explanation of what was seen by some of the DRDO scientists who visited Russia. The team worked from basics of vibration testing of wing panels provided by M/s Godrej and sample flat



panels coated with BOKMY. This paper gives highlights of milestones reached in perfecting the testing techniques.

Acoustic Topography Test for Quality of Brazed joints in the Wing Panels

Fig. 1 shows one view of the Brahmos missile. The four delta wings at mid-body and four small delta control fins on the rear can be seen. These are important parts of the guiding system to make the missile air worthy.



Fig. 1: Artistic View of the Missile

There are two types of wings and one type of fin. All are made of special titanium material. The two wings are named CB-130 and CB-180. Fig. 2 shows CB-130 wing panel.

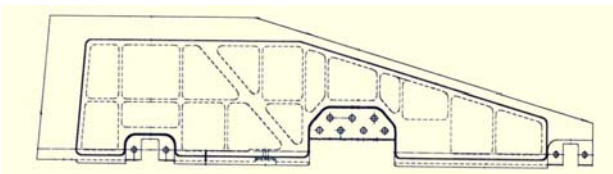


Fig. 2: Sketch of CB-130 wing panel

The panel has a special design. It is approximately 680 mm long, 180 mm wide and 22 mm thick. The dotted lines are boundaries of internal brazed joint not visible from above. Within the boundary, the area is hollow. The acoustic topography test was required to be carried out, to check the quality of the brazed joint.

The test involved spreading white powder on the surface and exciting the panel by a vibration shaker, so that the powder is displaced along the boundaries. The topography of formation of the powder gives visual impression of the brazed boundary. With this information, the team started working on finer details like

- Holding arrangement
- Frequency range of excitation
- Shaker parameters
- Selection of powder
- Density of spread of powder on the panel.

The biggest challenge was fixing the frequency range of excitation and connecting the shaker with the panel. More than 15 varieties of powders were tried. Fig. 3 shows the picture of initial trials when the results were far from acceptable.

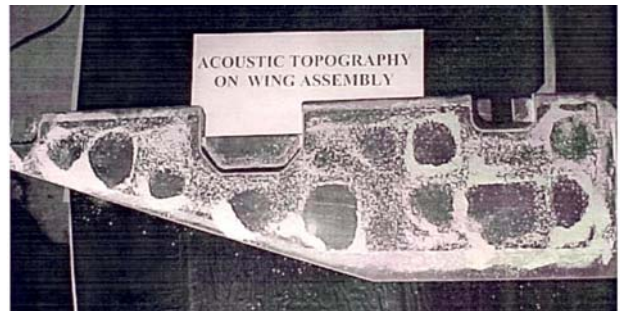


Fig. 3: Initial results of Acoustic Topography tests

For better results, piezoelectric shaker was directly clamped on the panel and excited between 45 to 100 KHz. The holding arrangement of the panel and clamping of the shaker to the panel is shown in Fig. 4.

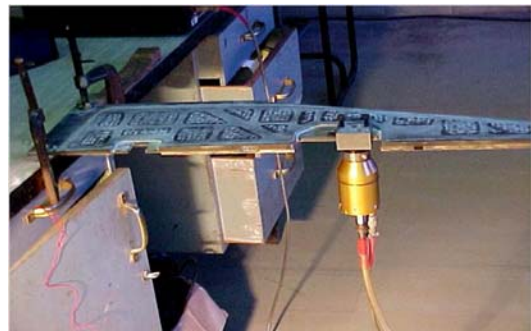


Fig. 4: Holding arrangement and attachment of shaker to the panel



Fig. 5 shows topography of the brazed boundary after the excitation. The deposit of powder on the boundaries clearly indicates formation of good brazed joint boundaries underneath.

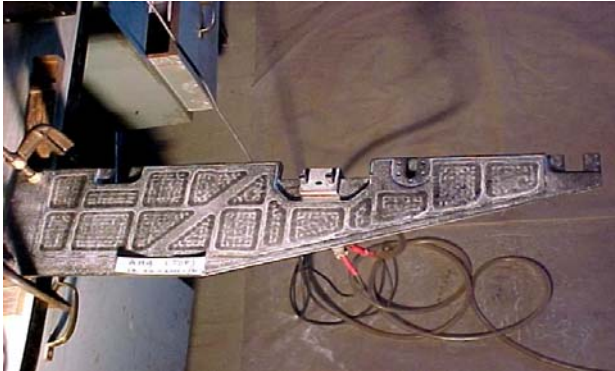


Fig. 5: Acoustic Topography of CB-130

After successful results of the test and approval of experts from Russia and DRDO, more than 150 panels and wings of production units were tested and certified in BARC. In view of increasing volume of work, the technology was transferred to Godrej on MoU with commercial and technical terms and conditions [2].

BOKMY testing

The F3 section of the missile is one of the important subsystems manufactured by Godrej. This section consists of an aluminum capsule, which acts as air intake for the engine. The high air intake results in high heat load on the capsule. In order to protect the capsule from the heat

load, it is covered with BOKMY coating. BOKMY is a rubber like material on the base of organo-silicon Indian rubber, glass micro spheres and fibrous additions. It is stuck on the aluminum capsule with a special sealant VIKSINT Y-10-28, applied uniformly on the outer surface of the capsule. As per the acceptance criteria, the quality of adhesion of BOKMY to the capsule needs to be checked by a non-destructive method. Good adhesion is a prerequisite for functional success of the subsection.

As the test was to be carried out from the rubber side, no well established NDT technique could be used. The team successfully tried vibration-based technique, to detect patches of poor bonding of BOKMY. Several test parameters were tried such as

- Rigid connection of piezoelectric shaker to the capsule
- Frequency range of excitation
- Selection of vibration sensor for measuring is response
- Spectrum Analysis.

Selecting the correct frequency range of excitation and distinguishing the discriminating feature in the frequency spectrum of the response of BOKMY, were the two important parameters for the success of testing. The test involved exciting the capsule in the range of 15 to 20 KHz and measuring the response of BOKMY with accelerometer. BOKMY responds to vibration depending on its bonding with the capsule. Fig. 6 shows comparison of frequency spectrum of BOKMY with good and bad bonding with the capsule.

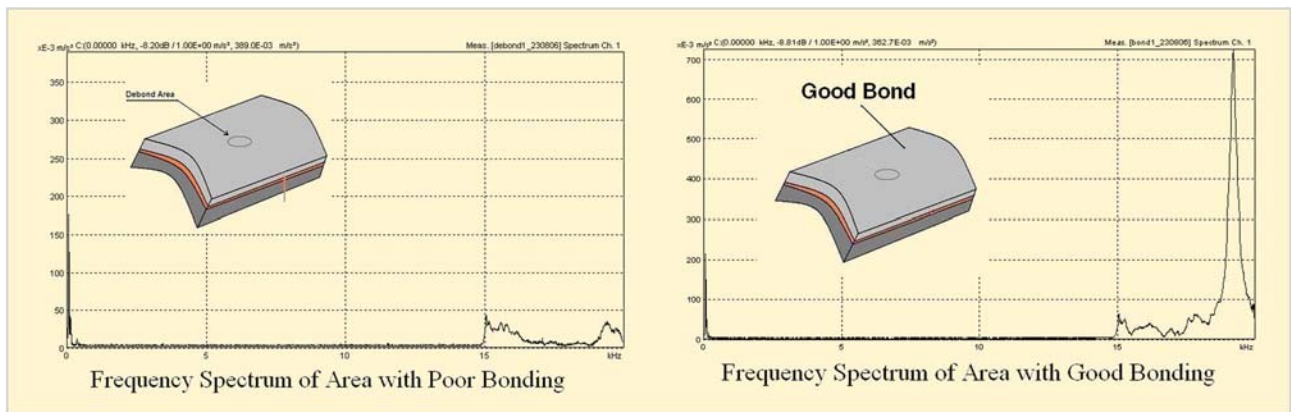


Fig. 6: Frequency Spectrum of BOKMY



It can be seen from the figure that BOKMY responds with higher amplitude around 20 KHz when the bond is good. The repeatability and accuracy of the technique was demonstrated to experts from Russia and DRDO. On request from DRDO and Godrej, BOKMY testing technology was also transferred to Godrej. Fig. 7 shows photograph of testing.

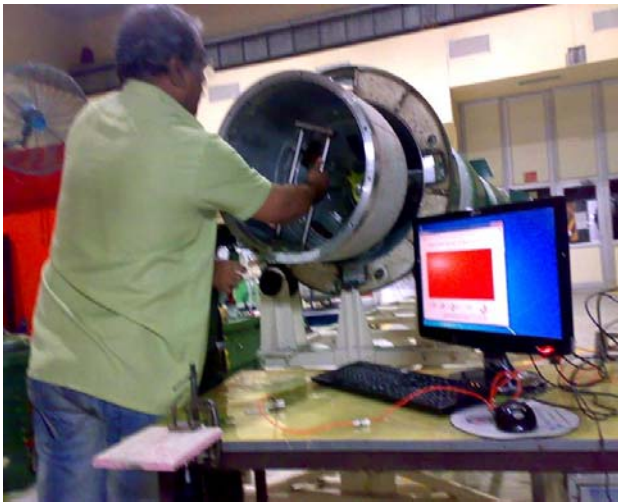


Fig. 7: BOKMY testing in progress

Conclusion

Two technologies were developed, implemented and inducted for testing the hardware developed for the DRDO project. Both are unique in characteristics and have nothing in common with machinery diagnostics. One was for testing the quality of brazed joints that are not visible on the surface of the hardware and the other was to check good bonding between two dissimilar materials. Both the technologies were based on rigorous vibration analysis of high frequency signals captured during testing. The repeatability and ease of operation are the highlights of the technologies.

Godrej invested in acquiring the hardware required for conducting both the tests. The team commissioned the test set up at Godrej and handed over to them. The commercial terms have been honored by Godrej.

This is a success story of developing innovative technology by BARC, on demand by the end user, for an important defence project of the country.

Acknowledgement

Authors would like to acknowledge the sustained moral support given by Dr. R.K. Sinha Director, BARC and Director RD&DG with a message to excel in this difficult field of vibration engineering and to deliver when demanded.

References

1. http://www.missilethreat.com/cruise/id.18/cruise_detail.asp
2. Technical Guidance for setting up test facility at Godrej for carrying out Acoustic Topography test on stabilising wings and panels and for testing quality of Bokmy coating on F3 section. MoU signed between BARC and Godrej May 2009.



Production of high specific activity ^{177}Lu and formulation of ^{177}Lu -DOTATATE for the treatment of neuroendocrine cancers

Sharmila Banerjee, Sudipta Chakraborty, Tapas Das, K.V. Vimalnath Nair,
Viju Chirayil and Archana Mukherjee
Radiopharmaceuticals Division

This paper received the DAE Group Achievement Award for the year 2009

Abstract

^{177}Lu has emerged as one of the highly useful radionuclide for the development targeted radiotherapy agents owing to its favorable nuclear decay characteristics, adequately long half-life and ease of its large-scale production with sufficiently high specific activity and excellent radionuclidic purity using medium flux research reactors. Extensive studies carried out in the Radiopharmaceuticals Division in the past ten years to optimize the production of ^{177}Lu with adequately high specific activity has resulted the commercial deployment of $^{177}\text{LuCl}_3$ suitable for various radiotherapeutic applications. On the other hand, research on development of ^{177}Lu -based radiotherapeutic agents has resulted in indigenous development of ^{177}Lu -DOTATATE, an agent presently being used in six nuclear medicine centers of our country for the treatment of patients suffering from malignancies of neuroendocrine origin.

Introduction

^{177}Lu is an attractive radionuclide for the development of targeted radiotherapeutic agents owing to its suitable nuclear decay characteristics [$E_{\beta(\text{max})}=0.49$ MeV, $E_{\gamma}=113$ keV (6.4%) and 208 keV (11%)], comparatively longer half-life [$T_{1/2}=6.65$ d] and ease of production with adequately high specific activity and excellent radionuclidic purity using the medium flux research reactors. [1]. The potential of ^{177}Lu in designing agents for therapeutic applications, more specifically targeted radiotherapy, was recognized as early as in 2000, in the Radiopharmaceuticals Division, BARC. Therefore, indigenous sourcing of this logistically ideal isotope in adequate quantities and specific activities became a necessity. Extensive studies have been carried out in the past ten years involving careful alterations

of various irradiation parameters such as, flux and duration of irradiation, enrichment of the target etc., for the production of ^{177}Lu with adequately high specific activity and radionuclidic purity. Using the present reactor facilities of our Institute, ^{177}Lu suitable for the preparation of various kinds of radiotherapeutic agents, is being routinely produced and regularly supplied to several nuclear medicine centers of our country since 2007. A direct outcome of the extensive research carried out in our Division on the production of ^{177}Lu has resulted the commercial deployment of the radionuclide through BRIT in 2011. On the other hand, efforts toward the development of ^{177}Lu -based radiotherapeutic agents has culminated in the indigenous formulation of ^{177}Lu -DOTATATE, an agent presently being used at different nuclear medicine centres across the country for the



treatment of inoperable malignancies of neuroendocrine origin.

Production of ^{177}Lu

^{177}Lu can be produced by two different routes, namely, by direct neutron activation of natural (^{176}Lu , 2.6%) or enriched (in ^{176}Lu) Lu_2O_3 target and also by indirect route involving the irradiation of enriched (in ^{176}Yb) Yb_2O_3 target followed by radiochemical separation of ^{177}Lu from Yb isotopes [2]. The above two production routes lead to the product having different specific activities. Although the specific activity obtained in conventional (n,γ) activation is usually low; owing to the high thermal neutron capture cross-section of ^{176}Lu ($\sigma = 2100$ b), direct neutron activation results in high specific activity of ^{177}Lu . In fact the cross-section of $^{176}\text{Lu}(n,\gamma)^{177}\text{Lu}$ is the highest encountered among all (n,γ) produced radionuclides presently used for therapy. Therefore, it is feasible to produce high specific activity ^{177}Lu suitable for developing agents for targeted radiotherapy applications by simple (n,γ) reaction using enriched ^{176}Lu as target in medium flux research reactors. However, a careful optimization of the time of irradiation is required in order to obtain the ^{177}Lu with maximum specific activity as there will be considerable target burn up owing to the high thermal neutron capture cross-section of ^{176}Lu . The ^{177}Lu activity produced at the end-of-bombardment (EOB) as a function of irradiation time at three different thermal neutron fluxes has shown in Fig. 1. It is evident from the figure, that depending on neutron flux, the activity of ^{177}Lu produced will be maximum after certain duration of irradiation, beyond which the activity will decrease owing to the high target burn up. Higher the thermal neutron flux of the reactor, shorter will be the time of irradiation for attaining maximum activity. Therefore, in order to obtain maximum specific activity using enriched ^{176}Lu target, the time of irradiation must be judiciously decided depending on the neutron flux available for the irradiation.

^{177}Lu is produced by irradiation of enriched (74% and 82% in ^{176}Lu) Lu_2O_3 target at a thermal neutron flux of

7×10^{13} – 1×10^{14} n/cm².s for a period of 21 d at the DHRUVA reactor. Following irradiation, the target is dissolved in suprapure 1 M HCl by gentle warming inside a lead-shielded plant. The resultant solution was evaporated to near-dryness and reconstituted in ultrapure water. The last step of the process was repeated twice. A maximum specific activity of ~ 1480 GBq/mg (40 Ci/mg) was achieved when irradiation was carried out with 82% enriched target at a thermal neutron flux of 1×10^{14} n/cm².s for 21 d. This corresponds to $\sim 36\%$ of the maximum achievable specific activity. The specific activity of ^{177}Lu obtained was significantly higher compared to the theoretically calculated value under the irradiation conditions employed (12.9 atom %), accounting for only thermal neutron capture. The observed difference could be partially accounted for by considering the contribution from epithermal neutrons (resonance integral=1087 b), which is not taken into account in theoretical calculations.

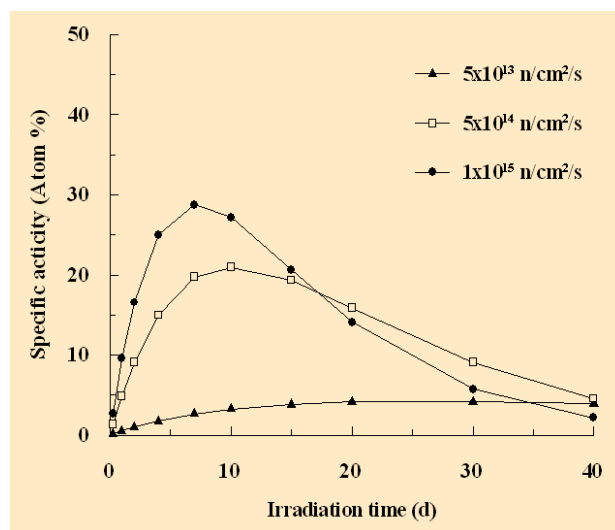


Fig. 1: Variation of ^{177}Lu specific activity with respect to duration of irradiation at different thermal neutron fluxes

The radionuclidic purity of ^{177}Lu could be determined by analyzing the gamma ray spectrum of radiochemically processed ^{177}Lu sample. The major gamma peaks observed are at 72, 113, 208, 250 and 321 keV, all of which correspond to the photopeaks of ^{177}Lu . The radionuclidic impurities that could be present in ^{177}Lu are $^{176\text{m}}\text{Lu}$, formed by $^{175}\text{Lu}(n,\gamma)^{176\text{m}}\text{Lu}$ ($\sigma=16.4$ b) and $^{177\text{m}}\text{Lu}$ produced via



$^{176}\text{Lu}(n,\gamma)^{177\text{m}}\text{Lu}$ ($\sigma = 7$ b). The presence of $^{176\text{m}}\text{Lu}$ ($T_{1/2} = 3.7$ h) can be eliminated by allowing 1 d cooling post-EOB. Therefore, $^{177\text{m}}\text{Lu}$ ($T_{1/2} = 160.5$ d) could be the only possible radionuclidic impurity present in ^{177}Lu . However, no peak corresponding to the photopeaks of $^{177\text{m}}\text{Lu}$ (128, 153, 228, 378, 414, 418 keV) could be visible in gamma ray spectra. This is expected as the radioactivity due to $^{177\text{m}}\text{Lu}$ produced will be insignificant and below the detectable limit on 21 d irradiation owing to its long half-life ($T_{1/2} = 160.5$ d) and comparatively low cross-section for its formation. The radionuclidic impurity burden due to the presence of $^{177\text{m}}\text{Lu}$ in ^{177}Lu could be determined by recording gamma ray spectrum of a sample aliquot after the complete decay of ^{177}Lu (8-10 half-lives of ^{177}Lu i.e. 55-70 days). The average level of radionuclidic impurity burden in ^{177}Lu due to $^{177\text{m}}\text{Lu}$ is reported to be ~ 5.5 kBq of $^{177\text{m}}\text{Lu}$ / 37 MBq of ^{177}Lu (~ 150 nCi / 1 mCi) at EOB, which indicates ^{177}Lu could be produced with 99.985% radiochemical purity using medium flux research reactors.

No carrier added (NCA) ^{177}Lu [theoretical specific activity 40.33×10^5 GBq/g (1.09×10^5 Ci/g)] can be produced following the indirect production route involving the neutron irradiation of enriched ^{176}Yb target followed by radiochemical separation of ^{177}Lu from the Yb isotopes. However, radiochemical separation of ^{177}Lu activity from irradiated Yb_2O_3 target is difficult owing to the similarity in the chemistry of the two adjacent members of the lanthanide series. Presence of Yb isotopes in ^{177}Lu will not only reduce the effective specific activity of the product but also interfere during the preparation of radiopharmaceuticals. Moreover, it can be shown by theoretical calculation that irradiation of 1 mg of 99% enriched (in ^{176}Yb) Yb_2O_3 target at a reasonably high thermal neutron flux of 5×10^{14} n/cm².s will produce only ~ 5.55 GBq (~ 150 mCi) of ^{177}Lu [1]. The use of enriched targets with low activation cross-section [$\sigma = 2.4$ b for $^{176}\text{Yb}(n,\gamma)^{177}\text{Yb}$] is not economical for isotope production, as a significant part of the target will be wasted.

^{177}Lu is being produced on a regular basis since the end of 2006 for carrying out clinical investigations of different

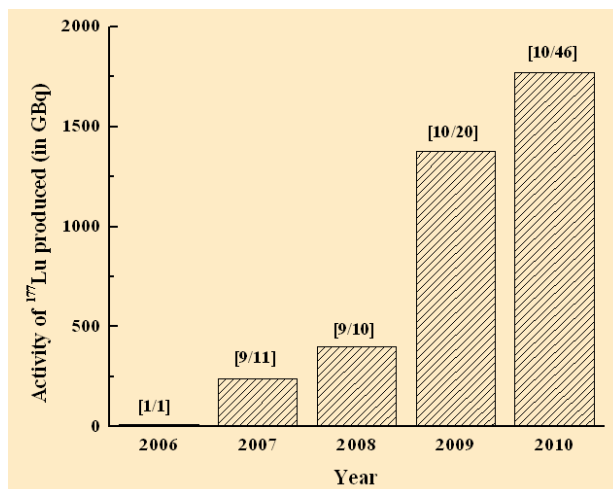


Fig. 2: Growth of ^{177}Lu production in India during 2006 to 2010

^{177}Lu -based radiochemical agents. Fig. 2 shows a graphical representation of the steady growth in the production and utilization of ^{177}Lu activity in India from 2006 to 2010. It is imperative from this representation that there is a substantial and steady growth in the use of ^{177}Lu in nuclear medicine. It is expected that with commercial supply and large-scale production, the utility of ^{177}Lu would be far more than experienced during these initial years of development.

Development of ^{177}Lu -DOTATATE for peptide Receptor Radionuclide Therapy (PRRT)

PRRT using radiolabeled somatostatin analogues is a novel therapeutic modality for treatment of somatostatin receptor-positive tumors. ^{177}Lu the promising radionuclide to develop new agents for PRRT which will be particularly useful for targeted therapy of smaller lesions owing to the small tissue penetration range of β^- particles of ^{177}Lu [3-4]. ^{177}Lu -labeled DOTATATE, where TATE is a somatostatin analog octapeptide, was envisaged as a promising agent for the treatment of patients suffering from inoperable tumors of neuroendocrine origin, over-expressing somatostatin receptors.

^{177}Lu -DOTATATE was prepared in the laboratory with high radiochemical purity ($>99\%$) following the optimized



protocol [3]. One of the challenges involved in carrying out targeted tumor therapy using ^{177}Lu -DOTATATE is the preparation of patient doses as the radiolabeled agent has to be prepared with adequately high specific activity so that sufficient activity can be deposited in the cancerous lesions without saturating the limited number of available receptors. As the specific activity of ^{177}Lu available at the time of preparation of the agent may vary considerably, it is crucial to optimize the labeling protocol, more importantly with respect to the amount of peptide, in order that it can be prepared with high radiochemical purity using minimum amount of DOTATATE. Therefore, an optimized protocol for the preparation of therapeutic dose (5.55-7.4 GBq, 150-200 mCi) with maximum achievable specific activity and stability was developed. As per the protocol developed, ^{177}Lu -DOTATATE, suitable for administration to the patients was prepared at the hospital radiopharmacies by adding the required volume of aqueous DOTATATE solution ($1\ \mu\text{g}/\mu\text{L}$ in de-ionized water) and $^{177}\text{LuCl}_3$ solution in 0.1 M ammonium acetate buffer (pH \sim 5) containing gentisic acid (40 mg/mL) such that DOTATATE:Lu molar ratio would be 4:1 [4]. Quick

quality control of ^{177}Lu -DOTATATE could be performed by paper chromatography using 50% acetonitrile in water as the eluting solvent. The extent of complexation can be subsequently determined with accuracy using HPLC [4]. More than 125 batches of ^{177}Lu -DOTATATE have been prepared following this protocol till date at six different nuclear medicine centers of India with a radiochemical purity of $>98\%$ and specific activity of 32.74-65.49 GBq/ μmol (885-1770 mCi/ μmol).

^{177}Lu -DOTATATE is presently being used to treat patients with neuroendocrine tumors in six major hospitals across India wherein therapeutic doses of ^{177}Lu -DOTATATE are prepared at the hospital radiopharmacies following the protocol developed. More than 150 patients suffering from various types of neuroendocrine originated tumors have been treated and more than 250 patient doses have been successfully dispensed to date. Fig. 3 shows the post-therapy scans (anterior and posterior) of patients with neuroendocrine originated primary cancer with extensive whole-body metastases and liver metastases, recorded at 1 d post-administration of 7.4 GBq (200 mCi)

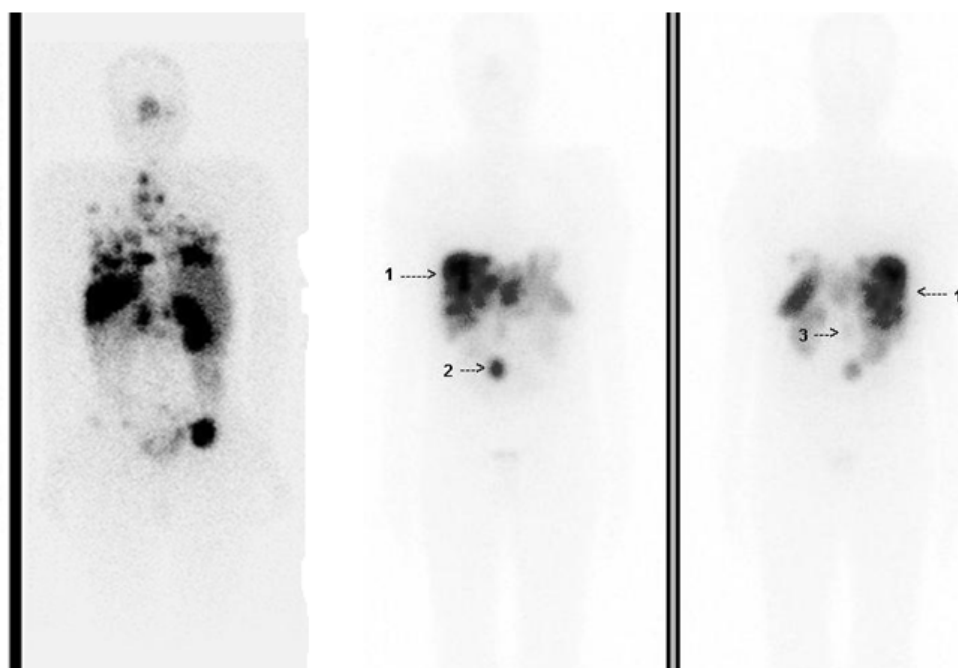


Fig. 3: Post-therapy scintigraphic images of patients with neuroendocrine tumors having extensive (a) whole-body metastases and (b) liver metastases, recorded at 24 h post-administration of 7.4 GBq (200 mCi) of ^{177}Lu -DOTATATE



of ^{177}Lu -DOTATATE. Ongoing clinical investigations carried out in our country, revealed symptomatic relief for majority of the patients who underwent ^{177}Lu -DOTATATE therapy.

Acknowledgements

The authors gratefully acknowledge previous Head of Radiopharmaceuticals Division BARC, Dr. Meera Venkatesh for her keen interest and encouragement. The guidance of Dr. M.R.A. Pillai, Head, Radiopharmaceuticals Division, right from initiating the program on development of ^{177}Lu based radiopharmaceuticals in India and bringing it to the present status is being gratefully acknowledged. The immense contribution of Dr. H.D. Sarma, Radiation Biology and Health Sciences Division, BARC for animal experimentation is gratefully acknowledged. The authors are thankful to Ex-Director, Radiochemistry and Isotope Group, Dr. V. Venugopal, for his constant support to the programme. The authors are thankful to the scientists and other staff members of Radiopharmaceuticals Division, for their valuable help and support in different capacities. The authors also gratefully acknowledge their clinical

collaborators for carrying out evaluation studies of ^{177}Lu -DOTATATE in human patients.

References

1. Pillai, M.R.A., Chakraborty, S., Das, T., Venkatesh, M., Ramamoorthi, N. Production logistics of ^{177}Lu for radionuclide therapy. *Applied Radiation and Isotopes* 59 (2003): 109-18.
2. Chakravarty, R., Das, T., Dash, A., Venkatesh, M. An electro-amalgamation approach to isolate no-carrier-added ^{177}Lu from neutron irradiated Yb for biomedical applications. *Nuclear Medicine and Biology* 37 (2010): 811-20.
3. Das, T., Chakraborty, S., Venkatesh, M., Banerjee, S. On the preparation of a therapeutic dose of ^{177}Lu labeled DOTATATE using indigenously produced ^{177}Lu in medium flux reactor. *Applied Radiation and Isotopes* 65 (2007): 301-8.
4. Das, T., Chakraborty, S., Kallur K.G., Venkatesh, M., Banerjee, S. Preparation of patient doses of ^{177}Lu -DOTATATE using indigenously produced ^{177}Lu : The Indian experience. *Cancer Biotherapy and Radiopharmaceuticals* 26 (2011): 395-400.



Cucurbituril-based Supramolecular Assemblies of Fluorescent Dyes: Their Prospective Applications

Jyotirmayee Mohanty

Radiation & Photochemistry Division

Dr. (Ms.) Jyotirmayee Mohanty was awarded the "APA Prize for Young Scientists-2010" at the Asian Photochemistry Conference (APC-2010) held at Victoria University, Wellington, New Zealand, during November 14-18, 2010.

Abstract

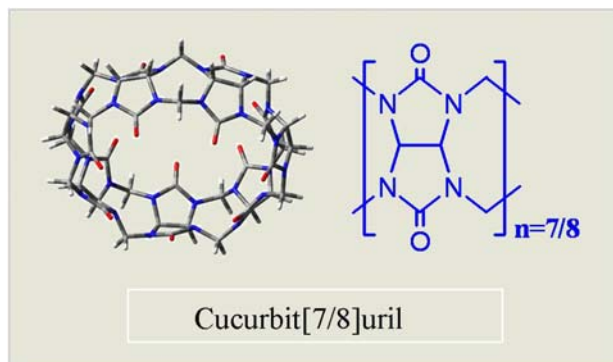
The molecular recognition behavior of versatile macrocyclic receptors, cucurbiturils (CBs) have been investigated, in relation to their host-guest interaction for organic chromophoric dyes, having technological and biological importance. Enhanced photostability of rhodamine dyes on their binding to cucurbit[7]uril (CB7) host have been applied successfully, to demonstrate the operation of highly efficient "supramolecular-based aqueous dye laser systems". These systems are environmentally more benign and more laboratory-safe as compared to the dye lasers based on organic solvents. For amyloid fibril diagnostic dye thioflavin T (ThT), its binding to CB7 and cucurbit[8]uril (CB8), leads to the formation of multiple inclusion complexes with a number of intriguing properties. Exploiting the effect of external stimuli on the non-covalent interaction between CB and ThT, we have illustrated the formation of novel *fluorescent molecular capsules* through cooperative metal ion binding to the 2:1 complex of CB7-ThT system and *on-off* fluorescence responses through the controlled dissociation of 2:2 complex to 1:2 assembly for CB8-ThT system in the presence of metal ions.

Key Words: Host-guest interaction, cucurbiturils, supramolecular-based aqueous dye laser, supramolecular assembly, fluorescence

Introduction

Encapsulation of guests through macrocyclic hosts, offers a convenient pathway for modulation of molecular properties, as it can introduce pronounced effects on, as well as fine-tune the physico-chemical properties of the included guest. Host-guest interaction finds immense importance in photostability, drug delivery, catalysis, and sensor applications. Cucurbiturils (CBs), the homologues of an interesting class of water soluble macrocyclic receptors, are composed of glycoluril units, coupled in a cyclic manner by pairs of methylene bridges.^{1,2} Structurally, the pumpkin-shaped CBs constitute highly symmetrical hydro-phobic cages of low polarity and polarizability with

two identical dipolar portal ends, composed of carbonyl functional groups. As a macrocyclic host, CBs have attracted considerable attention in recent years owing to their excellent physico-chemical properties and binding





abilities for a variety of guests. Among different CBs, the homologue cucurbit[7]uril (CB7, with 7 glycoluril units) forms stable inclusion complexes with many guest molecules, like organic dyes, protonated alkyl and aryl amines and cationic dyes, via a combination of hydrophobic and ion-dipole interactions.¹⁻³ The higher homologue cucurbit[8]uril (CB8), having a larger cavity size, can accommodate more than one guest molecules, to form 1:2 host-guest complexes or 1:1:1 ternary complexes with had many future prospects in various applications. Since the binding interactions in the host-guest systems are mainly non-covalent in nature, it is convenient to tune them by external stimuli like competitive binders, pH, temperature, light, redox control, etc. In this article, the supramolecular interactions of CB7 and CB8 hosts with the technologically important rhodamine dyes and biologically important thioflavin T dye, have been described in relation to the modulation of the guest properties, metal ion-induced tunability and their utilization for possible applications.

Supramolecular-based aqueous dye laser systems

Rh6G in ethanol is widely and traditionally used in tunable dye lasers, due to its very high fluorescence quantum yield ($\phi_f = 0.95$), significant photostability and large extinction coefficient. Such laser operation for Rh6G in aqueous solution is not realizable, because laser operation requires very high dye concentrations (>0.1 mM), at which significant amount of the dye exists as aggregates ($\sim 60\%$) and, therefore, not show strong fluorescence. Since CB7 prevents the aggregation and increases the photostability of Rh6G,³ the aqueous Rh6G-CB7 system offered a dye laser medium, which has been attempted successfully in our study. The effect of CB7 on the performance of aqueous Rh6G solution has been investigated in a broad-band dye laser set-up with respect to the practically relevant parameters like lasing efficiency, lasing stability, and beam quality. Large increase in lasing efficiency has been observed, predominantly due to the deaggregating action of CB7 on the dye. Thus the addition of millimolar concentration of CB7, to the aqueous solution of Rh6G

dye, makes it possible to develop "supramolecular-based aqueous dye laser system".⁴ For CB7•Rh6G system, however, the operation of a narrow-band aqueous dye laser system was unfortunately limited, due to the requirement of significantly high concentrations of CB7 and its associated cost as well as the sensitivity of the lasing efficiency of this system, towards minor but unknown impurities in the CB7 samples. Recent studies with two other important laser dyes, Rhodamine B (RhB) and sulforhodamine B (Kiton Red S; KRS), the use of which had previously been restricted to alcoholic lasing media, proved promising in aqueous solution in the presence of CB7. Since they form very strong inclusion complexes with CB7 with high binding constants ($K > 10^5$ M⁻¹)⁵ as compared to that of Rh6G ($K > 10^4$ M⁻¹),³ the dyes RhB and KRS require a 30-times lesser amount of CB7 stabilizer (200 μ M) than the previously tested CB7•Rh6G system. Moreover and unlike the case of Rh6G, the CB7•RhB and CB7•KRS lasing media are found to be insensitive towards minor impurities in the CB7 sample, e.g., both home-

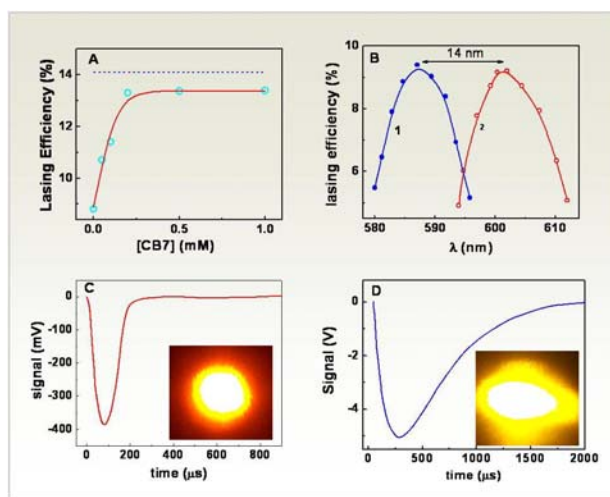


Fig. 1: (A) Dependence of the lasing efficiency of KRS (200 μ M) on CB7 concentration. Shown for comparison (dashed line) is the lasing efficiencies of KRS in optically matched ethanol solutions. (B) Tuning curves of KRS in EtOH (1) and in the presence of 200 μ M CB7 (2) at a pump energy of 6.3 mJ. Thermal deflection signals of KRS in water-CB7 (C) and in EtOH (D) systems. Insets of C and D show the laser beam profiles for the respective medium.



made and commercial CB7 samples afforded similar results which paves the way for their large scale use in the efficient as well as robust aqueous dye laser systems.^{2,5} The resulting dye lasers are environmentally more benign, more laboratory-safe, and less maintenance-sensitive than the presently employed dye laser systems based on organic solvents. The novel aqueous dye-CB7 systems are not only equally efficient with complementary tuning ranges, but also possess superior thermo-optic characteristics and unmatched beam profiles (Fig. 1), which should jointly enable new and revived photonic applications based on such dye lasers. The transferability of this supramolecular approach to UV dye lasers, which have been long sought after for use in replacing the operationally very vulnerable excimer and gas laser systems, is presently under investigation. At the other end, the method could also be applied to aqueous IR dye lasers, which are of great importance in biological and medical applications.

Fluorescent supramolecular capsule formation and potential uses

Thioflavin T (ThT) is a benzthiazolium dye, that has been extensively used in the early detection of amyloid fibril formation in tissues, to diagnose chronic disorders such as Alzheimer's and Parkinson's diseases.⁶ Detection is mainly based on the characteristic fluorescence of ThT ($\phi_f = 0.0003$) at 490 nm which increases dramatically (~ 1000 fold) upon binding to the cavities of the amyloid fibrils. Steady-state and time-resolved fluorescence studies illustrate significant enhancements/modifications in the fluorescence yield (40-fold), lifetime and spectral features of ThT on interaction with CB7 and has been assigned to the formation of 1:1 and 2:1 complexes between CB7 and ThT, leading to specific structural arrangements.^{2,6,7} As CBs act as like cation receptors, the effect of metal ions on the characteristics of CB7•ThT molecular assemblies, has also been investigated. Addition of metal cations to the 1:1 CB7•ThT complex displays expected competitive binding interactions with CB7, leading to decrease in the fluorescence intensity from ThT. However, addition of metal ions to the 2:1 (CB7)₂•ThT complex, leads to unusual enhancement in fluorescence emission

(~ 270 fold in the presence of Ca²⁺ and ~ 160 fold in the presence of Na⁺).^{2,7,8} These contrasting observations on the fluorescence enhancement for the stoichiometrically different CB7•ThT complexes, have been investigated explicitly for a feasible binding model. A detailed photophysical characterization with supporting data from NMR and anisotropy measurements, has led to the revelation of a novel stimulus responsive cooperative metal ion, binding to the stoichiometrically selected (CB7)₂•ThT complex, demonstrating a highly fluorescent supramolecular nanocapsule formation, as shown in Fig. 2.^{2,7,8} For the release mechanism of ThT from the novel supramolecular capsule, rupture of the capsular complex has been attempted with a strong competitive guest adamantly amine, which helped in disrupting the capsule to release the dye from the complex as shown in Fig. 2.^{2,7,8} The feasibility of a capsular molecular assembly formation and its rupture as in Fig. 2, is expected to have remarkable implications in targeted drug delivery, removal of toxins, on-off systems and with a potential as building blocks for tailor-made functional materials and molecular architectures, displaying unique properties.

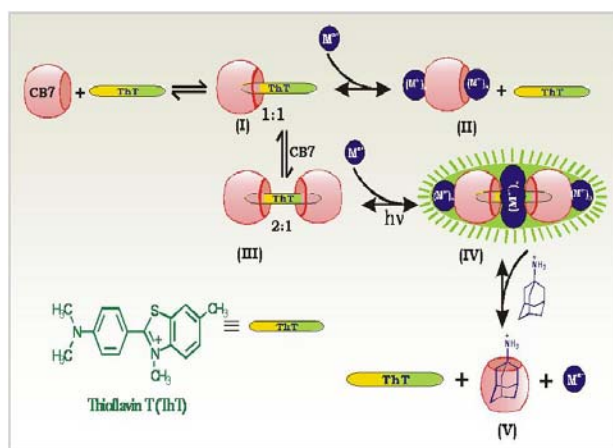


Fig. 2: Proposed scheme for the formation of highly fluorescent supramolecular capsule (IV) and its rupture by adamantly amine as the stimulant.

Supramolecular fluorescence on-off responses and their implications

The cucurbit[8]uril, having the larger cavity size, can co-host and stabilize two ThT molecules in a single CB8



cavity, as observed in other CB8-dye systems. On introducing CB8 to a dilute aqueous solution of ThT, significant spectral changes have been observed.^{2,7,9} Unlike CB7, with increase in CB8 concentration about 2 μ M, the absorption band of ThT shifted from 412 nm towards 445 nm with a well-defined isosbestic point at 428 nm. Surprisingly, on further addition of CB8, the absorption peak retracted to 415 nm with another isosbestic point at 426 nm and the final spectrum evolved, remained markedly different from the spectrum of ThT alone. Interestingly, the fluorescence of ThT in the presence of CB8 displayed striking features, a dual emission, with a distinct evolution of a hitherto unexplored intense emission band, having maximum at 570 nm which is assigned to the ThT excimer band. The modulations in the absorption and emission characteristics have been attributed to a π -stacked ThT excimer, co-localized in the CB8 cavity in a 1:2 (CB8•ThT) stoichiometry, which subsequently transforms into a 2:2 complex at higher concentration of CB8. After establishing the 2:2 binding for the CB8•ThT interaction with an intense fluorescence 'turn on' at 570 nm, we have attempted to make the system 'turn off' by engaging the CB8 portals through a competitive binder, i.e. Ca^{2+} ions. Gradual addition of Ca^{2+} ions decreases the emission intensity with concurrent changes in the absorption spectrum in the reverse order, achieving the dissociation of the 2:2 complex.^{2,7,9} This Ca^{2+} induced

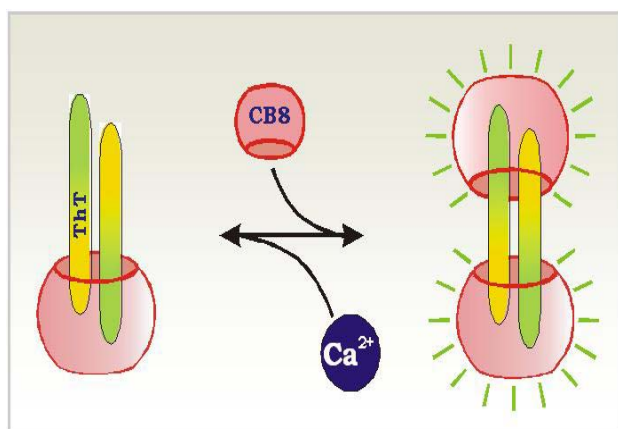


Fig. 3: Schematic representation of a 2:2 CB8•ThT assembly formation and dissociation, demonstrating the on/off mechanism.

control over the complexation equilibrium and excimer emission is projected as an on/off mechanism, as illustrated in Fig.3. The CB8-ThT host-guest assembly exemplified here, finds direct relevance to set fluorescence off/on sensors, stoichiometry controlled reactivity and provides lead information for tailor-made molecular architectures.

Acknowledgements

I acknowledge all my collaborators and co-authors of our published work. My special thanks to Dr. S. K. Sarkar, Head, RPCD and Dr. T. Mukherjee, Director, Chemistry group, BARC for their constant encouragement and support.

References

1. Lee, J. W., Samal, S., Selvapalam, N., Kim, H.-J., Kim, K. *Acc. Chem. Res.* 36, (2003): 621-630.
2. Bhasikuttan, A. C., Pal, H., Mohanty, J. *Chem. Commun. (Feature Article)* 47, (2011): p.9959-9971.
3. Mohanty, J., Nau, W. M. *Angew. Chem. Int. Ed.* 44, (2005): 3750-3754.
4. Mohanty, J., Pal, H., Ray, A. K., Kumar, S., Nau, W. M. *ChemPhysChem*, 8, (2007), 54-56.
5. Mohanty, J., Jagtap, K., Ray, A. K., Nau, W. M., Pal, H. *ChemPhysChem*, 11, (2010), 3333-3338.
6. Dutta Choudhury, S., Mohanty, J., Upadhyaya, H. P., Bhasikuttan, A. C., Pal, H. *J. Phys. Chem. B*, (2009): 1891-1898.
7. Bhasikuttan, A. C., Dutta Choudhury, S., Pal, H., Mohanty, J. *Isr. J. Chem. (Review Article)*, (2011): 634-645.
8. Dutta Choudhury, S., Mohanty, J., Pal, H., Bhasikuttan, A. C. *J. Am. Chem. Soc.*, (2010): 1395-1401.
9. Mohanty, J., Dutta Choudhury, S., Upadhyaya, H. P., Bhasikuttan, A. C., Pal, H. *Chem. Eur. J.*, (2009): 12362-12370.



Redox modulatory activities of dimethoxycurcumin, a synthetic analogue of curcumin

Amit Kunwar and K. Indira Priyadarsini
Radiation & Photochemistry Division

This paper received the Lester Pecker Young Investigator Award at the 5th International Niigata Symposium on Diet & Health held at Niigata, Japan, during October 29-31, 2010

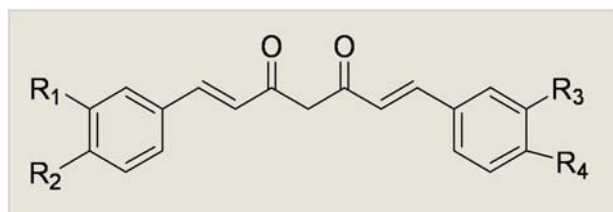
Abstract

To understand the anti-tumor activity of dimethoxycurcumin (Dimc), an analogue of curcumin, the redox modulatory activities have been examined and compared with those of curcumin. Reactions with reactive oxygen species (ROS), indicated Dimc to be as efficient as curcumin in scavenging superoxide radicals, while its reaction with peroxy radicals being much slower. These results were also supported by the observations on the scavenging of basal ROS levels in lymphocytes and *in vitro* antioxidant studies. Like curcumin, Dimc was a pro-oxidant and generated ROS in tumor cells. Accordingly, the compounds were non-toxic to lymphocytes, while exhibiting comparable cytotoxicity to tumor cells. Additionally, both curcumin and Dimc showed selective higher uptake in tumor cells than in normal lymphocytes.

Introduction

Curcumin, the major pigment from turmeric has been extensively researched for a wide variety of medicinal properties including antioxidant, anticancer, and anti-inflammatory activities [1]. New synthetic and natural analogues of curcumin are being explored for better metabolic stability and increased biological activity [2]. Among several analogues, dimethoxycurcumin (Dimc), a methoxylated derivative of curcumin, (Structure given in Scheme 1) showed superior anti-tumor activity and more metabolic stability over curcumin [3].

Although not fully established, it is proposed that the stability and pro-oxidant nature of Dimc could play a major role in its anti-tumor activity [3,4]. In order to understand the role of redox modulatory properties in anti-tumor activity, we compared the results on antioxidant and pro-oxidant effects of Dimc with those of curcumin under similar treatment conditions.



Scheme 1

Curcumin; $R_1=R_3=OCH_3$, $R_2=R_4=OH$
Dimethoxy curcumin (Dimc); $R_1=R_2=R_3=R_4=OCH_3$

Results

Differential antioxidant activity

Using pulse radiolysis technique, the rate constants for the reaction of curcumin with peroxy radicals such as lipid peroxy and trichloromethyl peroxy radicals, was estimated to be $7.3 \times 10^5 \text{ M}^{-1}\text{s}^{-1}$ and $1.5 \times 10^8 \text{ M}^{-1}\text{s}^{-1}$ respectively [5]. Reactions of above radicals with curcumin produced phenoxyl radicals, which could be regenerated back to curcumin by water-soluble antioxidants like



ascorbic acid. Similar studies on reactions of peroxy radicals with Dimc have also been attempted. However, due to the absence of the phenolic OH group, this reaction kinetics with Dimc was much slower and no intermediate phenoxyl radicals could be identified during such reactions. This observation confirmed, that the phenolic-OH is essential, and the central CH₂ group of the β-diketone moiety is not involved in the peroxy radical scavenging reactions [5]. Cyclic voltammetric studies of curcumin and Dimc in methanol indicated that, under identical experimental conditions, the peak potential for the oxidation of curcumin is ~150 mV less than that of Dimc. This suggested that the phenolic OH group is not only responsible for the reducing power but also the peroxy radical scavenging of curcumin [5]. Although Dimc is less efficient than curcumin in reacting with peroxy radicals, it is as efficient a scavenger of O₂^{•-} radicals as curcumin [6], indicating the involvement of the diketo group of curcumin or Dimc. The bimolecular rate constants for the reaction of O₂^{•-} radical with curcumin and Dimc were estimated to be 1.0 x 10⁵ M⁻¹s⁻¹ and 0.8 x 10⁵ M⁻¹s⁻¹ respectively [6]. Further, when curcumin and Dimc were checked for their ability to prevent the ROS induced lipid peroxidation in liposomal model system, curcumin was three to four times more effective than Dimc [5]. In line with these results, both curcumin and Dimc significantly reduced the basal levels of intracellular ROS in lymphocytes; however, curcumin was more effective than Dimc. All these studies portray that curcumin is a better antioxidant than Dimc under *in vitro* models.

Differential pro-oxidant activity

Extensive research in the last decade has indicated that, Curcumin exhibits pro-oxidant activity depending on the cell type through ROS production and alteration of the cellular redox homeostasis (e.g., depletion of GSH). Our group investigated the pro-oxidant activity of Dimc in human breast carcinoma, MCF7 cells as measured in terms of changes in cellular basal levels of ROS and GSH. The results on dihydroethidium (DHE) stained MCF7 cells, treated with Dimc for 2 h revealed that, it significantly elevated the basal ROS levels. Further, treatment with Dimc

also showed a dose (5-50 μM) dependent decrease of GSH/GSSH at 2 h, followed by an increase of this ratio at 6 h as estimated by change in the fluorescence of o-phthalaldehyde, which is a selective binder of free thiols. Comparing these results with another study by Shang et al [7] on curcumin modulating intracellular levels of ROS and GSH in MCF7 cells under similar treatment conditions suggested that, pro-oxidant effects of curcumin and Dimc are comparable.

Differential cytotoxicity in MCF7 cells vs. spleen lymphocytes

The pro-oxidative behaviour of curcumin and Dimc could be correlated with cytotoxicity. Therefore, we determined the relative cytotoxicity of Dimc and curcumin in two different cell types, MCF7 cells and normal splenic lymphocytes. The cell viability was monitored by both 3-4,5-dimethylthiazol-2-yl-2,5-diphenyl-tetrazolium bromide (MTT) assay and also by popidium iodide (PI)-staining assay. The results indicated that there was an increase in the cytotoxicity in both cell types with increasing concentrations of curcumin or Dimc treatment and both of them displayed similar cytotoxicity in MCF7 cells, however, Dimc was less toxic than curcumin in splenic lymphocytes.

Differential uptake in MCF7 cells vs. spleen lymphocytes

The cytotoxicity of any agent would be primarily governed by intracellular availability. Earlier we had reported, that the MCF7 cells selectively take up more curcumin than normal cells like lymphocytes [8,9]. Similar attempt was made to quantitatively estimate the uptake of Dimc in splenic lymphocytes and MCF7 cells. The results showed that the uptake levels of Dimc and curcumin were comparable in both the cells. MCF7 cells showed nearly two times more uptake than lymphocytes, for both curcumin and Dimc [10].

Conclusions

New improved analogues of curcumin are necessary to overcome the limited bioavailability and bio-stability problem of curcumin. Dimc, is more stable towards



hydrolysis and chemical oxidation than curcumin. This attracted many researchers to test its biological activity in different model systems. The results so far indicated that the pro-oxidant activity of Dimc is comparable to that of curcumin, while its antioxidant activity is much lower than that of curcumin. Since an ideal anti-cancer agent acts as an inhibitor of oxidative stress (antioxidant) in normal cells while acting as its inducer (pro-oxidant) in tumor cells, Dimc has the potential to be developed as an effective anti-tumor agent.

References

1. Aggarwal BB, Sundaram C, Malani N et al. Curcumin: the Indian Solid Gold. In *The Molecular Targets and Therapeutic Uses of Curcumin in Health and Disease*. Springer, New York, USA, 2007; p 1-76.
2. Anand P, Thomas SG, Kunnumakkara AB et al. Biological activities of curcumin and its analogues (Congeners) made by man and Mother Nature. *Biochem Pharmacol* 2008;76:1590–1611.
3. Tamvakopoulos C, Dimas K, Sofianos ZD et al. Metabolism and anticancer activity of the curcumin analogue, dimethoxycurcumin. *Clin Cancer Res* 2007;13:1269-1277.
4. Lee JW, Hong HM, Kwon DD et al. Dimethoxycurcumin, a structural analogue of curcumin, induces apoptosis in human renal carcinoma caki cells through the production of reactive oxygen species, the release of cytochrome C, and the activation of caspase-3. *Korean J Urol* 2010;51:870-878.
5. Priyadarsini KI, Maity DK, Naik GH et al. Role of phenolic O-H and methylene hydrogen on the free radical reactions and antioxidant activity of curcumin. *Free Radic Biol Med* 2003;35:475-484.
6. Singh U, Barik A, Singh BG et al. Reactions of reactive oxygen species (ROS) with curcumin analogues: Structure-activity relationship. *Free Radic Res* 2011;45:317-325.
7. Syng-Ai C, Kumari AL, Khar A. Effect of curcumin on normal and tumor cells: role of glutathione and bcl-2. *Mol Cancer Ther* 2004;3:1101-1108.
8. Kunwar A, Barik A, Mishra B et al. Quantitative cellular uptake, localization and cytotoxicity of curcumin in normal and tumor cells. *Biochim Biophys Acta* 2008;1780:673-679.
9. Kunwar A, Barik A, Pandey R et al. Transport of liposomal and albumin loaded curcumin to living cells: an absorption and fluorescence spectroscopic study. *Biochim Biophys Acta* 2006;1760:1513-1520.
10. Kunwar A, Barik A, Sandur SK et al. Differential antioxidant/pro-oxidant activity of dimethoxycurcumin, a synthetic analogue of curcumin. *Free Radic Res* 2011;45:959-965.



Autoclave Leaching of Refractory Uranium Minerals

**T. Sreenivas, K. Anand Rao, M. Manmadha Rao, K.C. Rajan, Md. Serajuddin,
P. Karthikayini and N.P.H. Padmanabhan**
Mineral Processing Division

This paper received the MISRA award for Best Paper in Hydro, Electro and Bio metallurgy Category instituted by the Indian Institute of Mineral Engineers, at the International Seminar on Mineral Processing Technology, held at Jamshedpur during Dec. 2010

Abstract

Autoclave circuits have been proven as reliable unit operations in hydrometallurgy, for treating refractory ores - either physical or chemical type. They yield high leach efficiency and produce stabilized leach residues, which are environmentally least harmful. Sustained R & D efforts in BARC have resulted in successful use of autoclave reactors, for the dissolution of refractory uranium minerals (viz. davidite, betafite, liandratite) and ores with extremely fine dissemination of uranium phases. This paper gives an overview of the studies.

Keywords: Uranium, Leaching, Autoclave, Pressure, Mineral processing.

Introduction

There are approximately 205 species of uranium minerals, occurring in 14 types of uranium deposits [1,2]. Uranium minerals can be grouped into various chemical categories such as oxides (uraninite, pitchblende), hydrated oxides (becquerelite, gummite), Nb-Ta-Ti complex oxides (brannerite, davidite), silicates (coffinite, uranophane, uranothorite), phosphates (autunite, torbernite), vanadates (carnotite, tyuyamunite) and hydrocarbons (thucholite, asphaltite). Simple oxide minerals like uraninite and pitchblende are relatively easily leachable, while the rest of them are not so leachable. Depending upon the ease of dissolution / leachability, the uranium minerals are categorized as (a) slightly refractory (oxidation is required prior to leaching e.g. coffinite & uranothorite), (b) moderately refractory (requires higher leach temperatures, greater free acid and oxidant concentration and longer leach periods (e.g. brannerite, thucholite & davidite); and (c) highly refractory (requires extreme leach conditions

e.g. betafite & pyrochlore). In addition to the chemical refractory nature of some of the uranium minerals, there exists certain uranium ores which inspite of having simple uranium oxide phases, yield low leach recovery due to the physical nature of occurrence of uranium in them. To this category, belong ores having uranium mineralization in very-fine to ultra-fine sizes, either in discrete form and/or as disseminations in various gangue minerals. These ores too demand rigorous leaching conditions for quantitative dissolution, which could be elevated temperature and pressure, finer grind, higher oxidation potential, higher leachant dosage, longer contact time etc.

Autoclave circuits have been proven as reliable unit processes, in maximizing the leachability of valuable minerals, which are not only chemically refractory in nature but also those ores which have the required minerals, in physically refractory form. Besides increasing the leach efficiencies and kinetics, the autoclave reactors also give



Table 1: Uranium plants with acid or alkaline pressure leach technology [4, 5].

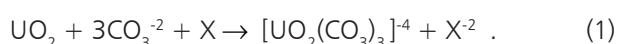
Plant Details and Year of commencement		Type of leaching
Eldorado Nuclear Ltd., Beaverlodge Mill, Uranium City,	1953	Alkaline
SaskatchewanAtlas Corp., Minerals Division, Moab Utah	1956	Alkaline
United Nuclear-Homestake, Partners, Grants New Mexico	1958	Acid
Cotter Corporation	1970	Alkaline
Canon City Colorado	1980	Acid
Lodeva Mill, France	1980	Alkaline
Rio Algom Corp., Lisbon Mill, Moab Utah	1980	Alkaline
Key Lake Mining Corp., Key Lake, Saskatchewan	1972	Acid
COGEMA Resources Inc., McClean Lake, Saskatchewan	1983	Acid
Uranium One Inc. Dominion Reefs Mill, S Africa	2008	Acid

stabilized leach residues, which can be safely disposed [3]. The use of autoclaves in uranium industry was in vogue since early 1950's [4,5]. Table 1 gives details of some prominent uranium mills using this technology. In the earlier days pressure leach technology was justified for only high grade uranium ores, due to its cost-intensive nature. However, increasing demand for uranium, upward trend in uranium metal price and growing environmental awareness, triggered the use of pressure leaching technology, even for low and medium grade uranium ore deposits. The technology is also being adopted by installations processing uranium bearing mine dumps or waste [6]. Uranium ore processing mills use either Pressure OXidizing autoclaves (POX) or HIgh Pressure Acid leach autoclave technology (HiPAL) depending upon the mineralogical characteristics of the ore, type of leaching followed – acid or alkaline, and on the type of oxidant as well as the level of oxidizing environment, necessary during the leaching reaction [4,5]. Similarly different types of autoclaves – vertical or cigar type/horizontal or in some cases, pipe autoclave reactors were investigated, for their suitability in uranium leaching application [4,7]. This paper discusses the recent R & D and pilot-plant scale studies, carried out in our Division, on the utility of autoclave reactors in processing various refractory uranium ores. An outcome of these studies is

the establishment of India's first uranium mill with alkaline pressure leach technology at Tummalapalle in Andhra Pradesh.

Leaching Chemistry of Uranium Minerals

The common oxidation states of uranium, in its minerals like uraninite, pitchblende, coffinite and numerous others, are +4 and +6. Amongst the two oxidation states, U⁺⁶ is soluble in aqueous media under suitable E_H – pH conditions, while U⁺⁴ is practically insoluble. The uranium minerals occurring in various ore deposits consist predominantly of uranous ion (U⁺⁴), necessitating the use of an oxidant and other lixiviants, for quantitative dissolution during leaching. The type of leaching - acid or alkaline mode depends upon the host rock. Sulfuric acid is the common leachant in acid leaching process, while Na₂CO₃ - NaHCO₃, (NH₄)₂CO₃ and NH₄HCO₃ are the widely used lixiviants in alkaline leaching of uranium ores. The oxidant reagents could be either chemical or gaseous in nature. A typical chemical reaction in alkaline leaching of UO₂ with carbonate ions and oxidant (X) is given in Equation 1, a similar equation can be written for the sulfuric acid leaching process.





Case Studies

Oxidative pressure leaching of uranium from a dolomitic limestone ore

India has a medium-tonnage, low-grade uranium ore deposit of siliceous dolomitic phosphatic limestone type, in Kadapa district of Andhra Pradesh. Detailed exploration carried out in a stretch of about 9 km in this area, established a resource of 29000 t of U_3O_8 with a cut-off grade of 0.025% U_3O_8 [8]. Mineralogical studies on an exploratory mine ore sample from this area, indicated the occurrence of uranium values predominantly as ultra-fine dissemination, in lighter gangue minerals (specific gravity less than 3.2). It also occurs, albeit to a minor extent, in the form of ultra-fine pitchblende in association with pyrite, as disseminations in collophane-rich parts, coffinite and as U-Ti complex. Carbonate minerals constitute the major gangue present in the form of dolostone (~80%). Siliceous minerals in the ore are quartz, feldspar and chlorite (13%). Collophane (4%) is the only phosphate bearing phase. Pyrite is the predominant sulphide ore mineral, along with few grains of chalcopryrite and galena. The iron bearing oxides are magnetite, ilmenite and goethite. Heavy media separation of various closely-sized feed fractions, using bromoform (BR) and methylene iodide (MI) liquids, have indicated that about 91% of the uranium values are present in lighter minerals (specific gravity <3.2) (Fig. 1), as ultra-fine disseminations. The remaining 9% of uranium values reported in methylene iodide heavy

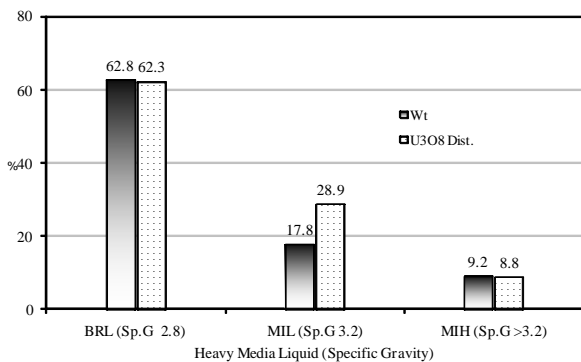


Fig. 1: Distribution of mass and uranium values of a dolomitic limestone ore, Kadapa district (A.P.) in various heavy media fractions

fraction, are accounted by discrete pitchblende, which is mostly associated with pyrite and collophane. Pitchblende occurring with pyrite is present as fine orbicular cluster, separated by thin disconnected rims of pyrite or as garlands around pyrite.

Atmospheric alkaline leaching studies, carried out on this ore sample, by varying important process parameters like mesh-of-grind, temperature, contact time, dosages of leachants - sodium carbonate and sodium bicarbonate, solids concentration and type of oxidant, gave a maximum U_3O_8 leachability of 65% (Fig. 2). Studies with other oxidants like NaOCl, Cu-NH₃, oxygen and air gave poor leachability in comparison to $KMnO_4$, emphasizing the need for strong oxidizing conditions during the dissolution

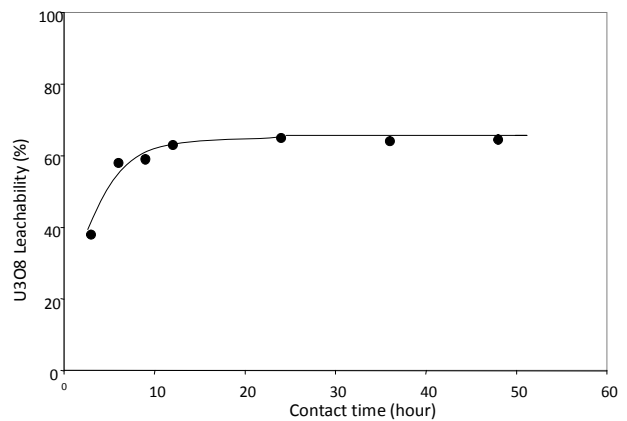


Fig. 2: Atmospheric leaching of uranium from dolomitic limestone type ore of Kadapa district (A.P.). Mesh of grind - 100#, Sodium carbonate 50 kg/t, Sodium bicarbonate 50 kg/t, $KMnO_4$ 10 kg/t,

process. However, as $KMnO_4$ cannot be used as an oxidant on commercial scale due to its expensive nature, the only alternative is to carryout the leaching reaction in a pressure reactor, using a gaseous oxidant. Since the solubility of oxygen diminishes with increasing temperature, adoption of higher partial pressure aids in increased dissolved oxygen concentration. Detailed analysis of the leach residue obtained in the atmospheric leaching experiments indicated, that uranium values associated with pyrite are not completely leached at temperatures <100°C. Further, some of the locked-up uranium values in various gangue



phases, require more aggressive diffusion conditions for penetration of the leachant to the desired mineral interface. Both these requirements can be realized only at elevated temperature and under sustained oxidizing conditions, possible in an autoclave reactor. Leaching at elevated temperature and pressure was initially carried out in a laboratory, 5 liter S.S. autoclave reactor equipped with necessary instrumentation and control to maintain pre-set temperature, overpressure and agitation speed of the impeller. All the autoclave leaching experiments were carried out, at optimum dosage combination of sodium carbonate and sodium bicarbonate evolved in atmospheric leaching, that is - 50 kg/ton and - 70 kg/ton respectively. The autoclave leaching studies mainly addressed the dissolution of uranium associated with pyrite and the scope of replacing $KMnO_4$ with industrial oxygen. Figs. 3 and 4, illustrate the effect of temperature and contact time on the leachability of uranium values, observed under

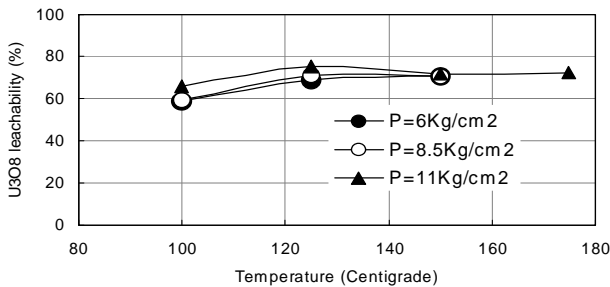


Fig. 3: Effect of temperature on leachability of uranium from dolomitic limestone ore in autoclave reactor. MOG 65% - 200#, Solids 50%, Contact time 6 h, Na_2CO_3 50 kg/t, $NaHCO_3$ 70 kg/t

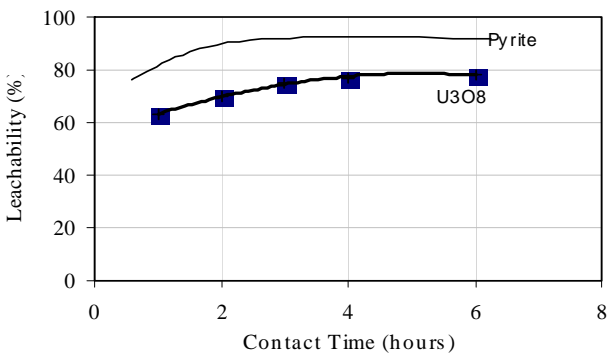


Fig. 4: Effect of Contact time on the leachability of uranium from dolomitic limestone ore in autoclave reactor. MOG 85% -200#, Solids 50%, Na_2CO_3 50 kg/t and $NaHCO_3$ 70 kg/t, pO_2 5.8 kg/cm².

aggressive conditions. About 75% of uranium values were leached at a reaction temperature of 125 - 130°C in 3 h of contact time, using a feed ground to 65% weight finer than 200#. Increasing the fineness of grind in -200# to 85% showed, an enhancement in leachability to about 80%. Based on these results, large-scale leaching studies were carried out, both on batch and continuous leach reactor, to generate necessary scale-up and engineering data for industrial scale reactor, besides verifying the reproducibility of results at higher-scale of operation. Both the batch and cigar type continuous reactor were of 850 liter capacity with inconel 600 as material of construction. The kinetic profile of the leaching reaction in pilot scale batch and continuous reactor is illustrated in Fig. 5. Large-scale studies confirmed the results generated in batch scale experiments. At present, DAE is setting-up a 3000 tpd capacity uranium mill at site, wherein two 720 m³ capacity autoclave reactors with inconel 600 cladding for the wetted parts will be used. This will be the first uranium plant, using autoclave leaching technology in India.

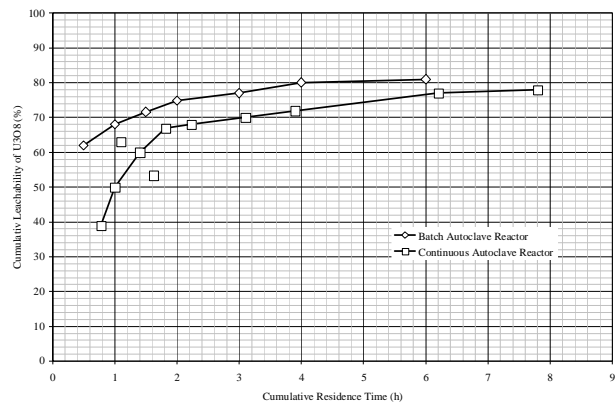


Fig. 5: Leaching kinetics of uranium from dolomitic limestone ore in batch and continuous autoclave reactor.

High acid pressure leaching of uraniumiferous alkali syenite ore containing betafite

Uraniferous alkali-syenite ore deposit in Vellore district of Tamilnadu, analysing 0.04% U_3O_8 containing betafite - $(Ca,U)_2(Ti,Nb,Ta)_2O_6(OH)$ as the main radioactive mineral, was studied for recovering uranium values. The other radioactive minerals in the ore include pyrochlore, uranothorite, thorite, cyrtolite, monazite and minor



concentrations of some secondary uranium minerals. Practically all the uranium-bearing phases are refractory in nature. The main gangue minerals in the ore are feldspar (83%), pyriboles (3.3%), iron oxides (2.9%), sulfides (0.1%), limonite (1.6%), barite (0.9%) etc. Since the major gangue of the ore is non-acid consuming in nature, the ore was processed by the sulfuric acid leaching route. Various process options were tried to extract the uranium values, which included physical beneficiation followed by acid leaching of the pre-concentrate, pug-cure-leaching, direct acid leaching of the ground ore at atmospheric pressure and normal temperature conditions and finally sulfuric acid leaching under aggressive temperature and pressure. Atmospheric leaching experiments indicated the scope of leaching to about 80% of the uranium values with high sulfuric acid dosage, about 200 kg/ton, at about 90°C. Though the leachability is reasonably satisfactory, the high residual SO_4^{2-}/HSO_4^- in the leach liquor, limits the efficiency of down-stream unit operations, particularly ion-exchange, tailings neutralization etc. Studies carried out at elevated temperature in an autoclave reactor, have indeed yielded twin benefits of reducing the acid consumption to 90 kg/ton and enhancing the leachability to 88-90% at about 150° C (Fig. 6) in 8 h contact time (Fig. 7). XRD analysis of feed and various leach residues have indicated, that the leachability of other-wise refractory uranium mineral phases could be accomplished within commercially acceptable operating conditions, due to the presence of both betafite and thorite in metamorphic form.

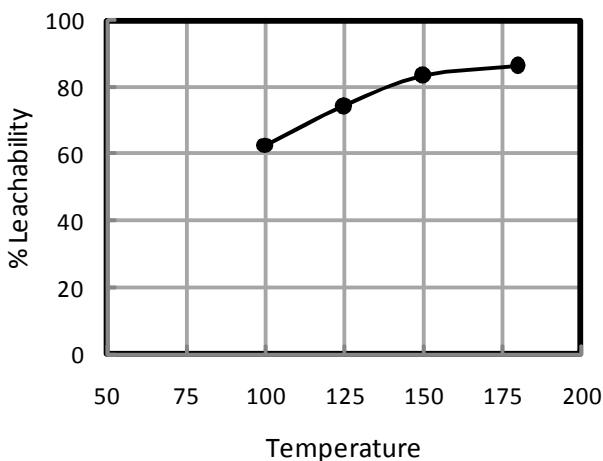


Fig. 6: Effect of temperature on autoclave leaching of betafite

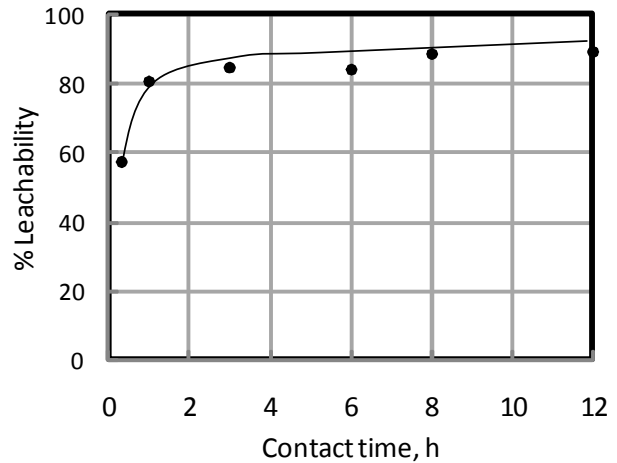


Fig. 7: Effect of contact time on autoclave leaching of betafite bearing uranium ore.

Encouraging results obtained in the autoclave reactor generated significant interest in the exploration geologists, working on this potential deposit.

High acid pressure leaching of uranium from liandratite

High sulfuric acid pressure leaching was also found successful in leaching uranium values from liandratite, a uranium bearing niobium-tantalum oxide refractory mineral, with the chemical formula $[U(Nb, Ta)_2O_8]$. As the chemical reactivities of uranium and Nb & Ta are different, a separate sequence of chemical conditions is required for maximal dissolution of individual metals. Leaching of niobium and tantalum oxides required, highly acidic or highly alkaline aqueous conditions, for quantitative dissolution at very high temperature. Unlike niobium and tantalum, the acidity or alkalinity necessary for uranium leaching is significantly lower. In view of this, the scheme for extracting the metal values from a liandratite bearing ore sample (Table 2), is formulated in such a way, that in the first stage, conditions were set to leach as much uranium values as possible, followed by re-adjustment of the chemical and experimental conditions, for dissolution of niobium and tantalum values. Optimal process conditions gave uranium leachability of about 80% at a reaction temperature of 180° C, sulfuric acid dosage



Table 2: Partial mineralogical and chemical composition of Madagascar Ore.

Partial Mineralogical Composition	Liandratite - $[U(Nb, Ta)_2O_8]$ Samarskite - $[(Y, Er)(Nb, Ta)_2O_6]$
Partial Chemical Composition	Nb_2O_5 39%, Th 1.5%, Ta_2O_5 5%, Fe_2O_3 11%, MnO 1.0% and U_3O_8 21%.

of 400 kg/ton, feed ground to finer than 150 μm and contact time of 48 h. There was no necessity of adding any additional oxidant during the leaching reaction, as sulfuric acid itself served as a strong oxidizing agent, due to its high concentration. The redox potential was consistently about 450 -500 mv (vs. SCE). The solution composition of the leach liquor indicated the presence of niobium and tantalum concentration of 5 mg/l and 30 mg/l against uranium concentration of 21 g/l, indicating that the leaching conditions are good for selective dissolution of uranium values. Thus, adoption of high acid autoclave leaching, could dissolve uranium quite selectively from the liandratite phase.

Conclusions

Leaching studies on different ores, having chemically refractory uranium minerals (betafite, liandratite) and on an ore where the uranium phases are in very-fine to ultra-fine dissemination in the host matrix, have indicated the scope of recovering uranium very efficiently, by using autoclave reactor. The investigations provide positive signals for exploration and exploitation even "difficult to process" uranium ores of India. This is a welcome technological advance, for augmenting the uranium resources, in order to meet the fuel demands of our ambitious nuclear power programme.

Acknowledgement

The authors are thankful to Dr. A.K. Suri, Director, Materials Group, BARC, for his interest in the investigations and for this encouragement.

References

1. Merrit, R.C., 1971, *The extractive metallurgy of uranium*, Colorado School of Mines Research Institute, Golden Colorado, United States Atomic Energy Commission, Colorado, p 50.
2. Edwards, C.R. and Oliver, J.A., 2000, Uranium processing: A review of currents methods and technologies, *Journal of Metals*, 52 (9), p 12.
3. Tong Deng, 1995, Aqueous pressure oxidation of minerals - a salient development in hydrometallurgy, *Mineral Processing and Extractive Metallurgy Review*, 12, p 185.
4. K.S. Fraser and K.G. Thomas, 2010, Uranium extraction history using pressure leaching, 3rd International conference on uranium (URANIUM 2010), 40th Annual Hydrometallurgy Meeting, Saskatoon.
5. BODU, R., et al., 1984, "The Lodeve plant: A complex alkaline process for a complex uranium ore", Mintek 50 (Proc. Conf. Sandton, 1984), The Council for Mineral Technology, Randburg, South Africa, p 707.
6. R.J.Verster and H.J.H. Pieterse, 1985, The use of autoclaves in uranium leach flowsheet., Technical publications of M/s. Bateman Engineering, SA, www.batemanengineering.co.za.
7. SORENSEN, E., JENSEN, E., 1985, "Uranium extraction by continuous carbonate leaching in a pipe autoclave", *Advances in Uranium Ore Processing and Recovery from Non-Conventional Resources* (Proc. IAEA Tech. Committee Mtg Vienna, 1983), IAEA, Vienna, p 41.
8. Anjan Chaki, 2009. *An Overview of Uranium Exploration Strategy in India*, International Symposium on Uranium Raw Material for the Nuclear Fuel Cycle: Exploration, Mining, Production, Supply and Demand, Economics and Environmental Issues (URAM-2009) Vienna, Austria, p 22.



Studies in Atomic Structure and Dynamics using Laser Spectroscopy

Asawari D. Rath

Laser & Plasma Technology Division

This paper received the Best Thesis Presentation Award at the Topical Conference on EM interaction with Atoms, Molecules and Clusters, held at RRCAT, Indore, during March 3-6, 2010

Abstract

The thesis deals with investigations relating to the structure and dynamics of atoms using high resolution and laser spectroscopic techniques. The experimental and theoretical work reported here, falls into three broad domains, namely, the high resolution laser spectroscopy for the study of atomic hyperfine interactions, the pulsed laser photoionization spectroscopy to investigate two-photon transitions and highly excited atomic levels including autoionization levels, and finally the multi-step isotope selective photoionization of atoms.

Introduction

High resolution spectroscopy is a prerequisite for investigations on the complex atomic structure of multi-electron atoms and their dynamics. The thesis presents studies in atomic structure and dynamics, using high resolution laser spectroscopic techniques, performed on uranium and erbium isotopic systems, representative of the actinide and lanthanide group of elements respectively. The atomic structure studies were performed on uranium, wherein the region at ~ 2 eV was investigated to understand effect of hyperfine interactions from isotope to isotope. The levels at ~ 4 eV and above including autoionization (AI) levels were studied using photoionization spectroscopy. The photoionization dynamics of erbium isotopes was investigated, both theoretically as well as experimentally.

Atomic Hyperfine Interactions

The hyperfine interactions in uranium isotopic system (^{233}U , ^{235}U , ^{238}U) were studied by investigations on Isotope Shifts (IS) and HyperFine Structures (HFS) of some transitions of uranium, starting from ground or lower meta-stable levels. These investigations were carried out by developing two independent high resolution techniques: - emission spectroscopy with a pressure scanned Fabry Perot spectrometer and scan averaged Opto-Galvanic (OG) spectroscopy, with a single mode tunable diode laser. A hermetically sealed, all metal, liquid air cooled hollow cathode lamp, specially designed and optimized to handle radioactive samples up to few milligrams, served as a spectroscopic source for both the techniques. The emission spectroscopic technique was extended to reduce the sample size to few tens of micrograms, to handle very rare / highly radioactive isotopes. The technique can be



gainfully utilized for off-line spectroscopic measurements of artificially produced isotopes of lanthanides and actinides, having moderate to long half-lives (> 1 day).

The recorded spectra were analysed using a spectral analysis code, developed on the basis of gradient minimization. The work generated new data on IS and HFS of ^{235}U and ^{233}U , hitherto unreported in literature. The Relative Isotope Shifts (RIS) and odd-even staggering (OES) of ^{233}U and ^{235}U were analysed using the IS values. Our data showed, that $\text{RIS}^{(233,235)} = 1.54 \pm 0.012$ and $\text{RIS}^{(234,235)} = 1.9 \pm 0.012$ and these values are in close agreement with the earlier reported work and the nuclear data of these isotopes. Further, the OES parameters for ^{235}U and ^{233}U based on our data are 0.368 ± 0.012 and 0.22 ± 0.012 respectively. Fig. 1 shows U I spectra recorded for the transition at 682.6 nm.

Photoionization Spectroscopy

For multi-step and multi-photon ionization studies, a versatile laser photoionization set-up was developed. It included both Resonance Ionization Mass Spectrometry (RIMS) and Photoionization Opto-Galvanic Spectroscopy (PIOGS) techniques developed from the first principles. For RIMS, a complete system consisting of a Time Of Flight Mass Spectrometer (TOFMS) of mass resolution of

~ 300 , photoionization chamber, collimated atomic beam generator, thermal ion suppressor and ion optics was designed and developed.

This set-up was used for studies on U I levels, in the region ~ 4 eV and above including Autolonization (AI) levels, which are of immense importance in the development of multi-step photoionization (PI) schemes for ultra-trace isotopic analysis and isotope selective photoionization experiments. In this work, two-photon transitions of U I were employed, to excite U atoms in ground or lower meta-stable levels to high lying two-photon resonant levels at ~ 4 eV and AI levels, connecting from these levels were studied, using two-colour three-photon ($2\lambda_1 + \lambda_2$) ionization, by two tunable dye lasers of wavelengths λ_1 and λ_2 . We investigated two schemes, involving two photon resonances, (a) 0 cm^{-1} ($J=6$) \rightarrow 33801.05 cm^{-1} ($J=8$) and (b) 620 cm^{-1} ($J=5$) \rightarrow 35886.88 cm^{-1} ($J=6$) and probed even parity AI levels in the energy region $51025\text{--}51760 \text{ cm}^{-1}$. These two-colour schemes for probing AI levels, offered experimental simplicity as compared to the usual three-colour schemes used earlier in the literature. While the scheme (a) was reported earlier, we extended in this work the scope of its application to a larger energy region of AI levels. On the other hand, the scheme (b) was explored for the first time. The analysis of the PI

resonances recorded using these schemes resulted in several new AI levels¹. Moreover, many highly excited odd parity levels in the region $33470\text{--}34800 \text{ cm}^{-1}$ were confirmed. An important criterion in the selection of the two-photon resonant levels in schemes (a) and (b), was their angular momenta $J = 8$ and 6 respectively. Consequently, the AI levels common to both the excitation schemes, were assigned $J = 7$, using angular momentum selection rules.

Isotope Selective Photoionization

Selective excitation and ionization of specific species is an important application of multi-step excitation and ionization spectroscopy. Isotope selective multi-step ionization was

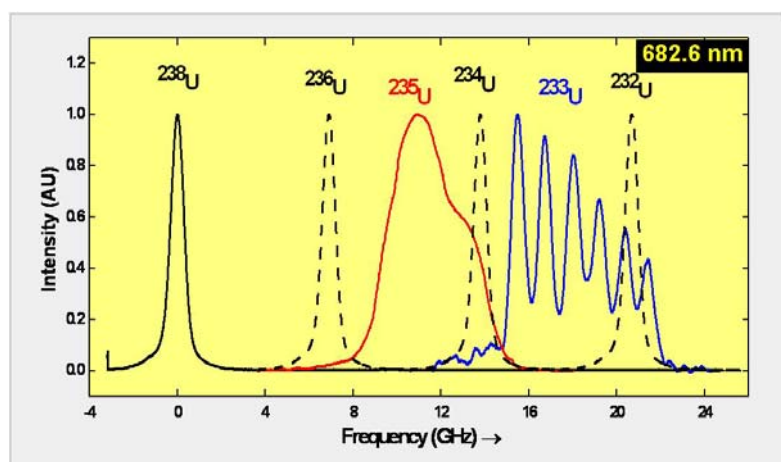


Fig. 1: Uranium spectra for the transition U I 682.6 nm. The (^{233}U , ^{238}U) and (^{235}U , ^{238}U) spectra are recorded using OG spectroscopy and emission spectroscopy respectively. The spectral peaks of other even isotopes (shown as dashed lines) are simulated using IS(^{234}U , ^{238}U) and the RIS parameters available in literature.



studied in natural erbium, both experimentally as well as theoretically. This system with 5 even ($A = 162-170$) and one odd isotope (^{167}Er) offers an excellent example for investigating various issues, concerning isotope selectivity since typical IS between adjacent even isotopes is ~ 1 GHz while the HFS of ^{167}Er extends over 3 GHz, thereby causing widespread spectral overlap. For experimental demonstration of isotope selective photoionization of erbium, first a three-step PI scheme was constructed with $4f^{12}6s^2 J = 6 \rightarrow 4f^{12}6s6p J = 7$, as the first step ($\lambda_1 = 582.7$ nm). The second and third step transitions were arrived at, by performing two- and three- colour three-photon PI spectroscopy to yield $\lambda_2 = 559.8$ nm and $\lambda_3 = 621.6$ nm. Isotope selective photoionization of natural erbium was then demonstrated using this level sequence and invoking isotope selectivity only in the first step by use of a single mode CW laser of line width of ~ 1 MHz; λ_2 and λ_3 were provided by two Nd:YAG pumped dye lasers of line width 3-5 GHz. The experiments were conducted in the RIMS chamber, where natural erbium was evaporated and collimated, to yield residual Doppler width of ~ 60 MHz. Complete isotope selective photoionization of erbium was achieved in these experiments².

Theoretical studies were performed, based on rate equation formalism developed for the populations of various isotopes in various levels of the three-step photoionization scheme, incorporating the effect of all atomic, vapour and laser parameters on the photoionization dynamics. They were solved numerically, to obtain the fractional ionization (f) and selectivity (α) of the process. Further, the effect of important operating parameters, i.e., saturation of the first step (See Fig. 2), vapour collimation and magnetic field, on fractional ionization and selectivity of the even isotopes was investigated. These results provided quantitative estimates of these quantities, for a realistic three-step photoionization experiment, where the first step is made isotope selective. The variation of selectivity and fractional ionization as a function of the operating parameters was studied, in terms of the IS and HFS of the first step. The experimental and theoretical investigations

are in general, applicable to isotope selective photoionization of lanthanide group of elements.

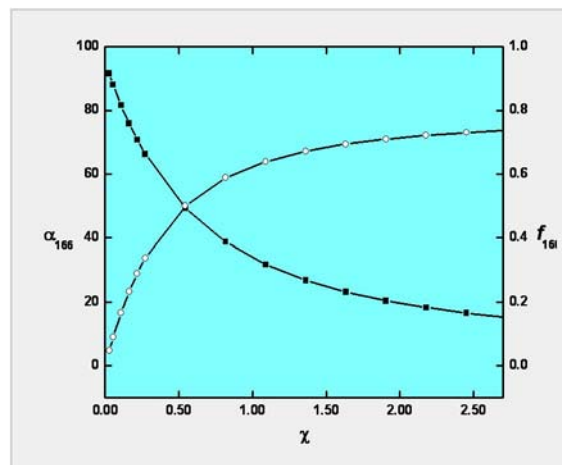


Fig. 2: Selectivity (·) and fractional ionization (o) for ^{166}Er as a function of saturation parameter χ for the first step with λ_1 tuned to the atomic transition of ^{166}Er .

Conclusions

The work carried out in this thesis, has resulted in the development of sophisticated spectroscopic techniques, new IS and HFS data for uranium isotopes and their relation to nuclear parameters, identification of several new AI levels of uranium and demonstration of isotope selective photoionization of natural erbium. The total work opens up several new and interesting possibilities in atomic spectroscopy and laser-atom interaction processes.

The author thanks Dr. B.N. Jagatap, Head, Atomic & Molecular Physics Division for his invaluable guidance during this work.

References

1. Asawari Rath et.al. "Autoionizing levels of uranium using quasi-resonant two-photon transitions" *BARC Newsletter Founders day Special Issue* (2010): 257-260.
2. A.P. Marathe et.al. "Separation of isotopes with overlapping spectra" *Proceedings of the 9th international workshop on Separation Phenomena in Liquids and Gases*, September 18-21, Beijing, China (2006) : 66-69.



Atoms, Molecules and Photons: From Precision Measurements to Quantum Control

B.N. Jagtap

Atomic and Molecular Physics Division

Dr. B.N. Jagtap is the recipient of the Platinum Jubilee Lecture Award (Physical Sciences) conferred on him at the 97th Indian Science Congress, held at Kerala University, Thiruvananthapuram, from 3-7 January 2010

Extended Abstract of the lecture

Spectroscopy is primarily concerned with making measurements on atoms and molecules, through their interactions with electromagnetic fields. These measurements played a very crucial role in the development of quantum mechanics, in the beginning of twentieth century and related developments in the later years. Spectroscopic measurements are continuing to contribute immeasurably, to our understanding of various atomic/molecular interactions and processes, even today. In a way, spectroscopic measurements encompass practically all endeavors in science and technology, be it basic sciences, astrophysics and astrochemistry, environmental and health sciences or energy generation and development of new industrial processes.

In recent years, however, the new and fast developing scheme in spectroscopy, is the control of the quantum world of atoms and molecules using laser photons. The theme is based on the realization, that light is not only a source of information on the structure of atoms and molecules, but it can also be used to act on, to manipulate them and control their various degrees of freedom. Coherent control, which is based on the atomic/molecular coherence and quantum interference in optical transitions, is an example of control of the internal degrees of freedom by laser photons. The world of coherent control today

covers several new aspects of laser-atom/molecule interactions, which include for example, control of chemical reactions, control of the optical properties of a medium, electromagnetically induced transparency and slow light propagation. Laser cooling of atoms is an example of controlling the external degrees of freedom, i.e., velocities and positions, using laser photons to realize atomic samples at unprecedented low temperatures. The field of ultra-cold atoms has expanded enormously in very recent years and it encompasses several new research directions, i.e., quantum degenerate gases, ultra-precision measurements, cold collision physics and atom optics to name a few. Current research in the area of quantum control of atoms and molecules holds an enormous promise, both as a platform for fundamental research and as a generator of new quantum technologies, e.g., ultra-precision atomic clock, ultra-sensitive magnetometer, quantum information processing and communication, and nano-technology.

For over twenty years, we have witnessed this paradigm shift in the outlook of spectroscopy, attempted to adopt it in our work and could succeed in advancing it by a few baby steps. In this presentation, we discuss the ideas underlying this progress with examples provided from our basic and applied work in high-resolution spectroscopy, coherent control and laser cooling and trapping of atoms.



Bioaccessibility of selenium from Se rich food grains of seleniferous region of Punjab, India as analyzed by Instrumental and Chemical NAA

Sumit K Jaiswal and N. Tejo Prakash

Department of Biotechnology & Environmental Sciences

and

Amit Goyal and Ranjana Prakash

School of Chemistry & Biochemistry, Thapar University, Patiala

and

R. Acharya and T.N. Nathaniel

Radiochemistry Division

and

A.V.R.Reddy

Analytical Chemistry Division

This paper received the IANCAS Best Paper Award (Oral Presentation), at the Fourth International Symposium on Nuclear Analytical Chemistry (NAC-IV), held at BARC, Mumbai, during November 15-19, 2010

Abstract

In the present study, selenium bioaccessibility was measured in rice and maize, cultivated in seleniferous soil of India, using *in-vitro* gastric digestion (GA) and gastro-intestinal digestion (GI) methods. The concentration of bioaccessible selenium was determined by Instrumental Neutron Activation Analysis (INAA). The total Se was observed to be about 58 mg kg⁻¹ and 29 mg kg⁻¹ in flours of rice and maize respectively. Total Se contents in maize flour sample after GA and GI were approximately 9.5 mg kg⁻¹ and 15 mg kg⁻¹; and in case of rice samples the levels were about 32 mg kg⁻¹ and 38 mg kg⁻¹. The results indicated that the bioaccessibility of GI digestion (51% in maize and 65% in rice) was higher compared to GA digestion (32% and 52% in maize and rice respectively). In addition, the bioaccessible levels of selenium were significantly more in the case of rice compared to maize.

Introduction

Selenium is an essential element for both human beings and animals. Se enters into the body as a dietary supplement through food. But it is also true that after digestion, all mineral contents present in diet may not be completely absorbed and utilized for physiological function of the body. It depends on the efficiency of the digestive system and chemical species of the elements. For example, Se as selenomethionine is more easily absorbed when ingested, than is selenite, selenate or selenocystine. In

short, bioaccessibility reflects the efficiency with which the nutrients are absorbed from the alimentary tract and available for further storage and use (Fairweather-Tait, 1992). Most of the cultivated plants possess the ability to absorb, metabolize and store significant amount of Se in their tissue when grown on soil containing available Se. Selenium dominantly enters the food-chain through plants (Rayman, 2008). Accumulation of Se by plants is due to their ability to transform inorganic Se into a variety of organoselenium species, including bioactive compounds,



which has important implications for human nutrition and health. The Tolerable Upper Level (TUL) Se-intake for adults is $400 \mu\text{g d}^{-1}$ against the daily requirement of $40 \mu\text{g}$ (Combs, 2001; Goldhaber, 2003). Bioavailability of Se is determined either by *in-vivo* administration to similar species to humans, for example murine models or *in-vitro* methods by simulating digestive system (Kulkarni et al., 2007). *In-vitro* methods were developed which are rapid and inexpensive (Miller et al., 1981). The results obtained by *in-vitro* methods are based on the formation of digestive products that are soluble or dialyzable (Ruby et al., 1999).

In the present study, the bioaccessible concentrations of selenium were determined in rice and maize collected from the seleniferous region of Punjab, by submitting the Se-rich samples to *in-vitro* gastric (GA) and gastrointestinal (GI) digestion. Selenium contents in the raw grains and the GA/GI digests were estimated by INAA.

Experimental

Harvested paddy and maize grains were collected from the seleniferous belt of Nawanshahr-Hoshiarpur region of Punjab India. The required amount of grains (about 25g) was washed with distilled water and dried overnight at 40°C . De-husked rice (semi milled) and whole maize grains were ground into fine powder using mortar and pestle. For total Se quantification in raw samples, approximately 100mg of rice and maize flour were taken in triplicate and packed in thin aluminum foils.

The *in-vitro* gastric digestion protocol was adapted from Kulkarni et al. (2007). Accurately weighed amounts (1.25 g) of rice and maize flour were transferred to 50 mL conical flasks, each containing 12.5 mL of gastric juice solution (6% w/v pepsin in HCl, $\text{pH} = 1.75$). Initially, the mixture was shaken vigorously for 1–2 min. The flasks were then sealed tightly with a parafilm and placed in shaker-incubator set at 37°C and 150 rpm for 3 h. Each sample was digested in triplicate and these digests were then cold centrifuged (Hitachi-RX II) at 4°C for 20 min at 5000 rpm. The supernatant was filtered through Whatman nitrocellulose membrane filters ($0.45 \mu\text{m}$, 25mm \varnothing).

For gastro-intestinal digestion, the pH of the each solution obtained after gastric digestion was adjusted up to pH 7, by drop-wise addition of a saturated solution of NH_4HCO_3 . To this mixture, 10 mL of pancreatic digestion solution (mixture of 2% w/v Pancreatin and 0.2% w/v bile salts) was added and shaken vigorously for 1 min. The flasks were incubated at 37°C , 150 rpm for 4h in a shaker incubator. The digests were then centrifuged at 4°C and filtered, following a procedure similar to the gastric digest. Clear supernatant of both gastric and gastro-intestinal digestion was taken for analysis. 200 μL of either gastric or gastro-intestinal digests were carefully transferred onto a Whatman filter paper (no. 41, 42.5mm \varnothing) with the help of micropipette and then air dried. This step was repeated 10 times so as to transfer a total solution of 2 mL. Each filter paper was folded 3-4 times to make it square shaped and packed in thin aluminum foil.

For Se quantification in raw samples and in GA and GI digests, all packed samples were co-irradiated in the self-serve position of the CIRUS reactor for 7 h duration at a neutron flux of $\sim 10^{13} \text{ cm}^{-2} \text{ s}^{-1}$ with Se ICP liquid standard (Spex) containing known amount of Se (5-25 μg), fused in pure amorphous silica powder and two reference materials namely CRM DOLT-1 (Dogfish Liver) from National Research Council of Canada (NRCC) and SL-1 (Lake Sediment) from IAEA. The samples were allowed to cool for about 9 days, and then the radioactive assay of the samples was γ -ray spectrometry using carried out by HPGe detector for 1–10 h, depending on Se concentration in samples. The peak areas were determined using peak-fit software PHAST. The peak areas were used for the calculation of the selenium concentration by relative method of NAA.

Results and Discussion

A typical gamma ray spectrum generated using data obtained from HPGe detector of the gamma-ray spectrometer with Compton suppressed detection system is presented in Fig. 1. The figure indicates gamma rays (136, 264.7 and 279 keV) that typically signify the presence of ^{75}Se (120d).

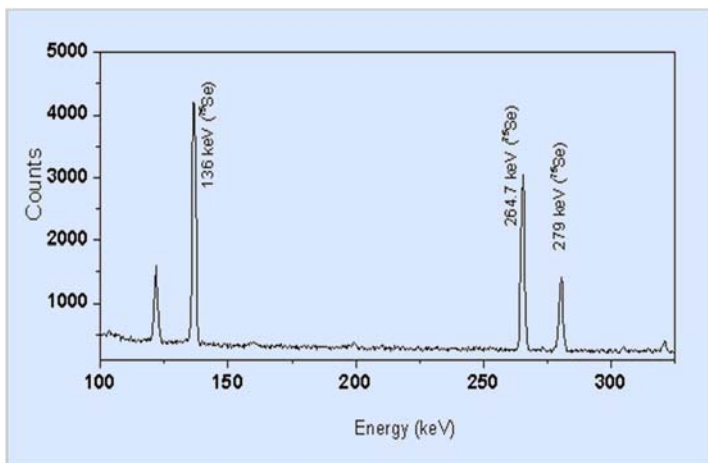


Fig. 1: Typical gamma ray spectrum of selenium as acquired after irradiation, using HPGe-BGO Compton suppressed detection system

The selenium concentrations determined in two reference materials, IAEA SL-1 and NRCC CRM DOLT-1 were $2.82 \pm 0.08 \text{ mg kg}^{-1}$ and $7.43 \pm 0.18 \text{ mg kg}^{-1}$ respectively as against the reported values of 2.9 and $7.34 \pm 0.42 \text{ mg kg}^{-1}$ respectively. The percent deviations from certified/information values are within $\pm 3\%$. The selenium concentration in raw flour, GA and GI hydrolysates (digests) are given in Table 1. The uncertainties quoted in Table 1 are the standard deviations at $\pm 1s$ confidence limits obtained from three independent sample analyses and the % relative standard deviations are in the range of 1.5-5%. INAA quantification of selenium in cereal grains, as reported by this group (Sharma et al. 2009) was found to agree with quantification by ICP-MS in the case of wheat (Cubadda et al., 2010).

Total Se concentrations in maize and rice flour were $29.05 \pm 3.5 \text{ mg kg}^{-1}$ and $58.2 \pm 5.9 \text{ mg kg}^{-1}$ respectively. In view of maize being taken as whole grain flour and rice as semi-milled (unpolished) in rural Punjab, daily consumption of 100 g of maize flour or semi-milled rice would possibly result in an approximate intake of Se between 7.5 to 15.0 fold, the tolerable upper intake level (TUL) for adults ($400 \mu\text{g Se d}^{-1}$). With reference to the estimates of bioaccessibility of selenium, the present study indicated that the bioaccessibility obtained by gastrointestinal digestion was higher compared to gastric digestion in both the samples investigated. In addition, the concentration of selenium in terms of its bioaccessible levels was significantly higher in

rice as compared to maize. This is due to the fact that the materials undergo pancreatic digestion in the gastrointestinal tract at neutral pH, resulting in higher accessibility of the bioavailable forms of the element. Pancreatin, which is a major enzymatic component, added in the GI, is a mixture of many enzymes that break complex nutrients into simple molecules, making various bioavailable forms of selenium more bioaccessible. The Se concentrations of the samples investigated in this study appeared to be very high in cereal grains for human consumption similar to wheat reported earlier by our group (Cubadda et al., 2010; Sharma et al., 2009). These levels of intake might lead to chronic toxic effects of selenium accumulation in humans through Se-rich food grains and livestock, fed on rice and maize straw as fodder. As an alternative to the social, economic and health impact caused by this Se-rich crop product in the region, exploring the opportunities of using

Table 1: Selenium content in cereal flours, gastric (GA) and gastrointestinal (GI) hydrolysates and their percent bioaccessibility (%B)

Sample	n	Se in flour (mg kg^{-1})	Se-after GA		Se-after GI	
			(mg kg^{-1})	% B	(mg kg^{-1})	% B
Maize	3	29.05 ± 3.5	09.53 ± 1.1	32	14.82 ± 2.3	51
Rice	3	58.25 ± 5.9	30.66 ± 2.8	52	38.01 ± 3.5	65

Merit Award



locally grown grains for fortification of low-Se grain batches or production of naturally enriched products as Se supplements for human and animal nutrition, is an alternative that is worth considering. Further studies are in progress to investigate the bioaccessible species of Se in products derived from high-Se grains grown in the study area.

References

1. Combs, G.F. (2001). Selenium in global food systems. *British Journal Nutrition*, 85, 517-547.
2. Cubadda, F., Aureli, A., Ciardullo, S., D'Amato, M., Raggi, A., Acharya, R., Reddy, A.V.R., & Tejo Prakash, N. (2010). Changes in Selenium Speciation Associated with Increasing Tissue Concentrations of Selenium in Wheat Grain. *Journal Agricultural Food Chemistry*, 58, 2295-2301.
3. Fairweather-Tait, S. (1992). Bioavailability of trace elements. *Food Chemistry*, 43, 213-217.
4. Goldhaber, S.B. (2003). Trace element risk assessment: essentiality vs toxicity. *Regulatory Toxicology Pharmacology*, 38, 232-242.
5. Kulkarni, S.D., Acharya, R., Rajurkar, N.S., & Reddy, A.V.R. (2007). Evaluation of bioaccessibility of some essential elements from wheatgrass (*Triticum aestivum* L.) by in vitro digestion method. *Food Chemistry*, 103, 681-688.
6. Miller, D., Schriker, B., Ramussen, R., & Van, C. D. (1981). An in-vitro method for estimation of iron availability from meals. *American Journal Clinical Nutrition*, 34, 2284-2256.
7. Rayman, M. P. (2008). Food-chain selenium and human health: emphasis on intake. *British Journal Nutrition*, 100, 254-268.
8. Ruby, M. V., Schoof, R., Brattin, W., Goldade, M., Post, G., Harnois, M., Mosby, D. E., Casteel, S.W., Berti, W., Carpenter, M., Edwards, D., Cragin, D., & Chappell, W. (1999). Advances in evaluating the oral bioavailability of inorganics in soil for use in human health risk assessment. *Environmental Science Technology*, 33, 3697-3705.
9. Sharma, N., Prakash, R., Srivastava, A., Sadana, U.S., Acharya, R., Tejo Prakash, N., & Reddy, A.V.R. (2009). Profile of selenium in soil and crops in seleniferous area of Punjab, India by neutron activation analysis. *Journal Radioanalytical Nuclear Chemistry*, 281, 59-62.



High Pressure Freezing of Cyanobacteria for Immunolocalization Studies

Rachna Agarwal

Molecular Biology Division

and

Michael Melzer

Leibniz Institute of Plant Genetics and Crop Plant Research, Gatersleben, Germany

and

Jayashree Krishna Sainis

Molecular Biology Division

This Paper received the Best Oral Presentation Award at the International Conference on advances in electron microscopy and related techniques and XXXI annual meeting of EMSI, held at Training School Hostel, Anushaktinagar, from 8-10 March, 2010

Abstract

Unicellular cyanobacteria *Synechocystis* 6803 and *Synechococcus* 7942 were cryofixed, using High Pressure Freezing (HPF), freeze substituted with 100% acetone, embedded in LR white and used for examining localization of components of the photosynthetic apparatus. The use of high pressure freezing and freeze substitution, enables us to analyze tissue that was fixed as faithfully as possible under "nearly" physiological conditions and therefore, increases significantly, the preservation of the ultra-structure and antigenicity as compared to conventional fixation, since no chemical cross linkers are used. The Calvin Cycle enzymes were preferentially located around thylakoid membranes as were the components of electron transport and CF_1 . Such intracellular location for soluble enzymes is in contrast to established conviction regarding their random location.

Introduction

Cyanobacteria are unicellular photosynthetic prokaryotes. The enzymes of the Calvin cycle of photosynthesis are known to be randomly distributed in the cytosol of these organisms. Such random location of these soluble enzymes, is in disparity with their precise function and regulation for photosynthetic carbon assimilation. This location has been conjectured from the fact that they can be isolated in soluble form. Immunoelectron microscopy can aid in deciphering their exact intracellular location. However, conventional electron microscopy suffers from

several drawbacks such as chemical fixation, which results in cross linking of immunological epitopes and also other structural artifacts due to crosslinking and substitution. Sample fixation represents a critical step in preparation of biological specimens for transmission electron microscopy. An ideal method should preserve the structure closest to *in vivo* within a minimum time frame. Cryo fixation techniques like High Pressure Freezing with freezing tissue within milliseconds are being used to reduce structural artifacts and a possible dislocation of molecules to a minimum. We have established a HPF protocol for cells of *Synechocystis* 6803 and *Synechococcus* 7942 and carried



out immunogold labeling studies for Ribose-Phosphate Isomerase (RPI), Phosphoribulokinase (PRK), Ribulose-1,5-bisphosphate carboxylase (RUBISCO), Phosphoglycerate kinase (PGK) and Glyceraldehyde-3-phosphate dehydrogenase (GAPDH) in the cryofixed (HPF) cells of *Synechococcus* 7942.

Materials and Methods

High pressure freezing and freeze substitution

A dense pellet of log phase cells was loaded into nitrocellulose tubes (Cat. No. LH 01843 VN, BAL-TEC, Balzer, Switzerland) by capillary force, cut into 2mm pieces and transferred onto a 0.15mm standard aluminum platelet (Engineering Office M. Wohlwend GmbH, Switzerland). As filler for the platelets, yeast paste was used. After covering with a 0.30 mm platelet, the samples were frozen under a pressure of ~2kbar using a Leica EM HPF (Leica Microsystems, Bensheim, Germany). Freeze substitution and infiltration in LR White resin was performed as described in the following section.

Freeze substitution and resin infiltration after high pressure freezing

100%Acetone, -90°C, 72h; 100%Acetone, -90°C to -70°C, 12h; 100%Acetone, -70°C, 24h; 100%Acetone, -70°C to -50°C, 12h; 100%Acetone, -50°C, 24h; 100%Acetone, -50°C to -35°C, 12h; 100%Acetone, -35°C, 24 h; 100%Acetone, -35°C to 20°C, 12 h.

Infiltration with LR White resin and polymerization

20%LRWhite/Acetone, RT, overnight; 40%LRWhite/Acetone, RT, 4h; 80%LRWhite/Acetone, RT, 4h; 100%LRWhite, RT, overnight; Polymerization in BEEM capsules, 60°C, 48 h.

Sectioning and Immunogold labeling

Ultrathin (70nm) sections were cut with a microtome (Leica Ultracut, Leica Microsystems, Bensheim, Germany) and used for immunolabeling. The grids were washed once with buffer containing 1mM Na₂HPO₄, 0.3 mM KH₂PO₄, 12 mM NaCl, 1 mM NaN₃, 0.1% Tween-20 and 0.1% BSA (IgG free), pH 7.6 (wash buffer) and blocked for 1 h with the above buffer containing 3% BSA (blocking buffer). Grids were blot dried and incubated with 20 μl each of appropriately diluted antibody (raised in rabbit) solution for 1 h. For controls, grids without any primary antibody were used. Excess liquid was removed and grids were washed several times with wash buffer and were further incubated with protein A conjugated with 5 nm or 10 nm gold for 1 h. Finally grids were washed twice with wash buffer and blot dried. Prior to the examination in a Tecnai Sphera G² transmission electron microscope (FEI Company, Eindhoven, Netherlands) at 120 kV, ultrathin sections were contrasted in a LEICA EM STAIN (Leica Microsystems, Vienna, Austria) with 0.5% uranyl acetate (Ultrastain 1, Laurylab, Sain-Fons, France) for 30 minutes, followed by an incubation in 3% lead citrate (Ultrastain 2, Laurylab, Sain-Fons, France) for 90 seconds.

Results and Discussion

Our studies involving comparison of various cell fixation techniques revealed that HPF was the most effective technique to gain improved preservation of structural integrity and antigenicity, in comparison with chemical fixation and Progressive Lowering of Temperature (data not shown). HPF frozen cells of *Synechococcus* 7942 showed elongated cells in LS (Fig. 1, D) and circular cells in TS (Fig. 1, A) with parallel concentric rings of thylakoid membranes. Carboxysomes were also observed in all the cells. The thylakoid membranes appeared uneven in diameter and the luminal space was barely visible. The

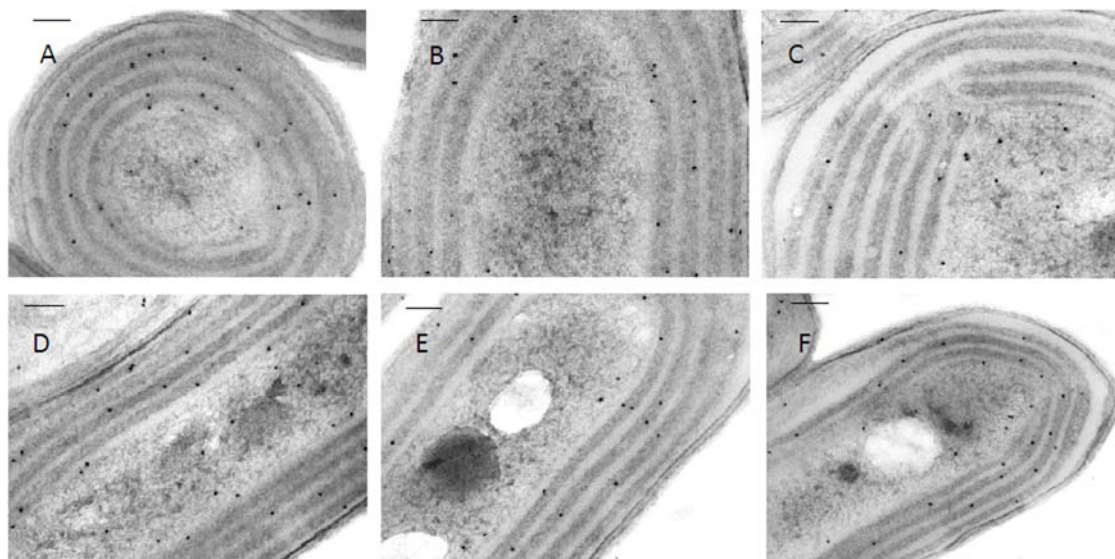


Fig. 1: Immunolocalisation of Calvin Cycle enzymes in HPF fixed samples of *Synechococcus* 7942: A) CF₁ B) PRK C) RPI D) RUBISCO E) PGK F) GAPDH. Arrows indicate the position of the gold particles. Bar Represents 100nm

contrast was weak probably due to non-availability of protein aggregates. The plasma membrane and outer envelope were preserved and looked pressed against each other which may be closer to the situation *in vivo*.

Immunogold labeling was carried out for PRK, RPI, RUBISCO, PGK and GAPDH (Fig. 1, B-F) with the catalytic portion of the chloroplast H⁺-ATP synthase (CF₁), serving as the positive control (Fig 1. A). Most of the label for PRK, RPI, PGK and GAPDH was seen around the thylakoid membranes, indicating the role of thylakoids in organization of these enzymes. RUBISCO was equally distributed between thylakoid membranes and carboxysomes (These structures are known to be RUBISCO reserves). The membrane bound particles accounted for ~70% of total for Calvin cycle enzymes in case of *Synechococcus*. Similar results were obtained from *Synechocystis* (3). These results have shown the intracellular location of soluble enzymes along the thylakoids and explained the efficiency of photosynthetic carbon reduction cycle, which remains unsubstantiated with the traditional concept of random and homogenous distribution of these enzymes.

References

1. Liberton M, Howard Berg R, Heuser J, Roth R and Pakrasi H B, Ultrastructure of the membrane systems in the unicellular cyanobacterium *Synechocystis* sp. strain PCC 6803. *Protoplasma* (2006) 227: 129–138.
2. Nevo R, Charuvi D, Shimoni E, Schwarz R, Kaplan A, Ohad I and Reich Z, Thylakoid membrane perforations and vesicles enable molecular traffic in cyanobacteria. *The EMBO Journal* (2007) 26, 1467–1473.
3. Agarwal R, Ortleb S, Sainis J K and Melzer M, Immunoelectron microscopy for locating calvin cycle enzymes in the thylakoids of *Synechocystis* 6803. *Molecular Plant*, 2 (2009) 32-42.

Acknowledgements

This work was carried out at the Structural Cell Biology Group, IPK, Germany, under the Indo German Collaborative project IND05/009.



Ion-transport characteristics in Nafion-117 membrane having mixed cationic composition

Sanhita Chaudhury, Chhavi Agarwal, A. K. Pandey and A. Goswami
Radiochemistry Division

This paper received the Best Oral Presentation Award (II prize) at the 2nd International Symposium on Application of Radiotracers in Chemical, Environmental and Biological Sciences (ARCEBS-2) held at SINP, Kolkata, during November 7-13, 2010

Abstract

Membrane (Nafion-117) composition dependent self-diffusion studies of different cations (Na^+ and Ba^{+2} ions) have been carried out, using radiotracer method. The choice of these two counterions in the membrane matrix was based on the fact, that these ions have significant difference in their self-diffusion coefficients in this membrane. Results indicate that the SDC of an ion in an ion exchange membrane, depends on the ionic composition of the membrane phase, and the mechanism of transport for bivalent ion is different from that of monovalent ion.

Introduction

Ion-exchange membranes can act as separators between two electrolyte solutions as they allow counter-ions to pass through while co-ions are excluded from the membrane. This property is utilized in the ion-exchange based separation processes as in Donnan dialysis and electrodialysis¹. Permeability of a diffusing species (permeant) in the membrane governs the transport flux across the membrane^{2,3}. The permeability coefficient of a species depends on its diffusion coefficient (D) and partition coefficient in the membrane which is the ratio of concentration of permeant in the membrane to that of the permeant in solution outside the membrane. Ratio of permeability coefficient of the two diffusing species across the membrane, determines the separation factor. The knowledge of diffusion coefficients is therefore important for modelling membrane transport process.

Radiotracers are extensively used for ion diffusion studies. Self-diffusion behavior of monovalent and multivalent ions in the Nafion-117 membranes has been widely studied^{4,5}. Self-Diffusion Coefficients (SDC) may be modified due to the presence of other ions in the membrane since ion exchange sites available for hopping reduce. However there is limited published experimental data, on SDC in membrane with mixed ionic composition. Okada et al⁶ determined ionic mobility in Nafion-117 in mixed ionic composition of H^+ ion and alkali metal cations. They observed no significant change in ionic mobility, depending upon the ionic composition of the membrane. Pourcelly et al⁷ observed from radiotracer studies, that SDCs of Na^+ and Ca^{+2} were independent of ionic composition of the membrane. In this paper, we report the measurement of SDC of Na^+ and Ba^{+2} in Nafion-117 membrane, having varying ionic composition of Na^+ and Ba^{+2} . The results are discussed in terms of possible mechanism of transport of the monovalent and bivalent ions.



Experimental

Nafion-117 membrane pieces (2cm X 2cm) were refluxed in ~7M HNO₃ for 1 h, and conditioned with alternate equilibrations with NaOH and HCl. Three different equilibrating solutions containing 0.1N NaCl and 0.1N BaCl₂ in different proportions of 1:1, 4:1 and 8:1 were used, keeping the total ionic concentration fixed at 0.1N. For each of the equilibrating solution, two experiments were carried out, one for the Na⁺ ion and another for the Ba⁺² ion. For each experiment, the membrane sample was kept in well-stirred (~52 rad/s) equilibrating solution (30 ml) at 27°C for ~3 hrs, to eliminate film-controlled diffusion at the membrane solution interface. After equilibration, the membrane was taken out and required (²²Na or ¹³³Ba) radiotracers were added to the respective solution. Filter paper standards were prepared by taking pieces of filter paper of the same dimensions (2 cm×2 cm) as the membrane sample and adding 100 μL of the radiolabeled solution. Separate standards were prepared for Na and Ba. To study the diffusion kinetics of the respective ions, the membrane was kept into the radio labeled equilibrating solution with continuous stirring and taken out intermittently. The samples were then thoroughly washed with deionised water to remove equilibrating solution clinging to the surface and were counted for uptake of respective (Na or Ba) activity using a NaI(Tl) detector connected to a 4k channel analyzer. The membrane sample was again placed in the equilibrating solution after counting. Experiments with Na and Ba radiotracer were done separately because the 511 keV gamma ray of ²²Na can cause huge background in the low energy gamma rays of ¹³³Ba. The equilibrium uptake of the radiotracers in the membrane gave ionic composition in the membrane as well as that of equilibrating solution which was used to obtain ion exchange isotherm. The same procedure was followed for equilibrating solutions of different ionic compositions.

Results and Discussion

The ion exchange isotherm is shown in Fig. 1. The higher selectivity of the membrane for Ba⁺² ion over Na⁺ is apparent from the figure. The isotherm gave composition

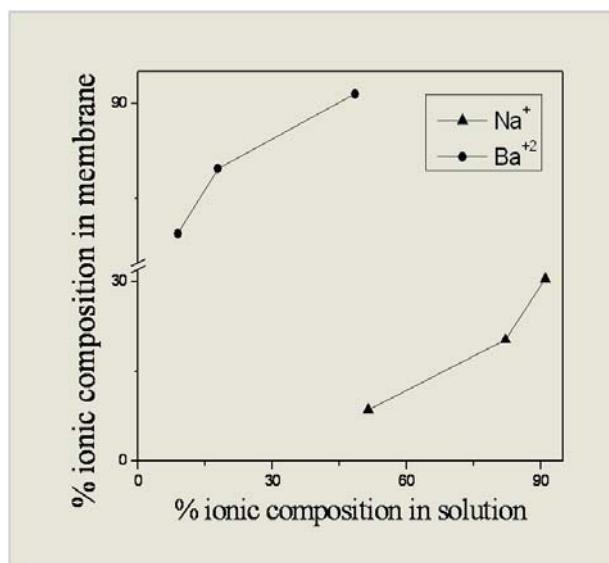


Fig. 1: Ion exchange isotherm for Na⁺ and Ba⁺² ions.

of the membrane and also the outside solutions, at which the isotopic exchange kinetics were studied

Fig. 2 shows the plot of kinetics of the isotopic exchange ${}^*Na^+_{(s)} \rightleftharpoons Na^+_{(m)}$ and ${}^*Ba^{+2}_{(s)} \rightleftharpoons Ba^{+2}_{(m)}$ respectively in three different equilibrating solution compositions, where * sign indicates the presence of radiotracer in the solution. It is seen from the figures, that the rate of isotopic exchange for Na⁺ ion does not change with change in ionic

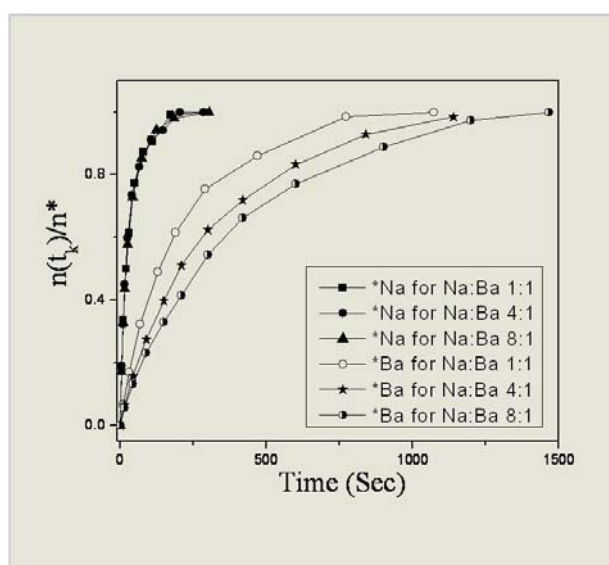


Fig. 2: Na⁺ and Ba⁺² diffusion kinetics for different ionic composition of the membrane

Technical Excellence Award



composition of the membrane, while that of Ba⁺² ion decreases significantly with increase in Na⁺ content in the membrane. The self diffusion coefficients of the Na⁺ and Ba⁺² ions were obtained from the least square fit to the plot, using the analytical solution of the Fick's second law as given by the equation:

$$n(t_k) = n^* \left[1 - \left(\frac{8}{\pi^2} \right) \left\{ \exp(-D\pi^2 t_k / L^2) + \frac{1}{9} \exp(-9D\pi^2 t_k / L^2) + \dots \right\} \right]$$

where n* is the total amount of the radiotracer ions in the membrane at equilibrium (t = ∞), n(t_k) is the amount of radiotracer at any time t_k in the membrane, D is the diffusion coefficient and L is the thickness of the membrane (200 mm). The D values are given in Table 1 along with the ionic composition of the membrane obtained from the ion exchange isotherm studies.

Table 1: SDC values of Na⁺ and Ba⁺² ions for different ionic composition of the membrane

% Na ⁺ (membrane)	D _{Na⁺} X 10 ⁷ (cm ² /sec)	D _{Ba⁺²} X 10 ⁷ (cm ² /sec)
8.55	9.4	1.2
20.26	9.6	0.84
30.44	9.2	0.64

For Na⁺ ion, the D values are reduced by about 8 % compared to the value of 1.03x10⁻⁶ cm²/sec for pure Na-form of membrane and it is independent of the composition of the membrane. For Ba⁺² ion, the D values are reduced by a factor of about 2 compared to pure Ba-form of the membrane (D ~ 1.4x10⁻⁷ cm²/sec) as the Na content in the membrane increases from 8.5% to 30.4%. These results indicate that Na⁺ ion possibly remains mostly dissociated in the water channels, and its transport is not hindered by the Ba⁺² ions which possibly remain in the proximity of the -SO₃⁻ ions. Increase in the Na-content in the membrane, increases the average distance of hopping of the Ba⁺² ions and hence its diffusivity is strongly effected by the ionic composition of the membrane.

Conclusion

Result of the present work shows, that the SDC of an ion in an ion exchange membrane depends on the ionic composition of the membrane phase. The effect is stronger for bivalent ions as compared to monovalent ions. This shows the mechanism of transport for bivalent ion is different than that of monovalent ion.

References

1. T. Sata, Ion-Exchange membranes-preparation, characterization, modification and application, Royal Society of Chemistry, (2004).
2. H. Yasuda, C.E. Lamaze, A. Peterlin, Diffusive and hydraulic permeabilities of water in water-swollen polymer membrane, *J. Polym. Sci., Part A* 29 (1971) 1117.
3. J. Crank, G.S. Park, Diffusion in Poymer, Academic Press, London (1968) Chapter 1.
4. A. Eisenberg, H.L. Yeager, Eds; Perflourinated Ionomer Membranes, ACS Symposium Series 180, American Chemical Society, Washington D.C.(1982) 41.
5. A. Goswami, Anjali Acharya, and A. K. Pandey, *J. Physical Chemistry B* 105 (2001) 9196.
6. Okada, T.; Satou, H., Okuno, M.; Yuasa, M. *J. Phys. Chem . B* 106 (2002) 1267.
7. Gerald Pourcelly, Phillippe Sstat, Agnes Chapotot, Claude Gavach, and Victor Nikonenko, *Journal of Membrane Science* 110 (1996) 69.



Nondestructive assay of Plutonium in empty stainless steel boxes by apparent mass method

C. Agarwal, S. Chaudhury, T. N. Nathaniel and A. Goswami

Radiochemistry Division

This Paper received the Best oral presentation award at the 4th International Symposium on Nuclear Analytical Chemistry (NAC-IV), held at Multipurpose Hall, TSH, BARC, from 15-19 Nov., 2010.

Abstract

Apparent mass method [1], initially standardized for the assay of Pu [2] has been used, to assess the amount of Pu in empty stainless steel boxes, generally used for storing and transferring plutonium oxide powders. The results have been compared with neutron coincidence counting results and found to match well. The advantage of this method is that, it can be used for any sample with nonstandard geometry and with uncertain source distribution.

Introduction

NonDestructive Assay (NDA) techniques are widely used throughout the nuclear fuel cycle for the assay of nuclear materials, which can be in a variety of shapes, sizes and matrices. Self attenuation corrections are generally important, due to the voluminous nature of the samples. Also, depending upon their origin, the samples can be homogeneous or inhomogeneous. For inhomogeneous samples, the usual gamma based nondestructive assay procedures cannot be used due to difficulty in calibrating the detector, for its efficiency for the required sample geometry. Along with this, attenuation correction procedures are not well established for such samples. Therefore, one needs a method to take care of both the factors for inhomogeneous samples. Apparent mass method [1] was proposed for such type of samples, where the exact knowledge of the sample matrix, its geometry and distribution is not available. The method takes advantage of the multiple γ -rays emitted by the nuclide monitored and correlates the self-attenuation of the sample, with the variation of apparent mass of the nuclide

monitored. The apparent mass ($m(E)$) at a given photon energy E is obtained, by correcting the measured count rate with the corresponding gamma ray abundance and the peak efficiency as given by:

$$m(E) = \frac{C_{net}}{I_{\gamma}\epsilon_{\gamma}w_A S_A} \quad (1)$$

where C_{net} is the net count rate of the γ -ray peak, I_{γ} is the intensity of the γ -ray, w_A is the weight fraction of the radioisotope in the sample and ϵ_{γ} is the peak efficiency of the detector for the required sample geometry and S_A is the specific activity of the isotope concerned. The apparent mass is an inverse function of self attenuation, taking place in the sample and therefore increases with decreasing energy. The apparent mass was fitted to the following functional form:

$$m(E) = m_0(1-B/E) \quad (2)$$

where, m_0 is the true mass of the nuclide monitored. When apparent mass $m(E)$ is plotted vs $1/E$, a straight



line is obtained. The intercept is the actual mass of the nuclide monitored (m_0), corresponding to the condition of infinite photon energy ($(1/E)0$), for which the attenuation correction becomes unity. 'B' in Eq. 2 is treated as free parameter in the fitting. This method has been used, to determine the plutonium amount in PuO_2 powder distributed in thin rectangular packets [2]. This method has also been extended for the assay of uranium. For this uranyl nitrate solutions were used as attenuating matrices [3].

Stainless steel boxes are used for storing and transferring plutonium oxide powder. For accounting the total Pu, the amount of Pu left in the stainless steel boxes after complete transfer, must be checked. There is no way to assess the distribution of plutonium in the empty boxes which can be inhomogeneous also. In the present work, the apparent mass method has been used, to obtain the plutonium amount in these empty stainless steel boxes. The results have been compared with the results of the neutron coincidence counting.

Experimental

The empty stainless steel box samples were counted in a 20 % coaxial HPGe detector coupled to a 4k channel analyzer. The detector had a resolution of 1.2 keV at 122 keV. Cd filters (1 mm) were used to reduce the count rate of 59.54 keV ^{241}Am gamma-rays. Since there was no way to find out the distribution of plutonium in the boxes, each sample was rotated manually by 180° in steps of 45° , and counting was done at each geometry, to average out any asymmetry in the actual distribution of the nuclide, monitored in the samples. The sample-to-detector distance was about 20 cm so that point source efficiencies could be used for the determination of Pu amount. Gamma ray spectra were analyzed using the PHAST software [4]. Point sources of ^{152}Eu and ^{133}Ba were counted in empty stainless steel boxes at the same distance used for obtaining peak efficiencies. A representative sample was also counted on the 2cc HPGe detector having a thin Be window for gamma-ray spectrum. This was required to obtain the

isotopic composition [5] needed to obtain total Pu amount. The samples were also counted using a shift-register based Neutron Well Coincidence Counter, having 24 ^3He counters of 2.54 cm diameter and 50 cm length arranged in an annular geometry. The counters were embedded in HDPE (moderator) of thickness 10.5 cm. The efficiency of the counter was 15 %.

Results and Discussion

The apparent masses at different energies were calculated, by correcting the measured count rate with the corresponding gamma ray abundances, peak efficiencies, specific activity and weight fraction of the radionuclide concerned. The gamma ray abundances were taken from LANL data⁶. The weight fractions of the radionuclide concerned was obtained by subjecting a representative sample to isotopic analysis by gamma-ray spectrometry. ^{242}Pu content was obtained from isotopic correlations [6]. The ^{241}Am content reported, is the percentage of ^{241}Am out of total Pu content. Fig. 1 shows the plot of apparent mass vs. $1/E$.

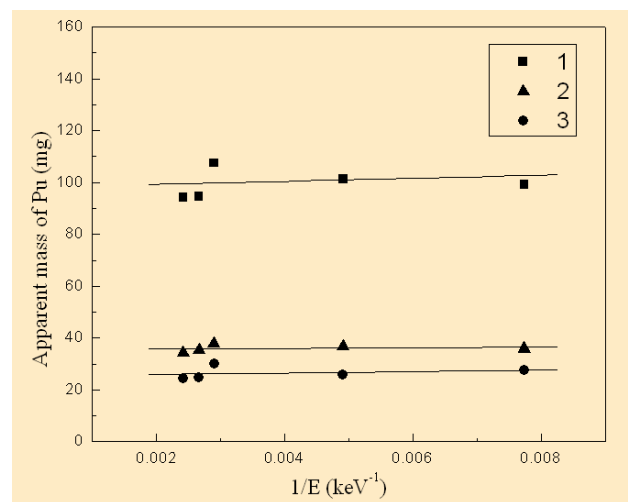


Fig. 1. Apparent mass of Pu as a function of $1/E$ for different samples where E is the γ -ray energy.

The slope of the curve is the measure of self-attenuation within the sample. Higher is the slope of the curve, more is the self-attenuation taking place in the sample. Here, the lines with zero slopes indicate no attenuation within



the sample. These curves were fitted to a functional form as given in Equation 2. The intercept of the fitted curves gives the true mass of the nuclide, monitored and as per Table 1. The error on the intercept gives the error on the measured Pu amounts as given in Table 1.

Table 1: The plutonium amount obtained in different stainless steel samples.

Sample No.	Pu amount (mg)	
	Apparent mass method	Neutron coincidence counting
1	101±6	111±4
2	36±2	39±2
3	27±5	29±2
4	27±3	29±2

The results of apparent mass method have been compared with neutron coincidence counting data (Table 1). The error on the Pu amounts is the propagated error of the real and accidental coincidence count rate. It can be seen, that the results by both the methods for all the four samples are within 10%. This shows the reliability of the apparent mass method for any sample with nonstandard source geometry and unknown source distribution.

Conclusion

In nondestructive assay of nuclear materials, often voluminous samples having nonstandard shapes, sizes and matrices are encountered. Matrix corrections for this type of samples are difficult. Apparent mass method can provide a reasonably good assay result in such cases provided the nuclides to be estimated have multiple gamma rays and the sample is not infinitely thick for those gamma rays.

References

1. Venkataraman R, Croft S (2003) *Nuclear Instruments & Methods in Physics Research A* 505:527.
2. Agarwal C, Poi S, Nathaniel TN, Mhatre A, Kalsi PC, Singh S and Goswami A (2007) *Journal of Nuclear Materials* 651: 386.
3. Agarwal C, Kalsi PC, Mhatre A and Goswami A (2007) *Applied Radiation and Isotopes* 65: 1386-1388.
4. Mukhopadhyaya PK (2001) Proceedings of Symposium on Intelligent Nuclear Instrumentation, Mumbai, 307.
5. Tripathi R, Tomar BS, Reddy AVR, Manohar SB and Murlidhar S (2002) BARC/2002/I/009.
6. Reilly D, Ensslin N, Smith Jr, Kreiner H (1991) Los Alamos National Laboratory, United States.



Catalytic decomposition of sulfuric acid over Fe_2O_3 and $\text{Pt}/\text{Al}_2\text{O}_3$: A comparative study

A.M. Banerjee, A.R. Shirole, M.R. Pai, A.K. Tripathi,
S.R. Bharadwaj and D. Das
Chemistry Division

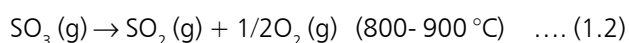
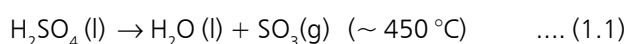
This paper received the Best Paper Award (II prize), at the International Symposium on Materials Chemistry (ISMC-2010), held at Mumbai, during December 7-11, 2010

Abstract

The catalytic activities of Fe_2O_3 and $\text{Pt}/\text{Al}_2\text{O}_3$ were compared for sulfuric acid decomposition reaction. In the temperature-dependent catalytic activity runs, it was found that at lower temperatures in the range of 725 – 750 °C, the SO_2 yield for the supported noble metal catalyst, was found to be higher than that of Fe_2O_3 while at higher temperatures in the range of 800 – 825 °C, the catalytic activities of the two catalysts were comparable. Both the spent catalysts and the fresh catalysts were characterized by XRD and FTIR, to evaluate any structural or surface modifications of the catalysts, due to their use in sulfuric acid decomposition at high temperatures. The investigation reveals that, Fe_2O_3 can be a good substitute for noble metal catalysts for sulfuric acid decomposition reaction, at temperatures of 750 °C and above.

Introduction

Large scale generation of hydrogen from water via thermochemical cycles or high temperature steam electrolysis employing nuclear/solar heat, appears to be promising options to meet the increasing global energy demands, without emitting green house gases. Owing to its higher efficiency (~47%) and other advantages, S-I (Sulfur–Iodine) cycle is widely considered as a preferred choice, among various thermochemical cycles, proposed for hydrogen generation via water-splitting¹. Decomposition of sulfuric acid is the most energy-demanding step of S-I thermochemical cycle and the efficiency of the cycle largely depends on the kinetics of this step. The sulfuric acid decomposition is comprised of the following two reactions in series:



Sulfuric acid can be decomposed to its anhydride SO_3 (Eqn.1.1) without a catalyst, while the decomposition of SO_3 (Eqn.1.2) has been known to be a catalytic reaction. Research on newer catalysts is vital from the view point of understanding the fundamental surface phenomenon and finally the development of active and stable catalysts, under high temperature and acid environments.

Various catalysts reported to be active for decomposition of sulfuric acid include noble metals, metal oxides and mixed metal oxides². Both the activity and the stability of the catalyst are very important, as the reaction environment is extremely hostile like high temperatures, presence of aggressive chemicals, including sulfur oxides, high temperature steam and oxygen. While noble metal catalysts are highly active for SO_3 decomposition reaction, loss of active metal has been reported during their long term use³. Earlier results from our laboratory have shown



effectiveness (chemical and thermal stability and high catalytic activity) of iron-oxide based catalysts, for decomposition of sulfuric acid⁴. In the present study, we compare the catalytic activities of iron oxide with a commercial Pt (1 wt.%) / Al₂O₃ catalysts, for decomposition of sulfuric acid in the temperature range of 700 °C to 825 °C.

Experimental

The Fe₂O₃ catalyst was prepared by precipitation method, using ferric nitrate as iron source and ammonia as the precipitating agent. The resulting precipitate was washed, dried in an air oven at 120°C and calcined in air at 750°C for 4 h. Calcined product was characterized using XRD, FTIR and N₂-BET surface area techniques. Sulfuric acid decomposition experiments were carried out in an indigenously developed flow, through quartz catalytic reactor as shown in Fig. 1. In a typical experiment, the powder catalyst sample (200 mg, 75 - 100 μ size) was loaded into the reactor at room temperature and a flow of nitrogen carrier (HP) at a rate of 40 ml min⁻¹ was initiated. The furnace temperature was increased to 700 °C, over a time interval of 1 h. Concentrated sulfuric acid was then pumped into the system (~ 25 g acid g⁻¹ h⁻¹) by syringe pump and it was carried by the carrier gas to the pre-heater, where the acid vaporized and then finally decomposed to SO₂, O₂ and H₂O over the catalyst bed. The unreacted SO₃ recombined with H₂O in the condenser downstream and was collected as a liquid solution. The gaseous SO₂ and O₂ products along with the carrier were passed through a NaOH solution, where SO₂ was trapped and the other gases (O₂ and N₂) were vented. For analysis of product SO₂, the decrease in concentration of the NaOH solution was measured by titration, with standardized sulfuric acid solution. Similarly, the unreacted sulfuric acid collected downstream of the reactor was determined by chemical titration, with standardized NaOH solution. The percentage conversion of sulfuric acid to sulfur dioxide was calculated based on the product yield of SO₂. The catalytic activities were measured in the temperature range 700 - 825 °C, at an interval of 25°C after equilibrating for ~ 1 h at each temperature.

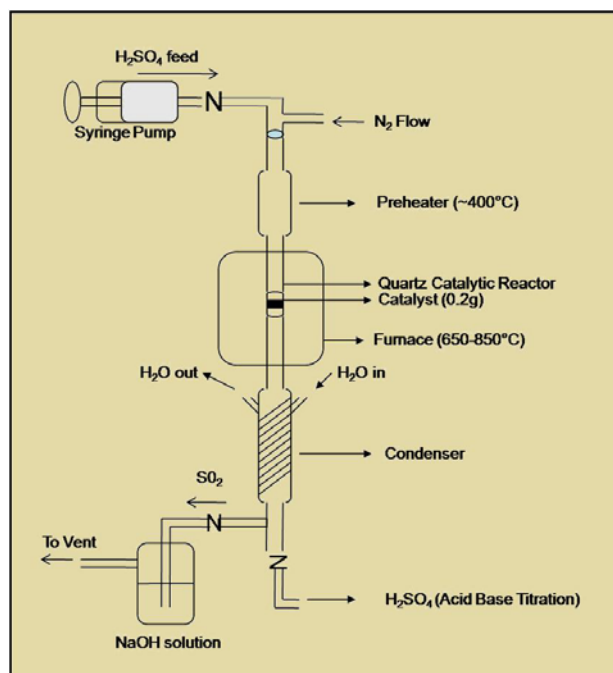


Fig. 1: Block diagram of the quartz experimental set up for carrying out sulfuric acid decomposition reaction

Results and Discussion

The temperature-dependent catalytic activity of the Fe₂O₃ and Pt (1 wt.%) / Al₂O₃ catalysts are shown in Fig. 2. Catalytic activity of both the samples increases with temperature, Fe₂O₃ showing maximum conversion of ~ 79% at 825 °C. At lower temperatures in the range of 725 – 750 °C, the SO₂ yield for the supported noble metal catalyst was found to be higher than that of Fe₂O₃, while at higher temperatures in the range of 800 – 825 °C, the catalytic activities of the two catalysts were comparable. It is pertinent to mention here, that blank experiments in the absence of catalysts verified that homogeneous vapor phase reaction did not occur under these conditions. Thus, Fe₂O₃ can be a good substitute for noble metal catalysts for sulfuric acid decomposition reaction at temperatures of 750 °C and above. Since the operation temperatures of the high temperature nuclear reactors would be high (>800 °C), Fe₂O₃ can be considered as a suitable catalyst for sulfuric acid decomposition. After two such temperature-dependent catalytic activity runs, the spent catalysts were collected and characterized by XRD and FTIR and compared

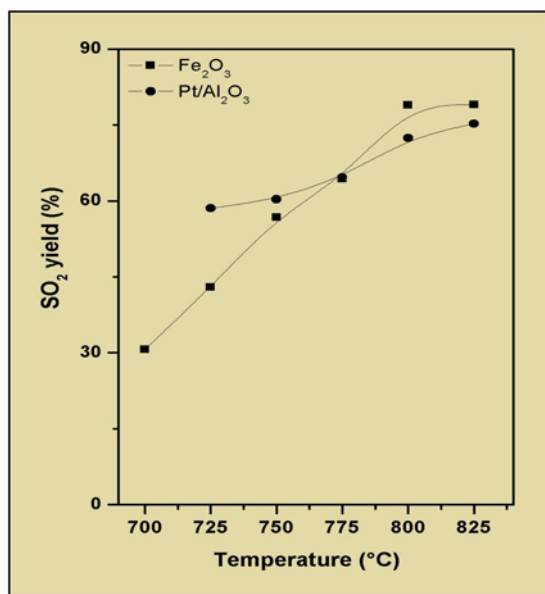


Fig. 2: Temperature dependent catalytic activities of iron oxide and noble metal catalyst for sulfuric acid decomposition reaction

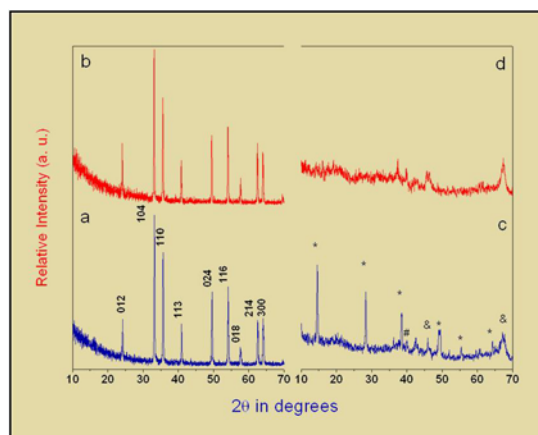


Fig. 3: Powder XRD patterns of (a) fresh Fe₂O₃ and (b) used Fe₂O₃ and (c) fresh Pt/Al₂O₃ and (d) used Pt/Al₂O₃ samples in catalytic sulfuric acid decomposition reaction Fe₂O₃ – (JC-PDS card No. 33-0664 hematite); * - AlO(OH) phase JCPDS card No.21-1307; &- $\bar{\alpha}$ -Al₂O₃ phase JCPDS card No.29-0063; # - Pt phase JCPDS card No. 04-0802

with the fresh catalysts to evaluate any structural or surface modifications of the catalysts, due to their use in sulfuric acid decomposition at high temperatures.

The N₂-BET surface area of the fresh Fe₂O₃ and Pt/Al₂O₃ samples were 17 m²g⁻¹ and 290 m²g⁻¹, respectively. The XRD patterns of the fresh and used catalyst samples are shown in Fig. 3. The XRD pattern of the fresh Fe₂O₃ sample, matches with the α -Fe₂O₃ or hematite phase (JC-PDS card No. 33-0664 hematite). From the XRD pattern of the spent Fe₂O₃ catalyst collected after the reaction, it is evident that there is no change in phase and neither is there any formation of other phases. Thus, the oxide catalyst retains its structural integrity during the course of the sulfuric acid decomposition reaction. On the other hand, the XRD of the fresh Pt/Al₂O₃ catalyst exhibited AlO(OH), $\bar{\alpha}$ -Al₂O₃ and Pt phases (marked in the fig) while the spent catalyst was less crystalline and showed only $\bar{\alpha}$ -Al₂O₃ phase as seen in Fig. 3c and 3d.

A comparison of the FTIR spectra of the fresh and spent catalyst samples is shown in Fig. 4. The prominent infrared absorption bands (cm⁻¹) for fresh Fe₂O₃ are observed at 479 and 560 cm⁻¹ while a weak IR band appeared at 440

cm⁻¹. In contrast, in the used catalyst sample, the two dominant bands and the weak band coexist at the same peak position. In addition to the characteristic peaks due to Fe₂O₃, there are four prominent peaks in the range of 1000–1200 cm⁻¹ which is an indication of C_{2v} symmetry and bidentate sulphate coordination, because a clear distinction between monodentate and bidentate coordination can be made, based on the number of observed bands (monodentate, C_{3v}, with three bands, and bidentate, C_{2v}, with four bands). The peaks arise due to SO bond stretching in metal sulfates with the lowest wave

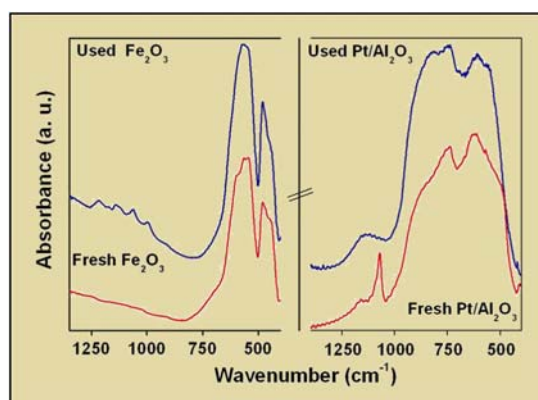


Fig. 4: FTIR spectra of the fresh and spent Fe₂O₃ and Pt/Al₂O₃ catalysts

Merit Award



number peak assigned to $\bar{\nu}_1$ stretching mode while the higher three peaks are due to $\bar{\nu}_3$ mode. Thus, the FTIR spectra of the spent catalyst samples, confirm the presence of bidentate sulfates species. These metal sulfates are probably the transient intermediates of sulfuric acid decomposition to sulfur dioxide, over these metal oxide catalysts. In the case of Pt/Al₂O₃, the spent catalysts does not show any evidence of sulfates.

From the comparison between the thermal analyses of metal sulfates and the activity of the corresponding metal oxides reported earlier in our work^{4,5}, we suggest, that the metal sulfate decomposition should be considered as the rate determining step for SO₃ decomposition. The presence of sulfate species on the used oxide samples is in agreement with the above hypothesis. On the other hand, it is reported⁶, that sulfur trioxide decomposition proceeds over Pt/Al₂O₃ through a different mechanism - adsorption and dissociation of SO₃ at the surface active sites, which are the active noble metal centre via the intermediate formation of adduct [SO₂.O] on the metal centre.

Conclusion

The catalytic properties of Fe₂O₃ and Pt/Al₂O₃ are compared for sulfuric acid decomposition reaction. At lower temperatures in the range of 725 – 750 °C, the SO₂ yield for the supported noble metal catalyst was found to be higher while at higher, temperatures in the range of 800 – 825 °C the catalytic activities of the two catalysts were comparable. The Fe₂O₃ catalyst retained its phase in the course of the reaction, while AlO(OH) phase present in the fresh Pt/Al₂O₃ catalyst disappeared after use in the decomposition. FTIR spectra suggest the formation of metal sulfates on the spent Fe₂O₃ samples, while spent Pt/Al₂O₃ catalysts do not show any evidence of sulfates. This along with the thermal decomposition data of the metal sulfates, suggested the formation and dissociation of metal sulfates as the probable mechanism over iron oxide catalysts, while a different mechanism is reported for SO₃ decomposition over Pt/Al₂O₃ catalyst. The investigation reveals that, Fe₂O₃ can be a good substitute

for noble metal catalysts, for sulfuric acid decomposition reaction at temperatures of 750 °C and above.

References

1. Brown L.C., Funk J.F., S.K. Showalter. GA report (GA-A23373).
2. O'Keefe D.R., Norman J.H., Williamson D.G. .*Catal. Rev. Sci. Eng.* 22 (1980) 325.
3. Petkovic L. M., Ginosar D. M., Rollins H. W., Burch K. C., Pinhero P. J., Farrell H. H. . *Appl. Catal. A*, 338 (2008) 27-36.
4. Banerjee A. M., Pai M. R., Bhattacharya K., Tripathi A. K., Kamble V. S., Bharadwaj S.R., Kulshreshtha S.K. .*Int. J. Hydrogen Energ.* 33 (2008) 319-326.
5. Banerjee A. M., Pai M. R., Meena S. S., Tripathi A. K., Bharadwaj S. R. . *Inter. J. Hyd. Energ.* 36, (2011) 4768-4780.
6. Golodates G. I. .Heterogeneous catalytic reaction involving molecular oxygen. Elsevier Science Publisher.



Chemical compatibility between U-6wt.%Zr alloy and T91 cladding

Santu Kaity, T.R.G. Kutty and Arun Kumar
Radiometallurgy Division

and

Renu Agarwal
Product Development Division

and

A. Laik
Materials Science Division

and

H.S. Kamath
Nuclear Fuels Group, BARC

This paper received the Best Poster Award at the 9th International Symposium on Materials Chemistry (ISMC 2010), held at BARC, Mumbai, during December 7-11, 2010

Abstract

Fuel-Clad Chemical Interaction (FCCI) is recognized as one of the major concerns for metallic fuels because of formation of low melting eutectic. The measured eutectic temperature between U-6wt.%Zr alloy and T91 steel was found to be almost similar to that of U-Fe system, i.e. 722°C. Addition of 6wt.% Zr in uranium and presence of alloying elements of T91 steel i.e. Cr, Mo, V, Nb etc. will not have significant effect on eutectic temperature. The interdiffusion between U-6wt.%Zr and T91 at 700°C resulted in formation of (U,Zr)(Fe,Cr)₂, Zr-rich and Zr-depleted layers at the interface, whereas at 750°C, reaction between these two caused eutectic melting and resulted in the formation of U₆Fe, U(Fe,Cr)₂ and Zr(Fe,Cr)₂ phases.

Introduction

Metallic fuel is considered for future Fast Breeder Reactors (FBRs), due to its high breeding potential, high thermal conductivity, high fissile and fertile atom densities, low doubling time and ease of fabrication as compared to other ceramic fuels¹. However, a few shortcomings of metallic fuels such as, low solidus temperature, high swelling rate and susceptibility to chemical and mechanical interaction with cladding materials, prevent them from achieving their full potential. Primarily, two design concepts have been proposed for the metallic fuel development programme for FBRs in India². One of them

is based on sodium bonded ternary U-15Pu-6Zr (composition in wt.%) alloy with T91 grade steel clad, and the other consists of binary U-15Pu alloy, mechanically bonded to T91 clad with a Zr liner between the fuel and clad. The schematic diagrams of cross-sections of conceptual fuel pin design, are shown in Fig. 1. Uranium, U-6Zr alloy are the proposed blanket materials. T91 cladding material is a 9Cr-1MoVNb steel, having ferritic-martensitic structure. In contrast to austenitic alloy steels, ferritic steels have the advantage of greater resistance to void swelling. T91 steel exhibits high mechanical strength,

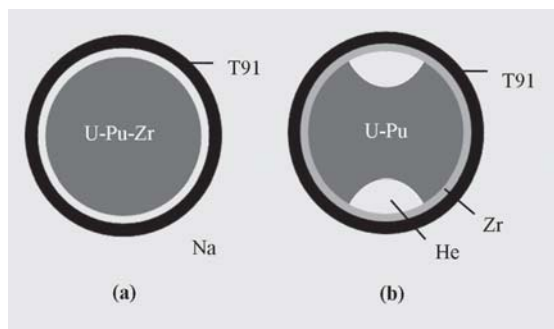


Fig. 1: Schematic diagram of cross sections of the proposed fuel pin design for fast reactors: (a) U-Pu-Zr ternary and (b) U-Pu binary metallic fuels.

and combines low thermal expansion with high heat conductivity³.

The chemical compatibility between fuel and clad material also known as Fuel-Clad Chemical Interaction (FCCI) is of prime importance, because of formation of low melting eutectic, which may sometime limit the life of the fuel pin, in a reactor. In the present investigation, chemical compatibility between U-6Zr alloy and T91 cladding has been studied, by measuring eutectic temperature by Differential Scanning Calorimeter (DSC), followed by diffusion couple experiments at 700°C and 750°C for heating upto 500 hrs.

Experimental

The purities of starting materials, uranium and zirconium, were 99.9% and 99.95%, respectively. U-6Zr alloy samples were prepared by following injection casting route. T91 grade steel was supplied by Larsen & Toubro. The heat treatment for T91 consists of austenization at 1050°C and air quenching followed by tempering at 750°C for 1 h.

Eutectic reaction measurement between U-6Zr and T91

For measuring the eutectic reaction temperature between U-6Zr and T91, U-Zr-T91 alloy (having 82 wt.% U, 5 wt.% Zr) was prepared by arc melting of U-6wt.%Zr and T91, in a highly purified helium atmosphere, on a water-cooled copper hearth. U-Fe alloy was (having 90 wt.% U) was also prepared to compare with the U-Zr-T91 alloy. The alloy samples were further heated at 700°C in high purity

argon atmosphere, to obtain perfect homogeneity. The eutectic temperature measurements were carried out, using a heat flux type Differential Scanning Calorimeter (DSC). The heating and cooling rates were programmed at 1 K/min. After the melting experiment, the microstructures of the polished samples were examined by Scanning Electron Microscope (SEM) and Energy Dispersive Spectroscopy (EDS).

Diffusion couple experiment between U-6Zr and T91

U-6Zr alloy and T91 steel were cut into small discs and then the surfaces of all these discs were polished using 1 μm diamond paste. The diffusion behaviour between U-6Zr and T91 was studied by diffusion couple experiment of U-6Zr/T91, where a disc of U-6Zr alloy was sandwiched between two discs of T91. These 'sandwiches' were kept inside a fixture made of Inconel 600 alloy. Ta foil was used to prevent any reaction between samples and fixture. The fixtures containing these samples were encapsulated in quartz tube under helium gas. The diffusion couples were annealed in a resistance heating furnace maintained at 700 and 750°C for up to 500 h. Subsequent to annealing, the couples were sectioned using a slow speed diamond cutting wheel. The exposed cross sections were polished to 1 μm surface finish. The extent of reaction and phases formed at the interface were analyzed by SEM/EDS. Further microstructural characterization was carried out using CAMECA SX-100 Electron Probe Micro-Analyzer (EPMA) equipped with Wavelength Dispersive Spectrometer (WDS).

Results and Discussion

Eutectic temperature

The DSC curves for different alloy compositions are shown in Fig. 2 indicating the eutectic reaction temperatures. The measured eutectic temperature between U-6Zr alloy and T91 was found to be 722°C, which is almost equal to that of U-Fe system. The results indicated that fuel-clad eutectic temperature was not changed with the addition of 6wt.% Zr in the fuel. Similarly, alloying elements of T91 grade steel i.e. Cr, Mo, V, Nb etc. have no

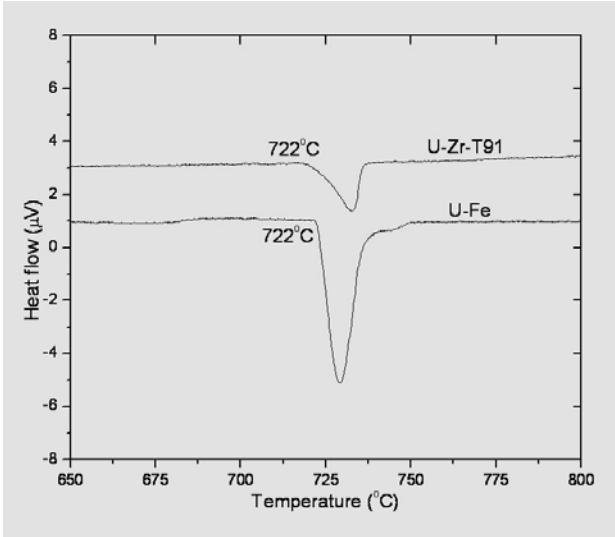


Fig. 2: DSC curve of U-Fe and U-Zr-T91 alloy showing eutectic reaction temperature.

remarkable effect on the eutectic temperature. These results concluded that the main contributors to the fuel-clad eutectic reaction are U of the fuel and Fe of the cladding. U-Fe alloy has the lamellar microstructure of U_6Fe (bright phase) and UFe_2 (dark phase) as shown in the Back Scattered Electron (BSE) micrograph (Fig. 3a). The BSE image as shown in the Fig. 3b reveals that the microstructure of U-Zr-T91 system is much different from the layered structure, as observed in case of U-Fe system.

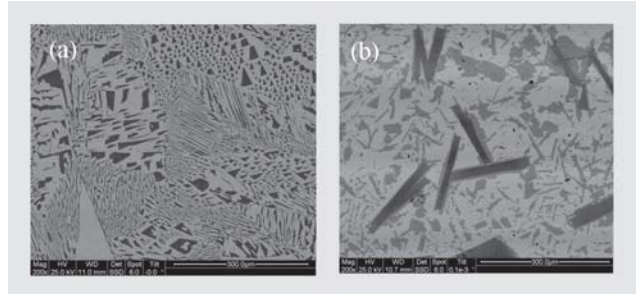


Fig. 3: Back-scattered electron (BSE) images of (a) U-Fe alloy (b) U-Zr-T91 alloy showing eutectic melted microstructure

The BSE image shows that three phases are formed in the alloy; bright matrix phase (U_6Fe), grey ($U(Fe,Cr)_2$) and a dark phase ($Zr(Fe,Cr)_2$). Zr has limited solubility in $U(Fe,Cr)_2$ and U has limited solubility in $Zr(Fe,Cr)_2$.

Diffusion behavior of U-6Zr and T91

Figs. 4(a-b) show the SEM micrographs of the reaction layer formed at the interface between U-6Zr and T91 after annealing at 700°C for 500 h. The intensity profile of U-Mα, Zr-Lα, Fe-Kα, Cr-Kα x-ray lines recorded across the interface, along the line AB is shown in Fig. 4(c). The interdiffusion between the two specimens resulted in the formation of three different layers at the interface: a diffusion reaction layer of thickness around 10 μm, a thin Zr-rich layer of thickness 2-3 μm and a Zr depleted layer of 15-20 μm. The formation of such diffusion layer can

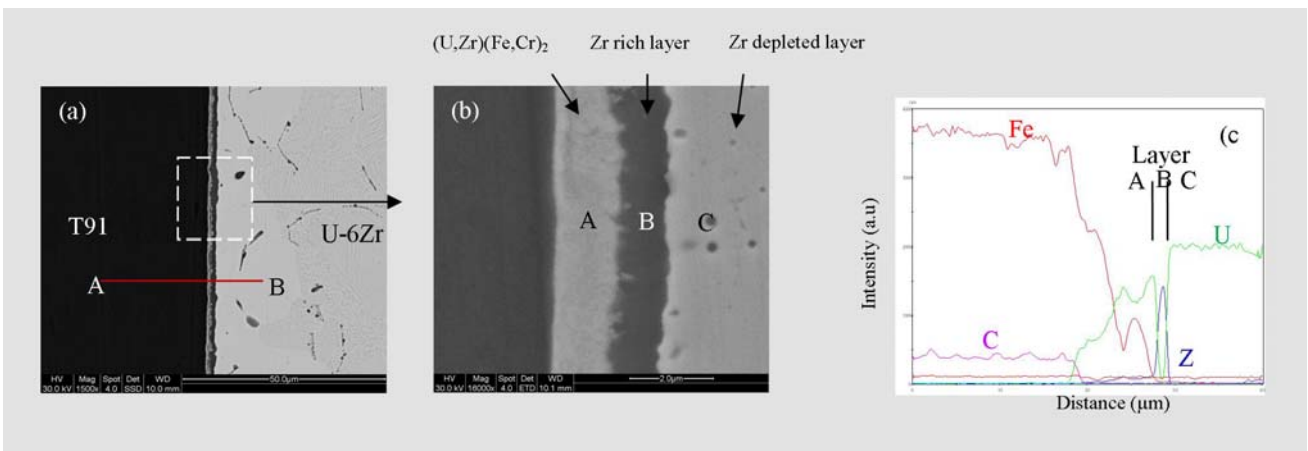


Fig. 4: (a) BSE micrograph of diffusion couple of U-6Zr/T91 annealed at 700°C for 500 h, (b) Magnified micrograph of the interface, (c) Intensity profiles of U-Mα, Zr-Lα, Fe-Kα and Cr-Kα x-ray lines along the line AB marked in Fig. 4(a) across the interface of U-6Zr/T91 diffusion couple annealed at 700°C for 500 h.



easily be explained with the help of the mechanism given by Hofman et al.¹. Zr diffuses out of U-Zr alloy due to its affinity for nitrogen on the surface. Due to the sluggish nature of diffusion reaction between Zr and Fe⁴, this Zr cannot react with T91 steel. Thus there is a Zr rich layer (layer B, Fig. 4b) on the surface and a Zr depleted inner zone (layer C) to maintain mass balance of Zr element. However, due to strong interaction of U with Fe of T91 steel, some uranium diffuses through this Zr-rich layer and comes in contact with Fe of the steel. This results in formation of a U-Fe layer (layer A) closer to T91 and outside Zr-rich layer. This outermost layer (layer A) has small amount of Cr and Zr, forming (U,Zr)(Fe,Cr)₂ with ~ 10 at.% Zr and ~ 5 at.% Cr. The Zr rich layer acts as a barrier, by reducing the penetration of Fe and Cr elements through it towards fuel lattice. Therefore, amount of Fe and Cr in layer C are negligible.

When the annealing temperature was increased to 750°C, eutectic-melted microstructure was observed as shown in Fig. 5 and they were much different from the layered structures formed below the eutectic temperature. The bright phase was identified by EDS as U₆Fe, the grey and dark phases are U(Fe,Cr)₂ and Zr(Fe,Cr)₂, respectively. The results indicate that the measured eutectic temperature between U-6Zr and T91, is very crucial from reactor safety point of view. In any case, if the clad temperature reaches

above the eutectic temperature, the direct contact of U-6Zr and T91 cladding would cause eutectic melting, as observed in this diffusion couple experiment.

References

1. G.L. Hofman, L.C. Walters, *Mater. Sci. Technol.* 10A (1994) 3.
2. B. Raj, *J. Nucl. Mater.* 385 (2009) 142.
3. R.L. Klueh, A.T. Nelson, *J. Nucl. Mater.* 371 (2007) 37.
4. K. Bhanumurthy, G.B. Kale and S.K. Khera, *J. Nucl. Mater.* 185 (1991) 208.

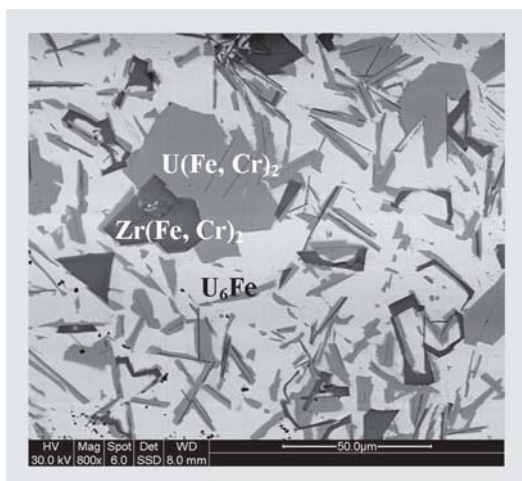


Fig. 5: BSE micrograph of the diffusion couple U-6Zr/T91 annealed at 750°C for 100 h.



Coincidence Doppler broadening studies of as grown CdSe nanoparticles

S.K. Sharma, P.K. Pujari, K. Sudarshan and P. Maheshwari

Radiochemistry Division

and

C.P. Shah, K.K. Singh, M. Kumar and P.N. Bajaj

Radiation and Photochemistry Division

This paper received one among the Best Poster Award at the 3rd Asia Pacific Symposium on Radiation Chemistry and DAE-BRNS 10th Biennial Trombay Symposium on Radiation & Photochemistry, held at Lonavala, during September 14-17, 2010

Abstract

Poly Vinyl Alcohol (PVA) capped CdSe nanoparticles, having size in the range of 7 - 17 nm, have been synthesized through chemical route and characterized, using X-Ray Diffraction (XRD) and Transmission Electron Microscopy (TEM). Positron Coincidence Doppler broadening (CDB) measurements have been carried out in these nanoparticles. It is observed that the electron momentum distributions, show a variation in the core electron momentum region with the particle size. In order to examine the influence of defects, first principle calculations of electron momentum distributions in bulk CdSe and in the presence of Cd as well as Se vacancy defects, have been performed. Comparison of experimental data with the calculated momentum distribution reveals the presence of Cd vacancy defects, the concentration of which decreases with increase in particle size. The present study also indicates possible Se enrichment on the surface of the nanoparticles, with decrease in particle size.

Introduction

CdSe (II-VI semiconductor) nanocrystals can be considered as model systems for colloidal nanocrystals. *Ab initio* calculations on CdSe nanocrystals have shown, that passivating the ligands on the surface does not produce the ideal wurtzite structure of the nanocrystals, and Se atoms relax outwards irrespective of the passivation [1].

Positron annihilation spectroscopy has emerged as a very sensitive technique, to study the outermost layers of nanoparticles [2]. The positrons trapped at the surface annihilate with the electrons of the surrounding atoms and the information about the surface of the nanoparticles can be obtained. In the present study, CDB studies were carried out in CdSe nanoparticles, to gain insight into

their surfaces. To elucidate the effect of vacancy defects on CDB ratio curves, these studies were corroborated with the theoretical calculation of CDB ratio curves.

Experimental

CdSe nanoparticles capped with PVA were synthesized by the chemical reaction of $\text{Cd}(\text{OCH}_2\text{COO})_2$ and Na_2SeO_3 as Cd and Se precursors, respectively. Two dimensional coincidence Doppler broadening spectra were recorded by using a ^{22}Na source and two HPGe detectors in coincidence. All the normalized momentum distribution spectra were analyzed, in the form of ratio curves with respect to Si crystal.



Results and Discussion

The ratio curves of all the CdSe samples, Cd and Se elements are plotted in Fig. 1. In the case of nanoparticles, a peak around $\sim 12 \times 10^{-3} m_0c$ having contributions from Cd (4d) and Se (3d) states, appears in all the samples. From the XRD and TEM, the size of the samples (S1, S2, S3 and S4) was calculated as 7, 11.5, 15.5 and 17 nm. It is clear from the figure that, the peak position and the area under the peak vary from sample to sample. The peak position for sample S1 is close to Se. As we go from S1 to S4, it is observed that the peak position shifts to the mid region of Cd and Se. The area under the peak also increases with the peak shifting from the lower to the mid region. This shows, that S1 has more contribution from Se as compared to Cd. It indicates the presence of Cd vacancies in the nanoparticles, where positrons are trapped and annihilate with the surrounding Se atoms. The concentration of the Cd vacancy defects, increases with decrease in the size of nanoparticles. Positrons are trapped at the surface of the nanoparticles where they annihilate with the surrounding atoms. It shows, that sample S1 has a Se rich surface, which is possible due to the outward relaxation of Se atoms in nanocrystals as reported in literature [1].

To investigate the effect of vacancy defects on momentum distribution ratio curves in CdSe, annihilating electron momentum distribution calculation in bulk CdSe supercells, as well as CdSe supercell, having vacancy defects of Cd and Se have been performed using 'MIKA/DOPPLER' package. The ratio curves of CdSe, Cd and Se, with respect to Si obtained from theoretical calculations are plotted in Fig. 2. The theoretical ratio curves for Cd and Se are very much similar to the experimental ratio curves for pure Cd and Se (Figs. 1 and 2). The ratio curves for bulk CdSe is not discernible from Cd in Fig. 2. This shows a very large contribution of Cd electrons as compared to Se electrons for positron annihilation in bulk CdSe. In the bulk CdSe, positron annihilates from the delocalized state, having positron density distributed in the interstitial regions of CdSe lattice. The *d*-electron density reaches far into the interstitial region and the electron density from (Cd) 4*d* state will be much higher than that from (Se) 3*d* state. The calculations show, that the fraction of the positrons annihilating with Cd (4*d* + 3*d*) electrons in pure Cd, is 80.17 % and with Se (3*d*) electrons is 6.32 % in pure Se. Thus, positron electron overlap for Cd electrons (4*d* and 3*d*) is much higher than Se electrons (3*d*) and the ratio curves of CdSe having 88.22 % fraction of positrons

Merit Award

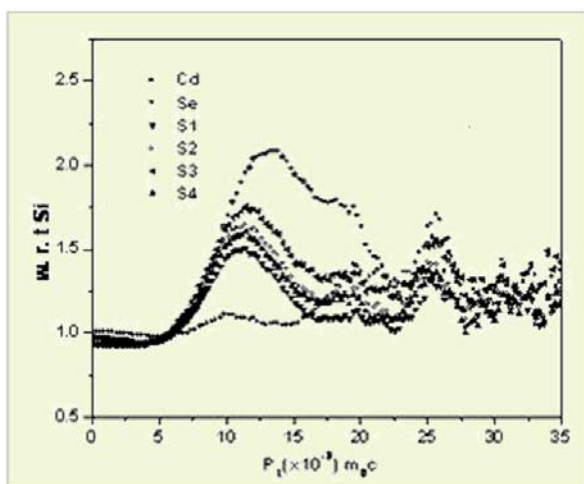


Fig. 1: CDB ratio curves of CdSe nanoparticle samples S1-S4, Cd metal and Se metal

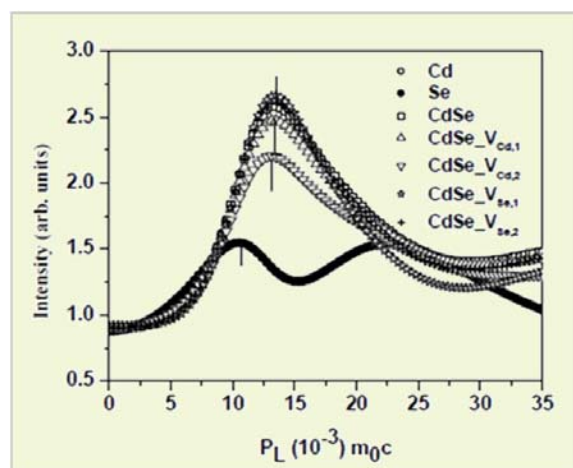


Fig. 2: Theoretically calculated momentum distribution ratio curves for CdSe, Cd and Se



annihilating with ($4d$ and $3d$) is indiscernible from pure Cd in this high momentum range.

In CdSe zincblende lattice, Se atom is surrounded by four Cd atoms and vice versa. In the presence of Se vacancies, positrons are trapped at Se vacancy defects and have maximum overlap with Cd electrons from the surrounding Cd atoms. Fig. 2 shows the ratio curves of CdSe having mono and di vacancy of Se where it is observed that the peak positions of the ratio curves in the presence of Se vacancy are at the same position as of bulk CdSe. This is because, in delocalized state, positrons have maximum overlap with Cd electrons which does not change significantly when the positrons are trapped at Se vacancy defects. When Cd vacancies are present in the CdSe supercell, positrons will be trapped at the Cd vacancy sites and will have maximum overlap with the surrounding Se atoms. This will enhance the contribution from Se electrons ($3d$) and the peak position would shift to lower P_L values as seen in Fig. 2. Due to the same reason, the area under the peak also decreases in the presence of Cd vacancy defects. In the presence of Cd di vacancy, contribution from Se electrons will further increase which shifts the peak position again to a lower value and the area under the peak further decreases. Thus, the presence

of Cd vacancy defects in CdSe lattice, shifts peak position to lower P_L values (towards Se peak position) and reduces the area under the peak (more contribution from Se electrons).

Conclusion

Electron momentum distributions in CdSe nanoparticles are seen to have a strong dependence on the size of the nanoparticles. Theoretical calculations show, that in bulk CdSe, Cd semi core electrons ($3d$ and $4d$) have major contribution in high momentum region. Comparison of experimental and theoretical ratio curves strongly suggests, that Cd vacancies are predominantly produced in CdSe nanoparticles during synthesis, the concentration of which reduces with increase in particle size. This study also provides an evidence of Se enrichment of the surface of CdSe nanoparticles, with decrease in particle size. .

References

1. A. Puzder, A. J. Williamson, F. Gygi, G. Galli, *Phys. Rev. Lett.*, 92, 217401 (2004).
2. S. W. H. Eijt, A(Tom) van Veen, H. Schut, P. E. Mijnders, A. B. Denison, B. Barbiellini, A. Bansil, *Nature materials*, 5, 23 (2006).



Depth Profile of Polychlorinated Biphenyls in Sediment Core from Thane Creek Area of Mumbai, India

S.K. Sahu, G.G. Pandit and V.D. Puranik
Environmental Assessment Division

This paper received the Best Poster Award at the International Symposium on Trace Organic Pollutants in the Environment, held at Bharathidasan University, Tiruchirapalli, Tamilnadu, India, on January 23, 2010

Abstract

In recent years there has been a growing concern all over the globe, about marine pollution due to persistent organic pollutants. Sediments, which are an important component of marine environment can serve as sorbents or concentrators for various persistent organic pollutants, including Polychlorinated Biphenyls (PCBs). In this study, the depth profile of accumulated PCBs in Thane Creek sediments of Mumbai, India was examined. The sediment core samples were collected using a gravity corer, processed & analysed for different PCB congeners. The surface segment showed the downward trend for these compounds, indicating a slow phase out of PCBs after the ban. The concentration and composition of different homologues vary at different depths.

Introduction

Ocean, seas and coastal areas form an integrated and essential component of the Earth's ecosystem. The sea receives the brunt of human waste, whether it is by deliberate dumping or by natural runoff from the land. Almost 80% of pollution comes from land-based activities and many pollutants are deposited in coastal water. The marine sediments act like sinks for most of the pollutants entering the aquatic environment. It becomes more critical in the case of creek ecosystem due to its landlocked and relatively stagnant nature. In recent years, there has been an increasing concern in persistent organic pollutants such as polychlorinated biphenyls (PCBs), dioxin, polycyclic aromatic hydrocarbons (PAHs) etc. in the aquatic environment. PCBs are ubiquitous in the environment due to their atmospheric transport in spite of the fact that they are not very volatile. Once released into the aquatic

environment, PCBs readily adsorb to particles and are then incorporated into the sediment due to their low water solubility and hydrophobic nature. Accumulation of PCBs in sediment, depends on sediment type. Sediments with high organic carbon content and a smaller particle size accumulate more pollutants as compared to coarser sandy sediments. The deposition of these particles in sea can lead to an accumulation of PCBs in the sediment. Sediments can serve as sorbents or concentrators for various inorganic and organic chemicals (Geostandards Newsletter, 1992).

In the present study, an attempt has been made to find the concentration of different PCB congeners at different depths in the Thane Creek sediment. The vertical distribution of PCBs in sediment could reflect the geochemical history of a given region, including changes due to anthropogenic releases into the system. Characterizing the chemical nature of the PCB congeners



may make it possible to suggest a potential contamination source. In this study, an attempt has also been made to find different possible sources contributing to the measured concentration of PCBs, using receptor modeling technique.

Materials and Method

The sediment core samples were collected using a gravity corer, of which inner and outer diameters were 5.2 and 6.0 cm respectively. The length of the core was 88 cm, collected with the help of an adjustable piston rod with silicon packing. The gravity-coring unit was lowered as slowly as possible into the sediments, to prevent lateral motion of the pressure wave created by the descent of the corer. The collected cores were extruded vertically and sliced at 2cm intervals. The collected core samples from the same depth were pooled, homogenized, freeze-dried and used for analysis.

Samples were extracted ultrasonically with n-hexane for 45 minutes. The extracts were then washed with de-ionized water to remove traces of acid. Silica gel column clean up was followed by elution with n-hexane. Extract volume was reduced to 0.5 ml under pure nitrogen flow, prior to analysis by Gas Chromatograph. For identification, the retention data was obtained by analyzing the individual standard. The quality assurance of the measurements was ensured, by analysis of standard reference material IAEA-408 Marine sediment.

Results and Discussion

Twelve PCB congeners were analyzed. The presence of different congeners indicated various sources of PCBs in the marine sediment. Diffusion, degradation and bio-turbation may have caused considerable deterioration of time resolution with the sedimentation rate. The concentration and composition of different congeners varied with depth and is given in Table 1. CB 180 was the predominant congener at the surface (0-12 cm segment) followed by CB 28, CB 44 and CB 52. At 13-24 cm depth, concentration of CB 28 (23.75 ng/g) and CB 52 (5.66 ng/g) was considerably high compared to other congeners. CB 44 and CB 28 were the predominant ones at 25-36 cm depth while the 49-60 segments showed higher concentrations of CB 52 and CB 44. In the deep sediment, the tetrachlorobiphenyls and trichlorobiphenyls contributed the most, towards the total PCBs. The vertical profile of different PCB congener concentrations in the core samples depicted a gradient from top to bottom, which indicated the influence of industrial contributions over the period (Fig.1). A sharp distinctive change suggested input from a source whereas gradual change indicated weathering. The percent contribution of different congeners is a very good indicator of processes like degradation, diffusion, accumulation etc., which drives the distribution of these congeners at different depths. When PCBs are stored in sediments for a prolonged period

Table 1: Concentration of different congeners at various depths

Depth (cm)	Concentration of PCB Congeners (ng/g)								
	CB 18	CB 28	CB 52	CB 44	CB 101	CB 180	CB 153	CB 126	CB 138
0-12	0.14	0.47	0.21	0.47	0.10	0.64	0.01	0.17	0.11
13-24	0.01	23.75	5.66	0.42	0.28	0.87	0.08	0.11	0.26
25-36	0.14	0.79	0.17	1.29	0.26	0.62	0.05	0.09	0.04
37-48	0.22	0.13	0.08	0.30	0.09	0.18	0.11	0.02	0.02
49-60	0.04	0.69	1.04	0.86	0.40	0.18	0.10	0.15	0.07
61-72	0.02	0.89	0.31	0.08	0.14	0.06	0.01	0.04	0.10
73-88	0.01	0.56	0.69	0.13	0.01	0.17	<0.010	<0.015	0.06

Merit Award

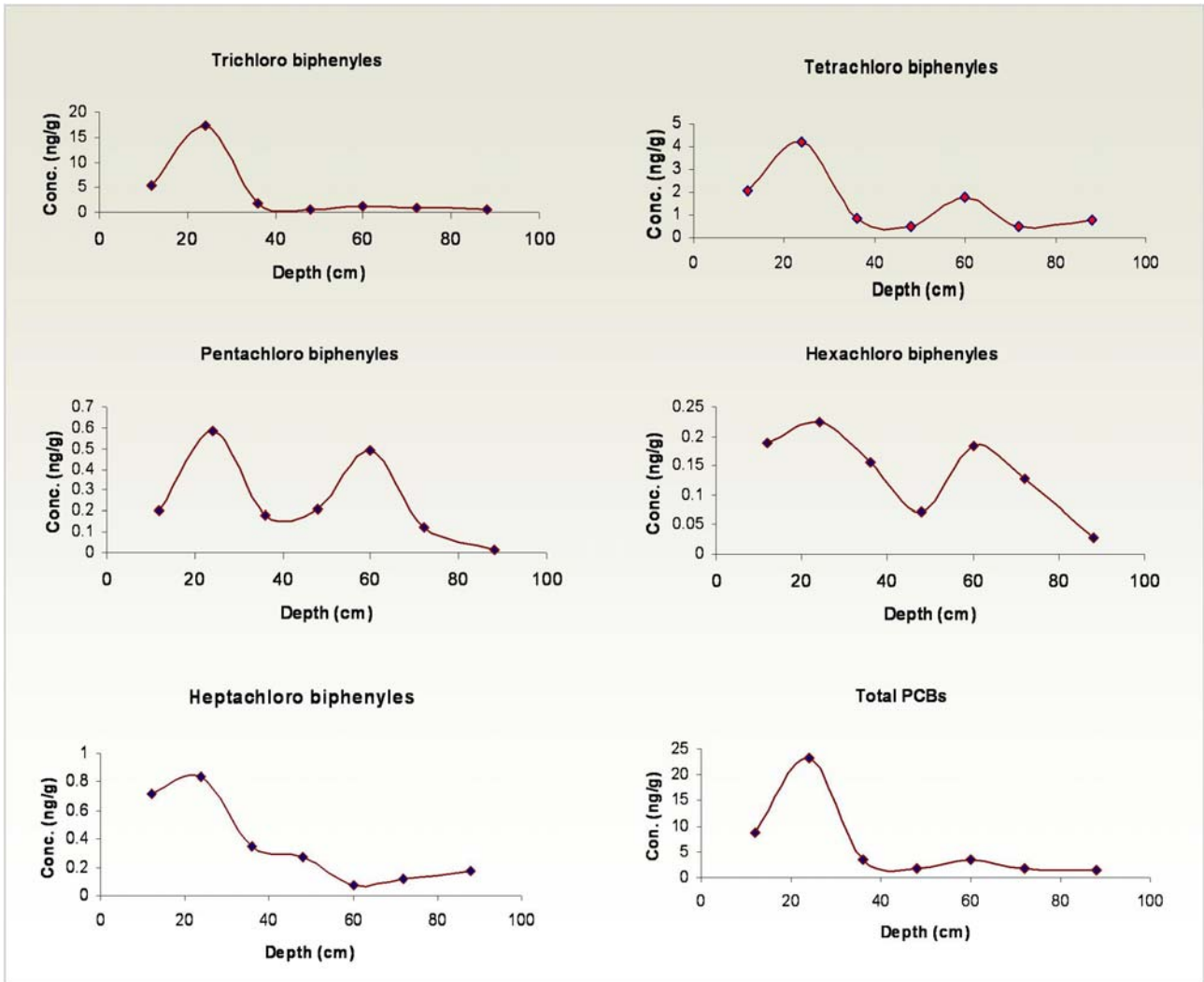


Fig. 1: PCB Concentration profile with depth

of time, they are subjected to biodegradation by bacteria. The process, along with other physico-chemical processes that change the composition of PCB congeners is called weathering. The longer the period, more change in composition is observed. Anaerobic conditions are best for decomposition of more chlorinated PCBs and Aerobic conditions are for less chlorinated PCBs. Anaerobic degradation in sediments would lead to the formation of less chlorinated congeners that are more mobile and would diffuse into overlying aerobic waters. The degradation decreases with increase in chlorination.

At the surface, concentration of the PCB congeners showed a downward trend, which indicated the phasing out of these compounds. The concentrations have been

reported to be slowly decreasing since their complete ban in the late seventies. Significant decrease was observed for tri, tetrachlorobiphenyles as compared to hexa and heptachlorobiphenyles. Phasing out of penta and hexachlorophenyles was more gradual than the tri and tetra congeners, while heptachlorobiphenyles with the high chlorination and low mobility were resilient to the phasing out processes. There was a decrease in the percent contribution of trichlorobiphenyles from 76% to 26%. This decrease in percent composition of trichlorobiphenyles contributed to an increase in percent composition of other homologues in all the segments. Another peak, though less in magnitude, was observed at the depth of 49-60 cm. Fresh input of compounds from this commercialization



along with diffusion of these compounds from the overlying layers could have contributed towards the elevated levels of concentration in this segment. The percent contribution of Pentachlorobiphenyles at this depth increased significantly, which could be due to degradation from higher chlorinated congeners as well as from use and manufacture of Aroclor during that period. Anaerobic degradation could be the predominant process in the deep sediment, which reflected the observed pattern. Degradation and other weathering processes helps in the conversions of higher chlorinated congeners to low chlorinated. Congeners that cannot be biodegraded will appear to be enriched, meaning that there will be an increase in percent composition but not in concentration. Low concentration of PCBs in the deep sediments, where industrial contribution cannot be the cause, could be due to depositions from the atmosphere, combustion, or biogenic in origin.

References

1. Bazzanti M., Chiavarini S., Cremisini C., and Soldati P., Distribution of PCBs congeners in aquatic ecosystem. A case study. *Environment Int.* 1997, 23(6), 799-813.
2. *Geostandards Newsletter, Special issue, July 1989*, 13, ISSN: 150-5505
3. Harkness, M.R., Mc Dermott, J.B., Abramowicz, D.A., Salvo, J.J., Flangan, W.P., Stephen, M.L., Mandello, F.J., May, R.J., Lobos. J.H., Carroll, K.M., Brennan, M.J., Bracco, A.A., In situ stimulation of aerobic PCB biodegradation in Hudson River Sediments. *Science*, 1993, 259, 503-507.



Functional characterization of a DNA repair polymerase from a radiation resistant bacterium, *Deinococcus radiodurans*.

Nivedita P. Khairnar and Hari S. Misra
Molecular Biology Division

Dr. (Ms.) Nivedita P. Khairnar received the Best Research Paper Award in the Poster session of the International Conference on "Mutagens & Genetic Diversity for Health & Agriculture", Annual Meetings of EMSI-2010, held at Chandigarh, during March 12-14, 2010

Abstract

Cells exposed to DNA damaging agents, produce different types of structural changes in the chromosome. Repair of these lesions requires synthesis of new DNA molecules, catalysed by specific DNA polymerases. A putative DNA polymerase has been characterized, for its role in DNA damage repair and radiation resistance in *D. radiodurans*, a bacterium best known for its extraordinary resistance to γ radiation. Transgenic *Escherichia coli* expressing this protein, showed an improved tolerance to both ionizing and non-ionizing radiations while *D. radiodurans* cells devoid of this protein become sensitive to DNA damage. Molecular studies suggest, this enzyme's involvement in base excision repair, a crucial process requires for correcting the DNA damage due to oxidative stress in all living systems.

Keywords: *Deinococcus*, Base excision repair, DNA strand breaks, radiation resistance

Introduction

Cells exposed to DNA damaging agents like UV and γ radiations, drought, salinity, chemicals and oxidants, produce different types of structural changes in their chromosomes, depending upon the nature of DNA damage. DNA strand breaks produced upon radiation exposure are repaired by a recombination process in bacterial system and also by non-homologous end joining processes, in higher organisms. Different types of nucleotide base damage, produced by chemical and physical mutagenic agents, are repaired by both excision and incision repair mechanisms. The ability of correcting these alterations, differs from organism to organism. Failures to correct these changes lead to mutation, which eventually results either in cell death or in cancer development in mammalian systems. Therefore, organisms

with higher tolerance to DNA damaging agents are believed to have efficient mechanisms for combating the deleterious effects of DNA damage.

Deinococcus radiodurans R1, a bacterium is characterized by its extraordinary tolerance to various kinds of DNA damaging agents, including UV and γ radiations [1, 2]. This bacterium can withstand ~ 6.5 kGy of γ radiation, a dose that can produce nearly 200 double strand breaks and 3000 single strand breaks per genome, without detectable loss of viability [2]. The genome of this bacterium, encodes proteins for different types of excision repairs and recombination repair of DNA strand break [3]. Many of these proteins have been implicated for their roles in the extraordinary radiation resistance of this bacterium. Unlike other bacteria, *Deinococcus* genome



encodes an X family DNA repair polymerase, having highest similarities with eukaryotic DNA polymerase-β[3]. Role of this enzyme has been demonstrated in UV lesion bypass and base excision repair functions in higher organisms. We have characterized this enzyme for its role in radiation resistance and DNA strand breaks repair. Different base excision repair mutant of *E. coli*, expressing DNA polymerase X (*polX*) from *D. radiodurans* became proficient in UVC tolerance as compared to respective untransformed controls. The *polX* mutant of this bacterium was less resistant to both γ and UVC radiations as compared to wild type. Molecular studies characterized this enzyme as a short length polymerase and its role in base excision repair in *D. radiodurans* [4]. A detailed study on various aspects of this enzyme, was presented during the annual meeting of Environmental Mutagens Society of India – 2010 (EMSI-2010) and at the International Conference on “Mutagens & Genetic Diversity for Health & Agriculture, which received the best paper award for poster presentation.

Experimental procedures

Deinococcus radiodurans strain R1 was a generous gift from Dr. M. Schafer [5] and *E. coli* mutants were obtained from Prof. Elzbieta Grzesiuk [7]. *Deinococcus* and *E. coli* were grown in respective nutrient media at 32 °C and 37 °C, respectively. Construction of expression plasmids and

genetic modification of bacterial cells were carried out, using protocols developed in our laboratory and described in [4]. Effect of various DNA damaging agents on cell survival of transgenic *E. coli* was monitored as described earlier [7]. *D. radiodurans* responses to these agents were evaluated as described earlier [8]. Recombinant Polymerase X was purified from transgenic *E. coli* and DNA Polymerase X activity was assayed as described in [9]. The 5’drPLYase activity was measured as detailed in [10], respectively.

Results and Discussion

Role of DNA polymerase X in bacterial resistance to radiations

The *polX* gene was PCR amplified from *D. radiodurans* genome and cloned in pET28a+ followed by in pRadgro [10], a shuttle expression vector works between *E. coli* and *Deinococcus radiodurans*. The recombinant plasmid, pGropoX (Fig 1A), was transformed into *E. coli* AB1157 and its various base excision repair mutant, derivatives and synthesis of recombinant protein along with hexahistidine tag, was ascertained by immunoblotting with (his)6 antibodies (Fig 1B). Genetically engineered *E. coli* cells expressing deinococcal-DNA polymerase X showed improved tolerance to UVC radiation (Fig 1C), indicating the role of this DNA polymerase in UV repair in *E. coli*. Higher tolerance of BER mutant expressing this protein,

Merit Award

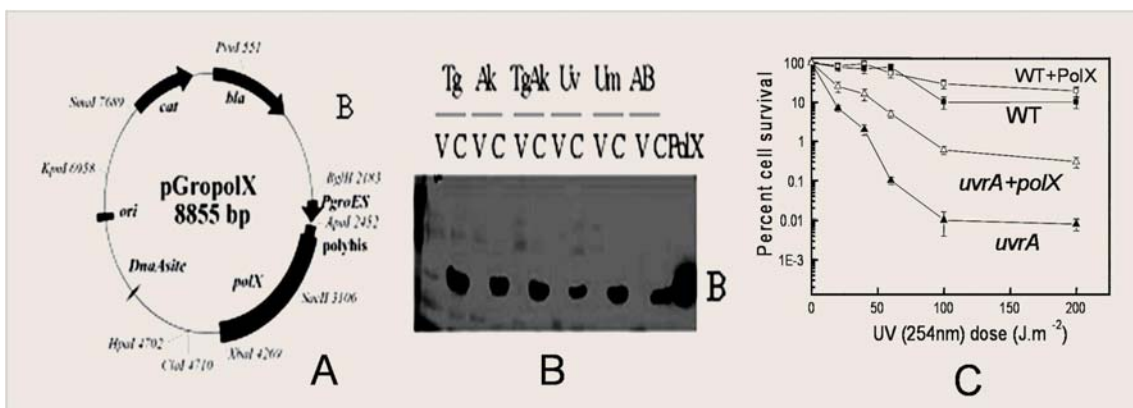


Fig. 1: Cloning (A), expression (B) and functional characterization of DNA polymerase X role in UV tolerance (C) of *E. coli* AB1157 (WT) and its excision repair mutant (*uvrA*). The data on other mutants are not shown.



might suggest the role of this enzyme in base excision repair.

The *polX* deletion mutant of *D. radiodurans* was generated and the effect of γ and UVC radiations, on survival of mutant and wild type, was evaluated. The γ radiation tolerance in mutant was nearly 3 log cycle less as compared to wild type at 8kGy dose, while this mutation showed insignificant effect on wild type response to UVC (Fig. 2A). Mutant cells became nearly 15 times more sensitive to 40mM hydrogen peroxide as compared to wild type (Fig. 2B). These results suggested an important role of X family DNA polymerase of *D. radiodurans* in bacterial response to DNA damage. Lack of a significant effect of *polX* mutation in UVC tolerance of *Deinococcus*, while an improvement in UVC tolerance of *E. coli* expressing this protein *in trans*, further indicated, that this X family DNA polymerase possibly works through UV induced SOS response, which is absent in *Deinococcus* [11] and present in *E. coli* [12].

Purification of recombinant polymerase X and activity characterization

The recombinant plasmid pETpolX (Fig. 3A) was transformed into *E. coli* BL21 and recombinant protein was induced with IPTG. The protein was purified to near

homogeneity and characterized for various putative functions *in vitro*. Enzyme catalyzed polymerization of only two deoxynucleotides at the 3' terminus of primer, complementary to template strand. Klenow fragment of *E. coli*, another DNA polymerase procured commercially and used as control, showed the full length copying of template DNA. This suggested that DNA polymerase X of *Deinococcus* is a short length polymerase (Fig. 3B).

The primary sequence of this enzyme contains a 5'dRPlyase functional domain, an activity integral to base excision repair function in protein. This activity was evaluated using modified oligos containing deoxyuridine (dU) base in dsDNA substrate. Enzyme was incubated with commercially available DNA glycosylase and AP endonuclease. Enzyme showed removal of 5'dR phosphate (5'dRP) from the apurinic site in dsDNA substrate (Fig. 3C). This suggested the presence of 5'dRP lyase activity in this DNA polymerase. Both DNA polymerase and 5'dRP lyase activities together, classified this enzyme as short patch base excision repair enzyme.

D. radiodurans confers extraordinary tolerance to various abiotic stresses including γ radiation, desiccation and hydrogen peroxide. These agents are known for inducing a strong oxidative stress in the cells. Oxidants produced

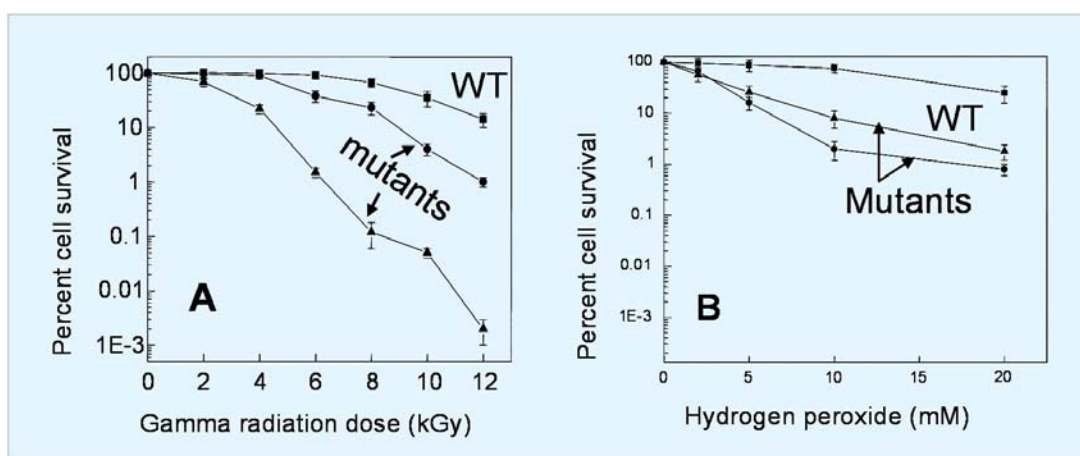


Fig. 2: Effect of γ radiation (A) and hydrogen peroxide (B) on cell survival of *Deinococcus radiodurans* (WT) and *polX* mutants (mutants).

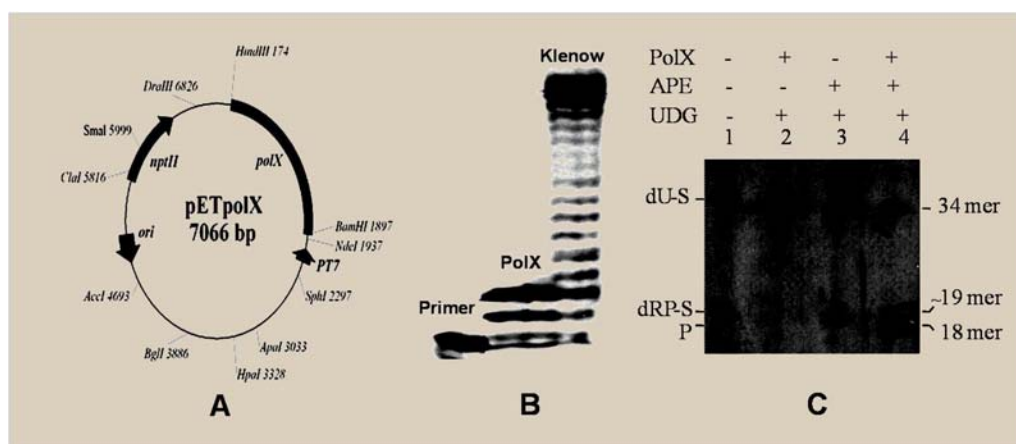


Fig. 3: Cloning of *polX* in *E. coli* expression vector (A) and characterization of polymerase (B) and dRPolase activity (C) of purified recombinant DNA polymerase X.

during this process, oxidize nucleotide bases in DNA, which become deleterious for cell survival. The replacement of damaged bases with correct base, therefore, becomes mandatory to the organism for avoiding mutation and cell death. This process requires both removal of the damaged base and then incorporation of new and correct base, at lesion site. This enzyme eventually showed both the functions i.e. removal of damaged base and filling of gap with new DNA base. These results suggested the role of this enzyme in bacterial resistance to radiations, by helping the bacteria in base excision repair mechanism.

Acknowledgement

Authors are grateful to Dr. S. K. Apte for his keen interest in subject, timely criticism and suggestion during the progress of this project.

References

- Blasius, M., Sommer, S. and Hubscher, U. "Deinococcus radiodurans: what belongs to the survival kit?" *Critical Reviews Biochemistry and Molecular Biology* 43 (2008): 221-238.
- Battista, J.R. "Radiation resistance: the fragment that remain". *Current Biology* 10 (2000): R204-205.
- Makarova, K. S., Aravind, L., Wolf, Y. I., Tatusov, R. L., Minton, K. W., Koonin, E. V. and Daly, M. J. "Genome of extremely radiation-resistant bacterium *Deinococcus radiodurans* viewed from the perspectives of comparative genomics". *Microbiology and Molecular Biology Reviews* 65 (2001): 44-79.
- Khairnar, N. P. and Misra, H. S. "DNA polymerase X from *Deinococcus radiodurans* implicated in bacterial tolerance to DNA damage is characterized as a short patch base excision repair polymerase". *Microbiology* 155 (2009): 3005-3014.
- Schaefer, M.; Schmitz, C.; Facius, R.; Horneck, G.; Milow, B.; Funken, K-H. and Ortner, J. "Systematic study of parameters influencing the action of Rose Bengal with visible light on bacterial cells: comparison between biological effect and singlet-oxygen production". *Photochemistry and Photobiology* 71 (2000): 514-523.
- Grzesiuk, E., Gozdek A. and Tudek, B. "Contribution of *E. coli* AlkA, TagA glycosylases and UvrABC-excinuclease in MMS mutagenesis". *Mutation Research* 480-481 (2001): 77-84.



7. Khairnar, N. P., Kamble, V. A., Mangoli, S. H., Apte, S. K., and Misra, H. S. "Involvement of a periplasmic protein kinase in DNA strand break repair and homologous recombination in *Escherichia coli*". *Molecular Microbiology* 65(2007): 294-304.
8. Misra, H.S., Khairnar, N.P., Kota, S., Srivastava, S., Joshi, V.P. and Apte, S.K. "An exonuclease I sensitive DNA repair pathways in *Deinococcus radiodurans*: a major determinant of radiation resistance". *Molecular Microbiology* 59 (2006):1308-1316.
9. Misra, H. S., Pandey, P. K., Modak, M. J., Vinayak, R., and Pandey, V. N. "Poly-amide nucleic Acid-DNA chimera lacking the phosphate backbone are novel primer for polymerase reactions catalysed by DNA polymerases". *Biochemistry* 37 (1998) : 1917-1925.
10. Prasad, R., Bebenek, K., Hou, E., Shock, D.D., Beard, W.A., Woodgate, R., Kunkel, T.A. and Wilson, S. H. "Localization of the deoxyribose phosphate lyase active site in human DNA polymerase by controlled proteolysis". *Journal of Biological Chemistry* 278 (2003):29649–29654.
11. Narumi, I., Satoh, K., Kikuchi, M., Funayama, T., Yanagisawa, T., Kobayashi, Y., Watanabe, H. and Yamamoto, K. "The LexA protein from *Deinococcus radiodurans* is not involved in RecA induction following gamma irradiation". *Journal of Bacteriology* 183 (2001): 6951-6956.
12. Walker, G.C. "The SOS response of *Escherichia coli*. In *Escherichia coli and Salmonella*" In *Cellular and Molecular Biology*, 2nd edn. Neidhardt, F.C., et al. (eds). Washington, DC: American Society for Microbiology Press, 1996.



Immobilization of glucose oxidase on synthetic and biological materials for biosensor development

Jitendra Kumar and S. F. D'Souza

Nuclear Agriculture and Biotechnology Division

This Paper received the Best Poster Award at the 3rd International Symposium on Materials Chemistry (ISMC-2010) held at BARC, from 7th-11th Dec., 2010

Abstract

A variety of synthetic as well as natural materials have been exploited, for immobilization of enzymes, for their use in biosensor development. Present study compared two different materials, PVA membrane and onion membrane for immobilization of glucose oxidase (GOD) enzyme and its application in glucose biosensor. PVA membrane has shown a more sensitive detection range (0.9-225 mg/dl glucose) but has less reusability (32 reactions) and low storage stability than that of the onion membrane, which has shown a less sensitive detection range (22.5-450 mg/dl glucose) but more reusability (127 reactions) and better storage stability.

Introduction

Biosensor: The Concept

A biosensor is described as a compact analytical device, incorporating a biological or biologically derived sensing element, either closely connected to, or integrated within, a transducer system. The principle of detection is the specific binding of the analyte of interest to the complementary biorecognition element immobilized on a suitable support matrix. The specific interaction results in a change in one or more physico-chemical properties (pH change, electron transfer, mass change, heat transfer, uptake or release of gases or specific ions) which are detected and may be measured by the transducer. The usual aim is to produce an electronic signal, which is proportional in magnitude or frequency to the concentration of a specific analyte or group of analytes, to which the biosensing element binds (1-2).

Biosensors can be classified by their bio-recognition system. The main biological materials used in biosensor technology are the couples enzyme/substrate, antibody/antigen and nucleic acids/complementary sequences. In addition, microorganisms, animal or plant whole cells and tissue slices, can also be incorporated in the biosensing system. Depending on the method of signal transduction, biosensors can also be divided into different groups: electrochemical (amperometric, potentiometric or conductometric), optical, thermometric, piezoelectric or magnetic.

Biosensors offer advantages over conventional analytical techniques. The selectivity of the biological sensing element, offers the opportunity for development of highly specific devices for real-time analysis in complex mixtures, without the need for extensive sample pre-treatment or large sample volumes. Biosensors also promise highly



sensitive, rapid, reproducible and simple-to-operate analytical tools.

Immobilization of biomaterials

The basic requirement of a biosensor is that the biological material should bring the physico-chemical changes in close proximity of a transducer. In this direction, immobilization technology has played a major role (1-2). Immobilization not only helps in forming the required close proximity between the biomaterial and the transducer, but also helps in stabilizing it for reuse. The biological material has been immobilized directly on the transducer or in most cases, in membranes, which can subsequently be mounted on the transducer. Biomaterials can be immobilized either through adsorption, entrapment, covalent binding, cross-linking or a combination of all these techniques.

A large number of techniques and supports have been used, for the immobilization of biocatalyst for development of biosensors. The choice of techniques and supports should be such that, it should retain the enzyme activity and have reusability as well as storage stability. A variety of synthetic as well as natural materials have been exploited in our laboratory, for immobilization of biocatalysts and their use in biosensor development (3-8).

Main objective

This study illustrates the comparison of two different materials, PVA membrane (5), a synthetic polymer and onion membrane (4), a biological material, for immobilization of glucose oxidase (GOD) enzyme and its association with dissolved oxygen probe, for the development of glucose biosensor.

GOD was selected for immobilization, because it is a well studied enzyme in the field of biosensors. Most of the glucose biosensors are based on the glucose oxidation catalysed by GOD. Immobilized GOD converts glucose

into gluconolactone with the consumption of oxygen. Amperometric response was monitored, by measuring the depletion of oxygen from sample using oxygen-sensitive DO electrode (Fig.1) (4-5). Glucose was detected on the basis of depletion of oxygen. In order to improve enzyme properties like reusability, operational stability and shelf storage stability, GOD was immobilized on different matrices and associated with transducers for biosensor application (4-5).

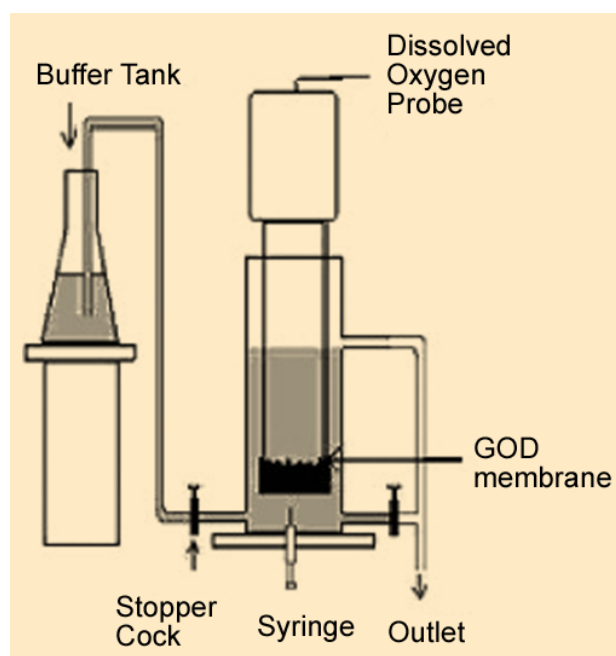


Fig.1: Schematic diagram of association of GOD immobilized membrane with the DO probe biosensor

Immobilization of glucose oxidase on PVA, synthetic membrane

Polyvinyl alcohol (PVA) is a synthetic polymer, that has been extensively used for immobilization of biocatalysts in a membranous form. It is a non-toxic and biocompatible polymer with good chemical and thermal stability. A large number of hydroxyl groups occur in the PVA, which provides a biocompatible microenvironment to the enzyme. However major limitation of the PVA membrane is its high swelling index and its solubility in water when not cross-linked. Swelling of the PVA membrane can be



reduced by cross-linking with a variety of chemical and physical methods (5).

Membrane composition was optimized on the basis of swelling index. Membranes were prepared using low and/or high degrees of polymerized (DOP) PVA (Polyvinyl alcohol (degree of hydrolysis 98–99%) with DOP ~360 and 1700–1800), acetone, and benzoic acid (BA) and were cross-linked by UV treatment. Swelling index was reduced after cross-linking the membrane with UV treatment, in the presence of benzoic acid as sensitizer. Study shows that the stability of the membrane was improved because of cross-linking. SEM study of the surface of PVA membranes before and after UV treatment showed, that surface of the membranes after UV treatment had less ridges and roughness and was smoother than the surfaces of the membrane before UV treatment. The membrane with smoother surfaces has greater antifouling capability for better quality and longevity (5).

A 10 ml homogenous mixture of 12% low DOP PVA, 8% high DOP PVA and 2% BA was prepared in 50 mM sodium phosphate buffer containing 20% acetone. 2 ml GOD (2000 units/ml) was added to the mixture and mixed homogeneously. The mixture was overlaid as a thin membranous layer, air-dried, peeled off carefully and placed under UV light for cross-linking. Cross-linked GOD–PVA membranes were stored at 4°C.

GOD–PVA membrane was used for the calibration of DO electrode response with different concentrations. (0.9–450 mg/dl) of glucose. Linear fit ($Y=0.1512+0.52X$) with a slope of 0.52 ($R^2 = 0.989$; S.D. = 1.9214) was estimated between 0.9 and 225 mg/dl of glucose. From the linear fit of calibration of DO electrode in response to standard concentration of glucose, the detection range of biosensor was estimated to be between 0.9 and 225 mg/dl.

GOD–PVA membranes were reused for 32 reactions without significant loss of activity. The low relative standard deviations 2.8×10^{-2} (mean = 46.2×10^{-2} ppm,

when $n = 6$) in the response of immobilized enzyme for 90 mg/dl glucose, demonstrated the high reproducibility of analysis. Additionally, a very low relative standard deviation 3.1×10^{-2} (mean = 46.78×10^{-2} ppm) of three different experiments carried out; using the same condition, further demonstrated the result. The immobilized GOD–PVA membranes were stable for 30 days of investigation with retention of 90% activity, when stored at 4°C and subsequently response decreased.

Immobilization of glucose oxidase on inner epidermis of onion natural membrane

Natural polymers in living organisms are composed of biomolecules like carbohydrates, lipids and proteins and therefore they can provide a biocompatible microenvironment for enzyme immobilization. The inner epidermis of the onion bulb scales consists of elongated tubular cells, blunt or tapering ends along with numerous guard cells. The cell wall is an elaborate extracellular matrix consisting of a microfibrillar cellulose phase and a matrix phase that contains a variety of polymers such as polygalacturonic acid (PGA), hemicelluloses, proteins, and phenolics, including lignin. This natural membrane is mechanically stronger because it consists of microfibrillar cellulosic biological components and can be a biocompatible immobilizing support, for optimum enzyme activity. Significance of the present work was to employ this natural polymer as a new support, for the immobilization of enzyme for biosensor application (4). Onions (*Allium cepa* L.) were cut into half, bulb scales were separated and inner epidermis from outer fleshy scale was stripped. Circular pieces of 1.5 cm diameter were cut and stored at 4°C in the refrigerator. An aliquot of 100 µl GOD (250 units/ml prepared in 50mM sodium phosphate buffer) was added on each membrane. After 30min, 10 µl of 2% glutaraldehyde solution was added to the surface of the membrane and spread uniformly. The cross-linking was allowed to take place for 30 min. Control membranes were prepared without glutaraldehyde treatment. SEM study showed that membrane consisted



of elongated tubular cells with blunt or tapering ends as reported in literature. After GOD immobilization on surface of the onion membrane, many changes like depressions and uneven distribution of microfibrillar structure were observed, on the surface morphology. Changes in surface morphology could be due to cross-linking of enzyme with membrane, using glutaraldehyde, which indicates that the enzyme was successfully immobilized on the surface of onion epidermal membrane.

GOD immobilized onion epidermal membrane was used for the calibration of DO electrode response with different concentrations (4.5 - 900 mg/dl) of glucose. A linear fit ($Y = 0.0517 + 0.0016X$; $R^2 = 0.999$; S.D. = 0.318) was estimated to be between 22.5 and 450 mg/dl of glucose. From the linear fit of calibration of DO electrode in response to standard concentration of glucose, the detection range of biosensor was estimated between 22.5 and 450 mg/dl (4).

The reusability of GOD onion membrane, prepared in the presence and absence of glutaraldehyde was observed. Glutaraldehyde treatment cross-linked the enzyme onto onion membrane and reduced the leaching of enzyme, thus increasing the reusability of the immobilized enzyme (127 repeated reactions). It was stable for 45 days of investigation with retention of 90% activity, when stored at 4°C. The low relative standard deviations 1.06×10^{-2} (mean = 23×10^{-2} ppm, when $n = 6$) in the response of the immobilized enzyme for 90 mg/dl glucose, also demonstrated the high reproducibility of analysis.

Conclusion

GOD immobilized PVA membrane has shown a high sensitivity (detection range 0.9-225mg/dl) for glucose detection, but low reusability (32 reactions) and stability (30 days) and GOD immobilized onion membrane has shown a high reusability (127 reactions) and stability (45 days) but low sensitivity (detection range 22.5-450 mg/dl) for glucose detection, for the development of the biosensor.

References

1. D'Souza, S. F. Immobilization and Stabilization of Biomaterials for Biosensor Applications. *Applied Biochemistry and Biotechnology - Part A Enzyme Engineering and Biotechnology* 96 (2001): 225-38.
2. D'Souza, S. F. Microbial Biosensors. *Biosensors and Bioelectronics* 16 (2001): 337-53.
3. Kumar, J., and D'Souza, S. F. An Optical Microbial Biosensor for Detection of Methyl Parathion using *Sphingomonas Sp.* Immobilized on Microplate as a Reusable Biocomponent. *Biosensors and Bioelectronics* 26 (2010): 1292-6.
4. Kumar, J., and D'Souza, S. F. Inner Epidermis of Onion Bulb Scale: As Natural Support for Immobilization of Glucose Oxidase and its Application in Dissolved Oxygen Based Biosensor. *Biosensors and Bioelectronics* 24 (2009): 1792-5.
5. Kumar, J., and D'Souza, S. F. Preparation of PVA Membrane for Immobilization of GOD for Glucose Biosensor. *Talanta* 75 (2008): 183-8.
6. Kumar, J., Jha, S. K., and D'Souza, S. F. Optical Microbial Biosensor for Detection of Methyl Parathion Pesticide using *Flavobacterium Sp.* Whole Cells Adsorbed on Glass Fiber Filters as Disposable Biocomponent. *Biosensors and Bioelectronics* 21 (2006): 2100-5.
7. Tembe, S., Inamdar, S., Haram, S., Karve, M., and D'Souza, S. F. Electrochemical Biosensor for Catechol using Agarose-Guar Gum Entrapped Tyrosinase. *Journal of Biotechnology* 128 (2007): 80-5.
8. Tembe, S., Karve, M., Inamdar, S., Haram, S., Melo, J., and D'Souza, S. F. Development of Electrochemical Biosensor Based on Tyrosinase Immobilized in Composite Biopolymeric Film. *Analytical Biochemistry* 349 (2006): 72-7.



Investigation of Magnetic Phase Transition in $\text{TbCo}_{2-x}\text{Fe}_x$

Madhumita Halder and S. M. Yusuf

Solid State Physics Division

This paper received the Best Poster Presentation Award at the
1) Advances in magnetism: Phenomena & Materials (AMPM-2010), at Manali, Himachal Pradesh
and at the 2) International Conference on Magnetic Materials (ICMM-2010) at held at
Saha Institute of Nuclear Physics, Kolkata, from 25th-29th Oct., 2010

Abstract

We have studied the nature of magnetic phase transition in $\text{TbCo}_{2-x}\text{Fe}_x$ laves phase compounds. For TbCo_2 , a structural phase transition is found to be associated with a magnetic phase transition but the nature of the magnetic phase transition is of second order. On Fe substitution, we find that the magnetic phase transition remains second order in nature and transition, spreads over a wide temperature range. From the critical exponent analysis, we conclude that TbCo_2 belongs to the three-dimensional Heisenberg class, while the phase transition for the Fe substituted compound can be described by the mean field theory.

Keywords: Magnetic phase transition, laves phase compounds

Introduction

$R\text{Co}_2$ compounds (R : rare earths) show interesting magnetic and electronic properties¹. These compounds with light rare earth elements like Nd, Sm, Gd and Tb are reported to show a second order magnetic phase transition, while with heavy rare earth elements like Dy, Ho and Er, a first order metamagnetic transition is reported². Among these, TbCo_2 is known to undergo a second order paramagnetic to ferrimagnetic phase transition along with a structural phase transition near the magnetic transition temperature T_c (231 K)³. Usually, a structural phase transition is associated with a first order magnetic phase transition. This motivated us to investigate the nature of magnetic phase transition in detail in TbCo_2 . Here, we present the critical exponent study in $\text{TbCo}_{2-x}\text{Fe}_x$ compounds. The nature of the magnetic interaction responsible for the

transition, has been brought out in the present critical exponent study.

Experimental Details

The polycrystalline $\text{TbCo}_{2-x}\text{Fe}_x$ samples ($x = 0$ and 0.1) with high purity constituent elements, were prepared by an arc-melting under argon atmosphere. After melting, the samples were annealed in vacuum-sealed quartz tube at 850°C for 7 days. Neutron diffraction patterns were recorded at various temperatures using the powder diffractometer - II ($\lambda = 1.249 \text{ \AA}$) at the Dhruva Research Reactor, Trombay. Magnetization measurements were carried out using a vibrating sample magnetometer (Oxford Instruments). For dc magnetization measurements, the samples were field-cooled (FC) under 0.02 T field down to 5 K . The measurements were then



carried out in the warming cycle from 5 to 320K under the same field. The magnetization isotherms were measured for $x = 0$ and 0.1 samples up to a maximum field of 5 T.

Results and Discussion

The FC magnetization versus temperature curves for both samples are shown in Fig. 1. The paramagnetic to ferrimagnetic transition temperature T_c is found to increase with Fe substitution (231 and 303 K for $x = 0$ and 0.1, respectively)

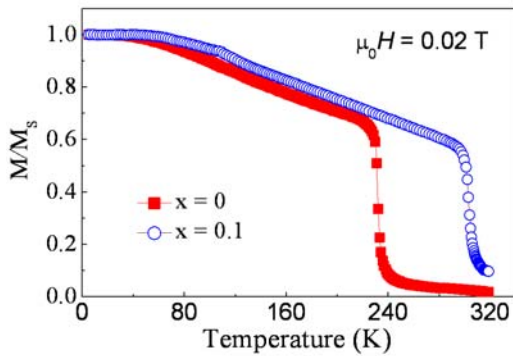


Fig. 1: Temperature dependence of normalized magnetization for $x = 0$ and 0.1 samples. Here M_s is the observed magnetization at 5 K.

Neutron diffraction patterns were recorded at different temperatures for both $x = 0$ and 0.1 samples (Fig. 2). For the $x = 0$ sample, the Rietveld refinement of the diffraction pattern, reveals that the low temperature (22 K) phase is

rhombohedral (space group $R\bar{3}m$) and the room temperature phase is cubic (space group $Fd\bar{3}m$), whereas for the $x = 0.1$ sample, the low temperature (22 K) phase is rhombohedral and at room temperature (Fig. 3) there is a co-existence of both rhombohedral and cubic phases. From the analysis of the diffraction patterns for $x = 0$ and 0.1 samples (Fig. 2), we find that the structural phase transition is coupled with magnetic phase transition. The magnetostructural transitions also broaden on Fe substitution⁴. The cubic and rhombohedral crystallographic phases coexist over the temperature ranges of around (205 K – 285 K) and (265 K – 365 K) for $x = 0$ and 0.1 samples, respectively.

The nature of the magnetic phase transition in $TbCo_{2-x}Fe_x$ has been studied by Arrott plot (M^2 vs H/M curves, where M is the magnetization and H is the magnetic field) method

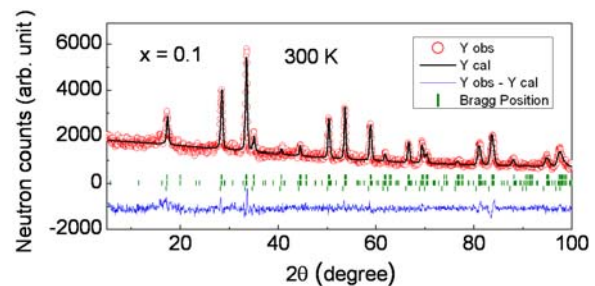


Fig. 3: Neutron diffraction patterns for $x = 0.1$ sample at 300 K. The vertical bars indicate the allowed Bragg peak positions (top for rhombohedral phase, middle for magnetic phase and bottom for cubic phase).

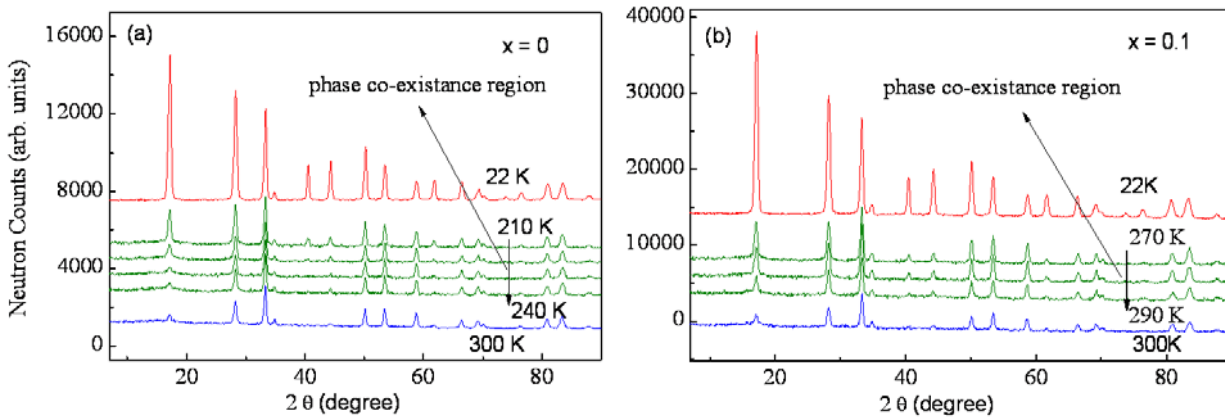


Fig. 2: Temperature dependent neutron diffraction patterns for (a) $x = 0$ and (b) $x = 0.1$ samples.

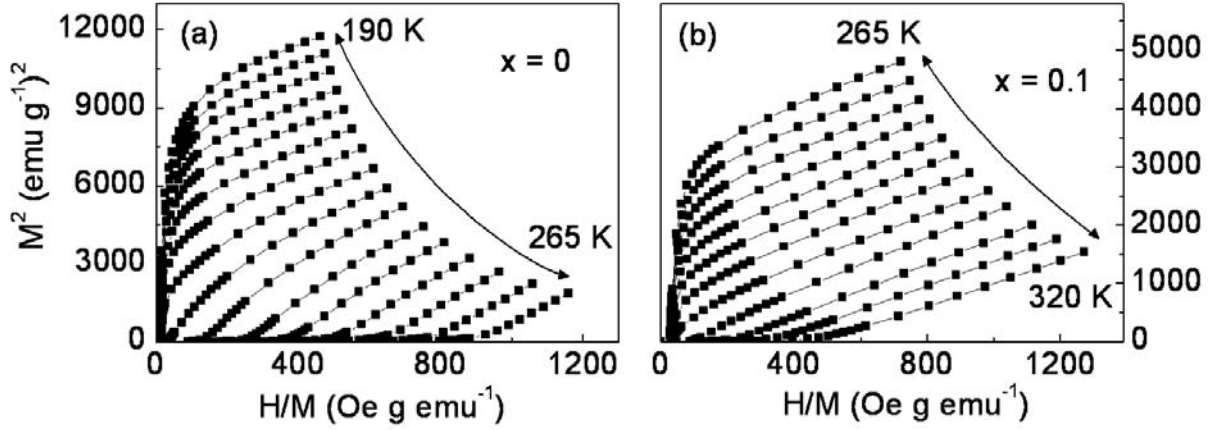


Fig. 4: Arrott Plots for (a) $x = 0$ and (b) $x = 0.1$ samples.

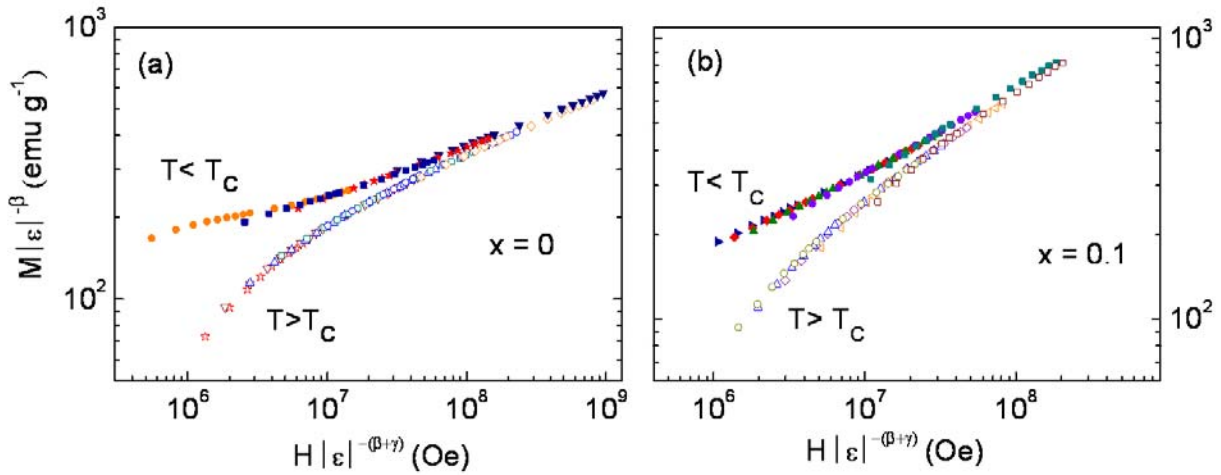


Fig. 5: Logarithmic scaling plot of $M|\epsilon|^\beta$ versus $H|\epsilon|^{-(\beta+\gamma)}$ in the critical region for (a) $x = 0$ and (b) $x = 0.1$ samples.

and a detailed investigation has been carried out by performing critical exponent study near T_c . A positive slope of the M^2 vs H/M curves has been observed, for both $x = 0$ and 0.1 samples (Fig. 4) indicating that the paramagnetic to ferrimagnetic transition is of second order in nature according to Banerjee criteria⁵.

The critical exponents are obtained by using the modified Arrott plot method⁶, the details of which are described elsewhere⁴. The value of critical exponents $\beta = 0.380(4)$ and $\gamma = 1.407(8)$ were obtained for the $x = 0$ sample. These values of β and γ are close to the values predicted

for a three-dimensional Heisenberg model ($\beta = 0.368$ and $\gamma = 1.396$)⁷ with a short-range exchange interaction. The values of $\beta = 0.541(1)$ and $\gamma = 1.023(2)$ were obtained for the $x = 0.1$ sample. The obtained values of β and γ for the $x = 0.1$ sample are close to the values predicted from mean-field theory ($\beta = 0.5$ and $\gamma = 1$)⁸. The obtained values of critical exponents can be justified by the $H\epsilon^{-\beta}$ vs $H\epsilon^{-(\beta+\gamma)}$ plot.⁹ The scaled data are plotted on a log scale as shown in Fig. 5 for $x = 0$ and 0.1 samples. It can be clearly seen that all data fall on either of the two branches of the universal curve, one for temperatures above T_c and the other for temperatures below T_c .



conclusion

Usually, a structural phase transition is associated with a first order magnetic transition. In case of $\text{TbCo}_{2-x}\text{Fe}_x$, we rather find that there is a structural phase transition coupled with a magnetic phase transition but the nature of the magnetic phase transition is of second order. We have investigated the critical behavior of the $\text{TbCo}_{2-x}\text{Fe}_x$ series. For the $x = 0$ sample, the values of critical exponents are close to that of 3D Heisenberg model with short-range exchange interaction, while for the $x = 0.1$ sample, the values of critical exponents are close to that of mean-field theory with a long-range exchange interaction.

References

1. J. Inoue and M. Shimizu. "First- and second-order magnetic phase transitions in $(\text{R-Y})\text{Co}_2$, and $\text{R}(\text{Co-Al})_2$, ($\text{R} = \text{heavy rare-earth element}$) Compounds". *J. Phys. F: Met. Phys.* 18 (1988): 2487-2497.
2. S. Khmelevskiy and P. Mohn. "The order of the magnetic phase transitions in RCo_2 ($\text{R} = \text{rare earth}$) intermetallic compounds". *J. Phys.: Condens. Matter* 12 (2000): 9453-9464.
3. N. Yoshimoto, J. Sakurai and Y. Komura. "X-Ray diffraction study on crystal deformation of TbCo_2 ". *J. Magn. Magn. Mater.* 31-34 (1983): 137-139.
4. M. Halder, S. M. Yusuf, M. D. Mukadam, and K. Shashikala. "Magnetocaloric effect and critical behavior near the paramagnetic to ferrimagnetic phase transition temperature in $\text{TbCo}_{2-x}\text{Fe}_x$ ". *Phys. Rev. B* 81 (2010): 174402-9.
5. S. K. Banerjee. "On a generalized approach to first and second order magnetic transitions". *Phys. Lett.* 12 (1964): 16-17.
6. A. Arrott and J. E. Noakes. "Approximate equation of state for nickel near its critical temperature". *Phys. Rev. Lett.* 19 (1967): 786-789.
7. M. Campostrini, M. Hasenbusch, A. Pelissetto, P. Rossi, and E. Vicari. "Critical exponents and equation of state of the three-dimensional Heisenberg universality class". *Phys. Rev. B* 65 (2002): 144520-20.
8. H. E. Stanley. *Introduction to Phase Transitions and Critical Phenomena*, Oxford University Press, New York, 1971.
9. H. E. Stanley. "Scaling, universality, and renormalization: Three pillars of modern critical phenomena". *Rev. Mod. Phys.* 71 (1999): S358- S366.



Large Sample Neutron Activation Analysis of Dross for Gold and Silver

K. K. Swain, Nicy Ajith, R. Verma and A. V. R. Reddy

Analytical Chemistry Division

and

R. Acharya

Radiochemistry Division

This Paper received the IANCAS Best Paper Award at the Fourth International Symposium on Nuclear Analytical Chemistry (NAC-IV), held at Mumbai from 15-19 November, 2010

Abstract

Large Sample Neutron Activation Analysis (LSNAA) of dross from the India Government Mint, Mumbai, was carried out, using the AHWR critical facility at BARC, for the determination of valuable elements namely Au and Ag. The k_0 -based Internal Monostandard NAA (IMNAA) using Na as internal monostandard was used, to calculate concentration ratios. The Au/Na values in the samples with varying mass were used to arrive at representative sample size for analysis, which has been determined as ≥ 2 g. Concentrations of Au and Ag were in the range of 200-400 mg kg⁻¹ and 1200-1700 mg kg⁻¹ respectively in three different samples of dross.

Introduction

Refining of precious metals is carried out in fireclay crucibles and during the refining process, some metals diffuse into the walls of the crucibles. At the end of the life cycle, these crucibles are crushed and ground in a ball mill, and this ground crucible is called dross [1]. The dross is washed repeatedly on James Tables to recover precious metals like gold (Au) and silver (Ag). After this operation, the exhausted dross still contains significant quantities of Au and Ag. Quantification of Au and Ag in dross is required, to recover these precious metals. It is difficult to dissolve dross sample as it is a complex and refractory material. Also quantitative leaching of Au and/or Ag from dross is difficult. In view of this, it is essential to choose those analytical techniques, which can analyze solids directly to obviate the chemical decomposition. It is expected that Au and

Ag are not homogeneously distributed in dross, though major matrix is assumed to be homogeneous. Therefore, estimation of Au and Ag using small size samples will be erroneous. For such samples, instead of replicate sub-sample analysis, LSNAA is used for obtaining better analytical representative sample size as well as reliable values [2, 3]. Analysis of large size sample is feasible by NAA due to high penetrating power of neutron and γ -rays [4]. A k_0 -based IMNAA using *in situ* relative detection efficiency [3, 5], is useful to analyze both large and small size samples. This method gives elemental concentration ratios with respect to the internal monostandard, chosen from the elements present in the sample. To arrive at absolute concentration values, knowledge of concentration of the internal monostandard is required. In the present work, applicability of IMNAA to large size samples of dross



from the India Government Mint, Mumbai has been explored.

Experimental

Dross samples, obtained from the India Government Mint, Mumbai, were sealed in clean polyethylene sheets and irradiated for 4-6 h at Graphite Reflector (GR) position of Advanced Heavy Water Reactor (AHWR) Critical Facility (CF) reactor at BARC. Indium standards with and without cadmium cover (0.8 mm) were irradiated for 4h for the determination of thermal to epithermal neutron flux ratio (f) in the irradiation position, by cadmium ratio method [6]. IAEA SL-1 was used as reference standard for sodium (Na) determination. After appropriate cooling periods, radioactivity assay was carried out using a 45% relative efficiency High Purity Germanium (HPGe) detector, coupled with a Multi Channel Analyzer (MCA). The ratio of mass of an element to mass of the internal monostandard element in the sample was calculated using IMNAA method^[6]. Relevant nuclear data was taken from Nuclear Data Tables^[7].

Results and Discussion

The graphite reflector position of CF was characterized for neutron flux parameters. The f-value obtained by the cadmium ratio method is $(8.6 \pm 0.3) \times 10^2$. The corresponding thermal equivalent neutron flux is $3.4 \times 10^7 \text{ cm}^{-2} \text{ s}^{-1}$ (>99.8 % thermal neutron component) [8]. To establish the distribution of sodium (Na) in the dross samples, four replicate small sub-samples from one of the dross sample (D-1) were collected and irradiated in Pneumatic Carrier Facility (PCF) of CIRUS reactor at BARC. The average concentration of sodium was $7.41 \pm 0.21 \text{ mg g}^{-1}$ in the sub samples, indicating homogeneous distribution of Na. Ideally internal standard is chosen that has uniform distribution in the entire sample and for this work, Na was chosen as internal monostandard. Activation products ^{140}La , ^{56}Mn and ^{24}Na , produced in the irradiated dross samples, were used for *in situ* efficiency calibration. An *in situ* relative detection efficiency plot for large size dross sample (100 g) is shown in Fig. 1, which covers an energy range of 329-2754 keV. To arrive at representative sample size for analysis of dross for precious metals, eight samples of small to large sizes (100 mg-100 g) of dross were analyzed. Concentration ratios of Au to Na were obtained using IMNAA method. Au/Na concentration values were plotted as a function

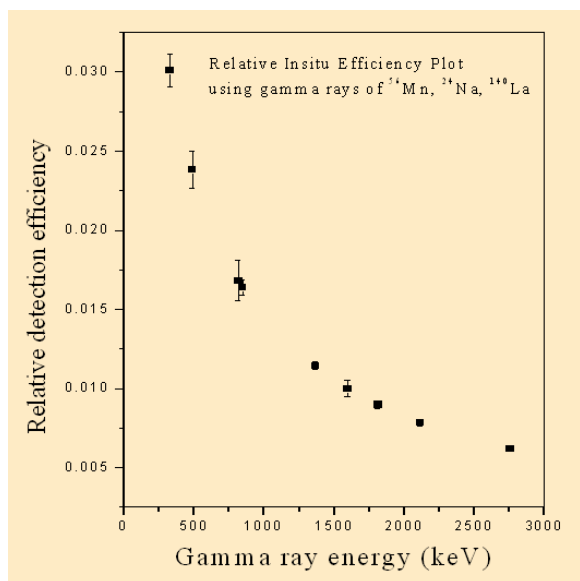


Fig. 1: Typical relative in-situ efficiency plot of neutron irradiated dross (100 g)

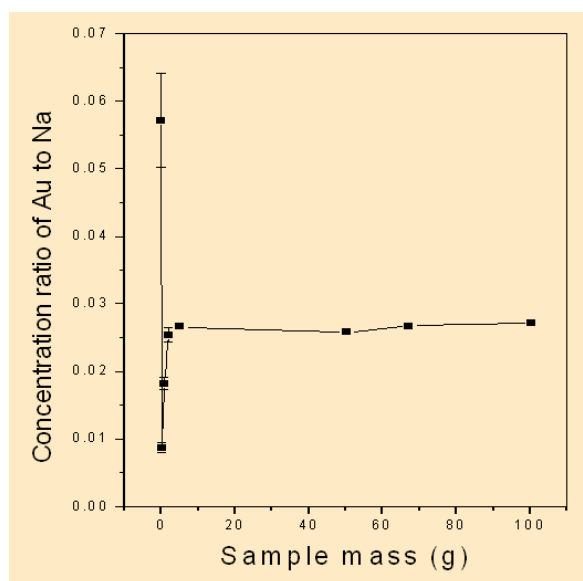


Fig. 2: Concentration ratios of Au to Na in small to large size samples of dross



Table 1: Relative and absolute concentrations in Au and Ag in three different dross samples

Element (X)	D-1 (100.4 g)		D-2 (67.2 g)		D-3 (50.6 g)	
	X/Na	Conc. \pm Unc. mg kg ⁻¹	X/Na	Conc. \pm Unc. mg kg ⁻¹	X/Na	Conc. \pm Unc. mg kg ⁻¹
Au	2.72 E-2	202 \pm 7	4.18 E-2	353 \pm 9	4.32 E-2	394 \pm 11
Ag	1.63 E-1	1208 \pm 98	1.70 E-1	1455 \pm 76	1.87 E-1	1705 \pm 68

of sample mass (Fig. 2). From Fig. 2, it is clear that representative sample size is ≥ 2 g. In the present study, large samples of dross in the mass range of 50-100g were used, to produce adequate activity, so as to obtain measured count rates that are statistically significant. The results thus obtained are given in Table 1. Concentrations of Au and Ag were found to be in the range of 200-400 mg kg⁻¹ and 1200-1700 mg kg⁻¹ respectively. To validate the results of large size sample analysis, replicate sub sample analyses of D-1 sample (50-100mg) were carried out. For this purpose, 200g of dross was ground and sub-samples were irradiated in PCF of CIRUS reactor. Relative method with IRMM SMELS-I as comparator was used, to determine Au and the average value was 198 \pm 12 mg kg⁻¹. This value is in good agreement with that obtained by LSNA (202 \pm 7 mg kg⁻¹), which validated the present large sample analysis method.

Conclusions

The IMNAA method using *in situ* relative detection efficiency was used, to determine concentrations of Au and Ag in large size dross samples. Low flux graphite reflector position of AHWR Critical Facility reactor, BARC was found suitable for irradiation of such large samples. Results indicated that Na is evenly distributed in the dross and thus it was chosen as a monostandard. The method was validated by determining Au in replicate ground samples of dross.

Acknowledgements

Authors thank the India Government Mint, Mumbai, for providing dross sample and the staff of AHWR Critical Facility, for the support during the irradiation of samples. This work was carried out as part of IAEA Coordinated Research Project (CRP Code: F2.30.27) on LSNA.

References

1. Murthy D. S. R., Prasad P. M., *Hydrometallurgy*, 42 (1996) 27-33.
2. Bode P., Overwater R.M.W., De Goeij J.J.M., *J. Radioanal. Nucl. Chem.* 216 (1997) 5.
3. Nair A.G.C., Acharya R., Sudarshan K., Gangotra S., Reddy A.V.R., Manohar S.B., Goswami A., *Anal. Chem.* 75 (2003) 4868.
4. Overwater R.M.W., Bode P., de Goeij J.J.M., Hoogenboom J.E., *Anal. Chem.* 68 (1996)341.
5. Sudarshan K., Nair A.G.C., Goswami A., *J. Radioanal. Nucl. Chem.* 256 (2003) 93.
6. Acharya R., Swain K. K., Sudarshan K., Tripathi R., Pujari P. K., Reddy A.V. R., (2010) *Nucl Instr Meth A*, 622 (2010) 460.
7. De Corte F., Simonits A., *Atom. Data Nucl. Data Tables* 85 (2003) 47.
8. Dasari K. B., Acharya R., Swain K. K., Lakshmana Das N., Reddy A. V. R., *J Radioanal. Nucl Chem.*, 285 (2010) 525-531.



Magnetic Ordering in $\text{La}_{1-x}\text{Ce}_x\text{CrO}_3$ ($0.0 \leq x \leq 1.0$) Nanoparticles

P. K. Manna, A. K. Bera and S. M. Yusuf

Solid State Physics Division

and

R. Shukla and A. K. Tyagi

Chemistry Division

This paper received the Best Poster Awards at the "Advances in Magnetism: Phenomena and Materials" (AMPM-2010), held at Manali, during June 3-5, 2010 and "International Conference on Magnetic Materials" (ICCM-2010) held at Saha Institute of Nuclear Physics, Kolkata, during October 25-29, 2010, respectively.

Abstract

We report the study of magnetic ordering in $\text{La}_{1-x}\text{Ce}_x\text{CrO}_3$ ($0.0 \leq x \leq 1.0$) nanoparticles by employing dc-magnetization and neutron diffraction techniques. The analysis of our experimental results shows some remarkable observations, such as occurrence of sign-reversals of magnetization and exchange bias field in a single system, tunability of unit cell volume (V_U) as well as Néel temperature (T_N) just by varying x . These sign-reversal phenomena have been explained by using a core-shell model, which is established from the high resolution transmission electron microscopy, and dc-magnetization measurement techniques. The tunable behavior of V_U has been ascribed to a lesser ionic radius of Ce^{3+} compared to that of La^{3+} , while tunability of T_N has been assigned to a decrease in the Cr-O-Cr angle with increasing x . We have also brought out the technological importance of these sign-reversal phenomena in volatile, and thermally assisted magnetic random access memory elements.

Keywords: Doped LaCrO_3 Nanoparticles, Magnetization and exchange bias sign-reversals.

Introduction

The interest in the substitution of the La-sites of LaCrO_3 compound, started mainly with an aim to improve the conductivity of the pure LaCrO_3 as an interconnect material, in solid oxide fuel cell technology. The substituent/dopant used for this purpose is mainly divalent ions, such as Ca^{2+} , Sr^{2+} . From magnetic point of view, no drastic change is observed upon substitution with these divalent ions. However, a new twist occurs, in the form of magnetization sign-reversal, when the La-sites are substituted with trivalent rare earth ions, such as Pr^{3+} [Ref. 1], and Nd^{3+} [Ref. 2]. The fundamental and

technological importance of the magnetization sign-reversal phenomenon, has attracted a lot of attention recently. This phenomenon was reported in molecular magnets,³ orthovanadates,⁴ and rare-earth based perovskite orthochromates,^{1,2} though its origin was found to be different for these different classes of materials.

In this paper, we show how the temperature-dependent magnetization behavior of $\text{La}_{1-x}\text{Ce}_x\text{CrO}_3$ nanoparticles changes from positive to negative upon Ce^{3+} substitution, leading to a sign-reversal of magnetization for $x \geq 0.8$. Interestingly, for the $x = 0.8$ nanoparticle system,



the sign-reversal of magnetization is accompanied by a sign-reversal of exchange bias (EB) field, which is another rarity.

The coexistence of these two novel phenomena has been explained by a core-shell model. We have also brought out the technological importance of magnetization and EB sign-reversals in the volatile, and Thermally Assisted Magnetic Random Access Memory (TA-MRAM) elements, respectively. Moreover, we found that the unit cell volume (V_U) and Néel temperature (T_N) of the $\text{La}_{1-x}\text{Ce}_x\text{CrO}_3$ nanoparticles can be tuned just by varying x .

Experimental

The $\text{La}_{1-x}\text{Ce}_x\text{CrO}_3$ ($0.0 \leq x \leq 1.0$) nanoparticles were prepared by a two-step synthesis route based on the gel combustion method.⁵ X-Ray Diffraction (XRD) measurement was carried out by using a Philips X-ray diffractometer. TEM images were recorded by using a Philips CM30/Super TWIN electron microscope. DC-magnetization measurements were carried out by using a vibrating sample magnetometer instrument (Oxford make). Neutron powder diffraction experiments ($\lambda = 1.249 \text{ \AA}$) were performed at Dhruva reactor, Trombay.

Results and Discussion

The single-phase nature of the nanoparticles was confirmed from the Rietveld refinement (using the FULLPROF program⁶) of room-temperature XRD pattern [Fig.: not shown]. The TEM image revealed [Fig.: not shown] the formation of nanoparticles with an average diameter of $\sim 43 \text{ nm}$.

The HRTEM image [Fig. 1(a)] shows the presence of roughness/defects at the particle-surface. Because of this, the spins located at the surface become magnetically different from those situated at the core part. Consequently, the nanoparticles can be considered as core-shell type. One way to check the existence of this shell, and its magnetic nature could be the thermoremanent (TRM) and isothermoremanent (IRM) magnetization measurements.⁷ Fig. 1(b) depicts the field-dependence of TRM and IRM at 5 K for the $x=0.8$ nanoparticles. A monotonically increasing TRM, and a negligible value of IRM, signify that the shell behaves like a diluted antiferromagnet (DAFF) under a magnetic field. The TRM

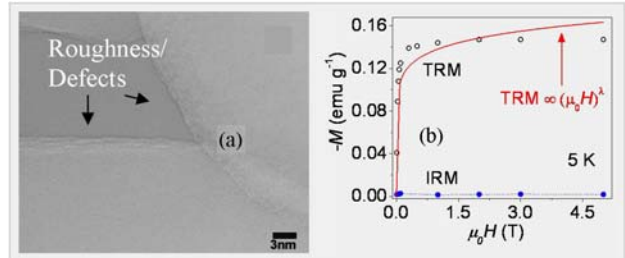


Fig. 1: (a) HRTEM image, and (b) field (μ_0H) dependence of TRM and IRM for the $x=0.8$ nanoparticles. In Fig. (b), solid line is a fitted curve, and the dotted line is a guide to the eye.

data have been fitted by the power law: $\text{TRM} \propto (\mu_0H)^\lambda$ [Fig. 1(b)]. In the present case, the best fitted value of λ is less than 1 (i.e. 0.10), which signifies that the shell behaves like a reduced dimensional DAFF. To explore the microscopic magnetic nature of the core-part, we performed the low-temperature neutron diffraction experiments on the $x=0.8$ nanoparticles at 22 and 300 K [Fig. 2].

An extra Bragg peak (indicated by an arrow) is clearly seen at 22 K, which signifies the presence of a long-range antiferromagnetic (AFM) ordering in the nanoparticles. The Rietveld analysis of the neutron diffraction pattern at 22K reveals a G-type antiferromagnetic (AFM) alignment of the Cr^{3+} ionic moments along the crystallographic b -axis. The neutron diffraction experiments on other

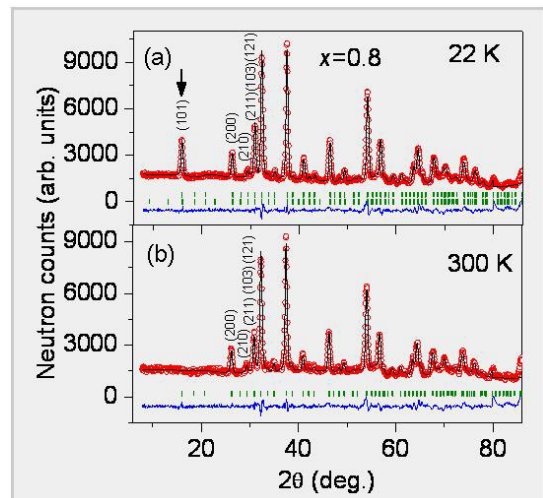


Fig. 2: Rietveld-refined neutron diffraction patterns for $x=0.8$ at (a) 22 and (b) 300 K.

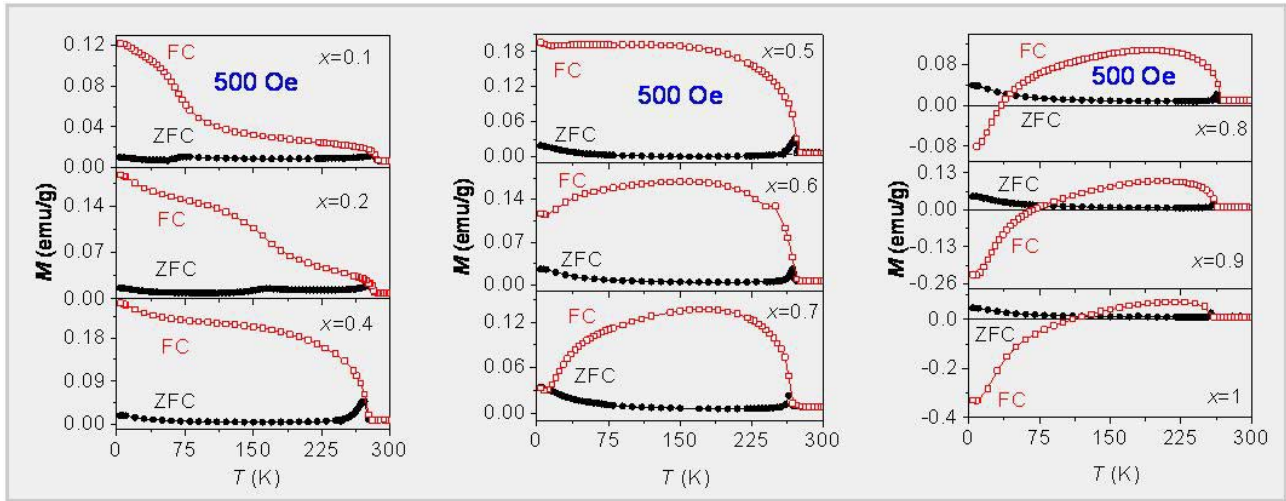


Fig. 3: FC and ZFC magnetizations of the $\text{La}_{1-x}\text{Ce}_x\text{CrO}_3$ ($0 \leq x \leq 1$) nanoparticles.

compositions also showed similar features. Therefore, from the HRTEM, dc-magnetization, and neutron diffraction experiments we concluded that the present nanoparticles were core-shell type consisting of an AFM core and a reduced dimensional DAFF shell.

Now, we shall discuss about the effect of Ce^{3+} -concentration (x) on the temperature-dependent magnetization behaviors of the $\text{La}_{1-x}\text{Ce}_x\text{CrO}_3$ nanoparticles. Fig. 3 shows the behavior of field cooled (FC) and zero-field cooled (ZFC) magnetizations for different x , under an applied magnetic field of 500 Oe. The ZFC curves of all the compositions show a typical peak, which can be considered as T_N for these nanoparticles. Apart from a change in T_N with x , all ZFC curves behave in a similar manner. However, the nature of the FC curve changes drastically with increasing x . Up to $x=0.4$, the FC curve shows an increase in the FC-magnetization below ~ 100 K. For the $x=0.5$ composition, below 100 K, the FC-magnetization is almost temperature-independent. For $x > 0.5$, the FC-magnetization decreases as the temperature goes down below 100 K. Interestingly, for $x \geq 0.8$, the down-turn in the FC-magnetization leads to a sign-reversal of magnetization. It can also be noted that the magnitude of the negative magnetization increases with increasing Ce^{3+} -concentration (x); clearly hinting the role played by Ce^{3+} . In fact, the Cr^{3+} ions creates an internal field at the Ce^{3+} sites so that the Ce^{3+} ions get polarized in a direction opposite to that of Cr^{3+} . As a result, the presence of more Ce^{3+} would imply an increase in the magnitude of the

negative magnetization. For the $x=0.5$ composition, a balance between the Cr- and Ce-moments occurs, so that below ~ 100 K, the FC-magnetization becomes almost independent of temperature.

The observed sign-reversal of magnetization can be exploited, for applications in thermomagnetic switches and volatile magnetic memory element.

Fig. 4 shows the switching behavior of the magnetization for $x=0.8$ nanoparticles under two (50 and 800 Oe) different magnetic fields applied in a cyclic manner. The magnetization of the nanoparticles switches between

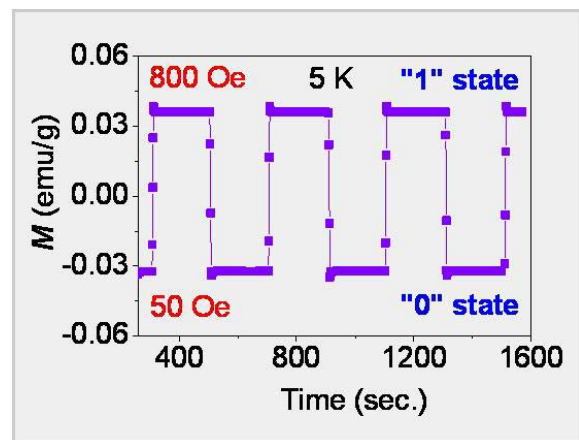


Fig. 4: Switching of the magnetization of $x=0.8$ nanoparticles at 5 K between positive and negative values under the application of two different magnetic fields in a cyclic manner.

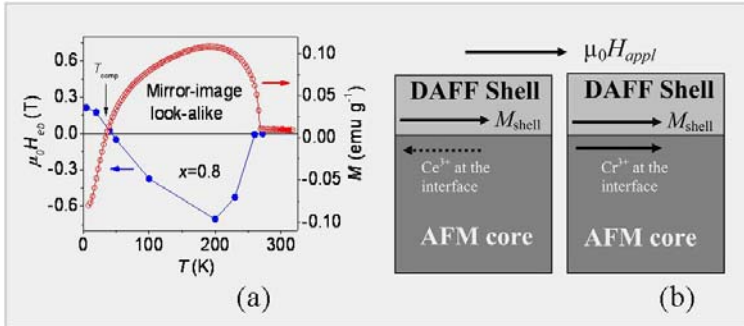


Fig. 5: (a) Mirror image-like behavior of the FC-magnetization and $\mu_0 H_{eb}$. (b) Schematic model to explain the sign-reversal phenomena. $\mu_0 H_{appl}$ is the externally applied magnetic field.

negative and positive values without any significant decay in its magnitude. The presence of the bi-stable states ('0' & '1') of the magnetization can be considered as equivalent to those of electrical resistance, electrical polarization, and reflectivity, which form the basis of a data storage material.³ However, once the external magnetic field is switched off, the corresponding magnetization-state does to exist, indicating that the present nanoparticles may be suitable for application in the volatile magnetic memories.

We have already given evidence that the nanoparticles are core-shell type in nature. Such core-shell systems are ideal for studying EB phenomenon, which is reflected mainly by a shift of the FC-hysteresis loop along the field-axis. The ZFC and FC hysteresis loops [Figs., not shown here] of the $x=0.8$ nanoparticles show that the ZFC-loop is symmetric around the origin, whereas the FC-loops are shifted along the field axis. Interestingly, below T_{comp} , the shift is along the positive field axis (positive EB), while above T_{comp} , the shift is along the negative field axis (negative EB). As a result, the temperature-dependence of the exchange bias field ($\mu_0 H_{eb}$) looks like a mirror-image [Fig. 5(a)] of the FC-magnetization.

To explain the coexistence of these two sign-reversal phenomena, we propose a schematic model based on the core-shell configuration [Fig. 5 (b)]. The net magnetization (M_{Net}) of the nanoparticles

results from the magnetization of the surface-shell (M_{Shell}) and the core consisting of Cr^{3+} (M_{Cr}) and Ce^{3+} (M_{Ce}) moments, and it can be expressed as, $M_{Net} = M_{Shell} + M_{Cr} - M_{Ce}$. The negative sign in M_{Ce} occurs because of the antiparallel orientation of the Ce^{3+} ionic moments, with respect to that of Cr^{3+} (discussed earlier). At $T > T_{comp}$, M_{Ce} is weak and thus, M_{Net} is positive, whereas at $T < T_{comp}$, the antiparallel orientation of M_{Ce} overcomes ($M_{Shell} + M_{Cr}$) giving rise to a negative magnetization in the presence of the magnetocrystalline anisotropy. To explain the

sign-reversal of EB, we now concentrate on the core-shell interface. Below T_{comp} , the AFM interface exchange coupling [Fig. 5(b), left side] between M_{Shell} and M_{Ce} predominates and thus, $\mu_0 H_{eb}$ becomes positive. Whereas, above T_{comp} , $\mu_0 H_{eb}$ becomes negative because of the dominant nature of the ferromagnetic (FM) interface exchange coupling between M_{Shell} and M_{Cr} [Fig. 5(b), right side]. The observed sign-reversal of EB-field can be used in TA-MRAM.

Let us now concentrate on the observed tunability in structural and magnetic parameters with changing x . A plot of the unit cell volume (V_U) of the nanoparticles obtained from the Rietveld refinement of the XRD patterns is shown in Fig. 6(a). A decrease in V_U is observed with increasing x . To explain this, we have plotted [Fig. 6(b)] the effective ionic radius (R_{eff}) of the La/Ce site, calculated using Shannon's table.⁸ A decrease in R_{eff} is found with increasing x , which signifies that the decrease in V_U is nothing but the effect of a relatively smaller ionic radius

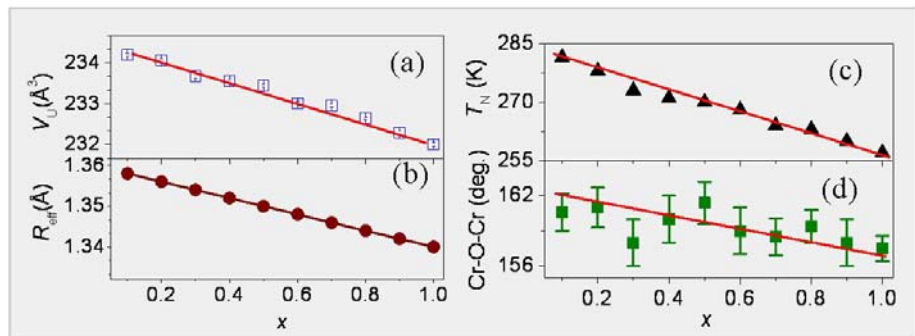


Fig. 6: Variation of (a) V_U and (b) R_{eff} ; (c) T_N and (d) Cr-O-Cr angle with x . The solid lines are guide to the eye.



of Ce^{3+} ions (1.34\AA) as compared to that of the La^{3+} ions (1.36\AA). From magnetic point of view, T_N of these nanoparticles can also be tuned by varying x . Fig. 6(c) shows the T_N vs. x plot of the nanoparticles, which shows a decrease in T_N with increasing x . To explain this behavior, we looked at the Rietveld-refined values of the Cr-O-Cr angles. With increasing x , Cr-O-Cr angle decreases [Fig. 6(d)] signifying a decrease in the AFM superexchange interaction between the Cr^{3+} ions. It is interesting to note that both V_U and T_N decrease almost linearly with x ; indicating the presence of an inter-link between structural and magnetic properties of the present nanoparticles.

Summary and Conclusion

We have observed the novel sign-reversal phenomena of magnetization ($x \geq 0.8$) and EB-field ($x = 0.8$) in the $\text{La}_{1-x}\text{Ce}_x\text{CrO}_3$ ($0.0 \leq x \leq 1.0$) nanoparticles. In order to explain these two phenomena, and explore the nature of magnetic ordering in these nanoparticles, we have employed different techniques, such as transmission electron microscopy, dc-magnetization, and neutron diffraction. The analysis of our experimental results shows that the nanoparticles are of core-shell type consisting of an AFM core and a reduced dimensional DAFF shell. The core-shell model has been used successfully, to explain both sign-reversal phenomena. We have also brought out the importance of these sign-reversal phenomena in volatile magnetic memory and TA-MRAM. Moreover, we observed that V_U and T_N of the nanoparticles can be tuned just by varying x , which provides a possible linkage between structural and magnetic properties.

References

1. Yoshii, K., Nakamura, A., Ishii, Y., and Morii, Y. "Magnetic Properties of $\text{La}_{1-x}\text{Pr}_x\text{CrO}_3$ ". *Journal of Solid State Chemistry* 162 (2001): 84-89.
2. Khomchenko, V. A., Troyanchuk, I. O., Szymczak, R., and Szymczak, H. "Negative magnetization in $\text{La}_{0.75}\text{Nd}_{0.25}\text{CrO}_3$ perovskite". *Journal of Materials Science* 43 (2008): 5662-5665.
3. Yusuf, S. M, Kumar, Amit, and Yakhmi, J. V. "Temperature- and magnetic-field-controlled magnetic pole reversal in a molecular magnetic compound". *Applied Physics Letters* 95 (2009) 182506.
4. Ren Y., Nugroho A. A., Menovsky A. A., Stremper J., Rütt U., Iga F., Takabatake T. and Kimball C. W. "Orbital-ordering-induced phase transition in LaVO_3 and CeVO_3 ". *Physical Review B* 67 (2003): 014107.
5. Shukla, R., Manjanna, J., Bera, A.K., Yusuf, S.M., and Tyagi, A.K. " $\text{La}_{1-x}\text{Ce}_x\text{CrO}_3$ ($0.0 \leq x \leq 1.0$): A New Series of Solid Solutions with Tunable Magnetic and Optical Properties". *Inorganic Chemistry* 48 (2009) 11691-11696, and references therein.
6. "FullProf Suite". <http://www.ill.eu/sites/fullprof/> (accessed on 15/07/2011).
7. Manna, P. K., Yusuf, S. M., Shukla, R. and Tyagi, A. K. "Coexistence of sign reversal of both magnetization and exchange bias field in core-shell type $\text{La}_{0.2}\text{Ce}_{0.8}\text{CrO}_3$ nanoparticles". *Applied Physics Letters* 96 (2010) 242508, and references therein.
8. Shannon, R. D. "Revised effective ionic radii and systematic studies of interatomic distances in halides and chalcogenides". *Acta Crystallographica* A32 (1976): 751-767.



Microstructural characterization of Al-base metallic foam developed by novel FSP technique

Kaushal Jha and K. N. Mahule

Engineering Design & Development Division

and

K. Bhanumurthy

Scientific Information Resource Division

and

G. K. Dey

Materials Science Division

This Paper received the 3rd Prize in poster presentation, at the International Conference on Advances in Electron Microscopy and Related Techniques, held at Mumbai from 8-11 March, 2010

Abstract

This paper discusses various microstructural features of Al-base metallic foams, prepared by FSP technique in 5052 Al alloy. Relative Density achieved was 50% of base metal. Pore sizes were observed in the range of 100 μm to 500 μm .

Introduction

In recent years, there has been a significant increase in interest, in the use of lightweight metallic foams for energy absorption roles, such as those in automotive applications and packaging materials. The metal foams are capable of absorbing a very large amount of energy at relatively low stresses i.e. they transmit lower force to the packaged material. This is due to large plateau stress. The other potential applications of foam include sandwich cores, lightweight structures, mechanical damping, flame arresters, heat shields, biocompatible inserts etc. All these properties of foams are sensitive to the macroscopic cellular structure, relative density, etc. [1,2].

Friction Stir Processing (FSP) is a relatively new solid state process and is used for microstructural modifications of metallic materials. FSP is based on the basic principle of

Friction Stir Welding (FSW) [3]. This method has been used for development of porous aluminium (5052) in the present investigation. The basic principle used for making metallic foam, is to distribute the blowing agent (TiH_2) in the metal and then heat it. FSP has been found to be a good technique, to distribute the blowing agent in the metal. Various steps involved in the development process include, diffusion bonding of Al plates with TiH_2 placed at pre-determined grooves, optimization of bonding process parameters, friction stir process and subsequently controlling the heating cycle, to get the desired porous aluminium structure.

Experimental

Friction Stir Processing (FSP) is based on the basic principle of FSW, but it is used to modify the local microstructure and control in the near-surface layer of the metal



components. It involves complex material movement and plastic deformation (results in proper mixing of TiH_2 powder in present case). Material undergoes intense plastic deformation at elevated temperature, resulting in generation of equiaxed recrystallised grains. This method has been used for the development of porous aluminium (5052) in the present investigation.

Various steps involved in the development processes were

- ❖ Making of channels in aluminium plate on a milling machine
- ❖ Mixing of Al + Titanium hydride powder for filling in the channels
- ❖ Diffusion bonding of Al plates with TiH_2 placed at pre-determined grooves
- ❖ Optimization of bonding process parameters
- ❖ Friction stir process of the plate with optimized parameter
- ❖ Heat the processed plate in a controlled way to get the desired porous aluminium structure.

The process has been shown in the flow chart in Fig. 1. The FSP tool used, is a shaped as a frustum of cone. The diameter of the tool shoulder is 18 mm. The diameter of tool probe is 6 mm and length of the tool probe is 4.8

mm. The thickness of bonded plate was 5mm. The rotation speed of the tool was 1120 rpm and tool was traversed on the plate at 40 mm/min. Initial study was done, by filling the channels with different amounts of TiH_2 (2%, 3% and 5% of weight of mixed powder placed in channels). The processing was done along the channels and also perpendicular to the channels. It was seen, that when the plate was processed perpendicular to the channels, it gave better foam. Hence, the plate was processed in a direction perpendicular to the channels. The processing has been done by overlapping approx. 2 mm. Yoshihiko Hangai et.al. [4] have processed along the channels and they have presented the effect of multi-pass on porosity. This was followed by heating the plate to yield foam.

Results and Discussion

The optical micrographs of the cross-section of the diffusion bonded specimens after friction stir processing, show nearly uniform distribution of TiH_2 particles. It was also seen that the density reduces with increase in the content of TiH_2 in the original grooves. The dissociation temperature was determined by DSC and it was found, that dissociation started at approx. 540° C. Based on this

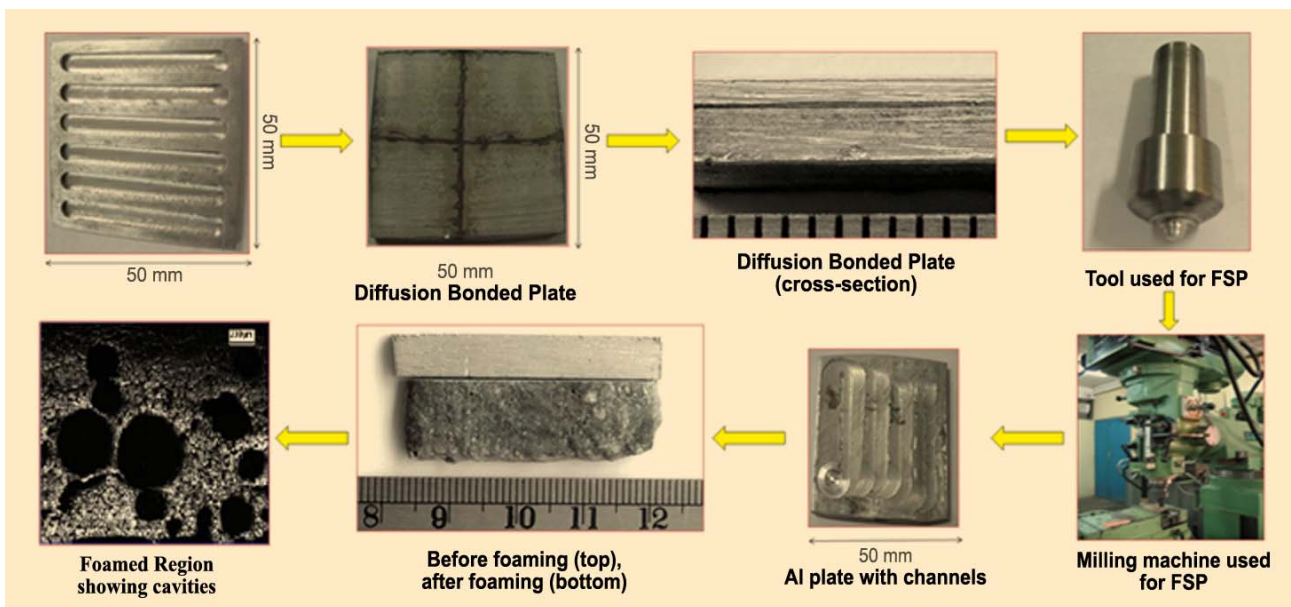


Fig. 1: Flow chart showing the complete process of foam fabrication by FSP



temperature, heating cycle for foaming was optimized. The density that could be achieved easily was close to 50% of the base metal with 5% TiH₂ filled in the grooves. Considering the total weight of the plate, hydride percentage in bulk comes to ~1%. To get lower density foams, percentage of hydride has to be increased. The optical micrographs of the cross-section of the diffusion bonded specimens after friction stir processing are shown in Fig. 2. This micrograph shows nearly uniform distribution of TiH₂ particles. A cross-section of typical foam is shown at lower magnification in Fig. 3(a) and at higher magnification in Fig. 3(b). It can be seen that, the pore size is in the range of 100 μm to 500 μm and these pores are nearly spherical in shape. Presence of micro-cracks can also be noticed in this micrograph.

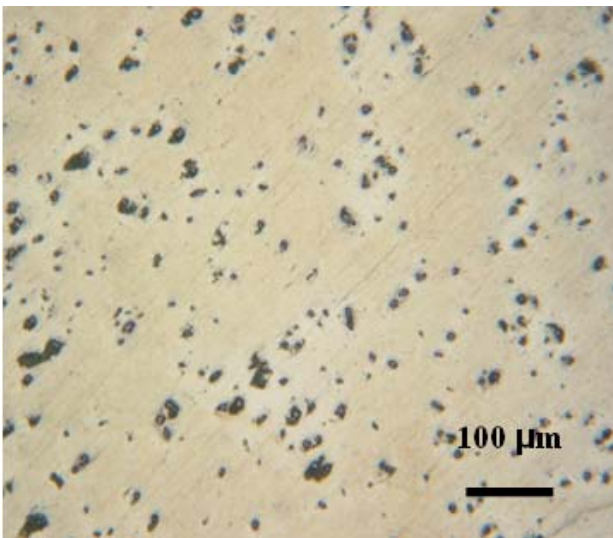


Fig. 2: Optical micrograph of the cross section of the diffusion bonded specimen after FSP showing the distribution of TiH₂ in base metal.

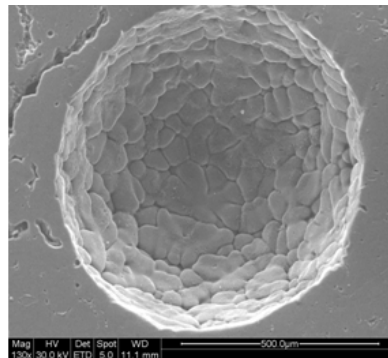
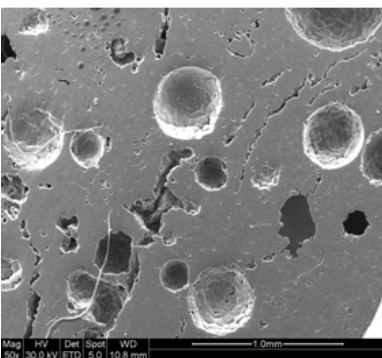


Fig. 3: Typical Secondary electron micrograph of Al-foam (a) Cross-section of foam (b) microstructure inside a single pore.

Conclusion

- (i) FSP on Al5052 alloy after diffusion bonding, seems to produce nearly uniform distribution of the blowing agent. The processing was done in the direction perpendicular to the channels.
- (ii) The optimum parameters for processing Al 5052 alloy were found to be 1120 rpm and 40 mm/min traverse speed.

FSP seems to be a promising technique, to produce foams with better mechanical properties as compared to other techniques. Initial trials with limited resources are successful and indicate that FSP has a high potential for fabrication of porous aluminium at a relatively lower cost.

References

1. M. Ashby, Tony Evans, N A Fleck, L J Gibson, J W Hutchinson, H N G Wedly, "Metal foam: A design guide", Butterworth-Heinemann (2000)
2. J. Baumeister, J. Banhart, M. weber, "Aluminium foam for transport industry", *Mat. & Des.* Vol. 18. 217-220, 1997.
3. R. S. Mishra, Z. Y. Ma, "Friction stir welding and processing", *Mat. Sc. Engg.* R 50 (2005) 1-78.
4. Yoshihiko Hangai, Takao Utsunomiya, Makoto Hasegawa, "Effect of tool rotating rate on foaming properties of porous aluminium fabricated by using friction stir processing", *J. Mat. Processing Tech.* 210 (2010) 288-292.



PROSPECTIVE APPLICATIONS OF BIOTECHNOLOGICAL METHODS IN SALT ACCUMULATOR HALOPHYTE *SESUVIUM PORTULACASTRUM* (L.) L.

Vinayak H. Lokhande and Tukaram D. Nikam

Department of Botany, University of Pune

and

Penna Suprasanna

Functional Plant Biology Section, Nuclear Agriculture and Biotechnology Division

This Paper received the Best Poster Award, at the International Conference on 'Biotechnology: A Global Scenario' organized by Department of Biotechnology, held at Kakatiya University, Warangal, Andhra Pradesh from 2-4 November, 2010

Abstract

Sesuvium portulacastrum (L.) L., (Aizoaceae) is a pioneer, psammophytic, salt accumulator and facultative halophyte, growing along the coastal and warmer zones of the world. The plant is used as a source of food and forage, has ability to grow under adverse abiotic stress conditions and shows significant potential for environmental protection. The plant contains secondary metabolite phytoecdysteroid- 20 hydroxyecdysone (20E), an insect molting hormone useful in sericulture industry. This paper demonstrates the establishment of plant tissue culture, *Agrobacterium rhizogenes* mediated-transformation, for the production of hairy root cultures, salt stress responses and detoxification of toxic, hazardous and carcinogenic textile dye Green HE4B (GHE4B), using *in vitro* grown plantlets. The results suggested use of axillary shoots as the best choice to study the salt stress responses, as compared to unorganized cell biomass or the whole plant. The *in vitro* grown plantlets were used for the study of detoxification of textile dye Green HE4B, using analytical methods viz., FTIR, HPLC and GCMS and degradation into non-toxic metabolites. In summary, we have successfully explored different dimensions of the halophytic plant system, *Sesuvium*, for both basic and applied applications. Further research in understanding the halophytic behavior of this plant, should enable it to develop into a valuable model system.

Introduction

Abiotic stresses such as drought, flooding, high salinity, sub-zero, low or high temperatures, inorganic nutrient imbalance, oxidative stress, heavy metals toxicity and natural or man-made toxic compounds, cause reduction in crop productivity and crop failure (Flowers 2004). Plants have evolved adaptative strategies to manage the changing environmental conditions, particularly with the available resources. Some plant species have retained their habitat in nutrient-rich marine environment and were found to be more successful in combating the adverse abiotic stresses, referred to as 'halophytes' (Flowers et al. 2010).

Sesuvium portulacastrum (L.) L., commonly known as 'seapurslane' is an important 'salt accumulator' facultative halophyte, belonging to the family Aizoaceae (Fig. 1). It grows naturally in the subtropical, Mediterranean, coastal and warmer areas around the world and in India, distributed along the coastal sides of eastern and western regions (Lokhande et al. 2009). The plant has shown its potential to continue growth under adverse environmental conditions such as salinity, drought and heavy metals (Slama et al. 2007; Lokhande et al. 2009, 2010, 2011a, b). *Sesuvium* has been used widely as pioneer species for environmental protection such as sand dune fixation, saline soil stabilization, desalination of saline soil, desert



Fig. 1: Habitat and flower variation (pink and white colour) of *Sesuvium portulacastrum*

greenification and as an ornamental plant. (Lokhande et al. 2009). The plant has revealed its importance in effective removal of heavy metals such as cadmium, lead and arsenic from contaminated sites (Ghnaya et al. 2007; Lokhande et al. 2011b). Recently, the plant has shown its application as a source of organic fertilizer, for improving the soil fertility and productivity of crop plants (Ravindran et al. 2007) and as a substitute for salt in the curing process of goatskins (Kanth et al. 2009). This plant is used in traditional medicine as a remedy for fever, kidney disorders and scurvy and showed positive activity against human immunodeficiency virus (HIV) (Padmakumar and Ayyakkannu 1997). The essential oil extracted from the leaves of *Sesuvium*, revealed notable antibacterial activity against both gram-positive and gram-negative bacteria and displayed significant antifungal and antioxidant activity (Magawa et al. 2006). Besides, *Sesuvium* contains a secondary metabolite phytoecdysteroid- 20-hydroxyecdysone (20E) with insect molting activity and

therefore, finds use in sericulture industry (Lokhande et al. 2009).

Considering its importance and application in sustainable agriculture towards desalinization, phytoremediation and environmental protection, research needs to be directed, for exploiting different biotechnological methods. In this article, our results on establishment of plant tissue culture, *Agrobacterium rhizogenes*-mediated transformation for the production of hairy root cultures, salt stress responses and detoxification of toxic, hazardous and carcinogenic textile dye Green HE4B (GHE4B), using *in vitro* grown plantlets are described.

In Vitro Propagation

Nodal explants (~ 10 mm, from plants grown in the Department of Botany garden, University of Pune, Pune) were surface sterilized with 0.1% (w/v) mercuric chloride for 5 min, according to standard protocol. These explants were cultured on MS (Murashige and Skoog 1962) medium containing 3 % sucrose, 10 μ M BA (6-benzyladenine), pH 5.8 and solidified with 0.8% agar. The cultures were maintained at $25 \pm 2^\circ\text{C}$ and 16 h photoperiod under cool white fluorescent light (Philips India, Ltd., 40 $\mu\text{mol m}^{-2} \text{s}^{-1}$) and 70 % relative humidity for one month. After one month, axillary shoots induced from nodal explants were excised and cultured on MS medium, supplemented with different concentrations (0, 10, 20, 40 or 60 μ M) of BA, Kinetin (Kin), thiodiazuron (TDZ) and 2-isopentenyl adenine (2iP) on freshly prepared shoot induction medium. After one month, data was recorded on number of shoots per explant, percent explants forming shoots, average shoot length (mm), number of roots per explants, percent shoots forming roots and average root length (mm) from 20 explants replicated at least thrice. For rooting, single axillary shoots were transferred to MS liquid medium supplemented with 0, 2.5, 5.0, 10 or 20 μ M NAA (α -naphthaleneacetic acid) or IAA (Indole-3-acetic acid). The rooted plantlets were further acclimatized under *ex vitro* conditions. Fig. 2 presents the different steps in tissue culture of *Sesuvium*.

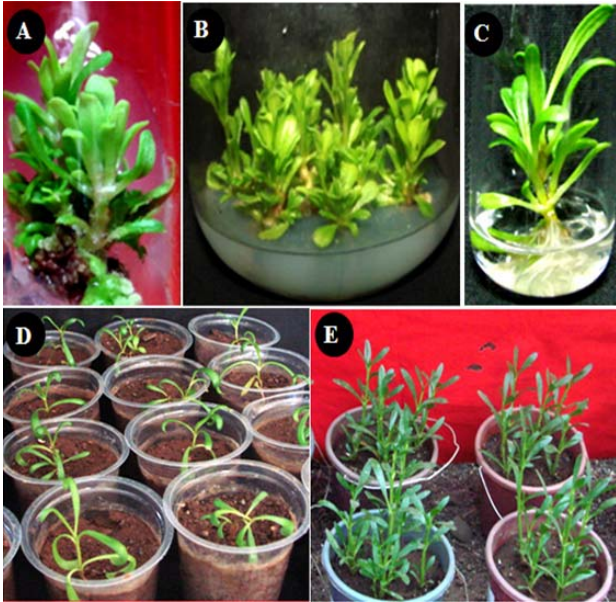


Fig. 2: Tissue culture of *S. portulacastrum*. A: shoot induction from nodal explant on MS + 10.0 uM BA; B: Multiple shoots maintained on MS + 20.0 uM BA; C: Rooting to the shoots on MS + 5.0 and 10.0 uM NAA; D and E: Rooted plants hardened in small and large plastic pots.

Among the different concentrations of cytokinins (BA, Kin, TDZ and 2iP), 20 µM BA and 40 µM, were found to be most effective for the production of significantly higher number of multiple shoots per explant, in comparison to other cytokinins. While higher concentrations of BA and 2iP inhibited growth and shoot formation frequency, TDZ and Kin were ineffective for shoot multiplication. Addition of NAA (5.0 or 10 µM) significantly increased root induction frequency, however, the highest number of roots

per axillary shoot, root elongation and root induction frequency were observed on MS medium, supplemented with 10 µM NAA. The hardened plants upon transfer to field conditions, showed greater than 85 % survival rate and similar morphology as their parent plants growing under natural conditions.

Hairy Root Production

The leaves and stem segments (nodal and internodal sectors) of *in vitro* grown axillary shoots were used as source of explants, for the production of hairy roots. The explants were pre-cultured on MS basal medium prior to infection with *A. rhizogenes* strain NCIM 5140 (ATCC 5140; procured from the National Chemical Laboratory, Pune). The explants were then infected with bacterial suspension for 30 min at 28°C, followed by co-cultivation for 48 hrs. The residual of the bacterium was removed by transferring the explants on antibiotic cefotaxime (400 mg l⁻¹), followed by final transfer on MS basal medium. After 20-30 days of culture initiation, observations were made on hairy root induction from the cut edges of explants. The transgenic nature of hairy roots was confirmed, by phenotypic observation as well as through PCR amplification, of 970 bp domain of T-DNA region of *A. rhizogenes* plasmid. Results on hairy root induction are presented in Fig. 3. Leaf explants revealed significantly the highest percentage of hairy root induction (70%) as compared to stem explants

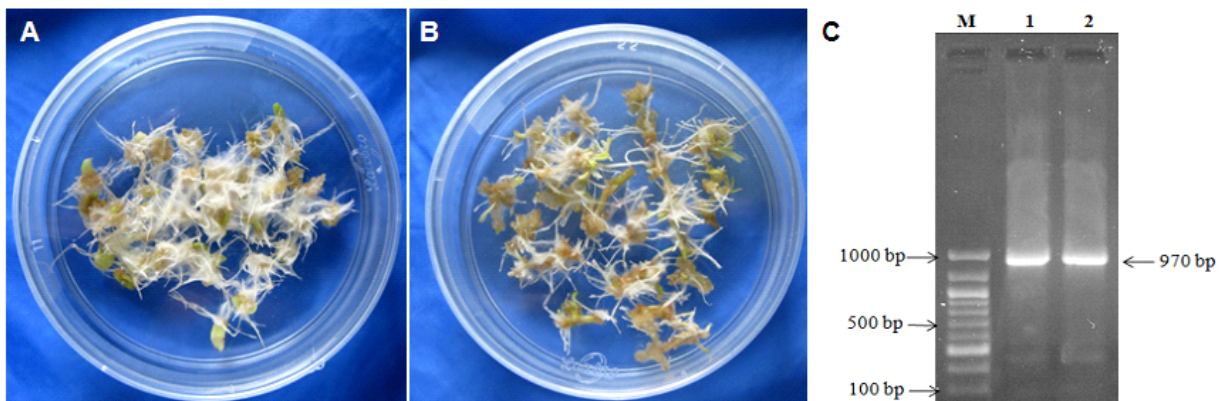


Fig. 3: Hairy root induction in *S. portulacastrum*. A and B: Hairy roots induced from *in vitro* grown leaf and nodal explants and C: PCR amplification of 970 bp TDNA region of Ri plasmid showing confirmation for transgenic nature of hairy roots (M: 100 bp DNA ladder; 1 and 2: PCR amplification product of genomic DNA extracted from hairy roots induced from leaf and nodal explants).



(52%) after 28 d of culture. The negative geotropism, growth on plant growth hormone free medium and fast growth, confirmed the phenotypic nature of transformed hairy roots, induced from leaf and stem explants of *S. portulacastrum*. Further, PCR amplification confirmed the successful integration of T-DNA from *A. rhizogenes* ATCC 1540 into the hairy root genomic DNA, which showed the transformed nature of hairy roots.

Physiological and Biochemical Responses to Salt Stress

Physiological and biochemical responses to salt stress were studied at *in vitro* (callus and axillary shoots) and *ex vitro* (whole plant) level, in relation to growth, water status (percent water content, FW/DW ratio), osmotic adjustment (accumulation of osmolytes- proline, glycine betaine and total soluble sugars- TSS), oxidative stress (membrane damage rate through MDR and MDA content) and activities of antioxidant enzymes (catalase- CAT, ascorbate peroxidase- APX and superoxide dismutase- SOD). The callus cultures were exposed to 0, 100, 200 and 400 mM NaCl for 15 days, axillary shoots to 0, 200, 400 and 600 mM NaCl for 8 days, whereas *ex vitro* grown plants were exposed to 0, 200, 400, 600 and 800 mM NaCl for 15 days. The results demonstrated, that the mechanism of salinity tolerance operating at cellular, axillary shoots and whole plant levels, were found to be similar and improved with increase in the levels of tissue organization. Besides, higher efficiency of saline ions accumulation and its sequestration into vacuoles, osmolytes synthesis, and antioxidant enzyme activities (for maintenance of higher osmotic balance and detoxification of excessively produced reactive oxygen species) significantly contributed to the tolerance. Further, the results suggested use of axillary shoots as the best choice to study the salt stress responses as compared to unorganized cell biomass (callus) or the whole plant.

Detoxification of Textile Dye GHE4B

Attempts have been made to study the decolorization of a toxic textile dye Green HE4B (GHE4B), using *in vitro*

grown *Sesuvium* plantlets. Results on decolorization of GHE4B are presented in Fig. 4. The plantlets exhibited significant (70%) decolorization of GHE4B (50 mg l⁻¹) in the presence of 200 mM sodium chloride (NaCl) within 5 days of incubation. The enzymatic analysis performed on the root and shoot tissues of the *in vitro* plantlets, subjected to GHE4B decolorization in the presence of 200 mM NaCl showed a noteworthy induction of tyrosinase, lignin peroxidase and NADH-DCIP reductase activities, indicating the involvement of these enzymes in the metabolism of the dye GHE4B. The UV-visible spectrophotometer, High Performance Liquid Chromatography (HPLC) and Fourier Transform Infrared Spectroscopy (FTIR) analysis of the samples, before and after decolorization of the dye, confirmed the efficient phyto-transformation of GHE4B

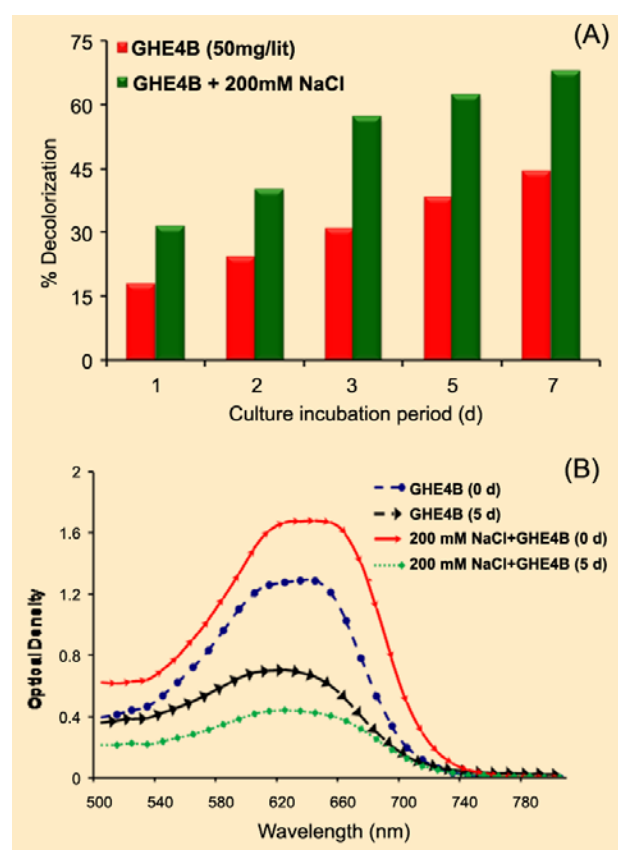


Fig. 4: Detoxification of toxic textile dye GHE4B using *in vitro* plants of *Sesuvium*. A: Percent decolorization of GHE4B (50 mg/lit) in presence or absence of NaCl (200 mM) under variable incubation period and B: Absorption spectra for decolorization of GHE4B in presence or absence of NaCl after initial (0 d) and final (5 d) incubation period.



in the presence of 200 mM NaCl. Gas Chromatography Mass Spectroscopy (GC-MS) analysis of the products revealed formation of three metabolites such as p-amino benzene, p-amino toluene and 1, 2, 7-amino naphthalene after phyto-transformation of GHE4B. The present study for the first time showed the prospect of *Sesuvium* for efficient degradation of textile dyes and its efficacy on the saline soil contaminated with toxic compounds.

Taken together, our studies indicated successful exploration of different dimensions of the halophytic plant system, *Sesuvium*, for both basic and applied applications. Further research in this plant should enable it develop into a useful model system.

Acknowledgements

The senior author is grateful to the Department of Atomic Energy (DAE), the Board for Research in Nuclear Science (BRNS), for the financial support under the BARC-UOP collaborative Ph.D. research program, and Dr. S. F. D'Souza, Associate Director (A), BMG & Head, NABTD for encouragement and support.

References

- Banerji A, Chintalwar GJ, Joshi NK, Chadha MS (1971) Isolation of ecdysterone from Indian plants. *Phytochem* 10:2225-2226.
- Flowers TJ (2004) Improving crop salt tolerance. *J Expt Bot* 55:307-319.
- Flowers TJ, Colmer TD (2008) Salinity tolerance in halophytes. *New Phytol* 179:945-963.
- Flowers TJ, Galal HK, Bromham L (2010) Evolution of halophytes: multiple origins of salt tolerance. *Funct Plant Biol* 37:604-612.
- Ghnaya T, Slama I, Messedi D, Grignon C, Ghorbel MH, Abdely C (2007) Effect of Cd²⁺ on K⁺, Ca⁺ and N uptake in two halophytes *Sesuvium portulacastrum* and *Mesembryanthemum crystallinum*: Consequences on growth. *Chemosphere* 67:72-79.
- Kanth SV, Keerthi PB, Selvi AT, Sarvanan P, Rao RJ, Nair BU (2009) Studies on the use of *Sesuvium portulacastrum*- Part II: preservation of skins. *J Amer Leather Chem Associat* 104:25-32.
- Lokhande VH, Nikam TD, Suprasanna P (2009) *Sesuvium portulacastrum* (L.) L., a promising halophyte: cultivation, utilization and distribution in India. *Genet Resour Crop Evol* 56:741-747.
- Lokhande VH, Nikam TD, Patade VY, Ahire ML, Suprasanna P (2011a) Effects of optimal and supra-optimal salinity stress on antioxidative defence, osmolytes and in vitro growth responses in *Sesuvium portulacastrum* L. *Plant Cell Tiss Org Cult* 104:41-49.
- Lokhande VH, Nikam TD, Suprasanna P (2010) Biochemical, physiological and growth changes in response to salinity in callus cultures of *Sesuvium portulacastrum* L. *Plant Cell Tiss Org Cult* 102:17-25.
- Lokhande VH, Srivastava S, Patade VY, Dwivedi S, Tripathi RD, Nikam TD, Suprasanna P (2011b) Investigation of arsenic accumulation and tolerance in *Sesuvium portulacastrum* (L.) L. *Chemosphere* 82:529-534.
- Magawa ML, Gundidza M, Gweru N, Humphrey G (2006) Chemical composition and biological activities of essential oil from the leaves of *Sesuvium portulacastrum*. *J Ethnopharmacol* 103:85-89.
- Murashige T and Skoog F (1962) A revised medium for rapid growth and bioassays with tobacco tissue cultures. *Physiol Plant* 15: 473-497.
- Padmakumar K, Ayyakkannu K (1997) Seasonal variation of antibacterial and antifungal activities of the extracts of marine algae from Southern coast of India. *Bot Mar* 40:507-515.
- Ravindran KC, Venkatesan K, Balakrishnan V, Cehllappan KP, Balasubramanian T (2007) Restoration of saline land by halophytes for Indian soils. *Soil Biol Biochem* 39:2661-2664.
- Slama I, Ghnaya T, Hessini K, Messedi D, savoure A, Abdely C (2007) Comparative study of the effects of mannitol and PEG osmotic stress on growth and solute accumulation in *Sesuvium portulacastrum*. *Environ Expt Bot* 61:10-17.



Radiation synthesized stimuli-responsive HEMA-co-MAETC hydrogels

N.K. Goel, V. Kumar, Y.K. Bhardwaj and S. Sabharwal
Radiation Technology Development Division

This paper received the Best Poster Award at the 3rd Asia Pacific Symposium on Radiation Chemistry and at the DAE-BRNS 10th Biennial Trombay Symposium on Radiation & Photochemistry (TSRP-2010), held at Lonavala, September, 14-17, 2010

Abstract

A stimuli-responsive 2-Hydroxyethylmethacrylate-co-[2-(Methacryloyloxy)-ethyl]trimethylammonium chloride (HEMA-co-MAETC) hydrogel, was synthesized via radiation polymerization/crosslinking process, using ⁶⁰Co-gamma radiation. The swelling extent as well as bulk morphology of hydrogel was significantly affected by concentration of MAETC in the co-monomer feed. HEMA-co-MAETC hydrogel exhibited a reversible swelling/volume transition, in response to the ionic strength of the swelling medium. The temperature of swelling medium enhanced the swelling rate without affecting the swelling extent of the hydrogel. In addition, the swelling of the copolymer hydrogel gel at 60°C reduced the swelling-deswelling cycle time by ~30 % of that at room temperature (~28°C) without altering the swelling extent.

Introduction

Hydrogels are three-dimensional networked structures of polymer chains, which swell in the aqueous environment without dissolving or losing their structural integrity¹. The network is often formed by covalently crosslinked polymers, but ionic bonds, crystalline regions, entanglements and Van der Waals forces can also lead to water swellable polymer networks^{2,3}. Water imbibing properties of hydrogels enable them to be employed for several pharmaceutical applications, superabsorbent materials for sanitary napkins, sensors, separation adsorbents and controlled drug delivery systems. The applications of hydrogels are mainly governed by factors such as, equilibrium swelling degree, dynamics of swelling and stimuli responsive property⁴⁻⁶. Introduction of a very small amount of ionic polymers in neutral hydrogel matrix is an easy method to regulate the swelling extent as well

as to induce stimuli responsive behavior into parent neutral hydrogel without compromising the properties of the parent matrix⁴⁻⁶.

Experiment/Method

Radiation induced synthesis of hydrogels

HEMA, MAETC solution (75% aq.w/v) and water were mixed in various ratios and filled in glass tubes, deoxygenated by purging N₂ and sealed. Polymerization was carried out by irradiating the sealed samples at room temperature for dose of 3.75 kGy by gamma rays from a ⁶⁰Co γ -source. The increase in the mass of the samples immersed in aqueous solutions was monitored gravimetrically and the swelling ratio and Equilibrium Degree of Swelling (EDS) of the gels was determined as

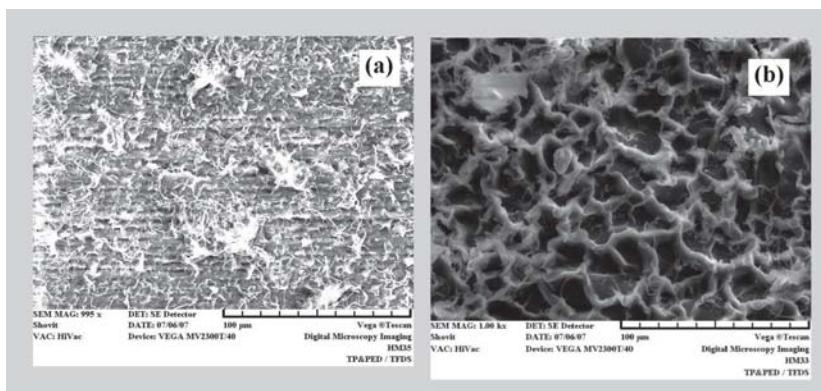


Fig. 1: SEM image of swelled hydrogel (a) Pure HEMA and (b) MAETC-co-HEMA

Swelling ratio = (Swelled weight-Initial weight)/Initial weight.

EDS (%) = (Swelled weight/Initial weight) x 100

Results and Discussion

FTIR and SEM analysis

The chemical characteristics and bulk morphology of the HEMA-co-MAETC hydrogels were investigated by FTIR spectroscopy and Scanning Electron Microscopy (SEM) techniques, respectively. The additional FTIR peaks at 1240 cm⁻¹ (–C–N stretching) in copolymer gels confirm the presence of MAETC in the HEMA matrix. Fig. 1 shows the SEM images of the gels, which clearly indicates that the pore size of the gel drastically is increased due to the presence of MAETC in the copolymer gel, which was further supported by the increase in the swelling ratio (Table 1).

Swelling of gels

EDS of copolymer gels with varying feed compositions were studied, at different concentration of electrolytes (NaCl), pH, and temperatures. EDS of gel was found to be proportional to the content of MAETC in the gel matrix (Fig. 2), and irregular trend was obtained in various pH (data not shown). The copolymer gel exhibited ionic strength responsive characteristics manifested by the drastic deswelling in the NaCl solutions (Table

1). The swelling-deswelling cycle in water-NaCl solution was repeated several times.

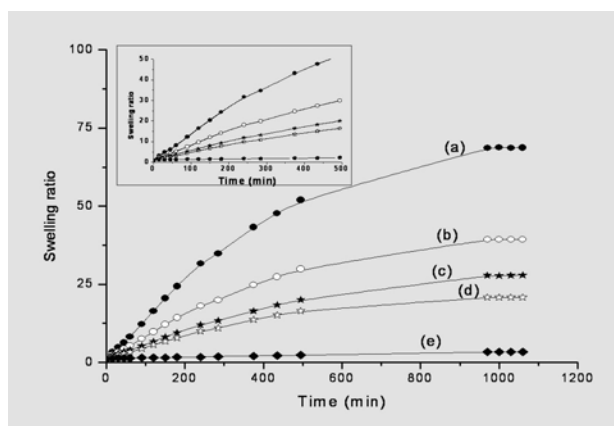


Fig. 2: Swelling kinetics of HEMA-co-MAETC gels in double distilled water at 28°C (a) HM31 (b) HM32 (c) HM33 (d) HM34 (e) HM35. Inset: Swelling kinetics at lower time

Table 1: Composition and EDS of hydrogels in water and NaCl solution

Sample	[HEMA] (mole fraction)	[MAETC] (mole fraction)	EDS (%)				
			Water	0.01N NaCl	0.05N NaCl	0.1N NaCl	0.5N NaCl
HM31	0.85	0.15	7394	2729.7	1191.1	766.1	325.7
HM32	0.89	0.11	3997	1665.3	742.3	500.1	207.9
HM33	0.91	0.09	2817	1436.3	581.3	393.4	165.6
HM34	0.93	0.07	2063	1316.7	471.9	326.4	139.8
HM35	0.97	0.03	268	198.9	115.4	98.6	71.9



The effect of temperature on the responsive behavior, (i.e., swelling-deswelling cycle in water-0.5N NaCl solution) of the co-polymer gels is shown in Fig. 3. Interestingly, temperature of the medium didn't affect the swelling ratio significantly but the swelling rate in water increased significantly with increase in the temperature. The increase in the temperature from 28° to 60° decreases the swelling-deswelling cycle duration by ~ 30%.

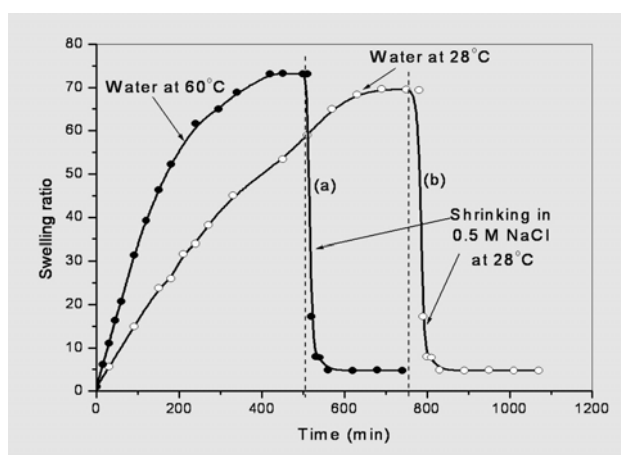


Fig. 3: Effect of temperature on the responsive behaviour of MAETC-co-HEMA gel.

Conclusion

Radiation polymerization/crosslinking is an easy process to develop an ionic strength responsive hydrogel, by incorporating an ionic polymer (PMAETC) into a non-ionic polymer matrix (PHEMA). The swelling extent and responsive behavior can be easily controlled by swelling medium conditions, such as electrolyte concentration and temperature.

References

1. Tokita, M., Tanaka, M. J. "Friction Coefficient of Polymer Networks of Gels". *J. Chem. Phys.* 95 (1991): 4613-19.
2. Peppas, N. A., Mikos A. G. *Hydrogels in medicine and pharmacy: Fundamentals*, CRC Press, Boca Raton Fla, 1986.
3. Park, K., Shalaby, W. S. W., Park H. *Biodegradable hydrogels for drug delivery*, Technomic, Lancaster PA, 1993.
4. Goel, N. K., Virendra Kumar, Bhardwaj, Y. K., Sabharwal. S. J. *Macromol. Sci. A-Pure Appl. Chem.* 43 (2006): 327-34.
5. Goel, N. K., Virendra Kumar, Bhardwaj, Y. K., Biswal, J., Sabharwal. S. J. *Macromol. Sci. A-Pure Appl. Chem.* 43 (2006): 1151-66.
6. Virendra Kumar, Chaudhari, C. V., Bhardwaj, Y. K., Goel, N. K., Sabharwal. S. *Eur. Polym. J.* 42 (2006): 235-46.



Room temperature synthesis of $MWO_4:Eu^{3+}$ ($M = Ca, Sr, Ba$) nanomaterials

B.S. Naidu, V. Sudarsan and R.K. Vatsa

Chemistry Division

and

B.Vishwanadh

Materials Science Division

This paper received the Best Poster Award, at the International Conference on Materials Chemistry (ISMC 2010), held at BARC, Mumbai, during December 7-11, 2010

Abstract

Undoped and Eu^{3+} doped MWO_4 ($M=Ca, Sr, Ba$) nanomaterials were prepared at room temperature by co-precipitation method and characterized by XRD, TEM and photoluminescence techniques. It is observed that average crystallite size of MWO_4 nanomaterials increases, with increasing M^{2+} ionic size. Strong red emission has been observed from Eu^{3+} doped MWO_4 nanomaterials and the emission intensity decreases with increase in ionic size of M^{2+} . The decrease in emission intensity is attributed to soft surrounding around Eu^{3+} ion in the host lattice having higher ionic radii M^{2+} ions.

Introduction

Tungstate materials have attracted much attention over the past two decades, due to their important properties and applications in photoluminescence, microwave devices, optical fibers, scintillator materials, humidity sensors and catalysis [1-4]. Preparing them in nanosize dimension and understanding their optical properties will be of interest and will be relevant for developing different types of optical materials, for various applications. Further, lanthanide ions once incorporated in the lattice can result in energy transfer from host to lanthanide ions, thereby leading to improved luminescence from such materials. Due to similarities in coordination number and ionic sizes of ions like calcium with trivalent lanthanide ions [5], it is easy to replace M^{2+} ion by Ln^{3+} ion in the MWO_4 ($M=Ca, Sr, Ba$) lattice. It will be interesting if lanthanide doped

MWO_4 nanoparticles can be obtained at low temperature with suitable ligand stabilization, so that they can be dispersed in different solvents for further processing. Such nanoparticles are also expected to have different luminescence properties as compared to those prepared through solid-state method. Keeping this in view, in the present study, a number of MWO_4 nanoparticles doped with Eu^{3+} were prepared. For the preparation of MWO_4 nanomaterials, sodium tungstate solution was added to ethylene glycol containing metal nitrates and stirred for two hours. The precipitate was collected by centrifugation and washed with methanol and acetone. The precipitate was dried under ambient conditions and used for characterization.



Effect of nature of metal ion on the particle size

Fig.1 shows XRD patterns of MWO_4 ($M = Ca, Sr, Ba$) nanomaterials. All the peaks are characteristic of nanocrystalline tetragonal MWO_4 with scheelite structure. The shifting of XRD peak maximum to lower 2θ values from Ca to Ba through Sr is due to increase in the ionic radii of cation and associated lattice expansion. Line widths of diffraction peaks are also found to decrease, with increase in the ionic radii of the metal ion. Average crystallite size was calculated by using Debye-Scherrer formula and was found to be 7, 10, 20 nm for $CaWO_4$, $SrWO_4$ and $BaWO_4$, respectively.

Lattice parameters were calculated by least squares fitting of the XRD patterns. These are found to be $a = 5.240 \text{ \AA}$, $c = 11.381 \text{ \AA}$ for $CaWO_4$, $a = 5.415 \text{ \AA}$, $c = 11.951 \text{ \AA}$ for $SrWO_4$ and $a = 5.613 \text{ \AA}$, $c = 12.703 \text{ \AA}$ for $BaWO_4$ nanoparticles. The increase in the lattice parameters is due to increase in the ionic sizes of metal ions. Increase in particle size with increase in ionic radius of the metal cation can be explained based on the difference in the extent of stabilization of ligand (EG moiety) on the surface of MWO_4 nanoparticles. As the stabilization of EG moiety on the nanoparticles occurs through cations like Ca^{2+} ,

Sr^{2+} and Ba^{2+} , the extent of stabilization of ligand will be the highest for $CaWO_4$ nanoparticles and lowest for $BaWO_4$ nanoparticles, due to the so called hard-hard and soft-soft interactions. Extent of stabilization of ligands with $SrWO_4$ is in between that of $CaWO_4$ and $BaWO_4$. Higher the extent of stabilization, lower will be the extent of growth and this result in smaller particles.

TEM images of $CaWO_4$, $SrWO_4$ and $BaWO_4$ nanomaterials are shown in Fig.2. $CaWO_4$ nanoparticles are relatively small with size in the range 5-10 nm and have uniform size distribution as can be seen in Fig.2 (a). The SAED pattern from these nanoparticles is shown in the inset of Fig.2 (a). The pattern consists of several rings, which are characteristic of very fine particles that are randomly oriented. HRTEM image of $CaWO_4$ nanoparticles is shown in Fig.2 (b). Distance between lattice fringes is found to be 3.1 Å and this matches well with that of (112) plane of $CaWO_4$. TEM image of $SrWO_4$ nanoparticles is shown in Fig.2 (c). It is clear from the image that particles have homogeneous size distribution with sizes in the range of 15-25 nm. Corresponding SAED pattern shown in the inset of Fig.2 (c) consists of both rings, and dots characteristic of nanocrystalline $SrWO_4$ phase with slight aggregation. TEM image of $BaWO_4$ nanoparticles is shown in Fig.2 (d). These particles are having rice shape with

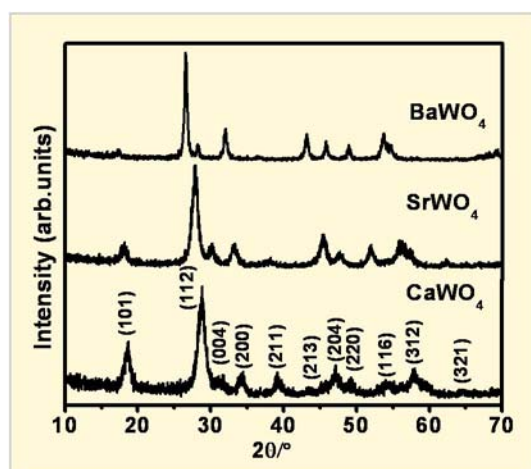


Fig.1: XRD patterns of MWO_4 ($M = Ca, Sr, Ba$) nanoparticles.

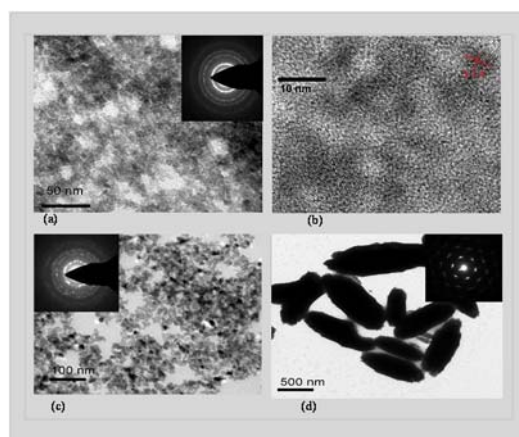


Fig. 2: TEM image of (a and b) $CaWO_4$, (c) $SrWO_4$ and (d) $BaWO_4$ nanomaterials and inset of the images shows corresponding SAED pattern.



length around 500-1000 nm. SAED pattern from $BaWO_4$ nanoparticles is shown in the inset of Fig.2 (d) and the pattern mainly consists of dots and is characteristic of single crystalline nature of $BaWO_4$ nanomaterials. Based on XRD and TEM studies it is inferred that $CaWO_4$ nanoparticles are relatively smaller in size compared to other two tungstates. It will be interesting to assess these MWO_4 nanomaterials for their luminescence properties. Hence, these nanomaterials are doped with representative lanthanide ion namely the Eu^{3+} and their luminescence properties are described in the following section.

Effect of metal ion on luminescence of $MWO_4:Eu^{3+}$ nanoparticles:

Emission spectra of Eu^{3+} doped (2%) MWO_4 ($M = Ca, Sr, Ba$) nanoparticles excited at 270 nm is given in Fig. 3 (a). It consists of four peaks at 590, 615, 650 and 700 nm and are attributed to $^5D_0 \rightarrow ^7F_1, ^5D_0 \rightarrow ^7F_2, ^5D_0 \rightarrow ^7F_3$ and $^5D_0 \rightarrow ^7F_4$ transitions of Eu^{3+} ions present in the lattice. The $^5D_0 \rightarrow ^7F_2$ transition is electric dipole allowed transition. It is hypersensitive and is highly dependent on the symmetry around the Eu^{3+} ion. Unlike this, $^5D_0 \rightarrow ^7F_1$ transition is a magnetic dipole allowed transition and is independent of the symmetry around Eu^{3+} ion in the lattice. Asymmetric ratio is ~ 12 for all the three tungstates. High value of asymmetric ratio indicates that Eu^{3+} ion occupies a highly asymmetric environment in MWO_4 ($M = Ca, Sr, Ba$) crystal lattice. The intensity of Eu^{3+} emission decreases with increase in the ionic size of the alkaline earth metal cations. Similar effect was observed by Blasse et al.[6] for UO_6 emission in the tungstate host. Presence of ions with large radius around the luminescent center is equivalent to soft surroundings. With increase in the softness of surroundings, Stokes shift increases and as a result, the excited tungstate group decays by a non-radiative route to ground state, instead of transferring energy to lanthanide ions. This explains the decrease in

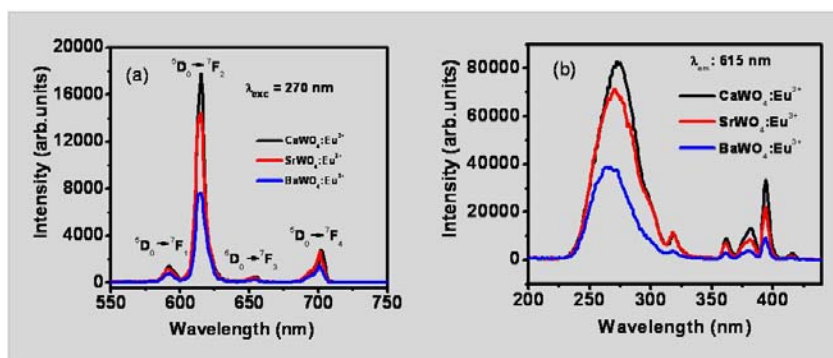


Fig. 3: (a) Emission spectra and (b) excitation spectra from $CaWO_4:Eu^{3+}$, $SrWO_4:Eu^{3+}$, $BaWO_4:Eu^{3+}$ nanoparticles. ($\lambda_{exc} = 270$ nm and $\lambda_{em} = 615$ nm)

luminescence intensity when going from $CaWO_4$ to $SrWO_4$ and then to $BaWO_4$. It is also known, that with increase in the stiffness of the lattice, non-radiative process decreases, leading to improvement in photoluminescence.

In the present case, the ionic radii of metal ion increases while going from $CaWO_4$ to $SrWO_4$ and then to $BaWO_4$. Hence, the stiffness of the lattice decreases in the same order and this explains the observed maximum in the luminescence intensity from $CaWO_4$ as compared to $SrWO_4$ and $BaWO_4$. Values of lattice parameters further confirm this. The excitation spectra corresponding to Eu^{3+} emission is shown in Fig.3 (b). The patterns consist of broad peak centred at 270 nm and sharp peaks above 310 nm. The broad band is assigned to the $Eu-O$ charge transfer transition and sharp peaks to f-f transitions of Eu^{3+} ion present in the lattice. As Eu^{3+} doped $CaWO_4$ nanoparticles showed highest luminescence intensity as compared to Eu^{3+} doped $SrWO_4$ and $BaWO_4$, detailed studies were carried out on luminescence properties of undoped and different lanthanide doped $CaWO_4$ nanoparticles.

Conclusions

Undoped and Eu^{3+} doped alkaline earth tungstate nanomaterials were prepared at room temperature. Increase in particle size with increasing ionic radii of metal ion was observed and is explained based on the ratio of hard-hard, soft-soft interactions between ligand and metal ions.



Strong red emission from Eu^{3+} doped tungstate nanomaterials was observed and emission intensity decreases with increasing ionic size, due to soft surrounding around the Eu^{3+} ions in the lattice.

References

1. Zhang, F; Yiu, Y; Aronson, M. C.; Wong, S. S. "Exploring the Room-Temperature Synthesis and Properties of Multifunctional Doped Tungstate Nanorods" *Journal of Physical Chemistry C*, 112 (2008): 14816–14824.
2. Nagornaya, L. L; Danevich, F. A; Dubovik, A. M; Grinyov, B. V; Henry, S; Kapustyanyk, V; Kraus, H; Vostretsov, Yu.Ya; "Tungstate and molybdate scintillators to search for dark matter and double beta decay", *IEEE Transactions on Nuclear Science*, 56 (2009): 2513-2518.
3. Dellwo, U; Keller, P; Meyer, J. U. "Fabrication and analysis of thick film humidity sensor based on MnWO_4 " *Sensors and Actuators, A: Physical*, 61 (1997): 298-302.
4. Jianhua, W; Ronghuan, H. "Synergetic catalytic effect of molybdate and tungstate on the hydrogen peroxide-iodide system and its analytical applications" *Analytica Chimica Acta*, 303 (1995): 241-246.
5. Shannon, R. D. "Revised effective ionic radii and systematic studies of interatomic distances in halides and chalcogenides." *Acta Cryst.*, A32 (1976): 751-767.
6. Blasse, G; Grabmaier, B. C. "Luminescent Materials", Berlin, Springer-Verlag, 1994.



Standardization of correlation between measured radioactivity and observed dose using an activated concrete sample

Sanhita Chaudhury, Chhavi Agarwal and A. Goswami

Radiochemistry Division

and

M. Gathibandhe

Reactor Projects Division

This paper received the Best Poster Award at the 4th International Symposium on Nuclear Analytical Chemistry (NAC-IV) held at Mumbai, during November 15-19, 2010

Quantitative correlation between observed radioactivity and the measured dose, is important for applications in nuclear reactor operations like decontamination of coolant channels. The quantitative correlation between observed radioactivity and measured dose was established for several locations in nuclear power reactors in our earlier work [1]. For this work, CdZnTe detector is preferred over HPGe, since online radioactivity measurement involves difficult-to-access locations, where a bulky HPGe detector cannot be used. In this present work, an attempt has been made to standardize the correlation between observed radioactivity and the measured dose and compare the results from CdZnTe and HPGe detector. A concrete sample was irradiated in the Dhruva reactor and the dose of the

sample was measured at different distances using a digital survey meter. The activated source was counted with HPGe and CdZnTe detectors at different distances as shown in the Table 1. The γ ray spectra showed the presence of radionuclides ^{59}Fe , ^{46}Sc and ^{60}Co , which emit high energy γ rays. The efficiencies of the detectors were simulated at different distances using Monte Carlo method and considering the concrete sample as a point source. The activities of the radionuclides were obtained by using the experimental count rates and the simulated efficiency values. The total dose rates for each source to detector distances was also calculated by simulating the dose rates for individual γ ray energies. Well reproduction of the experimental dose rate to simulated dose rate for HPGe

Table 1: Measured and simulated total dose rates at different distances.

HPGe			CdZnTe		
Distance (cm)	Observed dose($\mu\text{Sv/hr}$)	Simulated dose($\mu\text{Sv/hr}$)	Distance (cm)	Observed dose($\mu\text{Sv/hr}$)	Simulated dose($\mu\text{Sv/hr}$)
14.6	56	57.2	4.5	370	459.3
23.5	25	23.4			
36.5	10	9.2			
65.5	3	2.7	10	109	105.4



detector is seen from Table 1. It is also seen from the table that CdZnTe detector, inspite of having poor resolution, reproduced the measured values reasonably well, particularly at larger source-to-detector distances. So, it can be concluded that CdZnTe detector can be a good replacement for HPGe detector for γ -counting in inaccessible locations like nuclear reactors.

References

1. S. Chaudhury, C. Agarwal, A. Goswami, A. Mhatre, M. Gathibandhe, S. C. Dash, *J. Radioanalytical & Nuclear Chemistry*, (2010) 286 : 47-54.



Structural and electronic properties of Pd_n (n=1-8) clusters deposited on alumina surface

Sandeep Nigam and Chiranjib Majumder
Chemistry Division

This paper received the Best Poster Award (II Prize) at the International Symposium on Materials Chemistry (ISMC 2010), held at Mumbai, during December 7-11, 2010

Abstract

We report a systematic first-principles investigation, of the structure and electronic properties of Pd_n (n=1-8) clusters deposited on the α -Al₂O₃ surface. The results show that interaction with surface significantly distorted the gas phase Pd_n structure and the atoms arrange themselves in zig-zag pattern. Close competition between Pd-Pd and Pd-surface interactions drive the deposited structure to maximize the Pd-surface interaction, with minimum sacrifice in the Pd-Pd bonds. In case of Pd₇, the three dimensional gas phase geometry transforms into a hexagonal structure, which orients its atoms in parallel to the surface plane, to maximize the interaction with surface. After deposition, the electronic states of Pd_n cluster becomes broader and the amount of *spd* hybridization increases.

The growth and properties of metal clusters on oxides, are of considerable importance in applications viz sensor devices, microelectronics and heterogeneous catalysis¹⁻³. The chemical properties of the metal clusters are governed by the size and shape which is a trade-off between nucleation and growth kinetics, on one hand, and the metal-support interaction on the other. Therefore, it is not surprising that the physics and chemistry of the metal-oxide interface is being intensively investigated⁴⁻⁵. Many studies concerning the adsorption of transition metal atoms

on alumina supports, have been reported over the past few years⁴⁻⁵. Among transition metals, Pd exhibits a well-known ability to catalyze a large number of chemical reactions when deposited on alumina⁶. Moreover, Pd is of special interest due to its special position in the periodic table with *d¹⁰s⁰* electronic configuration, which changes in various situations depending on its chemical bonding and determines its specific chemical behaviour. Motivated by these facts, in the present work, we have theoretically investigated the growth of Pd_n cluster deposited on relaxed

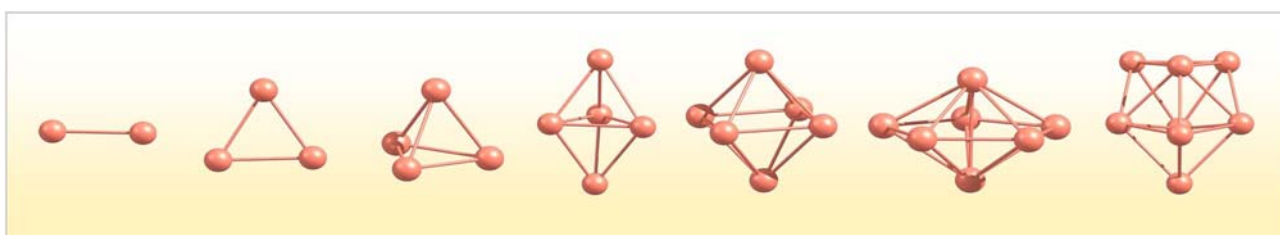


Fig. 1: Lowest energy structure of gas phase Pd_n clusters (n=2-8).



Al-terminated $\alpha\text{-Al}_2\text{O}_3(0001)$ surface under the density functional formalism. The current study aims to identify preferred adsorption sites and structure of deposited Pd cluster and in particular, analyze the relaxation in comparison to most stable gas-phase isomer.

In general, the palladium cluster favours three dimensional compact structures in the gas phase (tetrahedron, trigonal bipyramidal, octahedron, pentagonal bipyramid, bicapped octahedron) with spin moment of $2\mu_B$ (as shown in Fig. 1). Further, we have explored the potential energy surface for adsorption of these clusters on the alumina surface. The $\alpha\text{-Al}_2\text{O}_3(0001)$ surface was modelled with 18- atomic layer slab, containing 120 atoms. To make the reading easy, we have labelled each adsorption site with a letter and a number indicating the type of the atom and the atomic layer in the slab, respectively. Fig. 2(a) displays the top five atomic layers as represented is different colours and denoted by, Al(1), O(2), Al(3), Al(4), and O(5) throughout the article. Pd atom prefers to occupy

the O(2) atop site (Fig. 2(b)) with an adsorption energy of -1.40 eV. For the adsorption of Pd dimer, we have followed two approaches: (i) the Pd_2 dimer is placed on the surface in parallel and perpendicular orientations and (ii) two Pd atoms are placed far apart on the surface. The geometry optimization of all these configurations suggests that, Pd_2 dimer prefers to orient in parallel to the surface plane with elongation in bond from 2.48 to 2.56 Å (viz Fig.2(c)). In the second case, when two Pd atoms are placed far apart ($4\text{-}5$ Å away), on relaxation they are adsorbed on two different O(2) sites as two separate Pd atoms. Further, it is seen that the configuration having Pd-Pd bond is more stable on the surface, in comparison to the case where two Pd atoms are far apart. Based on these results we infer that the strong metal-metal interactions is preferred over metal surface interaction. Thus these results corroborate the Volmer-Weber (island formation) growth mode of Pd clusters on the Al_2O_3 surface.

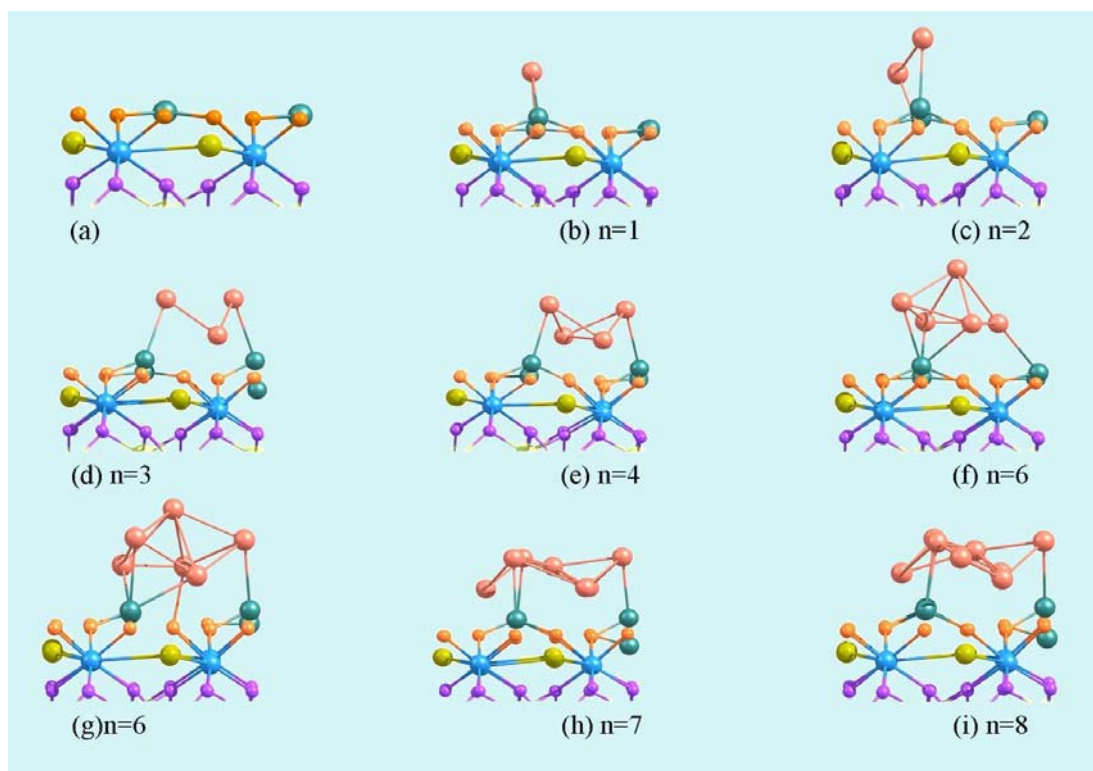


Fig. 2: Lowest energy structure of Pd_n clusters ($n=1\text{-}7$) deposited on alumina surface



Upon deposition on the Al_2O_3 surface, one of the angles of isolated Pd_3 cluster widens from 60° to 66° and therefore the opposite Pd-Pd distance increases upto 2.74 \AA (Fig.2(d)). Upon interaction with the Al_2O_3 surface, gas phase tetrahedral Pd_4 is distorted to a bent rhombus, where alternate Pd atoms are placed close and away from the surface atoms (viz Fig.2(e)). The trigonal bipyramidal structure of Pd_5 reorients into a square pyramidal geometry, after the adsorption on Al_2O_3 surface (viz Fig. 2(f)). The Pd_6 cluster, which forms octahedron geometry in the gas phase, deforms into a capped pentagon structure on the alumina surface (viz Fig.2(g)). The Pd_7 cluster forms pentagonal bipyramid structure as the lowest energy isomer in the gas phase. Remarkably this three dimensional geometry opens up after interaction with alumina surface (viz Fig.2(g)). The lowest energy structure of the Pd_7 on Al_2O_3 forms a zigzag patterned hexagonal structure with three Pd atoms binding atop aluminum Al(1) site and other three atoms occupying the top sites of Al(4) and the seventh atom (i.e. the central atom) resides over the Al(3) atom (viz Fig.2(h)). In line with the growth pattern of Pd_7 , the gas phase bicapped octahedron structure of Pd_8 also reorients to capped hexagonal structure having zig-zag pattern (viz Fig. 2(i)).

Thus from the above results it is clear, that isolated Pd_n clusters are significantly distorted after deposition on a substrate. In general, Pd_n cluster adsorbed in zig-zag orientation on the Al_2O_3 surface by placing the alternate

Pd atoms up and down. There is interplay between the strength of Pd-Pd and Pd-surface interaction, which primarily decides the interface geometry. The deposited clusters reorient in such a way, that it can maximize the Pd-surface interaction with minimum sacrifice in the Pd-Pd bonds. For Pd_5 and Pd_6 , not all atoms are interacting with the surface, as this will lead to rupturing of some Pd-Pd bonds. However, in case of Pd_7 and Pd_8 , the cluster could interact with all seven atoms, because simultaneously it is able to retain the Pd-Pd bonds. Therefore, even though Pd_7 cluster in the gas phase prefers a five-fold symmetry configuration, after deposition it has a six fold symmetry forced by the alumina surface as shown in Fig. 3.

From charge distribution analysis it was found, that down Pd atoms residing on bridge positions loses its charge to the nearby oxygen atom of the surface and to the Pd atoms which are connected directly to the top layer aluminium atom, there is finite amount of charge transfer from surface to the adsorbed atoms. From the electronic density of states (EDOS) spectrum it is found, that the hybridization among the s , p , and d orbitals increases, as the size of the clusters increases. This is also reflected by the broadening of the electronic states after deposition. In Fig. 4 we have plotted the average adsorption energy of the deposited cluster, vis-à-vis the average binding energy of the gas phase cluster. It is clear from the figure, that the trend in the average binding energy and adsorption energy is opposite. This can be explained that as the stability

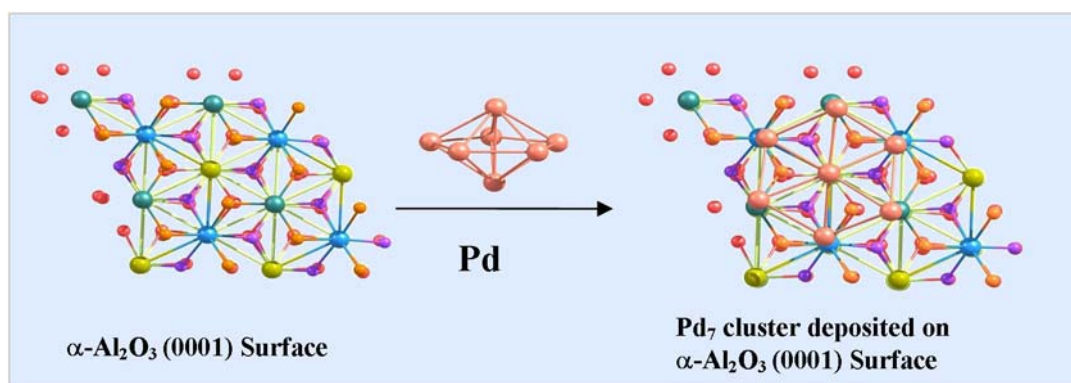


Fig. 3: Reorientation of Pd_7 cluster on $\alpha\text{-Al}_2\text{O}_3$ (0001) surface (top view)

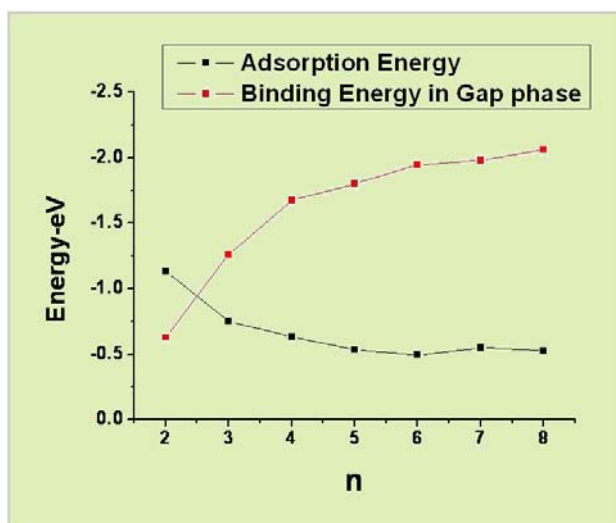


Fig. 4: Variation in the average binding energy of the gas phase cluster compared with average adsorption energy of deposited Pd_n Cluster.

of the cluster improves, its interaction energy with the surface decreases.

In conclusion, we have studied the adsorption of small Pd clusters on the $\alpha\text{-Al}_2\text{O}_3$ (0001) surfaces under the density functional formalism. The results show that the gas phase geometry of Pd_n clusters as significantly distorted after deposition, as the atom of the now arranges them in up-down-up type of a zig-zag pattern. The competition between Pd-Pd and Pd-surface interactions further governs the growth motif of larger clusters. In case of Pd_7 , the gas phase geometry with pentagonal symmetry changes to hexagonal zig-zag structure. After deposition, the electronic states of Pd_n cluster becomes broader and amount of *spd* hybridization increases.

References

1. Goodman, D.W. "Model studies in catalysis using surface science probes" *Chemical Reviews*, 95 (1995):523-536
2. R.M.Lambert, G. Pacchioni; (Eds.), *Chemisorptions and Reactivity on Supported Clusters and Thin Films: Towards an Understanding of Microscopic Processes in Catalysis*, Kluwer, Dordrecht, 1997.
3. Azad, A.M., Akbar, S.A., Mhaisalkar, S.G., Birkefeld, L.D., Goto, K.S., "Solid-state gas sensors. A review"

Journal of the Electrochemical Society, 139 (1992): 3690-3704

4. Nigam, S., Majumder, C.; "Growth pattern of Ag_n ($n = 1-8$) clusters on the $\alpha\text{-Al}_2\text{O}_3$ (0001) surface: A first principles study" *Langmuir* 26 (2010):18776-18787
5. Cruz Hernández, N., Márquez, A., Sanz, J.F., Gomes, J.R.B., Illas, F "Density functional theory study of Co, Rh, and Ir atoms deposited on the $\alpha\text{-Al}_2\text{O}_3$ (0001) surface" *Journal of Physical Chemistry B*, 108 (2004):15671-15678
6. Babu, N.S., Lingaiah, N., Gopinath, R., Reddy, P.S.S., Prasad, P.S.S. "Characterization and reactivity of alumina-supported Pd catalysts for the room-temperature hydrodechlorination of chlorobenzene" *J. Phys. Chem. C* 111 (2007): 6447–6453.



Studies on BaO-CaO-Al₂O₃-B₂O₃-SiO₂ glass system for use as SOFC sealant

M. Goswami, S. Singaravelan, A. Patil and G.P. Kothiyal

Glass and Advanced Ceramics Division

and

S. Bhattacharya

Technical Physics Division

This paper received the Best Oral Presentation Award at the International Workshop and Symposium on the Synthesis and Characterization of Glass (Glass-Ceramics (IWSSCGGC) held at C-MET, Pune, during July 7-10, 2010

Abstract

35BaO-15CaO-5Al₂O₃-(10-x)B₂O₃-35SiO₂-xA(BCABS) glasses (x = 2 mol.%, A = ZrO₂, TiO₂, P₂O₅ or Cr₂O₃) were prepared and characterized for thermo-physical and electrical properties and bonding with Crofer 22 interconnect. Thermal expansion coefficient (TEC) values varied from 11.58 to 12.81 x 10⁻⁶/°C (30-500°C) with different additives. Electrical conductivity showed an increase by an order of 10⁶ S/cm at 1023K from 10⁻¹² S/cm obtained at 323K. Seals were fabricated with TiO₂, Cr₂O₃ and P₂O₅ substituted BCABS glasses at max. 1000°C. Seals with TiO₂ substituted BCABS glass showed acceptable hermeticity (10⁻⁶ Torr) and high temperature stability and hermeticity after heat treatment at 775°C for 300 hrs.

Keywords: Glass-ceramics, Sealant, Solid oxide fuel cell, Microstructure.

Introduction

Solid oxide fuel cell (SOFC) is one of the most promising energy conversion devices, that combines high efficiency and fuel flexibility. The planar design is considered to be superior to the tubular design, due to its high current density and simple manufacturing process. Many studies have been reported on glass and glass-ceramics based sealant materials, to achieve desirable properties for SOFC application [1-2]. However, each system/category has its own drawbacks such as thermal expansion mismatch, high temperature stability or high chemical reactivity with other SOFC components. Alkaline earth silicate systems are considered among the potential systems, for use as high temperature sealing materials and considerable work has been reported, related to their synthesis and characterization [3-7]. The objective of present work was to study the effects of various additives such as TiO₂, ZrO₂,

P₂O₅ and Cr₂O₃ on thermo-physical, and electrical conductivity of 35BaO-15CaO-10B₂O₃-5Al₂O₃-35SiO₂ glass system and their bonding behaviour with Crofer 22 APU interconnect. We investigated high temperature phase stability of as prepared glass and seals by giving heat treatment at 775°C for 300 hrs. Microstructure at the interface and vacuum compatibility of these seals were measured. We have discussed a detailed study only for TiO₂ substituted BCABS glass in this paper.

Experimental

Glasses of nominal compositions of 35BaO-15CaO-5Al₂O₃-(10-x)B₂O₃-35SiO₂-xA (mol.%), with x = 2 mol.% of A = ZrO₂, TiO₂, P₂O₅ or Cr₂O₃ additives were prepared, using melt-quench technique. Thermal expansion coefficient was measured in the temperature range of 30 to 900°C using



TMA instrument (Model TMA-92, Setaram, France). Glass samples and seals were heat treated for max. 300 hrs at 775°C and phase identification was carried out on powdered samples, by using a Philips (PW1710) X-ray diffractometer with Cu K as radiation source. For electrical conductivity measurements, samples of approximately 2-3mm thickness with both ends flat were taken and coated with gold on both sides for good electrical contacts. Measurements were carried out using Impedance Analyzer (HP 4194 A) in the frequency range 10Hz to 15MHz, over the temperature range 323–1023K. Sealing of different glasses with Crofer 22 APU alloy was carried out, at temperatures between 950 and 1000°C (for BCABSP-950°C, BCABST-990°C and BCABSCr-1000°C), employing the sandwich geometry. Microstructure near the interface of such seals was then investigated using SEM (Model: Tescan Vega MV2300T/40) and elemental line scans were taken out across the interface.

Result and Discussion

TEC and T_g values for samples having ZrO_2 , are found to be higher than those of samples containing other additives. Fig. 1 shows the Secondary electron(SE) images of BCABST glass/ Crofer 22 APU interfaces of the as prepared seal. From this figure, a continuous crack-free and sharp interface without any reaction zone was observed. Elemental line scans taken across the interface showed interdiffusion of Ba, Si, Ba, Ti, Fe, Cr elements. Fig. 2 show the SE images of BCABST glass/ Crofer 22 APU interfaces of the seal, heat-treated at 775°C for 300 hrs durations. From the figure, formation of two different crystalline phases promoted by the presence of interconnect material in the glass matrix is clearly observed. These crystallites are identified as Ba rich

phase with brighter region and silica rich phases with little darker region. Further, a Cr rich region of around 3-5 mm thickness at the interface, for the sample heat treated for 300 hrs at 775°C, is observed. Elemental line scans shows enrichment of Cr at the interface and interdiffusion of Fe, Cr, Ba, Ti, and Ca across the boundary [Fig.2(b)]. The Cr enrichment at the interface may lead to formation of Cr_2O_3 layer helping in good bonding. Formation of Cr_2O_3 layer at the interface with 1-2mol% P_2O_5 additive has been reported by Ananthanarayan et al [3].

Fig. 3 shows the XRD patterns of BCABST glass samples, heat-treated at 775°C for different durations. XRD patterns of these samples remained unchanged upto 10hrs of heat treatment. It showed a marginal change in TEC of the

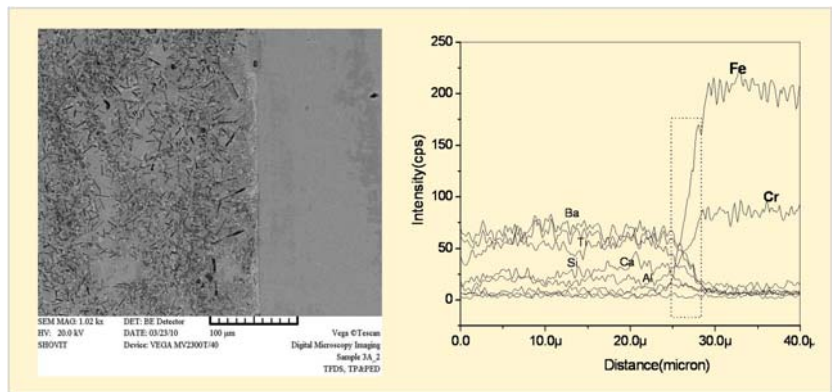


Fig. 1a & b: Microstructure and line scans at the interface of the TiO_2 substituted BCABS glasses with Crofer 22 APU seal.

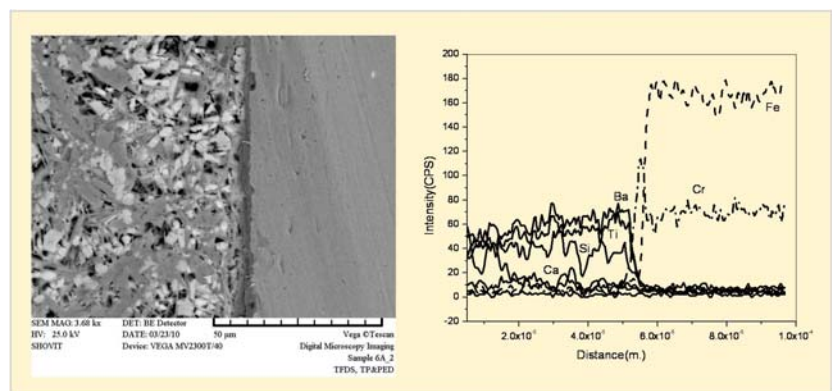


Fig. 2 a & b: Microstructure and line scans at the interface of the TiO_2 substituted BCABS glasses with Crofer 22 APU seals after heat treatment of 300hrs.

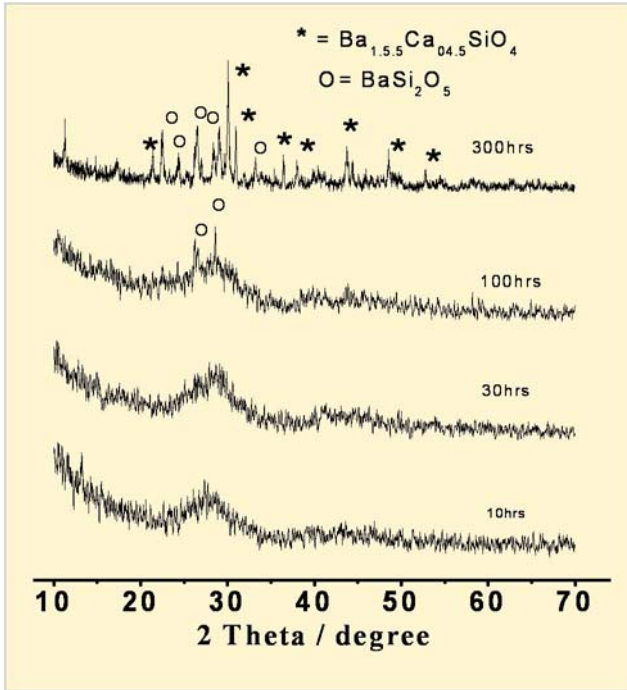


Fig. 3: XRD patterns of BCABS glass samples with TiO₂ heat treated at 775°C for different Durations.

sample. After heat treatment of 100 hrs, barium orthosilicate (BaSi₂O₅) developed as a minor crystalline phase whereas Ba_{1.5}Ca_{0.5}SiO₄ and BaSi₂O₅ phases were developed after 300 hrs of heat treatment. The TEC values were found to be 11.67 and 11.02 x 10⁻⁶/°C (30-300°C) for 100 and 300hrs heat-treated samples, respectively. Since TEC values of these developed phases are nearly the same as that of the base glass[1], the overall TEC did not show appreciable change after heat treatment.

Fig. 4 shows the conductivity of BCABST glass sample, as a function of frequency at different temperatures (323-1023K). The conductivities remain constant at each temperature over a wide frequency range, extending from 10⁴ to 10⁶ Hz, depending upon the temperature. The dc conductivity value increases from 5.01 x 10⁻¹¹ S/cm at a temperature of 323K to 4.6 x 10⁻⁶ S/cm at the temperature of 1023K. The conductivity values are nearly of the same order for all glass samples. These conductivity values are within the acceptable limit for their use as high temperature sealant.

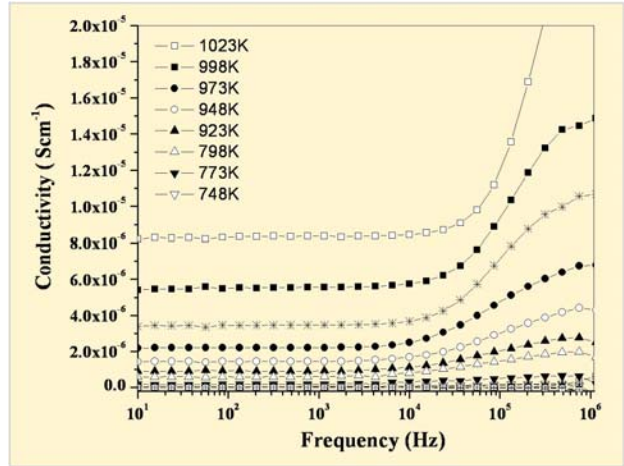


Fig. 4: Variation of ac conductivity (σ') with frequency for TiO₂ substituted BCABS glass at different temperatures.

Leak testing for these seals was carried out and seals were found to withstand a vacuum of 10⁻⁶ Torr at room temperature. Further *in-situ* leak testing of the seals was also carried out, at different temperatures upto 800°C, by holding them at a desired temperature and monitoring the changes in pressure gauge. Seals were found to withstand a vacuum of 10⁻⁶ Torr upto 800°C. To check the high temperature stability of these seals, they were kept at 775°C for different durations upto max.300hrs and tested again for vacuum at room temperature as well as at elevated temperatures. Seal with TiO₂ substituted BCABS glass was found to withstand a vacuum of 10⁻⁶ Torr, indicating their integrity upto 800°C after heat treatment at 775°C for 300 hrs.

Conclusion

35BaO-15CaO-5Al₂O₃-10B₂O₃-35SiO₂ glass samples with ZrO₂, TiO₂, P₂O₅ and Cr₂O additives, were prepared by melt-quench technique. TEC values of as prepared glasses were found to be in the range of 10.59 to 12.81 x 10⁻⁶/°C (30-300°C). Seals prepared with BCABS glass having TiO₂, P₂O₅ or Cr₂O₃ additive with Crofer 22 APU were found to withstand a vacuum of 10⁻⁶ Torr and seals with BCABS glass having TiO₂, maintained the hermeticity (vacuum did not deteriorate) at 800 °C even after heat treatment at 775°C for 300 hrs. For TiO₂ substituted BCABS glass, electrical conductivities showed an increase from 5.01



10^{-11} to 4.6×10^{-6} S/cm with increase in temperature from 323K to 1023K, which is in the acceptable range for use as sealing material in SOFC.

Acknowledgements

The authors wish to thank to Dr. A. K. Suri for encouragement and support to this work. Thanks are due to Drs. S. K. Gupta and A. K. Tyagi for providing SEM and XRD facilities, respectively and to Shri P. A. Wagh, Smt. Syamal Mohite and Shri Radhakrishanan Nair for sample preparation and other technical help.

References

1. Fergus J. W. "Sealants for solid oxide fuel cells" *J. Power Sources* 147 (2005): 46-57.
2. Sohn S.B., Choi S.Y., Kim G.H., Song H.S., Kim G.D., "Stable sealing glass for planar solid oxide fuel cell" *J. Non-Cryst. Solids* 297 (2002): 103-112.
3. Ananthanarayanan A., Kothiyal G. P., Montagne L., Tricot G., and Revel B., "Sintering and Sealing Properties of Barium Calcium Aluminum Boro-Silicate (BCABS) Glasses" *J. Mat. Chem. Phy.* 2011 (press).
4. Pascual M.J., Guillet A., Duran A., "Optimization of glass-ceramic sealant compositions in the system MgO-BaO-SiO₂ for solid oxide fuel cells (SOFC)" *J. Power Sources* 169 (2007): 40-46.
5. Haanappel V.A.C., Shemet V., Vinke I.C., Quadackers W. J., "A novel method to evaluate the suitability of glass sealant-alloy combinations under SOFC conditions" *J. Power Sources* 141 (2005): 102-107.
6. Ghosh Saswati, Das Sharma A., Kundu P., Mahanty S., Basu R.N., "Development and characterizations of BaO-CaO-Al₂O₃-SiO₂ glass-ceramic sealants for intermediate temperature solid oxide fuel cell application. *J. Non-Cryst. Solids* 354 (2008)" 4081-4088.
7. Ghosh S, Das Sharma A, Mukhopadhyay A.K., Kundu P., Basu R.N., "Effect of BaO addition on magnesium lanthanum alumino borosilicate-based glass-ceramic sealant for anode-supported solid oxide fuel cell." *Int. J. Hydrogen Energy* 35 (2010): 272-283.
8. Kulikovsky A. A, "A simple equation for temperature gradient in a planar SOFC stack" *Int. J. Hydrogen Energy* 35 (2010): 308-312.



Studies on the Production Feasibility of ^{64}Cu by (n, p) Reactions on Zn Targets in Dhruva Research Reactor

K.V. Vimalnath, A. Rajeswari, K.C. Jagadeesan, Viju C., P.V. Joshi, Meera Venkatesh
Radiopharmaceuticals Division

This Paper received the Best Paper Award at the Fourth International Symposium on Nuclear Analytical Chemistry (NAC-IV), held at Mumbai, India from 15-19 November 2010

Abstract

^{64}Cu is a useful radionuclide for both PET imaging and targeted therapy, as it decays by three different modes, namely, electron capture (41%), β^- (40%) and positron emission (19%). While ^{64}Cu is generally produced by $^{64}\text{Ni}(p,n)$ reaction in a cyclotron, $^{64}\text{Zn}(n,p)$ route to avail high specific activity 'no carrier added' grade ^{64}Cu is attractive for research studies and was hence explored. 10-500 mg zinc foil target (48.63% in ^{64}Zn) was irradiated in the medium flux reactor Dhruva, at a thermal neutron flux of $\sim 5.6 \times 10^{13} \text{ n.cm}^{-2}.\text{s}^{-1}$ for 3 days. Irradiated Zn foil was dissolved in 5 mL 10M HCl and ^{64}Cu was separated by anion exchange chromatography (Dowex 1 \times 8; 100-200 mesh) using 3M HCl for elution. ^{64}Cu radioactivity content and its radionuclide purity were ascertained by γ -ray spectrometry, using HPGe detector coupled to a 4K MultiChannel Analyser system (MCA). Radiochemical separation yielded a radionuclidic purity of 99.9% w.r.t ^{64}Cu .

Keywords: ^{64}Cu , no carrier added, reactor production, radionuclide purity.

Introduction

^{64}Cu is a unique radionuclide, owing to its transmutation through three different modes, namely, electron capture (41%), β^- (40%), β^+ (19%), which makes it useful in both PET imaging as well as targeted therapy. The therapeutic potential of ^{64}Cu , arises both from the beta rays of E_{max} 578.7 keV, and the considerable Auger e⁻ emission (avg e⁻ energy 6.54 keV (22.39%)). The 12.7 h half life of ^{64}Cu , is reasonably amenable for synthesis of radiopharmaceutical compounds and their subsequent human use.

Copper has several radioisotopes which are suitable for use in different applications. The well established complexation chemistry of Cu, which exists in +1 or +2

oxidation state, allows simple and quick radiolabeling¹. Positron emitters such as ^{11}C ($t_{1/2}$ 20.39 min), ^{13}N ($t_{1/2}$ 9.965 min), ^{15}O ($t_{1/2}$ 2.1 min), ^{18}F ($t_{1/2}$ 109.77 min) and ^{68}Ga ($t_{1/2}$ 67.629 min)^{2,3} used in PET imaging are all produced through reactions in cyclotrons. Most positron emitters identified for radiopharmaceutical applications are short-lived, among which the most widely used PET radionuclide is ^{18}F ($t_{1/2}$ 109.77 min). But in order to utilize ^{18}F products clinically, it is important to have the medical cyclotron either in the hospital or in vicinity, for quick transport. The high costs of cyclotrons for producing short-lived PET radionuclides and the special automated synthetic apparatus for preparation of the radiopharmaceuticals, is a major limitation for the wide spread use of PET technology. In this context, it is interesting to study the feasibilities of reactor production



of PET radionuclides such as ^{64}Cu in a vast country like India.

^{64}Cu can be produced in a research reactor employing (n,γ) and (n,p) reactions by neutron irradiation, on suitable targets. Radiative neutron capture reactions on copper oxide targets of natural or enriched composition, provides an easy option involving simple chemical dissolution, to avail ^{64}Cu radiochemical, albeit of low specific activity, which will have very limited applications. High specific activity 'no carrier added' (n.c.a) grade ^{64}Cu can be produced, by employing (n,p) reactions on zinc target in a research reactor. In such a case, radiochemical separation of radiocopper from the zinc target is an essential step, to avail radionuclidically pure n.c.a ^{64}Cu for nuclear medicine applications.

The thermal neutron cross section of 4.1 b and resonance integral cross section of 4.4 b for ^{63}Cu having 69.17% natural abundance indicate, that reasonable amounts of ^{64}Cu activity of a low specific activity can be produced in a reactor through (n,γ) route⁴. While the (n,γ) route leads to low specific activity product, the indirect route of (n,p) reaction on a Zn target, provides ^{64}Cu radiochemical of higher specific activity. However, it is recognized that although both $^{64}\text{Zn}(n,p)$ and $^{64}\text{Ni}(p,n)$ reactions lead to high specific activity ^{64}Cu , cyclotron irradiation of enriched ^{64}Ni target yields far higher quantities of ^{64}Cu .

This paper presents our studies on the production feasibility of ^{64}Cu in a medium flux research reactor such as DHRUVA at our institute Bhabha Atomic Research Centre, Trombay, India, using zinc foil and describes the logistics of radiochemical separation of ^{64}Cu from neutron-irradiated Zn target.

Experimental

Materials

Zinc foil (spectroscopic grade, >99.99% chemically pure),
CuO (spectroscopic grade, >99.99% chemically pure)

BDH-make were utilised, for production of ^{64}Cu . All other chemicals used were of AR grade and supplied by reputed chemical manufacturers. ^{64}Cu and ^{65}Zn radiotracers for various studies were prepared, by thermal neutron irradiation of CuO and Zn targets followed by dissolution in HCl solution. Zn targets encapsulated in cadmium shield was cold-weld sealed in standard Aluminum container (22 mm Ø, 43 mm ht.), for neutron irradiation. Radioactivity content and radionuclidic purity of ^{64}Cu prepared, were determined by recording γ -ray spectra using HPGe detector, coupled to a 4K multichannel analyzer (MCA) system. A ^{152}Eu reference source, was used for both energy and efficiency calibration of the detector².

Exchange studies using radiotracers

Distribution experiments were performed on the uptake of Cu and Zn, by Dowex 1×8 (50-100, 100-200 and 200-400 mesh) anion exchanger, using ^{64}Cu , ^{65}Zn radiotracers. 50 mg resin was equilibrated with radiotracers in 2mL HCl volume of varying concentrations at room temperature for 1 hour and the uptake of ions was calculated, as a function of acid concentration by measuring the radioactivity of the supernatant solution. 1g each of Dowex 1×8 resin, mesh 50-100, 100-200 and 200-400 were weighed and conditioned in 3M HCl in separate columns of dimension 5 mm Ø and 100 mm L. Zn Solution spiked with ^{65}Zn radiotracer of specific activity 1000 Bq/mg Zn was passed through the column, 0.5 mL fractions were collected separately and monitored in NaI(Tl) detector to record the breakthrough. The capacity of the column for Zn per g of the exchanger was determined.

Neutron irradiation of Zn target and radiochemical preparation

10 mg each of Zn foil unshielded and shielded (packed in cadmium foil) was encapsulated in a standard aluminum container by cold weld sealing and was neutron irradiated in Dhruva research reactor, at a flux of $5.6 \times 10^{13} \text{ n.cm}^{-2}.\text{s}^{-1}$ for 3 days. Subsequently, the irradiated



sample of Zn foils were retrieved by opening the aluminum can inside a 100 mm lead shielded glove box facility, with remote handling tong provisions. Irradiated samples were dissolved in 10 M HCl solution by gentle heating. The acid concentration of the resultant clear solution was adjusted to 3 M with respect to HCl. An aliquot was measured by γ -ray spectrometry, using HPGe detector coupled to a 4K MultiChannel Analyser system (MCA) for estimating the total radioactivity of ^{64}Cu and ^{65}Zn , $^{69\text{m}}\text{Zn}$ radionuclides produced.

Radiochemical Separation of ^{64}Cu from radioactive Zn

5 mL solution containing the mixture of copper and zinc radionuclides in 3 M HCl solution was loaded on to an anion exchanger column (Dowex 1 \times 8; 50-100 mesh; 10 mm Dia.; 300 mm ht.) for radiochemical separation of ^{64}Cu from Zn. 3 M HCl solution was passed through the column, to elute ^{64}Cu preferably. The eluate fraction containing ^{64}Cu collected in a 100 mL glass beaker, was concentrated by gentle heating to \sim 2 mL. A measured aliquot suitably diluted was dispensed in a standard 10 mL glass vial and measured in HPGe detector coupled to a 4K MultiChannel Analyzer (MCA) system, for assay of ^{64}Cu activity. These aliquots of the processed $^{64}\text{CuCl}_2$ solution were followed for sufficiently long span (greater

than 20 half lives of ^{64}Cu) to confirm the radionuclide purity. Similarly, radiochemical separation studies were also done with exchanger of size 100-200 and 200-400 mesh sizes.

Results and Discussion

Neutron irradiated zinc foil dissolves easily in 10 M HCl acid, resulting in a clear solution. Dose rate from the neutron-irradiated Zn foil at contact, was around 5 mGy/h, while in case of Zn foil sealed in Cd shield, irradiated under similar conditions, a dose rate of \sim 40 $\mu\text{Gy/h}$ was recorded. Very high amounts of $^{69\text{m}}\text{Zn}$ and ^{65}Zn , 7.4 GBq and 2.5 GBq respectively (Table 1), are co-produced under the stated neutron irradiation conditions, contributing to the increased dose rate. Use of a cadmium shield reduces the thermal neutron flux seen by the Zn target and thus reducing the production of undesired zinc radionuclides, without affecting production of ^{64}Cu , which is through fast neutrons that are not absorbed by the Cd.

Distribution studies on the uptake of Cu and Zn, by Dowex 1 \times 8 (50-100, 100-200 and 200-400 mesh) anion exchanger indicates that, at 3M concentration of HCl, greater than 95% uptake of Zn is achieved, while there was no uptake of Cu. Based on these studies, it was seen that the capacity for holding Zn was 40 mg, 60 mg & 80

Table 1: Yields of ^{64}Cu and co-produced radionuclides by neutron irradiation of zinc foil target in Dhruva research reactor at neutron flux $5.6 \times 10^{13} \text{ n.cm}^{-2}.\text{s}^{-1}$ for 3 days

Radionuclide	$T_{1/2}^{2,3}$	Activity at End of Irradiation	Activity per g Zn
<i>Zn foil neutron irradiated with no shielding</i>			
^{64}Cu	12.7h	1.4 MBq	146 MBq
$^{69\text{m}}\text{Zn}$	13.76h	73 MBq	7.4 GBq
^{65}Zn	244.1d	25 MBq	2.5 GBq
<i>Zn foil neutron irradiated in Cd Shield</i>			
^{64}Cu	12.7h	1.2 MBq	118 MBq
$^{69\text{m}}\text{Zn}$	13.76h	5.1 MBq	544 MBq
^{65}Zn	244.1d	0.51 MBq	55 MBq



mg Zn per g of 50-100, 100-200 & 200-400 mesh resin respectively. It is envisaged that for production of 5 mCi n.c.a ^{64}Cu by (n, p) reaction on Zn targets, about 1g Zn has to be used, which would require ~25g 50-100 mesh, 17g 100-200 mesh or 13g 200-400 mesh resins in suitably designed column. Among the three columns prepared, radiochemical separation using Dowex 1 × 8 (100-200 mesh) gave satisfactory results, yielding a fast separation of radionuclidically pure ^{64}Cu .

At 3M HCl condition, ^{64}Cu elutes out of column, while radioactive zinc is held in the column. Zn was eluted out of column using ultrapure water as eluate. Neat separation of ^{64}Cu from radioactive Zn was achieved. Fig. 1 shows the elution profile of ^{64}Cu from a solution of Zn over a Dowex 1 × 8 (100-200 mesh) anion exchanger column. It was seen, that the separation of ^{64}Cu and ^{65}Zn was very

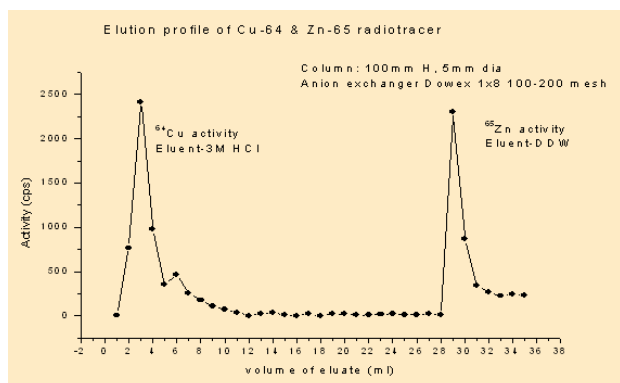


Fig. 1: Elution profile of ^{64}Cu and ^{65}Zn from anion exchanger column.

distinct. Fractions between 1 mL and 10 mL contained the ^{64}Cu activity. Optimizations of column condition for radiochemical separation were carried out, using the radiotracers of ^{64}Cu and ^{65}Zn of known specific activity. 5.5 kBq of ^{64}Cu activity loaded in the column could be recovered almost completely (>99.88 %), which was ascertained by HPGe-MCA measurements of 511 keV photo peak. 1112.5 keV gamma ray peak of ^{65}Zn was not detected in these spectra of ^{64}Cu fraction, confirming the strong retention of Zn in anion exchanger. Further, on eluting the column with ultrapure water, ^{65}Zn activity was released and the fractions between 28 mL and 32 mL

accounted for all the activity of ^{65}Zn . Uptake study of radioactive Zn in different acid concentrations showed, that the best elution efficiency (>95%) for copper was obtained under 3M HCl column condition. The elution profile of ^{64}Cu from Zn over Dowex 1 × 8 columns of 100-200 & 200-400 mesh sizes, was also similar and reproducible.

Based on these observations and inferences, samples of Zn foil shielded with Cd foil were neutron-irradiated and subjected to radiochemical processing, and ~118 MBq n.c.a ^{64}Cu was separated. The gamma spectra showed 511 keV and 1345 keV photopeaks, the first being annihilation peak as a result of positron emission and latter one, the characteristic photopeak of ^{64}Cu . Radionuclide purity of greater than 99.9% was recorded (Fig. 2).

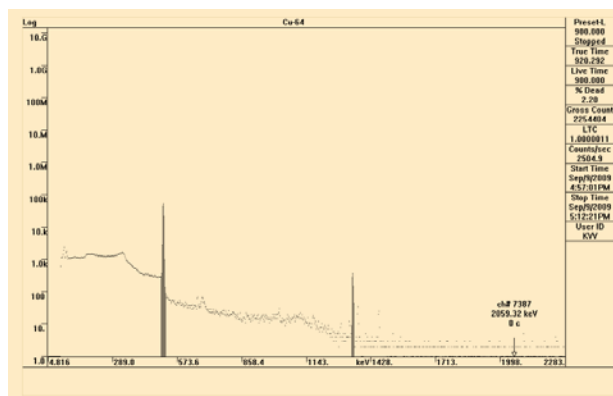


Fig. 2: Gamma Spectrum of ^{64}Cu recorded using HPGe-MCA system

The procedure demonstrated can be applied to routine production separation of MBq levels ^{64}Cu on a regular basis in radiochemical production laboratories. The post irradiation procedures are simple and the undesired co-production of large levels of ^{69m}Zn and ^{65}Zn can be suppressed, by appropriately designed cadmium shield. An irradiation duration of approximately 3-4 half lives for ^{64}Cu i.e., ~50 h resulted in production of about 0.55-0.74 GBq (15-20 mCi) of ^{64}Cu , when about 5g Zn targets were used. The separation procedure in such a case, requires large ion exchange column or multiple columns, that may be operated simultaneously. However, a good



alternate would be to trap the microscopic amounts of ^{64}Cu produced in +1 state, in a small cartridge of ion exchanger column, wash off the radioactive Zn and then elute copper as Cu^{+2} in a small definite volume of 3M HCl. In either case, the time required for radiochemical separation, volume concentration and radioactivity assessment would be not more than 3-4 h post irradiation. This would enable access to a few hundreds of MBq of ^{64}Cu , which can be utilized for radiolabeling studies. Presently, with no prospects for production of ^{64}Cu by cyclotron route in immediate future at our centre, the availability of activity from reactor production will enhance the prospects for evaluation of diagnostic and therapeutic formulations of ^{64}Cu based radiopharmaceuticals, in a modest way.

Conclusion

It is feasible to produce appreciable levels of ^{64}Cu in a medium flux research reactor by (n,p) reactions on Zn targets. It is envisaged that 0.55-0.74 GBq ^{64}Cu can be produced, by irradiating approximately 5g Zn, which is adequate for optimization and labeling studies of ^{64}Cu based radiopharmaceuticals.

Acknowledgements

The authors sincerely thank Dr V. Venugopal, Director Radiochemistry and Isotope Group, BARC for his keen

interest and support. The authors thank Shri V. K. Sharma, Head Safety Studies Section, Health Physics Division, BARC for evaluation of production feasibility using MCNP codes and discussions. Thanks are due to our colleagues in the Radiochemicals Section, Radiopharmaceuticals Division, BARC for their support and help rendered in various ways and to the personnel from Reactor Group for facilitating neutron irradiation of samples.

References

1. Wadas TJ, Wong EH, Weisman GR Anderson CJ. "Copper chelation chemistry and its role in copper radiopharmaceuticals". *Current Pharmaceutical Design* 13 (2007): 3-16.
2. Reus U, Westmeier W, Warnecke I. "Catalog of gamma rays from radioactive decay". *J At Nucl Data Tables* 29 (1983): 193-406.
3. Tuli JK. *Nuclear Wallet Cards*. 6th ed., Brookhaven National Laboratory, New York, 2000.
4. Rajeswari A, Vimalnath KV, Viju C, Sharad PL, Jagadeesan KC, Joshi PV, Meera Venkatesh. "Studies on preparation of ^{64}Cu using (n, γ) route of reactor production". Extended abstracts of the plenary lectures and contributed papers of the Second International Conference on Application of Radiotracers in Chemical, Environmental and Biological Sciences (ARCEBS-10) 3 (2010): 86-88.



Study of interfaces in organic semiconductor heterojunctions

P. Maheshwari, D. Dutta, K. Sudarshan, S. K. Sharma and P. K. Pujari

Radiochemistry Division

and

S. Samanta, A. Singh and D. K. Aswal

Technical Physics Division

This Paper received the Best Oral Presentation Award at the 12th International workshop on Slow positron Beam Techniques (SLOPOS-12) held at Magnetic Island, Australia, during 1-6 August, 2010.

Abstract

The defect structure at the organic heterojunctions is studied, using slow positron beam. The structural and electronic properties of heterojunctions are of technological and fundamental importance, for understanding and optimization of electronic processes in organic devices. Interface trap centres play a significant role in the electrical conduction through the junctions. Depth dependent Doppler broadened annihilation measurements have been carried out in p- and n-type organic semiconductor thin films (30-80 nm), both single as well as multilayers grown on quartz substrate. The objective of the present study is to investigate the defect structure and to understand the behavior of positrons at the charged organic interfaces. Our result shows the sensitivity of positrons to the interfacial disorders that may be a convoluted effect of the presence of defects as well as the influence of the charge dipole in multilayers.

Introduction

Organic electronics has attracted worldwide attention, due to the advantages of low-cost, ease of processing, compatibility with a wide range of substrates, large area and the ease of tailoring the material characteristics. The potential devices comprise of organic transistors [1], organic photovoltaic cells [2,3], organic light emitting diodes [4] and organic memory devices [5]. Organic heterojunctions are intrinsic to organic devices. Considerable work is focused on the heterojunctions towards understanding the physics of device operation and performance [6-9]. Many aspects of device operation are quite well understood. However, there is considerable knowledge gap in the understanding of structural and electronic properties of interfaces, between organic and

inorganic components, which are important for understanding and optimization of electronic processes in these devices. Engineering of the interfacial properties, to improve device performance by utilizing various surface modification schemes, is another area of current interest.

In organic devices, energy level alignment and interfacial dipole has been observed at the interfaces, due to charge transfer at the heterojunctions [10, 11]. The dependence of molecular orientation on charge transfer and interfacial dipole has also been reported [12, 13]. The molecular orientation near the interfaces, mainly governed by molecule-molecule and molecule-substrate interaction, can be crucial for the device efficiency [14, 15]. Phthalocyanines are a class of low molecular weight organic molecules, exhibiting semiconductor properties.



They represent one of the most promising candidates for ordered organic thin films as these systems possess advantageous attributes such as thermal and chemical stability, and, excellent film growth characteristics [16]. The electronic and optical properties of Organic semiconductor (OSC) thin films, strongly depend on their structure and morphology [17]. The fabrication of heterojunctions involves controlled growth of OSC thin films. However, fabrication of hetero-multilayered structure is a challenge, due to large anisotropy and relatively weak nature of interaction forces between organic molecules [16].

Beam-based positron annihilation spectroscopy has been found to be a very sensitive technique to probe open volume defects present at the surfaces and interfaces, which is not possible by any other conventional defect characterization techniques. The unique repulsive force between positron and ion cores of the material makes the positron ideal for probing defects, voids and free volumes. The presence of open volume defects / free volume manifests as increase in lifetime and narrowing of the momentum distribution. The latter is often described by a shape parameter, namely Doppler broadening S -parameter, defined as the ratio of the number of counts in the central part of 511 keV gamma line to the total number of counts under the peak. The increase in S -parameter corresponds to an increase in number or size of the defect or void.

The morphology of OSC thin films as a function of temperature and the type of substrate as well as the thickness of the films has been reported by us earlier [18]. In the present work, microstructure of the organic-organic as well as organic-inorganic (film-substrate) interfaces of the heterojunctions, has been studied. Doppler broadened S -parameter as a function of positron energy is seen to be sensitive to the interfacial microstructure. We have observed for the first time, sharp contrast in S -parameter at the interfaces in organic heterojunctions indicating the presence of considerable disorder, contrary to the reported

ordered superstructure obtained from X-ray measurements.

Experiment

Single layer and multilayer structure of n-type (copper-hexadecafluoro-phthalocyanine; $F_{16}CuPc$) and p-type (cobalt-phthalocyanine; $CoPc$) OSC materials, have been prepared on quartz substrate, by thermal evaporation using Hind high Vac thermal evaporation system (model no-12A4T), under vacuum better than 10^{-6} mbar. The substrate was cleaned by sonication with trichloroethylene, acetone and methanol separately for 5 minutes each, before the deposition. The films were deposited at the substrate temperature of $100^{\circ}C$ and the deposition rate was $0.2 \text{ \AA}/\text{sec}$. Single layer films of n and p-type material were 80 nm thick and the individual film thickness for p-n and n-p-n junction system was 60 nm and 30 nm, respectively. The thickness of the films was measured by quartz crystal monitor.

Depth-dependent Doppler broadening measurements were carried out, using slow positron beam at BARC in the energy range 200 eV-20 keV. A high-efficiency high-purity germanium detector, with a resolution of 2 keV at 1332 keV photopeak of ^{60}Co , was used for Doppler broadening measurements and spectra with 2×10^5 counts were acquired at each energy. The ratio of integral counts within ~ 2 keV energy windows centered at 511 keV and total photo peak area was used to evaluate the S -parameter.

Results and Discussion

The variation of S -parameter as a function of positron energy for the single layer (p and n-type OSC) and multilayer films (p-n and n-p-n junction) are shown in figs. 1-4, with solid lines as eye-guides. In general, there is a decrease in S -parameter with beam energy followed by an increase at the interface (organic-organic/ organic-inorganic, as the case may be) and reaching the bulk value of quartz at higher energies. The most important



observation is the enhancement of *S*-parameter at the interfaces.

Figs. 1 and 2 show the *S*-parameter variation, as a function of depth for n-type and p-type OSC, respectively. The *S*-parameter variation for single layer n-type and p-type films of F₁₆CuPc and CoPc on quartz substrate, reflects an organic-inorganic (film-substrate) interface. The energy

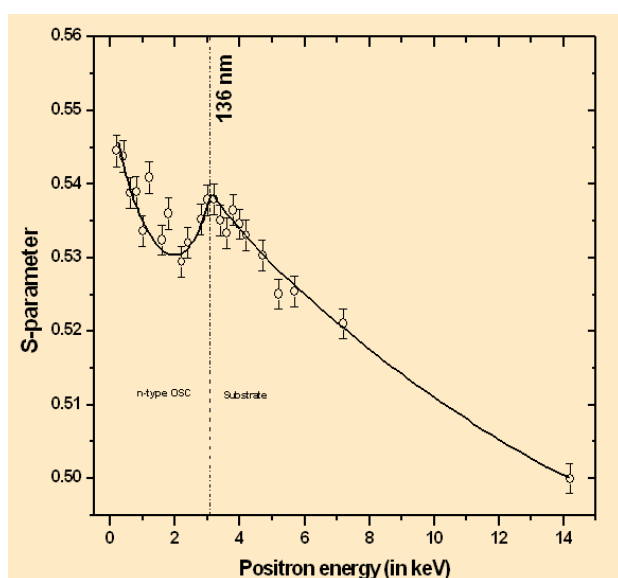


Fig. 1: *S*-parameter for 80 nm n-type OSC film grown on quartz

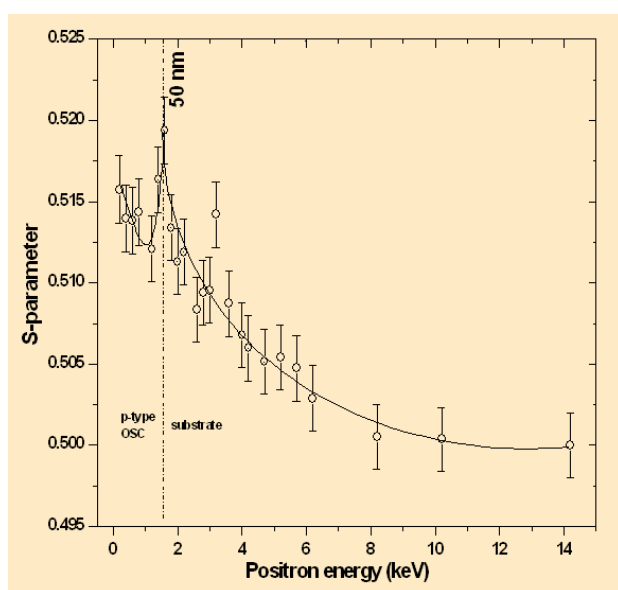


Fig.2: *S*-parameter for 80 nm p-type OSC film grown on quartz

corresponding to the maximum of *S*-parameter value, indicates the mean depth of the interface between the film and the quartz substrate as calculated from the range-energy relation given by, $\langle z \rangle = (40/\rho) * E^{1.6}$, where, ρ is the density of the material (1.7g/cm³ for OSC and 2.32g/cm³ for quartz) and *E* is the energy of positron in keV. The observed *S*-parameter profile, indicates the sharp contrasting interfacial characteristics between the film and the substrate. The high value of *S*-parameter at the interface, indicates the presence of open volume defects / domains (trap centers) and reveals the sharp microstructure variation between organic and inorganic materials, as indicated by the fall in *S*-parameter value thereafter. The epitaxial relation of film and the substrate is important not only in crystallographic sense but also for growth behavior. The organic molecules have large anisotropy and internal degrees of freedom, due to low symmetry and extended size [16]. The effect of size difference of unit cells of organic molecules and the inorganic substrate as well as molecule-substrate interaction, leads to translational and orientational domains, which are the sources of disorder [16]. The subsequent growth of the film is accomplished by the interplay of molecule-molecule and molecule-substrate interaction [19].

The organic-organic interfaces are distinctly clear in the case of multilayered structures; p-n and n- p-n heterojunctions. These interfaces experience weak van der Waals forces existing between the organic molecules. It has been reported in literature, that these structures exhibit ordered arrangement of molecules across the heterojunction [20]. Also, energy level bending due to charge transfer at the heterojunction, leads to the formation of charge accumulation layer and interfacial dipole [21]. However, the presence of defects / open volumes / domains of disorder are clearly revealed from our slow positron beam studies. Fig. 3 shows *S*-parameter profile for p-n junction. This structure comprises of both an organic-organic (n and p-type OSC) and organic-inorganic (OSC-substrate) interface. A sharp contrast in



S-parameter can be seen at the two interfaces corresponding to energies 1.8 keV and 5.7 keV respectively. Similar interfacial characteristics have also been observed for n-p-n junction represented by the sharp oscillatory behavior of S-parameter near to the interfaces between n-p and p-n type OSC materials (bulk film) as well as film-substrate as shown in Fig. 4. The increase in S-parameter value near the interface, is the convoluted effect of defects

arising due to the growth behavior of different types of organic molecules and the intrinsic electric field, due to interfacial dipole at the interface. It is to be noted, that for energies higher than 1.8 keV, the standard Makhovian profile for positron implantation shows wide (in comparison to film thickness) and smoothly varying form and should not lead to sharp interfaces (as reflected from oscillatory behavior of S-parameter). However, electric field at the interfaces due to charge accumulation, might have modified the standard Makhovian profile. This must be taken into account to explain the sharp oscillations in S-parameter. The mean depths of these interfaces as calculated by positron implantation profile, are observed to be shifted towards the larger depths. The shift in the depth appears to be due to the cumulative effect of increased diffusion of positrons on the substrate side, where diffusion length has been found to be high and leading to broadening of implantation profile. However, the role of electric field, especially in multilayers cannot be ruled out.

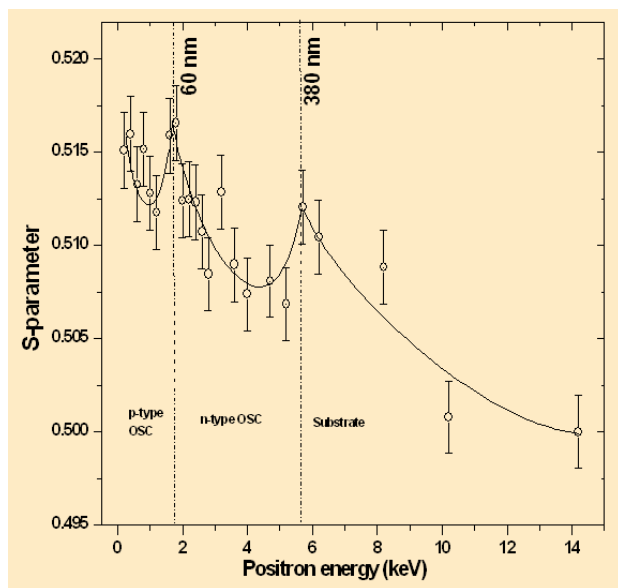


Fig. 3: S-parameter for p-n Junction (each layer 60 nm)

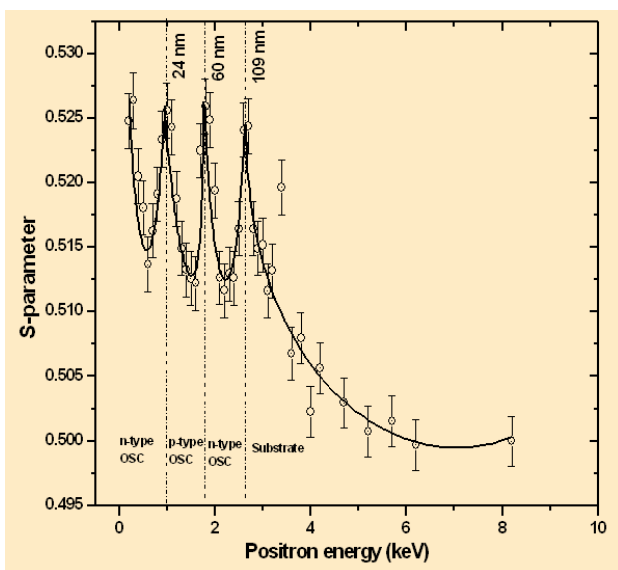


Fig. 4: S-parameter for n-p-n junction (each layer 30 nm)

In conclusion, we have reported positron studies on the organic heterojunctions. A large degree of disorder or presence of open volume defects at the interfaces are seen, which are believed to have ordered structure from X-ray studies. The observed contrast in the S-parameter at the interfaces, makes the positron beam technique a potential characterization tool in organic electronics and, we believe more detailed information on the heterojunction microstructure can be obtained through suitable modeling.

References

1. Dodabalapur A, Katz H E, Torsi L and Haddon R C 1995 *Science* 269 1560
2. Tang C W and Vanslyke S A 1987 *App.I Phys. Lett.* 51 913
3. Peumans P and Forrest S R 2001 *Appl. Phys. Lett.* 79 126



4. Tang C W and Vanslyke S A 1986 *Appl. Phys. Lett.* 48 153
5. Ma L, Liu J, Pyo S and Yamg Y 2002 *Appl. Phys. Lett.* 80 362
6. Akaike K, Kanai K, Ouchi Y and Seki K 2009 *Appl. Phys. Lett.* 95 113306
7. Tang J X, Zhou Y C, Liu Z T, Lee C S and Lee S T 2008 *Appl. Phys. Lett.* 93 043512
8. Liu Z T, Lo M F, Wang H B, Ng T W, Roy V A L, Lee C S and Lee S T 2009 *Appl. Phys. Lett.* 95 093307
9. Brumbach M, Placencia D and Armstrong N R 2008 *J. Phys. Chem. C* 112 3142
10. Haibo W, Liu Z, Ng T W, Lo M F, Lee C S and Lee S T 2010 *Appl. Phys. Lett.* 96 173303
11. Rajagopal A, Wu C I and Kahn A 1997 *J. Appl. Phys.* 83 2649
12. Chen W, Chen S, Huang H, Qi D C, Gao X Y and Wee A T S 2008 *Appl. Phys. Lett.* 92 063308
13. Chen W, Chen S, Huang Y L, Huang H, Qi D C, Gao X Y, Ma J and Wee A T S 2009 *J. Appl. Phys.* **106** 064910
14. Kowarik S, Gerlach A, Sellner S, Schreiber F, Cavalcanti L and Konovalov O 2006 *Phys. Rev. Lett.* **96** 125504
15. Thayer G E, Sadowski J T, zu Heringdorf F M, Sakurai T and Tromp R M 2005 *Phys. Rev. Lett.* **95** 256106
16. Brutting W, *Physics of Organic semiconductors* 2008 WILEY-VCH Verlag GmbH & Co. KGaA
17. Ribic P R and Bratina G 2007 *J. Vac. Sci. Technol. B* **25** 1152
18. Maheshwari P, Dutta D, Samanta S, Singh A, Aswal D K, Reddy A V R and Pujari P K 2009 *Phys. Stat. Solidi C* **6** 2589
19. Debnath A K, Samanta S, Singh A, Aswal D K, Gupta S K, Yakhmi J V, Deshpande S K, Poswal A K and Surgers C 2008 *Physica E* **41** 154
20. Akimichi H, Inoshita T, Hotta S, Noge S and Sakaki H 1993 *Appl. Phys. Lett.* **63** 3158
21. Chen W, Chen S, Huang H, Qi D C, Gao X Y and Wee A T S 2008 *Appl. Phys. Lett.* **92** 063308.



Study of structural and thermal properties of barium strontium silicate glasses

K. Sharma, A. Dixit, A. Arvind and G.P. Kothiyal
Glass and Advanced Ceramics Division

This paper received the Best Poster Award at the International Workshop and Symposium on the Synthesis and Characterization of Glass-Ceramics (IWSSCGGC) held at C-MET, Pune, during July 7-10, 2010

Abstract

We present some studies on barium-strontium silicate based glasses which are considered as potential sealant materials for solid oxide fuel cell application. Glasses are prepared by melt-quench technique and characterized for phase identification, glass transition temperature (T_g), thermal expansion coefficient (TEC) and microstructures. A few seals have been tested with Crofer-22APU interconnect. The average TEC of glass samples are found to be in the range $1-2 \times 10^{-5} \text{ } ^\circ\text{C}^{-1}$. With the addition of B_2O_3 and Cr_2O_3 , we observed a decrease in glass transition temperature of glasses and seals were prepared at lower temperatures. Microstructure near interface of these glasses with Crofer 22 APU revealed good bonding and found to withstand a vacuum of 10^{-6} Torr

Introduction

Glasses and glass-ceramics find wide application in hermetic sealing, coatings and more recently in the solid oxide fuel cells as prospective sealant materials [1-4]. However, sealants for high temperature applications such as SOFCs require additional constraints of long term chemical stability, under both oxidizing and reducing ambients in the temperature range 750-850°C. One of the major challenges for implementation of planar SOFC is the development of suitable sealant materials, to separate air and fuel.

The most common sealants employed in SOFC are based on alkaline earth oxide glass and glass-ceramics. The properties of the glass based sealant material can be fine tuned through altering the glass composition. Many studies have been reported on glass and glass-ceramics based sealant materials to achieve desirable properties [5-10].

In this paper, we present some studies on the structural, thermo-physical and sealing properties of barium-strontium silicate based glasses. A few glass-to-metal (Crofer) seals in sandwich geometry were prepared and the interfaces were studied by using SEM and EPMA. Some of the seals were also tested for hermeticity at room temperature in a specially designed system and were found to withstand a vacuum of $\sim 10^{-6}$ Torr.

Experimental

Nominal compositions (in mol.%) of glass samples with different additives given in Table 1 were prepared by using melt-quench technique. The precursor carbonates or oxides of 99.9% purity are mixed, ground and calcined at a maximum temperature of 800°C in alumina crucible. The calcined charge was then melted at 1450-1550°C. The melt was poured on stainless steel plate. The glass samples were annealed at around 650°C for 4 hrs. DTA was carried out in the temperature range of 30 to 950°C



Table 1: The compositions (in mol%) of the prepared glass samples

Sample ID	SiO ₂	SrO	BaO	La ₂ O ₃	Al ₂ O ₃	B ₂ O ₃	Cr ₂ O ₃
BSS	38	20	30	0	10	0	2
BBSS	30	20	30	05	05	10	0
BBSSCr	30	20	30	05	05	8	2

in an air ambient, using a TG/DTA instrument (Model Labsys, M/s Setaram, France). Thermal expansion coefficient (TEC) was measured in the temperature range of 30° to 900°C using TMA instrument (Model TMA-92, Setaram, France). The phase identification was carried out by using Philips (PW1710) X-ray diffractometer with Cu K_α as radiation source. For studying the adhesion/bonding, sealing with Crofer 22 APU alloy was carried out in sandwich geometry. Microstructure near the interface was investigated using SEM (Model: Tescan Vega MV2300T/40) and elemental line scan was taken across the interface to see the diffusion.

Result and Discussion

Glass transition temperature and thermal expansion coefficient (TEC) are determined from TMA plots. BSS glass has a glass transition temperature of 670°C and TEC value of 10 × 10⁻⁶ °C⁻¹. The glass transition temperature has decreased with addition of B₂O₃. Glass transition temperature has decreased to 650 °C when B₂O₃ content was added to 10 mol%. The TEC values of the glass samples are found to be around 11.4 × 10⁻⁶ °C⁻¹ and 12 × 10⁻⁶ °C⁻¹ with the addition of B₂O₃- and Cr₂O₃ in BSS glass, respectively.

In glass and glass-ceramics, the thermo-physical properties are strongly dependent upon the composition [11]. In glasses, SiO₂ acts as network forming oxide [12]. Decreasing of silica content will decrease the overall network and also decrease the rigidity of the network. Further, addition of Cr₂O₃ is also known to increase the thermal expansion coefficient of glasses as it decreases the glass polymerization. Thus, the net effect of addition of B₂O₃ and Cr₂O₃ shows an increase in thermal expansion coefficient of glasses, while the glass transition temperature decreases.

DTA plots of BSS and BBSS glass samples at 10 K/min are shown in Fig. 1a. It exhibits a glass transition endotherm at 800°C and two exotherms at around 1060°C and 960°C. With addition of B₂O₃, peak crystallization temperature is shifted to 784°C. The crystallization kinetics of the BSS glass was studied using the Avrami, Kissinger and Augis-Bennett [13,14] equations.

$$k = \nu \exp\left(\frac{-E}{RT}\right) \tag{1}$$

$$\ln\left(\frac{T_p^2}{\alpha}\right) = \frac{E}{RT_p} + \ln\frac{E}{R} - \ln \nu \tag{2}$$

$$n = \frac{2.5}{\Delta T} \times \frac{RT_p^2}{E} \tag{3}$$

Where, *E* is the effective overall activation energy for the crystal transformation process, *ν* an effective frequency factor, which is a measure of the probability that a molecule having energy *E* participates in the transformation, *R* the gas constant, and *T_p* the crystallization peak temperature. Peak crystallization temperatures found to shift from 960 to 985°C with increasing heating rate from 5 to 20 K/min.

According to equation (2) a plot of ln(*T_p²/α*) versus 1/*T_p* should be linear and slope of the straight line gives the activation energy for the crystallization. The plot of ln(*T_p²/α*) versus 1/*T_p* is shown in Fig 1b. The effective activation energy and crystallization index (*n*) are calculated using equation (2 and 3). The activation energy for crystallization was found to be around 422 kJ/mol. The glass has shown

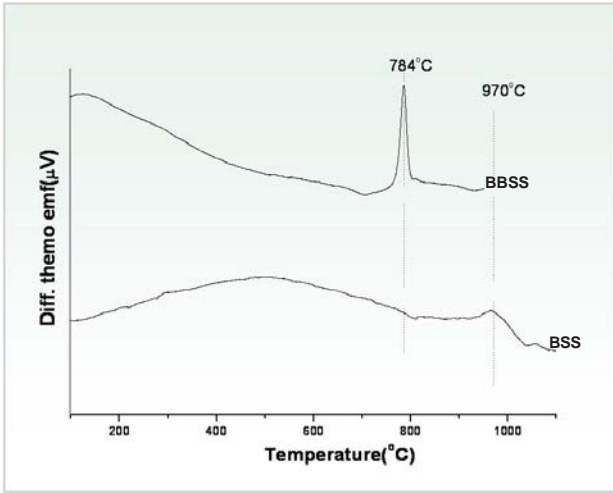


Fig. 1(a): DTA plots of BBSS & BSS glasses

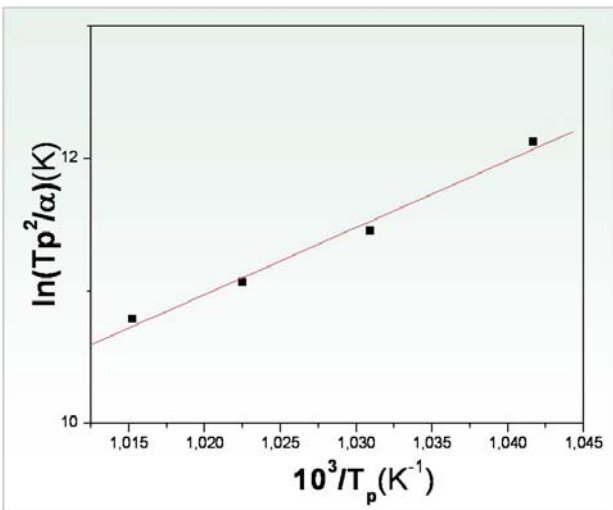


Fig. 1(b): The plot of $\ln(T_p^2/\alpha)$ versus $1/T_p$

a tendency to surface crystallize as value of n was found to be near 2.

The activation energy for crystallization for BSS glass is high which implies that it will take long time and high temperature for crystallizing this glass. We observed that the microstructure of glass does not show a significant crystallization when heat treated at 900°C (Fig. 2a). The appearance of the different crystallized phases was observed for glass samples when glass was heat treated at 1000°C and 1100°C (Fig. 2b&2c).

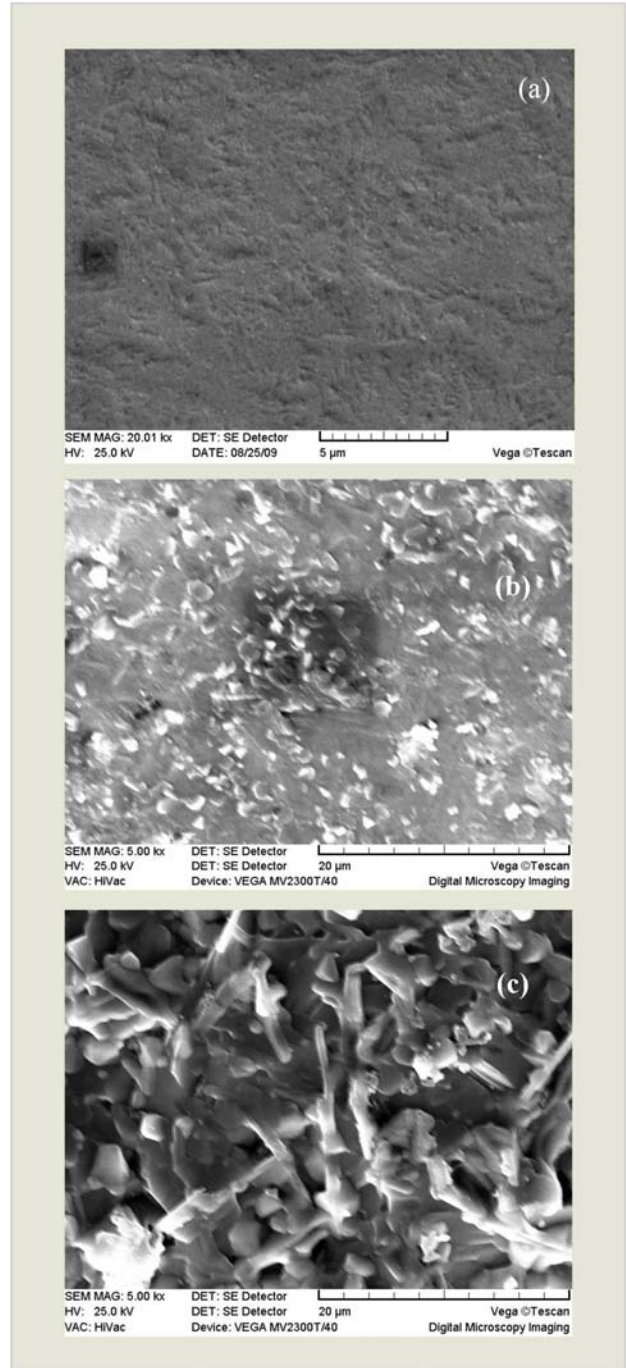


Fig. 2: microstructures of BSS glass after heat treatment at (a) 900°C for 6h, (b) 1000°C for 6h, (c) 1100°C for 6h,

XRD patterns of different glass samples after controlled heat treatment at different temperatures are depicted in Fig. 3. The BSS glass after heat treatment shows the formation of $BaSi_2O_5$ and $BaAl_2Si_2O_8$. However, the intensity

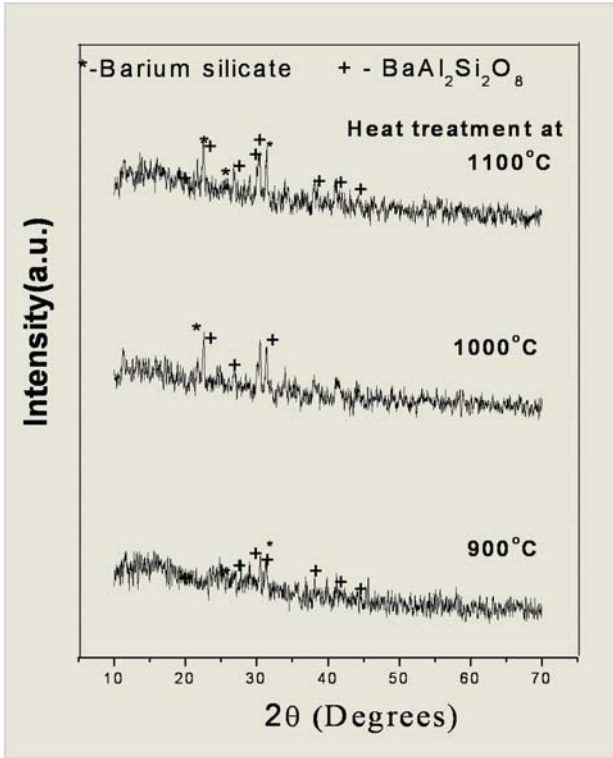


Fig. 3a: XRD plots of BSS after different heat treatment

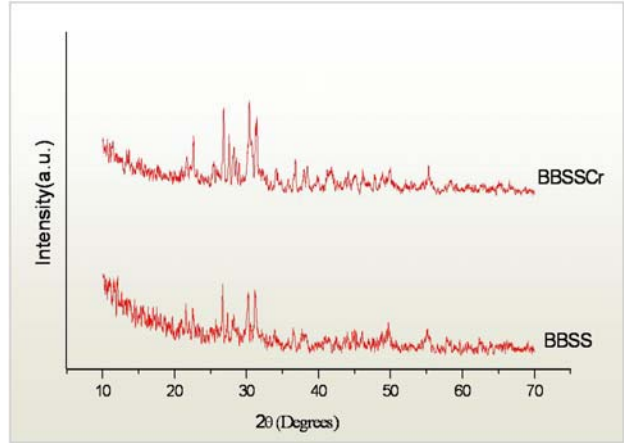


Fig. 3b: XRD plots of BBSS and BBSSCr after heat treatment at 800 C for 6h

using two flat crofer plates in sandwich geometry at the max. 1150-1200°C. However, for other composition we are able to get good bonding at around 1000°C. Microstructures near the interface of seals investigated are shown in Fig. 4. Elemental line scans for the seal confirm enrichment of Cr at the interface. We have

of major peaks is low, implying the samples are not well crystallized.

The others samples BBSS and BBSSCr showed relatively good crystallization behaviour. XRD patterns of these glass samples after controlled heat treatment at 800°C are depicted in Fig. 3b. The glass after heat treatment shows the formation of $BaSi_2O_5$, $BaAl_2Si_2O_8$, $Ba_{0.9}Sr_{0.1}Al_2Si_2O_8$ and Sr_2SiO_4 .

The glass transition temperature for BSS glass is around 800°C which corresponds to viscosity of $10^{11.3}$ Pa s. Viscosity of the glass decreases with increasing temperature. The significant wetting of metal by glass is possible at higher temperature (viscosity around $10^7 - 10^4$ Pa.s). Sealing behaviour of this glass with Crofer 22 alloy was assessed by making a seal with the glass,

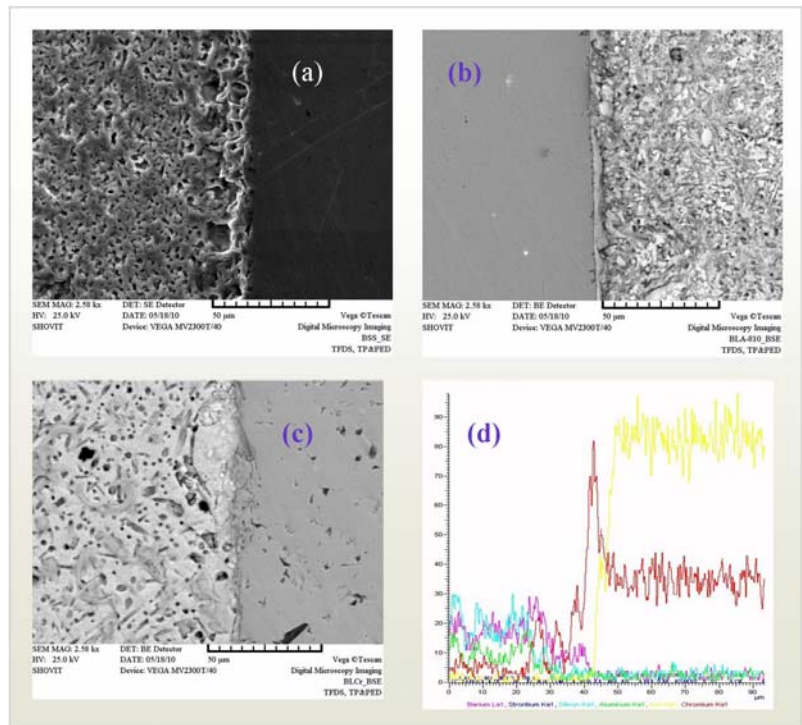


Fig. 4: Microstructure near the interface of glass with Crofer 22 APU (a) BSS (b) BBSS (c) BBSSCr (d) Elemental line scan across the interface of BSS glass.



observed an interdiffusion of Si from the glass into the metal to a depth of approximately 5-10 μm . EDAX has also shown interdiffusion of Fe, and Ba across the boundary implying the good wetting of metal by glass materials.

The elemental mapping of the seals after heat treatment at 800°C for 100 h is shown in Fig 5. It indicates the presence of some crystalline phases near the interface. From the mapping we conclude that these crystallites are rich in Ba, Si and Al and poor in Cr. The enrichment of

Cr at the interface of Crofer22 alloy was also observed, however, the diffusion of Cr in the glass (away from reaction zone) is minimal. Leak testing of some seals was carried out and these seals were found to withstand a vacuum of 10^{-6} Torr at room temperature.

Conclusion

The glass/glass-ceramics have been prepared and successfully used for the fabrication of hermetic seals.

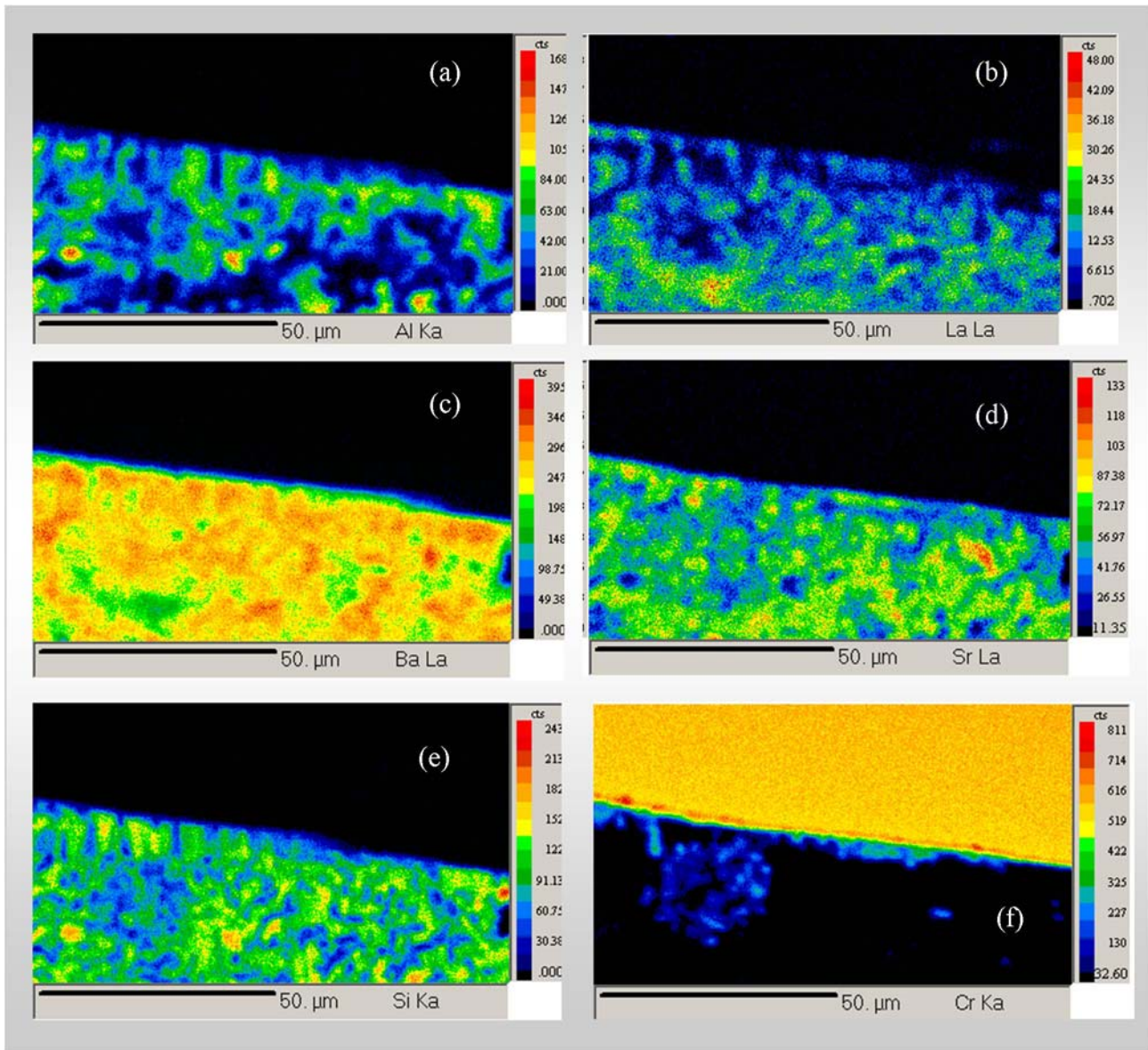


Fig. 5: Elemental mapping at BBSS glass - Crofer 22 APU seal interface after heat treatment at 800°C for 100 h

Merit Award



These glasses were optimized for sealing applications for Crofer-22 APU. The sealing at lower temperature was achieved by adding the additives like B_2O_3 , La_2O_3 and Cr_2O_3 . TEC values were found to be in the range of $10-12 \times 10^{-6}/^\circ C$ (30-300°C). Development of crystalline phases $BaSiO_3$ and $BaAl_2Si_2O_3$ upon heat treatment was observed which is not detrimental for SOFC sealant. The prepared glasses exhibited good sealing with Crofer 22 APU and thus has potential as a good sealant for high temperature applications.

Acknowledgements

The authors wish to thank Dr. A.K. Suri and Mr. V.K. Handu for encouragement and Drs. S. K. Gupta and A.K. Tyagi for providing SEM and XRD facilities respectively. We would also like to thank Shri Radhakrishanan Nair for vacuum testing of seals.

References

1. Steele B. C. H., Heinzl A. "Materials for fuel-cell technologies". *Nature* 414(2001): 345-352.
2. Pascual M. J., Guillet A., Duran A. "Optimization of glass-ceramic sealant compositions in the system $MgO-BaO-SiO_2$ for solid oxide fuel cells (SOFC)". *Journal of Power Sources* 169 (2007): 40-46.
3. Jeffrey W., Fergus, Sealants for solid oxide fuel cells. *Journal of Power Sources* 147 (2005): 46-57.
4. Ley K. L., Krumpelt M., Kumar R., Meiser J. H., Bloom I. "Glass-ceramic sealants for solid oxide fuel cells: Part I. Physical properties". *Journal of Materials Research* 11 (1996): 1489-1493.
5. Lara C., Pascual M. J., Prado M.O. "Sintering of glasses in the system $RO-Al_2O_3-BaO-SiO_2$ (R = Ca, Mg, Zn) studied by hot-stage microscopy". *Solid State Ionics* 170 (2004): 201-208.
6. Lara C., Pascual M. J., Duran A. "Glass-forming ability, sinterability and thermal properties in the systems $RO-BaO-SiO_2$ (R = Mg Zn)". *Journal of Non-Crystalline Solids* 348 (2004): 149-155.
7. Yang Z., Meinhardt, Kerry D., Stevenson J.W. "Chemical compatibility of barium-calcium-aluminosilicate-based sealing glasses with the ferritic stainless steel interconnect in SOFCs". *Journal of Electrochemical Society* 150 (2003): A1095-A1101.
8. Brochu M., Gauntt B.D., Shah R., Miyake G., Loehman R. E. "Comparison between barium and strontium-glass composites for sealing SOFCs". *Journal of the European Ceramic Society* 26 (2006): 3307-3313.
9. Lara C., Pascual M. J., Keding R. and Durán A., "Electrical behavior of glass-ceramics in the systems $RO-BaO-SiO_2$ (R=Mg, Zn) for sealing SOFCs". *Journal of Power Sources* 157 (2006): 377.
10. Sohn S. B., Choi S. Y., Kim G. H., Song H. S., Kim G. D. "Stable sealing glass for planar solid oxide fuel cell". *Journal of Non-Crystalline Solids* 297 (2002): 103-112.
11. Shelby J. E. *Introduction to glass science and technology*. The Royal Society of Chemistry, 2005
12. Micmillan P. W. *Glass Ceramic*. Academic Press, London, 1979.
13. Avrami M. "Transformation-time relations for random distribution of nuclei". *Journal of Chemical Physics* 8 (1940): 212-224.
14. Bansal N. P., Gamble E. A. "Crystallization kinetics of a solid oxide fuel cell seal glass by differential thermal analysis" *Journal of Power Sources* 47 (2005): 107-115.



Synthesis, characterization and luminescence study of $Y_2Sn_2O_7$: Tb nanoparticles co-doped with Sb^{3+}

Sandeep Nigam, V. Sudarsan and R. K. Vatsa
Chemistry Division

This paper received the Best Poster Award at the International Conference on Recent Trends in Materials Science and Technology (ICMST 2010), held at Thiruvananthapuram, Kerala, during October 29-31, 2010

Abstract

Tb^{3+} doped $Y_2Sn_2O_7$ nanoparticles were prepared at a relatively lower temperature ($700^\circ C$) by the polyol method. The crystal structure and particle size were characterized by XRD and TEM. As prepared samples show strong green emission, characteristic of Tb^{3+} , but very poor luminescence has been observed from samples heated at $700^\circ C$. Co-doping of these $Y_2Sn_2O_7$: Tb^{3+} nanoparticles with Sb^{3+} ions results in significant improvement of Tb^{3+} emission. Distortion of the symmetry around Tb^{3+} ions of pyrochlore lattice due to the substitution of Sb^{3+} is the reason for the improved luminescence.

During the last decade, pyrochlore-type oxides ($A_2B_2O_7$) have emerged as important host matrices for lanthanide-doped luminescent materials, due to their higher thermal stability¹⁻⁴. Among different types of pyrochlores, the ones based on Sn^{4+} ions are applicable as potential hosts for the incorporation of luminescent lanthanide ions. Chemical substitution of A or B sites of pyrochlore oxide by lanthanide ion, is a widely used approach, to prepare thermally-stable luminescent materials¹⁻⁴. In bulk $Y_2Sn_2O_7$, Y^{3+} ions are having a centro-symmetric environment (D_{3d}). For lanthanide ions occupying such sites, only the magnetic dipole transitions are allowed and all electric dipole transitions are forbidden. This will result in very poor luminescence from Eu^{3+} and Tb^{3+} ions when doped in such lattices⁴. This problem can be avoided by incorporating other ions like Sb^{3+} in the lattice so that the lattice gets distorted and luminescent intensity from the lanthanide ions increases. Sb^{3+} ions have been chosen in the present study as its ionic radius is comparable with

the Y^{3+} ions and additionally it has a valence shell electronic configuration of $5s^2$ and the luminescence of ions with s^2 valence shell configurations are very sensitive to the surrounding environment. Based on these facts, we have carried out the synthesis and characterization of $Y_2Sn_2O_7$ nanoparticles co-doped with Tb^{3+} and Sb^{3+} and subsequent investigation for luminescence properties.

For the preparation of Tb^{3+} and Sb^{3+} doped $Y_2Sn_2O_7$ nano-materials, Sn metal, $SbCl_3$, Tb_4O_7 , Y_2CO_3 , were used as starting materials. The solution containing Y^{3+} , Sn^{4+} , Tb^{3+} and/or Sb^{3+} in ethylene glycol medium was slowly heated up to $100^\circ C$ followed by the addition of appropriate amount of urea. The temperature was then raised to $150^\circ C$ and maintained at this value for 2 hours. After the reaction, the precipitate was collected by centrifugation and then washed twice with acetone and three times with ethyl alcohol, followed by drying under ambient conditions. The samples prepared were thus finally heated to $700^\circ C$ for 5 hours.



Fig. 1 shows the XRD patterns of as prepared and 700°C heated samples. From XRD studies it is confirmed, that as prepared sample is amorphous and heat treatment at 700°C results in the formation of highly crystalline $Y_2Sn_2O_7$ phase, having pyrochlore structure. Based on the line width of the diffraction peaks, average crystallite size was estimated to be around 5 nm for the nanoparticles (700°C heated sample). Lattice parameters were calculated based on the least square fitting of the diffraction peaks and were found to be $a = 10.553(1) \text{ \AA}$ for the $Y_2Sn_2O_7$ nanoparticles. Comparable lattice parameters were also observed for Sb^{3+} co-doped $Y_2Sn_2O_7:Tb^{3+}(2.5\%)$ nanoparticles. Transmission Electron Microscopic (TEM) images of the nanoparticles obtained at 700 °C show very fine spherical particles with a diameter in the range of 2-5 nm. Formation of small spherical particles has been attributed to the low concentration of the product nuclei (yttrium tin hydroxide) existing in the reaction medium after nucleation. High resolution image corresponding to a particular nanoparticle is shown in the same figure as an inset.

Luminescent measurements were carried out on different as prepared and heated samples (Fig. 2). As prepared sample of $Y_2Sn_2O_7:Tb^{3+}(2.5\%)$ showed a characteristic emission transition of Tb^{3+} ions. Contrary to this, 700°C heated sample of $Y_2Sn_2O_7:Tb^{3+}(2.5\%)$ nanoparticles does

not show any emission from Tb^{3+} ions. For as prepared sample, since it is amorphous, Tb^{3+} environment will be significantly distorted, thereby increasing both the electric magnetic dipole transition probabilities of Tb^{3+} ions. This results in strong Tb^{3+} emission from the sample. However for 700°C heated sample, Tb^{3+} ions replace the Y^{3+} ions of the $Y_2Sn_2O_7$ lattice, and have a centrosymmetric environment (D_{3d}) and hence the electric and magnetic dipole transition probabilities are very weak leading to poor Tb^{3+} emission from the sample.

Co-doping of $Y_2Sn_2O_7:Tb^{3+}$ nanoparticles with Sb^{3+} ions have resulted in significant improvement of the Tb^{3+} emission. Fig. 2 shows the emission spectrum from as prepared and 700°C heated Sb^{3+} co-doped $Y_2Sn_2O_7:Tb^{3+}$ nanoparticles. As observed for $Y_2Sn_2O_7:Tb^{3+}(2.5\%)$ sample, co-doped sample (as prepared) also showed Tb^{3+} emission. Additionally, Sb^{3+} co-doped $Y_2Sn_2O_7:Tb^{3+}(2.5\%)$ sample shows considerable enhancement in Tb^{3+} emission intensity, against Tb^{3+} alone doped sample i.e. $Y_2Sn_2O_7:Tb^{3+}(2.5\%)$. The improved emission characteristics of Tb^{3+} ions in the Sb^{3+} co-doped sample is attributed to the lattice distortion brought about by Sb^{3+} ion incorporation in the lattice of $Y_2Sn_2O_7$. This is understandable as the coordination numbers preferred by Sb^{3+} ions are generally 4-6. But in present $Y_2Sn_2O_7$ systems, Y^{3+} ion has a co-ordination number of 8. Therefore

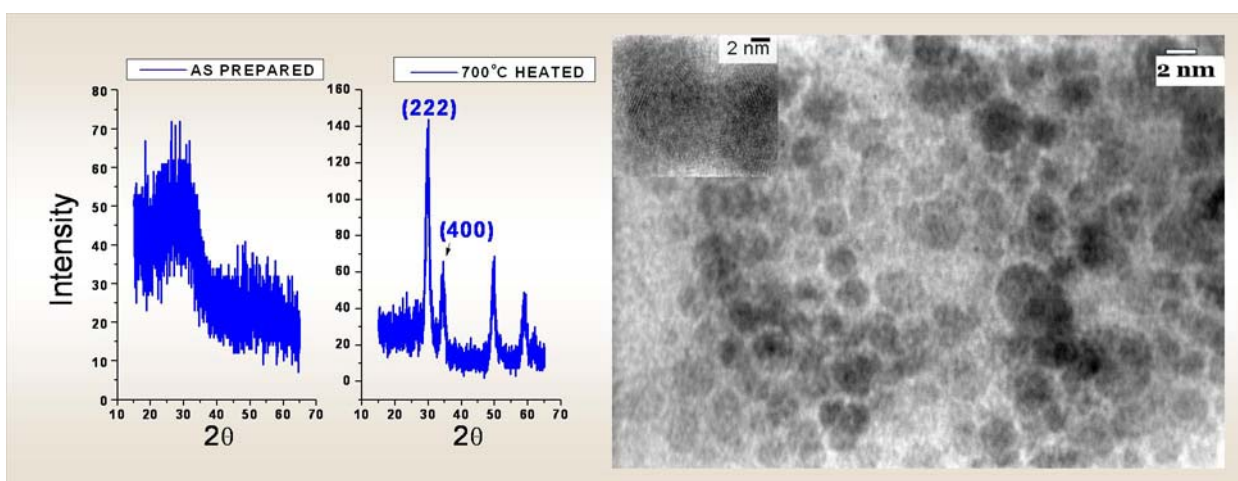


Fig. 1: XRD Pattern of as prepared and 700°C heated samples of $Y_2Sn_2O_7$, alongwith TEM image for 700°C heated sample. Inset of TEM image shows the HRTEM image of the nanoparticles.

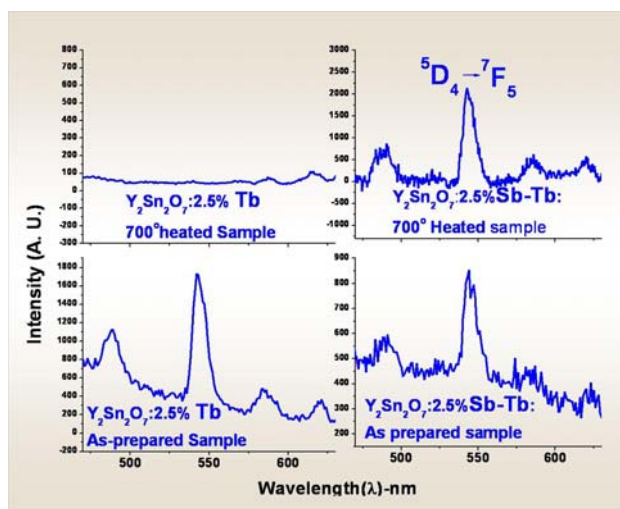


Fig. 2: Emission spectrum from as prepared and 700 °C heated samples of $Y_2Sn_2O_7: Tb^{3+}$ and Sb^{3+} co-doped $Y_2Sn_2O_7: Tb^{3+}$ nanoparticles. Intensity has been taken in arbitrary units (A.U.).

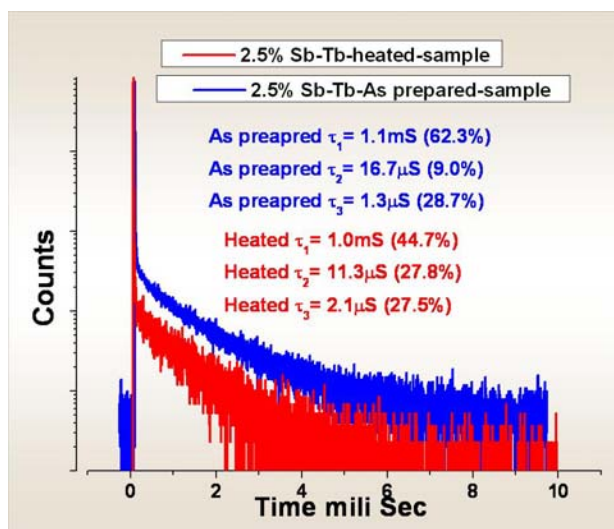


Fig. 3: Decay curve corresponding to 5D_4 level of Tb^{3+} ions in as prepared and 700 °C heated samples of Sb^{3+} co-doped $Y_2Sn_2O_7: Tb^{3+}$ nanoparticles

substitution of Y^{3+} site by Sb^{3+} ion is expected to significantly distort the lattice/environment around Y^{3+}/Tb^{3+} ions, thereby facilitating the electric dipole transitions of Tb^{3+} ions.

To get further insight, time resolved luminescence studies were also carried out (Fig. 3). The 5D_4 level of Tb^{3+} ions from Sb^{3+} co-doped $Y_2Sn_2O_7: Tb^{3+}$ (2.5%) nanoparticles has been found to decay multi-exponentially with a major component around 1 ms. Multi exponential decay corresponding to the 5D_4 level, further supports the presence of a variety of Tb^{3+} ions in the lattice associated with the lattice distortion, brought about by the Sb^{3+} incorporation in the lattice. The improvement in the luminescence from Sb^{3+} co-doped $Y_2Sn_2O_7: Tb^{3+}$ nanoparticles, has been further corroborated by estimating the approximate quantum yield of emission (η), using the emission spectrum and measured 5D_4 lifetime ($\tau_{measured}$). In the present study, to calculate the quantum yield, we have adopted a method based on the intensity of emission spectrum as mentioned in previous reports^{5,6} and we found quantum yield around 84 % for co-doped samples. These results have further proved that Sb^{3+} addition has considerably boosted the Tb^{3+} emission.

In the summing up, Tb^{3+} doped $Y_2Sn_2O_7$ nanoparticles were prepared at a relatively lower temperature (700°C) by the polyol method. The crystal structure, particle size were characterized by XRD and TEM. As prepared samples showed strong green emission, characteristic of Tb^{3+} , but very poor luminescence was observed from samples heated at 700°C. Co-doping of these $Y_2Sn_2O_7: Tb^{3+}$ nanoparticles with Sb^{3+} ions resulted in significant improvement of Tb^{3+} emission. Distortion of pyrochlore lattice due to addition of Sb^{3+} was the reason for the improved luminescence. Thus from these results one can infer, that Sb^{3+} co-doping is an effective way to improve the luminescence properties of lanthanide ions doped $Y_2Sn_2O_7$ nanoparticles.

References

1. Matteucci, F., Cruciani, G., Dondi, M., Baldi, G., Barzanti, A. "Crystal structural and optical properties of Cr-doped $Y_2Ti_2O_7$ and $Y_2Sn_2O_7$ pyrochlores" *Acta Materialia*, 55 (2007): 2229-2238
2. Shrivastava, A. M. "On the luminescence of Bi^{3+} in the pyrochlore $Y_2Sn_2O_7$ " *Mat. Res. Bull.* **37** ((2002):745-751



3. Shrivastava, A. M. "An interpretation of the optical properties of Cr⁴⁺-activated pyrochlores, Y₂Ti₂O₇, and Y₂Sn₂O₇" *Journal of Luminescence* **129** (2009): 1000-1002
4. Lu, Z.; Wang, J.; Tang, Y.; Li, Y.; "Synthesis and photoluminescence of Eu³⁺ -doped Y₂Sn₂O₇ nanocrystals" *J. Solid State Chem.* **177**, (2004): 3075-3079.
5. Peng, C.; Zhang, H.; Yu, J.; Meng, Q.; Fu, L.; Li, H.; Sun, L.; Guo, X.; "Synthesis, characterization, and luminescence properties of the ternary europium complex covalently bonded to mesoporous SBA-15" *J. Phys. Chem. B*, **109** (2005): 15278- 15287.
6. Ghosh, P.; Kar, A.; Patra, A.; " Energy transfer study between Ce³⁺ and Tb³⁺ ions in doped and core-shell sodium yttrium fluoride nanocrystals" *Nanoscale*, **2** (2010) 1196-1202.



Assessment of germplasm of Indian bread wheats for polymorphism at *Xgwm261* locus: Microsatellite analysis, sequencing and relationship with agronomic traits

Suman Bakshi and S.G. Bhagwat

Nuclear Agriculture and Biotechnology Division

This Paper received the Best Poster Award in the Biotechnology Section, at the Zonal Seminar on Physiological and Molecular Interventions for Yield and Quality Improvement in Crop Plant, held at the S.V. Patel University of Agriculture & Technology, Meerut, from 17-18 September, 2010

Abstract

Heat stress is emerging as a major threat to wheat grain quality and production in the country. The quantum jump in wheat yields was earlier achieved with Norin-10 gene(s). Experience revealed that varieties carrying these genes have reduced spikelet fertility and yield under heat stress. A search for alternative to the Norin-10 genes has revealed, that *Rht8* which is deployed in the European cultivars may confer reduced culm height without the adverse effects. The *Rht8* is tagged with a 192bp allele at *Xgwm261* locus. In this study, Indian bread wheat germplasm was assessed for allelic polymorphism at *Xgwm261* locus.

Introduction

Wheat grain with annual production of 550 million tonnes is the staple food for millions all over the world. In recent times, heat stress has emerged as a major problem in the sub-tropical wheat cultivation areas. Therefore, agronomically desirable plant types, with heat stress tolerance have become a necessity. Earlier, significant yield improvement was brought about with the use of GA₃ insensitive dwarfing genes. However, the varieties carrying 'Norin-10' genes are sensitive to heat stress and show reduced fertility under high temperature. Short stature varieties grown in Southern Europe, carry a different semi-dwarfing gene *Rht8*, which reduces plant height by 10% without significant reduction in yield (Worland et al. 1988). The microsatellite locus *Xgwm261* shows polymorphism with predominance of 165bp, 174bp and

192bp alleles. The 192bp allele in wheat shows plant height reduction as compared to 165 and 174bp. The semi-dwarfing effect of the 192bp is due to a tight linkage (0.6cM) with *Rht8*. The present study was undertaken with an aim to investigate polymorphism at *Xgwm261* locus and to investigate if there was a relationship between the allelic variation and agronomic traits in an experiment conducted at heat stress location.

Material and Methods

Microsatellite screening was done in 92 bread wheat genotypes, recommended for cultivation in different agro-climatic zones. GA₃ sensitivity test was done on seedlings. Genomic DNA was isolated and polymorphism at *Xgwm261* locus was studied. The alleles/genes *RhtB1b*, *RhtD1b*, *RhtB1a* and *RhtD1a* were amplified using allele



specific primers (Ellis et al. 2002). Sequencing was done using ABI 3730LX sequencer. DNA sequences from sequenced alleles were aligned by using the ClustalW program (<http://www.ebi.ac.uk/Tools/clustalw>). All the genotypes were grown at two locations: Trombay (longitude: 72°.9', latitude: 19°0' situated at sea level) and Niphad (longitude: 74°6', latitude: 20°6', altitude: 549m above mean sea level). Standard agronomic practices were followed.

Results and Discussion

Analysis showed five allelic variants based on size at *Xgwm261* locus. Three alleles; 165bp (44.5%), 174bp (10.8%), 192bp (39.1%) were more frequent (Table 2). A less frequent 200bp allele (4.3%) with sequence differences among genotypes was observed. A new 198bp allele was observed in cultivar NI179. Genotypes were analyzed using perfect markers to understand the basis of differences in plant height. The results confirmed, that tallness was associated with presence of *RhtB1a* and *RhtD1a* (Table 2&3). The Norin 10 genes brought about reduction in plant height at both the locations. The 192bp allele of *Xgwm261* locus however, did not show association with reduced plant height as a general effect. Also, there was no overall positive influence of 192bp allele on other agronomic traits.

Agronomic parameters and allelic variation

The two locations were different with respect to climatic conditions. The effect of location was reflected in the data on agronomic parameters. Values for all the parameters were lower at Trombay, except for the tiller number per plant (Table1). There was an absence of height reduction or Superiority in association with 192bp allele of the *Xgwm261* locus (Tables' 2&3). Absence of positive influence of 192bp indicated that, a height neutral 192bp allele may be present among the Indian cultivars. Ellis et al. (2007) reported lack of association between 192bp allele and reduction in plant height. In the Indian wheat programme, exotic germplasm from CIMMYT was used, to incorporate traits such as semi-dwarfing genes or the 1B/1R translocation. A genotype with 192bp allele not linked to *Rht8* from CIMMYT, could be a source of height neutral 192bp allele in the Indian varieties. It was also observed, that the 165bp allele was associated with superior means for some of the agronomic traits and numerically higher for almost all agronomic traits at Trombay location (Table 3). This indicated that the 165bp allele could be associated with advantage under heat stress conditions. Five of the analyzed genotypes showed new allelic variants with size 200bp and 198bp. The conspicuous feature of these genotypes was that all were tall (no major dwarfing gene), recommended for warmer

Table 1: Comparison of plant performance in the two environments

Agronomic trait	Niphad (Mean±SE)	Trombay (Mean±SE)	ANOVA significance
Plant height	84.47±1.55	59.0±1.15	**
Grain number per spike	48.33±0.98	34.45±0.81	**
Tillers per plant	8.56±0.25	13.11±4.08	**
Spikelets per spike	18.95±0.21	17.11±0.21	**
Grain yield per plant	11.31±0.40	8.15±0.39	**

** significant at 1% level



Table 2: Means for agronomic traits showing effect of allelic variation at *Xgwm261* locus in presence or absence of Norin-10 genes at Niphad location.

<i>Xgwm261</i> allele, Norin-10 gene	N	PHT	TLPLT ⁻¹	SPKLT	GNO SPK ⁻¹	GY PLT ⁻¹
165bp	41	80.87±1.72 ^a	8.20±0.33 ^{ab}	19.33±0.30 ^b	50.33±1.38 ^b	11.91±0.68 ^b
192bp	36	83.92±2.06 ^a	9.25±0.45 ^b	19.02±0.37 ^{ab}	49.43±1.57 ^{ab}	11.56±0.60 ^b
174bp	10	90.6±8.44 ^a	7.26±0.49 ^a	17.68±0.59 ^a	39.14±2.28 ^a	8.36±0.58 ^a
165bp, <i>RhtB1b</i>	15	80.33±1.18 ^a	8.71±0.57 ^a	19.45±0.41 ^a	52.73±2.17 ^a	12.47±1.01 ^a
192bp, <i>RhtB1b</i>	18	80.60±1.19 ^a	8.96±0.59 ^a	18.34±0.50 ^a	50.48±2.29 ^a	11.95±0.97 ^a
165bp, <i>RhtD1b</i>	20	77.40±1.85 ^a	8.0±0.49 ^a	19.09±0.46 ^a	49.33±1.94 ^a	11.55±1.07 ^a
192bp, <i>RhtD1b</i>	11	77.33±2.00 ^a	8.70±0.44 ^a	18.89±0.66 ^a	49.2±2.60 ^a	12.54±0.60 ^a
165bp, <i>RhtB1a, RhtD1a</i>	5	99.76±6.92 ^a	7.76±0.58 ^a	20.52±0.80 ^a	47.96±5.07 ^a	12.47±2.13 ^a
192bp, <i>RhtB1a, RhtD1a</i>	7	101.94±5.46 ^a	11.11±1.60 ^a	20.25±0.66 ^a	46.74±4.53 ^a	9.29±1.64 ^a
174bp, <i>RhtB1a, RhtD1a</i>	5	112.68±3.58 ^a	7.48±0.91 ^a	18.28±0.74 ^a	40.8±1.48 ^a	8.32±0.58 ^a

N: Number of varieties, PHT: Plant height, TLPLT: Tillers plant⁻¹, SPKLT: Spikelets spike⁻¹, GNO SPK⁻¹: Grain number spike⁻¹, GY PLT⁻¹: Grain yield plant⁻¹

Table 3: Means for agronomic traits showing effect of allelic variation at *Xgwm261* locus in presence or absence of Norin-10 genes at Trombay location

<i>Xgwm261</i> allele, Norin-10 gene	N	PHT	TLPLT ⁻¹	SPKLT	GNO SPK ⁻¹	GY PLT ⁻¹
165bp	41	60.0±1.32 ^a	14.84±0.62 ^b	17.90±0.31 ^c	37.32±1.15 ^b	10.21±0.60 ^b
192bp	36	57.44±1.99 ^a	11.28±0.58 ^a	16.82±0.32 ^b	33.2±1.35 ^a	6.56±0.50 ^a
174bp	10	57.27±5.19 ^a	11.6±0.95 ^a	15.04±0.57 ^a	31.02±1.24 ^a	6.10±0.57 ^a
165bp, <i>RhtB1b</i>	15	59.52±1.87 ^a	13.96±1.01 ^a	17.62±0.39 ^a	35.05±1.64 ^a	9.67±1.02 ^a
192bp, <i>RhtB1b</i>	18	54.48±2.64 ^a	11.98±0.95 ^a	16.6±0.57 ^a	31.7±2.53 ^a	6.82±0.92 ^a
165bp, <i>RhtD1b</i>	20	59.62±1.34 ^a	14.56±0.83 ^b	18.03±0.60 ^a	40.7±1.17 ^a	11.15±0.76 ^b
192bp, <i>RhtD1b</i>	11	53.54±1.79 ^a	10.28±0.84 ^a	16.89±0.52 ^a	36.43±1.56 ^a	7.18±0.69 ^a
165bp, <i>RhtB1a, RhtD1a</i>	5	70.08±4.44 ^a	17.12±2.67 ^a	18.16±0.67 ^b	32.88±4.27 ^{ba}	9.92±1.78 ^b
192bp, <i>RhtB1a, RhtD1a</i>	7	72.01±5.70 ^a	12.54±1.37 ^a	17.0±0.48 ^{ab}	27.66±2.98 ^a	4.61±0.98 ^a
174bp, <i>RhtB1a, RhtD1a</i>	5	72.08±1.71 ^a	13.44±1.14 ^a	15.68±1.68 ^a	31.44±2.07 ^a	7.13±0.85 ^{ab}

N: Number of varieties, PHT: Plant height, TLPLT: Tillers plant⁻¹, SPKLT: Spikelets spike⁻¹, GNO SPK⁻¹: Grain number spike⁻¹, GY PLT⁻¹: Grain yield plant⁻¹

zone and ancestors found in their pedigrees were different. There is a need to assess these new alleles, to ascertain their advantage under high temperature conditions.

Allele size and sequence determination

Sequencing of amplified products at *Xgwm261* locus (Fig. 1) revealed that 174bp and 165bp alleles contained (CT)₁₁AG and (CT)₆AG motifs, respectively as reported earlier (Liu et al. 2005). The genotypes C306 and PBW516

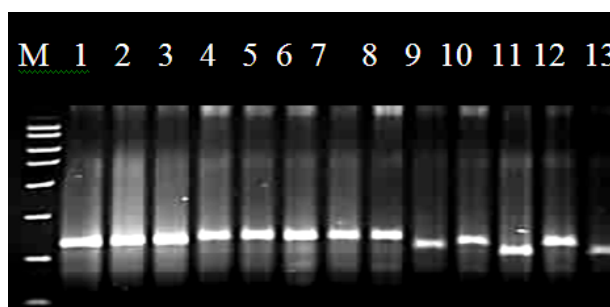


Fig. 1: Resolution of PCR products for sequencing.



showed 192bp allele with a sequence different from the previously known allele. The alignment of sequence with ClustalW indicated that the region after CT repeats is more liable to deletions or additions. A new allele (198bp) found in variety NI179 showed sequence (CT)₂₃GATATG. The alleles with higher molecular size of 198bp in NI179 and 200bp in NI5643, NI 747-19, NI5439 and HW2003 were observed in varieties recommended for warm areas. The allelic variability reported earlier (Liu et al. 2005) and in this study indicated that, this locus is variable and could have some adaptive value. Further investigation is needed to understand the effect of these alleles on plant height, yield and adaptation to high temperature stress. The varieties with 165bp allele were more frequent in the warmer zones and late sown conditions. The 165bp allele could be associated with advantage under heat stress conditions. With the predictions that wheat crop may face higher levels of heat stress, it would be important to incorporate known useful genes such as *Rht8*.

References

1. Ellis, M.H., Bonnett, D.G., Rebetzke, G.J. A 192bp allele at the *Xgwm261* locus is not always associated with *Rht8* dwarfing gene in wheat. *Euphytica* 157 (2007):209-214.
2. Ellis, M.H., Spielmeyer, W., Gale, K.R., Rebetzke, G.J., Richards, R.A. Perfect markers for the *RhtB1b* and *RhtD1b* dwarfing genes in wheat. *Theor. Appl. Genet.* 105 (2002):1038-42.
3. Liu, Y., Liu, D., Zhang, H., Wang, J., Sun, J., Guo, X. Allelic variation, sequence determination and microsatellite screening at the *Xgwm261* in Chinese hexaploid wheat (*Triticum aestivum*) varieties. *Euphytica* 145 (2005):103-12.
4. Worland, A.J., Law, C.N., Petrovic, S. Genetic analysis of chromosome 2D of wheat. II. The importance of this chromosome to Yugoslavian varieties. *Plant Breed.* 100 (1988):247-59.



Bull's Multirule Algorithm, (\bar{X}_M), An Excellent Means of Internal Quality Control for Hematology Analyzers

Shagufta. S, S.K.G. Shettigar, S. Gujral and R.K. Kulkarni

Medical Division, BARC

and

Manikchandra, T.

Tata Memorial Hospital, Mumbai

This paper received the Best Paper Award (II prize) at the All India Institute of Medical Technologists, 20th Congress of Biomedical Laboratory Science, held at Tiruchirapalli, Tamil Nadu, during December 18-19, 2010.

Abstract

Automated Hematology cell counters are extensively used in hematology laboratories and their functional accuracy is monitored using expensive commercial controls and retained specimens. In this present study we have tried to implement a computational method based on Bull's Multirule Algorithm (\bar{X}_M) along with the existing quality control method. The Algorithm works on the principle that mean of red cell indices - MCV, MCH, MCHC remain stable for any particular hospital population over a number of years. This mean can be used to check accuracy and calibration of the hematology analyzer. A batch of 20 blood samples is used to derive means of red cell indices and is compared to $\pm 3\%$ and $\pm 2\%$ action limits of the computed Bull's mean. The batch is re-analysed if it fails Bull's Multirule criteria; that is if (1) the mean is outside $\pm 3\%$ action limit (2) mean of three consecutive batches is outside $\pm 2\%$ action limit. In the current study we could identify calibration anomalies in the analyzer using this criteria in spite of following NABL and CAP recommendations on use of commercial controls. Thus we emphasize, that commercial controls within acceptable limits are not the surest way to know proper functioning of the analyzer and recommend \bar{X}_M should be incorporated in the daily quality control regimen

Introduction

The term quality control has been described, as a method of repeated assays of known standard materials and monitoring reaction parameters, to ensure precision and accuracy^[1] and taking necessary corrective measures to bring it in conformance with the specification.

Traditionally, quality control in hematology consisted of (1) analyzing stabilized control material with known manufacturer's means and limits, (2) between run controls - where recently analyzed patient samples were reanalyzed at designated time intervals and (3) Bull's moving average (\bar{X}_B), using patient data as a means of quality control^[2].

\bar{X}_B was first proposed by Dr Brian S Bull, Loma Linda University in 1974. It was subsequently refined by Korpman and Bull in 1976 known as Bull's Multirule Algorithm (\bar{X}_M), as a means of internal quality control using red cell indices - Mean Corpuscular Volume (MCV), Mean Corpuscular Hemoglobin (MCH) and Mean Corpuscular Hemoglobin Concentration (MCHC)^[2]. \bar{X}_B works on the principle that red cell indices are known to be stable blood parameters. Hence, the mean of red cell indices of a given patient population would not vary more than 0.5 % from day to day or year, to year provided the population does not change^[4]. Therefore, if the mean of



red cell indices is known, patient blood sample can be used to check calibration and drift of the hematology analyzer. The algorithm involved extensive calculation and hence was difficult for implementation, but in the later years its importance was established and \bar{x}_B was incorporated in the hematology analyzers, although publications on specific \bar{x}_M use in hematology analyzers are not readily available^[2]. The algorithm analyses the patient's red cell indices through instrument in batches of twenty. The mean of each batch is compared to Bull's mean and its action limits, i.e. the percent deviation of Bull's mean. The batch is rejected if either of the two Bull's Multirule criteria is satisfied (1) the mean of one of the batches is outside its $\pm 3\%$ action limit or (2) the mean of three consecutive batches is outside its $\pm 2\%$ action limit^[3]. The standard data established by Dr Bull obtained from 1,767 hospitals, yielded the following mean values MCV - 89.9 fl, MCH - 30.5 pg and MCHC- 33.9 g/dl^[4].

In the present study, similar attempts have been made to study Bull's Multirule Algorithm using patient's data from BARC hospital. The population taken for sampling purpose comprises of general Indian population of different ethnicities including men, women and children. This patient population would remain constant for a number of years since it involves people who are beneficiaries of the Contributory Health Service Scheme of Department of Atomic Energy.

Materials and Method

Patient's blood collected in EDTA vacutainers was processed on well calibrated five-part differential haematology cell counter, SYSMEX XS 1000i. Complete data of thousand patients was retrieved from the analyzer using Sysmex software^[5] and MCV, MCH and MCHC required for computing Bull's mean was exported to excel sheets. Standard deviation (SD) was calculated and $\pm 3SD$ limits were applied to the patient data and five percent grossly abnormal samples were rejected. Moving averages for forty seven batches, of twenty patients, each was obtained. $\pm 2\%$ and $\pm 3\%$ action limit was applied to Bull's mean, (\bar{x}_B) the weighted moving average of forty seven moving averages. Bull's mean, \bar{x}_M function in the analyzer was activated with this range. Thereafter the analyzer automatically plotted the Levy-Jennings (L-J) graph using MCV, MCH and MCHC data, obtained after processing the patient's sample. A single point on the graph corresponded to a batch of twenty processed patients' samples. The graph was studied prior to release of the reports for online viewing by the clinicians. Subsequently a graph with $\pm 3\%$ action limits as the criteria and also $\pm 2\%$ action limit was documented.

Observation and Results

As seen in Table 1, the computer simulation generated the above values for Bull's mean standard deviation and coefficient of variation and action limits of MCV, MCH, and MCHC. The graph so obtained from the analyzer

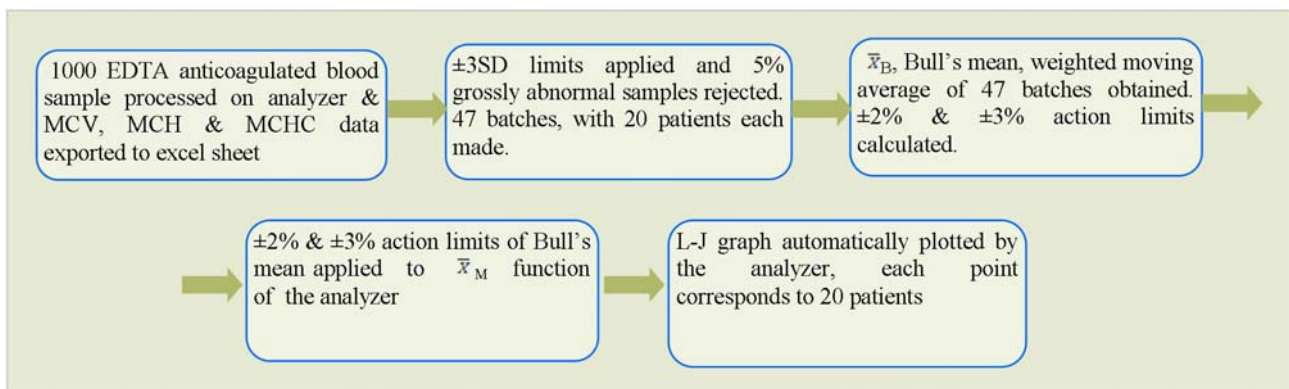


Fig. 1: Flow chart depicting the method for computing Bull's mean



Table 1: Table showing the Bull's mean for MCV, MCH and MCHC along with std.dev, coefficient of variation and action limit.

	MCV	MCH	MCHC
Bull's Mean	84.1(fl)	27.8 (pg)	33.1(g/dl)
Std. Dev.	0.4	0.1	0.1
CV %	0.4	0.5	0.3
3% Action limit	81.6-86.6	27.0-28.6	32.1-34.1
2% Action limit	82.4-85.8	27.2-28.4	32.5-33.7

using $\pm 2\%$ and $\pm 3\%$ action limits was well within the range. MCHC being the most stable parameter, followed a straight line graph whereas MCV and MCH were found to be scattered around the mean. A graph using the above data was also plotted manually with the help of Excel sheets and was found to be comparable with the analyzer graph. This further indicated the accuracy and proper functioning of the analyzer.

It was further observed that the standard data for MCV, MCH and MCHC obtained by Dr Bull was not in agreement with our data, which could be probably due to lower hemoglobin standards in Indian population. A study comprising data of 1000 patients was also done, to find out the MCV, MCH and MCHC values of the same population in three different seasons of the year. First thousand patient's data processed on well calibrated 3-part differential hematology analyzer Sysmex - KX 21 was retrieved from our data base and Bull's mean for each season was computed, the results of which are as shown in Table 2. Hence it should be noted that although there were variations between the data obtained in the present

study and those obtained by Dr Bull, the data obeyed Bull's Multirule Algorithm and hence was acceptable.

The graph shown below indicates the points plotted by the analyzer. Graph 1 has $\pm 3\%$ as its action limit and graph 2 has $\pm 2\%$ as its action limit. It is seen from the graph, that the MCHC plot followed a straight line graph whereas MCV and MCH were scattered around the mean. It is also seen, at some point during the analysis, the graph showed a sudden drift, even though two of the three QC samples analyzed after the start up procedure were within acceptable limits. According to NABL and CAP standards^[6], if two out of three QC samples are within acceptable limits, the analysis can be continued. Defective QC material was thought to be the reason for the failure of one of the QC. Continuation of the drift in the graph prompted the fact that the analyzer has gone out of calibration, since more than three points in the graph were out of $\pm 2\%$ limits satisfying second rule of Bull's Multirule for rejection. To confirm the calibration failure, a comparative study was done using our 3 part differential cell counter SYSMEX KX 21 and similar analyzer SYSMEX

Table 2: Bull's mean of first 1000 samples for 3 seasons with respect to Bull's mean from our study and Dr. Bull's standard mean

	October '09	January '10	July '10	Bull's Mean	Bull's Standard Data
MCV (fl)	84.8	84.0	84.6	84.1	89.9
MCH (pg)	29.3	28.8	27.3	27.8	30.5
MCHC (g/dl)	34.6	34.1	32.7	33.1	33.9



XS 1000i from another hospital. The results confirmed that our 5-part differential analyzer needed recalibration. It should be emphasized here that it was only because of the \bar{X}_M that malfunctioning of the analyzer was detected whereas the commercial QC failed to explain the reason for the drift. Thus, it is of utmost importance that the \bar{X}_M be incorporated along with the QC practices and monitored intermittently for any drifts in the \bar{X}_M graph. The analyzer was monitored post calibration and Bull's mean for the next 400 samples was computed and was found comparable with the results before the analyzer went out of calibration, as seen in Table 3.

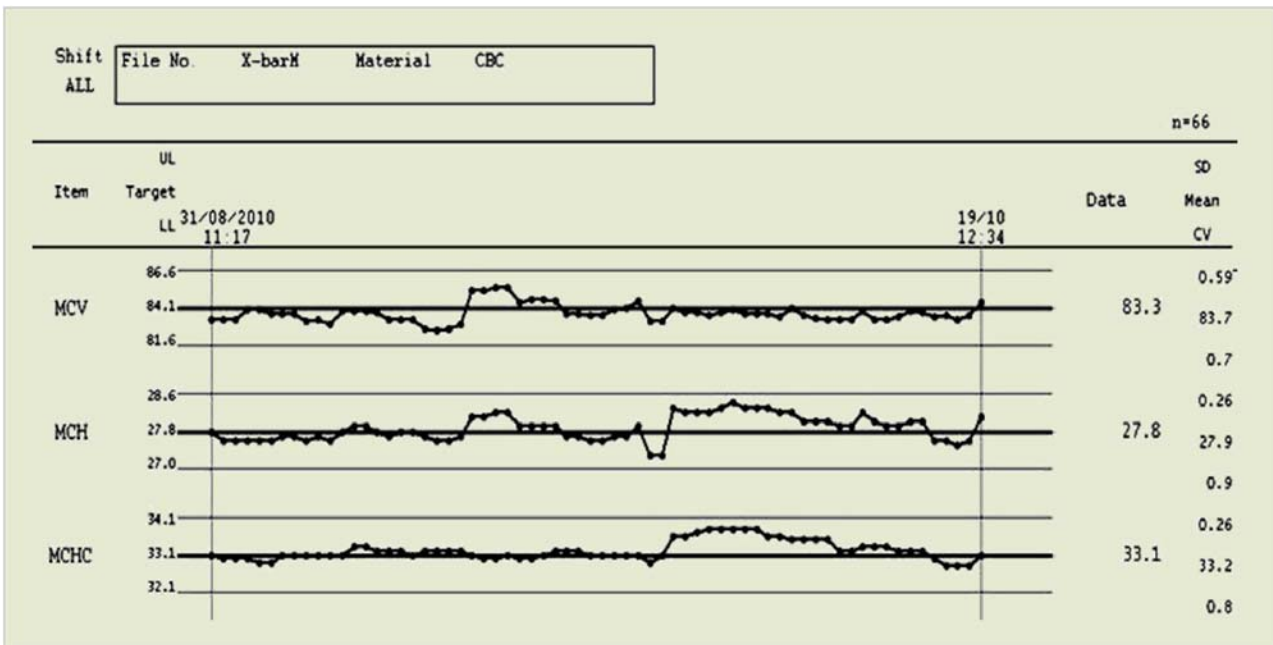
Table 3: Comparison of Bull's mean before the calibration error and after the recalibration of analyzer

	Bull's Mean before calibration error	Bull's Mean after calibration
MCV (fl)	84.1	83.7
MCH (pg)	27.8	27.8
MCHC(g/dl)	33.1	33.2

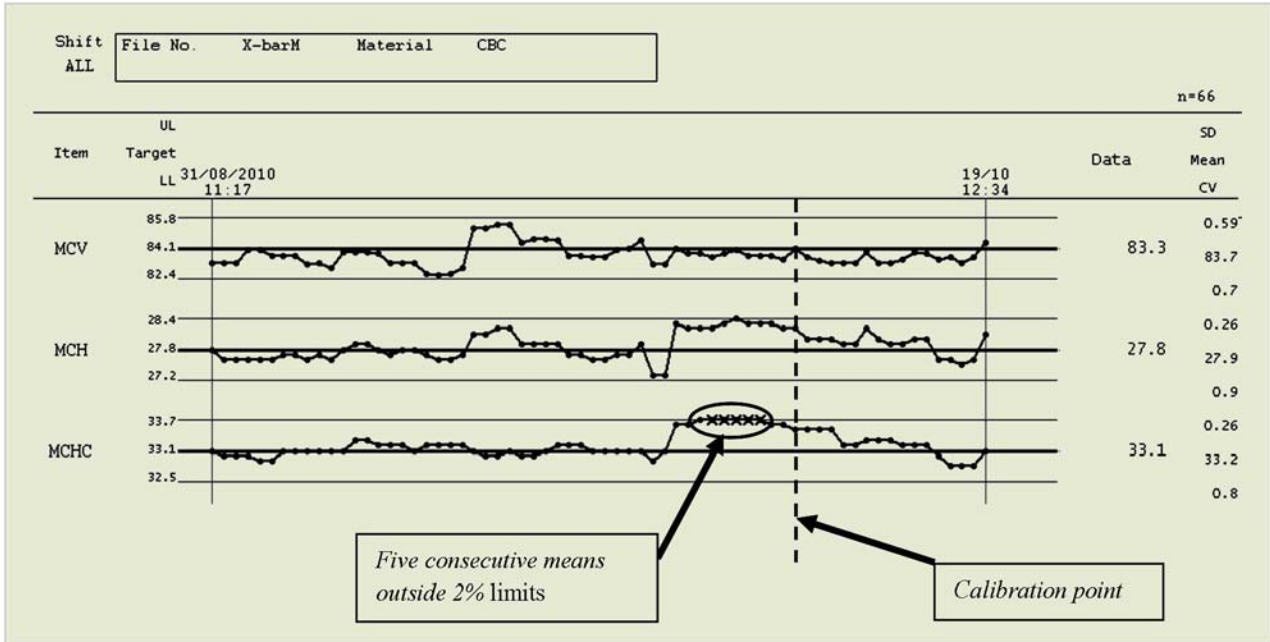
Conclusion and Discussion

- It was observed from the present investigation, that the Bull's mean obtained by Indian standards could not match those of international standards laid down by Dr Brian Bull owing to probable low hemoglobin standards. Hence, it is imperative for every laboratory to develop one's own standard mean using one's own patient population, as population variation is an important criterion to be considered while computing standard means.
- It is surprising to find that even though the analyzer went out of calibration at some point of time, two of the three QC values obtained, remained well within acceptable limits. However, the problem with the analyzer could be detected only with the drift in the \bar{X}_M graph and further action with regard to corrective measures were taken and the analyzer was recalibrated. Hence, it is of utmost importance to incorporate the use of \bar{X}_M function in the Quality control regimen, even if commercial controls and

Merit Award



Graph 1: Levy-Jennings chart output from Sysmex XS1000i with 3% action limit (UL = Upper limit, LL = Lower limit, Target – Bull's mean, SD = Std. Dev, CV = Coeff. Var)



Graph 2: Levy-Jennings chart output from Sysmex XS1000i with 2% action limit applied(UL= Upper limit, LL =Lower limit, Target – Bull's mean, SD= Std. Dev, CV = Coeff. Var)

retained specimen are already a part of it. Moreover it also permits quality control of the analyzer during the interval when control materials are not being analyzed.

- The use of \bar{X}_M is advocated for the reason that in the current environment of cost restriction, multiple repeats of the commercial control can be avoided.
- It was also observed that multiple repeats of the same abnormal sample within a given batch may also cause a non random population in that batch and a shift in result. Such shifts are usually corrected in the next batch of 20 when random analysis is made.
- Shift in the results is also observed in the cases, when a batch has predominance of a particular type of patient like from the oncology, paediatric or the dialysis unit.
- Change of reagents and their lot number also hold important significance as they too could be the reason for the shift in analyzer.

- A minimum of sixty specimens per day must be processed to yield 50% probability of detecting a 3SD shift^[7].

References

1. Moby's medical dictionary, 8th edition, 2009.
2. Beckman Coulter, Bulletin 9611, XM - Exponentially Weighted Moving Average.
3. Lunetzky ES, Cembrowski G. S., Performance characteristics of Bull's Multirule Algorithm for quality control of multichannel hematology analyzers, *Am J Clin Pathol.* Nov 88(5): 1987: 634-8.
4. Cell Dyn 3500, System Operators Manual; February 1996.
5. Sysmex XS-1000i Instruction Manual, May 2008.
6. Hematology - coagulation checklist ©2007. College of American Pathologists.
7. George, S Cembrowski; Quality Control in U.S. and Canadian Hematology Laboratories.



Carbondioxide Emissions and Alternative Electricity Generation Options

I.V. Saradhi, G.G. Pandit and V.D. Puranik
Environmental Assessment Division

This paper received the Best Poster Presentation Award (II prize), at the Workshop cum Seventeenth National Symposium on Environment (NSE-17), held at Indian Institute of Technology, Kanpur, during May 13-15, 2010

Abstract

Increasing concerns over climate change have limited the liberal usage of available energy technology options. The objective of the study, is to estimate the carbondioxide emissions from Indian electricity sector, for the projected future demand under different scenarios. The study has been carried out using MESSAGE model which evaluates the alternative energy supply strategies, with the user defined constraints on fuel availability, environmental regulations etc. The model predicted a share of 85 % - Thermal, 8 % - Hydro, 3.5 % - Nuclear and 3.5 % - Renewables in the base line scenario at the end of study period i.e 2035. In baseline scenario, the annual carbondioxide emissions during 2030 are about 2,300 million tones of CO₂ and with the use of high nuclear capacity and high renewables, the emissions reduced to 1800 million tonnes. In the scenario of high nuclear capacity, the carbondioxide emissions are reduced by 10 % when nuclear energy share increased to 9% from 3% in baseline scenario. Similarly, aggressive use of renewables reduces 4% of carbondioxide emissions.

Introduction

India, the largest democracy with an estimated population of about 1.05 billion, is on the road to rapid economic growth. Policy initiatives of the Government of India during the past decade, have resulted in a faster growth of GDP and forecasts by several agencies point towards continued growth of the India economy over the next the 30 to 40 years. Energy is a vital input into production and if India is to move with higher growth rate that is now feasible, reliable supply of energy, particularly electric power and petroleum products, at internationally competitive prices is needed. It is a matter of concern, that the annual per capita consumption of electricity in India, at about 750 kWh¹ (including captive power generation) is among the lowest in the world. Further, people in a large number of villages have no access to electricity.

Environmental concerns are associated with all forms of energy, including fossil fuels, nuclear energy, renewables

throughout the chain from their exploration/mining, transportation and generation to the end-use. Studies on global climate change carried out under Inter-governmental Panel on Climate Change indicate, that global warming due to increase in carbon dioxide levels as a result of human activities, is a fact of life. To address these issues in an integrated manner, a study has been carried out, wherein India's energy demand growth rates, electricity in particular, are reviewed and strategies to meet the projected demand have been chalked out under different scenarios.

Study of Indian Electricity Sector

To study the various technology options available for meeting the electricity demand in future upto 2030, an optimized energy system is developed for the given supplies and utilization requirements, using the software



MESSAGE² (Model for Energy Supply Strategy Alternatives and their General Environmental Impacts). In this model, the whole electricity supply system is represented as an oriented network of technologies and activities, starting from extraction or supply of primary energy, passing through energy conversion processes (e.g. electricity generation), to transmission and distribution, to meet the given demand for final energy in the industry, transportation, household and service sectors. Technologies are represented by a set of parameters such as investment costs, fixed and variable costs, energy conversion efficiencies, historical capacities, availability factors, emission factors and others. As a result of optimization using the MESSAGE model, a least-cost mix of energy supply technologies can be found for each scenario. In the present study, the projected future demands of the final electricity consumption by different categories, are studied under various scenarios. The growth rates of electricity considered for the present study is 1.063 per annum, upto 2025 and 1.049 from 2025 to 2030³ for business-as-usual scenario.

Scenario Development

Scenarios provide framework for exploring future energy perspectives, including various combinations of technology options and their implications. Five scenarios reflecting the varying technological progress have been developed, in the current study. The scenarios are briefly discussed below.

- a) *Business-as-usual scenario* : This scenario is characterized by the most likely path of development in the absence of any major intervention. This scenario incorporates existing government plans and policies. In this scenario, 8 % growth rate of GDP is considered over entire modeling framework. Deployment of clean technologies and penetration of technologies are assumed as per the existing trends and proposed projects for nuclear and renewables. The nuclear energy based power generation capacity is assumed to the extent of 20 GW and renewables upto 45 GW.
- b) *High nuclear scenario* : In this scenario, nuclear based power generation is expected to increase to 6.8 GW by 2012 and further to 14 GW by 2017, 55 GW by 2027 and 63 GW by 2032. The high nuclear energy based power generation has been assumed, in view of the latest development in the nuclear sector, due to enhanced international cooperation and Government of India's initiative in this direction. This scenario considers aggressive pursuit of nuclear energy based power generation, driven by the assumption that the country is able to import fuel.
- c) *Aggressive renewables scenario* : In this scenario, high penetration of renewable energy is considered. The lower bound of installed capacities considered by 2035 for 45 GW, 10 GW, 8 GW and 8 GW for wind, small hydro, solar and biomass respectively. The maximum capacities considered in the study are the expected potentials of these technologies.
- d) *Hybrid scenario* : In this scenario, both nuclear and renewable energy technologies are included aggressively becoming a combination of baseline scenario with high nuclear and aggressive renewables.
- e) *CO₂ limit scenario* : In this scenario, limitations are incorporated under each scenario and on CO₂ emissions the share of energy technologies are studied.

Results and Discussion

Business-as-usual Scenario

The total electricity consumption increased by 6.2 times during the study period in Business-as-usual scenario. Fig.1 shows the variation in percentage share of commercial fuels over the modeling time frame. At the end of the study period, the percentage share of coal, gas, oil, hydro, nuclear and wind are 62, 19, 4, 8, 3 and 4 respectively. The share of power technologies in future from 2005 to 2030 for the business-as-usual scenario is presented in Fig. 2. Coal remains the dominant fuel during the entire study period. Gas-based power generation is the next major contributor. This is in line with the policies of Government, to increase the share of gas based power generation by



increasing the resource extraction as well as the imports. Contribution from the nuclear-based power generation is becoming increasingly significant towards the end of the study period, without any special intervention. The contribution of hydro power steadily decreased to 8% during the study period. The contribution of wind power technology also significantly increased during the study period in this scenario, up to a maximum potential of 45 GW as it is available at competitive price. Although coal remains the dominant fuel during the study period, with limited domestic production capacity, the import dependence of coal were found to be much higher in 2030. Similarly, dependence on gas is also significant. The contributions from oil is forcibly limited in the study as the same will be utilized in other commercial energy sectors like transport industry. The model also indicates that hydro power is utilized upto the maximum potential of 84 GW.

Inter-scenario comparison

Different scenarios have been developed, using business-as-usual scenario as the base study. In high nuclear scenario, the share of nuclear increased to 9 % reducing the share of coal to 56 %. Under this scenario it is assumed, that 63 GW of nuclear power plants will be constructed in the wake of nuclear deal with many countries, for supply of fuel and technology. In high renewables scenario, the share of renewables increased

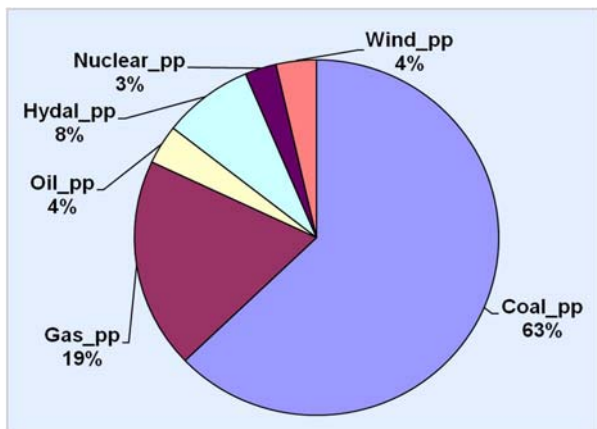


Fig. 1: Percent contribution of different technologies in Business-as-usual Scenario (2030)

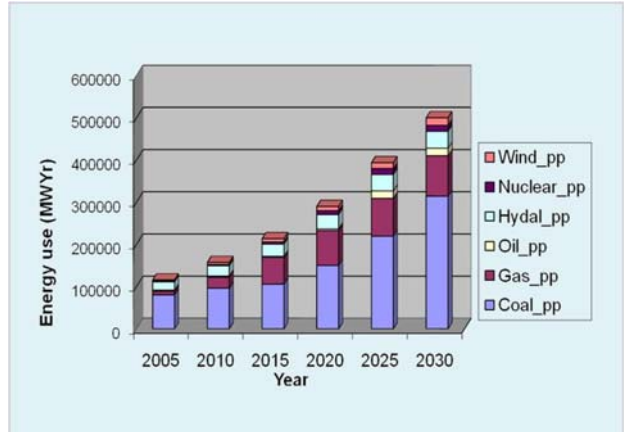


Fig. 2: Commercial Energy use in Business-as-usual Scenario (2005-2050)

from 4 % to 7% reducing the share of coal. Under this scenario the use of biomass, solar and small hydro projects are considered to their maximum potential. To examine the aggressive use of both nuclear and renewables technology a hybrid scenario is developed, wherein about 16 % of the power generation is contributed by nuclear and renewable technologies and the coal share is reduced to 54 %.

Carbondioxide emissions

To study the extent of reduction in CO₂ emissions by the use of cleaner technologies under different scenarios, the emissions from each technology are incorporated in the MESSAGE model as constraints and the total emissions are quantified based on the amount of the particular technology used during the study period. Fig. 3 shows the carbondioxide emissions for the study period from 2005 to 2030. for Business-as-usual Scenario Carbondioxide emissions from power generation steadily

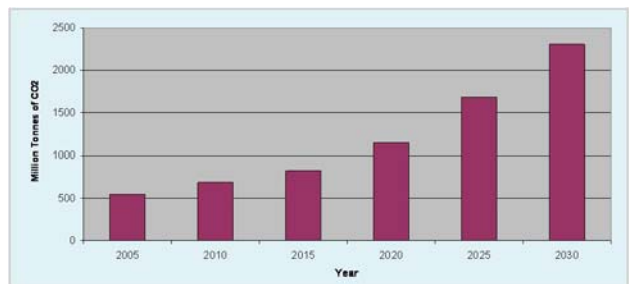


Fig. 3: CO₂ Emissions in Business-as-usual Scenario (2005-2030)



increased from 548 million tons in 2005 to 2305 million tons in 2030. These emissions are significant and difficult to meet, if restrictions on the carbondioxide emissions are imposed on India in future.

Additionally an attempt has been made to introduce limitations on the emissions of carbondioxide under each scenario and study the variations in the share of energy technologies. For this study the lowest possible CO₂ emissions under each scenario has been estimated. It is the level in each scenario below which, the model cannot generate a feasible solution for the given input data. The lowest possible CO₂ emission limit in 2030 under each scenario, is presented in the Table 1, As shown in the table, the lowest possible limit is 1800 million tons for the hybrid scenario. This gives an indication, that by adopting both nuclear and renewable technologies aggressively, it is possible to reduce around 500 million

3) Most importantly even after the use of hybrid scenario the reduction in carbondioxide emissions are only seen after 2025. This indicates the need for deployment of these technologies as early as possible.

References

1. TEDDY, TERI Energy Data Directory and Yearbook, 2004/2005, The Energy and Resources Institute, New Delhi (2006).
2. MESSAGE, Model of Energy Supply Strategy Alternatives and their General Environmental Impacts, User Manual, International Atomic Energy Agency (2003).
3. Grover and Subhash Chandra, A Strategy for Growth of Electrical Energy in India, Document No.10 (2004).

Table 1: Lowest possible limit on Carbondioxide emissions for different scenarios (Year - 2030)

Scenario	CO ₂ emissions (million tons)
Business-as-usual	2100
High Nuclear	1900
High Renewables	2000
Hybrid	1800

tons of CO₂ emissions as compared to that of the business-as-usual scenario.

The observations made in the study are

- 1) Coal remains the dominant fuel for production of electricity during the study period. However, the import dependency of coal increases.
- 2) Introduction of high nuclear capacity and renewables replaces coal to some extent and also contributes to 9 % and 4 % reduction in carbondioxide emissions respectively.



Chemical stability and proton conductivity of $\text{BaCe}_{0.8}\text{Y}_{0.2}\text{O}_{3-\delta}$

Pooja Sawant, A.N. Shirsat, S. Varma,
B.N. Wani and S.R. Bharadwaj
Chemistry Division

This paper received the Best Poster Award (III prize) at the 17th DAE-BRNS National Symposium and Workshop on Thermal Analysis (THERMANS 2010), held at Kurukshetra, Haryana, India, during March 9-11, 2010

Abstract

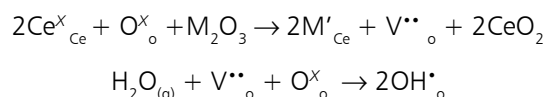
Rare earth doped barium cerate (BaCeO_3) is used as an electrolyte for proton conducting Solid Oxide Fuel Cell. Yttrium doped BaCeO_3 was prepared by solid state route and its chemical stability in different atmospheres was evaluated. In the presence of H_2O and CO_2 atmosphere, formation of byproducts like $\text{Ba}(\text{OH})_2$, BaCO_3 , CeO_2 was observed above 450°C . Proton conductivity was measured at different temperatures up to 500°C in moist N_2 atmosphere. Since, higher conductivity was observed in moist atmosphere, conduction can be attributed to the protonic species. Activation energy for proton conduction was also calculated.

Introduction

Solid oxide fuel cells (SOFCs) have presently become a promising system for generation of electric power due to their high conversion efficiency, the possibility of internal fuel reform, and their low pollutant emission. In 1980s Iwahara et al. [1,2] found several perovskite-type oxides exhibiting high proton conductivity at temperatures above 450°C . Perovskite materials such as BaCeO_3 or SrCeO_3 are considered the best candidates as electrolytes in SOFCs, because they possess high proton conductivity. Therefore, they have been considered as promising materials as electrolytes of SOFCs requiring direct energy conversion. They are mostly studied as electrolyte material in the fuel cells, hydrogen pumps, gas sensors, tritium technology and as reactor material for synthesis of ammonia at atmospheric pressure [3,4].

Among these electrolytes, Y doped BaCeO_3 oxides have been extensively studied, because of their excellent proton

conducting property at intermediate temperature [5,6]. Barium cerate has a perovskite-type structure, in which substitutions of Ce^{4+} by Y^{3+} cause the formation of oxygen vacancies. Proton conductivity of these electrolytes is dependent on the concentration of oxygen vacancies in the perovskite oxides. Kroger-Vink notation of incorporation of trivalent dopants and subsequent incorporation of water/protons can be described as



Water from the gas-phase dissociates into a hydroxide ion and a proton, where oxygen vacancies are replaced by hydroxide ions, protons form a covalent bond with lattice oxygen. This mechanism was proposed by H. Iwahara et al. [7] for proton conduction in perovskite oxides and is called "Hopping mechanism for migration of proton from one oxygen ion to another".



Although, Y doped barium cerate has been probed as a potential solid electrolyte material for applications to various ionic devices, its practical suitability has been hampered due to its chemical and structural instability in the presence of moisture (a common by-product in fuel cells that utilize hydrogen and hydrocarbons as fuels), and carbon dioxide (produced from oxidation of hydrocarbon fuels) at elevated temperatures [8]. In this work, we are reporting thermal as well as chemical stability of $\text{BaCe}_{0.8}\text{Y}_{0.2}\text{O}_{3-\delta}$ (BCYO) in different atmospheres.

Experimental

BaCeO_3 (BCO) and $\text{BaCe}_{0.8}\text{Y}_{0.2}\text{O}_{3-\delta}$ (BCYO) samples were prepared by a conventional solid-state reaction route, in air using stoichiometric amounts of BaCO_3 , CeO_2 and Y_2O_3 . The mixture was calcined in three steps: i) powder heated at 900°C for 2 days ii) pelletized and heated at 1200°C for 24 h and iii) the final sintering of the pellets was carried out at 1400°C for 10 h. The phase characterization was carried out using Philips diffractometer (PW 1729) with Ni filtered $\text{CuK}\alpha$ radiation and using silicon as external standard.

Stability of BCO and BCYO was studied, using thermogravimetry (TG) technique in CO_2 atmosphere. TG run was recorded in flowing CO_2 atmosphere up to 900°C at a scan rate of $10^\circ/\text{min}$ using the SETARAM

simultaneous TG/DTA instrument (Model 92-16.18). The residue was cooled to room temperature under flowing CO_2 atmosphere and it was characterized by XRD. Chemical stability in moist atmosphere as well as in boiling water was studied. Few milligrams of BCO and BCYO samples were exposed to water vapour for 2 h and separate sample of each was heated in boiling water for 2 h. Sample was removed, dried at room temperature and XRD pattern was recorded.

Proton conductivity measurements of BCO and BCYO pellet (sintered at 1400°C for 10 h in ambient atmosphere) was performed in moist nitrogen gas flow, using Pt-electrodes and employing AC impedance and gain phase analyser spectrometer (Solartron 1260) in the frequency range 0.1 Hz – 10 MHz. The applied ac voltage was 100 mV. Before each conductivity measurement, the sample was equilibrated at constant temperature for 30 mins.

Results and Discussion

To delineate the path of reaction, XRD powder pattern of BCO and BCYO mixture, heated at different temperatures, was recorded (Fig. 1 a,b). It was observed that pure phase could be obtained only after heating at 1200°C . The diffraction pattern shown in Fig. 1b corresponds to cubic structure with lattice constant $a_0 = 4.3968 \pm 0.001 \text{ \AA}$ and

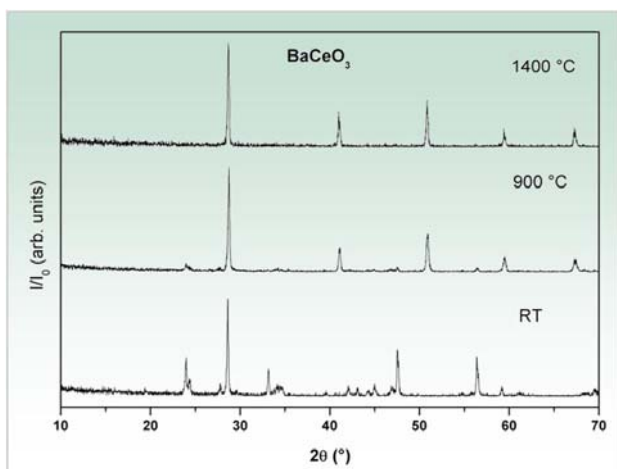


Fig. 1a: XRD pattern of BCO during calcination.

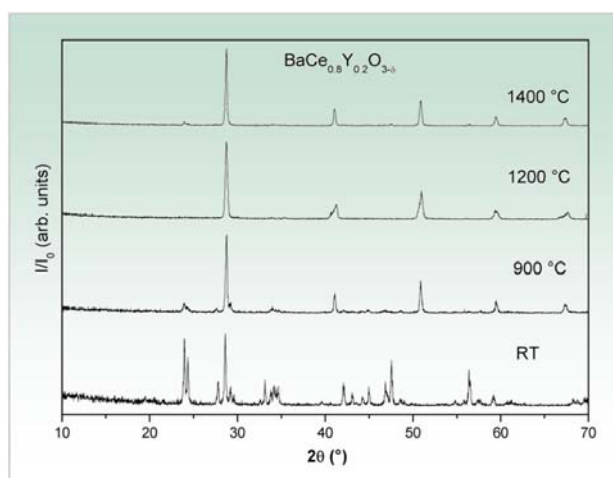
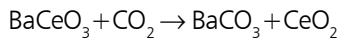


Fig. 1b: XRD pattern of BCYO during calcination.



cell volume = $58 \pm 1 \text{ \AA}^3$ which also agrees with the $(\text{BaCe}_{0.9}\text{Y}_{0.1}\text{O}_{2.95})$ JCPDS 82-2372.

TG scan of BCO as well as BCYO powders heated in flowing CO_2 atmosphere is shown in Fig. 2. It showed a weight gain above $\sim 450 \text{ }^\circ\text{C}$ and it continued up to $900 \text{ }^\circ\text{C}$ due to the following reaction,



When heated under identical experimental conditions, BaCeO_3 absorbs more CO_2 as compared to BCYO, indicating that BCYO is more stable as compared to BaCeO_3 . XRD pattern of the residue showed complex diffraction pattern, which is due to BaCO_3 and fluorite-like structure of CeO_2

as major phases along with BCYO as residual impurity (Fig. 3). Also, the characteristic diffraction peaks attributable to the formation of Y_2O_3 are absent in the decomposition products.

As these materials are known to be good proton conductors, stability of BCO and BCYO was studied in moist atmosphere as well as in boiling water. XRD pattern of moisture treated samples are shown in Fig. 4 a and b. In the presence of water, the following reaction is favored at low temperatures.

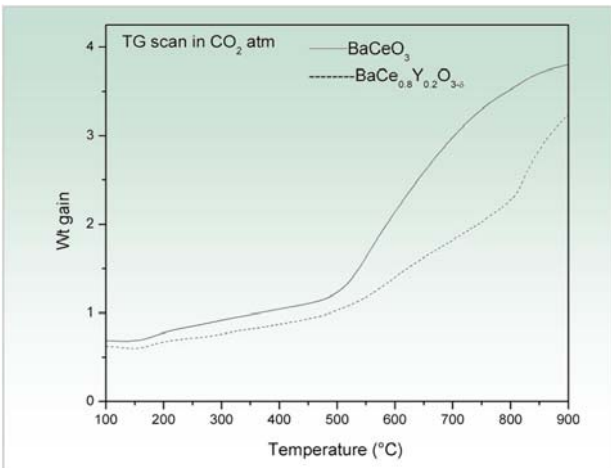
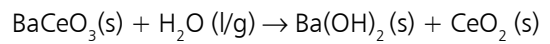


Fig. 2: TG plot of BaCeO_3 and BCYO in CO_2 atmosphere.

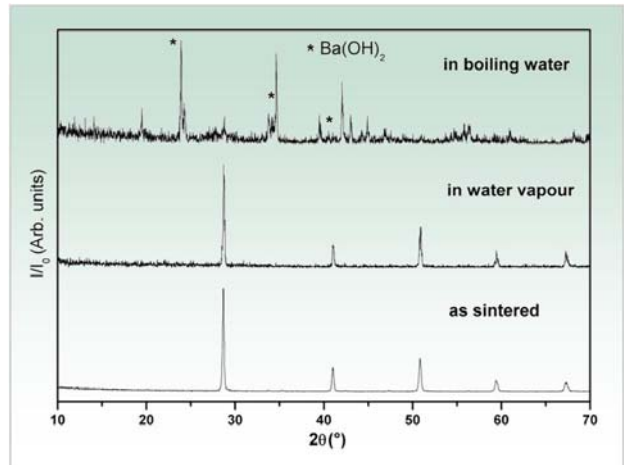


Fig. 4a: XRD Pattern of BCO after exposure to water for 2 h.

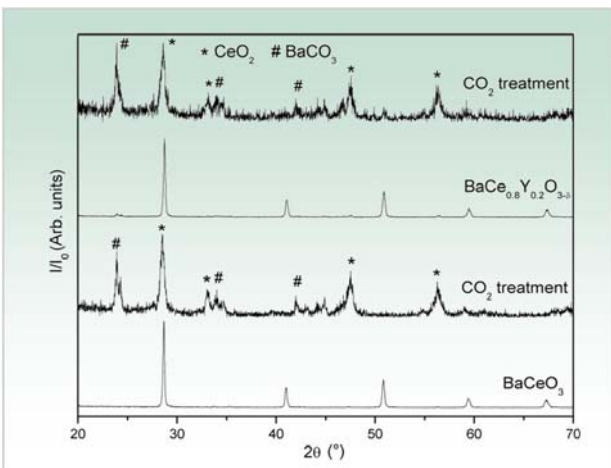


Fig. 3: XRD pattern of BaCeO_3 and BCYO, before and after CO_2 exposure.

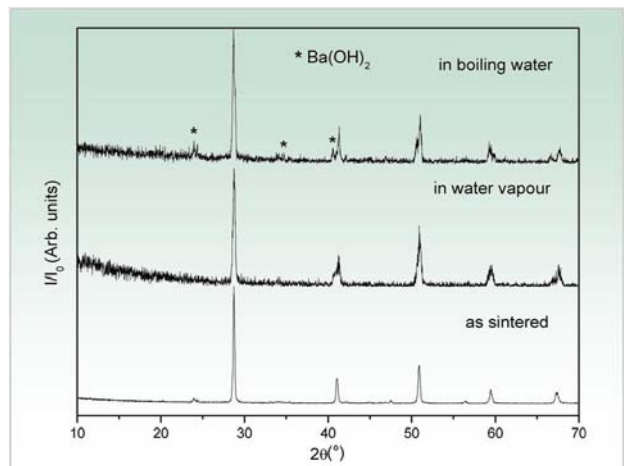


Fig. 4b: XRD Pattern of BCYO after exposure to water for 2 h.



Generally ceria-based compounds were found to conduct protons as well as oxygen ions and in reduced state they also conduct electrons. But in a humidified atmosphere at low temperatures, these compounds predominantly conduct protons. Representative Nyquist plots at 673 K for BCO and BCYO and equivalent circuit employed for its analysis, are shown in Fig. 5. The conductivity of undoped $BaCeO_3$ and $BaCe_{0.8}Y_{0.2}O_{3-\delta}$ as a function of temperature is shown in Fig. 6. It is found that protonic conductivity of Y doped $BaCeO_3$ is higher than undoped $BaCeO_3$ in the moist nitrogen. The conductivity increases under wet N_2 flow due to the increase in activated hydroxyl ion sites as generated in the presence of moisture. The

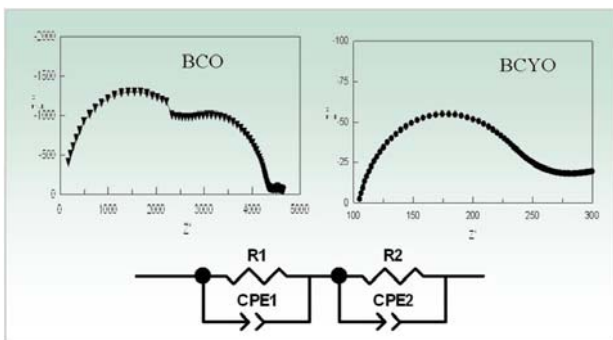


Fig. 5: Representative Nyquist plot at 673 K for BCO and BCYO and equivalent circuit employed for its analysis.

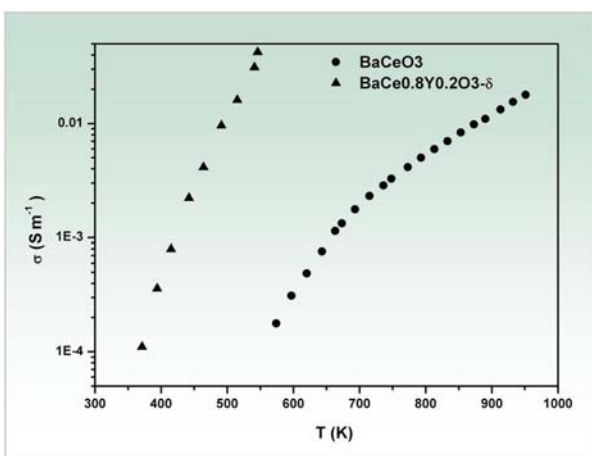


Fig. 6: Conductivity measurement of BCO & BCY sample using AC-impedance.

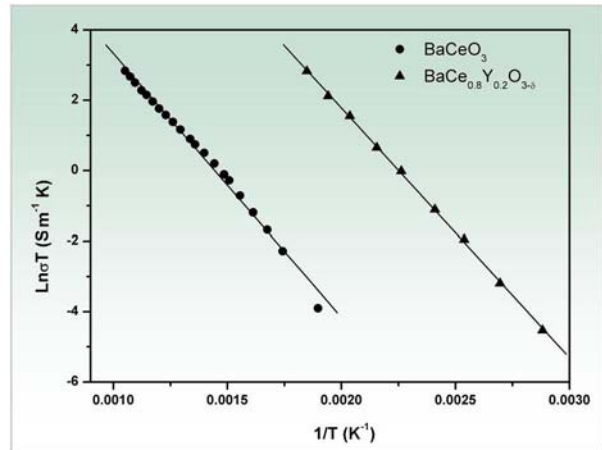


Fig. 7: Arrhenius plot of $\ln(\sigma T)$ against $1/T$ for BCO and BCY under Wet N_2 flow.

activation energies for proton conduction were found to be 0.64 eV and 0.61 eV for $BaCeO_3$ and $BaCe_{0.8}Y_{0.2}O_{3-\delta}$ respectively in moist atmosphere. (Fig. 7).

Conclusions

$BaCeO_3$ and $BaCe_{0.8}Y_{0.2}O_{3-\delta}$ powders were prepared by ceramic route. $BaCe_{0.8}Y_{0.2}O_{3-\delta}$ displays better chemical stability against CO_2 and H_2O as compared to pure $BaCeO_3$. Also, $BaCe_{0.8}Y_{0.2}O_{3-\delta}$ shows better proton conduction and less activation energy in humid atmosphere as compared to undoped $BaCeO_3$.

References

1. Iwahara H., Uchida H., Tanaka S.. High temperature type proton conductor based on $SrCeO_3$ and its application to solid electrolyte fuel cells. *Solid State Ionics* 9-10 (1983): 1021-25.
2. Iwahara H., Uchida H., Ono K. and Ogaki K.. Proton conductors in sintered oxides based on $BaCeO_3$, *J. Electrochem. Soc.* 135 (1988): 529-33.
3. Iwahara H., Asakurab Y., Katahirac K., Tanakad M.. Prospect of hydrogen technology using proton-conducting ceramics. *Solid State Ionics* 168 (2004): 299-310.



4. Schober T. Applications of oxidic high-temperature proton conductors. *Solid State Ionics* 162/163 (2003): 277-81.
5. Grover W. and Readey D.. Proton Conductivity Measurements in Yttrium Barium Cerate by Impedance Spectroscopy. *J. Am. Ceram. Soc.* 85 [11] (2002): 2637-40.
6. Longo A., Giannici F., Balerna A., Ingrao C., Deganello F., Martorana A.. Local Environment of Yttrium in Y-Doped Barium Cerate Compounds. *Chem.Mater.* 18 (2006): 5782-88.
7. Iwahara H.. Proton conducting ceramics and their applications. *Solid State Ionics* 86-88 (1996): 9-15.
8. Scholten M., Schoonman J., Miltenburg J., Oonk H.. Synthesis of strontium and barium cerate and their reaction with carbon dioxide. *Solid State Ionics* 61 (1993): 83-91.



Coherent Laser-Atom Interaction and its Application to Atomic Frequency Offset Locking

Y. B. Kale

Laser & Plasma Technology Division

and

Ayan Ray

Laser & Plasma Technology Division

and

B. N. Jagatap

Atomic & Molecular Physics Division

This Paper received Best the Poster Award, at the Topical Conference on Atomic and Molecular Physics (TC-2010), held at the Raja Ramanna Centre for Advanced Technology, Indore from 3-6 March, 2010

Abstract

We present here, the development and demonstration of a novel technique of atomic frequency offset locking, based on Electromagnetically Induced Transparency (EIT) resonance of sub-natural linewidth. Frequency stability of the lock is studied, in terms of Allan variance $s(2, t)$. It is found that the frequency stability of the EIT stabilized probe is superior ($s \sim 10^{-13}$) to that of the pump ($s \sim 10^{-12}$) stabilized on saturated absorption signal. This observation is in contradistinction with the conventional master-slave offset locking scheme and is in tune with the non-absorptive nature of EIT resonance, arising from the quantum interference in coherent laser-atom interaction.

Introduction

Electromagnetically Induced Transparency (EIT) refers to the phenomenon of rendering an otherwise opaque medium, transparent to a narrow band of light frequencies. Physics underlying this phenomenon and its use as atomic frequency standard has been discussed extensively in literature^{1,2}. An ultra-narrow linewidth of the EIT signal may be considered as a narrow band frequency filter, since it is associated with a sharp change in dispersion of the medium. It therefore can be used as a frequency reference for offset locking, where the offset is precisely equal to the known energy gap between two atomic levels. In this paper, we describe development and

demonstration of an Atomic Frequency Offset Locking (AOFL) scheme, using a sub-natural EIT resonance obtained using a three-level Λ system in the D_2 transition of Cs. The frequency offset here, corresponds to the frequency separation between the ground hyperfine transitions of Cs, i.e., the atomic clock transition.

Level scheme and Experimental Arrangement

Three-level scheme used in our experiments, is shown schematically in Fig. 1. Here ω , Ω and Δ are respectively the laser frequency, Rabi frequency and detuning, and the subscripts 'pu' and 'pr' denote the pump and probe lasers. In this configuration, the pump laser dresses the



transition $F=4 \rightarrow F'=3$ while the probe laser is scanned across $F=3 \rightarrow F'=3$ transition to generate an EIT signal.

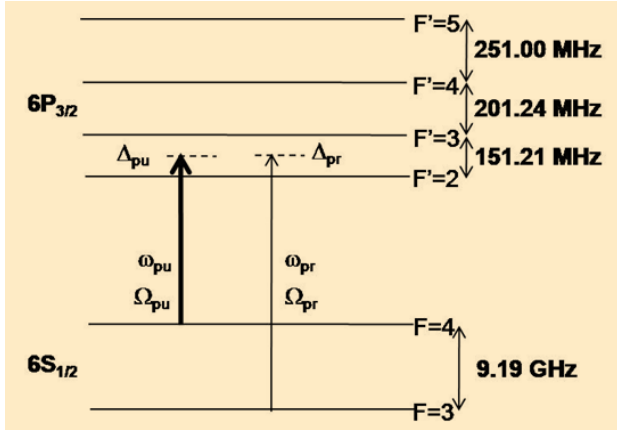


Fig. 1: Energy levels relevant for the experiments. Vertical arrows denote pump (thick arrow) and probe (thin arrow) lasers respectively.

The schematic representation of the experimental scheme is given in Fig. 2. Here ECDL1 and ECDL2 are tunable diode lasers, which are used as probe and pump beams respectively. Intensities of pump and probe beams are such that $\Omega_{pu} \sim 5\Omega_{pr}$. The pump beam is modulated at 30 KHz and stabilized on the third derivative signal of saturated absorption spectrum of $F=4 \rightarrow F'=3$ transition,

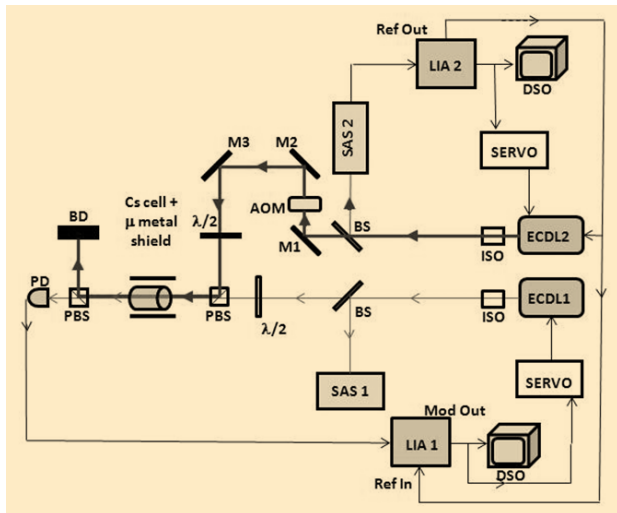


Fig. 2: Schematics of the experimental set-up. ECDL: external cavity diode laser, ISO: optical isolator, BS: beam splitter, M: mirror, AOM: acousto optic modulator, PBS: polarizing cubic beam splitter, BD: beam dump, PD: photodiode, LIA: Lock-in amplifier, SAS: saturated absorption spectroscopy set-up and DSO: digital storage oscilloscope.

to yield $\Delta_{pu} = 0$. The probe is scanned over the appropriate frequency range to generate an EIT signal. The third derivative of EIT signal is obtained simultaneously by demodulating the signal through a lock-in-amplifier. For frequency stabilization of probe, the zero point of the third derivative discriminator signal is selected as the lock point and the correction signal is processed through a servo loop and fed back to the piezo actuator. Under the closed loop condition, the output of the lock-in-amplifier is recorded with a DSO at a sampling speed of 50 k samples/s. The recorded output is used for obtaining frequency stability of AOFL in terms of the Allan variance.

Results and Discussion

Fig. 3 shows the EIT spectrum and its third derivative as a function of probe detuning. Fitting of the EIT profile to Lorentzian line shape, yields FWHM (Γ_{EIT}) = 1.2 MHz, which is substantially lower than the natural linewidth ($\Gamma = 5.3$ MHz) of the transition. Note here that the theoretical estimate of Γ_{EIT} for $\Omega_{pr} \ll \Omega_{pu}$ is given by³

$$\Gamma_{EIT} \cong \left(\sqrt{\frac{2\gamma}{\Gamma}} \Omega_{pu} \right) \quad (1)$$

where γ is the Raman coherence time for the ground hyperfine levels. For our experimental conditions, $\gamma = 20$ kHz as determined by the time of flight. Using Eq.(1), we estimate $\Gamma_{EIT} \sim 2$ MHz, which is close to the observed linewidth. This implies that Γ_{EIT} varies linearly with Ω_{pu} and further reduction in the linewidth is possible by reduction in Ω_{pu} . This, however, is not attempted, since the purpose of this work is to demonstrate a robust AOFL scheme based on EIT resonance.

The behaviour of Allan variance, $\sigma(2, \tau)$, for the EIT locked probe (σ_{EIT}) and for SAS locked pump (σ_{SAS}) is shown in Fig. 4. It may be seen, that $\sigma_{EIT} < \sigma_{SAS}$ for all τ . Specifically at $\tau = 10$ s, σ_{EIT} attains a minimum value = 2×10^{-13} whereas $\sigma_{SAS} = 2 \times 10^{-12}$. This behaviour clearly demonstrates that the EIT locked probe has better frequency stability that

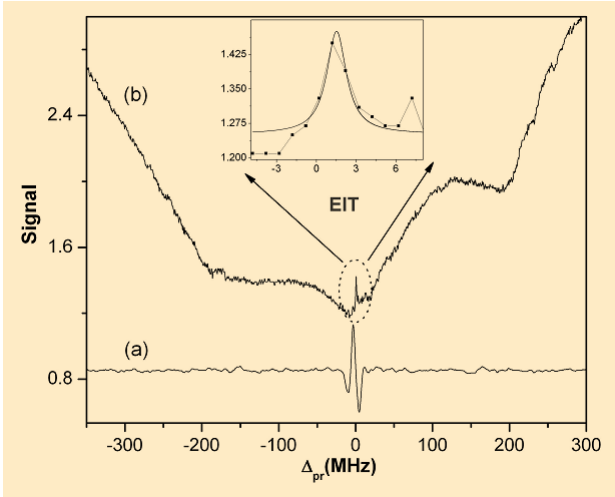


Fig. 3: Simultaneous recording of EIT (b) and its third derivative (a). Inset shows Lorentzian fit of EIT signal which gives FWHM of ~ 1.2 MHz.

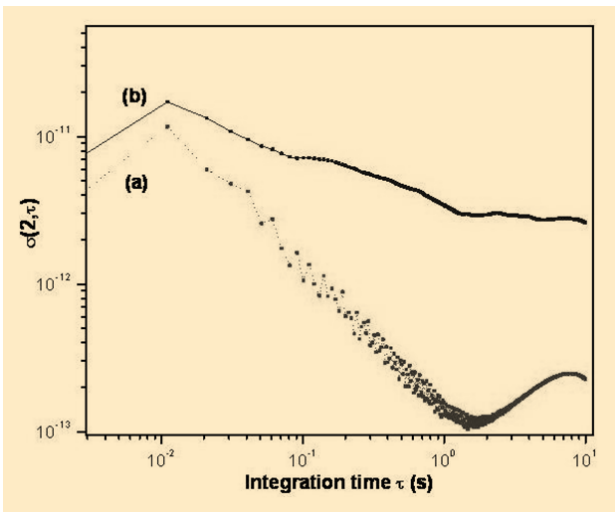


Fig. 4: Comparison of square root of Allan Variance (σ) for (a) EIT lock, (b) SAS lock.

the SAS locked pump. This observation is contrary to the conventional master-slave offset locking configuration, where it is the pump that governs the stability of the probe. This behaviour is a direct fall out of the quantum interference origin of EIT resonance.

In conclusion, we have demonstrated here a robust AFOL scheme based on EIT resonance, which arises from coherent laser-atom interaction. The frequency offset in the present scheme is precisely equal to the Cs clock transition.

References

1. M. Fleischhauer, A. Imamoglu and J. P. Marangos. "Electromagnetically Induced Transparency: Optics in coherent media" *Rev. Mod. Phys.* 77, (2005): 633-673.
2. D.J. Fullton, S. Shepherd, R.R. Moseley, B.D. Sinclair and M.H. Dunn. "Continuous-wave electromagnetically induced transparency: A comparison of V, \ddot{E} , and cascade systems" *Phys. Rev. A* 52, (1995): 2302-2311.
3. A. Javan, O. Korcharovskaya, H. Lee and M.O. Scully. "Narrowing of electromagnetically induced transparency resonance in a Doppler-broadened medium" *Phys. Rev. A* 66, (2002): 1-8.



Conformational Changes in the Chromatin Structure of Human Peripheral Blood Mononuclear Cells Exposed to Low Dose Radiation

Vinay Jain, Birajalaxmi Das and M.Seshadri

Low Level Radiation Studies Section
Radiation Biology & Health Sciences Division

and

P.A. Hassan

Chemistry Division

This paper received the Best Poster Award at the 7th International Conference on High Levels of Natural Radiation and Radon Areas (7HLNRRRA), held at Navi Mumbai, during November 24-26, 2010

Abstract

Ionizing radiations are known to challenge the integrity of the genome, by inducing several lesions like double strand breaks, single strand breaks and oxidative base damages in the DNA. Eukaryotic DNA is packaged inside the nucleus in the form of chromatin, which is formed by the interaction of histone proteins with DNA. Higher order chromatin structure acts as a barrier to the detection and repair of DNA damage. Modulations in chromatin structure are central in cellular responses to radiation-induced DNA damage. Such conformation changes may be monitored, by using a tool that studies the dynamic changes in size and shape of particles due to conformational modifications. Dynamic Light Scattering (DLS) is a sensitive and non-invasive tool, to study the dynamics of biomolecules in solution. In the present study, Dynamic Light Scattering (DLS) was used to analyze radiation-induced conformational changes in the structure of native chromatin.

Introduction

Ionizing radiations are known to challenge the integrity of the genome, by inducing several lesions like double strand breaks, single strand breaks and oxidative base damage in the DNA. Human cells have evolved efficient DNA repair processes, in response to DNA damage, by which the integrity of the genome is maintained. Emerging evidence indicates, that various modulations to chromatin structure are centrally important, to many aspects of the DNA damage response. DNA is compacted and packed in the form of chromatin in eukaryotic cells; the basic unit of chromatin is the nucleosome core particle, which consists of ~ 146 base pairs of DNA, wrapped in two left-handed superhelical turns around an octamer of

histone proteins. Higher order chromatin packaging acts as a barrier to the detection and repair of DNA damage. Hence, chromatin reorganization is thought to play a crucial role in cellular responses to DNA damage, by making damaged sites more accessible to repair machinery as well as transcriptional machinery of the cell. Dynamic Light Scattering (DLS) is a sensitive and non-invasive tool, to study the dynamics of biomolecules in solution. It measures time-dependent fluctuations in the scattering intensity, arising from particles undergoing random Brownian motion and relates it too particle size. In the present study, we have used Dynamic Light Scattering (DLS) as a tool to analyze radiation-induced conformational

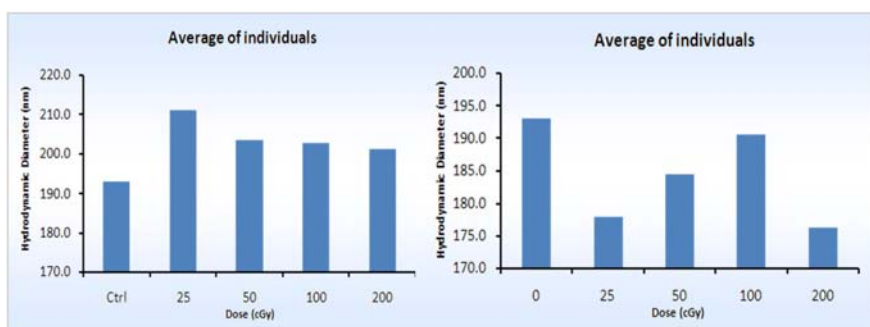


Fig. 1: Individuals divided in two groups on the basis of chromatin size profiles

changes, in the structure of native chromatin, in Peripheral Blood Mono Nuclear Cells (PBMCs) at resting stage (G_0).

Methodology

Venous blood samples were collected from 10 healthy donors with informed consent. Blood samples were irradiated at room temperature at various dose groups (25 cGy, 50 cGy, 100 cGy and 200 cGy) in addition to sham-irradiated control. Peripheral Blood Mononuclear Cells (PBMCs) were separated from whole blood using histopaque™ and resuspended in RPMI medium and irradiated using ⁶⁰Co gamma source (Blood irradiator 2000, BRIT) at a dose rate of 0.51 Gy/min. PBMCs were incubated for 2 hours at 37°C post irradiation in fresh medium. Native chromatin was isolated from each dose group, with an optimized concentration of micrococcal nuclease enzyme. Soluble chromatin was dialyzed and concentration (yield) was measured, using UV spectrophotometer. Chromatin obtained from each dose group was analyzed using Dynamic Light Scattering.

Results and Discussion

Post-irradiation alterations in the chromatin structure were studied at five different dose points (Cntl, 25 cGy, 50cGy, 1 Gy and 2 Gy) in 10 random and healthy individuals. Dose response studies done on 10 individuals have shown a significantly different chromatin size profile in the cells exposed to 25 cGy and 50 cGy as compared to control sample. All the individuals studied showed maximum change at 25 cGy which recovers to unirradiated levels at 1 Gy exposure. Interestingly, on further analyses we

observed that the individuals studied could be divided in to two groups on the basis of their response to radiation exposure. In both the groups maximum change was observed at 25 cGy, however their response was reverse. One group showed maximum increase in hydrodynamic diameter at 25 cGy which reduced in dose dependent manner upto 1 Gy

whereas other group showed maximum decrease in hydrodynamic diameter ay 25 cGy which increased in dose dependent manner upto 1 Gy to reach the size comparable with unirradiated state (Fig. 1).

Based on the above observations, time-dependent experiments were done on 4 individuals, to determine if during 2 hr incubation cells exposed to higher doses recover back to original conformation. In time-dependent experiments, cells were exposed to 1 Gy dose and incubated in CO₂ incubator for different time points such as 15 min, 45 min, 90 min, and 120 min after irradiation and then chromatin was isolated and analyzed using DLS. Interestingly, we have observed a time-dependent recovery in the chromatin structure at 1 Gy dose with maximum change observed at 15 min or 30 min, which recovers back to unirradiated levels after 120 min. (Fig.2)

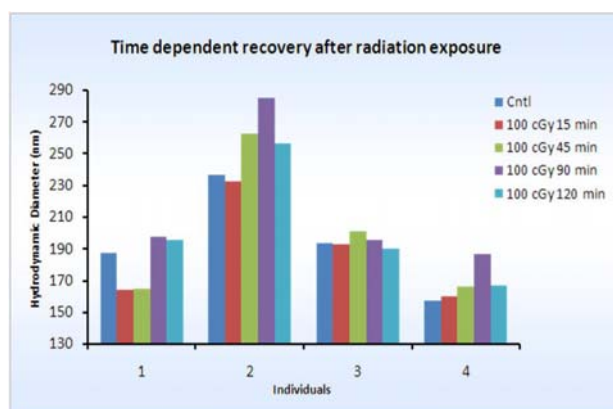


Fig. 2: Time dependent recovery after radiation exposure



Conclusion

Dynamic Light Scattering is a useful and innovative tool, to study the minute structural alterations occurring in chromatin after radiation exposure. Radiation-induced alterations in the conformation of chromatin fibers were observed, at doses as low as 25 cGy. Time dependent experiment using 100 cGy exposure shown, that recovery in chromatin conformation after radiation exposure is faster at higher dose (100 cGy), as compared to lower dose (25 cGy).

References

1. Pandita, T.K. and Richardson, C. (2009) Chromatin remodeling finds its place in the DNA double strand break response. *Nucleic Acid Research*, 37, 1363-1377
2. Downs, J.A., Nussenzweig, M.C. and Nussenzweig, A. (2007) Chromatin dynamics and the preservation of genetic information. *Nature*, 447, 951-958.
3. Kruhlak, M.J., Celeste, A., Dellaire, G., Capetillo, O.F., Muller, W.G. , McNally, J.G., Bazett-Jones, D.P. and Andre Nussenzweig (2006) Changes in chromatin structure and mobility in living cells at sites of DNA double strand breaks. *The Journal of Cell Biology*, 172, 823-834.
4. Pinto, M., Prise, K.M. and Michael, B.D. (2005) Evidence for complexity at the nanometer scale of radiation induced DNA DSBs as a determinant of rejoining kinetics. *Radiation Research*, 164, 73-85.
5. Holde, K.V., Leuba, S.H. and Zlatanova, J. (1998) Physical approaches to the study of chromatin fibers. *Gene Therapy and Molecular Biology*, 1, 475-482.
6. Lee, K.S., Mandelkern, M. and Crothers, D.M. (1981) Solution structural studies of chromatin fibers. *Biochemistry*, 20, 1438-1445.
7. Eisenberg, H. , Borochoy, N. ,Kam, Z. and Voordouw, G. (1979) Conformation of plasmid DNA and of DNA-histone chromatin like complexes by Laser Light Scattering. *Phil. Trans. R. Soc .Lond.*, 293, 303-313.
8. Campbell, A.M., Cotter, R.I and Pardon, J.F. (1978) Light Scattering measurements supporting helical structures for chromatin in solution. *Nucleic Acid Research*, 5, 1571-1580.
9. Schmitz, K.S. and Shaw, B.R. (1977) Hydrodynamic evidence in support of spacer regions in chromatin. *Science*, 197,661-662.



Development of a plastic scintillator based large area ground surface contamination monitor

P. Ashokkumar, Anand Raman, D.A.R. Babu and D.N. Sharma
Radiation Safety Systems Division

This paper received the Best Poster Award at the 29th National Conference on (IARP NC 2010) Recent Advances in Radiation Dosimetry held at Mumbai, during February 3-5, 2010

Abstract

This paper presents the features of a recently developed ground surface contamination monitor based on wide area plastic scintillation detector and investigates the design and performance characteristics of the system. The system incorporates an innovative methodology for suppressing the general background radiation influence on the detector response. The methodology involves the incorporation of a suitably positioned gamma sensitive Geiger Muller tube, the output of which is used to compensate for the general background interference in the response from the plastic scintillation detector. This paper reports on the performance evaluation of the system and the parameters considered for setting the alarm levels.

Introduction

Radiation protection is an integral component in the operation of all nuclear facilities and within that, contamination monitoring plays a major role. For nuclear facilities in India, the Atomic Energy Regulatory Board stipulates that, surface beta contamination levels should be below the specified derived working levels (DWLs) [AERB Safety Manual (Rev-4)] which happen to be 3.7 Bq/cm² for beta/gamma contamination. This entails regular area contamination monitoring to be carried out as per the regulatory stipulations, to ensure the zonal status of the working areas.

Generally, surface contamination monitoring in nuclear facilities, involves the routine collection of smear samples and later counting them, using laboratory installed GM counting setups. The alternate detector system used for these applications is the gas-filled proportional counter based monitoring system, which has its own merits and demerits [Alfred Klett et al, IRPA 2006]. The ground surface contamination monitor which is the subject matter of

this paper, incorporates a large area based plastic scintillator in correlation with a geiger muller detector.

Design features

General Hardware

The system hardware comprises of two large area plastic scintillation detectors, characteristics of which have been discussed elsewhere [Anand Raman et. al., NSRP 2009] covering an area of approximately 1000 cm². The detectors are mounted on a mobile trolley, at a distance of 10mm from the ground surface. An energy compensated Geiger Muller tube is placed above the detector plane, at a distance equivalent to 30mm above the ground surface. The signal processing hardware and the HV bias for the PMT coupled to the plastic scintillation detectors, is housed adjacent to the detectors, along with a rechargeable battery on the trolley. The detector signals processed by this module is then input to the data processing module, which is mounted at a height of 60 cm above the ground



surface, on the rotatable handle of the trolley. The data processing module is based on the NXP make 89LPC935 microcontroller and incorporates an embedded program for computation of contamination and the interface with the display and alarm segments. The total system operates on 12V rechargeable battery, housed in the system. The block diagram of the system is shown in Fig. 1.

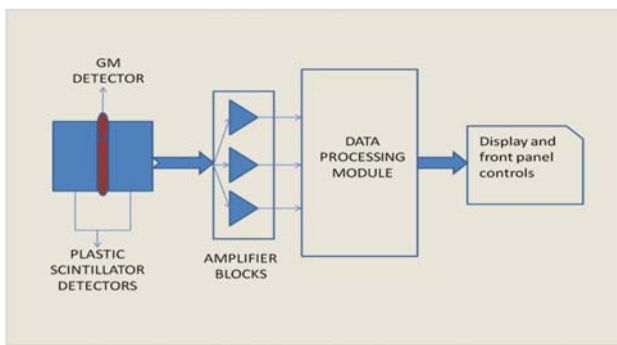


Fig. 1: Block Diagram of the ground surface contamination monitor

Data processing Software

The system software records the individual counts from each of the three detectors over a 5 second interval, and further to that, deducts the correlated counts from the values recorded for the plastic scintillation detectors in relation to that measured by the Geiger Muller counter. The output of the data processing module in terms of contamination levels of Bq/cm² is displayed on the front panel. In addition, a selectable switch on the front panel, also helps to obtain the individual count rate from each of the detectors as well as the general background exposure rate measured by the GM detector in μ R/hour.

Evaluation of detector parameters

Detector efficiency

The beta efficiency of the bare large area plastic scintillator with respect to distance from a Sr⁹⁰-Y⁹⁰ source of 1876 Bq, was obtained and found to be 40% when the source was in close contact. In order to provide protection against contamination of the detector surface, a thin 50 micron plastic film was used, the advantage being, that these sheets can be replaced whenever the accumulated

contamination on these sheets increase beyond the background threshold levels. At 50 micron thickness, the cutoff beta energy is 60 kev [Herman Cember]. The beta efficiency of the detectors when bare as well as used with the contamination protection sheet, is given in Fig. 2. The efficiency of the detector reduces from a maximum of 35% on contact to 5% over a distance of 30 mm. A source to detector distance of 10 mm has to be maintained, for achieving a beta efficiency of 20%.The gamma sensitivity of the system was measured to be in the range of 2.2cps/iR/hr.

Uniformity of response over the sensitive area

The variation of the response of the detector over the surface, with a beta source located at different positions just above it has also been obtained and the efficiency variation along the central line, parallel to the longer side of the detector is shown in Fig. 3. An electroplated standard Sr⁹⁰-Y⁹⁰ source was used for the purpose. The scintillator shows reductions in efficiency at the borders of the detector on both the sides. The profile is slightly asymmetric and the maximum is centered. The relative yields are well within 20% of the maximum.

Any beta/gamma contamination application will have to account for the general background based gamma compensation. This has been realized by carrying out simultaneous gamma background measurement and then subtracting the correlated gamma counts from the plastic scintillation detector.

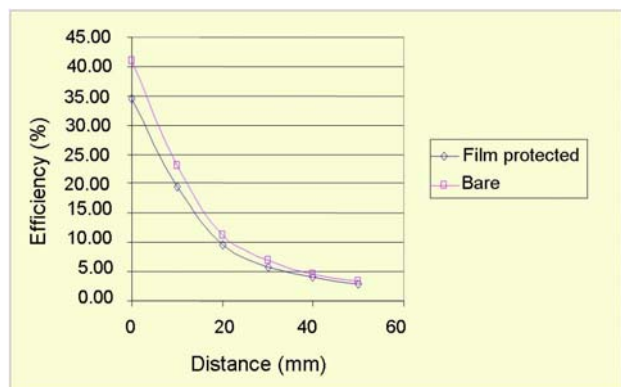


Fig. 2: Distance vs. Efficiency plot for bare plastic scintillator detector and when provided with contamination protection film

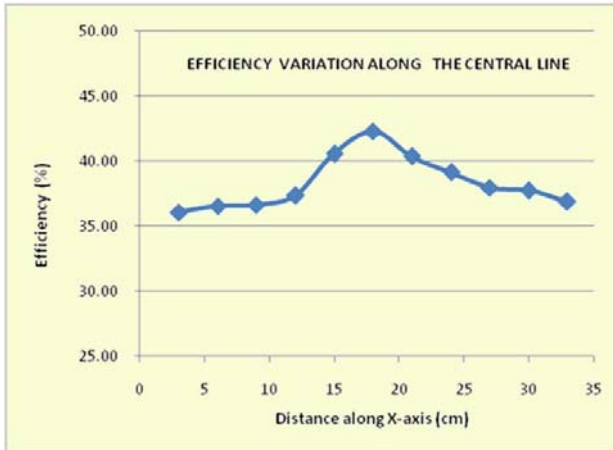


Fig 3: Efficiency variation over the surface of the detector

Calibration and estimation of contamination

The calibration of the individual plastic scintillation detectors was carried out for different gamma dose rates, and the same has been set up in a look up table in the system software. Further the GM tube also has been calibrated for the same dose rates and the data fitted in to the software to convert the GM counts in to the ambient gamma dose rate. Holding this GM based dose rate data, the corresponding contribution in to the counts recorded by the plastic scintillation detector is computed, through extrapolation from the lookup table and then compensated for, in the absolute counts recorded by the two detectors individually. The net counts thereby obtained are considered as the contamination measured by the system. A Sr⁹⁰-Y⁹⁰ source of area 500 cm², with a source distribution of approximately 4 Bq/cm², was used as a test source and the contamination as measured by the system was obtained in the order of 3.7 to 4 Bq/cm². The minimum detection level for the system was computed to be of the order of 0.2 Bq/cm².

Parameters for setting alarm levels

The AERB limits being 3.7 Bq/cm², it was decided that the alert levels should be at least one tenth of this limit value. With an effective area of 1000 sq cms, the total contamination under the frame of the detector would be 3700 Bq. Since the efficiency for beta contamination at a distance of 10 mm is obtained to be 20%, 740 counts

would be approximately recorded for this contamination level. One tenth of this would be 74 counts approximately, which is the limit set for the alert levels of the system. Any count value recorded above this value would be considered as a definite indication of contamination, requiring health physics intervention.

Conclusion

The large area plastic scintillator is suitable for incorporation in contamination monitoring applications. The detectors have been used for beta contamination monitoring in ground surface contamination monitoring applications. A prototype ground surface contamination monitor has been developed, based on the large area plastic scintillator and the minimum detectable level of this system has been established to be 5% of the stipulated Derived Working Levels.

Acknowledgements

We gratefully acknowledge the guidance and encouragement of Shri. H.S.Kushwaha , in carrying out this study. We thank our colleagues, Smt. Shubhangi Wani and Shri Satish Joshi for their able support and cooperation during the course of this development work. We thank our colleagues at RSSD workshop in the fabrication of the mechanical assembly.

References

1. Alfred Klett, Peter Haefner, Wilfried Reuter, Comparison Of Scintillation And Gas Filled Detectors For Contamination Monitoring. 2nd European IRPA Congress On Radiation Protection,2006.
2. G.F Knoll , Radiation Detection and Measurement,
3. Herman Cember, Introduction to health physics, Pergamon press, New York.
4. Radiation Protection for Nuclear Facilities: AERB Safety Manual (Rev-4)
5. Anand Raman, P Ashokkumar, D A R Babu and D N Sharma; Study and Characterisation of large area plastic scintillator detector for beta/gamma contamination monitoring applications. NSRP18, (November 2009).



Electrocatalysis of Fe(III)/Fe(II) Redox Reaction on Polyaniline Coated Platinum Electrode : Influence of Ionic Speciation of Analyte

Saurav K. Guin, Ruma Chandra, H.S. Sharma(Retd.) and S.K. Aggarwal
Fuel Chemistry Division

This paper was awarded the Best Poster Presentation (III prize) at the 4th ISEAC Triennial International Conference on ElectroAnalytical Chemistry and Allied Topics (ELAC-2010) held at Puri, Orissa, during March 16-18, 2010.

Introduction

Electrochemical charge transfer reactions of polyaniline (PANI) film with the redox species present in electrolyte solution are of interest both from fundamental and practical point of view of electrocatalysis. It is well known that, PANI can exist in various oxidation states at the molecular level, such as fully reduced leucoemeraldine base (LB), half-oxidized emeraldine base (EB) and fully oxidized pernigraniline base (PB). All these base forms are insulators. In strong mineral acids, EB transforms into the conducting emeraldine salt (ES) through acid doping. Electrochemical reactions at PANI coated platinum electrode depends on three factors, which are (i) transport of charge within the PANI layer, (ii) diffusion of the solution species towards and within the PANI layer and (iii) Charge transfer between the diffusing species with PANI. The first factor is constant for a PANI coated electrode, where PANI exists in ES form. Thus the second and third factors have major influence on the electrocatalytic activity of PANI to redox couple. The formal potential of Fe(III)/Fe(II) redox couple is $\sim 0.45-0.5$ V (vs. Ag/AgCl reference electrode), depending on the medium of concern. Thus the third factor, i.e., charge transfer between the Fe-species with PANI (in ES form) is thermodynamically possible. The electrocatalytic activity of PANI to Fe(III)/Fe(II) redox reaction

is studied [1-2] and there it is evidenced, that the catalytic activity is influenced by the nature of medium and that may be caused due to variation of the diffusing species within the PANI film. In this context, it is therefore of interest, to investigate the role of speciation of Fe-species, in the catalytic activity of PANI.

Experimental

Cyclic voltammetric experiments were carried out at room temperature with CHI 440A electrochemical workstation, by employing a three electrode voltammetric cell, having platinum disk working electrode ($\phi = 0.2$ cm²), platinum wire counter electrode and Ag/AgCl (3 M KCl) reference electrode. All the potentials quoted in this paper are with respect to the Ag/AgCl (3 M KCl) reference electrode. All chemicals used here were of high purity. All the reagents were prepared in Millipore water. Prior to performing the experiments, the working solution was purged with high purity nitrogen for 15 min, for purging out the dissolved oxygen from the solution. PANI film was electrodeposited potentiodynamically from 0.1 M aniline in 0.5 M H₂SO₄ solution. The potential was cycled between -0.2 V and 1.3 V at the scan rate of 0.1 Vs⁻¹. After synthesis, the PANI film was washed with 0.5 M H₂SO₄ and was employed in other experiments.



Results and Discussion

Potentiodynamic growth of PANI film on platinum electrode

The evolution of the cyclic voltammogram of the potentiodynamic growth of PANI film is shown in Fig. 1. The peak 'A' in the first cycle indicates the oxidation of aniline. From the second cycle on, peak 'A' disappears and a new peak 'C' generates, suggesting that short chain oligomers formed on the surface are being oxidized. The current increases with the number of cycles and the peak 'C' shifts slowly to peak II, indicating the regular growth of PANI film having longer chain length. The peak I/I* and Peak II/II* represent the redox transformations between LB/EB and EB/PB, respectively. There exists a difference of opinion about the current peak B/B*. According to some researchers they originate due to the presence of polymer containing phenazine rings [3], while others presumed that they are the result of oxidation and reduction of the degradation products (mainly, benzoquinone/hydroquinone) trapped inside the polymer matrix [4]. The peak I shifts slightly to more positive potential as the growth proceeds and it is probably due to the thickening of PANI film during its polymerization. Therefore, Fig. 1 depicts that PANI film exists in conducting ES form in $0.5 \text{ MH}_2\text{SO}_4$, between the potentials $\sim 0.2 \text{ V}$ and $\sim 0.7 \text{ V}$.

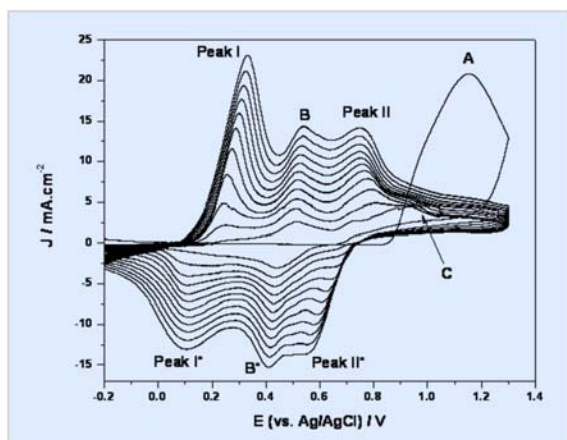


Fig. 1: Potentiodynamic polymerization of aniline for 12 consecutive cycles in 0.1 M aniline solution by potential scanning between -0.2 V and 1.3 V with a scan rate of 0.1 Vs^{-1} .

Electrocatalytic effect of PANI film to 50 mM FeCl_3 solution in 1M HCl

Cyclic voltammetry experiments were carried on bare platinum electrode and PANI coated platinum electrode with 50 mM FeCl_3 solution in 1 M HCl by cycling the potential between -0.2 V and 0.8 V at a scan rate of 10 mV.s^{-1} . The cyclic voltammograms are shown in Fig. 2(A) which shows that, the PANI film enhances the rate of charge transfer for both the reduction and oxidation of Fe(III) and Fe(II), respectively. The small current peak at $\sim 0.2 \text{ V}$ for the PANI film electrode arises due to the redox transformation of PANI from LB to EB state. It can be observed from Fig. 2(B), that both the oxidation and the reduction peak currents of Fe(III)/Fe(II) redox process, enhance rapidly as the thickness of the PANI film increases. This is attributed to the increase in the available active area for the charge transfer of the Fe-species with the electrode through the polymer itself. Most interestingly, the separation of the cathodic and anodic peak (i.e. ΔE_p) of Fe(III)/Fe(II) redox couple decreases as the thickness of the PANI film increases. For FeCl_3 solution 1 M HCl, tetrahedral $[\text{FeCl}_4]^-$ is expected to be the predominant species, whereas in the acid doped (i.e. protonated) ES state of the PANI film, almost half of all nitrogen atoms of the polymer chain bear a positive charge. As a consequence, a strong electrostatic attraction between positively charged PANI chain and negatively charged $[\text{FeCl}_4]^-$, induce the penetration of the analyst PANI film, resulting in a low overpotential (i.e. small ΔE_p) for the redox process of Fe-species in 1 M HCl solution.

Electrocatalytic effect of PANI film to 50 mM FeCl_3 and 50 mM $\text{Fe}_2(\text{SO}_4)_3$ solution in 0.5M H_2SO_4

Cyclic voltammetry experiments were carried on bare platinum electrode and PANI coated platinum electrode (12 cycles) with 50 mM FeCl_3 solution in 0.5 M H_2SO_4 and by cycling the potential between -0.2 V and 0.8 V at a scan rate of 10 mV.s^{-1} . The cyclic voltammograms are shown in Fig. 3(A). Similar experiments were carried out with 50 mM $\text{Fe}_2(\text{SO}_4)_3$ solution in 0.5M H_2SO_4 and the

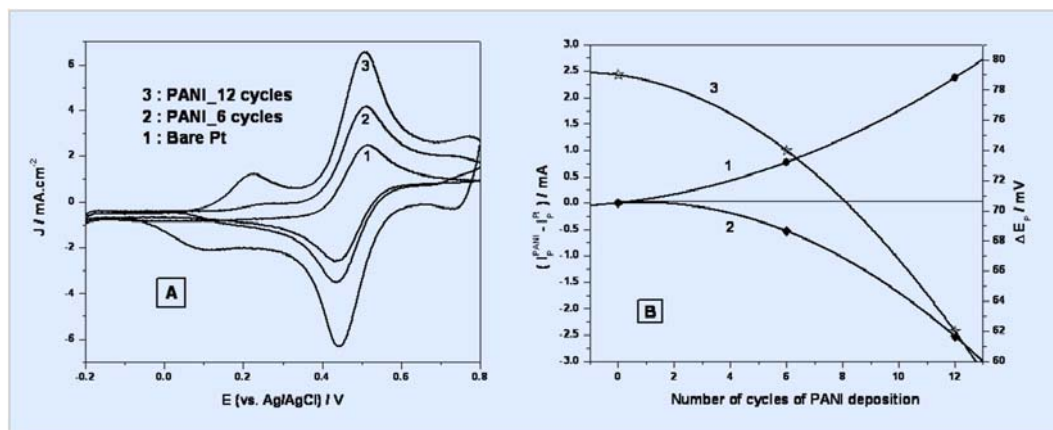


Fig. 2 (A) Comparison of cyclic voltammograms for 50 mM FeCl_3 in 1 M HCl at (1) bare platinum electrode, (2) PANI film electrode deposited by 6 consecutive potential cycles and (3) PANI film electrode deposited by 12 consecutive potential cycles. In all the cases scan rate is kept constant at $10 \text{ mV}\cdot\text{s}^{-1}$. (B) The difference in peak currents ($I_p^{\text{PANI}} - I_p^{\text{Pt}}$) between the PANI film electrode and bare platinum electrode (1) anodic peak current, (2) cathodic peak current and (3) the potential difference (ΔE_p) between the cathodic and anodic peaks with the variation of the thickness of the PANI film.

cyclic voltammograms are shown in Fig. 3(B). It is evidenced from both the figures, i.e.; Fig. 3(A) and Fig. 3(B), that for PANI film, the current i.e. the rate of charge transfer increases almost to an equal extent irrespective of the analyte. However, the suppression of the LB/EB redox peak at $\sim 0.2 \text{ V}$ in the presence of the Fe-species may be due to the presence of a thin layer of Fe(II), which has higher oxidation potential as compared to LB, at the

interface after completion of the scanning towards the negative potential. Table 1 presents the variation in relative peak currents ($I_p^{\text{PANI}}/I_p^{\text{Pt}}$) and the peak separations (ΔE_p) for different Fe-species. It can be observed that, though the relative peak currents are almost independent of the speciation of the analyte, it strongly influences the overpotential of the Fe(III)/Fe(II) redox reaction. For the anionic $[\text{FeCl}_4]^-/[\text{FeCl}_4]^{2-}$ species the overpotential of the Fe(III)/Fe(II) redox reaction decreases significantly on PANI

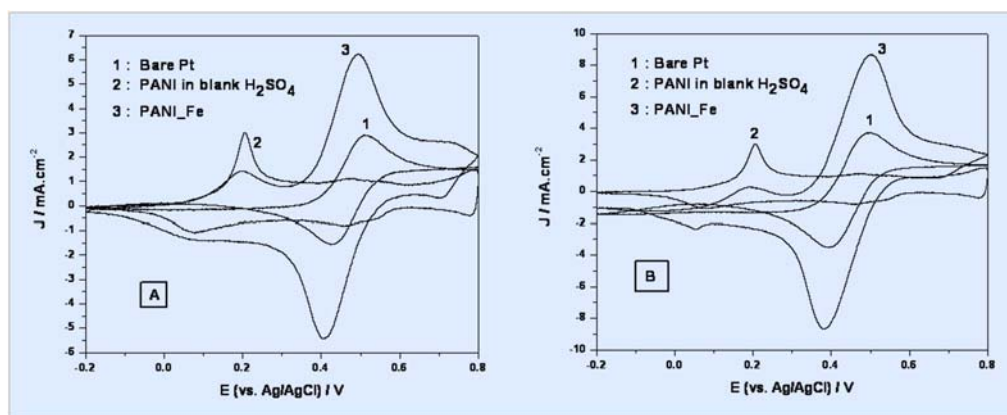


Fig. 3: Comparison of cyclic voltammograms for (A) 50 mM FeCl_3 in 0.5 M H_2SO_4 and (B) 50 mM $\text{Fe}_2(\text{SO}_4)_3$ in 0.5 M H_2SO_4 at a scan rate of $10 \text{ mV}\cdot\text{s}^{-1}$. In each figure, the electrochemical signal generates form (1) bare platinum electrode, (2) PANI film electrode in blank 0.5 M H_2SO_4 solution and (3) PANI film electrode in the analyte solution.



Table 1: The relative peak currents ($I_p^{\text{PANI}}/I_p^{\text{Pt}}$) and the peak separation (ΔE_p) for different speciation of Fe in the reaction medium (* : Probable)

Chemical	Solvent	Speciation*	$I_p^{\text{PANI}} / I_p^{\text{Pt}}$	$\Delta E_p^{\text{Pt}} / \text{m}$	$\Delta E_p^{\text{PANI}} / \text{mV}$
FeCl ₃	1M HCl	[FeCl ₄] ⁻	1.9	79	62
FeCl ₃	0.5 M H ₂ SO ₄	[Fe(H ₂ O) ₆] ³⁺	1.9	83	91
Fe ₂ (SO ₄) ₃	0.5 M H ₂ SO ₄	[Fe(H ₂ O) ₆] ³⁺	1.8	103	120

film because of the coulombic attraction and as a result, induced penetration of the redox species within and through the positively charged PANI polymer backbone. However, the reverse phenomena happens for the cationic [Fe(H₂O)₆]³⁺ / [Fe(H₂O)₆]²⁺ species. In this case, the coulombic repulsion between the analyte and positively charged PANI polymer backbone, hinders the penetration of the analyte through the polymer film on the electrode surface and thus the overpotential of the redox reaction increases significantly on PANI film as compared to the bare platinum electrode. The increase in overpotential for PANI coated platinum electrode to Fe³⁺/Fe²⁺ redox couple in H₂SO₄ medium, also gets support from the literature [1].

Conclusion

Electrocatalysis of Fe(III)/Fe(II) redox reaction to PANI coated platinum electrode is greatly influenced by three parameters, viz. (i) the redox state of the PANI film, which determines the conductive nature of the film and passes the current signal to the platinum electrode, (ii) the area of interaction of the PANI film with the analyte, which controls the charge transfer between the diffusing analyte and PANI active sites. This decides the current value during the redox reaction and finally, (iii) the speciation of the analyte i.e., the overall ionic nature of the analyte, which governs the diffusion of the analyte and solution species towards and within the PANI film. This exhibits the variation in the overpotential during the redox reaction of the analyte.

References

1. Z. Mandic and L. Duic, *J. Electroanal. Chem.* 403 (1996) 133.
2. K. R. Prasad and N. Munichandraiah, *Synth. Met.* 126 (2002) 61.
3. E. M. Genies, M. Lapkowski and J. F. Penneau, *J. Electroanal. Chem.* 249 (1988) 97.
4. D. E. Stilwell and S-M. Park, *J. Electrochem. Soc.* 135 (1988) 2254.



Electrochemical Oxidation of Ascorbic Acid on Gold Nanoparticles Coated Pt

Manoj K. Sharma and Arvind Ambolikar

Fuel Chemistry Division

This paper was awarded the Best Poster Presentation (III prize) at the 4th ISEAC Triennial International Conference on ElectroAnalytical Chemistry and Allied Topics (ELAC-2010) held at Puri, Orissa, during March 16-18, 2010

Introduction

Nanomaterials exhibit unique chemical [1-3], physical [4-7] and electronic [8] properties that are distinctly different from those of bulk materials and depend on size, shape and surface composition of the nanostructured materials. Nanomaterials of noble metals are finding worldwide interest in research communities [9-12]. Several reviews have highlighted the role of metal nanoparticles in catalysis [13-15]. The small size of the nanoparticles endows them with a high surface area, providing more active sites to catalyse reactions and with the ability to electronically interact with the reactant molecules, providing significant improvement in both detection and catalytic capabilities. Because of these properties, nanoparticles are finding applications in electroanalysis and electrochemical based sensors. In electrochemical experiments, nanoparticles based electrodes are rapidly replacing the conventional macroelectrodes because of the large effective surface area, increased mass transport, high catalytic activity and the ability to exert control over the local environment at the nanoparticles-modified electrode surface [16]. Gold nanoparticles have found applications as catalysts and biosensors in various chemical and biological reactions of interest, including biological labeling in medical imaging, because of the nanoparticles' biocompatibility and easy functionalization of the surfaces. The surface of the gold nanoparticles is generally functionalized to prepare sensors, but some of the analytes can be detected at the

nanoparticles-modified electrode. Electrochemical deposition is commonly used to synthesize and deposit metal nanoparticles onto the substrate simultaneously, with easy control of particle morphology. Therefore, electrochemical deposition is a potentially powerful and convenient technique, to regulate catalytic properties of the nanoparticles. This paper describes the electrochemical oxidation of ascorbic acid on nanostructured gold coated Pt electrode. The dependence of peak current (i_p) and peak potential (E_p) of ascorbic acid oxidation, on the numbers of cyclic voltammetry (CV) cycles used for gold deposition was studied.

Experimental

Chemicals such as HAuCl_4 , ascorbic acid and mono- and di-sodium phosphate salts were used without purification. Ultrapure water, filtered by a Millipore water system at a resistivity of $>18 \text{ M}\Omega \text{ cm}$, was used for solution preparation. Electrochemical experiments were carried out in a conventional three-electrode glass cell, using Autolab PGSTAT 30 (Eco Chemie, The Netherlands) electrochemical workstation. The platinum electrode and gold nanoparticles-modified Pt electrodes were used as working electrodes. The counter and reference electrodes were platinum wire and Ag/AgCl/3M KCl , respectively. The deposition of gold nanoparticles was carried out by CV



techniques. The potential was cycled between 1.2 V and -0.2 V in an aqueous solution of 2 mM HAuCl_4 in 1 M KCl. The electrooxidation of ascorbic acid was carried out in 0.1 M phosphate buffer solution, using Differential Pulse Voltammetry (DPV). Atomic Force Microscopic (AFM) images were recorded in air, using a Nanosurf EasyScan 2 instrument. The measurements were carried out in a contact mode, by using a silicon cantilever with a force constant of 0.2 N/m

Results and Discussion

The surface characteristics of electrodes influence almost all the processes taking place at their surface. Therefore, the surface of an electrode plays an important role in applied electroanalysis. The metal-deposition is a widely used technique for surface modification and metal nanoparticles of varying shapes, sizes and compositions can be obtained, by carefully tuning the electrochemical deposition parameters. The gold deposition on Pt surface was carried out by CV technique and the parameter varied was the number of cycles in CV used for the gold deposition. The surface modification of the platinum electrode was investigated by studying the electrochemical

oxidation of ascorbic acid in phosphate buffer. Fig. 1 shows the DPV of 5 mM ascorbic acid in 0.1 M phosphate buffer on Pt and gold deposited Pt. The peak oxidation current (i_p) increased and the peak width at half maxima decreased on increasing the numbers of CV cycles. Fig. 2 shows the variation of ascorbic acid oxidation peak current and peak potential as a function of numbers of CV cycles. The oxidation peak potential (E_p) decreased exponentially and peak current (i_p) showed sigmoidal increase with increase in numbers of CV cycles. The E_p and i_p on bare Pt electrode were 0.408 V and 4.720 μA , respectively. The E_p shifted to lesser positive potential by 97 mV and 151 mV on gold deposited Pt, after one and two CV cycles of gold electrodeposition, respectively.

The Electrochemical Impedance Spectroscopy (EIS) is a powerful, non-destructive, and informative technique, to study the specific microscopic events of interest at the electrode surface, by measuring the interfacial impedance of the electrode/solution interface. Parameters such as solution resistance (R_u), charge transfer resistance (R_{ct}) and C_{dl} , are evaluated from the EIS measurement and used to investigate the interface of the electrode/solution. Here,

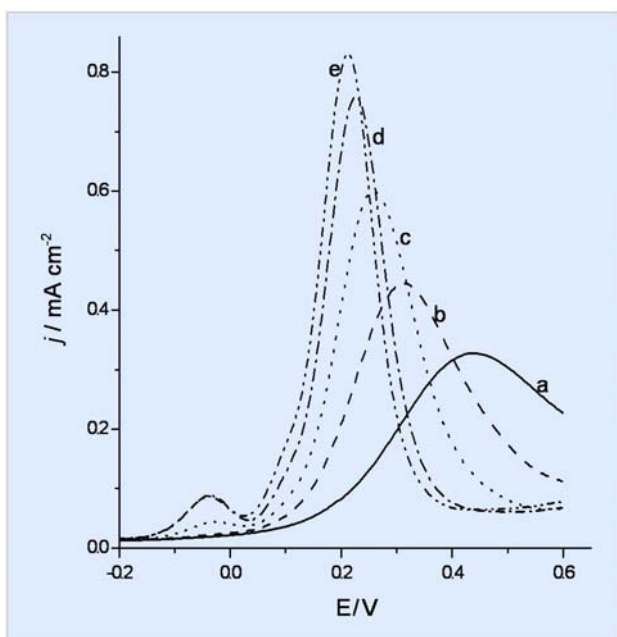


Fig. 1: DPV response for 5 mM ascorbic acid on (a) Pt and gold deposited Pt after (b) 1 (c) 2 (d) 5 (e) 7 CV scans. Electrolyte: 0.1 M phosphate buffer (pH 7)

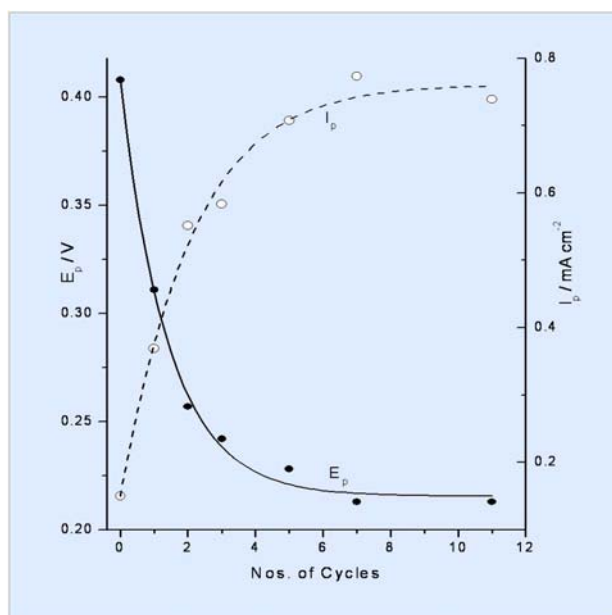


Fig. 2: E_p and I_p response for 5 mM ascorbic acid as a function of numbers of CV scan.



the change in surface morphology of the electrode surface on gold electrodeposition and its effect on electron transfer kinetics is studied by EIS measurements. Fig. 3 shows that the charge transfer resistance (R_{ct}) on gold deposited Pt electrode decreased, therefore, indicating the fast electron transfer kinetics on increasing the number of CV cycles for electrodeposition of gold. The height distribution profile (Fig. not shown here) in AFM measurements revealed that percentage of particles with smaller dimensions increased in first 3-4 CV cycles and the particle height distribution profiles are almost similar in case of higher number of CV cycles. Therefore, a significant improvement in catalytic behaviour of electrode, for ascorbic acid oxidation, was observed in initial 3-4 CV cycles and for latter CV cycles, the electrochemical behaviour is almost similar.

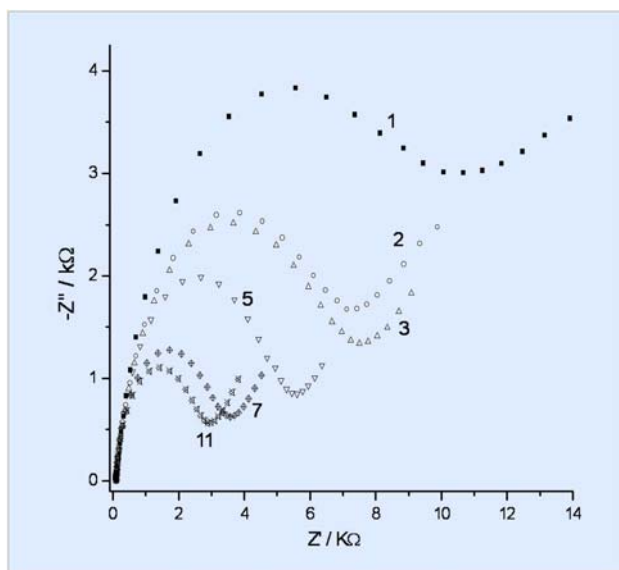


Fig. 3: Impedance plots obtained in 0.1 M H_2SO_4 containing 5 mM $[Fe(CN)_6]^{3-/4-}$ for Pt and gold deposited Pt electrodes. The numbers in the plots indicate the number of cycles used for gold deposition on Pt.

Conclusion

The nanostructures of gold synthesized on Pt are responsible for the electrocatalytic oxidation of ascorbic acid. The change in surface morphology of gold nanoparticles occurred in successive CV cycles, due to repetitive

reduction-oxidation of gold deposits in each CV cycle. The different morphology of AuNPs deposits resulted in varying electrochemical response on AuNPs-modified electrodes. Therefore, by carefully selecting the experimental parameters for electrodeposition of metal nanostructures, the morphology of nanostructure metals can be tuned, to obtain desired catalytic properties.

Acknowledgements

Authors are thankful to Dr. H. S. Sharma, Head, Electrochemistry Section and Dr. S. K. Aggarwal, Head, FCD for their support and encouragement.

References

1. L. N. Lewis, *Chem. Rev.* 93 (1993) 2693.
2. V. Kesavan, P. S. Sivanand, S. Chandrasekaran, Y. Koltypin and A. Gedankin, *Angew. Chem. Int. Ed.* 38 (1999)3521.
3. R. Ahuja, P. I. Caruso, D. Mobius, W. Paulus, H. Ringsdorf and G. Wildburg, *Angew Chem. Int. Ed.* 32 (1993) 1033
4. P. Mulvaney, *Langmuir*, 12 (1996) 788.
5. M. M. Alvarez, J. T. Khoury, T. G. Schaaff, M. N. Shafiqullin, I. Vezmar and R. L. Whetten, *J. Phys. Chem. B* 101 (1997) 3706.
6. A. P. Alivisatos, *J. Phys. Chem.* 100 (1996) 13226.
7. L. E. Brus, *Appl. Phys. A* 53 (1991) 465.
8. R. F. Khairutdinov, *Colloid J.* 59 (1997) 535.
9. R. Fahrner (Ed.) *Nanotechnology and Nanoelectronics, Materials, Devices, Measurement Techniques*, Springer 2005.
10. D. J. Lockwood (Ed.) *Nanostructure Science and Technology*, Springer, New York 2002.
11. Z. L. Wang, (Ed.) *Micro-manufacturing and Nanotechnology Nanowires and Nanobelts: Volume 1: Metal and Semiconductor Nanowires, Volume 2: Nanowires and Nanobelts of Functional Materials*, Springer, New York 2006.



12. G. Z. Cao, (Ed.) *Nanostructures and Nanomaterials: Synthesis, Properties and Applications*, Imperial College Press, London 2004.
13. R. Schloglm and S. B. A. Hamid, *Angew. Chem. Int. Ed.* 43 (2004) 1628.
14. D. Astruc, F. Lu and J. R. Aranzaes, *Angew. Chem. Int. Ed.* 44 (2005) 7852.
15. A. Roucoux, J. Schulz and H. Patin, *Chem. Rev.* 102 (2002) 3757.
16. E. Katz, I. Willner and J. Wang, *Electroanalysis* 16 (2004) 19.
17. Y. M. Yan, R. Tel-Vered, O. Yehezkeli, Z. Cheglakov and I. Willner, *Adv. Mater.* 20 (2008) 1.



Electromagnetically induced transparency in a tripod atomic system

Niharika Singh

Homi Bhabha National Institute

and

R. D'Souza and B. N. Jagatap

Atomic and Molecular Physics Division

and

Q. V. Lawande

Theoretical Physics Division

This paper received the Best Poster Award at the National Laser Symposium (NLS-19), held at Raja Ramanna Centre for Advanced Technology, Indore, from 1-4 December, 2010

Abstract

We investigate theoretically, Electromagnetically Induced Transparency (EIT) in a medium consisting of four-level atoms in tripod configuration and interacting with three laser fields, i.e., a weak probe, a strong pump and a strong control beam. Using Master equation approach, analytical results are obtained for the absorption spectrum of the weak probe in the presence of strong pump and control fields for both stationary and mobile atoms. These results are then used to understand the behaviour of double dark resonances, in terms of the laser-atom interaction parameters.

Introduction

Electromagnetically Induced Transparency (EIT) is a phenomenon that originates from coherence induced changes in the susceptibility of the medium and provides an experimental basis for sub-natural resolution. Three-level systems^{1,2} driven by a pair of pump and probe laser beams have been investigated in detail in this context. In recent years, however, considerable attention is being paid to four-level atomic systems, which offer avenues for studying richer quantum interference effects³. One such system is a tripod system³, which is an extension of a three-level Λ system with an additional transition from a nearby ground level, that is driven by a third control field. The resultant configuration then becomes a double dark resonant system³. At the practical

level, the situation may be viewed as an interesting way of controlling the coherent dynamics of the standard Λ system and thereby tailoring the characteristics of the ensuing EIT by the control field. In this paper, we investigate theoretically, the double dark resonances, i.e., two EIT windows in a tripod system using Master equation formalism.

Theoretical formulation and results

A tripod system as shown in Fig. 1 can be realized with Zeeman states of ^{87}Rb D_2 transition. Here the levels $|1\rangle$, $|3\rangle$ and $|4\rangle$ constitute a three-level Λ system where probe and pump lasers excite $|1\rangle \rightarrow |4\rangle$ and $|2\rangle \rightarrow |4\rangle$ transitions respectively. Level $|3\rangle$ is an additional level that is connected to the excited level $|4\rangle$ by a control laser. For $|i\rangle \rightarrow |j\rangle$



transition, the relevant Rabi frequencies, detunings and decay rates are denoted by $2\alpha_{ji}$, Δ_{ji} and $2\gamma_{ji}$ respectively.

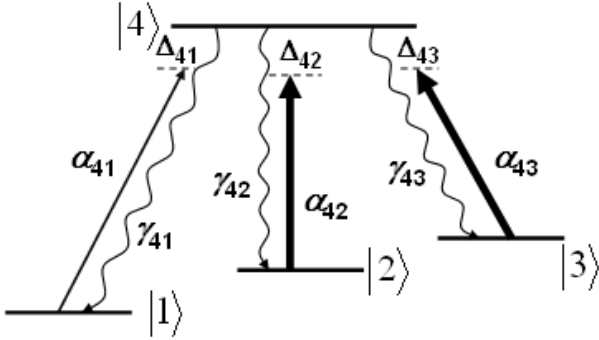


Fig. 1: Schematic representation of a four-level tripod system

The master equation for this system is

$$\frac{\partial \rho}{\partial t} = -i[H_0, \rho] - \sum_k \gamma_{jk} (A_{jk}\rho - 2A_{jk}\rho A_{jk} + \rho A_{jk}), \quad (1)$$

where ρ is the reduced atomic density operator, A_{mn} is the atomic operator and H_0 is the semi-classical atom-field interaction Hamiltonian in rotating wave approximation, i.e.,

$$(2)$$

Eq.(1) describes a set of 16 coupled equations involving components $\rho_{ij} = \langle i|\rho|j\rangle$, $i, j, = 1, 2, 3, 4$, of the density matrix. Of particular interest in experiments relating to EIT is the induced polarization ρ_{14} in steady state, since the probe absorption is given by $A = \text{Im}(\rho_{14}\gamma_{41}/\alpha_{41})$. A closed form analytical solution for ρ_{14} is therefore instructive to understand the dressed state and EIT resonances. For weak probe field, i.e., $\alpha_{41} \ll \alpha_{42}, \alpha_{43}$, steady state polarization ρ_{14} can be obtained perturbatively up to first order in α_{41} ,

$$\rho_{14} = \frac{-\alpha_{41}(\Delta_{41}-\Delta_{42})(\Delta_{41}-\Delta_{43})}{\alpha_{43}^2\Delta_{42} + \alpha_{42}^2\Delta_{43} - \Delta_{41}(\alpha_{42}^2 + \alpha_{43}^2) + (\Delta_{41}-\Delta_{42})(\Delta_{41}-\Delta_{43})(\Delta_{41} + i\gamma_4)} G(v) \quad (3)$$

where $\gamma_4 = \gamma_{41} + \gamma_{42} + \gamma_{43} = \Gamma/2$, $\Gamma = 6.1$ MHz is the natural linewidth of ^{87}Rb D_2 transition and $G(v)$ is the Maxwell-Boltzmann distribution of atomic velocities. It may be noted here, that in the absence of the control laser ($\alpha_{43} = \Delta_{43} = 0$), Eq. (3) reduces to the familiar result

for a three-level Λ system. EIT spectrum then can be generated, by averaging Eq.(3) over $G(v)$.

Inspection of Eq.(3) reveals a number of interesting features of coherent spectroscopy of a tripod system. In particular, the susceptibility of the medium vanishes identically at $\Delta_{41} = \Delta_{42}$ and $\Delta_{41} = \Delta_{43}$ and these correspond to the positions of two EIT resonances. This is in contrast to the Λ system, which exhibits a single EIT resonance at $\Delta_{41} = \Delta_{42}$. In order to understand the nature of the EIT resonances and their FWHM (Γ_{EIT}), it is instructive to discuss the dressed state resonances, i.e., absorption spectrum for a stationary atom. The dressed state resonances of tripod system appear at $\Delta_{41} = \delta_1, \delta_2$ and δ_3 , where δ_i are the roots of the cubic equation,

$$\Delta_{41}^3 - \Delta_{41}^2(\Delta_{42} + \Delta_{43}) + \Delta_{41}(\Delta_{42}\Delta_{43} - \alpha_{42}^2 - \alpha_{43}^2) + \alpha_{42}^2\Delta_{43} + \alpha_{43}^2\Delta_{42} = 0 \quad (4)$$

A special case of this is when $\Delta_{42} = \Delta_{43}$, which corresponds to two dressed state resonances at $(\Delta_{42} \pm \sqrt{\Delta_{42}^2 + 4\alpha^2})/2$,

where $\alpha^2 = \alpha_{42}^2 + \alpha_{43}^2$. Doppler averaging of this result yields a single EIT resonance at $\Delta_{41} = \Delta_{42}$, which is analogous to the EIT in a Λ system. We may now consider a somewhat general case, where $\alpha_{43} < \alpha_{42}$. In this situation, we observe that the dressed state spectrum is a triplet corresponding to $\delta_{1,2} \sim (\Delta_{42} \pm \sqrt{\Delta_{42}^2 + 4\alpha^2})$ and $\delta_3 \sim \Delta_{43}$. Doppler averaging of this result, yields two EIT resonances at $\Delta_{41} = \Delta_{42}$ and $\Delta_{41} = \Delta_{43}$. We further observe, that $\Gamma_{\text{EIT}}(\Delta_{41} = \Delta_{42})$ is of the same order as that observed in a Λ system for identical pump-probe parameters, whereas $\Gamma_{\text{EIT}}(\Delta_{41} = \Delta_{43})$ is significantly narrower. Thus, the possibility of observing an ultra-narrow EIT profile by use of a control laser field makes the tripod system interesting in applications related to precision and metrology.

We now investigate the linewidth of EIT resonances as a function of control field parameters α_{43} and Δ_{43} . These results are shown in Fig. 2. It may be noted here, that $\Gamma_{\text{EIT}}(\Delta_{41} = \Delta_{42})$ and $\Gamma_{\text{EIT}}(\Delta_{41} = \Delta_{43})$ are both subnatural for low α_{43} . However, $\Gamma_{\text{EIT}}(\Delta_{41} = \Delta_{42})$ exhibits weaker dependence,



i.e., it remains almost constant over a wide range of α_{43} . Further both the EIT widths show minima at the respective two-photon resonance conditions, i.e., at $\Delta_{41} = \Delta_{42}$ and $\Delta_{41} = \Delta_{43}$ as shown in Fig. 2(b).

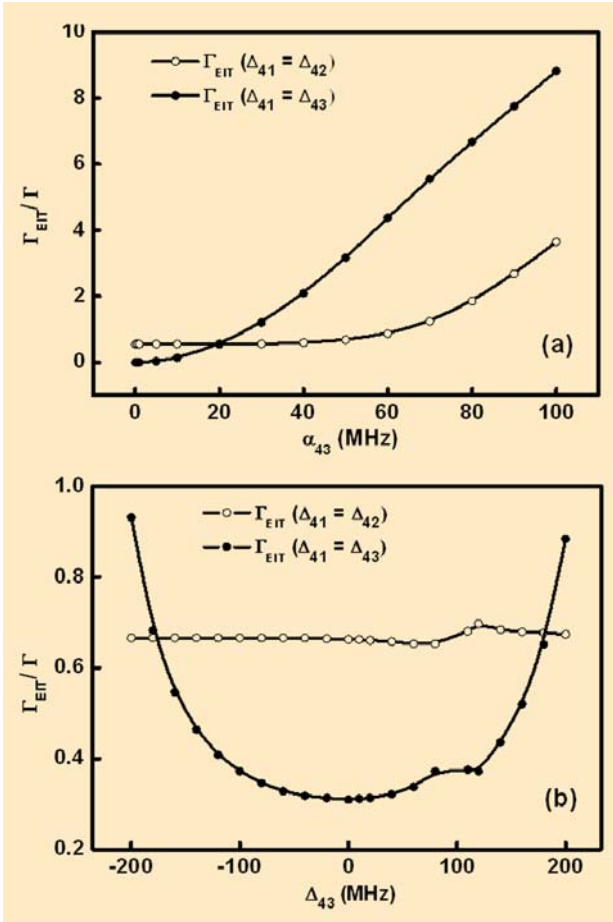


Fig. 2: Variation of Γ_{EIT} with (a) α_{43} and (b) Δ_{43} . For frame (a) $(\alpha_{42}, \Delta_{42}, \Delta_{43}) = (20, 0, 20)$ MHz and for frame (b) $(\alpha_{42}, \alpha_{43}, \Delta_{42}) = (20, 15, 100)$ MHz.

Conclusion

In this paper we have studied the EIT resonances in a tripod system interacting with a coherent tri-chromatic field and provided an analysis of parametric dependence of two EIT resonances and their linewidths. The presence of two strong fields makes the tripod configuration a 'double control system' providing more flexibility to this system than the system, where there is only one controllable optical beam.

References

1. Marangos J. P. "Electromagnetically Induced Transparency". *J. Mod. Opt.* 45 (1998): 471-503.
2. Wynands R and Nagel A. "Precision spectroscopy with coherent dark states". *Appl. Phys. B* 68 (1999): 1–25.
3. Gavra N, Rosenbluh M, Zigdon T, Gordon A. D.W and Friedmann H. "Sub-Doppler and sub-natural narrowing of an absorption line". *Opt. Comm.* 280 (2007): 374-378.



Estimation of Distribution Coefficient of Uranium and its correlation with soil parameters around Turamdih Uranium Tailings Pond

Sukanta Maity, S. Mishra, S. Bhalke, C. B. Dusane, G.G. Pandit and V. D. Puranik

Environmental Assessment Division

and

H. S. Kushwaha

Health Safety and Environment Group

This paper received the Consolation award in Poster Presentation Session, at the Workshop cum Seventeenth National Symposium on Environment (NSE-17), held at Indian Institute of Technology, Kanpur, from 13-15 May, 2010

Abstract

Distribution coefficients (K_d) of uranium and its daughter products are very important for migration studies around uranium mining sites. Since the distribution coefficient depends very much on the soil chemistry, generation of site-specific K_d is very important. In the present study, soil and water from various locations around Turamdih uranium tailings pond were collected and chemically characterized, for various parameters. The distribution coefficient of uranium at the top and at one meter depth soil samples from the above locations, were estimated using the laboratory batch method and found to vary from 69 to 5524 l/kg. The correlation among distribution coefficient of uranium and the soil parameters like pH and CaCO_3 was carried out.

Keywords: Uranium, Distribution coefficient, Laboratory batch method, Correlation, Soil, Water

Introduction

Predicting the transfer of radionuclides in the environment for normal release, accidental, disposal or remediation scenarios, in order to assess exposure, requires the availability of important generic parameter values. One of the key parameters in environmental assessment, is the solid liquid distribution coefficient, K_d , which is used to predict radionuclide-soil interaction and subsequent radionuclide transport in the soil column (H. Vandenhove et al., 2009). Distribution coefficient values of uranium are very much dependent on various physics-chemical parameters of soil and ground water, that's why site

specific distribution coefficient is necessary for the prediction of contaminant transport in geological matrices. Uranium sorption is affected by soil properties other than soil texture such as pH, CaCO_3 , content of amorphous iron oxides, soil organic matter content, cation exchange capacity and phosphate status (EPA, 1999).

In the present study, the soil and ground water samples collected around Turamdih tailings pond were characterized and distribution coefficient for uranium was estimated in soil samples. Since distribution coefficient is a strong function of soil parameters, its correlation with various soil parameters was also observed.



Experimental

Sample collection and processing

From nine different villages around Turamdih uranium mining site, in the Jharkhand state of India, surface and one meter depth soil and ground water samples were collected twice. Soil samples were air-dried and passed through a 2mm mesh sieve, then homogenized and used for chemical characterization as well as estimation of distribution coefficient of uranium.

Methodology

pH and CaCO₃ in soil samples were determined, using procedures given in IS 2720 Part No.26 and IS 2720 Part No.23 respectively. The estimation of distribution coefficient of uranium was carried out, using the laboratory batch method (EPA-1999). Sorption kinetics of Uranium was estimated with respect to contact time. Uranium analysis was carried out using DPASV (Metrohm-663 VA stand). Both in water and soil samples pH was analyzed using a pH meter.

Results and Discussion

The pH in the soil samples, collected from various places around Turamdih tailings pond, were found to vary from 5.55 to 8.55. Similarly, the concentration of CaCO₃ of the

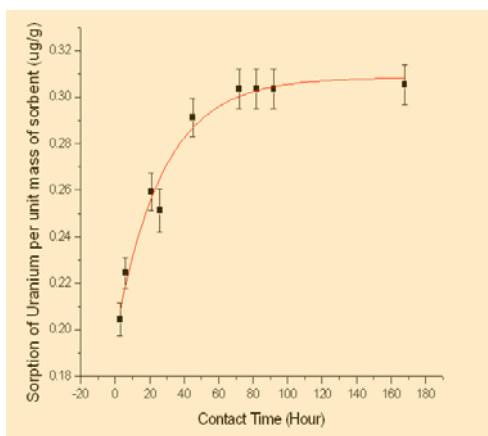


Fig. 1: Variation of uranium sorption with respect to contact time

soil samples varied from 0.229 to 1.14 %. From sorption kinetics of uranium it was observed, that within 72 hours, uranium reached equilibrium with soil and water as shown in Fig. 1. Distribution coefficient of uranium varied from 69 to 5524 l/kg in different sampling locations around Turamdih uranium tailings pond, as shown in Fig. 2. No significant difference in uranium K_d values was observed, both at the top and in one meter depth soil samples.

Effect of pH with distribution coefficient of uranium

In the present study, it is observed that the K_d(U) values are increasing in the pH range of 5 to 6, because at this pH, uranyl ion (UO₂²⁺) hydrolyzes, forming a number of aqueous hydroxide complexes and decreasing in the pH range of 6 to 9, due to formation of strong anionic uranyl-carbonate complexes with dissolved carbonate, as shown in Fig. 3. Vandenhove et al. (2007) examined the effect of soil pH on uranium availability for 18 spiked soils, and a similar linear decrease of log K_d with pH was observed for soils with pH ≥ 6, which was explained by the increased amount of soluble uranyl-carbonate complexes at high pH.

Effect of concentration of CaCO₃ with distribution coefficient of uranium

In the soil samples it is observed, that with increase in the concentration of CaCO₃, the distribution coefficient value

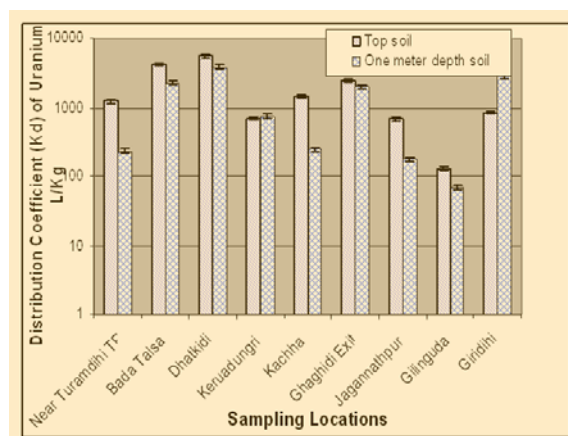


Fig. 2: Distribution coefficient of uranium in top and one meter depth soil samples around Turamdih uranium tailings pond.

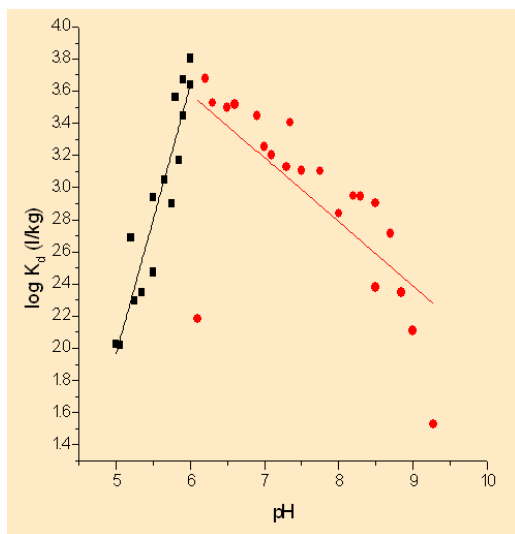


Fig. 3: Variation of distribution coefficient of uranium with pH in soil samples around Turamdih uranium tailings pond

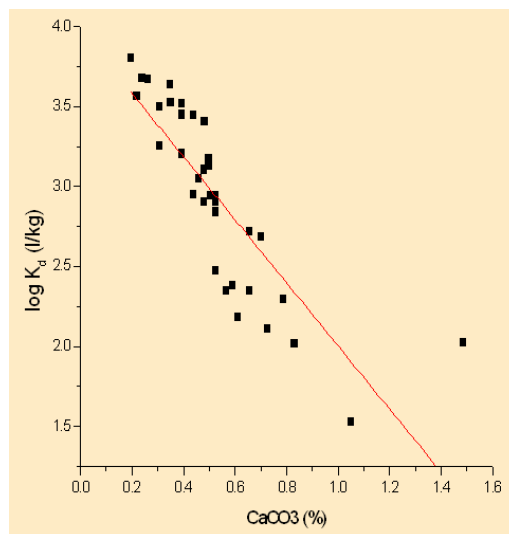


Fig. 4: Variation of distribution coefficient of uranium with CaCO₃ in soil samples around Turamdih uranium tailings pond

of uranium decreases as shown in Fig. 4. In the presence of CaCO₃, U (VI) forms dissolved uranyl carbonate complex, so adsorption of uranium in solid matrix decreases. According to McKinley *et al.* (1995) and Duff and Amrhein (1996), dissolved carbonate has a significant effect on the aqueous chemistry and solubility of U(VI).

Conclusion

The distribution coefficient of uranium varied from 69 to 5524 l/kg in the soil samples collected around Turamdih tailings pond. No significant difference in uranium K_d values was observed at the top and in one meter depth soil samples. A good correlation was observed between distribution coefficient of uranium and soil parameters like pH and concentration of CaCO₃. Using this correlation equation, distribution coefficient values for other sites of the same type of soil, can be estimated. These site-specific K_d values, will help in the migration study of uranium from uranium tailings.

References

1. Duff, M. C., and C. Amrhein. "Uranium(VI) Adsorption on Goethite and Soil in Carbonate

Solutions." *Soil Science Society of America Journal*, 60(5) (1996): 1393-1400.

2. EPA (Environmental Protection Agency), 1999. Understanding Variation in Partitioning Coefficients, K_d Values: Volume II: Review of Geochemistry and Available K_d Values for Cadmium, Caesium, Chromium, Lead, Plutonium, Radon, Strontium, Thorium, Tritium and Uranium. US-EPA, Office of Air and Radiation, Washington, USA. EPA 402-R-99-004B.
3. McKinley, J. P., J. M. Zachara, S. C. Smith, and G. D. Turner. "The Influence of Uranyl Hydrolysis and Multiple Site-Binding Reactions on Adsorption of U(VI) to Montmorillonite." *Clays and Clay Minerals*, 43(5) (1995):586-598.
4. Vandenhove, H., Van Hees, M., Wouters, K., Wannijn, J., Canwe predict uranium bioavailability based on soil parameters? Part 1: Effect of soil parameters on soil solution uranium concentration. *Environ. Pollut.* 145,(2007) 587–595.
5. Vandenhove H., Gil-García C., Rigol A., Vidal M. 2009, New best estimates for radionuclide solid–liquid distribution coefficients in soils. Part 2. Naturally occurring radionuclides. *Journal of Environmental Radioactivity*.



Estimation of radiation doses to members of the public in the northern corridor of India from intake of ^{238}U in drinking water

Sunil Bhalke, S. Mishra, Sukanta Maity, Chetan B. Dusane, G.G. Pandit and V.D. Puranik
Environmental Assessment Division

This paper received the Consolation award in Poster Presentation, at the Workshop cum Seventeenth National Symposium on Environment (NSE-17), held at Indian Institute of Technology, Kanpur from 13-15 May, 2010.

Abstract

In the present paper, radiological quality in drinking water collected from northern corridor of India has been evaluated, on the basis of ^{238}U activity. The uranium activity concentration in water samples vary from 2.0 to 2802 mBq L⁻¹. These values are compared with safe limit values, recommended for drinking water, by WHO and USEPA. Annual committed effective doses due to ^{238}U was evaluated, for the adult members of the public through the ingestion of the water. The dose due to ^{238}U for all analysed samples of drinking water, are in the range of 0.07 – 92.1 mSv yr⁻¹.

Keywords: Uranium, Activity concentration, Adsorptive stripping voltammetry, Committed effective dose

Introduction

The geology of the area strongly influences the presence of natural radionuclides in drinking water. Various physico-chemical procedures and water–host-rock interactions influence their preferential mobilisation from soil/rock to water (Remy and N. Lemaitre 1990). Because of this, the concentrations are uneven and depend on the nature of the aquifer rock types and the prevailing lithology, thus the daughter products of radioactive series in water, cannot be assumed to be in radioactive equilibrium with their parents. Increased level of radionuclides present in drinking water, can become potential source of exposure to the public. Uranium is a chemotoxic and nephrotoxic heavy metal. The purpose of this study, is to estimate the concentration of uranium in drinking water and to evaluate the area-specific committed effective dose to adult members of the public, from intake of naturally occurring

^{238}U through drinking water in the northern corridor of India.

Experimental

Bore-well, well, river, surface and stream water samples were collected from northern corridor (Panjab, East Singhbhum of Jharkhand and Domiasiat sector of Meghalaya) of India and processed and analysed for uranium by Adsorptive stripping Voltammetry DPASV (Metrohm-663 VA stand), after complexing with chloroanilic acid (Bhalke *et al.*, 2005).

Results and Discussion

The activity concentrations of ^{238}U in drinking water samples, collected from different areas of Panjab, East Singhbhum of Jharkhand and Domiasiat sector of Meghalaya, are reported



in Table 1 and Figs. 1 and 2. Uncertainty reported for uranium individual analysis is at 1σ .

Activity Concentrations of ^{238}U in drinking water

Water samples were collected from four districts of Punjab state. Uranium activity concentration varies from 2.9 ± 0.3 to $2802 \pm 312 \text{ mBq L}^{-1}$ in Faridkot district, shown in Fig. 1. In 91% of water samples from Punjab, uranium concentration was found within the safe limit

recommended by AERB, India ($60 \mu\text{g L}^{-1}$ or 740 mBq L^{-1}). The elevated levels of uranium observed in few samples from Punjab, could be due to granite rock of Tusham Hills, Bhiwani district of the neighboring Haryana state of India, which contains high level of radioactivity (Kochhar, 1989) or extensive use of phosphate and other fertilizers. However based on limited number of water samples and parameters analysed, clear conclusion cannot be derived regarding the source of high uranium concentration in water, in Punjab region.

Table 1: ^{238}U activity concentrations and associated Committed Effective Dose to adult member of the public in East Singhbhum District of Jharkhand State from intake of drinking water.

Location	$^{238}\text{U}(\text{mBq L}^{-1})$	$^{238}\text{U}(\mu\text{Sv yr}^{-1})$	Location	$^{238}\text{U}(\text{mBq L}^{-1})$	$^{238}\text{U}(\mu\text{Sv yr}^{-1})$
Suvarna rekha	6.68-14.6	0.22-0.48	Bada Thalsa	25.97 ± 0.25	0.855
UCIL Barrage	6.55 ± 0.59	0.216	Turamadhi	34.62 ± 1.2	1.141
Matiguda	4.20 ± 0.49	0.138	Kudada	4.58 ± 0.025	0.151
Rakha Mines	4.58 ± 0.37	0.151	Ghagdih	10.76 ± 0.62	0.354
UCIL Colony	33.51-369	1.1-12.1	Gilindoda	5.56 ± 0.37	0.183
Bhatin School	14.84 ± 1.0	1.1	Kachha	39.57 ± 1.1	1.303
Rankini temple	4.58 ± 0.37	0.151	Kamalpur	4.08 ± 0.62	0.134
Chatikocha	3.46 ± 0.37	0.114	Trilindhi	7.42 ± 0.74	0.244
Tilaitand	32.40 ± 1.1	1.670	Keherva Dungri	8.66 ± 0.37	0.285
Chibasa	8.66 ± 0.62	0.285	Sundarnagar	13.60 ± 0.62	0.448
Dhamdum	50.70 ± 1.0	1.670	Neeldungri	27.20 ± 2.47	0.896
Matigoda	76.66 ± 1.1	2.526	Rughridhi	5.07 ± 0.74	0.167
Kerdadih	7.42 ± 0.49	0.244	Range	3.46-369	0.114-12.14

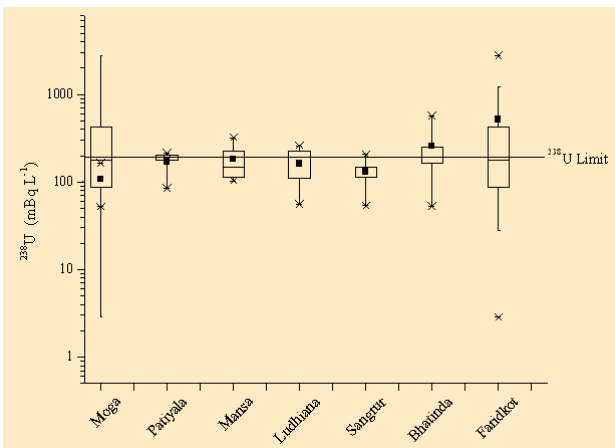


Fig. 1: ^{238}U concentrations in water samples collected from Punjab, India.

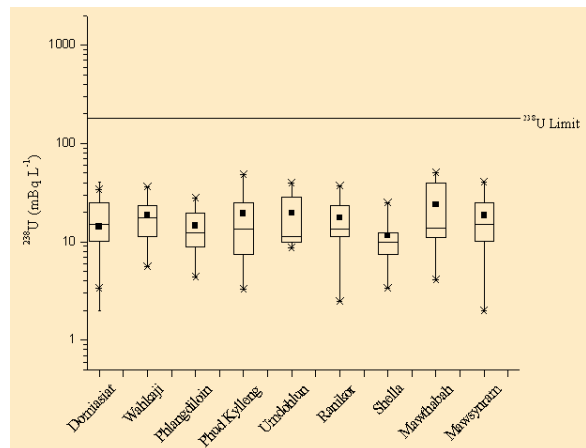


Fig. 2: ^{238}U concentrations in water samples collected from Meghalaya, India.



^{238}U concentrations in the drinking water samples are in the range of 3.46 ± 0.37 to 369 ± 9 mBq L^{-1} around East Singhbhum district of Jharkhand and are presented in Table 1. Uranium concentration in water samples collected from East Singhbhum district of Jharkhand are well within the safe limit recommended by USEPA (2004) for drinking water ($30 \mu\text{g L}^{-1}$ or 370mBqL^{-1}). Fig. 2 shows activity concentration of uranium around Domiasiat, Meghalaya which was found in the range of 2.0 ± 0.1 to 50.8 ± 2.2 mBq L^{-1} for uranium and belong within the safe limit of $15 \mu\text{g L}^{-1}$ (185mBq L^{-1}) uranium in drinking water recommended by WHO.

Estimation of the committed effective dose for adult

In order to estimate the committed effective doses for adults (20-70 y), due to drinking water intake, a consumption rate of 730L yr^{-1} , per person, was assumed. Using isotopic activity concentration in each water sample, the annual intake and the dose coefficients of the ^{238}U isotopes per unit intake ($4.5 \times 10^{-8} \text{Sv/Bq}$, for ingestion by adult members of the public, recommended by the International Commission on Radiological Protection (ICRP 1993, 1994)), the annual committed effective doses to the adult population were estimated and summarised in Table 1, Figs. 3 and 4. The Committed effective dose to adult members of the public, due to the ^{238}U in drinking water around Punjab, East Singhbhum district, Jharkhand and Domiasiat sector, Meghalaya, are in the range of $0.10 - 92.10 \mu\text{Sv yr}^{-1}$, $0.114 - 12.14 \mu\text{Sv yr}^{-1}$ and $0.07 - 1.6 \mu\text{Sv yr}^{-1}$ respectively, for ^{238}U . In Punjab region, only 5% samples showed a dose $>33 \mu\text{Sv yr}^{-1}$ for ^{238}U . The committed effective doses to the adult members of public, due to the ^{238}U in drinking water around north Indian corridor, are in the range of $0.061 - 92.10 \mu\text{Sv yr}^{-1}$. Doses from all the drinking waters are well below the reference level of the committed effective dose ($100 \mu\text{Sv yr}^{-1}$) as recommended by the WHO.

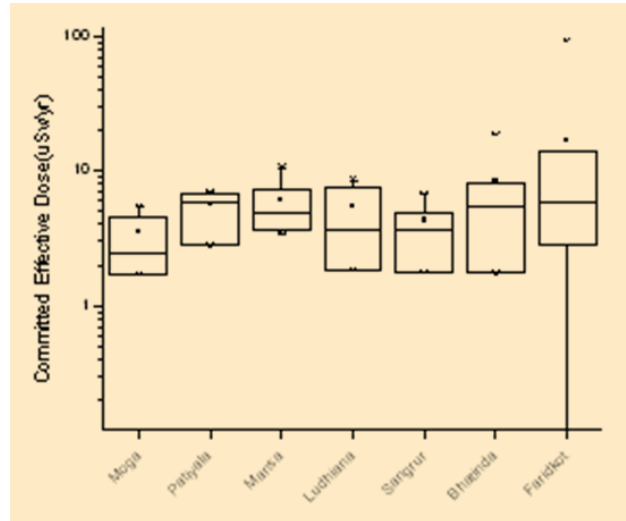


Fig. 3: Associated Committed Effective Dose to adult member of the public in Punjab state from intake of ^{238}U through drinking water.

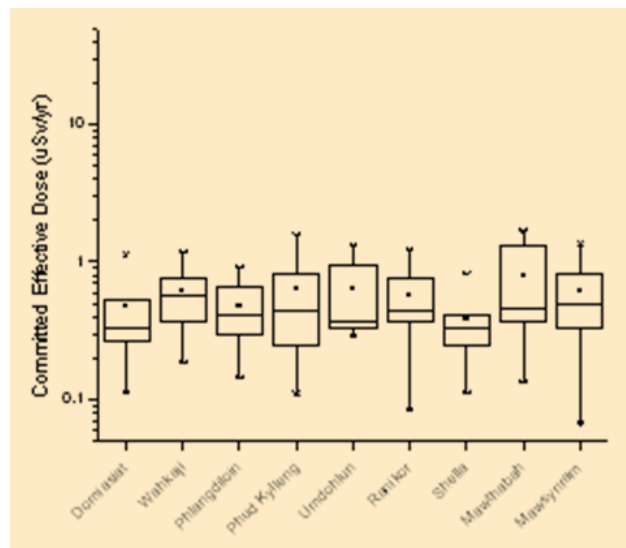


Fig. 4: Associated Committed Effective Dose to adult member of the public in Domiasiat sector, Meghalaya State from intake of ^{238}U through drinking water.

Conclusion

Uranium concentration in water ranges from 2 – 2802 mBqL^{-1} . Except for some places in Punjab, uranium concentration in all the places under study from northern



Indian corridor, are well within the limit recommended by WHO (2004). The committed effective doses to the adult members of public due to the ^{238}U for all the analysed drinking water samples are in the range of 0.07 – 92.1 $\mu\text{Sv yr}^{-1}$. Individual dose from ^{238}U are all being well below the reference level of the committed effective dose, recommended by WHO.

References

1. Bhalke, S., R. Raghunath, S. Mishra, B. Suseela, R. M. Tripathi, G.G. Pandit, V. K. Shukla and V. D. Puranik (2005). "Estimation of Uranium in Different Types of Water and Sand Samples by Adsorptive Stripping Voltametry." *Environmental Geochemistry*, Vol.8, NO.1&2, pp.180-185.
2. ICRP, International Commission on Radiological Protection, 1993. Annals of the ICRP 23, ICRP, International Commission on Radiological Protection, Publ. No. 68. Ann ICRP 24 (4), 1994.
3. Kochhar, N., *Indian Miner.*, 45, (1989): 339.
4. Remy, M.L. and N. Lemaitre, *Hydrogeologie*, 4, (1990):267.
5. USEPA, United States Environment Protection Agency. Review of RSC analysis. Report prepared by Wade Miller Associates, Inc. for the US Environmental Protection Agency. *Health Phys.*, 45, (2003): 361.
6. WHO, Guidelines for Drinking Water Quality, Third edition. Geneva, Switzerland (2004).
7. WHO, Genf. Available from: http://www.who.int/water_sanitation_health/.



Feasibility Study of phosphorus determination in (Th-U) O₂ sample using different types of solvents for the extraction of phosphomolybdic acid

B.N. Mahanty, R. Gaikwad, V.R. Sonar, S. Raul, D.K. Das, A. Prakash, Md. Afzal and J.P. Panakkal

Advanced Fuel Fabrication Facility, Bhabha Atomic Research Centre, Tarapur 401502

This Paper received the Best Paper Poster Award at the Symposium SESTEC-2010 held at IGCAR, Kalpakkam, from 1-4 March, 2010

Abstract

A simulated study has been carried out, for the determination of phosphorus in the synthetic mixture of known amount of phosphorus with equal concentration of uranium and thorium in perchloric acid medium, by optical fiber-based uv-visible spectrophotometer, using conventional molybdenum blue technique. Isobutyl methyl ketone and isobutanol solvents are used for the extraction of phosphomolybdic acid, formed in the intermediate steps of the molybdenum blue technique. The mean percentage recovery of phosphorus in the extraction with isobutyl methyl ketone and isobutanol solvents is found to be 93.3 % and 88.0% respectively.

Introduction

Phosphorus is an important chemical specification of the fuel, for the proposed Advanced Heavy Water Reactor (AHWR)¹. The AHWR fuel comprises a composite fuel cluster of (Th-²³³U)O₂ and (Th-Pu)O₂ fuel pins. Trace amount of phosphorus gets incorporated in these kinds of fuels, because of the monazite ore which contains phosphorus in the form of phosphate and the use of tri butyl phosphate in the processing of uranium, thorium and plutonium from spent nuclear fuels. The presence of phosphorus more than the specified limit, may affect the fracture toughness of the zircaloy cladding material, resulting in failure of the fuel pin². Hence, it is desirable to know and control this impurity in the nuclear fuel, before encapsulating it into the zircaloy cladding tube. Accurate determination of phosphorus at low levels is difficult, even with very sensitive analytical techniques like Inductively Coupled Plasma Mass Spectrometry (ICP-MS) or Graphite Furnace Atomic Absorption Spectrometry

(GFAAS)³. However, a sensitive and selective spectrophotometric method could be employed, for the determination of total phosphorus in the (Th-U) O₂ fuel, using conventional molybdenum blue technique⁴, which follows measurement of the concentration at 725nm. Solvent extraction is performed in one of the steps of this method, in order to increase the sensitivity of the determination.

A simulated study has been performed by preparing a synthetic mixture, on adding known amount of phosphorus with equal concentrations (4mg/ml) of uranium and thorium solutions in perchloric acid medium, followed by determination of the phosphorus using molybdenum blue technique. In the present work, the phosphomolybdic acid formed in the intermediate step by reaction with sodium molybdate and o-phosphate in the acidic medium, is extracted into two different types of solvents, viz. isobutyl methyl ketone and isobutanol and subsequently reduced to molybdenum blue. The absorbance of the



molybdenum blue was measured, using an optical fiber-based UV-Visible spectrophotometer, in the range of 710 -725 nm.

It is an endeavor to study the percentage recovery of phosphorus in the form of phosphate for both the extraction and compared.

Experimental

The uranyl nitrate and thorium nitrate solutions were separately brought to perchloric acid medium, by repeated evaporation upto dryness using 70% perchloric acid. The solutions were made up to the mark in a 50 ml volumetric flask as per required concentration of 4mg/ml of U and Th respectively. Synthetic mixture was prepared by mixing 1.5ml each of these two solutions, containing 4mg/ml of U and Th in perchloric acid medium, with 2ml of the standard solution of tri-sodium o-phosphate, having 25 μ g/ml of phosphorus in a 100ml borosilicate beaker. The mixture was heated on a hot plate until a dense white fume was observed. Subsequently it was allowed to cool at room temperature and mixed with 40ml doubly distilled water, followed by addition of 5ml 10% (w/v) sodium molybdate solution, to produce light yellow coloured phosphomolybdate acid. Afterwards, the whole reaction mixture was taken in a clean 125 ml separating funnel and was allowed to stand for 5 minutes, in order to complete the reaction. 40 ml of either isobutanol or isobutyl methyl ketone was added to this mixture and vigorously shaken for 1 minute, to extract the phosphomolybdate complex. After discarding the aqueous phase, the organic phase containing the phosphomolybdate was washed twice with 50ml of doubly distilled water. Subsequently, the aqueous phase was discarded and the organic phase was equilibrated with 25ml of stannous chloride solution for 15 seconds, so that all the phosphomolybdate gets converted to molybdenum blue. The aqueous phase was discarded and the organic phase was transferred into a 50ml volumetric flask and the inner wall of the separating funnel was

washed with a few ml of the organic phase, to collect back any traces of molybdenum blue sticking to the inner wall of funnel and finally made up to 50ml with the organic phase. The absorbance of the solutions was measured in the range of 710 - 725 nm, using a commercial optical fiber-based uv-visible spectrophotometer. All the extraction work was carried out in the fume hood, in order to avoid exposure to hazardous organic solvents.

Results and Discussion

Calibration curves of spectrophotometric measurement were performed, using standard solution of tri sodium o-phosphate in the identical way as described above, except for the addition of Th and U in HClO₄, 3ml of 70% HClO₄ was added in the initial step. The working standard of 0.5, 1.0 and 1.5 ppm of P was used. The correlation coefficients were found to be 0.999 and 0.997 for the extraction with isobutanol and isobutyl methyl ketone respectively, indicating an acceptable precision of linear calibration curves. Table 1 and Table 2 show the calibration data using isobutanol and isobutyl methyl ketone respectively, for the extraction of phosphomolybdate. Table 3 contains the data in the analysis of the synthetic mixture.

Table 1: Calibration of the spectrophotometer using tri sodium o-phosphate in the extraction with isobutanol

Concentration of P (ppm)	Absorbance (Avg. of 3 no. of data)
0.5	0.295
1.0	0.622
1.5	0.979

Table 2: Calibration of the spectrophotometer using tri sodium o-phosphate in the extraction with isobutyl methyl ketone

Concentration of P (ppm)	Absorbance (Avg. of 3 no. of data)
0.5	0.130
1.0	0.303
1.5	0.506



Table 3: Phosphorus determination in the synthetic mixture using isobutyl methyl ketone & isobutanol for the extraction

P added (ppm)	Absorbance		% Recovery	
	Extracted with isobutyl methyl ketone	Extracted with isobutanol	With isobutyl methyl ketone	With isobutanol
1.0	0.290	0.541	93.9	86.7
1.0	0.279	0.558	91.0	89.2
1.0	0.294	0.551	94.9	88.2

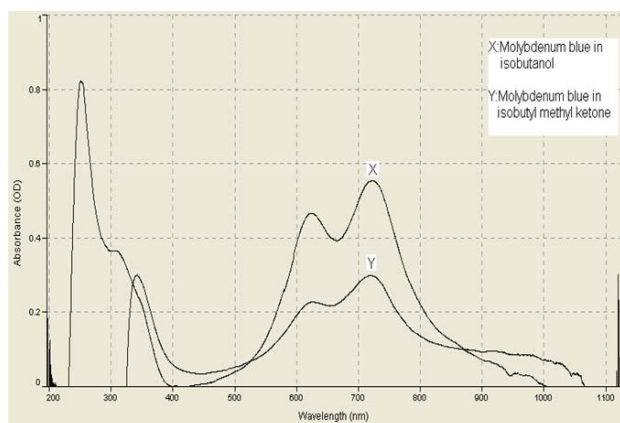


Fig. 1: UV-visible spectra of molybdenum blue in the analysis of the synthetic mixture containing 1 ppm phosphorus

The mean percentage recovery of phosphorus was found to be 88.0% and 93.3% for 1-ppm phosphorus with the precision, expressed in terms of standard deviation (σ) as 0.013 (n =3) and 0.020 (n=3) for the extraction with

isobutanol and isobutyl methyl ketone respectively. The better recovery with isobutyl methyl ketone may be because of its lower solubility in the aqueous medium as compared to that of isobutanol. It is obvious from Fig. 1 that the hump in 650-700nm ranges of molybdenum blue spectra becomes flattened and also a decrease of absorbance in presence of isobutyl methyl ketone is seen.

Conclusion

Even though the sensitivity of the determination of phosphorus with isobutyl methyl ketone is poorer as compared to that of isobutanol, the percentage recovery of phosphorus with the former solvent, is found to be better as compared to the latter. Further work is under progress, in order to optimize the process of determination of phosphorus in this kind of matrix.

References

1. T.R.G. Kutty , M.R. Nair , P. Sengupta , U. Basak , Arun Kumar , H.S. Kamath ; *Journal of Nuclear Materials* 374 9 (2008).
2. S.M. Dhavile, R. Shekhar, S. Thangavel, S.C. Chaurasia, J. Arunachalam; *Talanta* 76 134 (2008).
3. D.M. Hughes, D.C. Gregoire, H. Naka, C.L. Chakrabarti; *Spectrochim. Acta*, B53, 1079(1998).
4. Annual book of ASTM standards, Vol.12.01, C799, p460 (1986).



High Speed Cryogenic Turboexpander Rotor for stable operation up to 4.5 kHz Rotational Speed

Rajendran Menon, Anindya Chakravarty, Mukesh Goyal, Mohananand Jadhav,
Arun S., Satish Kumar Bharti and Trilok Singh
Cryo-Technology Division

This paper received the Best Paper Award at the Twenty Third National Symposium on Cryogenics (NSC-23) held at NIT, Rourkela, during October 28-30, 2010

Abstract

BARC has been working towards the development of gas-bearing-supported, high-speed turboexpander rotors, for use in indigenous helium liquefiers and refrigerators. Extensive experiments have been carried out, to obtain the dynamic characteristics of the rotor, both during coast-up as well as coast-down operations. The objective of these experiments is to identify the critical speeds of the rotor and relate it with the bearing clearance. This would enable design of radial bearings with proper clearance, so as to avoid the occurrence of critical speed near the range of rated rotor operational speeds. The present paper documents the experience of stable rotation of several 16 mm diameter cryogenic turboexpander rotors, during recent laboratory test runs. Snap shots from FFT analyzer during the experiments as well as synchronous response to unbalance for coast-up and coast-down operations, have been included.

Keywords: Cryogenic Turboexpander, Helium liquefier/ refrigerator plant, Gas Bearing, synchronous response to unbalance

Introduction

Turboexpander is a key focus area for BARC, in its program for indigenous development of helium refrigerators and liquefiers [1, 2]. From a consideration of the process cycle design of these liquefiers and refrigerators, turbine with rotor speeds in excess of 4kHz and size of 16mm is envisaged and developed. The exceptionally high rotating speeds coupled with the stringent requirement of line purity, necessitate the use of process gas (helium) as lubricant.

The vertically oriented turboexpander rotor [Fig.1] has a turbine and brake wheel at its two ends. The shaft consists of a collar, which together with the thrust bearings on its either side, forms the axial bearing system. Improvements have been made, over a period of time, in the thrust bearing design and configuration, to enable a jump in the stable operating speed of the rotor from 3.3 kHz [3]

to 4.2 kHz [4] and now to 4.5 kHz (theoretical design speed). The present design incorporates a top thrust bearing of tilting pad type [Fig.2] while the bottom one is helical grooved [Fig.3]. Damping, in the form of silicon rubber, is provided around the pad pivot. This combination of bearing has emerged to be the best during our laboratory trials, being particularly successful in passing over critical speeds, owing to the conformability and tilting action of the pads and good load bearing characteristics of the grooves. The journal bearing system constitutes the shaft and a pair of tilting pad bearings [Fig.4], designed to align the rotor and takeup any load due to unbalance. The weight of the rotor is taken up by a passive magnetic bearing, consisting of repelling magnets lodged in shaft and housing [Fig.1]. This system also aids in smooth take off and landing of the rotor.

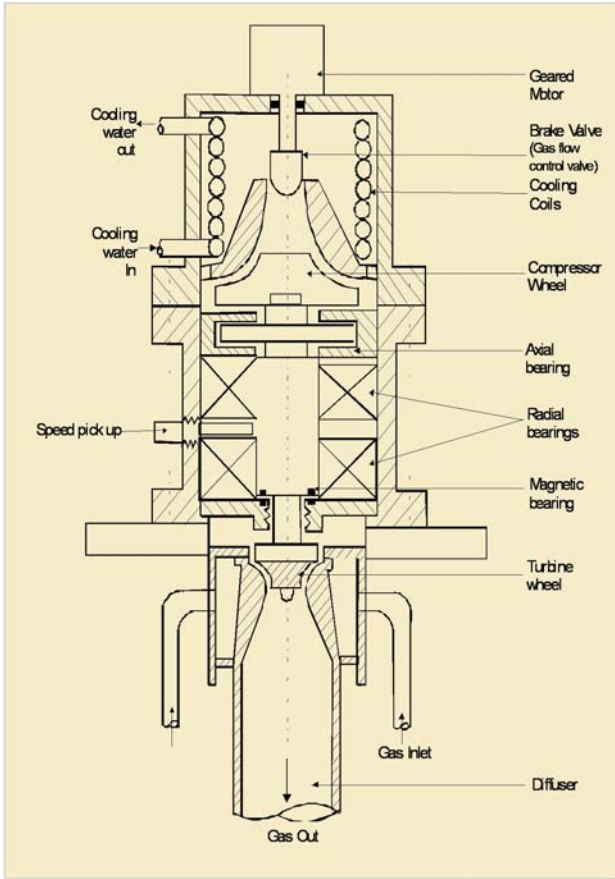


Fig. 1: Schematic of a typical cryogenic turboexpander



Fig. 2: Tilting Pad Top Thrust Bearing.



Fig. 3: Helical Grooved Bottom Thrust Bearing.



Fig. 4: Tilting Pad Journal Bearing.

**Rotor Bearing System – Major Specifications
Thrust Bearing**

Clearance (End Float): 70 to 150 microns (varies from unit to unit).

Pad material: AISI 4140 Steel.

Journal Bearing

Diametral Clearance: 75 to 100 microns (varies from unit to unit).

Pad material: Graphite impregnated with Babbit alloy.

Merit Award



Rotor

Unbalance: less than 6 mg at 8mm radius, both at the turbine as well as the brake compressor ends.

Rotor Bearing Run out: 10 microns or less is tolerated on the thrust bearing face. The shaft cylindricity and run out of the collar (thrust bearing face) is of the order of 2 microns. Shaft Material: K Monel 500.

Magnetic Bearing

Magnetic material: Samarium Cobalt.

Field strength: 1.65 K Gauss on flange and 0.5 K Gauss on rotor (for a rotor lift of 350 – 400 microns).

Clearance between turbine and diffuser

200 to 300 microns (varies from unit to unit).

Turboexpander Housing Design/Assembly Issues

Fig. 5 shows a sectional view of a typical cryogenic turboexpander housing. The major design and assembly issues for the system are discussed below.

- a) Tolerance build up effects are taken care of through spacers. These spacers are used to control the total thrust bearing clearance (axial end float), axial clearance between the turbine impeller and diffuser as well as the clearance between the brake compressor and its inducer.

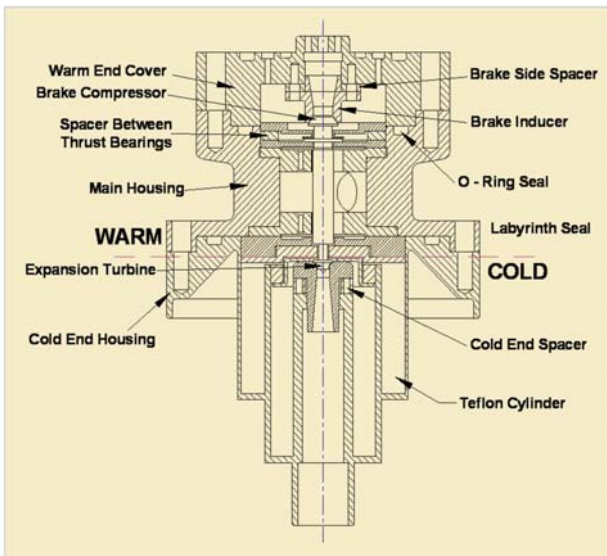


Fig. 5: Sectional view of a typical cryogenic turboexpander housing.

- b) The assembly is based on axial sealing using O-rings.
- c) Cold leakage is prevented by use of hollow and thin members at the cold end, Teflon® cylinder and labyrinth seal.
- d) High quality fabrication and run out of the order of 10 microns is required for proper alignment.
- e) Permanent joint (welding) is used at the cold end.

Rotordynamic Evaluation of the Turboexpanders

Several rotors are assembled and rigorous rotor dynamic trials conducted at the CrTD laboratory, to gauge the dynamic characteristics of the unit. The parameters of significance for these tests are the vibration signature and the starting/takeoff pressure at each successive run. The rotors tested have survived more than 20 start-stops without any significant change in starting pressure (1.5 bar gauge at HP turbine inlet) and vibration signature.



Fig. 6: Laboratory Experimental Rig.

Merit Award



The Experimental Rig

The rotor dynamic test rig consists of a small cold box with the turboexpander unit mounted on top of it. [Fig.6]. Helium gas is fed to the system from a screw compressor (13 bar HP to 1 bar LP) with a maximum delivery of 2 Nm³/min.

The Vibration Analyzer System

The instrumentation involves Industrial ICP® accelerometers, make IMI, model M621B40 (weight: 2.8 g, range 1.6 to 30000 Hz, sensitivity: 10mV/g, resonant frequency: 85kHz) mounted on the turboexpanders and signals fed to an OROS® vibration analyzer system [Fig. 7] with real time Fast Fourier Transform (FFT) capabilities using OROS® NVGate® software. It is possible to record the vibration signatures and play back for post analysis.

The rotor speed sensing system

The rotor speed is sensed through a magnetic type speed pickup [Fig.8] and a magnetic target fixed to the shaft and located in between the two journal bearings. This target is shrink fitted in a diametral hole drilled through the non magnetic shaft. The speed pick up tracks the rate of change of magnetic flux linkage above a threshold limit and twice per shaft revolution.

At any given rotor speed, the FFT shows all the components of vibration, synchronous, sub-synchronous

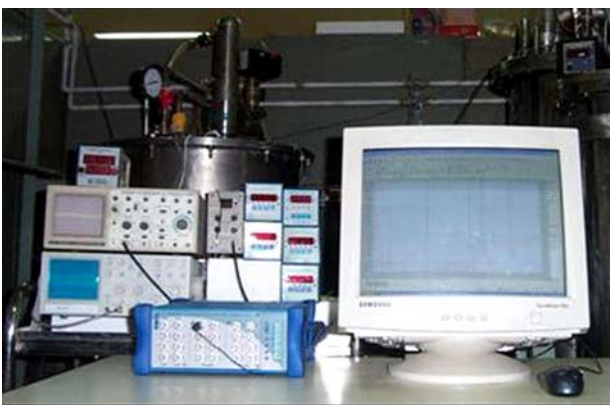


Fig. 7: OROS® Vibration Analyzer System



Fig. 8: Magnetic type speed pick-up

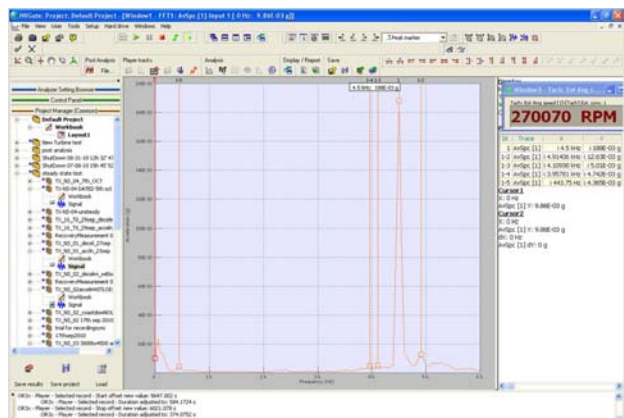


Fig. 9: FFT snapshot of "tx-ns-01" at maximum operating speed of 2,70,070 RPM.

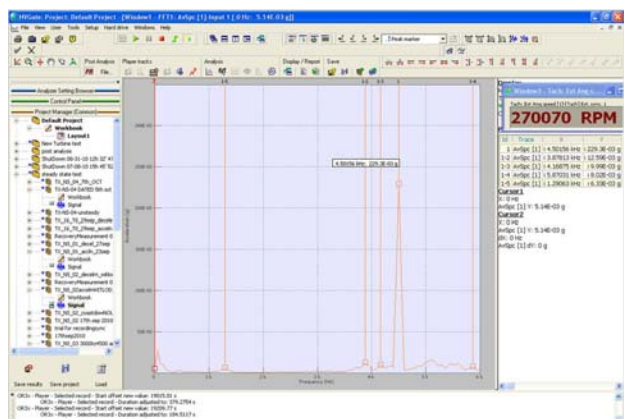


Fig. 10: FFT snapshot of "tx-ns-02" at maximum operating speed of 2,70,070 RPM.

Merit Award

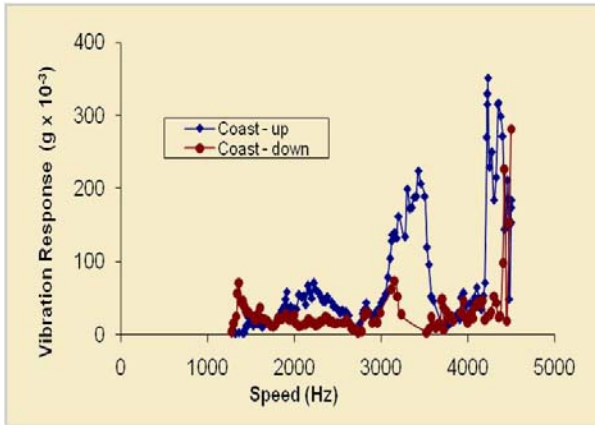


Fig. 11: Synchronous Vibration Response Plot for "tx-ns-01".

as well as super synchronous. Snapshots from the FFT response at highest operating speeds of 2,70,070 RPM for two different assembled rotors "tx-ns-01" and "tx-ns-02" are shown on Figs. 9 and 10 respectively. Synchronous vibration response in terms of 'g' – the acceleration due to gravity for the full range of speeds right from start-up and up to the maximum operating limit for the two turboexpander rotors "tx-ns-01" and "tx-ns-02" are shown in Figs. 11 and 12. Both the coast-up and coast-down responses are represented in the same graph.

Observations and Discussions

It is clear from Fig. 9 and 10 that the vibration levels at the maximum operating speed of 4.5 kHz is very low, 0.18 g and 0.22 g respectively. The same is true for all other rotors tested in the laboratory. All along, during the coasting up (and also during coasting down), no evidence of any half speed whirl is seen. Even the snapshot does not show any significant half speed vibration component. This concludes that the current design of rotor bearing system is stable for the range of operation of our interest.

The synchronous vibration plots of Figs. 11 and 12, throws light on some other aspects of the rotordynamic system. It is very much conclusive from the curves, especially during coast-up, that a system critical speed is present in the vicinity of 4 kHz. The critical speed is also seen to be split. The bearing x-y asymmetry, due to

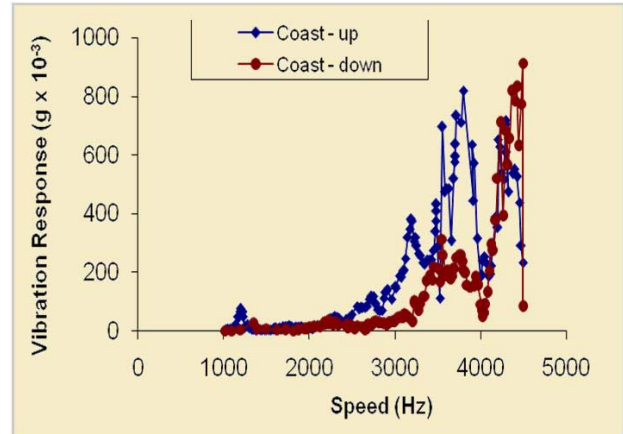


Fig. 12: Synchronous Vibration Response Plot for "tx-ns-02".

3 tilting pads being arranged symmetrically in 360°, may be the cause of this split.

It is also observed that the peak vibration response varies slightly from unit to unit. It is not possible to replicate the exact journal bearing clearance on all units and hence, the bearing radial stiffness, which is a strong function of this clearance, varies from unit to unit. The critical speed, in turn, shows slight variation too. The damping available in the current design is sufficient for all the rotors to pass through the critical speed to maximum operating speed. However, future higher efficiency turboexpanders with smaller gaps between turbine and diffuser might require smaller bearing clearance backed up by more effective radial damping to pass through critical speeds without any glitch. To achieve those tight clearances, a much higher quality of machining is required though.

References

1. Singh, T., Chakravarty, A. et al. "Cryogenic Refrigeration and Liquefaction Technology Development in BARC", *Indian Particle Accelerator Conference InPAC – 2006, BARC/TIFR, Mumbai* November 1 – 4, 2006
2. Singh T, Chakravarty A, et al., "Development of Helium Liquefaction/Refrigeration System at BARC", *Indian Journal of Cryogenics Special Issue Vol. 1*, pp 53-58. (2005)

Merit Award



3. Singh T, Chakravarty A. et al., "Stable Operation of a Cryogenic Turboexpander with Flexible Thrust Bearings", *Advances in Vibration Engineering* Vol. 3, pp 114-122. (2004)
4. A. Chakravarty, R. Menon, et al., "Development of Tilting Pad Thrust Bearings for Cryogenic Turboexpanders" *Indian Journal of Cryogenics* Vol. 35, pp 39-44. (2010)



Laser Assisted Decontamination of Nuclear Fuel Elements

J. Padma Nilaya and Dhruba J. Biswas

Laser & Plasma Technology Division, BARC

and

Aniruddha Kumar and Chandrakant Sharma

AFFF, BARC, Tarapur

This paper received the Best Paper Award at the National Laser Symposium held at RRCAT, Indore, during December 1-4, 2010

Abstract

Nuclear fuel elements get contaminated on their outer surface during the pellet loading operation, by powdery radioactive oxide particulates. The high radiotoxicity and hard gamma activity associated with the MOX fuel, render the conventional methods of cleaning impractical. We report here the satisfactory laser assisted cleaning of PFBR fuel elements, contaminated by UO_2 and PuO_2 particulates remotely inside a fume hood. The residual activity here was found to be well within permissible limits, thus making the laser assisted cleaning an attractive and viable alternative to the currently employed ultrasonic method of cleaning.

There is an ever-growing demand of plutonium bearing fuels mainly in the form of mixed oxide (MOX) in the nuclear industry. MOX fuels ($\text{UO}_2 + \text{PuO}_2$) are successfully being used in several BWRs and PWRs world-wide. The second stage of India's nuclear energy programme relies on Fast Breeder Reactors that will utilize MOX fuels with high plutonium content. AHWR will also utilize plutonium bearing MOX fuel along with Thoria- Urania fuel. The cylindrical MOX fuel pellets are loaded into a thin walled tube called the fuel element, after which it's two ends are welded with end plugs. The pellet loading operation, that involves pushing the fuel pellets literally into the element, leads to the accumulation of loose contamination on the tube surface in general and the tube ends in particular. The high radiotoxicity associated with Plutonium and hard γ activity associated with the daughter products of U^{232} , makes the handling of fuel elements highly hazardous, and therefore, the need arises for

developing a remote method of decontamination. Conventional methods of surface cleaning e.g., the mechanical or the chemical methods are always abrasive in nature and therefore cannot be applied to the fuel elements, due to the possibility of damage to the clad surface. The most common method of decontaminating the fuel elements until recently, has been to clean the elements inside the glove box with a soft wet cloth and repeat the procedure after their removal from the glove box through a transfer port. This process leads to undue exposure to the individuals, generates large secondary wastes, may release air borne activity in the working area in addition to being time consuming. Of late, ultrasonic cleaning has been found effective for this application. This process, that requires the fuel elements to be submerged in specially designed ultra-sonic tanks with fume hoods, generates large liquid waste necessitating an additional step of treating the active liquid.



The use of lasers to decontaminate radioactive metal surfaces has generated considerable interest in recent years, as it has two major advantages over the conventional methods¹. First of all, it is a dry process generating very little secondary waste and secondly it is a non-contact process, which can take place inside the glove box, without any manual interference, as the laser beam can be transported into the box either through transmissive optics or by an optical fibre. Motivated by these facts, we have now attempted to employ laser as a decontamination tool, for the cleaning of nuclear fuel elements after the pellet loading operation.

The loosely bound fuel particulates are attached to the substrate predominantly, by Van-der-Waal's forces [2], the removal of which can be achieved at a laser intensity much lower than that required for surface melting/vapourisation. The absorption of the incident energy by the substrate and/or the particulates causes rapid rise in the local temperature, leading to their sudden expansion. If the resulting force exceeds the Van-der-Waal's force, the particulates can be dislodged. The laser parameters that play a major role in the cleaning process are the fluence, pulse duration, and its wavelength. We carried out initial cleaning experiments with suitable contamination, simulated on samples made out of commonly used clad materials, to have a rough estimate of the laser parameters that are appropriate for cleaning²⁻⁴. These experiments involved the study of the cleaning efficiency as a function of the wavelength and fluence of the incident radiation. In addition to obtaining a firsthand experience in laser assisted cleaning of loose contamination of various kinds of substrates, these studies also revealed some interesting facts, hitherto unknown, with regard to the physical mechanism underlying the particulate removal, when irradiated by a laser. Absorption of the incident radiation by the substrate, was found to play a dominant role as against absorption in the particulates, leading to a better cleaning efficiency in the former case. Further, small signal absorption measurement of the incident coherent radiation by the metal surface, revealed an increase in the absorption by the surface, in the presence of transparent/semitransparent particulates on

it. This effect, identified as field enhanced surface absorption, has been found to increase with reduction in the average particulate size. Consequently, higher laser assisted removal efficiency of contamination from a metal surface has been observed, for smaller transparent contaminant particulates⁴.

Following these precursor studies, we then attempted to clean the PFBR fuel element surface (6.6 mm dia, SS, over a length of 30 cm) contaminated with plutonium and uranium oxide particulates. A work station capable of providing simultaneous rotational and translational motion to the fuel rod was made use of for this work. The pitch of rotation and the repetition rate of the laser were adjusted so as to expose the entire surface area of the fuel element to the laser beam. It may be noted here, that owing to the circular shape of the laser beam and the need to expose the entire surface, some amount of overlap between the successive exposures was essential. The cleaning of fuel elements was performed inside a fume hood in a laboratory at AFFF, BARC, Tarapur. The laser beam, steered into the fume hood by means of appropriately arranged mirrors, irradiated the fuel rod. A schematic diagram of the experimental set-up is shown in Fig 1. The negative pressure gradient maintained inside the fume hood ensured that ejected particulates found their way into the filter attached to the fume hood outlet and no air borne activity contaminated the working area. Further, usage of an inert purge gas prevents re-deposition of the ejected particulates and facilitates their efficient arresting in the filter.

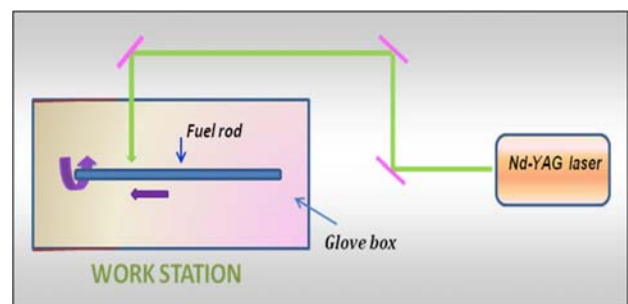


Fig. 1: Schematic diagram of the laser assisted decontamination set-up.



Decontamination experiments with PFBR clad surface contaminated with both UO_2 and PuO_2 particulates, were performed for two wavelengths viz., 1064 nm and 532 nm. The threshold fluence that was required to bring down the activity to the permissible level, was ascertained for both the wavelengths. The alpha activity on the surface of the fuel tube was measured before and after laser irradiation, by taking a swipe from a small area, counting the activity using a ZnS scintillation detector and then extrapolating the value for the entire surface area.

Laser assisted cleaning of PFBR clad surface contaminated with UO_2

Powdery UO_2 contamination smeared on to a part of the clad surface of PFBR element (6.6 mm dia, over a length of 30 cm) could be successfully removed, by making use of 532nm and 1064 nm coherent radiation derived from an Nd-YAG laser. The residual activity on the clad surface after laser irradiation was measured. The fluence of the incident laser pulse required to reduce the residual activity to well within the permissible levels (which normally is taken as the background activity) was determined. Detailed results of this investigation are summarized in Table 1. As

can be seen from the table, 532 nm radiation appears more effective in cleaning UO_2 contamination off SS surface. No observable change was found to occur on the clad surface, as a result of exposure to either of the wavelengths

Laser assisted cleaning of PFBR clad surface contaminated with PuO_2

PFBR fuel elements, 30 cm long with end plugs welded and surface contamination of PuO_2 at the same level as that of a loaded PFBR fuel element, have been successfully cleaned by exposing the fuel element surface to laser radiation of appropriate fluence and wavelength. Laser cleaning could bring down the contamination level to within the acceptable limit. In contrast to the finding in case of UO_2 contamination, here the residual activity could be brought down to the background level, with much lower fluence for 1064 nm radiation. Further, while oxidation of the tube was observed when cleaned with 532nm radiation, no such effect was apparent on visual inspection when cleaned with 1064 nm radiation. Detailed results of this investigation for both 532 nm and 1064 nm coherent radiation are summarized in Table 2.

Table 1: Summary of work on the laser assisted cleaning of UO_2 contamination off PFBR clad surface

S. No	Wavelength	Fluence (mJ/cm ²)	Initial activity (α) (Bq/cm ²)	Final Activity (Bq/cm ²)	Acceptable level of activity (Bq/cm ²)
1	532 nm	861	2.13	0.008	0.04
		470	2.11	0.008	0.04
		313	2.14	0.032	0.04
2	1064 nm	855	2.11	0.008	0.04
		400	2.15	0.02	0.04

Table 2: Summary of work on the laser assisted cleaning of PuO_2 contamination off PFBR clad surface

S. No	Wavelength	Fluence (J/cm ²)	Initial activity (\acute{a}) (Bq/cm ²)	Final Activity (Bq/cm ²)	Acceptable level of activity (Bq/cm ²)
1.	532 nm	1.17	27.47	0.018	0.04
		1.06	27.1	0.185	0.04
		0.86	27.24	0.66	0.04
2.	1064 nm	0.9	27.35	0.01	0.04
		0.77	27.51	0.02	0.04
		0.64	27.49	0.078	0.04



Table 3: Laser assisted cleaning of PuO_2 & UO_2 contamination off PFBR clad surface for most optimized operating conditions (Wavelength – 1064 nm, Fluence – 1.19 J/cm², Repetition Rate – 3.3 Hz, linear speed = 1.52 mm/sec)

S. No. of the fuel rod	Initial activity (Bq/cm ²)	Final Activity (Bq/cm ²)	Acceptable level of activity (Bq/cm ²)
1	6.47	0.006	0.04
2	6.43	0.008	0.04
3	6.39	0.008	0.04
4	6.51	0.004	0.04
5	6.45	0.005	0.04
6	6.58	0.006	0.04

Taking a clue from these studies, we next fixed the laser parameters for the highest cleaning efficiency and conducted the next experiment, wherein a number of loaded and end plug welded PFBR fuel tubes with varied initial surface contamination, comprising of UO_2 and PuO_2 , were laser cleaned. It may be noted here, that the measured α activity of the contaminated PFBR fuel element, owes its origin primarily to the presence of Pu due to its much higher specific activity. The results have been summarized in the Table 3.

It would be seen from this table that laser cleaning could always bring down the activity well below the permissible level. The time required to clean a 30 cm fuel element was found to be ~200 seconds. By suitably modifying the motor parameters and the repetition rate of the laser, the cleaning time can be reduced. It is of interest to note, that the two steps that are compulsorily followed in the currently adopted process of fuel element decontamination, viz., ultrasonic cleaning followed by manual cleaning, can be totally dispensed with, if laser is employed as the cleaning tool.

Acknowledgements

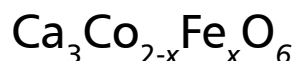
The authors gratefully acknowledge A. K. Das, J. P. Panakkal, L. M. Gantayet and H. S. Kamath for their constant encouragement and support.

References

1. L. Li, The potential role of high-power lasers in nuclear decommissioning, *Nuclear Energy* 41, 2002: (397-407).
2. J. P. Nilaya, A. Kumar, P. Raote, and D. J. Biswas, Laser assisted decontamination: A wavelength dependent study, *Appl Surface Science* 254, 2008: (7377-7380).
3. J. P. Nilaya, A. Kumar, P. Raote, M. B. Sai Prasad, and D. J. Biswas, Study of laser assisted decontamination of commonly used clad surfaces, *J. Laser Applications* 18, 2006:(294-296).
4. J. P. Nilaya and D. J. Biswas, Laser assisted decontamination of metal surface: Evidence of increased surface absorptivity due to field enhancement caused by transparent/semi-transparent contaminat particulates, *Applied Surface Science* 256, 2010: (1867-1870).



Magnetism of geometrically frustrated quasi-one-dimensional-spin-chain compounds



A. Jain and S.M. Yusuf

Solid State Physics Division

This paper received the Best Poster Award at the Conference on Advances in Magnetism: Phenomena and Materials (AMPM-2010), held at Manali, Himachal Pradesh, during June 3-5, 2010

Abstract

We report the effect of Fe substitution on magnetic properties of the compounds $\text{Ca}_3\text{Co}_{2-x}\text{Fe}_x\text{O}_6$ ($x = 0.2$ and 0.4), crystallizing in the space group $R\bar{3}c$. Rietveld refinement of neutron diffraction patterns and Mössbauer study confirmed, that Fe ion was located at trigonal prism site. Above 50 K, magnetic susceptibility obeys the Curie-Weiss law. The value of paramagnetic Curie temperature (θ_p) for $x = 0.2$ and $x = 0.4$ samples are 7.5 and -1.6 K, respectively. The neutron diffraction patterns at 1.5 K can be fitted with the amplitude modulated structure as well as the partially disordered antiferromagnetic structure.

Keywords: Neutron diffraction, spin-arrangement in spin-chain compounds, frustration

Introduction

Among the A_3MXO_6 type [$A = \text{Ca}, \text{Sr}$, and (M, X) = alkali or transition metal ions] quasi one-dimensional spin-chain compounds, the compound $\text{Ca}_3\text{Co}_2\text{O}_6$ and its derivative [1-5], crystallizing in the rhombohedral structure (space group $R\bar{3}c$), have recently attracted much interest, because of their peculiar magnetic properties. The crystal structure of the compound $\text{Ca}_3\text{Co}_2\text{O}_6$ consists of spin-chains, made up of alternating face sharing CoO_6 octahedra (OCT) and CoO_6 trigonal prism (TP). These chains are arranged on a triangular lattice and are separated by Ca^{2+} ions. The ferromagnetic (FM) intrachain and antiferromagnetic (AFM) interchain interactions, combined with a triangular lattice arrangement of spin-chains, give rise to geometrical frustration in this compound. Due to crystalline electric field, the Co^{3+} ions in this compound are in low spin ($S = 0$) and high spin ($S = 2$) states at the OCT and TP sites,

respectively. Below 25 K, the compound $\text{Ca}_3\text{Co}_2\text{O}_6$ undergoes a very complex 3D magnetic ordering due to the effect of geometrical frustration [4].

In order to examine the effect of 3d electron filling at octahedral/tetrahedral sites on the crystal structure and magnetic properties of the compound $\text{Ca}_3\text{Co}_2\text{O}_6$, we have substituted cobalt with iron. Here we report the results of the x-ray, Mössbauer, dc magnetization, and neutron diffraction studies of the compounds $\text{Ca}_3\text{Co}_{2-x}\text{Fe}_x\text{O}_6$ ($x = 0.2$ and 0.4).

Experimental

Polycrystalline samples of the compounds $\text{Ca}_3\text{Co}_{2-x}\text{Fe}_x\text{O}_6$ ($x = 0.2$ and 0.4) were prepared by the conventional solid state reaction method [1]. Neutron diffraction experiments at room temperature were carried out on a



powder diffractometer ($\lambda = 1.249\text{\AA}$), at the Dhruva research reactor, Trombay. The neutron diffraction experiments in the temperature range 1.5-100 K were performed using the cold neutron powder diffractometer DMC ($\lambda = 2.46\text{\AA}$) at the Paul Scherrer Institute (PSI), Switzerland. The diffraction data was analyzed by the Rietveld refinement method, using the FULLPROF [6] program. The dc magnetization measurements were carried out using a commercial (Oxford Instruments) vibrating sample magnetometer. Mössbauer spectra for Fe doped samples were recorded at room temperature, using ^{57}Co as γ -ray source.

Results and Discussion

Rietveld refinement of neutron diffraction patterns for $x = 0.2$ and 0.4 compounds at 297 K, confirms the single phase formation of these compounds in the space group $R\bar{3}\bar{c}$ [1]. In Figs. 1 (a) and (b), we show Rietveld refined

x-ray and neutron diffraction patterns only for the $x = 0.4$ compound. The refinement confirmed that Fe ion was located at TP site (6a).

Fig. 1 (c) depicts Mössbauer spectra for $\text{Ca}_3\text{Co}_{2-x}\text{Fe}_x\text{O}_6$ ($x = 0.2$ and 0.4) at room temperature, fitted well with asymmetric doublet. Analysis of these spectra gives the quadruple splitting $|QS|$: 1.23, 1.23 mm/s and isomer shift (IS): 0.40, and 0.40 mm/s for $x = 0.2$ and 0.4 samples, respectively. From these values, we can conclude that for both compounds, Fe is located at trigonal prism site and it is in Fe^{+3} high spin state ($S = 5/2$).

Temperature dependence of inverse magnetic susceptibility, shown in Figs. 2 (a) and (b), obeys the Curie-Weiss law in high temperature region for both compounds. The values of paramagnetic Curie temperature (θ_p) for $x = 0.2$ and $x = 0.4$ compounds are 7.5 and -1.6 K, respectively. In literature, reported value of θ_p for

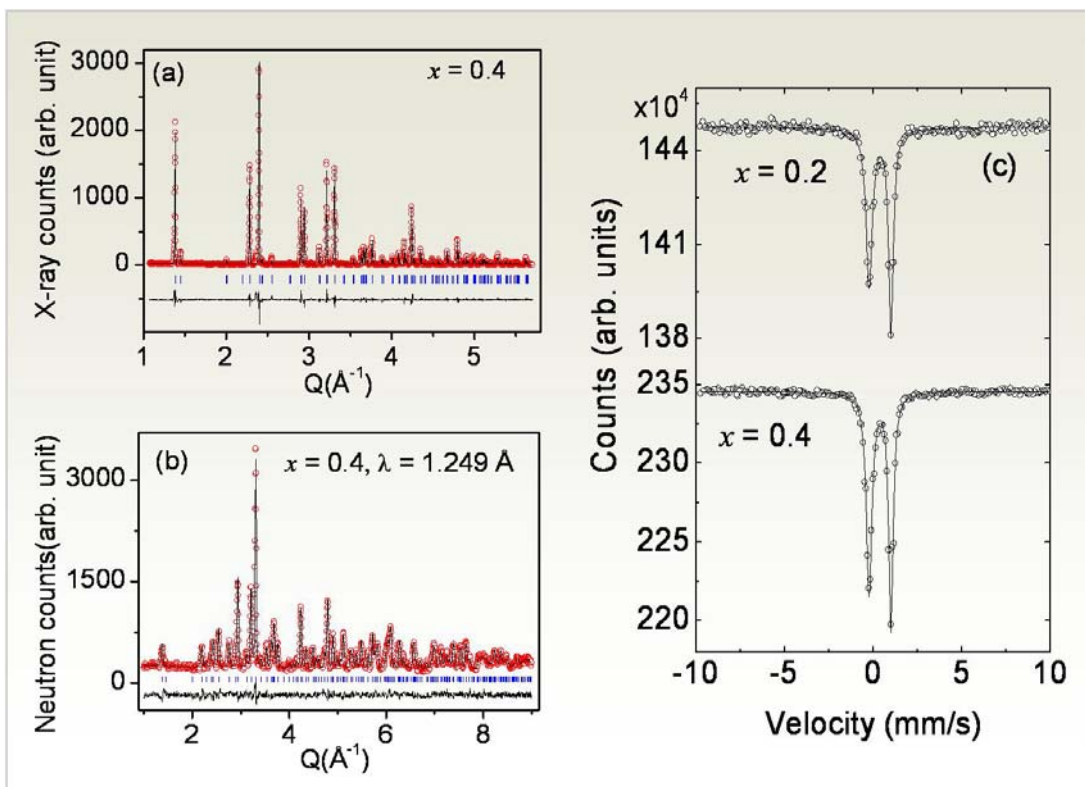


Fig. 1: Rietveld refined (a) x-ray (b) neutron diffraction patterns at room temperature. (c) Mössbauer spectra for $x = 0.2$ and 0.4 compounds.

Merit Award

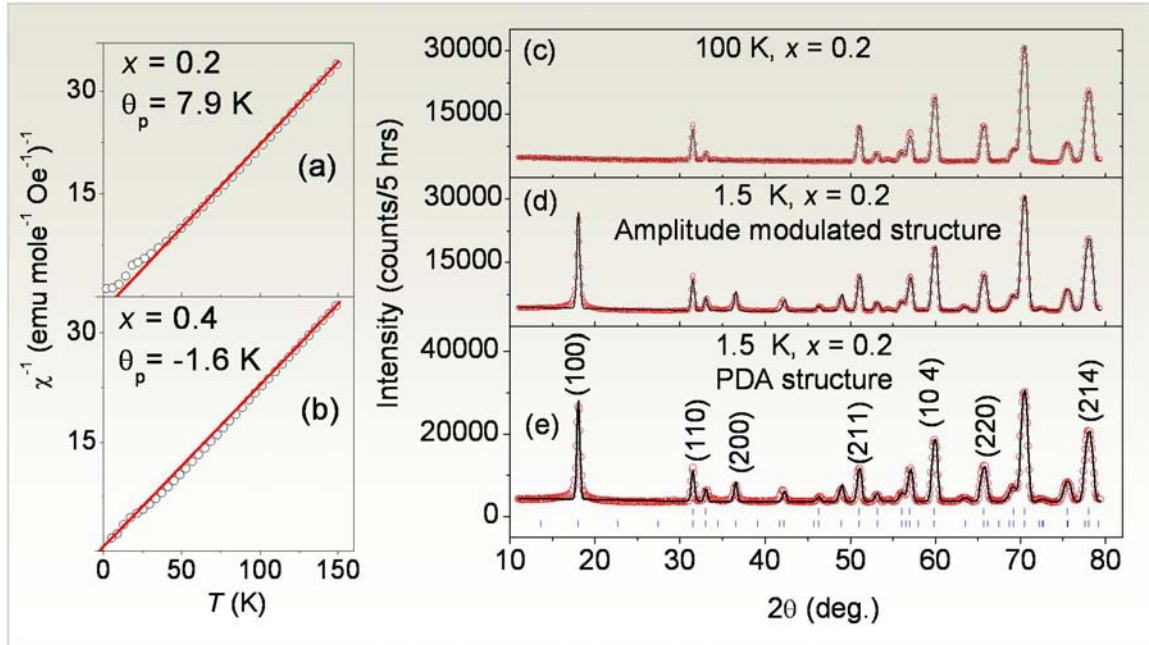


Fig.2: χ_{dc}^{-1} vs T for (a) $x = 0.2$ and (b) $x = 0.4$ compounds. The Rietveld refined neutron diffraction patterns of $\text{Ca}_3\text{Co}_{1.8}\text{Fe}_{0.2}\text{O}_6$ at (c) 100 K (only nuclear phase), (d) 1.5 K, and (e) 1.5 K. The vertical marks in (e) corresponds to the position of all allowed Bragg reflections for the crystal (top row) and magnetic (bottom row) reflections.

$\text{Ca}_3\text{Co}_2\text{O}_6$ is 27.9 K [1]. The observed negative value of θ_p for $x = 0.4$ compound indicates, that at this higher concentration of iron, AFM interaction dominates over FM interaction.

Additional Bragg peaks appear in the neutron diffraction patterns below 20 K and 17 K for $x = 0.2$ and $x = 0.4$, respectively, which can be ascribed to the onset of an antiferromagnetic ordering of Co^{3+} and Fe^{3+} spins. Figs. 3 (c) – (e) depict the neutron diffraction patterns ($\lambda = 2.46 \text{ \AA}$) for $x = 0.2$ compound at 100 K and 1.5 K. The observed extra reflections at 1.5 K can be fitted with two magnetic structures (i) amplitude modulated structure with a propagation vector $k = (0, 0, 1)$, and (ii) partially disordered antiferromagnetic (PDA) structure (a state in which $2/3$ ferromagnetic chains order antiferromagnetically, while $1/3$ are left incoherent). In both of these structures, net moment in the unit cell is zero. Both structures are able to fit the same neutron diffraction patterns, because the Fourier coefficients for each solution differ only in a global phase factor, that can't be determined by the diffraction experiment.

Conclusion

In summary, Rietveld refinement of room temperature x-ray and neutron powder diffraction patterns confirmed the single phase formation of these compounds in the space group $R\bar{3}c$. Rietveld refinement of neutron diffraction patterns and Mössbauer study confirmed, that Fe ion was located at trigonal prism site, $6a (0, 0, 1/4)$ of Co. High temperature magnetic susceptibility obeys the Curie-Weiss law. The value of paramagnetic Curie temperature (θ_p) for $x = 0.2$ and $x = 0.4$ samples are 7.5 and -1.6 K, respectively. The negative value of θ_p for $x = 0.4$ sample indicates, that antiferromagnetic interaction dominates over ferromagnetic interaction at higher concentration of iron. The additional Bragg peaks in the low temperature neutron diffraction patterns indicates, the antiferromagnetic ordering. At 1.5 K two different magnetic structures (i) amplitude modulated structure and (ii) PDA structure are able to fit the same neutron diffraction pattern because Fourier coefficient for each structure differs in global phase that can't be determined by the neutron powder diffraction experiment.



References

1. A. Jain, Sher Singh, and S. M. Yusuf. "Structural and magnetic properties of spin chain compounds $\text{Ca}_3\text{Co}_{2-x}\text{Fe}_x\text{O}_6$ ". *Phys. Rev. B* 74 (2006):174419.
2. I. Nowik, A. Jain, S. M. Yusuf, and J. V. Yakhmi, "Effect of Fe substitution on the magnetic ordering in $\text{Ca}_3(\text{Co}_{1-x}\text{Fe}_x)_2\text{O}_6$ ". *Phys. Rev. B* 77 (2008): 054403.
3. A. Jain, S. M. Yusuf, J. Campo, and L. Keller. "Magnetic ordering in the spin-chain compounds $\text{Ca}_3\text{Co}_{2-x}\text{Fe}_x\text{O}_6$ ($x = 0.2$ and 0.4): A neutron diffraction study". *Phys. Rev. B* 79 (2009):184428.
4. S. Agrestini, L. C. Chapon, A. Daoud-Aladine, J. Schefer, A. Gukasov, C. Mazzoli, M. R. Lees, and O. A. Petrenko. "Nature of the Magnetic Order in $\text{Ca}_3\text{Co}_2\text{O}_6$ ". *Phys. Rev. Lett.* 101 (2008): 097207.
5. T. Burnus, Z. Hu, M. W. Haverkort, J. C. Cezar, D. Flahaut, V. Hardy, A. Maignan, N. B. Brookes, A. Tanaka, H. H. Hsieh, H.-J. Lin, C. T. Chen, and L. H. Tjeng. "Valence, spin, and orbital state of Co ions in one-dimensional $\text{Ca}_3\text{Co}_2\text{O}_6$: An x-ray absorption and magnetic circular dichroism study". *Phys. Rev. B* 74, (2006) 245111.
6. J. Rodriguez-Carvajal. "Recent advances in magnetic structure determination by neutron powder diffraction" *Physica B* 192, (1993) 55-69.



Protactinium Recovery from Short-Cooled Spent Fuel and High-Level Waste Solutions in Thorium Fuel Cycle

Neelam Kumari, P.N. Pathak, D.R. Prabhu and V.K. Manchanda
Radiochemistry Division

This paper received the Best Paper Award at the "Emerging Trends in Separation Science and Technology (SESTEC-2010)" held at Indira Gandhi Centre for Atomic Research (IGCAR), Kalpakkam, during March 1-4, 2010

Abstract

Conditions have been optimized for selective removal of protactinium from short-cooled spent fuel dissolver solution and from high-level waste solution, employing diisobutyl carbinol as extractant. The study includes: effect of acidity, extractant and thorium concentration. Selectivity of the extractant has been investigated with respect to U, Pu and Th.

Introduction

Several thermal reactor systems have been proposed, for thorium utilization in India's nuclear power programme. Amongst them, the development of *Advanced Heavy Water Reactor (AHWR)* is relatively at an advanced stage. Other important options for thorium utilization programme are: (a) *Molten Salt Breeder Reactor (MSBR)*, (b) *Aqueous Suspension Reactor (ASR)*. These reactors are expected to work on circulating fluid fuel (molten fluoride/slurry of thorium oxide in water) and provide an option for on-line fuel reprocessing, which removes fission products and minimizes the losses of neutrons. Therefore, there is a need to develop processes for selective extraction of ^{233}Pa from spent fuels in these reactors. On the other hand, AHWR spent fuels are expected to initially reach a burn up of 15000 MWd/Te, which will be enhanced up to 24,000 MWd/Te, under equilibrium conditions. It would be necessary to reprocess some of the fuel bundles after short-cooling every year, to achieve a burn up of $\sim 40,000$ MWd/Te. This again necessitates the knowledge of extraction behavior of protactinium under process conditions [1]. A process to recover ^{233}Pa prior to the

processing of short-decayed fuel would minimize inventory charges of stored fissionable material. The separated ^{233}Pa , which will decay to isotopically pure ^{233}U , can reduce the volume of radioactive product to be stored. In addition, this would lead to significant decrease in the activity of the solutions, in the thorium-uranium recovery procedure.

The presence of long-lived alpha emitter ^{231}Pa (3.3×10^4 y) and significant amount of aluminium along with fluoride, adds new dimensions in high-level waste (HLW) management of AHWR spent fuel. Pentavalent ^{231}Pa is of special concern in AHWR-HLW, as it is capable to migrate much more in water/soil as compared to other ions. Therefore, there is a need to establish a suitable process, employing an appropriate solvent for this specific task. The amount of ^{231}Pa produced in $(\text{Th}-^{233}\text{U})\text{O}_2$ MOX fuel is expected to be 3 g/Te at 20,000 MWd/Te of burn-up and its concentration in AHWR-HLW is expected to be ~ 1 mg/L [2].



This paper deals with the extraction behavior of protactinium, thorium and uranium, employing diisobutyl carbinol (DIBC: 2,6 dimethyl 4-heptanol, Fig.1) as an extractant.

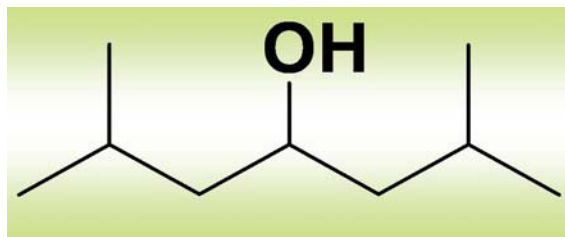


Fig. 1: 2,6 dimethyl 4-heptanol

Experimental

DIBC (Aldrich), *n*-dodecane (Lancaster) were used as received. ^{233}U tracer ($\sim 10^{-4}\text{M}$) was purified by anion exchange procedure. The purity was checked by alpha and gamma ray spectrometry. ^{233}Pa was separated from irradiated ^{232}Th (in APSARA reactor) by a radiochemical technique using DIBC as the extractant. Its purity was checked by gamma ray spectrometry. Thorium (nitrate form) obtained from Indian Rare Earths Limited, Mumbai, was used wherever necessary. The inner sides of the glass tubes were coated using 5% solution of dimethyl dichlorosilane (DMDCS) in toluene prior to Pa extraction studies. The solution was then drained out after a minimum of 3 hours and dried, before to use in solvent extraction studies.

Equal volumes (0.5-1.0 mL) of the pre-equilibrated organic phases and the aqueous phases under desired conditions were kept for equilibration, in a water bath for 30 minutes at 25°C. Gamma spectrometry was carried out for measuring ^{233}Pa activity. ^{233}U was estimated by liquid scintillator counting. Thorium estimation was carried out by EDTA complexometric titration, employing xylenol orange as indicator, and by spectrophotometry using Thoron as chromophore. The distribution ratio of the metal ion (D_{Th} , D_{Pa} , D_{U}) was defined as the ratio of concentration of metal ion in the organic phase to that in the aqueous phase. Material balance and the

reproducibility of the distribution data was within error limits ($\pm 5\text{-}10\%$).

Results and Discussion

Acid Uptake Behavior of DIBC

The understanding of acid uptake behavior of an extractant, is important in devising process flow sheet. In this context, nitric acid extraction studies were carried out in two different conditions viz. (a) at different acidities (1-6 M HNO_3) using 100 % DIBC (5.1 M), and (b) at different DIBC concentrations (10-100 %; 0.51-5.1 M) in *n*-dodecane at 4 M HNO_3 . For 100 % DIBC, the acid uptake in the organic phase increased gradually from 0.05 M to 1.5 M HNO_3 with increased initial aqueous phase acidity from 1 to 6 M HNO_3 . On the other hand, DIBC concentration variation (10-100 %; 0.51-5.1 M) experiments for acid uptake at 4 M HNO_3 , indicated towards the formation of predominantly 1:1 species (slope: 1.32). Similar observations have been reported during the extraction of HCl by DIBC [3].

Optimization of DIBC concentration

Fig.2 shows the variation of D_{Pa} values with aqueous phase acidity for pure DIBC (100%; 5.05 M) and 40 % (2.02 M) DIBC/*n*-dodecane. As expected, D_{Pa} values are

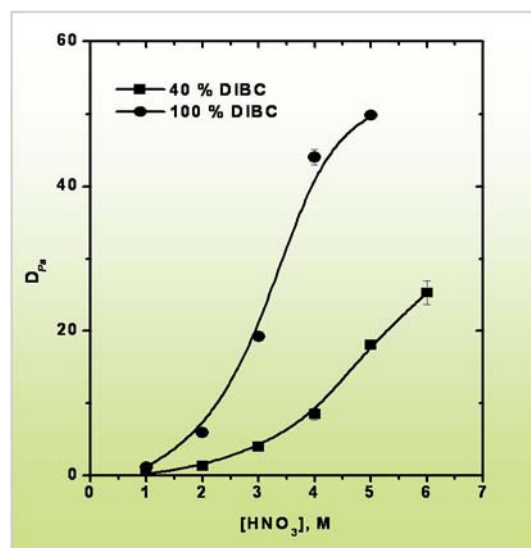


Fig. 2: D_{pa} as a function of nitric acid concentration; Diluent *n*-dodecane; T: 25°C



significantly higher for 100% DIBC in the entire range of acidity. However, 40% DIBC solution was chosen for Pa recovery experiments in view of the relatively lower concentration of ²³³Pa (in dissolver solution) and ²³¹Pa (in HLW solution), and sufficiently high D_{Pa} value

Extraction behavior of Pa, U and Th

Fig.3 shows the involvement of ~1-2 DIBC molecules during Pa extraction process, through the formation of ion-paired complex [4]. Similar solvation has been observed during nitric acid extraction. Therefore, the nitric acid is extracted as an ion pair of the type $[H(DIBC)_{1-2}]^+ \cdot [NO_3^-]$ [4]. The activity of this species increases with increased nitric acid concentration and that of free DIBC decreases. Therefore, it is logical to conclude that, Pa forms a complex with protonated DIBC rather than with free DIBC. Also, equal solvation numbers of nitric acid and Pa-species indicate, that they interact in 1:1 ratio. Thus, protactinium is extracted as monobasic complex of general formula $HPa(OH)_m(NO_3)_n \cdot 1-2$ DIBC, with $m + n = 6$, and $n e^- = 1$. Hardy et al. have reported that the hydrolyzed cationic, neutral and anionic species $[Pa(OH)_2(NO_3)_4]^+$ of Pa in nitric acid are in equilibrium and depending on the aqueous phase acidity, the interchange between them is fast [5].

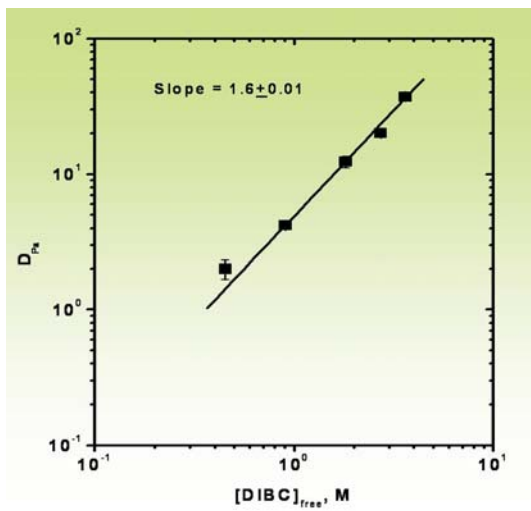


Fig. 3: Variation of D_{Pa} with DIBC concentration; Diluent n-dodecane; $[HNO_3]_4$ M; T: 25°C

Effect of Thorium

Fig.4 shows the variation of D_{Pa} with increasing concentrations of Th (up to 200 g/L) at different acidities. Generally, there is an increase in D_{Pa} values with increased aqueous phase acidity, which can be attributed to the formation of protonated species of DIBC $[H(DIBC)_{1-2}]^+$ and anionic $Pa(OH)_2(NO_3)_4^-$ species. This observation is further supported by enhanced extraction of Pa at lower

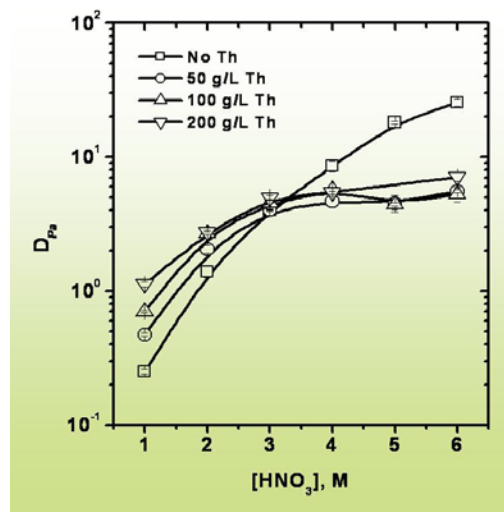


Fig. 4: Effect of Th on D_{Pa} as a function of acidity; Extractant: 40% DIBC *n*-dodecane; T: 25°C

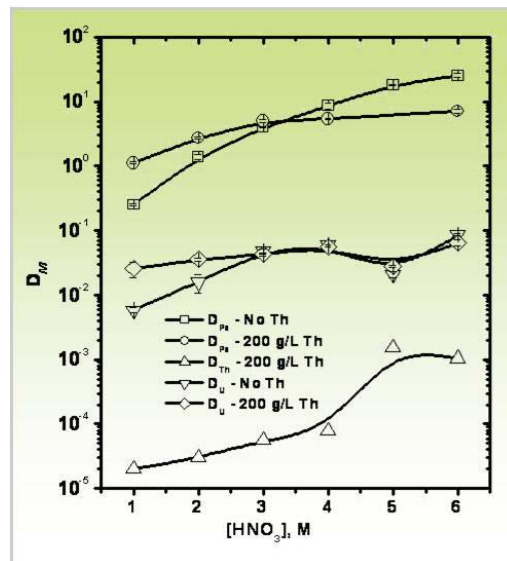


Fig. 5: Effect of Th on D_{Pa} , D_o , D_{Th} at different acidities; Extractant: 40% DIBC *n*-dodecane; T: 25°C



acidities (up to 4 M) with increased Th concentration (up to 200 g/L). However, there is a decrease in D_{Pa} values beyond 4 M HNO_3 , indicating a decrease in the activity of $[H(DIBC)_{1,2}]^+$ species, due to partial loading of organic phase with thorium, even though the distribution ratio values are too low (Fig.5).

Typically, in the presence of 200g/L at 4 M HNO_3 , the separation factor (SF) values of Pa over U and Th are ~ 100 , $> 10^5$, respectively. The relatively lower SF value of Pa over U was attributed to the latter's tendency to form anionic species, which is more favored at higher nitrate concentrations.

Conclusions

The conditions for Pa extraction from short-cooled dissolver and HLW solutions have been optimized. Protactinium is

extracted as monobasic complex of general formula $HPa(OH)_m(NO_3)_n \cdot 1-2 DIBC$, with $m + n = 6$, and $n e^- = 1$.

References

1. R.K. Sinha, A. Kakodkar, *Nuclear Engineering and Design* 236 (2006) 683–700.
2. B. Bhattacharjee, 14th Annual Conference of Indian Nuclear Society (INSAC-2003), IGCAR, Kalpakkam, December 17-19, 2003, IT-1.
3. Hans-Ludwig Scherff, G. Herrmann, *Radiochim. Acta*, 6(2) (1966) 53-60.
4. J. R. Oliver, J. R. Meriwether, R. H. Rainey, ORNL Report-2668, 1959.
5. C.J. Hardy, D. Scargill, J.M. Fletcher, *J. Inorg. Nucl. Chem.*, 7 (1958) 257-275.



Prussian Blue Analogue Molecular Magnets: Controlling Structural Disorder and Magnetic Properties

N. Thakur, S.M. Yusuf and A. Kumar
Solid State Physics Division

and

J. V. Yakhmi
Physics Group

This paper received the Best Poster Award at the "Advances in Magnetism: Phenomena and Materials" held at Manali, Himachal Pradesh, during June 3-5, 2010

Abstract

Prussian blue analogue molecular magnets $Ru_xNi_{3-3x/2}[Cr(CN)_6]_2 \cdot zH_2O$ and $Ba_xMn[Fe(CN)_6]_{2(x+1)/3} \cdot zH_2O$ have been investigated by dc magnetization and neutron diffraction techniques. The structural disorder has been quantified by Reverse Monte Carlo analysis of neutron diffraction patterns. The role of Ru substitution in controlling magnetic properties of these Prussian blue analogues has been brought out.

Introduction

The fascinating features of molecular magnets e.g. low density, multifunctionality, photoinduced magnetization, spin crossover, etc. when combined with various magnetic parameters such as high transition temperature (T_C), coercive field (H_C) and saturation magnetization (M_S) can lead to future smart devices [1-5]. We have synthesized a number of Prussian Blue Analogue (PBA) molecular magnets with general formula $A_kM_m\{M'(CN)_6\}_n \cdot zH_2O$ (M, M' = transition metal ions, A = alkali metal ion) using precipitation method. In the present paper, we have done a detailed structural disorder study of the $Ba_xMn[Fe(CN)_6]_{2(x+1)/3} \cdot zH_2O$ ($x = 0$ and 0.3) molecular magnets by carrying out the Reverse Monte Carlo (RMC) simulations of neutron diffraction data. We have also studied the effect of a $4d$ ion (Ru^{3+}) substitution on structural disorder and magnetic ordering in the cyanide-bridged molecular magnets, $Ru_xNi_{3-3x/2}[Cr(CN)_6]_2 \cdot zH_2O$

($0 \leq x \leq 0.5$). The present results of structural investigation are useful in designing molecular magnets as well as controlling their magnetic and other physical properties.

Experimental

Polycrystalline samples of PBAs $Ru_xNi_{3-3x/2}[Cr(CN)_6]_2 \cdot zH_2O$ ($0 \leq x \leq 0.5$), and $Ba_xMn[Fe(CN)_6]_{2(x+1)/3} \cdot zH_2O$ ($x = 0$ and 0.3) were synthesized by the co-precipitation method, maintaining the charge neutrality. Neutron diffraction patterns were recorded for these samples using the powder diffractometer-II ($\lambda = 1.249 \text{ \AA}$) at Dhruva research reactor, Trombay. DC magnetization measurements were carried out using a vibrating sample magnetometer as a function of temperature and magnetic field.

Results and Discussion

$Ru_xNi_{3-3x/2}[Cr(CN)_6]_2 \cdot zH_2O$ ($0 \leq x \leq 0.5$) PBAs

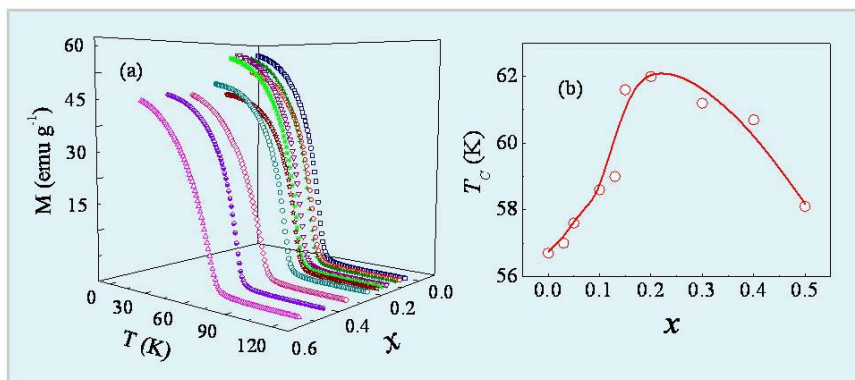


Fig. 1: (a) Magnetization vs. temperature curves at 500 Oe field for $Ru_xNi_{3-3x/2}[Cr(CN)_6]_2 \cdot zH_2O$ compounds with $x = 0, 0.03, 0.05, 0.1, 0.13, 0.15, 0.2, 0.3, 0.4$ and 0.5 (from right to left). (b) Variation of T_c with the composition (x).

Fig. 1 (a) shows the field cooled (FC) magnetization (M) versus temperature (T) plots for all compounds of the series $Ru_xNi_{3-3x/2}[Cr(CN)_6]_2 \cdot zH_2O$ ($0 \leq x \leq 0.5$) [4] at 500 Oe field. The variation of the transition temperature (T_c) with x is depicted in Fig. 1 (b). With $x > 0.2$, a combined effect of the stronger magnetic interaction between the $3d/4d-3d$ spin carriers (due to reduction in vacancies) and the reduction in the average spin of the Ru/Ni site, leads to a decrease in the T_c . An antiferromagnetic coupling of Ru^{3+} (low spin, $S = 1/2$) moments with both Ni^{2+} ($S = 1$) and Cr^{3+} ($S = 3/2$) moments is found.

The Rietveld refinement of the neutron diffraction pattern, confirms the face centered cubic crystal structure (space group: $Fm\bar{3}m$) for these compounds. We have performed the Reverse Monte Carlo (RMC) simulations, for a quantitative analysis of the observed diffuse scattering in neutron diffraction data, to quantify the total structural disorder present in these compounds. The nuclear diffuse scattering arises due to various structural disorders present in the samples: (i) presence of $[Cr(CN)_6]$ vacancies which are occupied by oxygen atoms of coordinated water molecules; and (ii) substitutional disorder which increases as x increases. Fig. 2 (a) depicts the RMC analyzed pattern for the $x = 0.2$ sample where $F(Q)$, the sum of the scattering amplitudes from all atoms in the reciprocal space at a given Q value, is plotted. As the diffuse scattering is a measure of the disorder present in a sample, it is essential to quantify the disorder. For this purpose, in Fig. 2 (b), we have plotted the area (α) under the $F(Q)$ vs. Q curves for different compositions (x). It is clear from Fig.2 (b) that the area under the curve (a measure of disorder) increases with x .

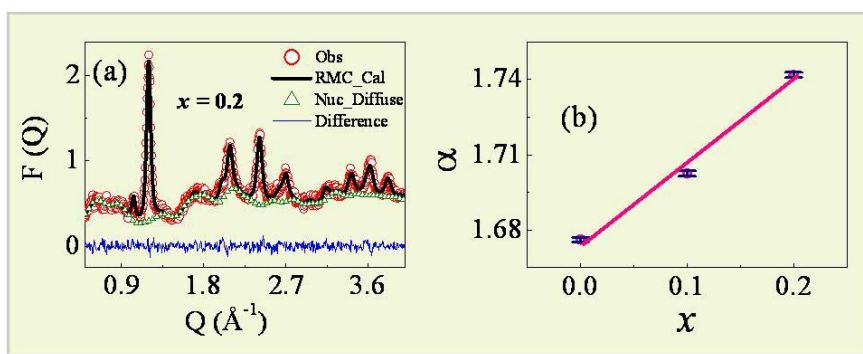
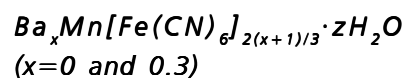


Fig. 2: (a) RMC calculated total scattering contribution (thick line) compared with the experimental data (open circles) at 100 K for $x = 0.2$. RMC calculated nuclear diffuse scattering contribution is shown by open triangles. Solid line at the bottom of the curve is the difference between the observed and the RMC calculated total intensities. (b) The variation of area (α) under the $F(Q)$ vs. Q curves (diffuse scattering contribution) with x (error bars are also shown).



From our temperature and magnetic field dependent dc magnetization measurements, a ferrimagnetic coupling of Mn^{2+} ($S = 5/2$) spins and the Fe^{3+} ($S = 1/2$) spins is found for compounds $Ba_xMn[Fe(CN)_6]_{2(x+1)/3} \cdot zH_2O$ ($x = 0$ and 0.3) [5]. The Rietveld refinement of the neutron diffraction pattern, confirms the face-centered cubic crystal structure (space group: $Fm\bar{3}m$) for these compounds. A large diffuse scattering is present in

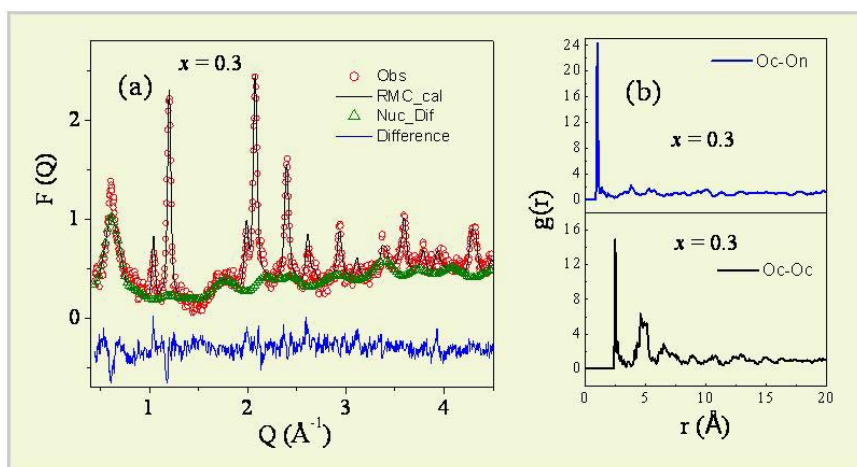


Fig. 3: (a) RMC analyzed neutron diffraction pattern at 100 K for $x = 0.3$. (b) Partial pair correlation function for coordinated (O_c) and noncoordinated (O_n) oxygen atoms for $x = 0.3$.

neutron diffraction patterns of both compounds in the form of a modulated background. The presence of diffuse scattering implies a deviation from a perfect periodic crystal structure and thus indicates, the presence of a prominent disorder in the compounds. A quantitative analysis of the observed diffuse scattering in the neutron diffraction patterns is carried out by using RMC simulations technique. RMC analyzed pattern for $x = 0.3$ sample is shown in Fig. 3 (a). Fig. 3 (b) shows partial pair correlation functions for coordinated (O_c) and noncoordinated (O_n) oxygen atoms for the $x = 0.3$ compound, as obtained from our RMC simulation study. Our investigations show that (i) around the coordinated oxygen atoms (located at the 24e crystallographic sites with $[\text{Fe}(\text{CN})_6]$ vacancies), there are formations of small clusters of noncoordinated oxygen atoms and, (ii) Ba substitution leads to a reduction in structural disorder. There is a decrease in the number of water molecules and vacancies of $[\text{Fe}(\text{CN})_6]$, leading to a decrease in the structural disorder in the Ba-substituted compound.

Summary and Conclusion

We have shown that the structural disorder and the magnetic properties of PBA compounds can be controlled by an appropriate chemical substitution. The novelty of the present work lies in the fact, that with the help of the RMC modeling of the diffuse neutron scattering, one

could quantify the structural disorder in a compound. The experimental procedure employed here, to determine structural disorder using neutron scattering, can be used in many other compounds as well and thus can serve as a guideline to control the structural disorder with the help of substitution in PBAs. The structural disorder plays an important role in the manifestation of many interesting phenomena in PBAs such as, photo-induced magnetization, pressure-induced magnetization, spin crossover, etc. [2] and, hence, the

outcome of the above results can help in the rational design of molecular magnets, suited for practical applications.

References

1. A. Kumar, S. M. Yusuf, and L. Keller, *Phys. Rev. B* 77 (2005): 054414.
2. A. Kumar, S. M. Yusuf, L. Keller, J. V. Yakhmi, J. K. Srivastava, and P. L. Paulose, *Phys. Rev. B* 75 (2007): 224419.
3. A. Kumar, S. M. Yusuf, L. Keller, and J. V. Yakhmi, *Phys. Rev. Lett.* 101 (2008): 207206.
4. S. M. Yusuf, N. Thakur, A. Kumar, and J. V. Yakhmi, *J. Appl. Phys.* 107 (2010): 053902.
5. N. Thakur, S. M. Yusuf, and J. V. Yakhmi, *Phys. Chem. Chem. Phys.* 12 (2010): 12208.



Response of aleurone layers from *Triticum dicoccum* genotypes to gibberellic acid (GA₃): Time course of amylase stimulation

Chun Mei Chang and S.G. Bhagwat
Nuclear Agriculture and Biotechnology Division

This Paper received the Best Poster Award (Third Place) at the Zonal Seminar on Physiological and Molecular Interventions for Yield and Quality Improvement in Crop Plants, held at S.V. Patel University of Agriculture & Technology, Meerut in 2010

Abstract

The height of a wheat plant is a trait which is related to gibberellin metabolism. The cells of GA insensitive semi-dwarfs have a defect in GA₃ utilisation. In the present study, the GA₃ response characteristics of aleurone layers from a *Triticum dicoccum* tall parent and its semi-dwarf mutant have been studied and compared to a variety containing *RhtB1b* semi-dwarfing gene. The results showed significant differences in the pattern of amylase secretion between the tall and semi-dwarf varieties. After 24h of incubation in 10⁻⁴M GA₃, the semi-dwarf mutant showed about half the amount of amylase activity as compared to the parent. The *RhtB1b* semi-dwarf showed intermediate amylase activity as compared to the parent and mutant.

Introduction

Gibberellic acids (GAs) form a large family of diterpenoid compounds, some of which are bioactive growth regulators, that control diverse developmental processes such as seed germination, stem elongation, leaf expansion, trichome development and flower and fruit development (Olszewski *et al.*, 2002). Introduction of the Norin-10 gene(s) resulted in semi-dwarf varieties of wheat that were lodging-resistant, and could accumulate biologically active gibberellic acids to higher levels than are found in wild-type controls (Sun, 2000), and these mutations behave as dominant altered-function mutations (Gale *et al.*, 1983). The wheat aleurone layer consists of a single layer of uniform, highly differentiated cells and provides an ideal system to study gibberellic acid (GA) response, with GAs specifically promoting the rapid expression of genes encoding hydrolases such as α -

amylases and its secretion occurring in a time bound manner. Therefore, any mutation/block in the GA signaling pathway or its utilisation would affect the production and secretion of amylases. Thus measurements of amylase stimulation/activity can be used to study any change in the GA action. The present study was carried out to understand the effect of GA on amylase production from aleurone layers of wheat plants with difference in height, using a tall parent and its semi-dwarf mutant.

Materials and Methods

The *Triticum dicoccum* varieties used were NP200 (tall parent), HW1095 (semi-dwarf mutant) and DDK1029 (*RhtB1b* carrier).

Chemicals used were procured from standard sources and were of analytical grade.



Aleurone incubation

Seeds were surface sterilized, the edges of the seeds including the embryo were cut off with a blade and the cylindrical portions were incubated in sterile distilled water for 24h. The starchy endosperm of each seed was removed and the aleurone layers were washed thoroughly with sterile distilled water and incubated in the incubation buffer containing 0.001M sodium succinate, 0.02M CaCl₂ (Bhagwat and Bhatia, 1994) and 1 mg/mL Cefotaxime, for up to 80h. The GA treated samples contained 10⁻⁴M GA₃. The aleurones were incubated in a rotary shaker at 28°C and 85rpm. Aliquots were collected every 12h in sterile environment and assayed for total protein content and amylase activity.

Amylase assay and protein estimation

Amylase activity was measured by incubating an aliquot at 37°C in acetate buffer (pH 4.8) along with starch for 30min. The enzyme reaction was stopped by adding 0.1M NaOH and placed in a boiling water bath for 5min with 1% DNSA. The resulting colour was measured at 540nm. Total protein was measured by Lowry's method.

Results:

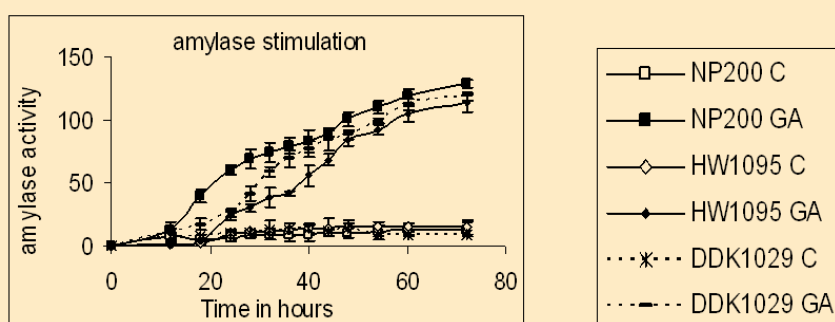


Fig. 1: Time course of amylase secreted into the medium. 1 amylase activity = mg maltose produced per mg protein at 37°C in 30min.

Protein and amylase secretion

The time course of each of the varieties showed that after a period of 18-24h there was stimulation of amylase

which was secreted into the medium. There was no stimulation in the absence of GA₃ (Fig. 1) throughout the incubation time. The total secreted protein in the medium was comparable in the GA treated and the control (Fig. 2).

Comparison of the varieties

Amylase stimulation in the varieties under identical conditions showed that stimulation began at 18h incubation in the variety NP200, and at 24h in HW1095 and DDK1029, following which, the amylase was secreted at a steady rate up to 54h. Subsequently, there was decrease in the rate (Fig. 1).

Total amylase activity

Total amylase activity over 72h showed that the variety NP200 produced more amylase as compared to HW1095 and DDK1029 was intermediate.

Discussion

The dicoccum wheat is less explored as compared to the bread wheat and macaroni wheat and information on the response of aleurones of dicoccum has not been reported. In this study, a tall variety NP200 and its gamma ray-

induced semi-dwarf mutant have been compared for their amylase stimulation in response to externally applied gibberellin. The time course study revealed that the response of dicoccums is comparable to that of other wheats, however, with its own characteristic time for stimulation under the experimental conditions used. Comparison of the parent and the mutant revealed that the total amount of amylase synthesized and

secreted in the medium up to 48h, was highest for the parent, lowest for the mutant and intermediate for the *RhtB1b* carrier semi-dwarf and the differences were significant. The results indicated that the *T. dicoccum*

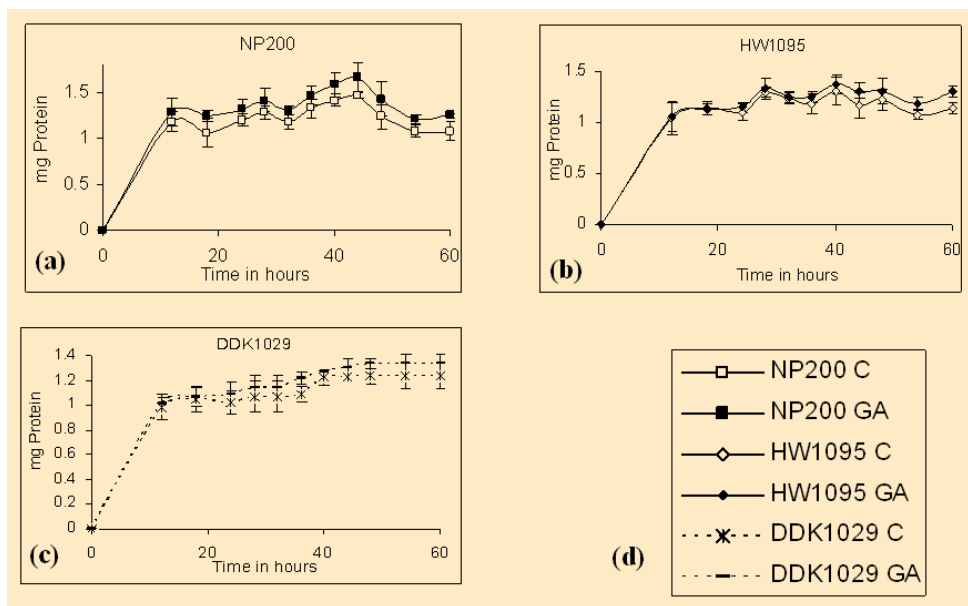


Fig. 2: Time course of total protein content secreted into the medium. (a) NP200 (b) HW1095 (c) DDK1029 (d) key

mutant HW1095 has altered GA metabolism as a result of which, the plant height is reduced and stimulation of amylase in aleurone is altered. The mutation appears to be different than the earlier known semi-dwarf gene *RhtB1b* since the stimulation pattern is different for the two semi-dwarfs. The activation of GA-stimulated amylase is also relevant to grain quality. Grains exposed to untimely rain at harvest would undergo amylase stimulation in pre-harvest sprouting. Lower stimulation of amylase may result in lower damage to the grain quality.

Conclusions

Aleurone layers of tall dicoccum variety showed amylase stimulation *in vitro* by externally applied GA₃. A semi-dwarf mutant showed reduced stimulation. A Norin10 (*RhtB1b*) carrying semi-dwarf showed different time course, which indicated that the mutation in HW1095 may be different in the *RhtB1b* mutation. The aleurone layers provide a useful system to study the effect of mutation or GA metabolism.

References

1. Bhagwat S.G. and Bhatia C.R. Quantitative differences in the gibberellin induced alpha amylase activity from aleurone layers of tall and semi-dwarf wheat cultivars. *Cereal Research Communications*. 22 (1994): 129-134.
2. Nayeem K.A., Sivasamy M. HW1095: Pusa dwarf dicoccum has high yield performance across the Indian zones. *AWN* 52 (2006):66.
3. Olszewski N., Sun T-P., and Gubler F. Gibberellin signaling: Biosynthesis, catabolism, and response pathways. *The Plant Cell* (2002) S61-S80.
4. Sun T-P. Gibberellin signal transduction. *Current Opinion in Plant Biology* 3(2000):374-380.
5. Gale M.D., Chojecki A.J., and Kempton R.A. Genetic control of α -amylase production in wheat. *Theor. Appl. Genet.* 64(1983):309-316.



The Central Monitoring Station of Indian Environmental Radiation Monitoring Network (IERMON): The Architecture and Functions

**Saurabh Garg, M.P. Ratheesh, T. Mukundan, M.D. Patel,
A. Vinod Kumar and V.D. Puranik**
Environmental Assessment Division
and
C.K.G. Nair
Ex-EAD, BARC

This paper received the Best Poster Award (I prize) at the Workshop cum 17th National Symposium on Environment held at Indian Institute of Technology (IIT), Kanpur, during May 13-15, 2010

Abstract

The Indian Environmental Radiation Monitoring Network (IERMON) is being established across the country by BARC, Mumbai. The network consists of stations with automated systems for environmental radiation monitoring, with online data communication facility. Currently about 110 stations are operational. The network is established with different objectives, the main objective being the detection and reporting of any nuclear emergency, anywhere in the country. The central monitoring station of the network is established in Mumbai.

This paper describes the architecture and functions of IERMON Central Station. The Central Station consists of a server room for online data collection from remote stations and maintenance of databases for various applications; central monitoring room for user interaction with database and IERMON website maintenance and development room, for the development of new applications. The functions of IERMON Central Station include: detection and reporting of nuclear emergency, maintenance of remote stations, and enhancement of public awareness on environmental radiation through public display systems and website, etc.

Introduction

Indian Environmental Radiation Monitoring Network (IERMON) was initiated in April, 2002 by Dr. Anil Kakodkar, then Chairman, Atomic Energy Commission, as he felt the need for a countrywide network for continuous monitoring of environmental radiation, which would have the capability to detect and inform any sudden increase in radiation level, for response action planning. IERMON thus took shape with the following objectives:

- Provide online information about radiation levels at various locations to Emergency control rooms of DAE.
- To facilitate environmental impact assessment of nuclear emergencies
- To provide environmental radiation awareness to the public.
- To facilitate R&D on new systems and methods for environmental radiation monitoring.



- To develop and validate mathematical models for atmospheric dispersion of radioactive pollutants in environment.

Currently IERMON is networking about 110 monitoring systems installed throughout the country. IERMON system is solar powered and data communication is through GSM network. These two features make the IERMON system ready to install at any remote place.

Locations for IERMON system installation were chosen on the basis of the following criteria:

- Nuclear establishments and other strategic locations:* For online reporting of emergency situation.
- National Border District:* To monitor cross-border transport of radionuclide.
- Cities with heavy population.*
- Coastal regions:* To monitor any nuclear emergency from the sea like nuclear powered ship or submarine etc.

IERMON Central Station

IERMON Central Station is established at Anushaktinagar, Mumbai. The layout of the Central Station is shown in Fig. 1. Data messages in the form of SMS messages from field systems, are received by the Receiving Systems at the central station. Complete format of the received SMS at Central Station is as follows:

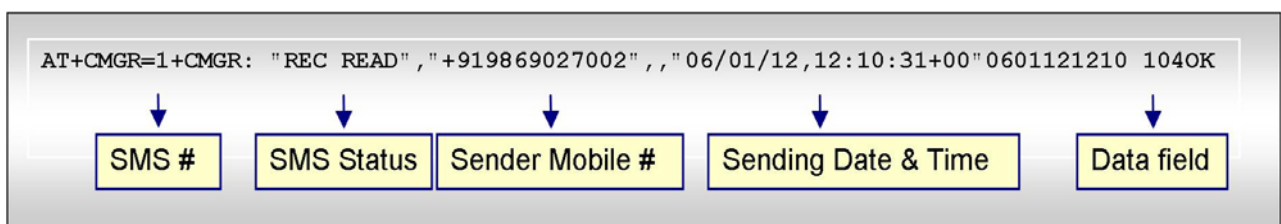


Fig. 1: Layout of IERMON Central Station

multiple such servers, with mirror images of each other data. Generic schema of database of IERMON Central Station is shown in Fig. 2.

All application and database servers are installed in the IERMON Server Room with UPS backup for 8 hours. The actual view of the server room is shown in Fig.3 and the internal view of a section of the monitoring room is shown in Fig. 4.

User can view data from all the stations in the network. The data can be displayed on a large plasma monitor as shown in the picture.

The Receiving System decodes the messages and extracts the data. The data is sent to a Data Server. The Data Server has redundancy by duplicating the data into a cluster of servers for different applications. Users can access the data through a LAN of PCs in the monitoring room.

All servers in the cluster, update the database in Data server. The Data Server again attains redundancy, by way of RAID configuration, multiple HDDs and above all

Functions of IERMON Central Station

- Linkage of IERMON Database to Emergency Response Centres (ERC) and Emergency Control Rooms (ECR) of Department of Atomic Energy using the Department's VSAT network (ANUNET)

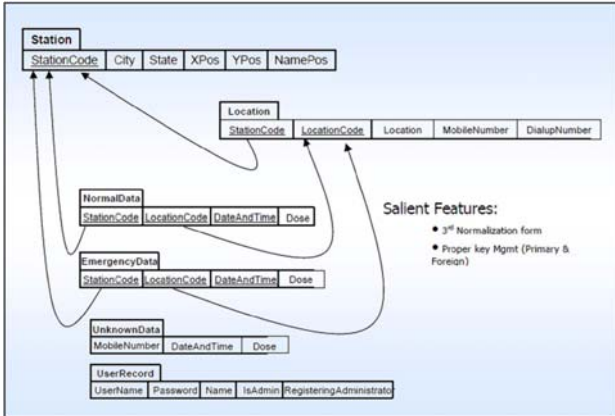


Fig. 2: Database Schema of IERMON Central Station (Generic Format)

- Detection of Nuclear Emergency by continuously monitoring the SMS messages from Remote Stations of IERMON
- Notification of Emergency by sending Alert Messages to ERCs/ECRs and also to designated authorities
- Report Generation (Hard Copy) at periodic intervals for distribution to designated authorities
- Installation and maintenance of public awareness display systems for generating awareness on environmental radiation.

Automated Alarm Messaging System (AAMS):

To notify emergency to ERCs/ECRs and designated authorities by sending Alarm SMS, IERMON Central Station had incorporated AAMS in the Central Broadcasting Station (CBS). For sending such SMS, CBS continuously checks the database for any emergency data, and if found, it sets up some flags and confirms the genuineness of the emergency and only then sends the SMS.

Public Awareness Display System & IERMON Website:

IERMON Central Station uses its data to educate the public about radiation by its Public Awareness Displays (PAD). These displays show a presentation containing figure and facts about the radiation, backed by actual radiation values at different places. PAD also educates the public about



Fig. 3: IERMON Server Room



Fig. 4: IERMON Central Station (Internal view)

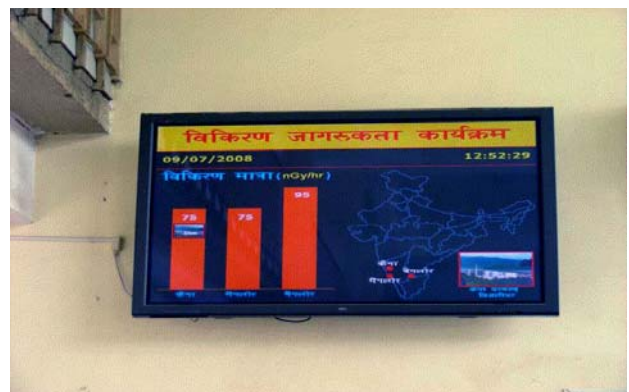


Fig. 5: Installed Public Awareness Displays

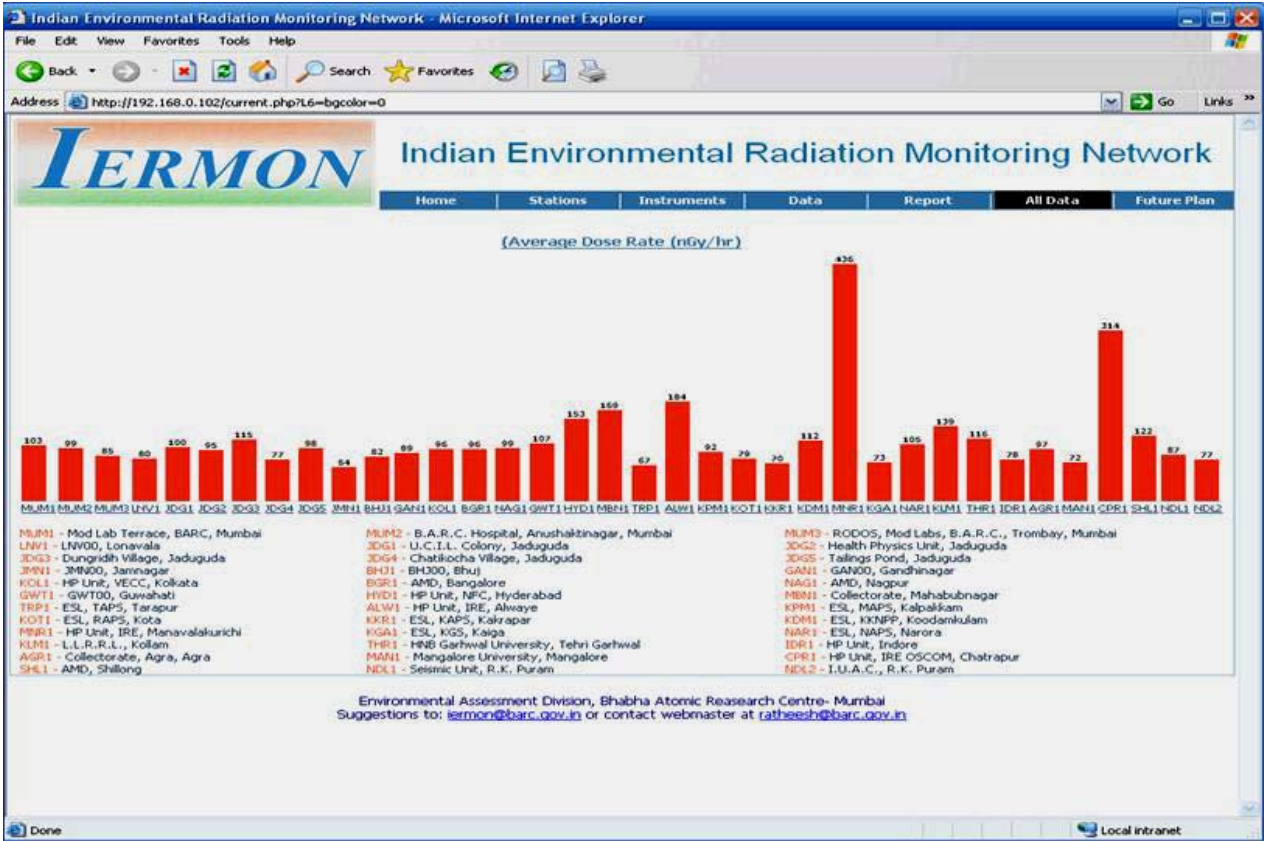


Fig. 6: Screen-shot of IERMON Website

the medical source of the radiation to the general public. Such PADs are designed in multiple languages (eg. Hindi, English and Khasi) with every display showing information in minimum two languages. PADs are installed with big sized plasma displays supported by Ultra-micro PC and provided with GSM communication for online data communication.

IERMON Central Station has also designed and in maintaining a website with all the online data and other features. This website is accessible within DAE, wherever ANUNET connectivity is available.





Thermal cyclic hydrogen absorption desorption behavior of Ti_2CrV alloy

Asheesh Kumar, K. Shashikala and C.G.S. Pillai
Chemistry Division

This paper received the Best Oral Presentation Award (III prize) at the 17th DAE-BRNS National Symposium and Workshop on Thermal Analysis, held at Kurukshetra, Haryana, during March 9-12, 2010

Abstract

Ti-Cr-V series is being extensively studied, because of its high hydrogen storage capacity. In the present work, we have studied the hydrogen absorption-desorption properties of the Ti_2CrV alloy. The alloy and its hydrides have been characterized for the structure, and the pressure composition of isotherms, kinetics of hydrogen absorption, hydrogen storage capacity, cyclic hydrogen absorption properties and desorption temperature have been studied in detail. The Ti_2CrV alloy shows a maximum hydrogen storage capacity of 4.37 wt% at room temperature. From the cyclic hydrogen absorption study it was seen that the hydrogen storage capacity decreases progressively with cycling initially, but the alloy can maintain steady cyclic hydrogen absorption capacity of 3.5 wt% after the 5th cycle. The DSC measurement of both saturated hydrides show, that the cycled hydride desorbs hydrogen at lower temperature as compared to the hydride not subjected to cycling.

Introduction

Though in the recent years hydrogen storage has attracted many new materials such as carbon nanotubes, porous metal-organic frameworks, complex hydrides, alanates, etc.¹⁻³, but still alloys and intermetallic based hydrides, continue to be the most important materials for practical applications⁴. The conventional AB_2 and AB_5 type of alloys, exhibit low gravimetric hydrogen storage capacity of ~1.2 to 1.4 wt%. The new series of Ti-V and Ti-Cr-V-based body-centered cubic (bcc) alloys are being explored extensively, due to their high hydrogen absorption capacity of ~3 wt%, which is almost twice that of conventional alloys. These alloys are considered to be promising third generation hydrogen storage materials^{5, 6}. The body centered cubic solid solution alloys show high reactivity

with hydrogen at room temperature⁵. Due to the higher gravimetric storage capacity, these alloys are preferred over the conventional AB_5 alloys, used in the Ni-MH batteries. The hydrogen storage properties such as reversibility, desorption capacity hydrogen storage capacity, and desorption temperature of the alloys can be improved, by changing the composition⁶⁻⁸.

Recently, we studied stoichiometric TiCrV alloy and Zr-substituted TiCrV alloys, for their hydrogen storage properties. The 5 at% Zr-substituted TiCrV alloy is found to show maximum hydrogen storage capacity of 3.53 wt% with less hysteresis loss and good cyclic stability⁸.

In the present study, the cyclic hydrogen absorption-desorption properties of the Ti_2CrV alloy has been



investigated. The alloy has been characterized for the structure, pressure composition isotherms, hydrogen storage capacity, hydrogen absorption kinetics and the desorption temperature. The cyclic hydrogen absorption properties of Ti_2CrV alloy is systematically investigated upto 10th cycle.

Experimental

The Ti_2CrV alloy was prepared by arc-melting the high purity elements, in a water-cooled copper hearth, under argon atmosphere. For achieving homogeneity, the alloy button was turned over and remelted 4 times. The crystal structure of the as-cast alloy and hydride was examined by X-ray Diffraction (XRD) technique, using monochromatic $Cu K_\alpha$ radiation.

The hydrogen absorption and desorption studies were done, using a Sieverts set up described in our earlier studies⁸. The activation procedure involved heating the alloy under vacuum (10^{-6} mbar) for 2 hours at 673 K. Pressure-composition isotherms were studied in the temperature range 298 K and up to a hydrogen pressure of 2 MPa, using a Sievert's type set up. The kinetic study was done at room temperature and a hydrogen pressure of 2 MPa after one absorption-desorption cycle. The cyclic hydrogen absorption study was also done. For cyclic hydrogen absorption study, the alloy was activated after each cycle as described above. The hydride sample was surface-poisoned before being taken out. The hydrogen desorption behavior of the saturated hydride sample was studied by DSC measurement. The DSC measurement was done by using DSC823^e Mettler-Toledo instrument under argon flow, at a heating rate of 10K/min for both the samples of uncycled and cycled Ti_2CrV hydrides.

Results and Discussion

Crystal structure

Fig.1 shows the XRD pattern of Ti_2CrV alloy before and after hydrogen absorption. The Ti_2CrV alloy forms pure body centered cubic (bcc) structure, with a lattice parameter of 3.10 Å. After hydrogenation, the alloy forms a hydride with a composition $Ti_2CrVH_{9.05}$. The saturated hydride shows face centered cubic (fcc) structure with a

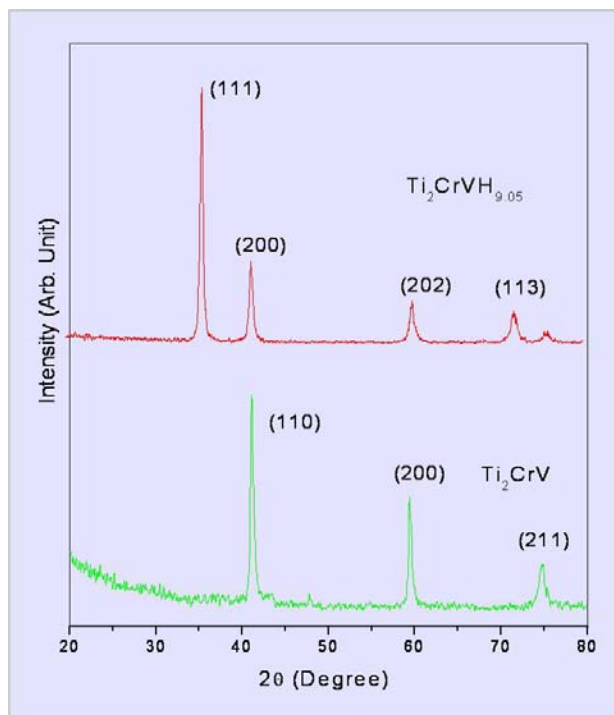


Fig. 1: XRD of Ti_2CrV alloy and its hydride

lattice parameter of 4.35 Å. Contrary to the $TiCrV$ alloy⁸, on cycling, the hydride of Ti_2CrV does not show phase separation, indicating good cyclic stability of the hydride

Hydrogen Absorption Study

The hydrogen absorption and desorption properties have been studied, using a Sievert's type set up. Fig. 2a shows the room temperature pressure-composition isotherms of Ti_2CrV alloy. The absorption isotherm measured at room temperature shows quite a flat plateau and the plateau pressure is less than 0.02 atm. The Ti_2CrV alloy shows a maximum hydrogen storage capacity of 4.37 wt% at room temperature and a hydrogen pressure of 2.5 MPa.

The rate of hydrogen absorption has been measured at room temperature, after one cycle of absorption-desorption. The rate of hydrogen absorption as a function of time is shown in Fig. 2b. The kinetics of hydrogen absorption is found to be fast for the Ti_2CrV alloy. As can be seen from Fig. 2b, Ti_2CrV alloy absorbs hydrogen without any incubation time. The alloy Ti_2CrV reaches the 2/3rd of the saturation value in about 290 seconds.

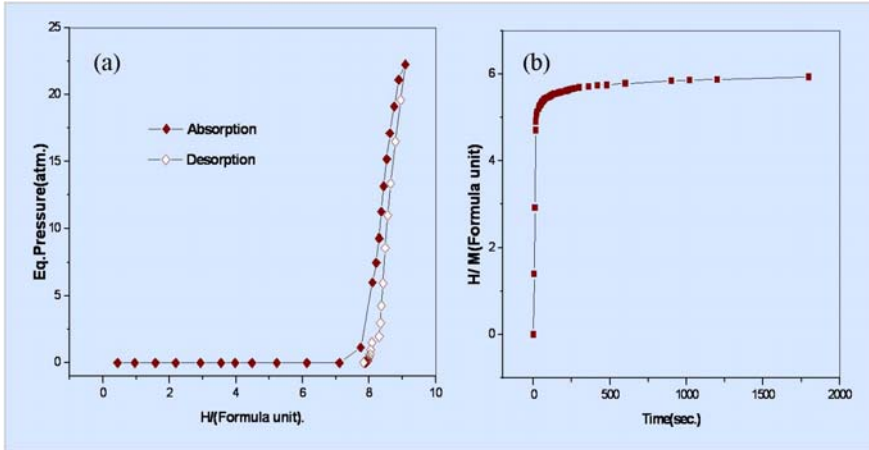


Fig. 2: (a) PC isotherms of Ti_2CrV alloy at room temperature, and (b) Kinetics study of Ti_2CrV alloy

Fig. 3 shows the cyclic absorption isotherm of Ti_2CrV alloy at room temperature, studied using Sievert's type setup. In this figure, we have plotted the pressure composition isotherm of some selected cycles viz. 1st, 2nd, 3rd, 4th, 6th, 8th and 10th. It has been found from literature, that upon cycling, the hydrogen absorption capacity decreases initially, however, after a few cycles it remains the same. The Ti_2CrV alloy absorbs a maximum of 9.05 H/ formula unit. All the absorption isotherms show the same plateau

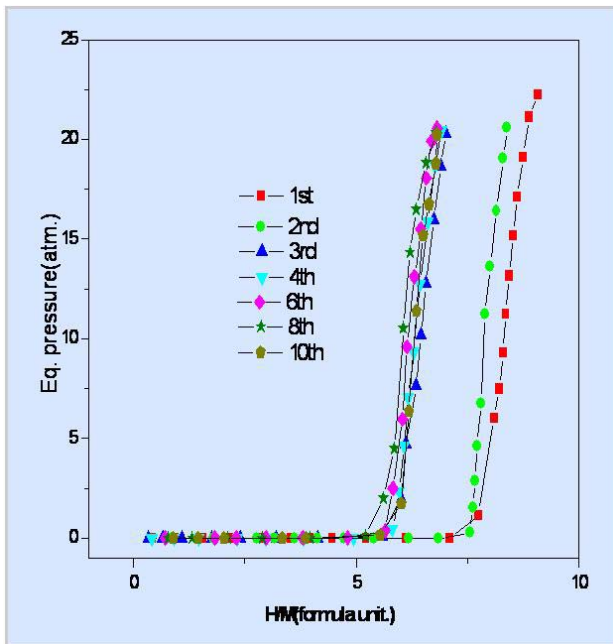


Fig. 3: Cyclic absorption isotherms of the Ti_2CrV alloy.

pressure below 0.02 atm. The plateau pressure remains unaltered with cycling. The alloy shows maximum absorption of 7.21, 7.19 and 7.21 H/Formula unit in the 6th, 8th and 10th cycles, respectively. After a few cycles, a stable absorption capacity of 3.5% is found for the Ti_2CrV alloy. The decline in hydrogen absorption capacity may be due to the formation of irreversible stable hydride. Many researchers have found similar cyclic absorption

capacity trend in the Ti-Cr-V based alloys^{9, 10}.

Hydrogen desorption Study

In order to investigate the hydrogen desorption process, and desorption temperature, Differential Scanning Calorimetric (DSC) measurement was performed on the saturated hydride, $Ti_2CrVH_{9.05}$ and $Ti_2CrVH_{7.21}$. Fig. 4 shows the DSC curve of uncycled and multi cycled hydride. From the figure it can be seen, that both hydrides of the Ti_2CrV

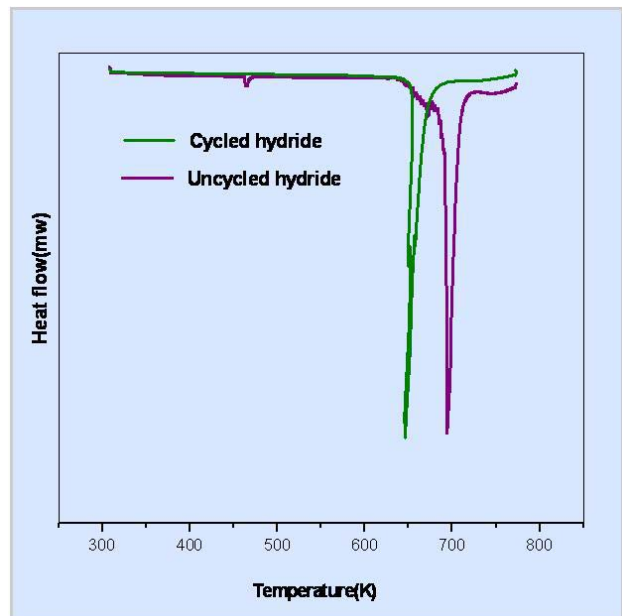


Fig. 4: DSC graphs of uncycled and multi-cycled Ti_2CrV hydrides



alloy show single endothermic peak. The main dehydrogenation peaks for the multicycle hydride and hydride after one hydrogen absorption desorption cycle, are found at 650 and 695K, respectively. It has been found, that the multi cycled hydride releases hydrogen at slightly lower temperature as compared to uncycled Ti_2CrV hydride. The cyclic study reveals, that the hydrogen desorption temperature decreases with cycling of the alloy.

Conclusions

The cyclic hydrogen absorption-desorption properties of Ti_2CrV alloy have been studied. This alloy was found have a maximum storage capacity of 4.37 wt%. The kinetics of hydrogen absorption was found to be fast for Ti_2CrV alloy without any incubation time. The cyclic hydrogen absorbing ability decreased progressively during the first few cycles and after that it remained almost constant at 3.5 wt% hydrogen absorption capacity. From the DSC analysis, the multicycled hydride showed hydrogen desorption at lower temperature as compared to uncycled hydride of Ti_2CrV . The plateau pressure was found to be less than 0.02 atm. at room temperature, indicating that this alloy forms stable hydride at room temperature. Due to the high storage capacity, this alloy could be used in Ni-MH batteries.

References

1. Zuttel A, Sudan P, Maunon Ph, Kiyobayashi T, Emmenegger Ch, Schlabach L. "Hydrogen storage in carbon nanostructures", *Int. J. Hydrogen Energy* 27 (2002): 203-204.
2. Zaluski L, Zaluska A, Ström-Olsen JO. "Nanocrystalline metal hydrides". *J. Alloys Compds* 253–254 (1997): 70–9.
3. Genma R, Okada N, Sobue T, Uchida HH. "Mechanically milled alanates as hydrogen storage materials". *Int. J. Hydrogen Energy* 31 (2006): 309-11.
4. Sakintuna B, Farida LD, Michael H. "Metal hydride materials for solid hydrogen storage: a review". *Int. J. Hydrogen Energy* 32 (2007):1121– 40.
5. Iba H, Akiba E, The relation between microstructure and hydrogen absorbing properties in Laves phase solid solution multiphase alloy, *J. Alloys Compd* 1995;231:508-512.
6. Yu XB, Wu Z, Xia BJ, Xu NX. "Enhancement of hydrogen storage capacity of Ti–V–Cr–Mn BCC phase alloys". *J. Alloys Compds* 372 (2004): 272–77.
7. Basak S, Shashikala K, Sengupta P, Kulshreshtha SK. "Hydrogen absorption properties of Ti-V-Fe alloys: effect of Cr substitution". *Int. J. Hydrogen Energy* 32 (2007): 4973-77.
8. Shashikala K, Banerjee S, Asheesh Kumar, Pai MR, Pillai CGS. "Improvement of hydrogen storage properties of TiCrV alloys by Zr Substitution". *Int. J. Hydrogen Energy* 34 (2009): 6684-89.
9. Lin HC, Lin KM, Wu KC, Hsiung HH, Tsai HK. "Cyclic hydrogen absorption-desorption characteristics of TiCrV and Ti0.8Cr1.2V alloys". *Int. J. Hydrogen Energy* 32 (2007): 4966-72.
10. Wang JY, Jeng RR, Nieh JK, Lee S, Lee SL, Bor HY. "Comparing the hydrogen storage alloys TiCrV and vanadium-rich TiCrMnV". *Int. J. Hydrogen Energy* 32 (2007): 3959-64.



Thorium Intake due to consumption of locally grown vegetables by inhabitants of High radiation background areas by INAA

R.S.Sathyapriya, Suma Nair, R.K. Prabhath, Madhu Nair and D.D.Rao

Internal Dosimetry Section, Health Physics Division

and

V. Kamesh

SRM University, Tamilnadu, India

and

R. Acharya

Radiochemistry Division

This Paper received the Best Paper Award at the Fourth International Symposium on Nuclear Analytical Chemistry (NAC-IV), held at Mumbai, from 15-19 November, 2010

Abstract

A study was conducted, to estimate thorium concentration in locally grown vegetables, in High Background Radiation Area (HBRA), of southern coastal region of India, using Instrumental Neutron Activation Analysis (INAA). The daily intake of ^{232}Th ranged between 0.27-5.35 mBq d⁻¹. The annual ingestion dose due to thorium from these food categories, was $0.47\mu\text{Sv y}^{-1}$ for female and $0.59\mu\text{Sv y}^{-1}$ for males.

Introduction

Humans are exposed to external and internal radiation, due to natural radioactivity. Internal radiation is due to inhalation of radon and thoron gases and their progeny and by ingestion of terrestrial isotopes from thorium and uranium series. According to UNSCEAR report, ingestion dose from thorium and uranium series is 0.12 mSv [1]. There are many areas in the world such as Guarapari in Brazil, Yanjiang in China, Chavara, Manavalkurichi and chatrapur in India possessing high levels of natural radiation. The cause of this high level of natural radioactivity, is due to monazite deposits in these regions. The ingestion doses received by the inhabitants of these regions, is mainly from intake of ^{232}Th , through consumption of food, milk etc. ^{232}Th is a long-lived

naturally occurring radionuclide, present in the earth's crust and forms 100% of the Thorium present in the earth's crust. Once in the human body, Thorium accumulates in lungs, liver and skeleton. Instrumental Neutron Activation Analysis (INAA) was used, to determine thorium concentration in different food products. The concentration of ^{232}Th obtained along with the regional food consumption rate and ICRP dose conversion factor were used, to evaluate the rate of ^{232}Th intake and annual committed effective dose.

Experimental

The National Nutrition Monitoring Board (NNMB) of India, has classified the food consumed into 14 categories, so that a characteristic everyday meal is reproduced[2]. In



this work, focus is on the typical locally grown and consumed vegetables and fruits. According to NNMB, vegetables were classified further into green leafy, roots, tubers and others. Vegetables and fruits were collected from kitchen gardens of houses from Chavara and Manavalakurichi regions.

The collected samples were processed, away from the sampling location, so as to reduce the contamination from dust. The samples were brought back to the laboratory and washed to remove sand or soil and to prevent the entry of ²³²Th as extraneous contaminant. Only the edible part was taken up for further analysis. The samples were then freeze-dried, homogenized and preserved for further analysis[3].

About 100 mg each of the powdered samples, along with NIST standard reference material (orchard leaves), were packed in an Al-foil and irradiated at the CIRUS research reactor at a thermal neutron flux of 1.0×10^{13} n/cm²s, for 21 hours. On irradiation, ²³²Th present in the sample is

converted to ²³³Th, which decays by β emission to ²³³Pa. Samples were assayed by measuring 311.8 keV γ -ray, using a 40% relative efficiency HPGe detector coupled to a 8k-Multi Channel Analyzer (MCA). The resolution of the detector was 2.1 keV at 1332 keV of ⁶⁰Co. The minimum detection limit for 80,000sec Counting was 0.2 ng/g-dry.

Results and Discussion

The reliability of the procedure, for estimation of ²³²Th in environmental samples by INAA was assessed by analyzing standard reference materials, orchard leaves (NIST-SRM-1571), Apple Leaves (NIST-SRM-1515) and Tomato leaves (NIST-SRM-1573a) under similar irradiation, cooling and counting conditions. The analytical results of our work agreed with the certified values. The concentration of ²³²Th was measured in four food categories: namely green leafy vegetable, Other vegetable, Roots & Tubers and Fruits (Table 1). The concentration in fresh weight ranged between 0.09 ng/g-fresh to 45.21 ng/g-fresh. The highest concentration was found in Tora root (45.21 ng/g-wet)

Table 1: Thorium concentrations in food samples

	Food Item	Concentration Of Th(ng/g dry wt)	Concentration Of Th(ng/g Fresh wt)	Concentration Of Th(μ Bq/g Fresh wt)
Green Leafy Veg.	Curry leaves	35.63 \pm 0.64	15.22 \pm 0.27	61.95 \pm 1.09
	amaranthus	89.51 \pm 3.37	15.28 \pm 0.58	62.19 \pm 2.36
	Drumstick leaves	26.78 \pm 0.99	6.35 \pm 0.23	25.84 \pm 0.94
Other Veg.	Brinjal(Blue)	22.25 \pm 0.86	1.92 \pm 0.07	7.81 \pm 0.28
	Brinjal(Long)	23.21 \pm 1.25	2.09 \pm 0.11	8.51 \pm 0.45
	Ivy gourd	12.1 \pm 0.16	0.92 \pm 0.01	3.74 \pm 0.04
	Ladies finger	15.36 \pm 0.93	2.09 \pm 0.13	8.51 \pm 0.53
	Tomato	2.34 \pm 0.08	0.09 \pm 0.01	0.37 \pm 0.01
	Yard long bean	9.42 \pm 0.17	0.81 \pm 0.02	3.29 \pm 0.04
	Drumstick	13.45 \pm 0.46	1.18 \pm 0.06	4.8 \pm 0.24
Tubers and Roots	Yam	30.25 \pm 1.03	15.71 \pm 0.09	63.94 \pm 0.37
	Taro root	69.56 \pm 2.17	45.21 \pm 1.13	184.1 \pm 4.59
	Tapioca	47.63 \pm 1.94	21.23 \pm 0.86	86.41 \pm 3.52
Fruit	Banana	6.59 \pm 0.11	01.99 \pm 0.03	8.09 \pm 0.01
	Guava	2.57 \pm 0.07	0.86 \pm 0.02	3.51 \pm 0.08
	Papaya	19.1 \pm 0.13	1.99 \pm 0.01	8.18 \pm 0.04



Table 2: Daily intake of ²³²Th in four food categories for the population Annual committed effective dose due to ²³²Th (H_{Th}) intakes for female and male

Food category	female (g/d)	male (g/d)	²³² Th concentration (μBq/g Fresh)	Daily intake (Female) (mBq/d)	Daily intake (Male) (mBq/d)	H _{Th} , Female, (10 ⁻⁸ Sv y ⁻¹)	H _{Th} , Male, (10 ⁻⁸ Sv y ⁻¹)
Leafy vegetable	9	12	49.94 ± 0.92	0.449 ± 0.008	0.599 ± 0.011	3.77 ± 0.07	5.03 ± 0.09
Other vegetables	41	55	12.34 ± 0.36	0.506 ± 0.015	0.678 ± 0.019	4.25 ± 0.12	5.69 ± 0.17
Root and Tuber	39	48	111.5 ± 1.92	4.348 ± 0.075	5.352 ± 0.092	36.51 ± 0.63	44.93 ± 0.77
Fruit	41	53	06.59 ± 0.02	0.270 ± 0.008	0.349 ± 0.003	2.27 ± 0.01	2.91 ± 0.01

followed by Tapioca (21.23 ng/g- wet). In Amaranthus, curry leaves, Tora root, Yam and Tapioca, the concentration was higher than the UNSCEAR values (0.1-33 μBq/g-fresh). Daily intakes of ²³²Th, due to consumption of the four food categories by the inhabitants of the region, were calculated using the consumption rate data as given by the NNMB (Table 2). The range was between 0.270 ± 0.008 to 4.348 ± 0.075mBq d⁻¹ for females and between 0.349 ± 0.003 and 5.352 ± 0.092 mBq d⁻¹ for males. The highest intake is from consumption of roots and tubers. ²³²Th intake was higher in males as compared to females as the consumption rate was higher for males than in females. The ingestion dose was evaluated as $H_{Th} = (U_i * C_{i,Th})g_{Th}$. Where i denotes the food category, U_i denote the annual consumption rate of food i (kg/y), C_{i,Th} is the activity concentration of the radionuclide ²³²Th in food i(Bq/kg), and g_{Th} is the dose co-efficient for ingestion of ²³²Th, which is 2.3 x 10⁻⁷ Sv/Bq for adult members of the public[4]. Dose from ingestion can be considered as negligible to that of natural external exposure.

Conclusion

The study shows that INAA can be used for estimation of ²³²Th concentration in food samples effectively. Tapioca,

Tora root and Amaranthus have higher concentrations of ²³²Th as compared to other food categories and they being widely used are major contributors to the effective dose.

Acknowledgements

Authors are thankful to Dr. P.K. Sarkar, Head, Health Physics Division, BARC for his keen interest in the work.

References

1. United Nations Scientific Committee on the Effects of Atomic Radiation(UNSCEAR)(2000). United Nations, New York.
2. National Nutrition Monitoring Board Diet and Nutritional Status of Rural Population, (2006) NNMB Technical Report 24.
3. Measurement of Radionuclides in Food and Environment Guidebook, Technical Report Series No. 295, (1989) IAEA, Vienna.
4. International Commission on Radiological Protection. ICRP 69) Annals of ICRP 25(1), (1995) Oxford.



Transgenic tobacco plants expressing fungal copper and zinc transporter genes show enhanced acquisition of copper and zinc

Sudhir Singh, Prachy Dixit and Susan Eapen

Nuclear Agriculture & Biotechnology Division

This paper won the Best Poster Award at "The National Symposium on Plant Tissue & Organ Culture: the present scenario", held at University of Calcutta. during March 3-5, 2010

Abstract

Copper (Cu) and zinc (Zn) are micronutrients essential for growth and differentiation of all organisms, but are often deficient in human diet. In the present study, transgenic tobacco plants expressing two fungal genes - namely a copper transporter (*tcu-1*) and a zinc transporter (*tzn1*) gene from *Neurospora crassa* were developed and the plants showed enhanced acquisition of Cu and Zn respectively compared to wild-type plants.

Introduction

Copper (Cu) and zinc (Zn) are essential micronutrients, indispensable for life of all organisms, Zinc and to a lesser extent Cu are normally deficient in human diet, especially in the diet of the population of developing countries. Phyto-fortification – enrichment of edible parts of crop plants with essential elements can be achieved, by forthcoming plants using conventional plant breeding methods or by transgenic technology. Although, plants have the inherent potential to take up these metals, their ability can be further enhanced by development of transgenic plants, with potential genes from heterologous sources. In the present work, a copper transporter (*tcu-1*) and a zinc transporter (*tzn1*) gene from fungus *Neurospora crassa* were cloned in binary vector pCAMBIA1301 and introduced individually into *Nicotiana tabacum* plants, through *Agrobacterium tumefaciens*-mediated plant transformation for developing transgenic plants with enhanced acquisition of Zn and Cu in plant biomass.

Experimental

Cloning of Cu and Zn transporter from *Neurospora crassa* and development of transgenic plants

Based on Cu and Zn accumulation studies in *N. crassa*, a Cu transporter gene referred as *tcu-1* (NCU00830.2) and a Zn transporter gene *tzn1* (NCU07621.3) of *N. crassa* having higher affinity for Cu and Zn, respectively, were chosen for the present work. The complete cDNA of the *tcu-1* and *tzn1* were cloned in plant binary vector pCAMBIA1301 (CAMBIA, Brisbane, Australia) [1,2]. The resulting plasmid has *hpt II* as a plant selectable marker and *uidA* as the reporter gene, apart from *tcu-1/tzn1*. Plasmids were finally introduced individually into *Agrobacterium tumefaciens* EHA 105 cells, using an electroporator 2510 (Eppendorf, Hamburg, Germany).

Transgenic *Nicotiana tabacum* L. cv Havana 425 plants were developed using *Agrobacterium tumefaciens*, according to the procedure described earlier [1].



Stable integration of *tcu-1/tzn1* in the genome of transgenic plants was confirmed by Southern blot hybridization. Expression of *tcu-1/tzn1*, as well as other transgenes in plants, was confirmed by reverse-transcription PCR (RT-PCR) using Affinity Script Multiple Temperature cDNA Synthesis kit (Stratagene, La Jolla, CA, USA)[1,2]

Copper/Zinc acquisition in transgenic (T₀) plants grown in hydroponics

Initially, ten independently transformed and confirmed T₀ tobacco lines in triplicate, (multiplied by micropropagation of shoots for developing same clones) along with control, were grown in Hoagland's liquid medium spiked with different concentrations of Cu/⁶⁵Zn. Copper content was estimated by GBC 932 B+ Atomic Absorption Spectrophotometer (GBC, Melbourne, Australia) using air-acetylene flame. ⁶⁵Zn estimation was done through gamma ray spectrometry [1].

Results and Discussion

Cloning of tcu-1/tzn1 and development of transgenic tobacco plants

A high affinity copper transporter gene *tcu-1* and zinc transporter gene *tzn1* were cloned from *Neurospora crassa*

and introduced into plant expression vector pCAMBIA1301. Transformation of tobacco was conducted by *Agrobacterium tumefaciens*-mediated co-culture method, using leaf discs and transgenic plants selected on medium containing hygromycin B.

In Southern blot analysis with genomic DNA, all transgenic lines selected for the study showed a single fragment, while control plant did not show any signal, suggesting stable integration of single copy of *tcu-1/tzn1* in selected transgenic lines as well as absence of homologous DNA sequence in control plants (Fig. 1). Results of RT-PCR using total RNA from transgenic plants confirmed that *tcu-1/tzn1* gene (as well as *hptII* and *uidA*) expressed in all selected transgenic lines, while there was no expression in control plants (Fig. 2).

Acquisition of copper/zinc by plants grown in hydroponics

When the performance of different T₀ transgenic lines in hydroponic solution with basal Cu level (ie 0.32 μM) was compared, all the transgenic lines showed higher Cu content in shoots with C-2-1 and C-2-4 plants showing up to 2.5 times higher Cu accumulation compared to control plants. Similarly, accumulation of Cu in roots was

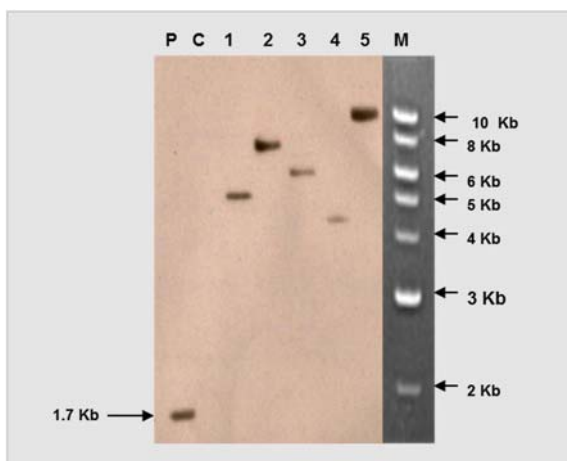


Fig. 1: Southern blot hybridization of total genomic DNA of control and T₀ *tcu-1* transgenic tobacco plants P-positive control, 1-5-DNA from selected transgenic lines showing single band > 1.7 kb, C-DNA from control tobacco plant, M-1kb ladder.

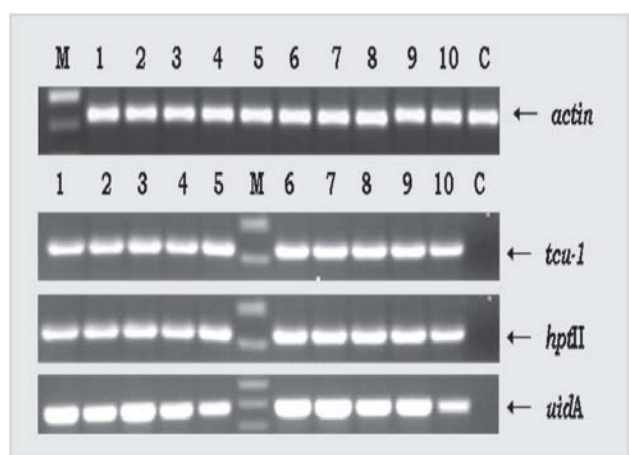


Fig. 2: Reverse transcription PCR of cDNA prepared from total RNA of transformed, PCR positive tobacco plants using *actin* (housekeeping), *tcu-1*, *hptII* and *uidA* specific primers. 1-10-T₀ Transgenic plants, C-control plant, M-100 bp ladder.

Merit Award



higher in most of the transgenic lines compared to control. Among them the best performing line C-2-4 showed 2.8 times higher accumulation of Cu in roots from solutions than control plants.

When the effectiveness of heterologous Cu transporter for Cu acquisition in tobacco plants exposed to a broad range of Cu concentrations (0.32µM, 3.2µM, 9.6µM and 96µM), using three better performing transgenic lines (C-1-1, C-2-1 and C-2-4) were tested, they showed higher accumulation of Cu in both shoots and roots compared to control plants at all Cu concentrations tested. Line C-2-4 showed the highest uptake of Cu from solution at all four concentrations of Cu tested. It accumulated 2.8 times more Cu in roots and up to 2.5 times more Cu in shoots compared to control plants.

When studies on uptake of Zn by control and ten independently transformed and confirmed transgenic plants grown in hydroponics spiked with ⁶⁵Zn was conducted, transgenic plants showed significantly enhanced uptake of Zn compared to control (Fig. 3). When the accumulation of Zn in root and shoot biomass was studied, roots showed higher accumulation of Zn compared to shoots. Roots of transgenic tobacco line Z5 showed up to 11 times more Zn acquisition compared to control. Levels of Zn in shoot biomass of all transgenic lines were also significantly higher than the control. These results demonstrated that transgenic tobacco plants with

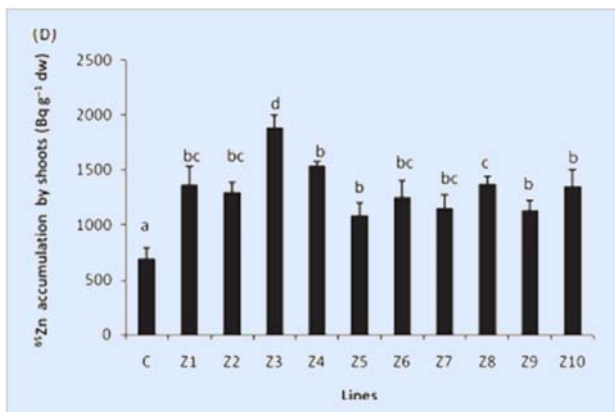


Fig. 3: ⁶⁵Zn accumulation in transgenic and control plants exposed to ⁶⁵Zn in hydroponics at the end of 10 days. (a) roots (b) shoots.

tzn1 could take higher Zn at all Zn concentrations compared to control. Accumulation of Zn was higher in roots compared to shoots.

For further studies, best performing transgenic line Z5 along with control tobacco plants were exposed to different concentrations of Zn. Zinc uptake by Z5 transgenic and control tobacco plants increased with increase in concentration of Zn, with the roots of Z5 plants showing significantly higher levels of Zn (~2.7, 4, 6.5, 8, 5.5 times, respectively, at 0.7, 7, 70, 350 and 700 µM Zn concentrations) compared to control plants (Fig. 4). Shoots of Z5 transgenic plants exposed to different concentrations of Zn also showed enhanced Zn acquisition compared to control plants. Although the levels of Zn in roots and shoots of Z5 transgenic tobacco plants were significantly higher at all Zn concentrations compared to control (Fig.4a,b), accumulation of Zn was higher in roots compared to shoots.

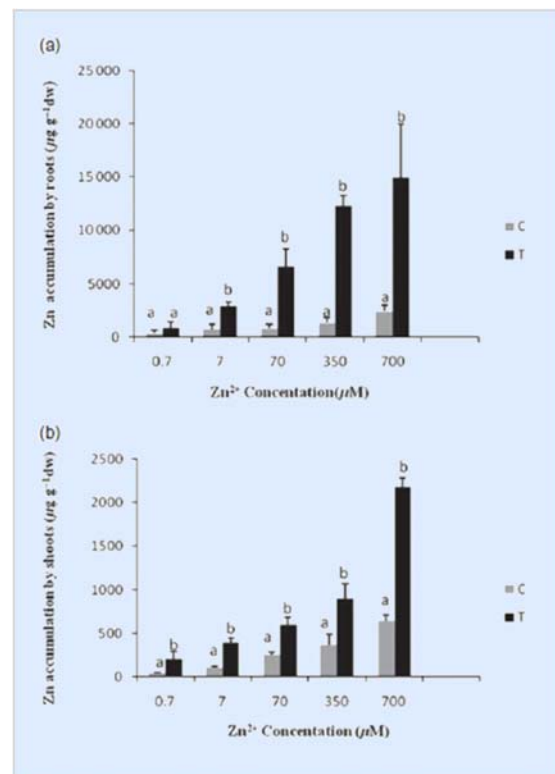


Fig. 4: Zinc accumulation by control and transgenic plants Z5 grown in hydroponics spiked with different concentrations of Zn (unlabelled ZnCl₂) at the end of 10 days. (a) Roots (b) Shoots.



Bio-fortification of crop plants for enhanced accumulation of mineral elements is one of the priority areas of research and transgenic technology can be used to enhance the levels of Zn and Cu in plant tissues. Over-expression of zinc and copper transporters can enhance the acquisition of Cu and Zn in plants. Another strategy to improve Cu/Zn acquisition in plants, is to introduce efficient heterologous Cu/Zn transporters in plants. In the present study, we cloned a high affinity copper transporter gene (*tcu-1*) and a zinc transporter gene from the fungus *N. crassa* and introduced them into tobacco plants. Transgenic tobacco plants (T_0) expressing *tcu-1* and *tzn1* were used for studies on Cu and Zn acquisition from solution. All the transgenic lines tested, showed higher levels of Cu/Zn acquisition compared to control plants and the levels of Cu/Zn in shoot biomass of transgenic lines were higher than wild-type plants. Although the shoots of transgenic plants accumulated higher levels of Cu/Zn compared to control plant, roots retained a high proportion of Cu/Zn which was taken up.

The present work perhaps is the first study, where heterologous Cu/Zn transporter genes were successfully transferred and expressed in a model plant-tobacco to

enhance Cu/Zn acquisition. Development of transgenic tobacco with heterologous Cu/Zn transporter genes, which was shown to take up high levels of Cu/Zn from solution and retaining high levels of Cu/Zn in roots, may find use in biofortification of Cu/Zn in crop plants such as carrot and cassava, where root is the edible part. To enhance Cu/Zn transport to shoots and seeds of crop plants, other genes involved in translocation of these essential elements to shoots, need to be co-transferred along with copper/zinc transporter genes.

References

1. Dixit, P., Singh, S., Ramchandran, V., Kiranmayi, P., Eapen, S. Expression of a *Neurospora crassa* zinc transporter gene in transgenic *Nicotiana tabacum* enhances plant zinc accumulation without co-transport of cadmium. *Plant Cell & Environment* 33 (2010):1697-707.
2. Singh, S., Korripally, P., Ramchandran, V & Eapen, S. Transgenic *Nicotiana tabacum* plants expressing a fungal copper transporter gene show enhanced acquisition of copper. *Plant Cell Reports* (2011) DOI 10.1007/s00299-011-1101-3.



Transient plane source technique for measurement of thermal conductivity of U and T91 for fast reactor application

Santu Kaity, M.R. Nair, A.K. Sengupta and Arun Kumar
Radiometallurgy Division

This paper received the Best Poster Award at the 17th National Symposium on Thermal Analysis (THERMANS 2010) held at Kurukshetra, Haryana, during March 9-11, 2010

Abstract

Transient Plane Source (TPS) method is one of the most precise, simple and convenient techniques for measurement of thermal conductivity of materials. In the present investigation the principle of the Transient Plane Source method has been described and thermal conductivity data generated for uranium metal and T91 cladding material has been highlighted. Thermal conductivity of uranium agrees well with those reported in the literature over the temperature range investigated. Thermal conductivity of T91 in the reactor operating temperature was found to be 25-29 Wm⁻¹K⁻¹. The thermal conductivity of T91 is higher than that of D9 and HT9 cladding in the temperature range room temperature (RT)-700°C.

Introduction

Thermal conductivity is one of the most important properties of both fuel and cladding material and the maximum LHR of the fuel without causing any centre melting is determined by the thermal conductivity of the fuel. As a part of that, thermal conductivity of U and T91 cladding material (Mod. 9Cr1Mo steel) was estimated by Transient Plane Source (TPS) technique. TPS technique was first demonstrated by Gustafsson^{1, 2}. It is a modern technique, giving information on thermal conductivity, thermal diffusivity and specific heat per unit volume of the material. This method has been used for studying a large number of different materials with thermal conductivities ranging from 0.005Wm⁻¹K⁻¹ (evacuated powders) to 500Wm⁻¹K⁻¹ (graphite)³. The sensor is sandwiched between two identical halves of the sample (solid sample) or embedded in the sample (powders, liquids). A direct current is passed through the sensor to increase the sensor temperature by a fraction of a degree up to several degrees. As a result the resistance of the

sensor changes which causes voltage drop over the sensor. By recording the voltage variation over a certain time period from the onset of the heating current, it is possible to obtain precise information on the heat flow between the sensor and the test specimen. Sensor acts both as a heat source for increasing the temperature of the sample and a "resistance thermometer" for recording the time-dependent temperature increase. The sensor consists of an electrically conducting pattern in the shape of a double spiral etched out of a thin sheet of nickel. Thin Polyimide (Kapton) films and Mica are used as insulator materials to support the Nickel spiral. Solution of the thermal conductivity equation is based on the assumption that the sensor is located in an infinite material. The "thermal wave" or "thermal penetration depth" generated in an experiment must not reach the outside boundaries of the sample pieces during the transient recording and determined by the probing depth given by $\Delta_p = 2(\kappa t)^{1/2}$, where κ is thermal diffusivity of sample



and t is measuring time of the experiment. A consequence of this equation is that the distance from any point of sensor to any point on the surface of the two sample pieces must not exceed Δ_p if the total measuring time is t .

Theory of TPS technique

A constant electric power supplied to the sensor results in an increase in temperature which is directly related to the variation in the sensor resistance $R(t)$ by the equation:

$$R(t) = R_0 \{1 + \alpha[\Delta T_i + \overline{\Delta T(\tau)}]\} \quad (1)$$

R_0 is resistance of the disk at time $t = 0$, α is the Temperature Coefficient of Resistivity (TCR), ΔT_i is small temperature drop over the electrically insulating layer which are covering the two sides of the sensor material. After a short initialization period, this temperature drop will stay constant due to liberation of constant power. If $\overline{\Delta T(\tau)}$ is the average temperature increase of the TPS element, we get the temperature increase recorded by the sensor as:

$$\overline{\Delta T(\tau)} + \Delta T_i = \frac{1}{\alpha} \left(\frac{R(t)}{R_0} - 1 \right) \quad (2)$$

Here ΔT_i is a measure of thermal contact between sensor and sample with $\Delta T_i = 0$ representing perfect thermal contact closely realized by a deposited (PVD or CVD) thin film. ΔT_i becomes constant after very short time Δt_i which can be estimated as:

$$\Delta t_i = \frac{\delta^2}{\kappa_i} \quad (3)$$

Where δ is the thickness of the insulating layer and κ_i is the thermal diffusivity of the layer material. It is assumed, that the disk consists of a certain number (m) of concentric ring sources located in an infinitely large sample. The time-dependent average temperature increase is given by theory^{1,3} as $\overline{\Delta T(\tau)} = P_0 (\pi^{3/2} a \lambda)^{-1} D(\tau)$ (4)

where P_0 is total output of power from sensor, a is radius of sensor, λ is thermal conductivity of sample that is being tested and $D(\tau)$ is a dimensionless time-dependent function. τ is defined accordingly: $\tau = (t/\theta)^{1/2}$ and $\theta = a^2 / \kappa$ (5)

where t is the time measured from the start of the transient recording; θ is the characteristic time; κ is the thermal diffusivity of the sample material. In most cases it is

advisable to introduce a time correction, because of unavoidable hardware and software delays. This is accomplished by replacing τ by τ_c where: $\tau_c = [(t - t_c) / \theta]^{1/2}$ (6)

Time corrections are a fraction of a second and should not be larger than the time between two consecutive temperature recordings. By making a computational plot of the recorded temperature increase versus $D(\tau)$, a straight line is obtained, the intercept of which is ΔT_i and the slope is $P_0 / (\pi^{3/2} a \lambda)$ using experimental times much longer than Δt_i . Since κ and θ are not known before the experiment, the final straight line from which the thermal conductivity is calculated, is obtained through a process of iteration.

Experimental

TPS technique is based on a specially designed Wheatstone bridge with sensor as one of the arms as shown in Figs. 1(a-b). The TPS unit was calibrated by Inconel 600 from RT to 700°C. Two identical cylindrical pure uranium samples (dia. 20 mm and height 10 mm) and two identical T91 samples (30 mm x 30 mm x 13.5 mm) were prepared for the experiment. The surfaces of the samples were polished to have good thermal contact with the TPS sensor and to minimize contact resistance. The experimental set

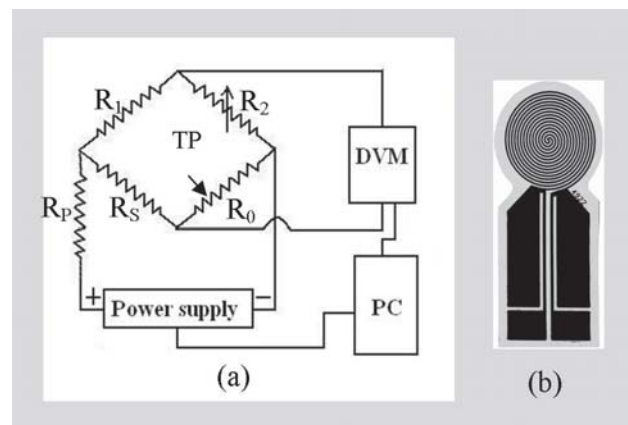


Fig. 1. (a) Schematic diagram of the electrical circuit for TPS method; R_p - standard resistance, which limits the current from a power supply; R_1 and R_2 - two block resistances (ratio arm); Digital Voltmeter (DVM); R_0 - TPS element; and R_2 - adjustable resistance. (b) TPS sensor

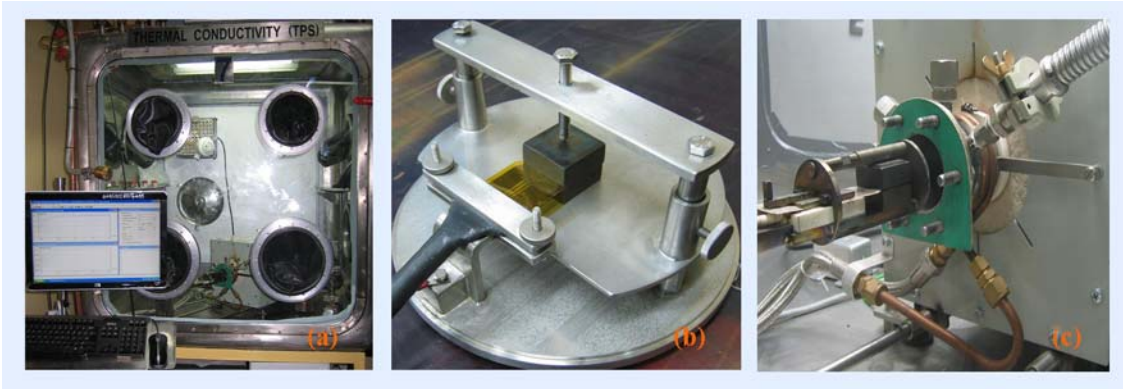


Fig. 2: (a) TPS unit inside a glove box, (b) Room temperature measurement set up with kapton sensor, (c) High temperature measurement set up with Mica sensor

up for room temperature and higher temperature measurement are shown in Fig. 2. The sensor is sandwiched between two halves of the sample. For high temperature measurement, the samples were heated in high purity argon atmosphere, to avoid oxidation. The samples were kept 30 min at each set of temperature before measurement to avoid temperature drift inside the samples. A Keithley 2400 source meter supplies a constant voltage across the bridge. Before the measurement, the bridge is automatically balanced and as the resistance of the sensor increases, the bridge becomes increasingly unbalanced. A Keithley 2000 digital voltmeter equipped with a scanner or multiplex card, records the unbalance voltage. From these recorded voltages it is possible to determine the temperature increase of the sensor and consequently the thermal conductivity of the sample.

Results and Discussion

Thermal conductivity data by Laser Flash method is estimated from the measured thermal diffusivity and heat capacity using $\lambda = \alpha C_p \rho$ relation, where λ is the thermal conductivity, α is thermal diffusivity, C_p is the specific heat capacity, and ρ is the density. Hence error from these two measurements can lead to lower accuracy in the thermal conductivity data. But in TPS method, thermal conductivity is estimated directly. The thermal conductivity plot of Uranium using TPS method and Laser Flash method are shown in Fig. 3 (a). The result of Uranium agrees well with those in the literature⁴ over the temperature range investigated. Since uranium is one of the major components of fast reactor metallic fuel, the thermal conductivity of uranium plays a significant role in optimization of fuel composition for fast reactor. Thermal conductivity of

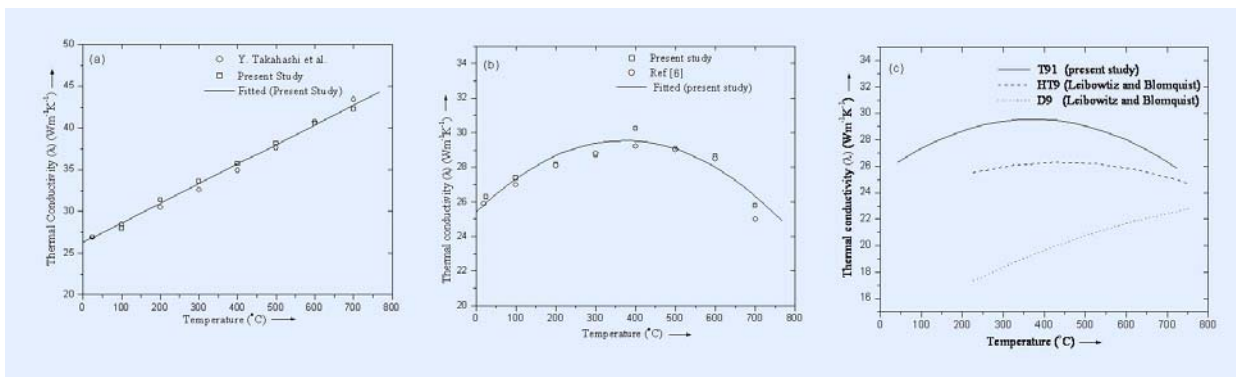


Fig. 3: (a) Thermal conductivity of uranium, (b) Thermal conductivity of T91, (c) Comparison of thermal conductivity of different cladding material for fast reactor



uranium estimated by TPS method can be represented in the range RT- 700°C by

$$\lambda \text{ (Wm}^{-1}\text{K}^{-1}\text{)} = 26.297 + 2.344 \times 10^{-2} T \quad (\text{T in } ^\circ\text{C})$$

Thermal conductivity of T91 is shown in Fig. 3(b). Thermal conductivity of T91 steel increases gradually from RT to 400°C and then decreases. In fact, it has been reported in the literature⁵ that the thermal conductivity of ferritic steel gradually increases from RT to 400°C and then decreases upto 750-800°C. After that it increases gradually. The Curie transition (i.e. ferromagnetic to paramagnetic transition) of T91 occurs at 742°C and ferrite (α) to austenite (λ) transition takes place at 837°C. The decrease in thermal conductivity of T91 may be due to both Curie transition and ferrite (α) to austenite (λ) transition. The thermal conductivity of T91 cladding was found to be higher than that of D9 and HT9⁵ as shown in Fig. 3(c). High thermal conductivity of T91 is one of the most important criterion for its selection as fast reactor cladding material. In a reactor operating condition, the cladding temperature for fast reactor is around 500°C to 650°C. In the temperature range the thermal conductivity of T91 is in between 25-29 Wm⁻¹K⁻¹. Thermal conductivity of T91 by TPS method is represented in the temperature range RT-700°C by

$$\lambda \text{ (Wm}^{-1}\text{K}^{-1}\text{)} = 25.420 + 2.223 \times 10^{-2} T - 2.988 \times 10^{-5} T^2 \quad (\text{T in } ^\circ\text{C})$$

Conclusions

Thermal conductivity of Uranium measured by TPS method in the present study agrees very well with published results. Thermal conductivity of T91 cladding is higher than D9 and HT9 cladding. Higher thermal conductivity of T91 is one of the important properties for choosing it as a cladding material for fast reactors.

References

1. S.E. Gustafsson, *Rev. Sci. Instrum.* 62(3)(1991) 797.
2. S.E. Gustafsson, International Patent Application No. PCT/SE89/00137.
3. Hot Disk Thermal Constants Analyser, Instruction Manual, Software version 5.9, Hot Disk, Sweden, 2007.
4. Y. Takahashi, M. Yamawaki, K. Yamamoto, *Journal of Nuclear Material* 154(1988)141.
5. L. Leibowitz and R.A. Blomquist, *International Journal of thermophysics*, 9(5)(1988)873.
6. G.M. Roux, O. Blanchot, R. Billardon, Identification of thermal boundary condition and thermo-metallurgical behaviour of X10CrMoVNb9-1 steel, DEN/SAC/DM2S/SEMT/LM2S,2006.



Sources identification using organic molecular markers in fine particulate matter collected at Trombay, Mumbai

S.K. Sahu, G.G. Pandit and V.D. Puranik

Environmental Assessment Division

This paper received the Best Poster Award at the Workshop cum Seventeenth National Symposium on Environment on advances in Environmental Monitoring and Modeling, held at the Centre for Environmental Science & Engineering, IIT Kanpur, from 13-15 May, 2010

Abstract

Positive Matrix Factorization (PMF), a useful factor analysis method, was applied to 24-hr $PM_{2.5}$ speciation data, collected at Trombay, Mumbai. The $PM_{2.5}$ fraction was found to have mass concentration ranging between $22.7 \mu\text{g}/\text{m}^3$ and $79.0 \mu\text{g}/\text{m}^3$, with a mean concentration of $56.7 \mu\text{g}/\text{m}^3$. In $PM_{2.5}$ samples, the total Polycyclic Aromatic Hydrocarbons (PAHs) level ranged from $12.8 \text{ ng}/\text{m}^3$ to $96.92 \text{ ng}/\text{m}^3$ and the mean concentration was $52.6 \text{ ng}/\text{m}^3$. For this study, a 5 factor model was found to provide the most physically interpretable solution, with 90.7% of the measured mass apportioned. The sources were identified as diesel combustion emissions, biomass burning and incineration, coal-fired power plant emissions, local gasoline traffic emissions and refinery emissions.

Introduction

Particulate matter has been implicated in a number of health effects, including respiratory symptoms, bronchitis, heart attack and premature deaths. The airborne Particulate Matter (PM) in an urban atmosphere, is a complex mixture of inorganic and organic substances, and their origin could be either natural or anthropogenic, or both. Among the organic compounds of anthropogenic origin, the PAHs make up an important group, because, of the way they endanger human health and also because, they can be used as source-specific marker molecules. Understanding the contribution of various emission sources is critical, to appropriately manage PAHs in the environment. Receptor models have been used, to assess contributions of PAHs from all major sources based on observations at sampling. Receptor models are the application of multivariate statistical methods to the identification and quantitative apportionment of pollutants to their sources. Positive Matrix Factorization (PMF), an advanced receptor models

has been successfully used, for quantitative identification of sources of organic pollutants in aerosols. PMF rotates the matrices of factor loadings and scores with positive constraints, which makes factor axes less orthogonal and makes factor loadings and factor scores more interpretable. In this paper, organic molecular markers PAHs were used in PMF analysis, to identify possible sources of $PM_{2.5}$ measures, at an urban location in Mumbai.

Sample Collection and Analysis

$PM_{2.5}$ samples were collected, using a fine particulate sampler. Sampling was done for a 24 hour period, at a height of 8 meters from the ground level. Pre-weighted filter papers were used, to collect the samples. A strict regime of quality control and quality assurance was followed. Field blanks were collected to quantify possible contamination of the samples during collection, transport and storage. The characterization and quantification of different PAHs were carried out, using a Shimadzu HPLC



system (LC-10 AD) with UV-visible detector. Before analysis, the filter paper samples were extracted ultrasonically, with hexane as solvent.

Results and Discussion

The PM_{2.5} fraction was found to have a mass concentration, ranging between 22.7 µg/m³ and 79.0 µg/m³, with a mean concentration of 56.7 µg/m³. In PM_{2.5} samples, the total PAHs ranged from 12.8 ng/m³ to 96.92 ng/m³ and the mean concentration was 52.6 ng/m³. Maximum concentration of PAH was observed during winter in PM_{2.5} samples, while a minimum value was observed during the monsoon. Lower concentration of PAHs was recorded during summer than in winter. This could be due to photo-oxidation of PAHs and the meteorological conditions, favoring the dispersion of these compounds during summer. Maximum concentration of fluoranthene was recorded during summer at the sampling site. Fluoranthene is the marker species of coal combustion, industrial oil burning and petrol and diesel powered vehicles. Due to longer retentivity of submicron particles in the atmosphere, Fluoranthene emitted around the industrial site shows a higher concentration during summer.

For this study, a five factors model was found to provide the most physically interpretable solution. 90.7% of the measured mass was apportioned. The sources were identified as diesel combustion emissions, biomass burning and incineration, coal-fired power plant emissions, local gasoline traffic emissions and refinery emissions. Fig.1 shows the percentage of concentrations of individual PAHs to different sources as obtained by PMF analysis.

Factor 1 explains about 30% of the sum of the measured PAHs and was dominated by

Benzo(k)Fluranthene, Benzo(b)Fluranthene, Phenanthrene and Perylene. According to Hwang et al. (2003) the presence of PAHs with 3 and 4 aromatic rings, such as Benzo(k)Fluranthene, Benzo(b)Fluranthene and Phenanthrene, indicates the dominance of diesel combustion. Therefore, the presence of these compounds can be attributed to diesel exhausts. Factor 2 explains 22% of the total PAHs and was dominated by Benzo (a) Anthracene, Benzo (a) Pyrene and Dibenzo (a,h) Anthracene. Kulkarni and Venkataraman (2000) have

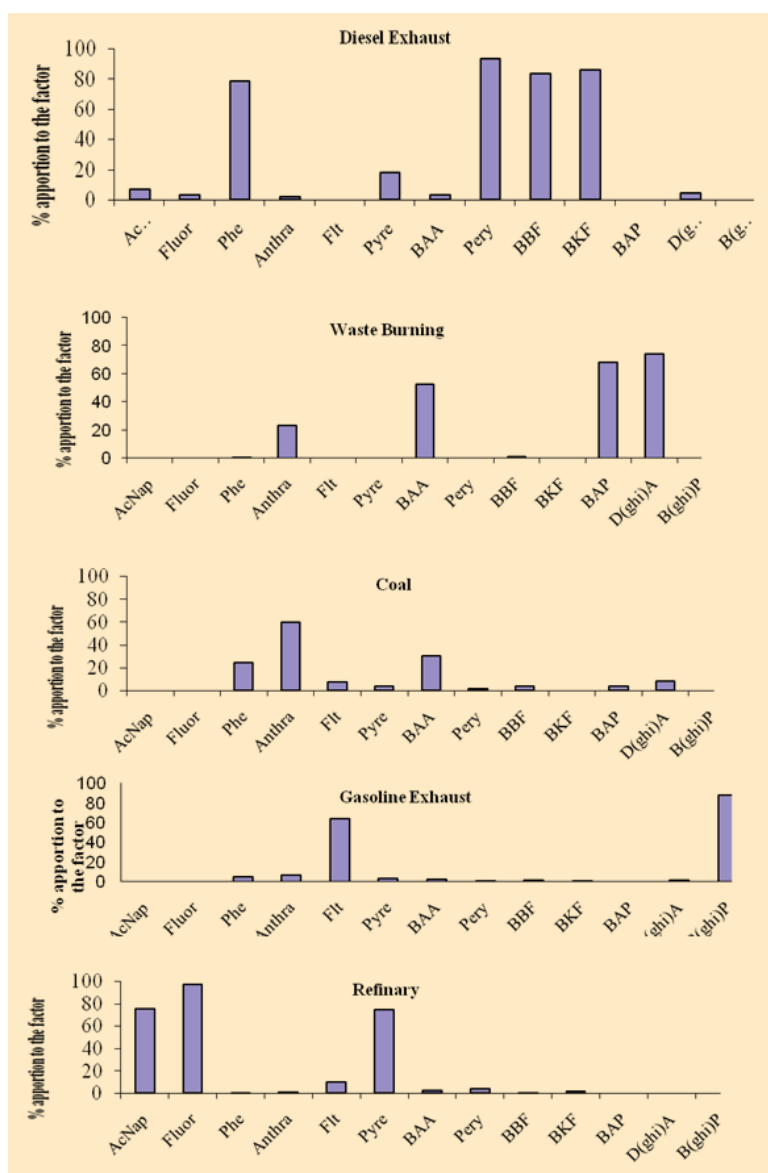


Fig.1 percentage contribution of individual PAH to different sources



shown, that Benzo(a)Pyrene can be a good tracer for wood burning, while Freeman and Cattell (1990) showed that this compound could be associated with combustion of vegetation. Masclat et al. (1986) have shown that, Dibenzo(a,h)Anthracene can be a typical tracer for incineration. Therefore, it is very difficult to assign any specific source for this factor. However, it is more appropriate to attribute this factor to biomass burning and incineration. Factor 3 is responsible for 16% of the sum of determined PAHs. This factor is predominantly weighted in Anthracene and Benzo(a)Anthracene. Khalili et al. (1995) identified that Anthracene, Phenanthrene and Benzo(a)Anthracene were tracers for coal combustion. Therefore coal combustion could be characterized as the source for this factor. Factor 4 accounted for 12% of the total measured PAHs. This factor is weighted in Benzo(ghi)Perylene and Fluranthene. Miguel et al. (1998) have shown, that Benzo(ghi)Perylene is characteristic of vehicular emissions from gasoline engines. Therefore this factor could be attributed to the vehicular emissions for gasoline exhausts. Factor 5 explains 10% of the variance and has a high load for Fluorene and Pyrene. According to Masclat et al. (1986), light PAHs (3 and 2 aromatic rings) are predominant in emissions from petrol refinery and are characterized by high concentration of Fluorene and Pyrene. Thus, in this work, this factor was associated with refinery emissions.

References

1. Kulkarni, P., and Venkataraman, C., (2000), "Atmospheric polycyclic aromatic hydrocarbons in Mumbai, India", *Atmospheric Environment*, 34, 2785-2790.
2. Khalili, N.R., Scheff, P.A., and Holsen, T.M., (1995), "PAH source fingerprints for coke ovens, diesel and gasoline engines, highway tunnels and wood combustion emissions" *Atmospheric Environment*, 29, 533-542.
3. Masclat, P., Nikolaou, K., and Mouvier, G., (1986), "Relative decay index and sources of Polycyclic aromatic hydrocarbons", *Atmospheric Environment*, 20, 439-446.
4. Miguel, A.H., and Pereira, P.A.P., (1998), "Benzo(k)fluoranthene, benzo(ghi)perylene and indeno(1,2,3-cd)pyrene: new tracer of automotive emissions in receptor modeling", *Aerosol Science Technology*, 10, 292-295.
5. Hwang, H.M., Wade, T.L., and Sericano, J.L., (2003) "Concentrations and source characterization of polycyclic aromatic hydrocarbons in pine needles from Korea, Mexico, and United States", *Atmospheric Environment*, 37, 2259-2267.
6. Freeman, D.J., and Cattell, C.R., (1990), "Wood burning as a source of atmospheric polycyclic aromatic hydrocarbons in urban air of Hon King", *Atmospheric Environment*, 24, 1581-1585.



Spectral narrowing of emission from ZnO inverse photonic crystals

Sunita Kedia

Department of Physics, Indian Institute of Technology, Bombay, Mumbai

and

R. Vijaya

Department of Physics, Indian Institute of Technology Kanpur, Kanpur

and

Alok K. Ray, Sucharita Sinha and K. Dasgupta

Laser and Plasma Technology Division

This paper received the Best Paper Award at the 9th DAE-BRNS National Laser Symposium (NLS-09), held at BARC, Trombay, Mumbai from 13th to 16th January, 2010

Abstract

Three dimensional photonic crystals are fabricated with polymethyl methacrylate (PMMA) colloidal spheres, by inward growing self-assembly technique. The voids present in the crystal are filled with zinc oxide (ZnO), prepared by sol-gel process and subsequently the polymer template is removed by chemical method, to get ZnO inverse photonic crystal. Structural and optical characterization of the crystal, establishes the quality of the crystals. Laser-induced emission studies on ZnO inverse photonic crystal, carried out at two different excitation conditions, help to establish the effect of the photonic crystal environment, on the emission of ZnO.

Introduction

Three-dimensional (3D) photonic crystals are structured dielectrics, with a periodically varying dielectric constant, in all three orthogonal directions in space. The structures are more popular because these can control the propagation of electromagnetic waves in a selective manner. In the absence of absorption, these crystals can show high reflection, associated with low transmission for a range of wavelength, known as the photonic stop band of the crystal. The photonic crystal is called a *pseudo* photonic band gap (PBG) material, when the wavelength of the stop band does not overlap for all angles of incidence. Earlier work shows that PBG crystals can be

used to suppress or enhance the spontaneous emission of radiative materials such as, laser dyes, quantum dots [1,2] and rare earth ions [3], embedded into the structure. When the position of the stop band of the crystal is independent of all conditions, one obtains a *complete* PBG structure. The photonic crystal with complete band gap is realizable when the constituent materials of the crystal have a high index contrast and can be used to design low threshold lasers, resonators and waveguide structures. There are a number of techniques by which 3D photonic crystals can be fabricated, among which self-assembly technique is the simplest and the least expensive [4]. In earlier work, a high index contrast in self-assembled polymeric photonic crystals has been



achieved, by infiltrating the direct 3D photonic crystals with a higher index material such as silica, ZnO, titania, silicon and germanium by different techniques [5-8] and the polymer template is subsequently removed, to get the inverse photonic crystal.

ZnO is a direct band gap semiconductor with a high refractive index ($RI \sim 2.0$) in the visible range. It is a widely used material because of its optical, electrical and acoustical characteristics and is well known for UV light-emitting device applications, due to the band gap at 3.3eV. In view of these qualities, ZnO inverse photonic crystal can be used to produce a blue laser [9]. Scharrer et al. infiltrated the ZnO into polystyrene (PS) photonic crystal by atomic layer deposition technique and observed a high UV photoluminescence (PL) in the inverse crystal, after removing the PS template by heat treatment [6]. Yang et al. infiltrated ZnO into PS-photonic crystal by electro-deposition technique and showed the broadening of PBG of inverse crystal, due to higher dielectric constant ratio [8] and discussed the effect of the photonic stop band on the PL of inverse crystal. An earlier work in our labs [7] reported the infiltration of SiO_2 and ZnO, prepared by sol-gel chemistry, into PS photonic crystals and a shift of nearly 100 nm in the reflection spectrum of the infiltrated crystal towards higher wavelengths, due to the increased effective index in the structure. Scharrer et al. obtained UV lasing with 3D ZnO inverse photonic crystal by pumping the sample along (111) direction with the third harmonic of Nd:YAG laser at 355nm. The lasing wavelength was tuned by changing the lattice constant of the crystal [9].

The aim of the present work is to fabricate large area ZnO inverse photonic crystals and understand their emission properties. In this context, 3D photonic crystals are fabricated by inward growing self-assembly method [4] using PMMA colloids. The crystal contains periodically arranged PMMA spheres (RI of 1.49) surrounded by air voids. The voids are infiltrated with ZnO prepared by sol-gel process. The infiltrated crystal is inverted by heat treatment [10] and chemical methods [8]. All the crystals

are analyzed by structural characterization, reflection measurements and laser-induced emission studies, to understand the effect of the photonic crystal environment on the active species of ZnO.

Experimental details

Commercially available aqueous suspensions of PMMA with a mean colloidal sphere diameter of 287nm (from Micro-particles, Germany), are used for self-assembly. The chosen diameter of the colloid results in a photonic stop band in the visible range. Simple glass slides are used as substrates and crystals are grown within 3 hrs in ambient conditions. Details of the fabrication process can be found elsewhere [11]. ZnO is prepared by sol-gel technique [7]. The PMMA photonic crystals are heated at 50°C for 10 min and dipped into the sol and withdrawn after 30 sec, in a controlled way. Since the crystals are at a slightly higher temperature than the sol, the crystal soaks the sol into its voids. The infiltrated crystals are allowed to dry in air for 12 hrs. The color of the infiltrated sample changes when it dries completely. The infiltration cycle was repeated 3 times with fresh sol. A longer duration of 3-days and 1 week was required, for complete drying of the crystal, after second and third infiltration cycles, respectively. The samples appeared opaque after the third infiltration cycle, perhaps due to a layer of ZnO formed on the surface of the photonic crystal after all the voids are fully infiltrated. To increase the index contrast further, PMMA template is removed by dipping the infiltrated crystal, in toluene for 30 min. The ZnO inverse photonic crystal looks blue in color to the naked eye.

The morphology of the photonic crystals is characterized with scanning electron microscope (SEM), atomic force microscope (AFM) and optical microscope (OM) images. The reflection and transmission spectra of the crystals are recorded with Perkin-Elmer Lambda 950 Spectrophotometer. A halogen lamp with unpolarized light and (12.5 × 5) mm spot size is used as the source. Laser induced emission study is performed with an excitation wavelength at the third harmonic of a Q-switched, pulsed



Nd:YAG laser at 355 nm. The laser is operated at 10 Hz repetition rate. The emission spectra are recorded using an optical fiber based spectrophotometer from Ocean optics (model no. 2000). Laser induced emission is also studied at an excitation wavelength, of 325nm from a continuous wave He-Cd laser, at an excitation power of 3.4 mW.

Results and Discussion

visible.

The reflectance and transmittance spectra are recorded from the (111) plane of the PMMA photonic crystal, ZnO infiltrated PMMA photonic crystal and ZnO inverse photonic crystal. The reflection spectra of PMMA photonic crystal for different angles of incidence are shown in Fig. 2a. The PMMA photonic crystal has a maximum reflectance of 25% at 597 nm at an incident angle of 8°.

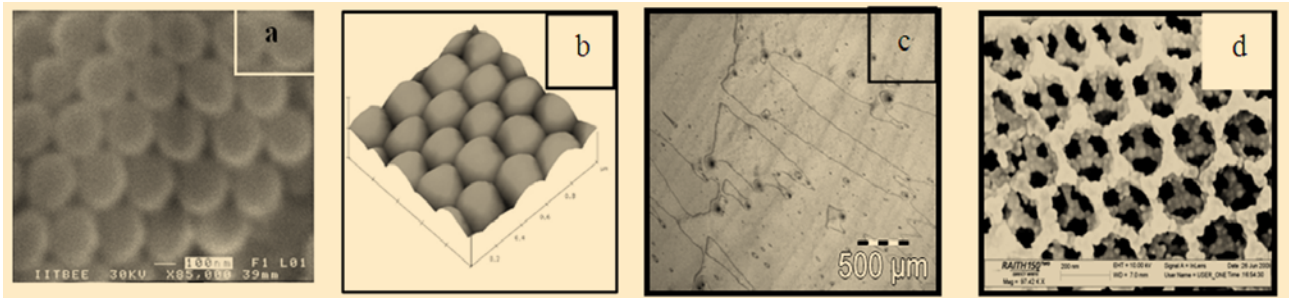


Fig. 1a: SEM image of 3D PMMA photonic crystal shows the hexagonal arrangement of spheres from the (111) plane of the fcc lattice. (Scale bar 100nm), 1b: AFM image of 3D PMMA photonic crystal gives an average sphere diameter of 283 nm (Scan area 1µm x 1µm), 1c: OM image of the (111) plane of the 3D PMMA photonic crystal. Dark lines are grain boundaries, which separate different domains (Scale bar 500µm), 1d: SEM image of the (111) plane of the ZnO inverse photonic crystal. Air spheres surrounded by ZnO net are observable. Well-ordered underlying layers are also visible. (Scale bar 200nm at 10 KV).

Fig. 1a is the SEM image of PMMA photonic crystal showing well arranged spheres in hexagonal geometry, indicating the (111) plane of the cubic lattice. Fig. 1b is the 3D AFM image of the (1 x 1) micron area of the same plane of the photonic crystal. It confirms the hexagonal arrangement of the spheres and gives an average diameter of 283 nm for the PMMA colloids. The SEM and the AFM images provide information from a small area of a few µm² of the crystal. OM image of the crystal is recorded to observe a larger area. Fig. 1c is the OM image of the (111) plane of the crystal, which shows domain sizes of about (2.0 x 0.8) mm, separated by grain boundaries (dark lines). Fig. 1d is the SEM image of the inverse photonic crystal, obtained by the chemical method. The average diameter of the hollow sphere is 277 nm which is nearly equal to the diameter of the original PMMA spheres. Well-connected ZnO net is observed throughout the domain and the underlying layer of the crystal is also

The wavelength of maximum reflection (λ) of the photonic crystal is related to the other crystal parameters and the geometry through the modified Bragg's law $\lambda = 2d_{hkl} \sqrt{n_{eff}^2 - \sin^2 \theta}$, where $d_{hkl} = \frac{\sqrt{2}}{\sqrt{3}} d$ for (111) plane in fcc arrangement, d is the diameter of the colloidal spheres and $n_{eff} = \sqrt{n_1^2 f_1 + n_2^2 f_2}$ where n_1 and n_2 are the refractive indices and f_1 and f_2 are the packing fractions of the constituent materials, in the crystal and θ is the angle of incident light. For PMMA photonic crystal, n_{eff} is 1.37. The value of λ calculated from Bragg's law for 8° is 642 nm, which differs from the experimental value, perhaps due to the poly-dispersity in the colloidal sphere diameter and the disordered packing in some areas.

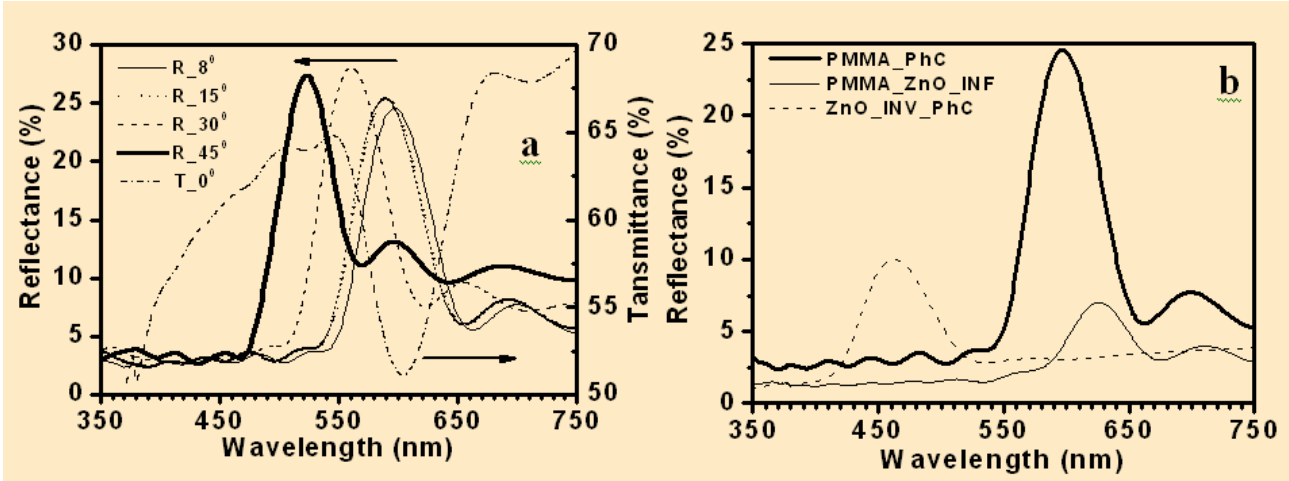


Fig. 2a: Transmittance (dash-dotted line) and reflectance of PMMA photonic crystal for incident angles of 8° (thin line), 15° (dotted line), 30° (dashed line) and 45° (thick line) 2b: Reflection spectra at 8° from PMMA photonic crystal (thick line), ZnO infiltrated PMMA photonic crystal (thin line) and ZnO inverse photonic crystal (dashed line).

When the angle of incident light increases, the reflection spectrum shifts towards the lower wavelength range as shown by an arrow pointing to the left in Fig.-2a. The full width at half maximum of the reflection spectra for different angles is nearly constant at 67 nm, which represents good quality of the crystal. Fabry-Perot oscillations are observed on both sides of the reflection maximum. The peak in reflection at near-normal incidence, matches with the dip in transmission. When the PMMA photonic crystal is infiltrated with ZnO, the effective index of the composite crystal is calculated to be 1.63, assuming 100% infiltration

of the voids. The infiltrated crystal has a maximum reflectance (at 8°) of 7% at 625 nm, as shown in Fig. 2b, which implies a shift of 28 nm after infiltration. For comparison, the reflection spectrum of PMMA photonic crystal for the same angle is shown by a thick line in the same figure. The reflection maximum in the case of infiltrated sample is reduced perhaps, due to a layer of ZnO formed on the top of the crystal, after the third infiltration. The dashed curve in Fig. 2b gives a maximum reflectance of 10% at 462nm, for the ZnO inverse photonic crystal. The shift in the reflection maximum to the lower

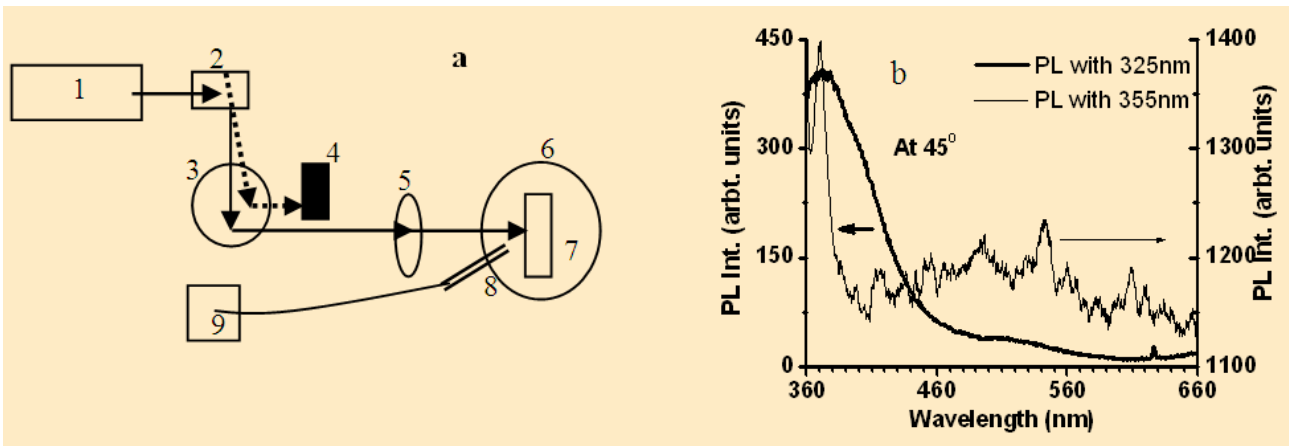


Fig. 3a: Schematic diagram of experimental set-up used for laser induced emission studies. 1-Nd:YAG laser with harmonic generators, 2- Pellin-Broca prism (dotted line is 532 nm and solid line is 355 nm), 3-mirror, 4-beam dump, 5-focusing lens, 6-rotating stage, 7-sample, 8-detector and 9- data acquisition system. 3b: thin line and thick lines are the emission spectra of ZnO inverse photonic crystal when excited at 355nm and 325nm respectively.

Merit Award



wavelength range, is due to the lower effective index of 1.33 for the inverse crystal.

For laser induced emission studies (schematic shown in Fig. 3a), the ZnO inverse crystal is excited with the third harmonic of Nd:YAG laser at 355nm, with a pulse energy of ~ 0.34 mJ and an average pulse duration of 6ns. The emission is collected at 45° since the stop band effect is expected between 340 nm to 440 nm at this angle. The emission spectrum of ZnO inverse crystal (thin line in Fig. 3b) shows a strong UV peak with a weak visible emission. The UV peak is due to the band-to-band transition of ZnO and the visible emission is from the presence of deep level defects due to oxygen vacancies and interstitial ZnO ions [8, 12]. On the other hand, when excited by He-Cd laser at 325nm, the emission recorded at 45° (thick line in Fig. 3b) has a broad UV peak but visible emission was feeble. Additionally, the larger excitation pump power at 355nm is leading to the narrowing of the spectral line. This has to be confirmed with emission studies at much lower excitation powers. In [8], the ZnO inverse crystal prepared by chemical method showed a large UV peak with a broad visible emission under excitation at 325nm. In another work [6], ZnO inverse crystal prepared by heat treatment showed only the UV peak. In [9], spontaneous emission followed by lasing at the PBG position was obtained for the ZnO inverse crystal when excited at 355nm with 20ps pulses. In the present work, even though the ZnO infiltrated into the PMMA photonic crystal has been obtained by the inexpensive sol-gel route, good quality inverse photonic crystal as well as photonic stop band effect in emission are clearly obtained.

The authors acknowledge the Board of Research in Nuclear Sciences, DAE for financial support.

References

1. S V Gaponenko, V N Bogomolov, E P Petrov, A M Kapitonov, A A Eychmueller, A L Rogach, I I Kalosha, F Gindele and U Woggon, *Journal of Luminescence*, 87-89, 152 (2000).
2. S V Frolov, Z V Vardeny, A A Zakhidov and R H Baughman, *Optics Communication*, 162, 241 (1999).
3. S V Gaponenko, V N Bogomolov, E P Petrov, A M Kapitonov, D A Yarotsky, I I Kalosha, A A Eychmueller, A L Rogach, J McGilp, U Woggon and F Gindele, *J. Lightwave Technology*, 17, 2128 (1999).
4. Q Yan, Z Zhou and X S Zhao, *Langmuir*, 21, 3158 (2005).
5. G A Emelchenko, A N Gruzintsev, V V Masalov, E N Samarov, A V Bazhenov and E E Yakimov, *J. Opt. A: Pure Appl. Opt.*, 7, 213 (2005).
6. M Scharrer, X Wu, A Yamilov, H Cao and R H Chang, *Appl. Phys. Lett.*, 86, 151113 (2005).
7. R V Nair and R Vijaya, *J. Phys. D: Appl. Phys.*, 40, 990 (2007).
8. Y Yang, H Yan, Z Fu, B Yang, J Zuo and S Fu, *Solid State Communications*, 139, 218 (2006).
9. M Scharrer, A Yamilov, X Wu, H Cao and R P H Chang, *Appl. Phys. Lett.*, 88, 201103 (2006).
10. K H Yeo, L K Teh and C C Wong, *Journal of Crystal Growth*, 287, 180 (2006).
11. R V Nair and R Vijaya, *Appl. Phys. A*, 90, 559 (2008).
12. K H Yeo, L K Teh and C C Wong, *Journal of Crystal Growth*, 287, 180 (2006).